NASA
Technical
Paper
2712

July 1987

Multiaxis Control Power From Thrust Vectoring for a Supersonic Fighter Aircraft Model at Mach 0.20 to 2.47

Francis J. Capone
and E. Ann Bare

NASA

NASA Technical Paper 2712

1987

Multiaxis Control Power From Thrust Vectoring for a Supersonic Fighter Aircraft Model at Mach 0.20 to 2.47

Francis J. Capone
and E. Ann Bare

Langley Research Center
Hampton, Virginia

National Aeronautics
and Space Administration

Scientific and Technical Information Office

Summary

The aeropropulsive characteristics of an advanced twin-engine fighter aircraft designed for supersonic cruise have been studied in the Langley 16-Foot Transonic Tunnel and the Lewis 10- by 10-Foot Supersonic Tunnel. The objective of this investigation was to determine multiaxis control-power characteristics obtainable from thrust vectoring. A two-dimensional convergent-divergent nozzle was designed to provide geometric yaw vector angles of 0°, −10°, and −20° combined with geometric pitch vector angles of 0° and 15°. Yaw thrust vectoring was provided by yaw flaps located in the nozzle sidewalls. Roll control was obtained from differential pitch vectoring. This investigation was conducted at Mach numbers from 0.20 to 2.47. Angle of attack was varied from 0° to about 19°, and nozzle pressure ratio was varied from about 1 (jet off) to 28, depending on Mach number.

The results of this investigation indicate that the nozzle resultant pitch vector angle was greater than the geometric pitch vector angle once nozzle pressure ratio was high enough to eliminate separation on the lower expansion ramp of the nozzle. The nozzle resultant yaw vector angle was less than the geometric yaw vector angle at all test conditions. This loss in yaw vector effectiveness was attributed to the small size of the yaw flaps relative to the total sidewall area of the nozzle. There was no effect of pitch vectoring on resultant yaw vector angle for simultaneous pitch-yaw vectoring. However, at low nozzle pressure ratios, yaw vectoring decreased resultant pitch vector angle for 0° pitch vectoring and increased resultant pitch angle for 15° pitch vectoring.

The effect of nozzle pressure ratio and pitch vectoring on the longitudinal aerodynamic characteristics followed expected trends as both lift and pitching moment increased with increased nozzle pressure ratio and/or geometric pitch vector angle. Similar effects to lateral aerodynamic characteristics resulted from yaw vectoring. Both the jet-off and powered increments in the force or moment coefficients that result from pitch or yaw vectoring remained essentially constant over the entire angle-of-attack range tested at all Mach numbers. There was no effect of pitch vectoring on the lateral aerodynamic forces and moments and only very small effects of yaw vectoring on the longitudinal aerodynamic forces and moments. This result indicates little cross-coupling of control forces and moments for combined pitch-yaw vectoring.

Longitudinal and directional control power was a function of nozzle pressure ratio and Mach number. Powered controls were very effective at low Mach numbers, and their effectiveness decreased as Mach number increased as a result of a reduction in available thrust coefficient. Longitudinal and directional control power from thrust vectoring was greater than that provided by aerodynamic control effectors for this and other configurations at Mach numbers up to 0.40. At Mach numbers from 0.40 to 1.20, control power was less; at Mach numbers from 2.00 to 2.47, control power from thrust vectoring was comparable with that provided by aerodynamic controls.

Introduction

The mission requirements for the next generation of fighter aircraft may dictate a highly versatile vehicle capable of operating over a wide range of flight conditions. This aircraft may be required to have short take-off and landing characteristics, in order to operate from bomb-damaged airfields, required to cruise supersonically, and required to have greater transonic and supersonic maneuverability at higher operational angles of attack than current fighters. (See refs. 1 to 4.) Several studies have shown that significant advantages in air combat are gained with the ability to perform transient maneuvers at high angles of attack including brief excursions into post-stall conditions. (See refs. 4 to 6.) However, the angle-of-attack envelope of an advanced fighter can be limited because of degraded stability characteristics and inadequate aerodynamic control power at high angles of attack. Also, the effectiveness of aerodynamic controls can be reduced by cross-axis coupling of the control moments, which then complicates the design of the flight control system.

One promising method of providing large control moments that are not dependent upon angle of attack and dynamic pressure (as are aerodynamic controls) is vectoring of the engine exhaust. Studies have shown that the control power provided from 10° to 15° of combined pitch-yaw vectoring can significantly enhance aircraft agility up to and including stall angle-of-attack range. (See refs. 4 and 7 to 10.) Also, thrust vectoring provides control moments that are essentially uncoupled from airframe aerodynamics. Use of powered controls affords the aircraft designer the opportunity to reduce the size of or to eliminate tails and control surfaces, which reduces aircraft drag and weight. Because aerodynamic control surfaces are usually sized for low-speed operation, they generally provide more control power than is required at high speed.

An extensive research program at the Langley Research Center has shown that pitch thrust vectoring can be provided from multifunction (nonaxisymmetric) nozzles. (See, e.g., refs. 11 to 14.) Recent efforts have been aimed at evaluating several yaw vectoring concepts at static (wind-off) conditions (refs. 14 and

15) and at forward flight conditions (ref. 16). Multifunction nozzles are also designed to provide thrust-reversing capability which can be used not only for STOL operation (ref. 3), but also to provide superior deceleration and closure-rate control for enhanced maneuverability and agility (refs. 6 and 7).

This paper presents results from a wind-tunnel investigation of a tactical fighter model designed for supersonic cruise. This model simulated a Mach 2.00, 49 000-lb vehicle with a close-coupled canard and underwing propulsion units that featured multifunction, two-dimensional exhaust nozzles originally designed with only pitch thrust vectoring capability. The objective of this investigation was to determine multiaxis control-power characteristics obtainable from thrust vectoring. Modifications were made to a two-dimensional convergent-divergent nozzle to provide geometric yaw vector angles of 0°, −10°, and −20° combined with geometric pitch vector angles of 0° and 15°. Yaw thrust vectoring was provided by yaw flaps located in the nozzle sidewalls. Roll control was obtained from differential pitch vectoring. This investigation was conducted in the Langley 16-Foot Transonic Tunnel and the Lewis 10- by 10-Foot Supersonic Tunnel at Mach numbers from 0.20 to 2.47. Angle of attack was varied from 0° to about 19°, and nozzle pressure ratio was varied from about 1 (jet off) to 28, depending on Mach number. A summary of these results is presented in reference 16. The aeropropulsive and flow-field characteristics of this configuration with various nonaxisymmetric nozzle designs are presented in references 13 and 17 to 20.

Symbols

All model longitudinal forces and moments are referred to the stability-axis system, and all lateral forces and moments are referred to the body-axis system. The model moment reference is located at fuselage station 69.81 in., which corresponds to $0.28\bar{c}$. A detailed discussion of the data-reduction and calibration procedures, as well as definitions of forces, angles, and propulsion relationships used herein, can be found in references 21 and 22.

A_t nozzle throat area, in^2

b wing span, 37.80 in.

C_D drag coefficient, $C_D \equiv C_{(D-F)}$ at NPR = 1.0 (jet off)

$C_{(D-F)}$ drag-minus-thrust coefficient, $\frac{\text{Drag - Thrust}}{q_\infty S}$

$C_{F,j}$ thrust coefficient along stability axis, $\frac{\text{Thrust}}{p_a S}$

C_L aerodynamic (thrust component removed) lift coefficient, $C_L \equiv C_{L,t}$ at NPR = 1.0 (jet off)

$C_{L,j}$ jet-lift coefficient, $\frac{\text{Jet lift}}{p_a S}$

$C_{L,t}$ total lift coefficient including thrust component, $\frac{\text{Lift}}{q_\infty S}$

C_{L_δ} lift effectiveness, per degree

$C_{L_{\delta_v}}$ lift effectiveness due to pitch vectoring, per degree

C_l aerodynamic (thrust component removed) rolling-moment coefficient, $C_l \equiv C_{l,t}$ at NPR = 1.0 (jet off)

$C_{l,j}$ jet rolling-moment coefficient, $\frac{\text{Jet rolling moment}}{p_a S b}$

$C_{l,t}$ total rolling-moment coefficient including thrust component, $\frac{\text{Rolling moment}}{q_\infty S b}$

C_{l_δ} lateral control power, per degree

$C_{l_{\delta_v}}$ lateral control power due to differential pitch vectoring, per degree

C_m aerodynamic (thrust component removed) pitching-moment coefficient, $C_m \equiv C_{m,t}$ at NPR = 1.0 (jet off)

$C_{m,j}$ jet pitching-moment coefficient, $\frac{\text{Jet pitching moment}}{p_a S \bar{c}}$

$C_{m,t}$ total pitching-moment coefficient including thrust component, $\frac{\text{Pitching moment}}{q_\infty S \bar{c}}$

C_{m_δ} longitudinal control power, per degree

$C_{m_{\delta_v}}$ longitudinal control power due to pitch vectoring, per degree

C_n aerodynamic (thrust component removed) yawing-moment coefficient, $C_n \equiv C_{n,t}$ at NPR = 1.0 (jet off)

$C_{n,j}$ jet yawing-moment coefficient, $\frac{\text{Jet yawing moment}}{p_a S b}$

$C_{n,t}$ total yawing-moment coefficient including thrust component, $\frac{\text{Yawing moment}}{q_\infty S b}$

C_{n_δ} directional control power, per degree

$C_{n_{\delta_v}}$	directional control power due to yaw vectoring, per degree
C_Y	aerodynamic (thrust component removed) side-force coefficient, $C_Y \equiv C_{Y,t}$ at NPR = 1.0 (jet off)
$C_{Y,j}$	jet side-force coefficient, $\frac{\text{Jet side force}}{p_a S}$
$C_{Y,t}$	total side-force coefficient including thrust component, $\frac{\text{Side force}}{q_\infty S}$
C_{Y_δ}	side-force effectiveness, per degree
$C_{Y_{\delta_v}}$	side-force effectiveness due to yaw vectoring, per degree
$\bar{c}$	wing mean geometric chord, 31.67 in.
F_i	ideal isentropic gross thrust, $w_p\sqrt{\frac{RT_{t,j}}{g^2}\left(\frac{2\gamma}{\gamma-1}\right)\left[1-\left(\frac{p_a}{p_{t,j}}\right)^{(\gamma-1)/\gamma}\right]}$, lbf
F_j	measured thrust along body axis, lb
F_N	measured jet normal force, lbf
F_r	resultant gross thrust, $\sqrt{F_j^2+F_N^2+F_S^2}$, lbf
F_S	measured jet side force, lb
g	gravitational constant, 32.174 ft/sec^2
ℓ_j	distance from c.g. to nozzle throat, in.
ℓ_t	distance from c.g. to quarter chord of horizontal- or vertical-tail mean geometric chord, in.
M	free-stream Mach number
NPR	nozzle pressure ratio, $p_{t,j}/p_\infty$ or $p_{t,j}/p_a$
p_a	ambient pressure, psi
$p_{t,j}$	average jet total pressure, psi
p_∞	free-stream static pressure, psi
q_∞	free-stream dynamic pressure, psi
R	gas constant, 1716 ft^2/sec^2-°R
S	wing reference area, 936.68 in^2
S_t	horizontal- or vertical-tail area, in^2
$T_{t,j}$	average jet total temperature, °R
$\bar{V}$	powered- or tail-volume coefficient
w_i	ideal weight-flow rate, lbf/sec
w_p	measured weight-flow rate, lbf/sec
x, y	nozzle coordinates with origin at FS 89.92 and WL 9.26 (fig. 7(c)), in.
α	angle of attack, deg
β	nozzle boattail angle, deg
δ_c	canard incidence angle, positive for leading edge up, deg
δ_p	resultant pitch vector angle, $\tan^{-1}\frac{F_N}{F_j}$, deg
δ_{te}	trailing-edge flap deflection, positive trailing edge down, deg
$\delta_{v,p}$	geometric pitch vector angle measured from nozzle centerline, positive for downward deflection angles (fig. 7(c)), deg
$\delta_{v,y}$	geometric yaw vector angle, positive to left looking upstream, (fig. 7(b)), deg
δ_y	resultant yaw vector angle, $\tan^{-1}\frac{F_S}{F_j}$, deg
γ	ratio of specific heats, 1.3997 for air

Abbreviations:

C-D	convergent-divergent
c.g.	center of gravity
FS	fuselage station
NRP	nozzle reference plane
STOL	short-field take-off and landing
2-D	two-dimensional
WBL	wing butt line, in.
WL	water line, in.
16 FTT	Langley 16-Foot Transonic Tunnel
10 × 10 T	Lewis 10- by 10-Foot Supersonic Tunnel

Model

This investigation was conducted with a 10.5-percent scale model of a twin-engine fighter aircraft designed to cruise at supersonic speeds. A sketch showing the general arrangement of the model and support system is presented in figure 1. A photograph of the model is shown in figure 2. The model featured a cambered and twisted wing and canard and had two single-engine podded nacelles mounted under the wing.

Wing-Canard-Fuselage Design

The configuration was designed for self-trimming ($\delta_c = \delta_{te} = 0°$) at a cruise speed of Mach 2 and a design lift coefficient of 0.10. The trim condition for the vehicle was established from the criterion that the vehicle be 5 percent unstable subsonically, which resulted in the vehicle being 4 percent stable for the supersonic design case.

The aerodynamic design of the lifting surfaces was accomplished by use of the FLEXSTAB code (ref. 23). This code uses the aerodynamic influence coefficient method and includes the effects of nonplanar surfaces such as a canard above the wing plane. The method is based on a linearized potential-flow theory with constant-pressure panels. The twist and the camber of both the canard and the wing surfaces are determined simultaneously such that the induced drag is minimized. Figure 3 illustrates the modeling of the vehicle for the FLEXSTAB code and the resulting wing and canard design.

The planform geometry of the wing is shown in figure 4. The wing had a leading-edge sweep of 68°, an aspect ratio of 1.53, a reference area of 936.68 in^2, and a wing mean geometric chord of 31.68 in. A wing trailing-edge flap, also shown in figure 4, was tested at deflection angles of 0° and 7°. The planform geometry of the canard is shown in figure 5. The canard incidence angle was remotely controlled about the canard hinge axis located at FS 46.18. The canard also had 10° dihedral (fig. 5).

Nacelle-Nozzle Installation

The nacelle with the 2-D C-D nozzle, shown in figure 6, was located under the wing in an inboard position. This is the baseline nacelle position of reference 13. The nacelle, which was toed-in 2°, had a faired-over inlet. The effects of the faired-over inlet on the longitudinal aerodynamic characteristics of this configuration are given in reference 18.

The 2-D C-D nozzle full-scale design allows independent actuation of the throat-area control flaps and the divergent flaps. The nozzle area ratio can therefore be set, within mechanical limits, independently from the nozzle throat area for good internal performance over a wide variety of flight conditions. The length of the divergent flaps was selected to provide good internal nozzle performance at the supersonic design point. To reduce nozzle weight and cooling flow, the full-scale design incorporated sidewalls which were cut back to 56 percent of full length (full-length sidewalls contain exhaust flow completely from nozzle throat to nozzle exit). For pitch thrust vectoring, the upper and lower divergent flaps are differentially deflected (one toward nozzle centerline and the other away from nozzle centerline). The full-scale nozzle design did not have provisions for yaw thrust vectoring.

The 2-D C-D nozzle model geometry is presented in figure 7. This nozzle had a throat area of 4.90 in^2, a duct aspect ratio of 1.0, an expansion ratio of 1.50, and a design nozzle pressure ratio of 6.24. The nozzle was tested in a subsonic afterburner power setting at all Mach numbers. Geometric pitch thrust vector angles of 0° and 15° (fig. 7(a)) were tested during the current investigation. References 13 and 17 present results of thrust vectoring at $\delta_{v,p} = 30°$.

The nozzle sidewalls on the model were modified so that yaw thrust vectoring flaps could be installed as shown in figure 7(b). This scheme is similar to the downstream-flap yaw vectoring concept of reference 15, in which the flaps were installed in the nozzle sidewalls downstream of the nozzle throat. When both flaps are deployed, one flap deflects into the nozzle internal flow, and the other flap deflects away from the exhaust flow. There should be little or no degradation of the total vectoring effectiveness of each nozzle as a result of interaction of the vectored nozzle exhausts, because the nacelle-mounted nozzles are essentially isolated from each other. This may not be the case for closely spaced twin-engine configurations.

The sidewall yaw flaps were sized to operate such that there would be no interference with the upper and lower divergent flaps at pitch vector angles of 0° and 15°. The yaw flap is short enough so that its upper and lower sides remain within the envelope formed by the upper divergent flap at $\delta_{v,p} = 15°$ and the lower divergent flap at $\delta_{v,p} = 0°$. (See fig. 7(b).) The hinge line of the yaw vector flap was kept downstream of the nozzle throat to eliminate any thrust losses that could result from being located forward of the throat (ref. 15). The yaw vector flap of the current test was sized for an afterburning nozzle configuration. Therefore, yaw thrust vectoring with the current configuration could not be accomplished at dry-power settings because of the physical interference of the yaw vector flap with the nozzle divergent flaps.

Apparatus and Procedure

Wind Tunnels and Support System

This investigation was conducted in the Langley 16-Foot Transonic Tunnel (16 FTT) and the Lewis 10- by 10-Foot Supersonic Tunnel (10 × 10 T). The 16 FTT is a single-return, atmospheric tunnel with a slotted, octagonal test section and continuous air exchange. The wind tunnel has a variable airspeed up to a Mach number of 1.30. A complete description

of this facility and its operating characteristics can be found in reference 22.

The 10×10 T is a single-return, variable-pressure tunnel with a square test section. The contour of the nozzle sidewalls is remotely adjustable and can provide a Mach number range from 2.00 to 3.50. A description of this facility can be found in reference 24.

The model was supported in both wind tunnels by the same sting-strut (fig. 1) support system in which the strut replaced the vertical tail. The strut had an NACA 0006 airfoil section with a sweep of 60° and a maximum thickness of 1.75 in.

Propulsion Simulation System and Instrumentation

External high-pressure air systems at each facility provided a continuous source of clean, dry air at a controlled temperature of about 70°F at the nozzles. The air was brought to a plenum mounted within the wind-tunnel support system ahead of the sting and was divided into two separate flows. The air was then routed through the sting-strut and forward through the fuselage from the bottom of the strut, as shown in figure 8. Three bellows were installed in each air line to provide a three-axis, flexible air-line bridge across the force balance and model. The air was then routed out through each wing to the respective nacelles and nozzles.

At the end of the round-to-rectangular transition section in the nacelle, a choke plate and two screens were installed to regulate and smooth the flow prior to entry into the nozzle instrumentation section. (See fig. 6.) The transition sections were made to interface with the flow supply pipe on the right and left ducts. Nine total-pressure probes, arranged in an equal-area-weighted, cruciform fashion, were used to determine average nozzle total pressure in each duct. The 18 total-pressure probes (left- and right-hand sides) were averaged to give overall nozzle total pressure. Two total-temperature probes in each duct measured stagnation temperature of the exhaust flow.

In the 10×10 T, mass flow through each nozzle was measured by individual critical-flow venturis located in the air lines prior to being routed through the sting-strut. These venturis were previously used during the investigations of references 13 and 19. In the 16 FTT, a single critical-flow venturi system (ref. 25) located outside the wind tunnel was used to measure total mass flow through the two nozzles. Discharge coefficient w_p/w_i was within 0.003 of that in reference 13.

Data Reduction

For each data point, multiple frames of data were averaged in each facility. Average values of the recorded data were used to compute standard force and moment coefficients based on wing area and mean geometric chord or span for reference area and length, respectively. A complete description of the data-reduction procedures for the 16 FTT is found in reference 21. Engineering-units data were transmitted by telephone from the Lewis complex to the Langley computer complex. Final reduction of the Lewis data was acccomplished at Langley with the Langley code (ref. 21).

Normal and axial forces of the balance were corrected for tare forces that resulted from pressurizing the air supply lines and bellows. These tare forces were determined with jets operating, using the 2-D C-D dry-power nozzle tested in reference 13. Also, the air supply system was capped off at the wings, and balance data were recorded as the lines were pressurized. From these calibration procedures, no corrections due to pressurization were found to be necessary for the other balance components.

The adjusted forces and moments measured by the balance were transferred to the body axis (WL 11.53), and the longitudinal forces and moments were transferred to the stability axis. Angle of attack α was obtained by applying deflection terms, caused by model support and balance bending under aerodynamic loads, and a flow angularity term to the angle of the model support system. A flow angularity adjustment of 0.1°, which is the average tunnel upflow angle measured in the Langley 16-Foot Transonic Tunnel, was applied. No flow angularity adjustments were made to the data from the Lewis 10- by 10-Foot Supersonic Tunnel.

Thrust-removed aerodynamic force and moment coefficients were obtained by determining the components of thrust for each of the three force terms and three moment terms and subtracting these values from the measured total (aerodynamic plus thrust) forces and moments. The thrust coefficients for the forces and moments at forward speeds were determined from measured static ($M = 0$) data and were a function of the free-stream static and dynamic pressure. Forces and moments were measured at static conditions by the force balance for each combination of pitch and yaw vector angle tested. Details of this procedure are contained in reference 21.

A comparison of static ($M = 0$) nozzle force and moment coefficients between the two wind tunnels is shown in figure 9. These results indicate excellent agreement between the data from the facilities.

To facilitate the analysis of control-power characteristics, a powered-volume coefficient similar to the usual tail-volume coefficient is defined. (See ref. 16.) The horizontal tail-volume coefficient is

$$\bar{V} = \frac{S_t}{S}\frac{\ell_t}{\bar{c}}$$

where S_t is the horizontal tail area and ℓ_t is the distance from the c.g. to the quarter chord of the tail. The pitch vectoring powered-volume coefficient is defined as

$$\bar{V} = \frac{2A_t}{S}\frac{\ell_j}{\bar{c}}$$

where A_t is nozzle throat area and ℓ_j is the distance from the c.g. to the nozzle throat. Throat area is multiplied by 2, because the configuration reported herein is twin engine. A yaw vectoring powered-volume coefficient is defined by replacing the mean geometric chord $\bar{c}$ with the span b.

Tests

Data were obtained in the 16 FTT at Mach numbers from 0.20 to 1.20 at angles of attack from 0° to about 19°. Reynolds number per foot varied from 3.0×10^6 to 4.1×10^6. Data were obtained in the 10 × 10 T at Mach numbers from 2.00 to 2.47 at angles of attack from 0° to about 19°. Reynolds number per foot varied from 1.4×10^6 to 1.8×10^6. Nozzle pressure ratio varied from 1 (jet off) to about 28, depending on Mach number. Basic data were obtained by varying nozzle pressure ratio at 4° angle of attack and by varying angle of attack at jet off and at a fixed (different value for each M) nozzle pressure ratio. The fixed nozzle pressure ratio tested at each Mach number represented a typical operating pressure ratio for a turbofan engine at that Mach number. A schedule of operating pressure ratio as a function of Mach number is presented in figure 10. Nozzle pitch vector angles of 0° and 15° were tested with yaw vector angles of 0°, −10°, and −20° in the 16 FTT. In the 10 × 10 T, nozzle pitch vector angles of 0° and 15° were tested with a yaw vector angle of 0°, and a nozzle pitch vector angle of 0° was tested with yaw vector angles of −10° and −20°. Differential pitch vector angles of 15° for the left nozzle and 0° for the right nozzle were tested with 0° yaw vectoring. The canard incidence was held at 0° for all tests.

All tests were conducted with 0.10-in-wide boundary-layer transition strips consisting of silicon carbide grit sparsely distributed in a thin film of lacquer. These strips were located 2.00 in. from the tip of the forebody nose and nacelle and on both the upper and lower surfaces of the wings and canard at 0.20 in. normal to the leading edges. Number 100 and number 60 silicon carbide grits were used in 16 FTT and 10 × 10 T, respectively.

Presentation of Results

Comparison and summary plots of the results from this investigation are presented in figures 11 to 34, which are organized as follows:

Thrust-removed aerodynamic characteristics derived from the measured total aerodynamic characteristics are presented in appendix A as figures 35 to 55. The effect of wing trailing-edge flap deflection on the longitudinal aerodynamic characteristics at $M = 2.00$ to 2.47 is presented in appendix B as figure 56. Trailing-edge flap effects at $M = 0.60$ to 1.20 are given in reference 17.

Results and Discussion

Static Performance

Pitch thrust vectoring. The effects of pitch vectoring on resultant thrust vector angles and nozzle performance parameters for the nozzles with geometric pitch vector angles of 0° and 15° are presented in figure 11. For the $\delta_{v,p} = 0°$ nozzle, values of the resultant pitch angle of approximately −4.5° result because the thrust axis was inclined downward −4.77°. This indicates that the gross thrust vector for this nozzle is aligned with the thrust axis. The variation of resultant pitch vector angle with nozzle pressure ratio for $\delta_{v,p} = 15°$ follows expected trends (refs. 26 and 27). The increase in δ_p as NPR increases is typically due to a reduction in flow separation over the lower flap of the nozzle. Maximum measured turning occurred at NPR = 5.0 and, for this type nozzle, usually occurs at or just below design nozzle pressure ratio, where the nozzle flow is fully expanded. Since peak thrust performance also occurs between NPR = 5.0 and NPR = 5.5 (fig. 11(b)), these results indicate that the nozzle is operating at an effective expansion ratio of 1.34 to 1.40 rather than at the geometric expansion ratio of 1.50 (design NPR = 6.24). This reduction in effective expansion ratio is caused by the cutback sidewalls of the nozzles (ref. 28).

The $\delta_{v,p} = 15°$ nozzle produced more than 15° of turning at NPR > 3.3 (Maximum $\delta_p = 12.7° - (-4.5°) = 17.2°$). This excess turning results from a large pressure gradient between the upper and lower divergence flaps of the nozzle, which causes a positive normal force. This pressure gradient, because of the large turning angle near the nozzle throat, causes an overexpansion of the flow which does not fully recompress on the lower divergent flap (refs. 26 and 27).

Resultant thrust ratio F_r/F_i, internal thrust ratio F_j/F_i, and discharge coefficient w_p/w_i are shown in figure 11(b) for the pitch vectored nozzle at static conditions. As can be seen, discharge coefficient measured in the 10×10 T was about 1 percent lower than that measured in the 16 FTT. As previously noted, excellent agreement was found for w_p/w_i measured in the 16 FTT between the current test (using a single venturi system) and that conducted for reference 13 (using two venturis). The same two venturis used in reference 13 were also used in a previous investigation in the 10 × 10 T (ref. 19), and the agreement between these two tests was also good. The reason for the difference in w_p/w_i shown in figure 11(b) for the current two investigations is not known. Since ideal isentropic gross thrust F_i is directly proportional to w_p, the absolute levels of the thrust ratios presented in figure 11(b) for the 10 × 10 T may be as much as 1 percent in error. However, it is believed that data measurements between the nozzle configurations are valid and provide correct data trends between the two facilities.

Yaw thrust vetoring. The effects of yaw vectoring on resultant thrust vector angles and nozzle performance parameters for the nozzles with 0° and 15° pitch vectoring are presented in figures 12 and 13, respectively. Resultant thrust vector angles are summarized in figure 14. Since the concept of using two sidewall flaps to direct the nozzle internal flow for yaw thrust vectoring is similar to typical 2-D C-D pitch thrust vectoring, the resultant yaw vector characteristics are also similar to pitch vector characteristics. As seen in figure 12(a), resultant yaw vector angle for $\delta_{v,y} = -10°$ increases (becomes more negative) as nozzle pressure ratio increases. Yaw vector peak thrust ratio performance (fig. 12(b)) also occurs at NPR between 5.0 and 6.0, which is similar to pitch thrust vectoring results (fig. 11(b)). For a significantly overexpanded nozzle (NPR << Effective design NPR of approximately 5.0 to 6.0), internal flow tends not to expand out over the yaw vector flaps. At higher NPR, the internal flow fully expands over the yaw flaps and is essentially invariant with nozzle pressure ratio for underexpanded nozzle conditions. It is expected that the resultant yaw vector angle for the other nozzle configurations would exhibit similar characteristics if they were tested to higher pressure ratios.

The measured resultant yaw vector angle was smaller than the geometric yaw vector angle for all test conditions (figs. 12(a) and 13). The reduced effectiveness is mainly attributed to the small size of the yaw vector flaps relative to the total sidewall area. The flaps were designed to operate between pitch vector angles of 0° and 15° and thus utilized only a portion of the total available sidewall area. For example, the flaps would have been about 23 percent larger if they were only required to operate at $\delta_{v,p} = 0°$. Because the yaw vector flaps do not cover the entire sidewall area, a portion of the internal exhaust flow can bypass the yaw flaps and not be turned. Similar results were obtained in reference 15. Also, some loss in yaw flap effectiveness is caused by the cutback sidewalls (fig. 7), which reduced the length of the flaps from that possible with the full sidewalls. This smaller flap probably reduces the turning capability of the left flap, which was turned into the exhaust flow.

Resultant thrust vector angles in the presence of both pitch and yaw vectoring are summarized in figure 14. Resultant yaw vector angle varies nearly

linearly with geometric yaw vector angle (fig. 14(a)). There was little or no effect of simultaneous pitch thrust vectoring on resultant yaw vector angle at NPR up to 3.0. It is expected that this would also be true at NPR > 3.0. This result suggests that there would be no coupling of lateral control moments with longitudinal control moments, which is important since control of an aircraft would require combined pitch-yaw vectoring.

The effect of yaw thrust vectoring on resultant pitch vector angle is shown in figure 14(b). At nozzle pressure ratios less than 3.5, resultant pitch vector angle δ_p decreased (became more negative) with increasing amounts of negative yaw flap deflection when $\delta_{v,p} = 0°$. However, for $\delta_{v,p} = 15°$, δ_p increased with increasing yaw flap deflection. This was especially true at NPR = 2.0, where δ_p nearly doubled as yaw flap deflection increased from 0° to −10°. For this case, the jet-lift component nearly doubled for $\delta_{v,p} = 15°$, and the axial component of thrust increased 3.4 percent compared with values at $\delta_{v,p} = 0°$ (these results are not shown). As previously noted, these results may indicate a reduction in the flow separation over the lower nozzle divergent flap.

Differential pitch thrust vectoring. The effects of differential pitch thrust vectoring on resultant thrust vector angles and nozzle performance parameters are presented in figure 15. Differential pitch thrust vectoring was employed to produce roll-control moments. In an actual airplane application, equal values of $\delta_{v,p}$ but of opposite sign would probably be used to provide these moments. In this application, there should be no effect of differential pitch thrust vectoring on either resultant pitch or yaw vector angles. However, since only $\delta_{v,p} = 0°$ and 15° nozzles were built, it was not possible with the current model hardware to test such a configuration. Consequently, the combination of $\delta_{v,p} = 15°$ for the left nozzle and $\delta_{v,p} = 0°$ for the right nozzle was tested; this hardware combination should produce pitch vectoring characteristics similar to a configuration having $\delta_{v,p} = 7.5°$ for both nozzles. Also, a small positive resultant yaw vector angle is induced because the model nozzle horizontal axis is rolled 6.5° with respect to the model (fig. 6).

Resultant pitch vector angle resulting from differential pitch thrust vectoring (fig. 15(a)) has the same characteristics as described previously for 15° of symmetrical pitch thrust vectoring. For NPR > 3.5, the differential pitch thrust vectored configuration produced over a 7.5° increase in δ_p from the unvectored configuration (fig. 15(a)). Thus, there is an overturning of the flow as was previously noted for 15° of pitch thrust vectoring. The resultant thrust ratio was higher from differential pitch vectoring than for 0° of pitch vectoring. Although the reason for this difference in performance is not known, similar characteristics of resultant thrust ratio were obtained during the investigation of reference 13 for $\delta_{v,p} = 15°$; that is, thrust ratio was higher for $\delta_{v,p} = 15°$ than for $\delta_{v,p} = 0°$. Also, a repeat static run for the $\delta_{v,p} = 15°$ nozzle made during the investigation of reference 13 produced resultant thrust ratio nearly equal to that shown in figure 11(b). These results suggest the possibility of flow separation and reattachment in the $\delta_{v,p} = 15°$ nozzle that may vary with nozzle pressure ratio.

Effects of Thrust Vectoring at Forward Speeds

Pitch thrust vectoring. The effects of pitch thrust vectoring on the total longitudinal aerodynamic characteristics are presented in figures 16 and 17 and are summarized in figure 18. Two types of basic data presentations are made to illustrate the effects of nozzle pressure ratio and angle of attack. First, the total longitudinal aerodynamic characteristics are shown in figure 16 as a function of nozzle pressure ratio at $\alpha = 4°$, which is a typical cruise angle of attack for this aircraft configuration. Second, the variation of the total aerodynamic characteristics with angle of attack (or total lift coefficient) is presented in figure 17 at jet-off conditions (NPR = 1) and at the scheduled nozzle pressure ratio for each Mach number tested (see fig. 10). At jet-off conditions (NPR = 1), aerodynamic and total performance parameters are identical (e.g., $C_L = C_{L,t}$).

The effects of nozzle pressure ratio on the total longitudinal aerodynamic characteristics at $\alpha = 4°$ (fig. 16) followed expected trends. At $\delta_{v,p} = 0°$, there was little or no effect of nozzle pressure ratio on total lift coefficient $C_{L,t}$ except at $M = 0.20$. The increment in $C_{L,t}$ between $\delta_{v,p} = 0°$ and 15° at jet-off conditions (NPR = 1) is a result of the aerodynamic flap effect from the deflected nozzle flaps at $\delta_{v,p} = 15°$ (see fig. 7). As nozzle pressure ratio increases for the $\delta_{v,p} = 15°$ configuration, $C_{L,t}$ also increases. The increase in $C_{L,t}$ is caused primarily by the jet-lift component of the nozzle gross thrust and some jet-induced supercirculation lift.

Jet-induced supercirculation lift, which for this configuration is quite small, can be seen from the thrust-removed aerodynamic characteristics presented in appendix A. (See, e.g., fig. 35.) Supercirculation lift is small because of the longitudinal location of the nozzle exits with respect to the wing and because of the underwing position of the nozzles. A more detailed discussion of the thrust-induced effects for this configuration is contained in reference 13.

The variation of pitching-moment coefficient with nozzle pressure ratio for the two nozzles tested is determined by the location of the nozzle gross thrust vector for the respective nozzle. The nozzle gross thrust vector at $\delta_{v,p} = 0°$ induces a nose-up pitching moment, because the thrust axis is located below the moment reference center (see fig. 6). For $\delta_{v,p} > 5°$, the gross thrust axis lies above the moment reference center; consequently, nose-down pitching moments occur as indicated by the $\delta_{v,p} = 15°$ data.

Drag-minus-thrust coefficient varies nearly linearly with nozzle pressure ratio regardless of pitch thrust vector angle. The differences between $C_{(D-F)}$ for $\delta_{v,p} = 0°$ and 15° result from thrust losses caused by turning the exhaust vector away from the axial direction and from generally higher drag on the $\delta_{v,p} = 15°$ configuration (see fig. 35). Increasing the magnitude of negative numbers for $C_{(D-F)}$ indicates improved performance from either higher thrust or lower drag.

The effects of angle of attack on the total longitudinal aerodynamic characteristics are presented in figure 17. The increment in lift or pitching-moment coefficient that results from changing nozzle pitch vector angle from 0° to 15°, at either jet-off or jet-on conditions, remains essentially constant over the entire angle-of-attack range for all Mach numbers tested. Thus, there is also no effect of pitch thrust vectoring on lift-curve slope and longitudinal stability characteristics. Reference 18 contains a complete discussion of the unpowered lift-curve slope and longitudinal stability characteristics.

The variation of total lift and pitching-moment coefficients with pitch vector angle is summarized in figure 18 for $\alpha = 0°$ and 14°. The results from reference 13 for $\delta_{v,p}$ up to 30° are also presented and show that both lift and pitching-moment coefficients vary nearly linearly with pitch thrust vector angle. Figure 18 also shows that the increment in both $C_{L,t}$ and $C_{m,t}$ between $\delta_{v,p} = 0°$ and 15° is essentially the same for $\alpha = 0°$ and 14°. The absolute levels of $C_{L,t}$ and $C_{m,t}$ are different because of the difference in angle of attack.

Yaw thrust vectoring. The effects of yaw thrust vectoring on the total aerodynamic characteristics of configurations with geometric pitch thrust vector angles of 0° and 15° are presented in figures 19 to 22. Lateral aerodynamic characteristics are summarized in figures 23 and 24. The basic data presentation is similar to that already described for pitch vectoring. The variations of the total aerodynamic characteristics with nozzle pressure ratio are nearly linear at each of the Mach numbers tested. A comparison of the lateral aerodynamic components ($C_{l,t}$, $C_{n,t}$, and $C_{Y,t}$) of figures 19 and 20 shows little or no difference between the data for 0° and 15° of pitch thrust vectoring. This indicates no coupling of the yaw thrust vectoring lateral control forces and moments with pitch thrust vectoring, which is important for the design of an airplane flight control system. The rolling-moment coefficients shown in figures 19 and 20 for configurations with yaw thrust vectoring result from a side-force component of the nozzle thrust which lies below the model moment reference center (see fig. 6).

Since the current yaw vectoring concept is similar to the pitch vectoring concept utilized, total side-force coefficient has similar characteristics to total lift coefficient. The increment in $C_{Y,t}$ between $\delta_{v,y} = 0°$ and $-10°$ or $-20°$ at jet-off conditions is the result of the aerodynamic flap effect of the deflected yaw flaps. At power-on conditions, this increment has a side-force thrust component and a jet-induced component. The jet-induced components shown in appendix A (fig. 39) can be as much as 30 percent of the total increment (e.g., at $M = 0.60$).

Yaw vectoring had little or no effect on lift or pitching-moment coefficient (except at $M = 0.20$) at $\delta_{v,p} = 0°$ (fig. 19). This was expected since yaw thrust vectoring had only a small effect on resultant pitch vector angle (fig. 12(a)). At $\delta_{v,p} = 15°$ (fig. 20), there were small increases in $C_{L,t}$ as $\delta_{v,y}$ varied from 0° to −20°. These variations result from the larger effects of geometric yaw vector angle $\delta_{v,y}$ on resultant pitch vector angle δ_p shown in figure 13 for $\delta_{v,p} = 15°$. The differences between $C_{(D-F)}$ for $\delta_{v,y} = 0°$ and for $-10°$ or $-20°$ result from turning the exhaust flow away from the axial direction and from differences in external nozzle drag (see figs. 36 and 37). Except at the higher values of NPR, yaw flap deflection generally increased drag. Some additional (unrealistic) drag may occur for the yaw vectored configurations, because the brackets used to attach the yaw flaps were exposed to external flow rather than being flush mounted (fig. 7(b)).

The effects of angle of attack on the total aerodynamic characteristics for $\delta_{v,p} = 0°$ and 15° are presented in figures 21 and 22, respectively. Both the jet-off and powered increments for either side-force, yawing-moment, or rolling-moment coefficients that result from changing yaw vector angle from 0° to $-10°$ or $-20°$ remain essentially constant over the entire angle-of-attack range for all Mach numbers tested. This result and the result obtained for pitch thrust vectoring confirm that the forces and moments from thrust vectoring are essentially constant over the angle-of-attack range tested. These results are in contrast to conventional aerodynamic

controls, which usually lose effectiveness as angle of attack is increased. Similar results from thrust vectoring at angle of attack for two different configurations are presented in reference 16.

The variations of the total lateral aerodynamic characteristics with geometric yaw vector angle at $\alpha = 0°$ and 14° for $\delta_{v,p} = 0°$ and 15° are summarized in figures 23 and 24, respectively. As with the pitch thrust vectoring results on longitudinal characteristics with varying geometric pitch vector angle, the variation of the lateral characteristics with geometric yaw vector angle is nearly linear. A comparison of figures 23 and 24 shows no effect of $\delta_{v,p}$ on the lateral aerodynamic characteristics with varying geometric yaw vector angle.

Differential pitch thrust vectoring. The effects of differential pitch thrust vectoring on the total aerodynamic characteristics are shown in figures 25 and 26, and the effects of differential pitch thrust vectoring on rolling-moment coefficient are summarized in figure 27. Differential pitch thrust vectoring was obtained by pitch thrust vectoring only the left nozzle at $\delta_{v,p} = 15°$. The rolling-moment coefficient that results from differential pitch vectoring has characteristics similar to those discussed previously for control moments generated by pitch and yaw thrust vectoring. As nozzle pressure ratio increases, rolling-moment coefficient increases nearly linearly (fig. 25), and both the jet-off and powered increments that result from differential pitch thrust vectoring are constant over the angle-of-attack range for all Mach numbers tested (figs. 26 and 27). The relative magnitude of the rolling-moment coefficient shown in figures 25 to 27 is similar to those estimated for 7.5° of symmetrical pitch thrust vectoring. The lift and pitching-moment coefficients and the side-force and yawing-moment coefficients that occur are a result of the combination of $\delta_{v,p} = 15°$ for the left nozzle and $\delta_{v,p} = 0°$ for the right nozzle. The lift and side-force increments are generated from the left nozzle only. In an actual airplane application, rolling moment would be generated by differential geometric pitch thrust vector angles of equal values but in opposite directions. For this case, it is probable that only increments of rolling-moment coefficient would result from differential pitch thrust vectoring if jet interaction and induced effects were negligible.

Powered Control-Power Parameters

An assessment of the multiaxis control-power characteristics from thrust vectoring is made from comparisons of the effectiveness of the various powered and aerodynamic control effectors available on this aircraft model and other configurations. The control-power parameters from thrust vectoring were evaluated at each nozzle pressure ratio at a constant angle of attack or at each angle of attack at a constant pressure ratio. As noted previously, angle of attack has little or no effect on the forces or moments generated by thrust deflection (powered controls).

The various powered control-power parameters that result from multiaxis thrust vectoring at $\alpha = 4°$ are presented in figures 28 to 30. These parameters at a constant Mach number are only a function of nozzle pressure ratio, because the aerodynamic coefficient increments that resulted from thrust vectoring were independent of angle of attack. The decrease in control power that occurs as Mach number increases is the result of a decrease in thrust coefficient (at constant NPR). The decrease in thrust coefficient is caused primarily by a decrease in thrust caused by the decrease in static pressure (as M increases) and, to a lesser extent, dynamic pressure effects. Longitudinal control power and lift effectiveness due to pitch thrust vectoring are presented in figure 28. The effects of nozzle pressure ratio on directional control-power, side-force, and rolling-moment effectiveness due to yaw thrust vectoring are shown in figure 29 for $\delta_{v,p} = 0°$ only. However, similar results were obtained for $\delta_{v,p} = 15°$. Lateral control power from differential pitch vectoring is given in figure 30.

Comparison of Powered and Aerodynamic Control Power

Longitudinal control. A comparison of longitudinal control power C_{m_δ} and lift effectiveness C_{L_δ} from powered and aerodynamic control effectors is presented in figure 31 as a function of Mach number at $\alpha = 0°$. Longitudinal control power from pitch thrust vectoring was obtained at the scheduled nozzle pressure ratio (fig. 10) for all Mach numbers. Longitudinal control power from pitch thrust vectoring on an F-18 aircraft model with 2-D C-D nozzles (ref. 12) is also shown in figure 31. Longitudinal control power generated by the canard (ref. 18) and wing trailing-edge flaps (ref. 17) of the current configuration as well as by aerodynamic control effectors on other fighter configurations (refs. 29 to 32) is also presented in figure 31. Negative values of canard control power have been presented to facilitate data comparisons. Figure 31 illustrates the dependence of control power on volume coefficient; at subsonic speeds, control power increases with increasing volume coefficient for both powered and aerodynamic controls.

The superiority of powered controls over either the canard (ref. 18) or trailing-edge flaps (ref. 17) for the current configuration at low speeds ($M < 0.40$) is

evident in figure 31. The low-speed values of control power from the aerodynamic controls were assumed to be those shown at $M = 0.60$. The decrease in value of the powered controls with increasing Mach number is caused by the decrease in thrust coefficient discussed previously. As can be seen, the effectiveness of the aerodynamic controls tends to increase slightly with increasing Mach number at subsonic speeds. Therefore, aerodynamic controls are usually sized for low speed and are therefore generally more effective than is required at high speeds. At Mach numbers from 2.00 to 2.47, powered controls provided nearly as much longitudinal control power as the canard or wing trailing-edge flaps. Pitch thrust vectoring also provided levels of longitudinal control comparable to aerodynamic controls at low speed. Thus thrust vectoring could be used to augment the control power provided by aerodynamic controls, particularly at low speeds. For an airplane design utilizing pitch thrust vectoring to augment aircraft control, the size of the aerodynamic surfaces could be reduced, and this reduction would reduce the drag of the configuration.

It is believed, however, that the main advantage of powered controls is at high angles of attack. This advantage is illustrated in figure 32, where longitudinal control power from pitch thrust vectoring at $M = 0.20$ and NPR = 2.5 is compared with control power at angles of attack up to 40° from both horizontal tails of an F-15 type aircraft (ref. 31) and from canards of a supersonic cruise fighter (ref. 32). The longitudinal control power from pitch vectoring was extrapolated linearly up to $\alpha = 40°$ because previous results from reference 16 for other configurations showed no decrease in control power up to $\alpha = 37°$. Longitudinal control power generated by thrust vectoring is not dependent upon angle of attack, whereas control power from the aerodynamic controls decreased with increasing angle of attack. For actual applications, levels of longitudinal control power from thrust vectoring could change as a result of decreases in thrust that may occur from inlet effects at high angles of attack. The horizontal tails and canards of reference 32 lost about 90 percent of their control power at $\alpha = 35°$ to 40°. It was also found in reference 32 that deflection of the horizontal tail was laterally stabilizing, whereas canard deflection was laterally destabilizing. This cross-coupling of the lateral stability with the longitudinal stability or control characteristics is typical for configurations with aerodynamic controls and most likely would not occur with powered controls.

Directional control. A comparison, at $\alpha = 0°$, of directional control power C_{n_δ}, side-force effectiveness C_{Y_δ}, and induced rolling moment C_{l_δ} from powered and aerodynamic controls is presented in figure 33. Directional control power from yaw thrust vectoring was obtained at the scheduled nozzle pressure ratio (fig. 10) for each Mach number shown. Directional control power from various aerodynamic control effectors for several fighter configurations (refs. 30 and 32 to 35) are also shown in figure 33. These configurations included the F-15 aircraft (ref. 30), an F-15 type aircraft (ref. 31), a supersonic cruise fighter (refs. 32 and 33), a tactical fighter (ref. 33), and an F-16 type aircraft (refs. 34 and 35).

Directional control power from yaw thrust vectoring exhibits similar characteristics with Mach number as those previously noted for longitudinal control power from pitch thrust vectoring. At low speeds ($M < 0.40$), directional control power from yaw thrust vectoring was greater than that provided by the various aerodynamic control effectors for those configurations shown. In fact, directional control power from yaw thrust vectoring was even greater than the various aerodynamic control effectors at the minimum nozzle pressure ratio tested (NPR = 2.0) at $M = 0.20$ (fig. 29(a)). Similar results are presented in reference 16 for a configuration with canted nozzles. Directional control power provided by the rudders was greater than that provided by yaw thrust vectoring at Mach numbers from 0.50 to 2.00. These aerodynamic controls are also generally sized for low-speed operation. Figure 33 also shows that yaw thrust vectoring generally provided more directional control power than that provided by unconventional aerodynamic means such as differential horizontal-tail deflection (ref. 32), direct side-force generators (vertical canards, ref. 34), and differential canard deflection (ref. 35).

The effects of angle of attack on directional control power (not shown) are also similar to those on longitudinal control power (fig. 32). For example, the configuration of reference 32 begins to lose directional control at about $\alpha = 20°$, and directional control is nonexistent at about $\alpha = 45°$. The direct side-force generators of reference 34 lose nearly all of their effectiveness at angles of attack of 15° and above. However, the level of directional control power provided by yaw thrust vectoring remains constant with varying angle of attack.

Generally, use of a rudder for directional control results in adverse rolling moments; that is, for positive rudder deflections, a nose-left yawing moment is accompanied by a positive rolling moment. This adverse rolling moment is caused by a side force generated on the vertical tail that acts above the c.g. of the aircraft. This is not the case for the current configuration. For this configuration, proverse roll is

generated by yaw thrust vectoring, because the nozzles are located below the c.g. of the aircraft. Thus, the vertical location of the nozzles relative to the aircraft c.g. becomes another design option, depending on the desired coupling of rolling moment with yawing moment.

Lateral control. A comparison between lateral control C_{l_δ} from differential pitch thrust vectoring and from aerodynamic controls is presented in figure 34. As expected, lateral control power from differential pitch thrust vectoring shows similar trends with Mach number to those previously discussed for longitudinal and directional characteristics. The levels of roll-control power from differential pitch thrust vectoring shown in figure 34 result from a large moment arm created by the wide-spaced nozzles of the current configuration. These levels would be reduced for a more conventional close-spaced twin-engine fighter aircraft (ref. 16).

Conclusions

The multiaxis control-power characteristics from multiaxis thrust vectoring for an advanced tactical fighter designed for supersonic cruise have been determined over a Mach number range from 0.20 to 2.47. The results from investigations in the Langley 16-Foot Transonic Tunnel and the Lewis 10- by 10-Foot Supersonic Tunnel indicate the following conclusions:

1. The nozzle resultant pitch vector angle was greater than the geometric pitch vector angle once nozzle pressure ratio was high enough to eliminate separation on the lower divergent flap of the nozzle.
2. The nozzle resultant yaw vector angle was less than the geometric yaw vector angle at all test conditions. This loss in effectiveness was attributed to the small size of the yaw vector flaps relative to the total sidewall area of the nozzle.
3. There was little or no effect of pitch thrust vectoring on resultant yaw vector angle. However, at low nozzle pressure ratios, yaw thrust vectoring decreased resultant pitch vector angle for 0° geometric pitch vector angle and increased resultant pitch angle for 15° geometric pitch vector angle.
4. The effects of nozzle pressure ratio and pitch thrust vectoring on the longitudinal aerodynamic characteristics followed expected trends. Both lift and pitching-moment coefficients increased with increasing nozzle pressure ratio and/or geometric pitch vector angle. Similar effects on the lateral aerodynamic characteristics resulted from yaw thrust vectoring.
5. Increments in force or moment coefficient that result from pitch or yaw thrust vectoring remain essentially constant over the entire angle-of-attack range for each Mach number tested.
6. There was no effect of pitch vectoring on the lateral aerodynamic forces and moments and only very small effects of yaw vectoring on the longitudinal aerodynamic forces and moments. This result indicates little cross-coupling of control forces and moments for combined pitch-yaw vectoring.
7. Longitudinal and directional control power resulting from thrust vectoring were functions of nozzle pressure ratio and Mach number. Powered controls were very effective at low Mach numbers, and their effectiveness decreased as Mach number increased because of a reduction in thrust coefficient.
8. Longitudinal and directional control power from thrust vectoring were greater than those provided by aerodynamic control effectors for this and other configurations at Mach numbers less than 0.40. At Mach numbers from 0.40 to 1.20, control power was less, and at Mach numbers from 2.00 to 2.47, control power from thrust vectoring was comparable to that provided by aerodynamic controls.

NASA Langley Research Center
Hampton, VA 23665-5225
April 2, 1987

Appendix A

Thrust-Removed Aerodynamic Characteristics

This appendix presents the thrust-removed aerodynamic characteristics for the various configurations tested. Thrust-removed aerodynamic force and moment coefficients were obtained by determining the components of thrust in axial force, normal force, side force, pitching moment, rolling moment, and yawing moment and subtracting these values from the measured total (aerodynamic plus thrust) forces and moments. These thrust coefficients at forward speeds were determined from measured static data and were a function of the free-stream static and dynamic pressures. Forces and moments were measured for each combination of nozzle pitch and yaw vector angles tested. Further details of this procedure are contained in references 13 and 21.

Thrust-removed aerodynamic characteristics are presented in figures 35 to 55 as follows:

Thrust-induced forces and moments, such as supercirculation lift, can be determined from the results presented in this appendix. For example, from figures 35 to 41, the thrust-induced forces and moments are simply the difference between the specified coefficient at some nozzle pressure ratio and NPR = 1.0 (jet off) for a particular nozzle configuration. The aerodynamic flap effect is the difference between the deflected and undeflected nozzle at jet-off conditions. The thrust-induced forces and moments at angle of attack (figs. 42 to 55) are the differences between coefficient values at the specified nozzle pressure ratio and at the jet-off condition (NPR = 1.0).

Appendix B

Wing Trailing-Edge Flap Characteristics

This appendix presents the effects of wing trailing-edge flap deflection on the longitudinal aerodynamic characteristics at $M = 2.00$ to 2.47. The effects of trailing-edge flap deflection at $M = 0.60$ to 1.20 are given in reference 17. Figure 56 shows that deflection of the trailing-edge flaps resulted in a decrease in lift coefficient accompanied by a nose-down pitching-moment coefficient. Except at low lift coefficients, deflection of the trailing-edge flap increased drag coefficient.

References

1. Barlow, Robert C.; and Richey, G. Keith: Trends in Modern High Performance Aircraft. *Proceedings—International Conference—Forward Swept Wing Aircraft*, R. K. Nangia, ed., Univ. of Bristol (Bristol, U.K.), c.1983, pp. (i)2.1–(i)2.11.
2. Rosen, Cecil C., III; Burger, Robert J.; and Sigalla, Armand: Aeronautical Technology 2000: A Projection of Advanced Vehicle Concepts. AIAA-84-2501, Oct.–Nov. 1984.
3. Selegan, David R.: STOL and Maneuver Technology Program. *Powered Lift Systems Plus an Overview of the JVX Program*, SP-555, Soc. Automot. Eng., Inc., Dec. 1983, pp. 1–7. (Available as SAE Paper 831425.)
4. Herbst, W.: Future Fighter Technologies. *J. Aircr.*, vol. 17, no. 8, Aug. 1980, pp. 561–566.
5. Well, K. H.; Faber, B.; and Berger, E.: Optimization of Tactical Aircraft Maneuvers Utilizing High Angles of Attack. *J. Guid., Control, & Dyn.*, vol. 5, no. 2, Mar.–Apr. 1982, pp. 131–137.
6. Skow, Andrew M.; Hamilton, William L.; and Taylor, John H.: Advanced Fighter Agility Metrics. AIAA-85-1779, Aug. 1985.
7. Nelson, B. D.; and Nicolai, L. M.: Application of Multi-Function Nozzles to Advanced Fighters. AIAA-81-2618, Dec. 1981.
8. Pennington, J. E.; and Meintel, A. J., Jr.: Performance and Human Factors Results From Thrust Vectoring Investigations in Simulated Air Combat. *Proceedings of the 1980 Joint Automatic Control Conference*, Volume I, IEEE: 80CH1580-0, American Automatic Control Council, c.1980, Paper TA1-A.
9. Lacey, David W.: Air Combat Advantages From Reaction Control Systems. SAE Tech. Paper Ser. 801177, Oct. 1980.
10. Hienz, Egon; and Vedova, Ralph: Requirements, Definition and Preliminary Design for an Axisymmetric Vectoring Nozzle, To Enhance Aircraft Maneuverability. AIAA-84-1212, June 1984.
11. Capone, Francis J.: Summary of Propulsive-Lift Research in the Langley 16-Ft. Transonic Tunnel. *J. Aircr.*, vol. 13, no. 10, Oct. 1976, pp. 803–808.
12. Capone, Francis J.; and Berrier, Bobby L.: *Investigation of Axisymmetric and Nonaxisymmetric Nozzles Installed on a 0.10-Scale F-18 Prototype Airplane Model.* NASA TP-1638, 1980.
13. Capone, Francis J.; and Reubush, David E.: *Effects of Varying Podded Nacelle-Nozzle Installations on Transonic Aeropropulsive Characteristics of a Supersonic Fighter Aircraft.* NASA TP-2120, 1983.
14. Leavitt, Laurence D.: Summary of Nonaxisymmetric Nozzle Internal Performance From the NASA Langley Static Test Facility. AIAA-85-1347, July 1985.
15. Mason, Mary L.; and Berrier, Bobby L.: *Static Investigation of Several Yaw Vectoring Concepts on Nonaxisymmetric Nozzles.* NASA TP-2432, 1985.
16. Capone, Francis J.; and Mason, Mary L.: *Multiaxis Aircraft Control Power From Thrust Vectoring at High Angles of Attack.* NASA TM-87741, 1986.
17. Capone, Francis J.; and Reubush, David E.: *Effect of Thrust Vectoring and Wing Maneuver Devices on Transonic Aeropropulsive Characteristics of a Supersonic Fighter Aircraft.* NASA TP-2119, 1983.
18. Capone, Francis J.; Bare, E. Ann; and Arbiter, Dorothy: *Aerodynamic Characteristics of a Supersonic Fighter Aircraft Model at Mach 0.40 to 2.47.* NASA TP-2580, 1986.
19. Capone, Francis J.; Bare, E. Ann; and Head, Verlon E.: *Effects of Multifunction Nozzle Installations on Supersonic Aeropropulsive Characteristics of a Supersonic Fighter Aircraft.* NASA TP-2703, 1987.
20. Reubush, David E.; and Bare, E. Ann: *Investigation of a Supersonic Cruise Fighter Model Flow Field.* NASA TM-86361, 1985.
21. Mercer, Charles E.; Berrier, Bobby L.; Capone, Francis J.; Grayston, Alan M.; and Sherman, C. D.: *Computations for the 16-Foot Transonic Tunnel—NASA, Langley Research Center.* NASA TM-86319, 1984. (Revision 1, 1987.)
22. Peddrew, Kathryn H., compiler: *A User's Guide to the Langley 16-Foot Transonic Tunnel.* NASA TM-83186, 1981.
23. Tinoco, E. N.; and Mercer, J. E.: *FLEXSTAB—A Summary of the Functions and Capabilities of the NASA Flexible Airplane Analysis Computer System.* NASA CR-2564, 1975.
24. Aiello, Robert A.: *NASA Lewis 10- by 10-Foot Supersonic Wind Tunnel.* NASA TM X-71625, 1974.
25. Berrier, Bobby L.; Leavitt, Laurence D.; and Bangert, Linda S.: *Operating Characteristics of the Multiple Critical Venturi System and Secondary Calibration Nozzles Used for Weight-Flow Measurements in the Langley 16-Foot Transonic Tunnel.* NASA TM-86405, 1985.
26. Capone, Francis J.: *Static Performance of Five Twin-Engine Nonaxisymmetric Nozzles With Vectoring and Reversing Capability.* NASA TP-1224, 1978.
27. Re, Richard J.; and Leavitt, Laurence D.: *Static Internal Performance Including Thrust Vectoring and Reversing of Two-Dimensional Convergent-Divergent Nozzles.* NASA TP-2253, 1984.
28. Yetter, Jeffery A.; and Leavitt, Laurence D.: *Effects of Sidewall Geometry on the Installed Performance of Nonaxisymmetric Convergent-Divergent Exhaust Nozzles.* NASA TP-1771, 1980.
29. Re, Richard J.; and Capone, Francis J.: *Longitudinal Aerodynamic Characteristics of a Fighter Model With a Close-Coupled Canard at Mach Numbers From 0.40 to 1.20.* NASA TP-1206, 1978.
30. Mello, J. F.; and Kotansky, D. R.: Aero/Propulsion Technology for STOL and Maneuver. AIAA-85-4013, Oct. 1985.
31. Lallman, Frederick J.: *Preliminary Design Study of a Lateral-Directional Control System Using Thrust Vectoring.* NASA TM-86425, 1985.
32. Klein, John R.; Walck, Kenneth J.; and Hahne, David E.: Airframe Component Effects on the Aerodynamic Stability and Control Characteristics of a Supersonic Cruise Fighter Aircraft at High Angles of Attack. AIAA-84-2110, Aug. 1984.

33. White, S. N.: *Feasibility Study for Integrating Thrust Vectoring as Primary Flight Control System.* NASA CR-165758, 1981.

34. Capone, Francis J.: *Effect of Direct Side-Force Generators on the Aerodynamic Characteristics of a Swept-Wing Fighter Model at Transonic Speeds.* NASA TM X-2874, 1973.

35. Re, Richard J.; and Capone, Francis J.: *An Investigation of a Close-Coupled Canard as a Direct Side-Force Generator on a Fighter Model at Mach Numbers From 0.40 to 0.90.* NASA TN D-8510, 1977.

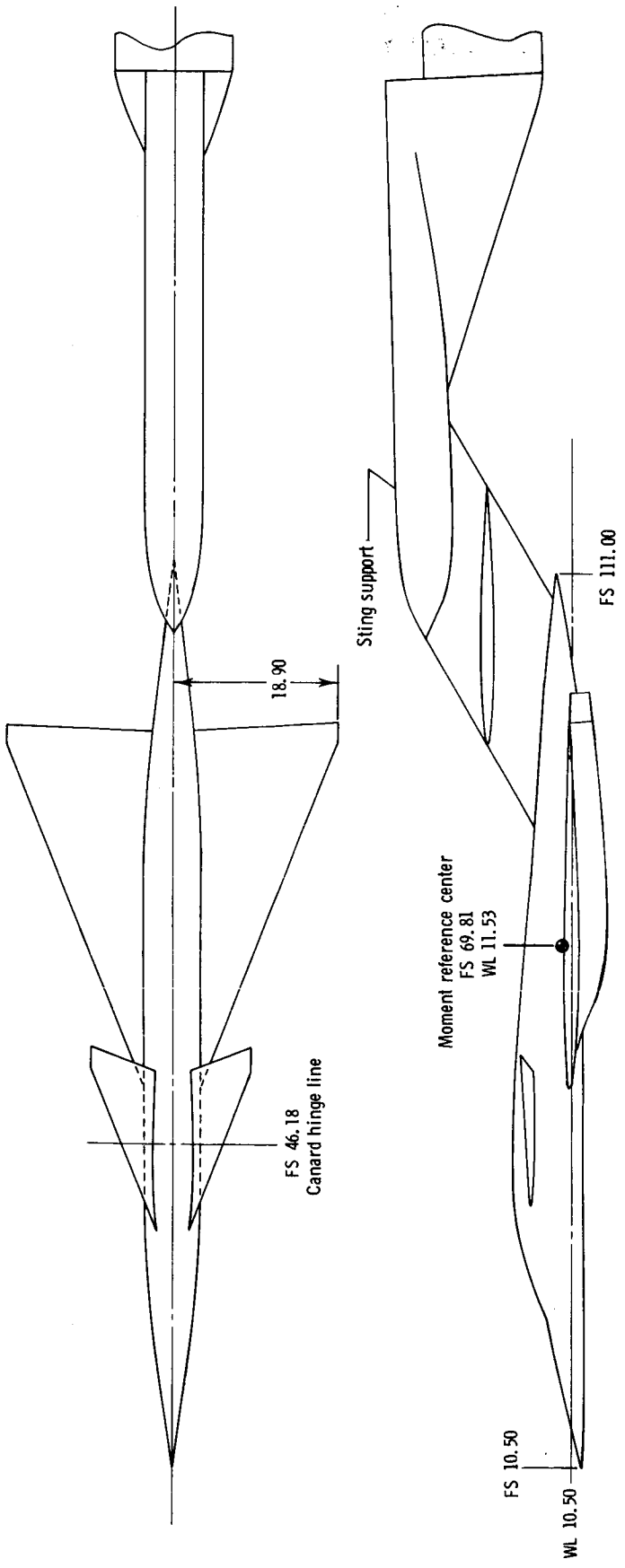

Figure 1. Sketch showing general arrangement of model and support system. All linear dimensions in inches.

L-80-1228

Figure 2. Photograph of model in 16 FTT.

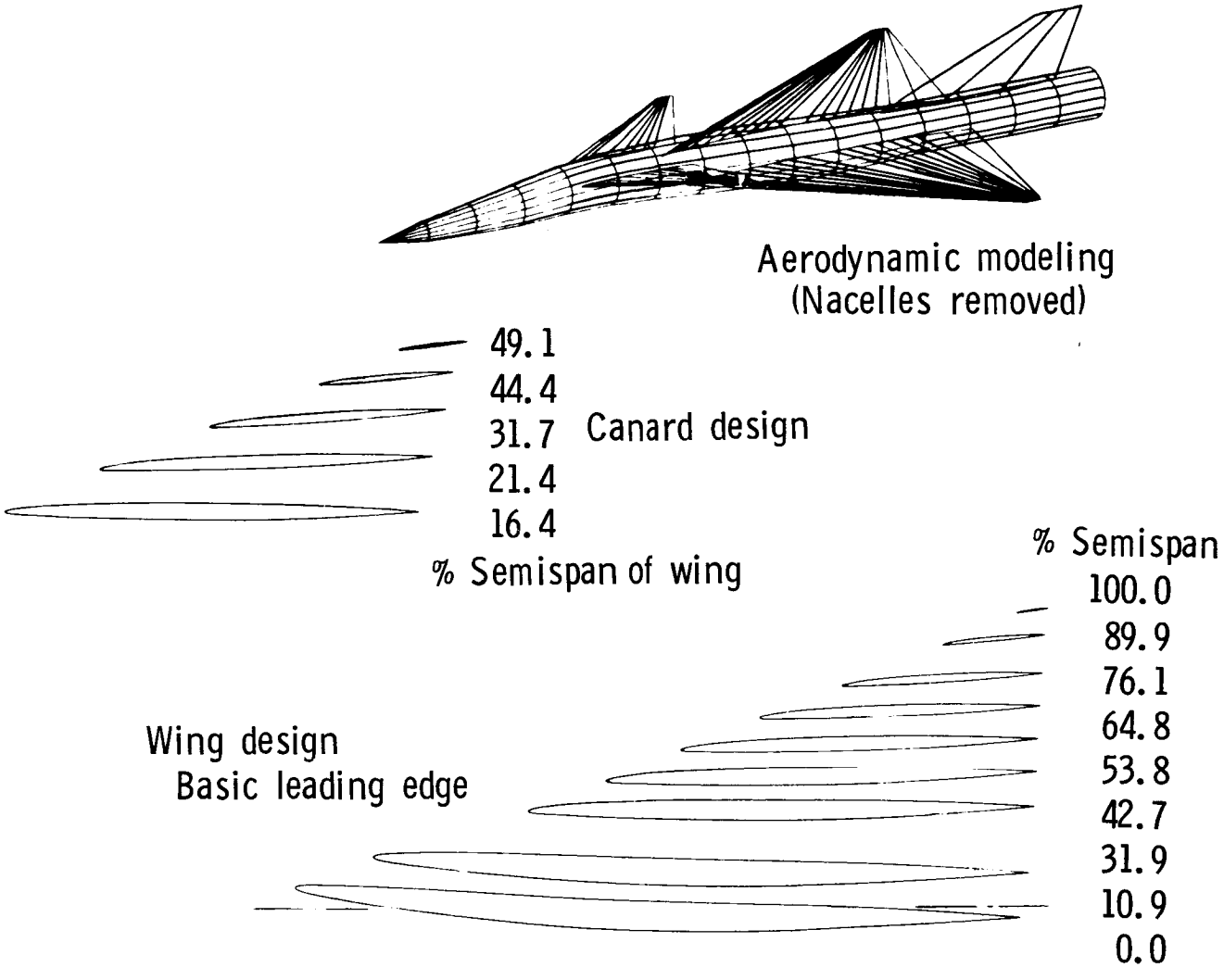

Figure 3. Wing-canard design characteristics.

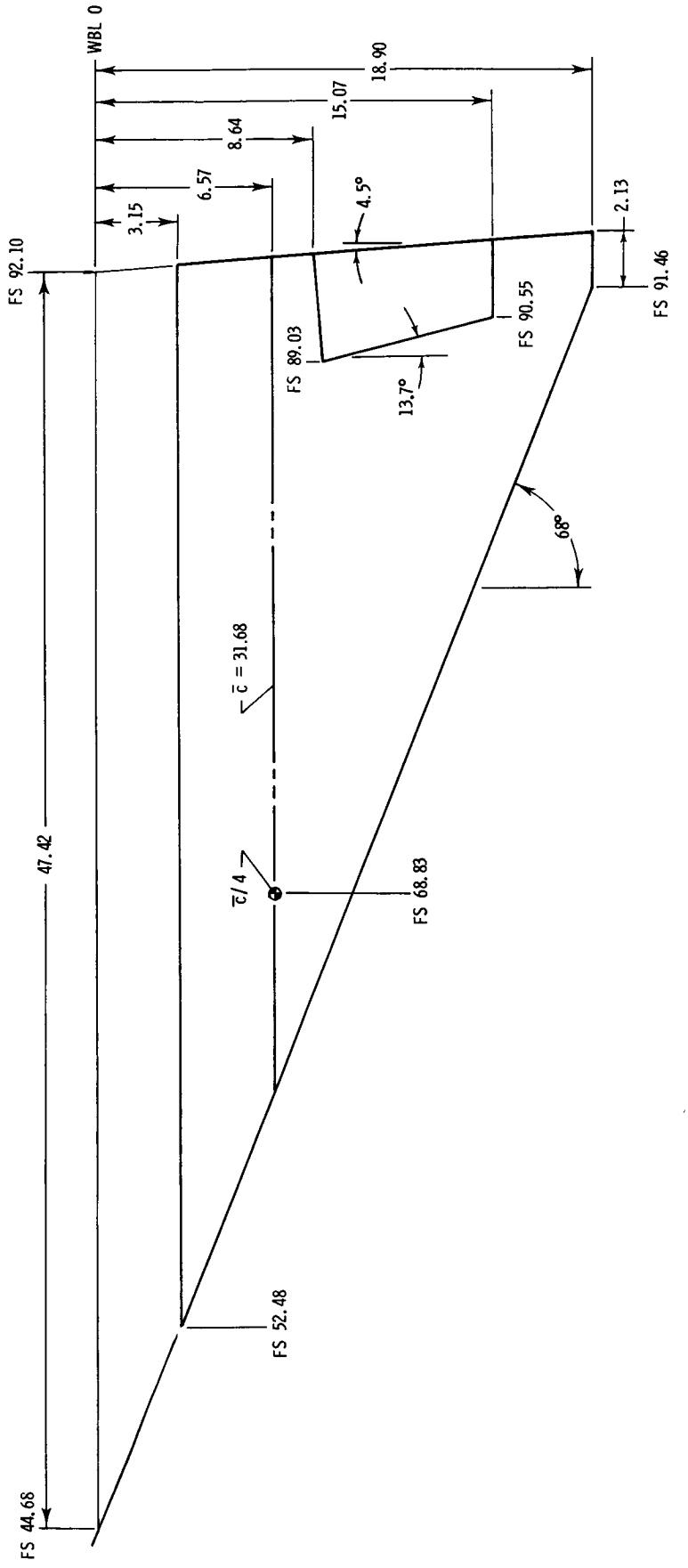

Figure 4. Sketch showing geometry of wing. All linear dimensions in inches.

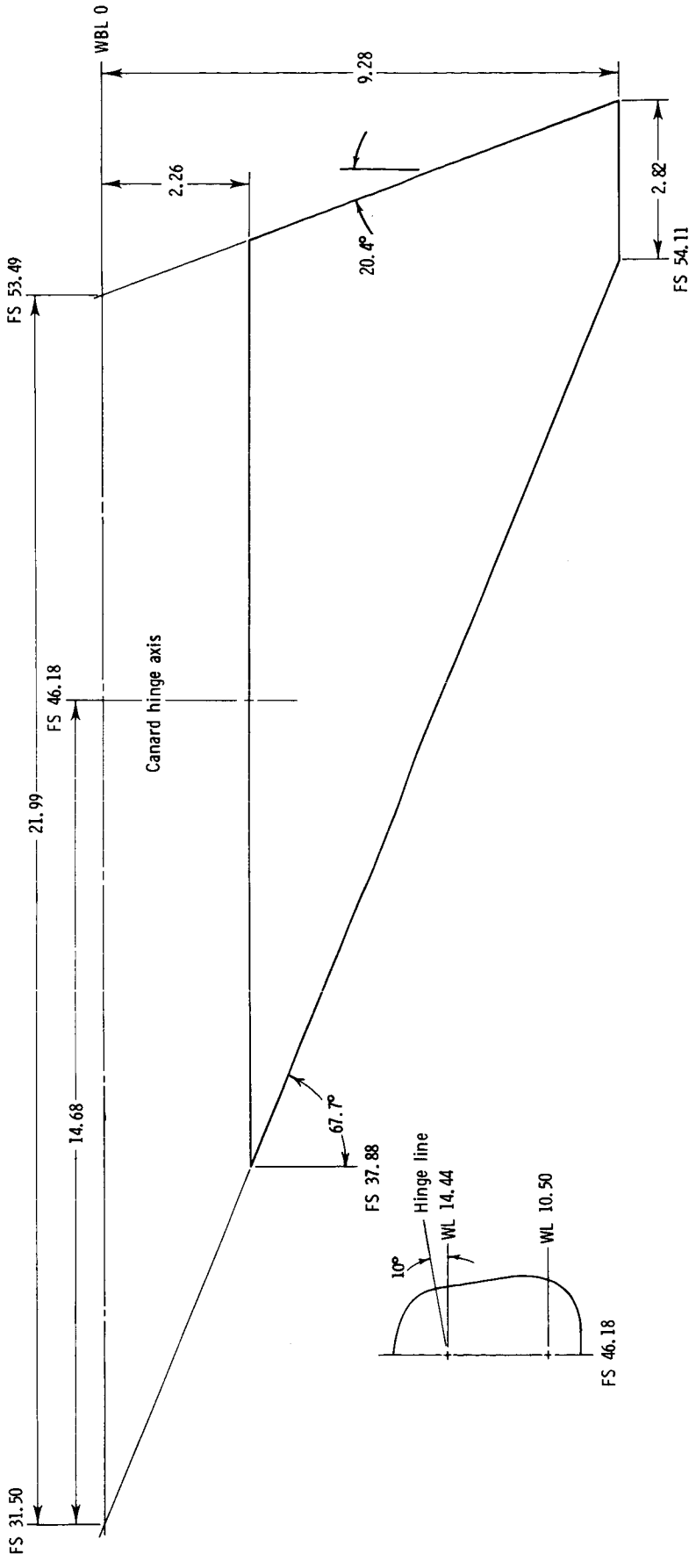

Figure 5. Sketch showing planform geometry of canard. All linear dimensions in inches.

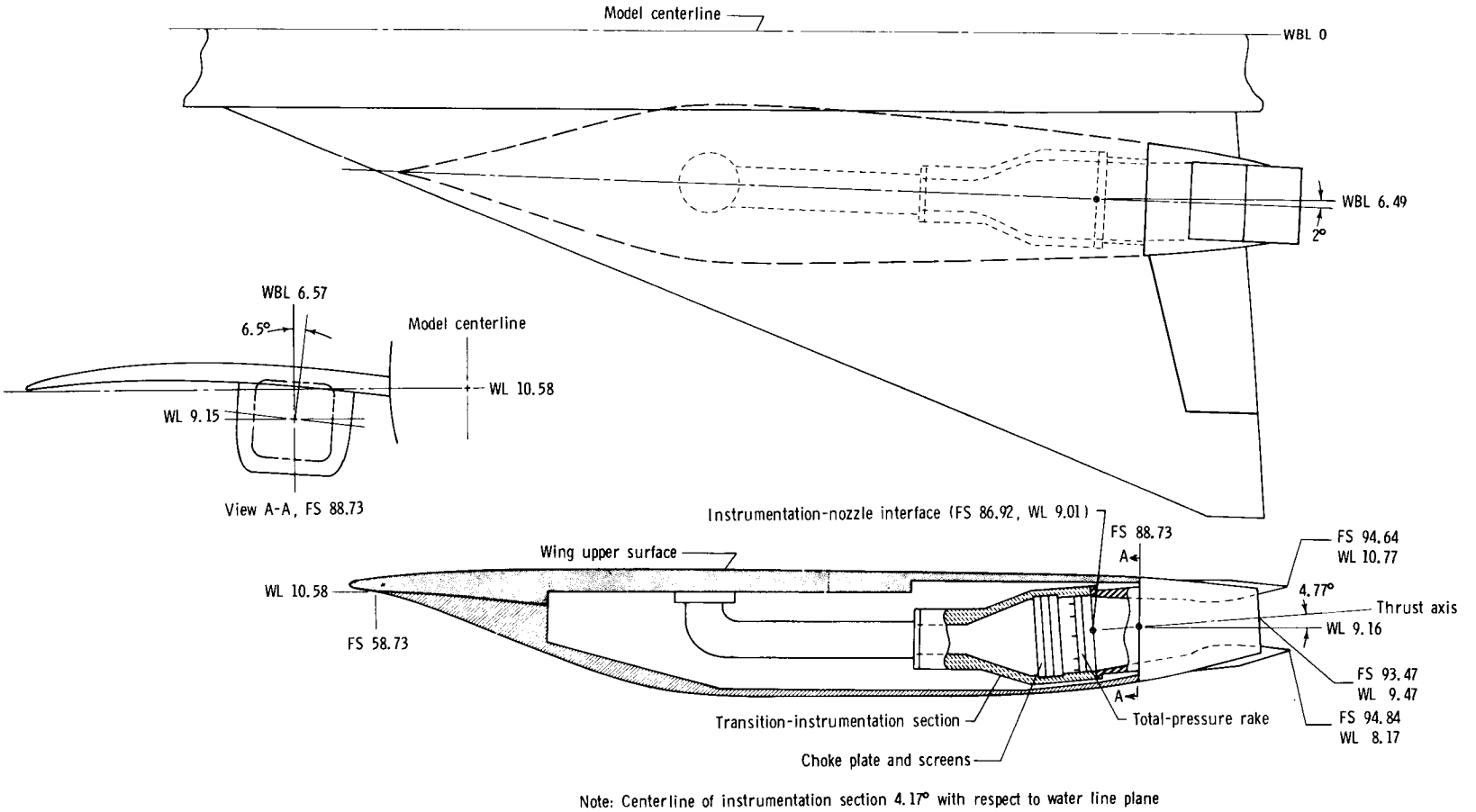

Figure 6. Nacelle-nozzle installation for 2-D C-D nozzle. All linear dimensions in inches.

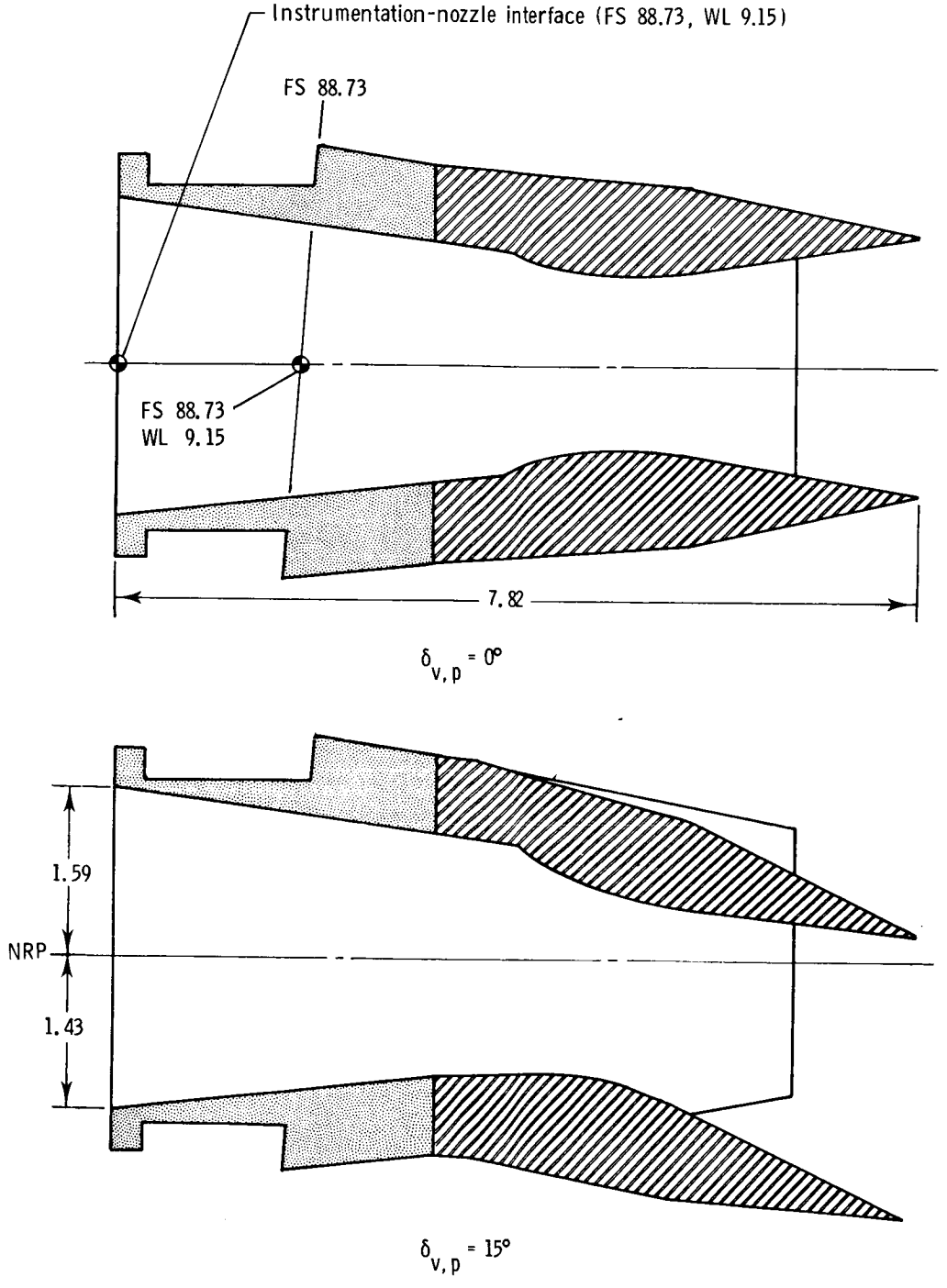

(a) Pitch vectoring configurations.

Figure 7. Details of 2-D C-D nozzle configurations. All linear dimensions in inches.

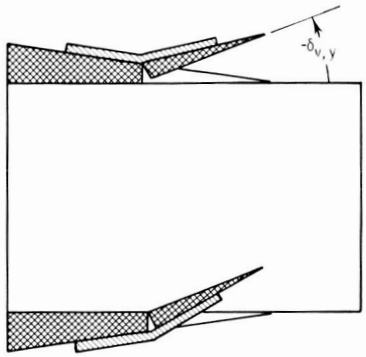

Note: $\delta_{v,y}$ = -20° shown. $\delta_{v,y}$ = -10° also tested.

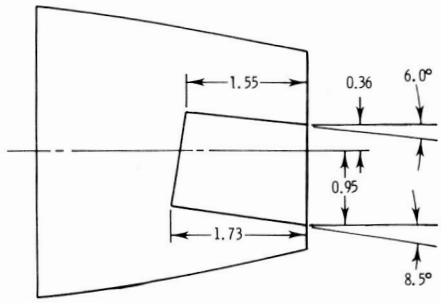

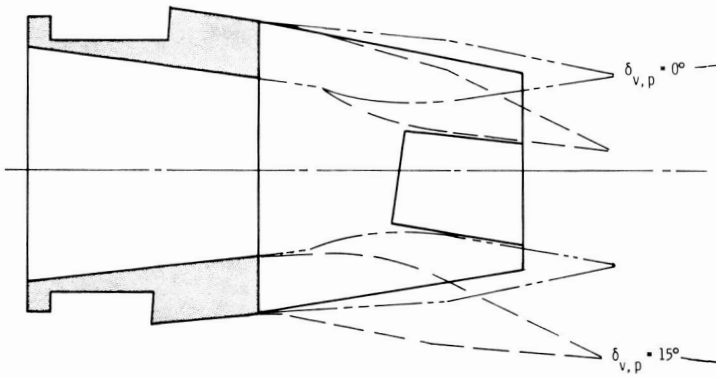

L-84-4961

$\delta_{v,p}$ = 0°, $\delta_{v,y}$ = -20°

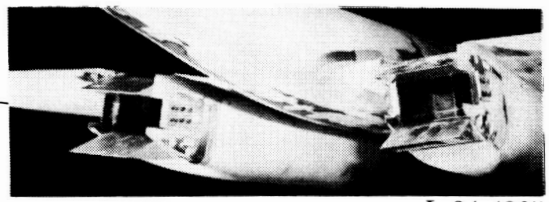

L-84-4965

$\delta_{v,p}$ = 15°, $\delta_{v,y}$ = -20°

(b) Yaw vector configurations.

Figure 7. Continued.

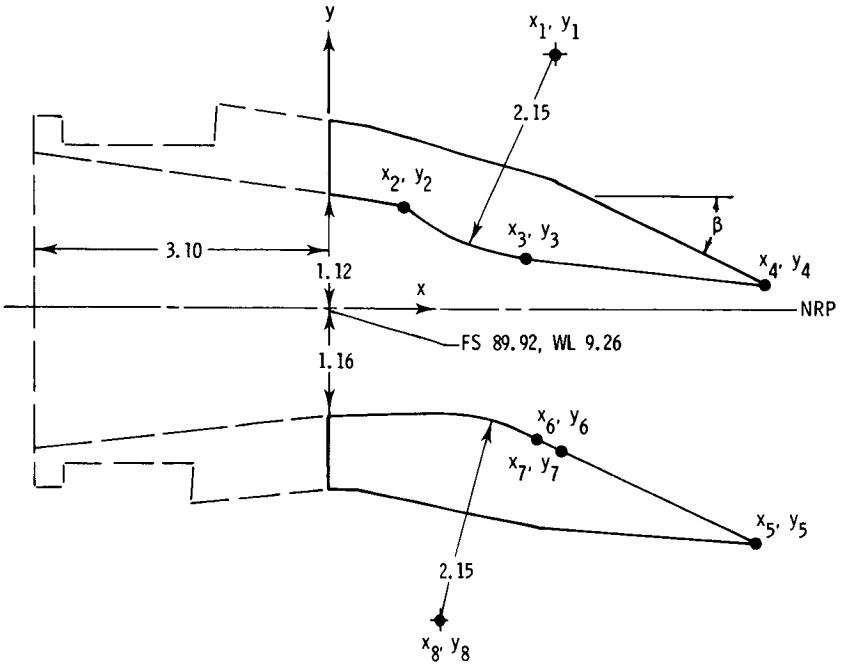

	$\delta_{v,p}$, deg	
	0	15
x_1	1.81	2.44
y_1	2.96	2.65
x_2	0.80	0.80
y_2	1.60	1.60
x_3	2.13	2.00
y_3	0.83	0.51
x_4	4.72	4.60
y_4	1.23	0.23
x_5	4.71	4.51
y_5	-1.23	-2.44
x_6	2.13	2.34
y_6	-0.83	-1.35
x_7	2.13	2.16
y_7	-0.83	-1.26
x_8	1.81	3.18
y_8	-2.96	-3.19
β, deg	12.13°	27.16°

(c) Nozzle details.

Figure 7. Concluded.

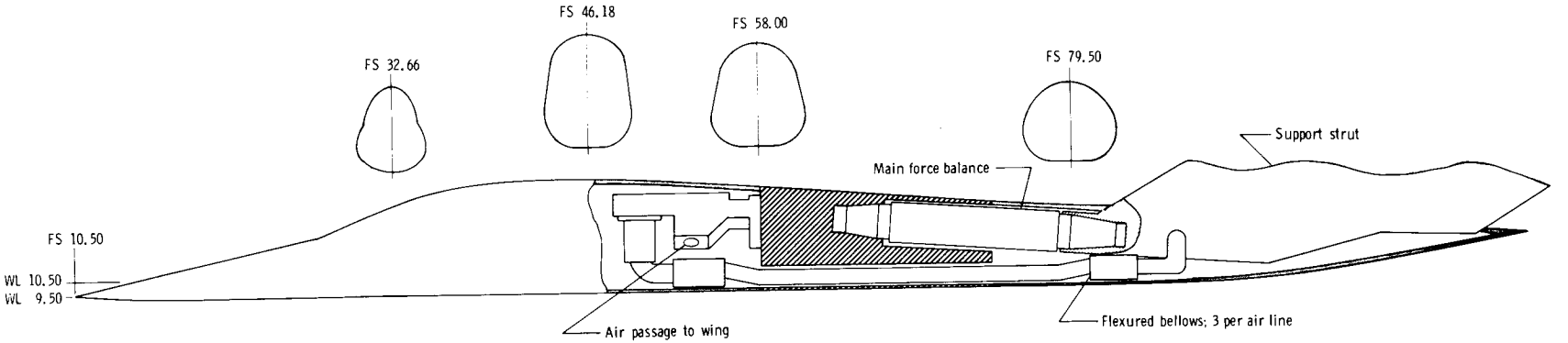

Figure 8. Sketch showing body arrangement and internal-flow hardware. All linear dimensions in inches.

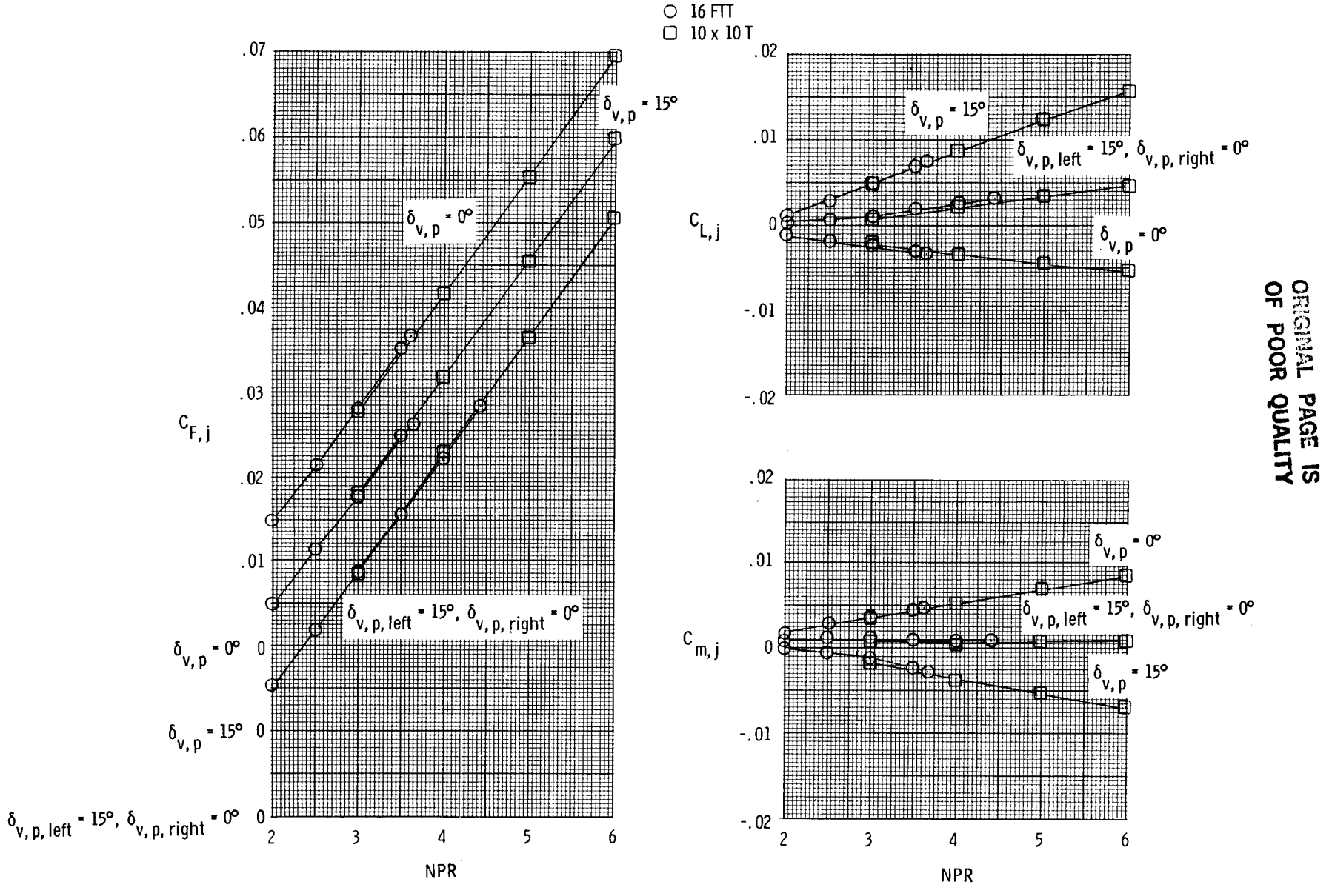

(a) Longitudinal characteristics; $\delta_{v,y} = 0°$.

Figure 9. Comparison between 16 FTT and 10 × 10 T nozzle force coefficients at static conditions.

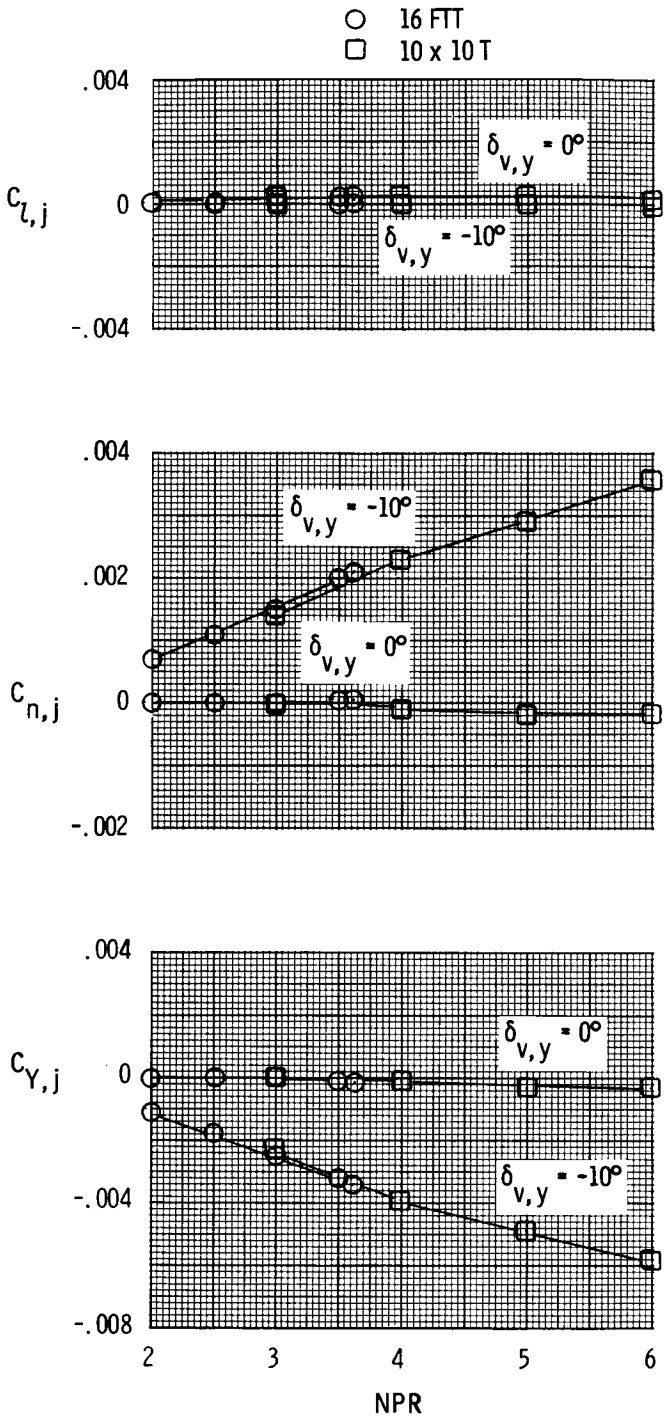

(b) Lateral characteristics; $\delta_{v,p} = 0°$.

Figure 9. Concluded.

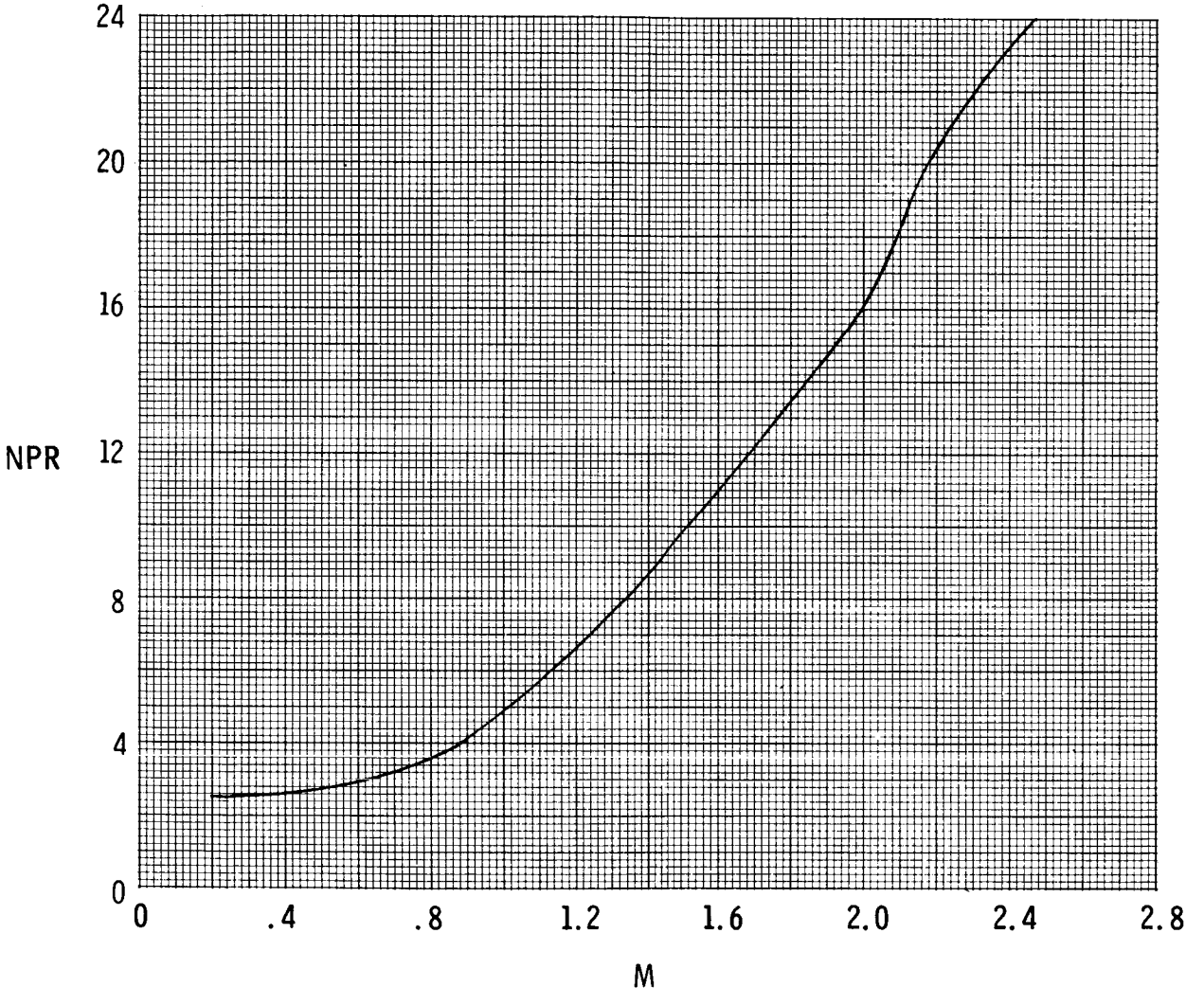

Figure 10. Typical nozzle pressure ratio operating schedule for turbofan engine.

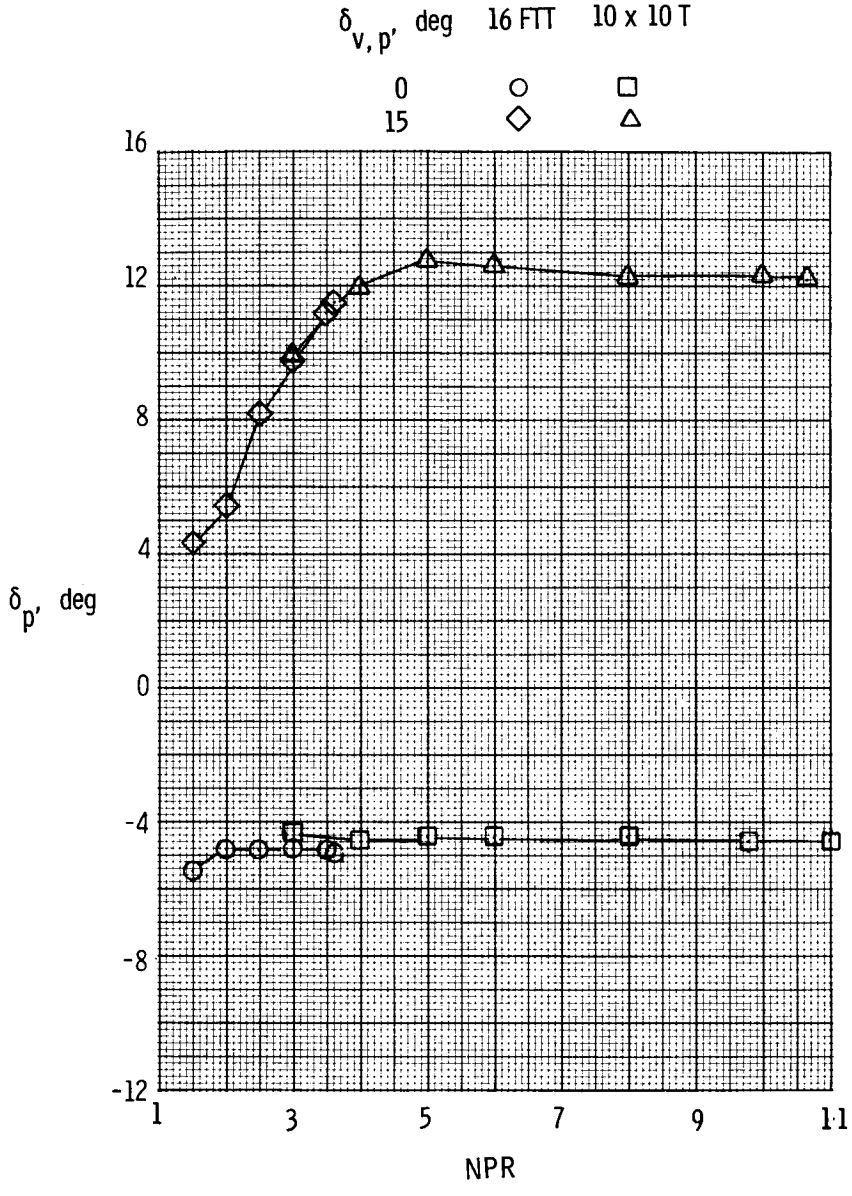

(a) Resultant thrust vector angles.

Figure 11. Effect of pitch vectoring on resultant thrust vector angle and nozzle performance parameters for $\delta_{v,y} = 0°$ and $M = 0$.

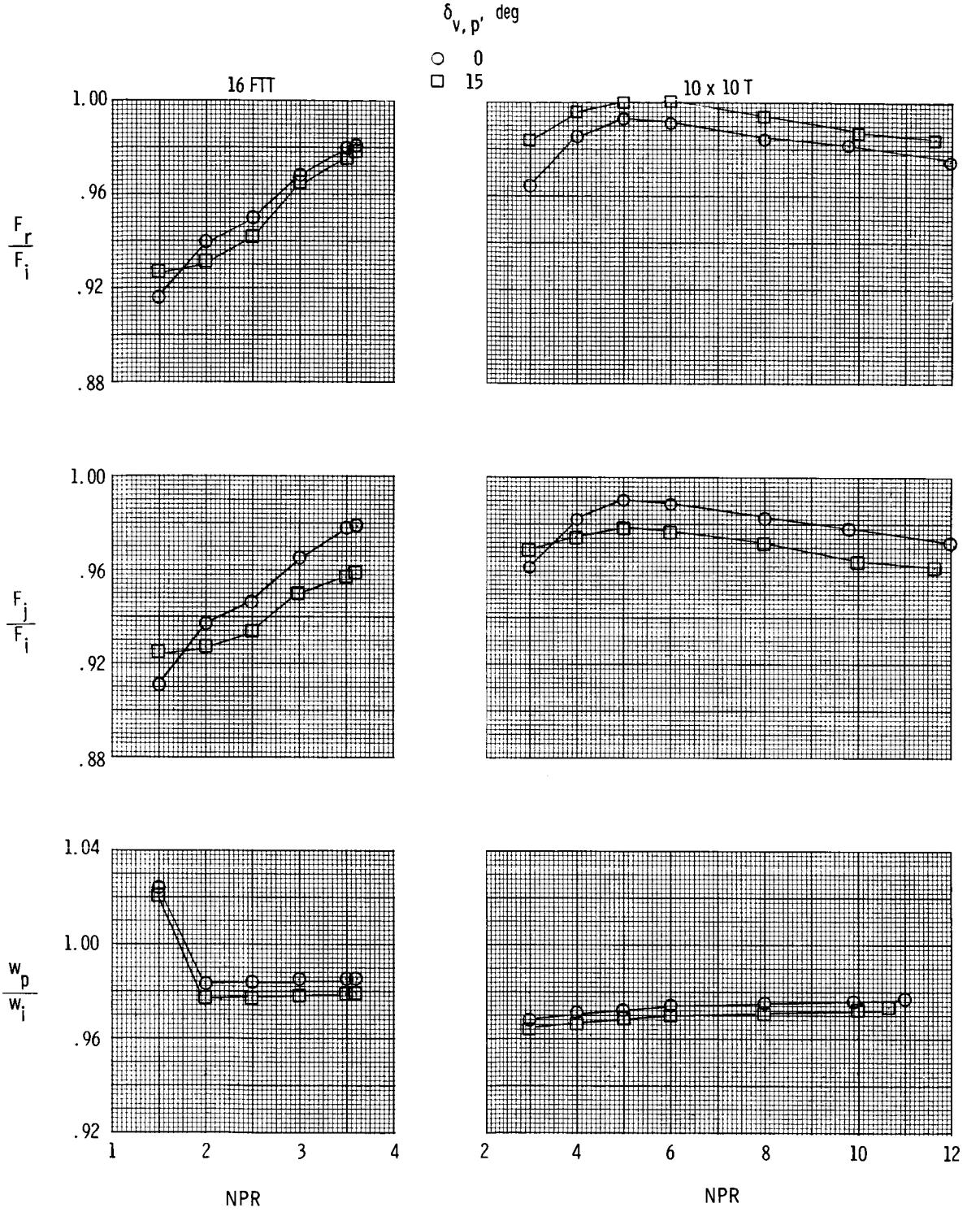

(b) Nozzle performance parameters.

Figure 11. Concluded.

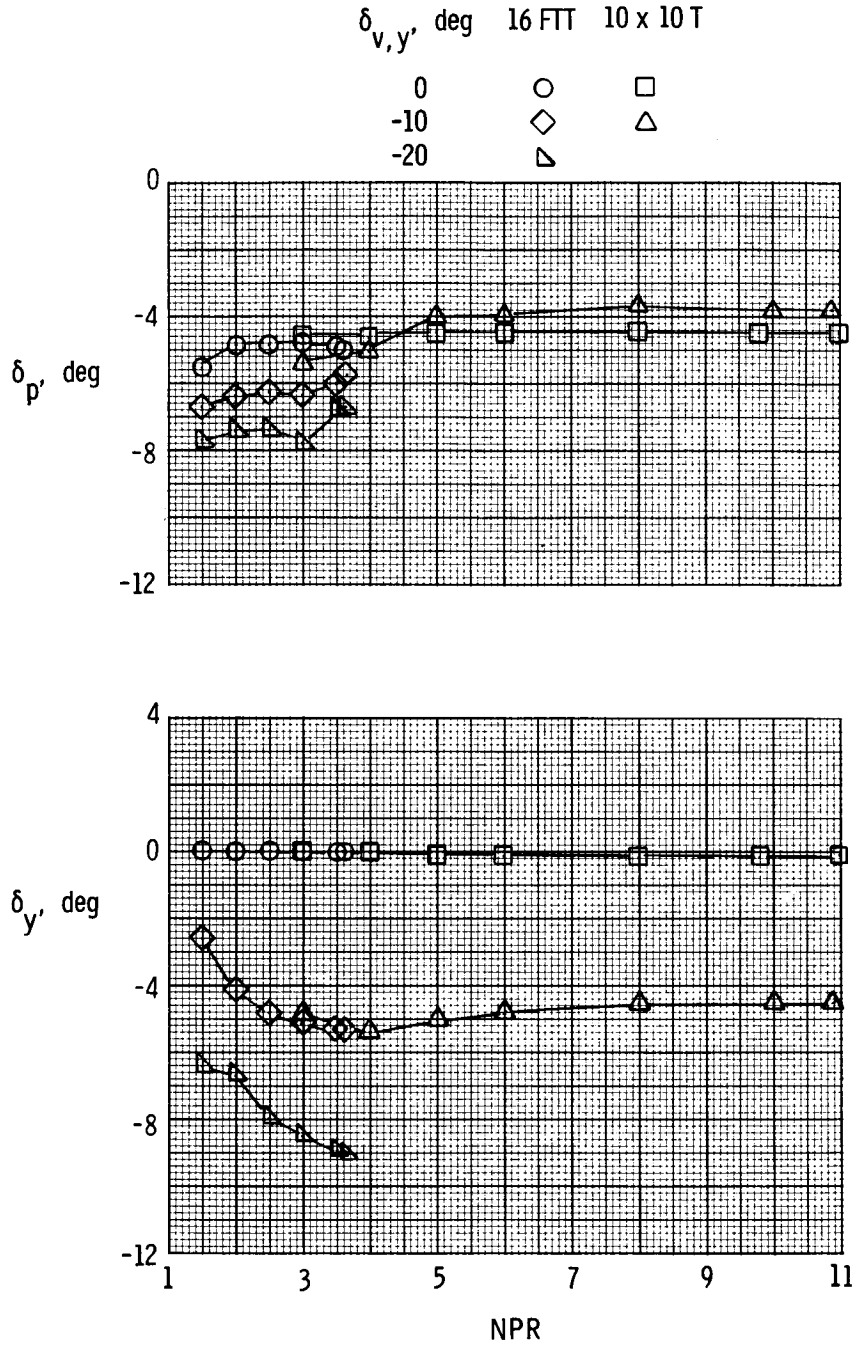

(a) Resultant thrust vector angles.

Figure 12. Effect of yaw vectoring on resultant thrust vector angles, and nozzle performance parameters for $\delta_{v,p} = 0°$ and $M = 0$.

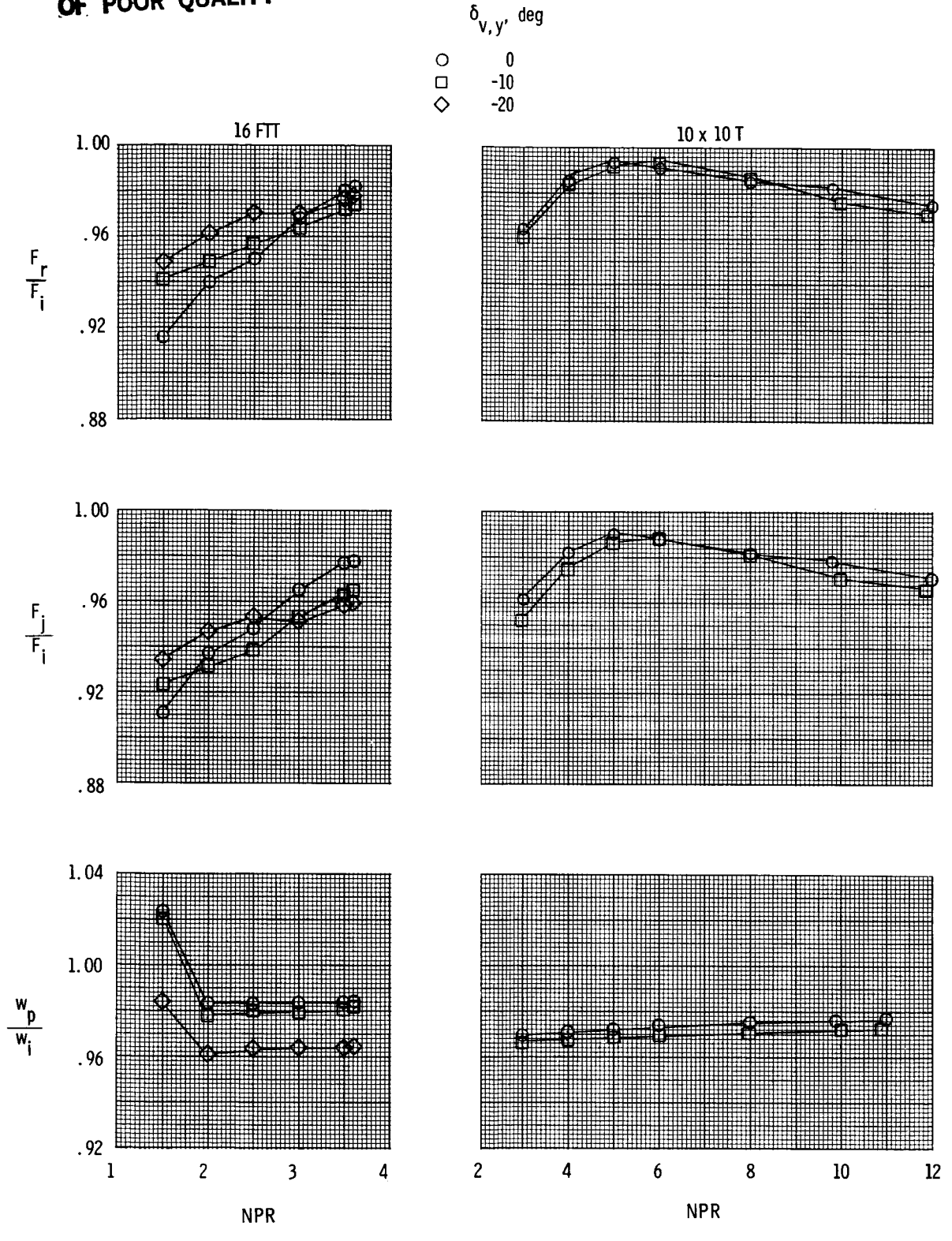

(b) Nozzle performance parameters.

Figure 12. Concluded.

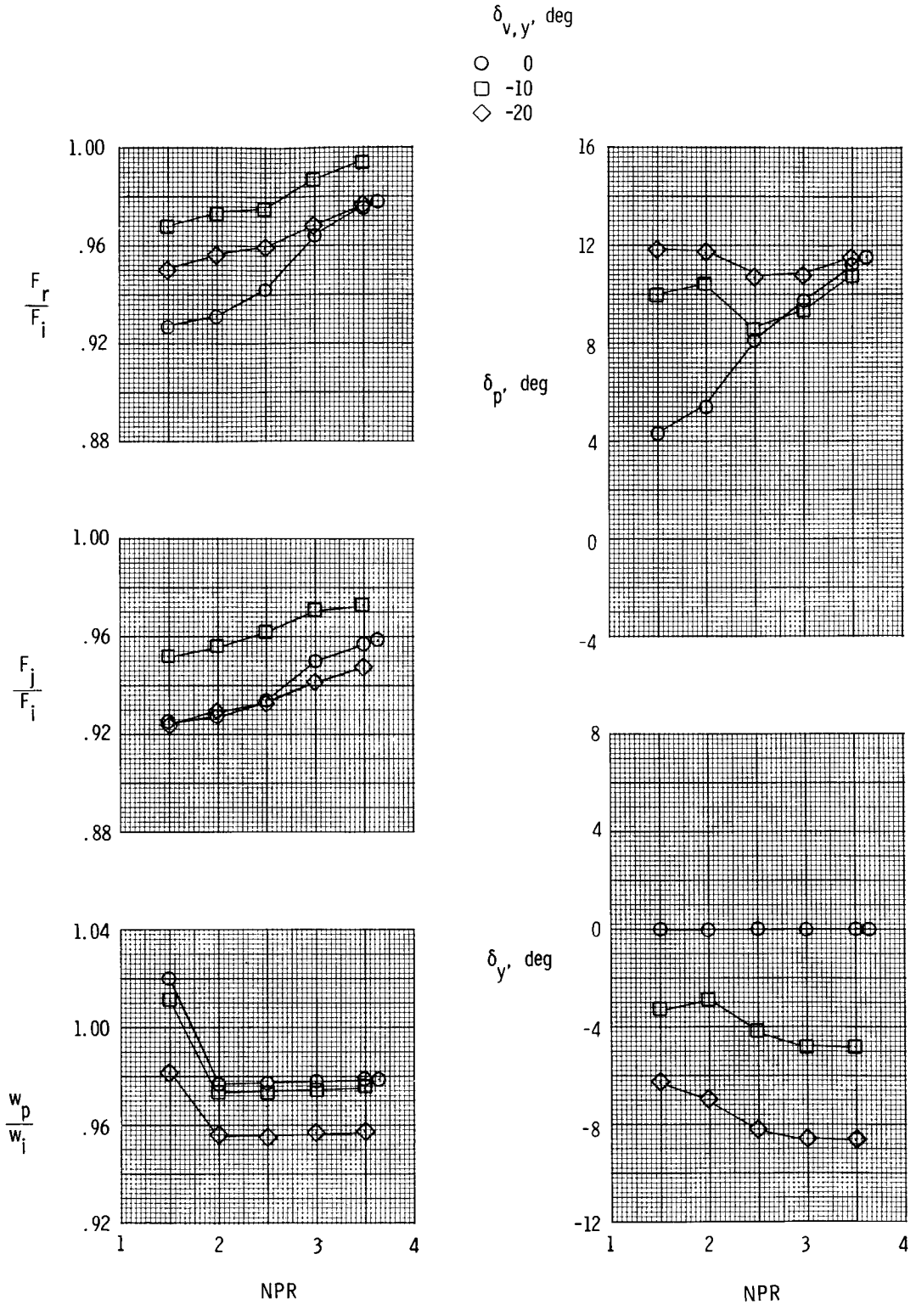

Figure 13. Effect of yaw vectoring on resultant thrust vector angles and nozzle performance parameters for $\delta_{v,p} = 15°$ and $M = 0$ in 16 FTT.

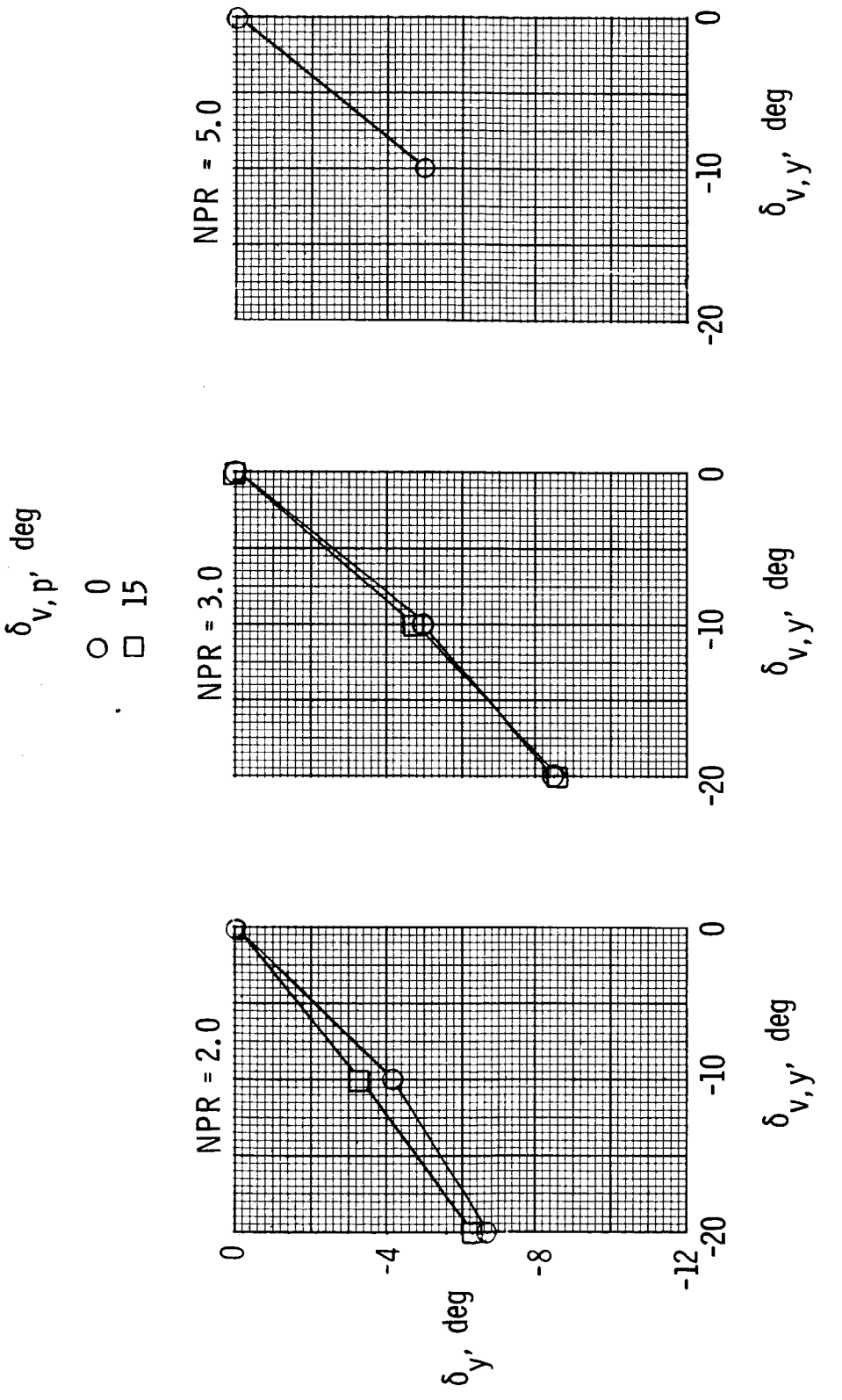

(a) Resultant yaw vector angle.

Figure 14. Summary of resultant thrust vector angles from combined pitch and yaw vectoring for $M = 0$.

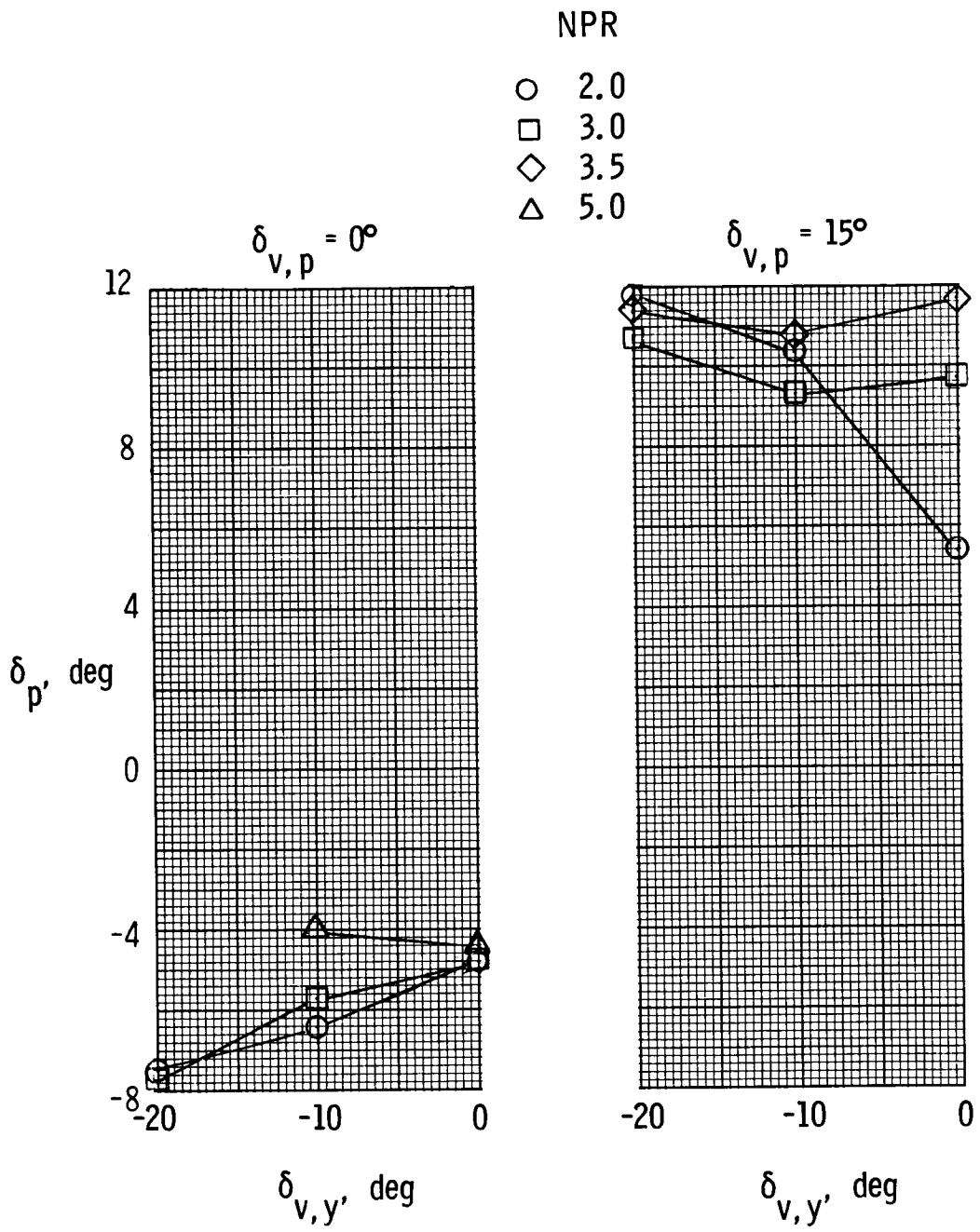

(b) Resultant pitch vector angle.

Figure 14. Concluded.

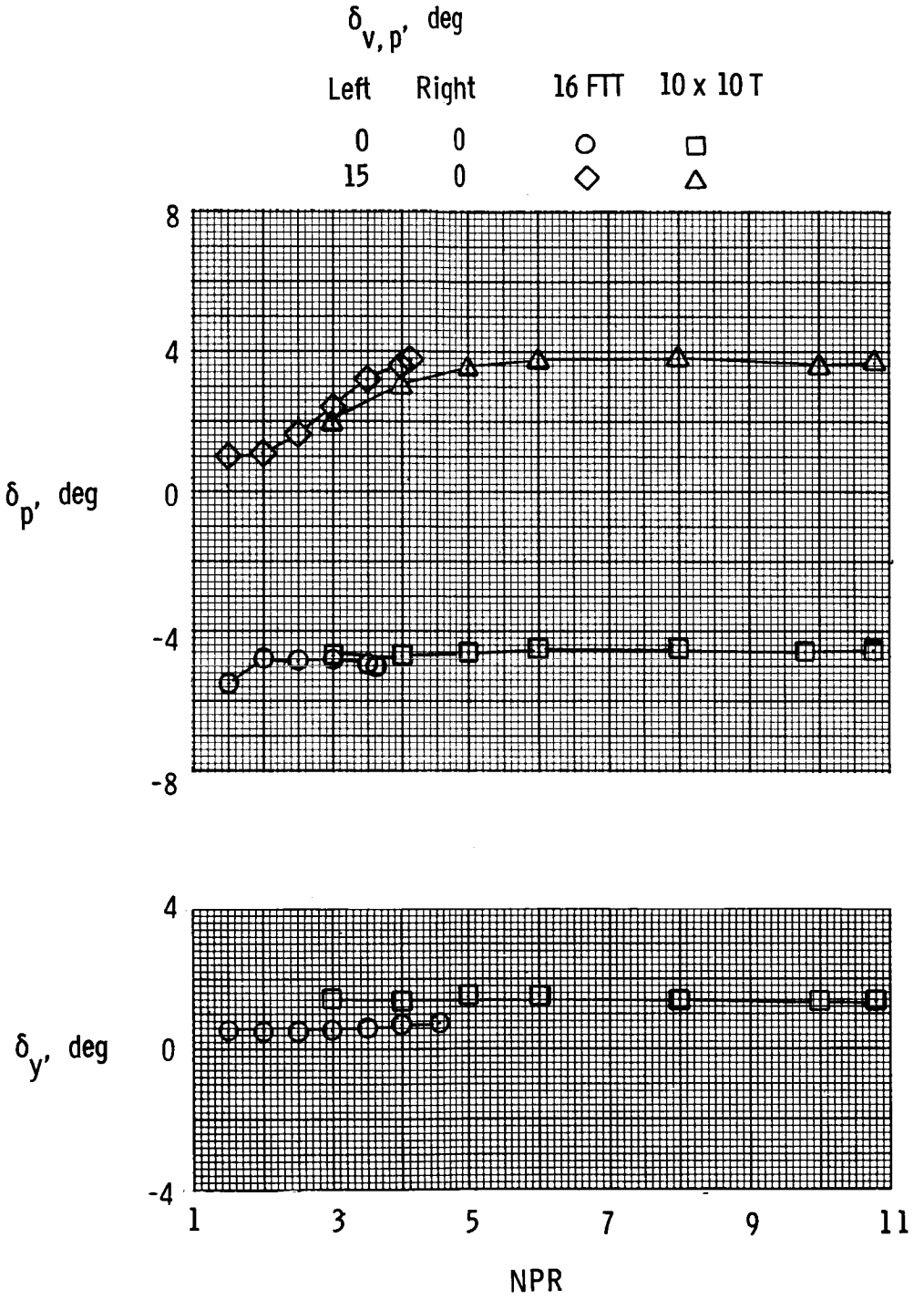

(a) Resultant thrust vector angles.

Figure 15. Effect of differential pitch vectoring on resultant thrust vector angles and nozzle performance parameters for $\delta_{v,y} = 0°$ and $M = 0$.

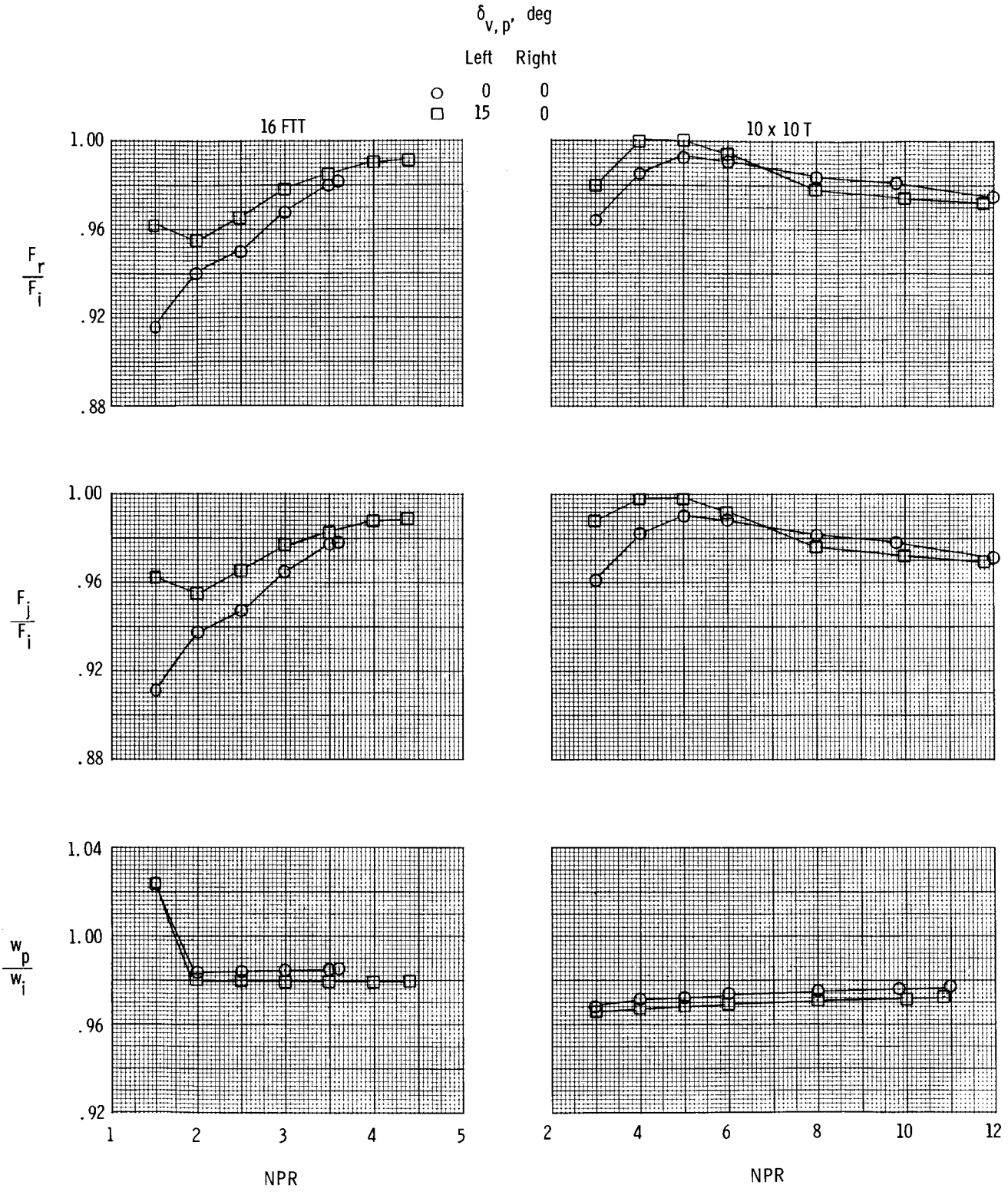

(b) Nozzle performance parameters.

Figure 15. Concluded.

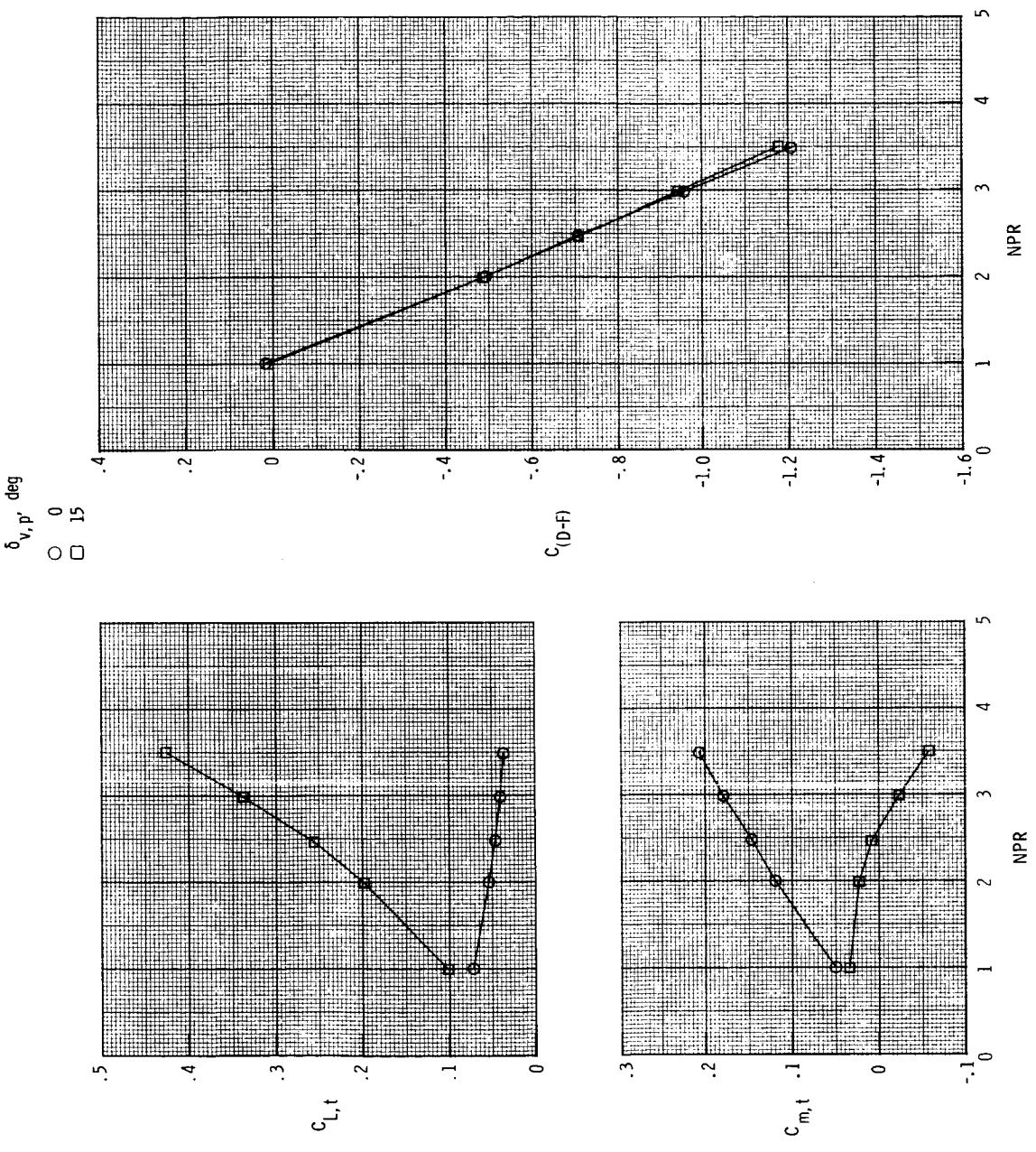

(a) $M = 0.20$.

Figure 16. Effect of nozzle pressure ratio and symmetric pitch vectoring on total longitudinal aerodynamic characteristics for $\delta_{v,y} = 0°$ and $\alpha = 4°$.

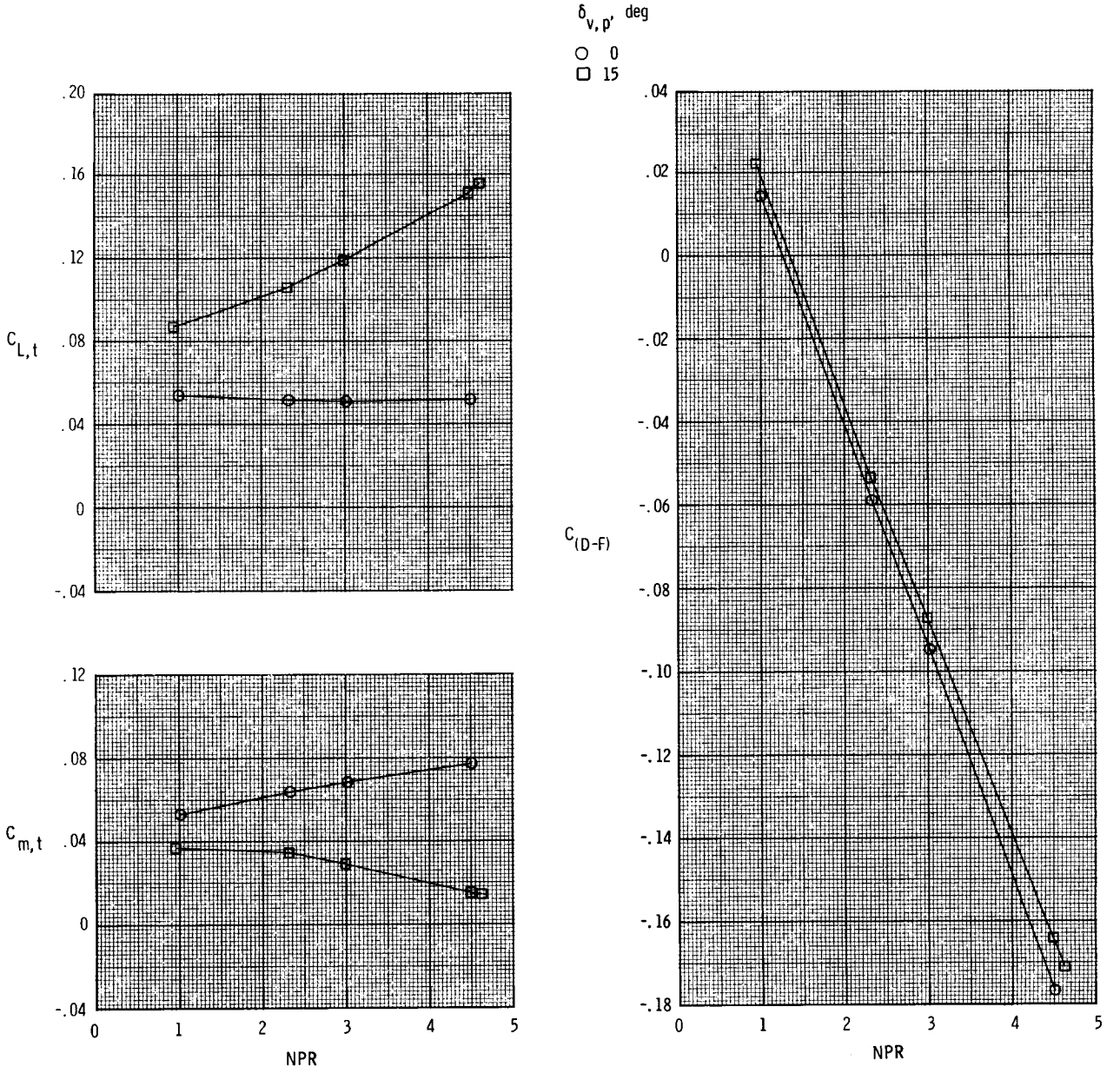

(b) $M = 0.60$.

Figure 16. Continued.

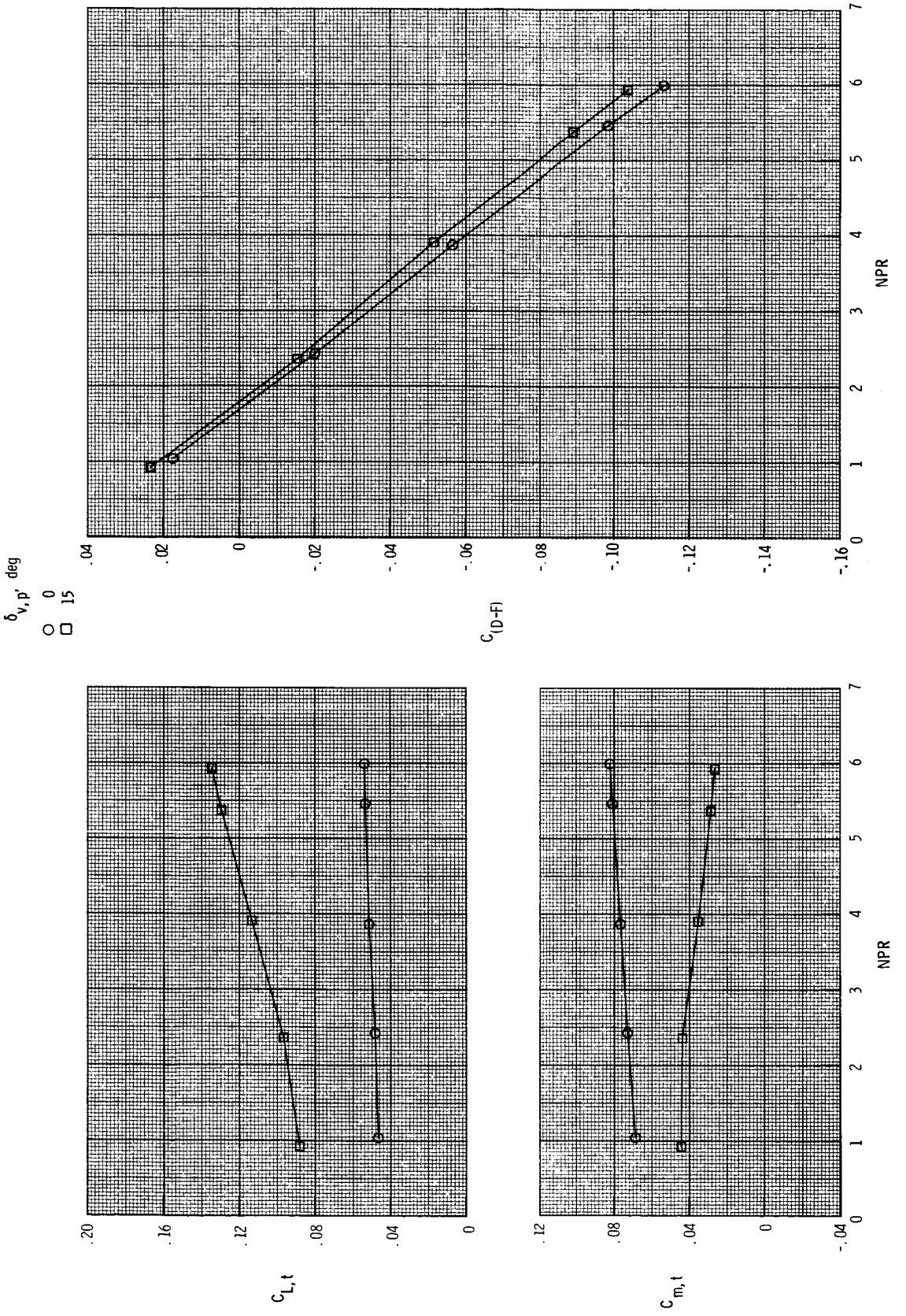

(c) $M = 0.87$.

Figure 16. Continued.

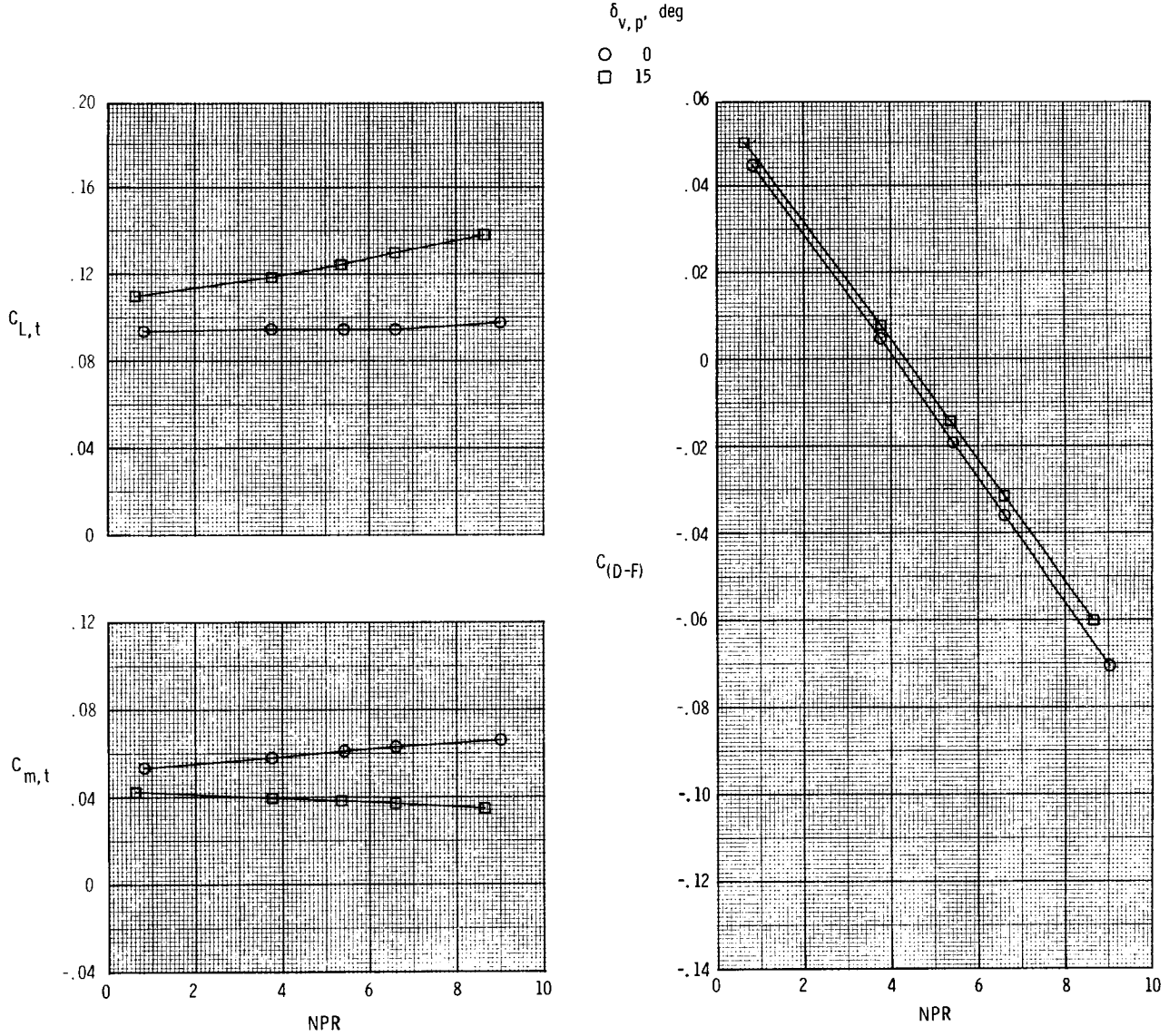

(d) $M = 1.20$.

Figure 16. Continued.

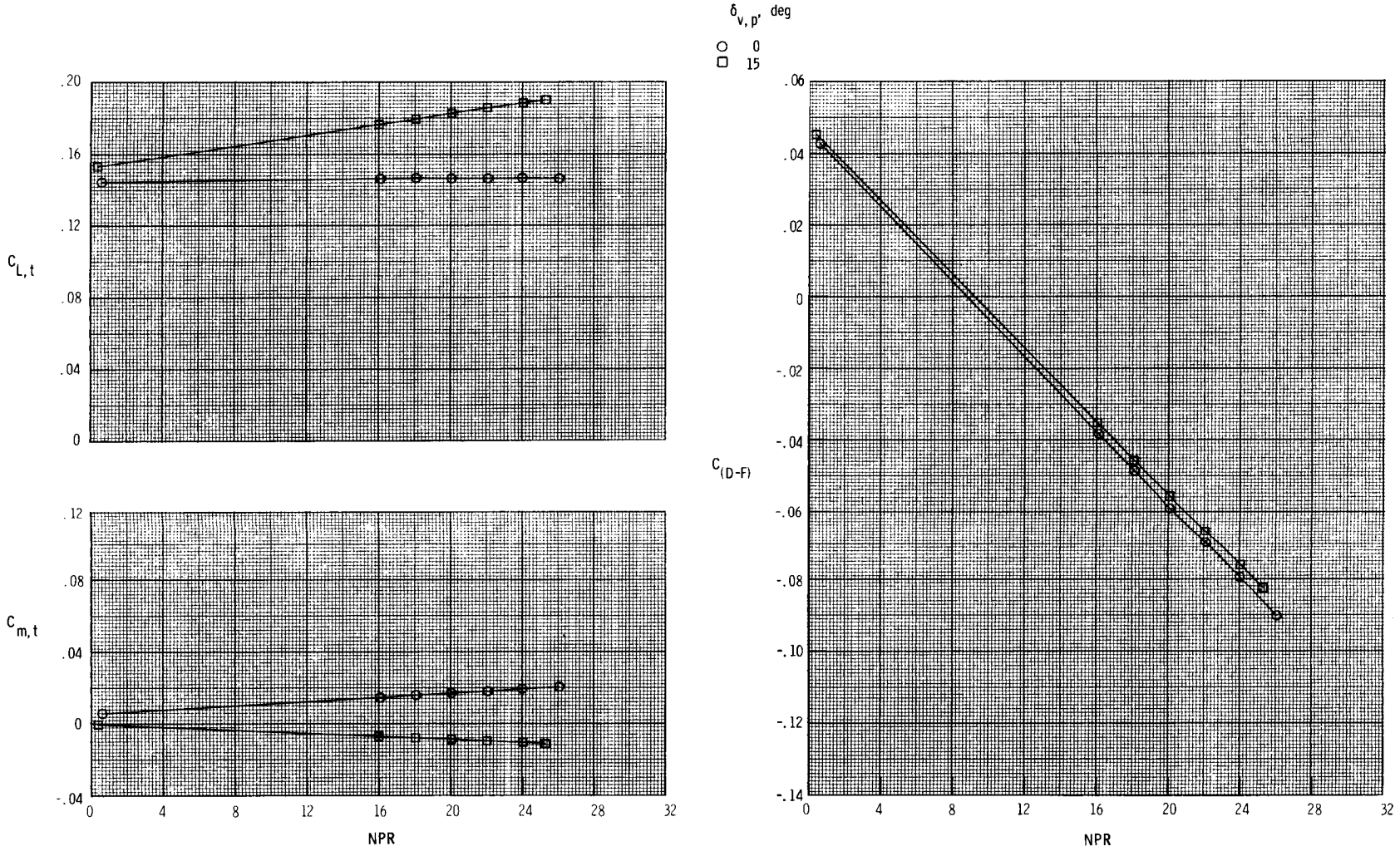

(e) $M = 2.00$.

Figure 16. Continued.

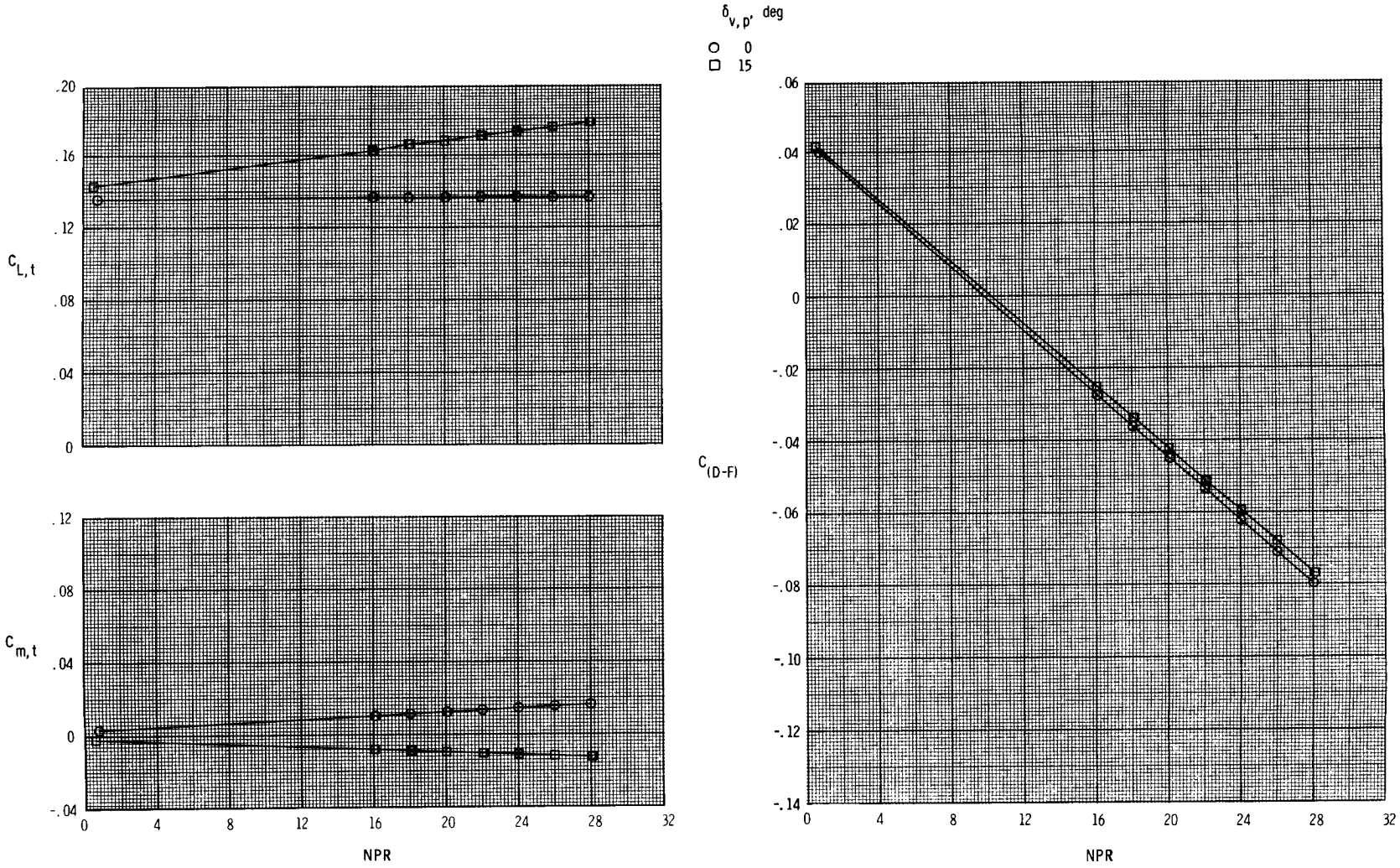

(f) $M = 2.17$.

Figure 16. Continued.

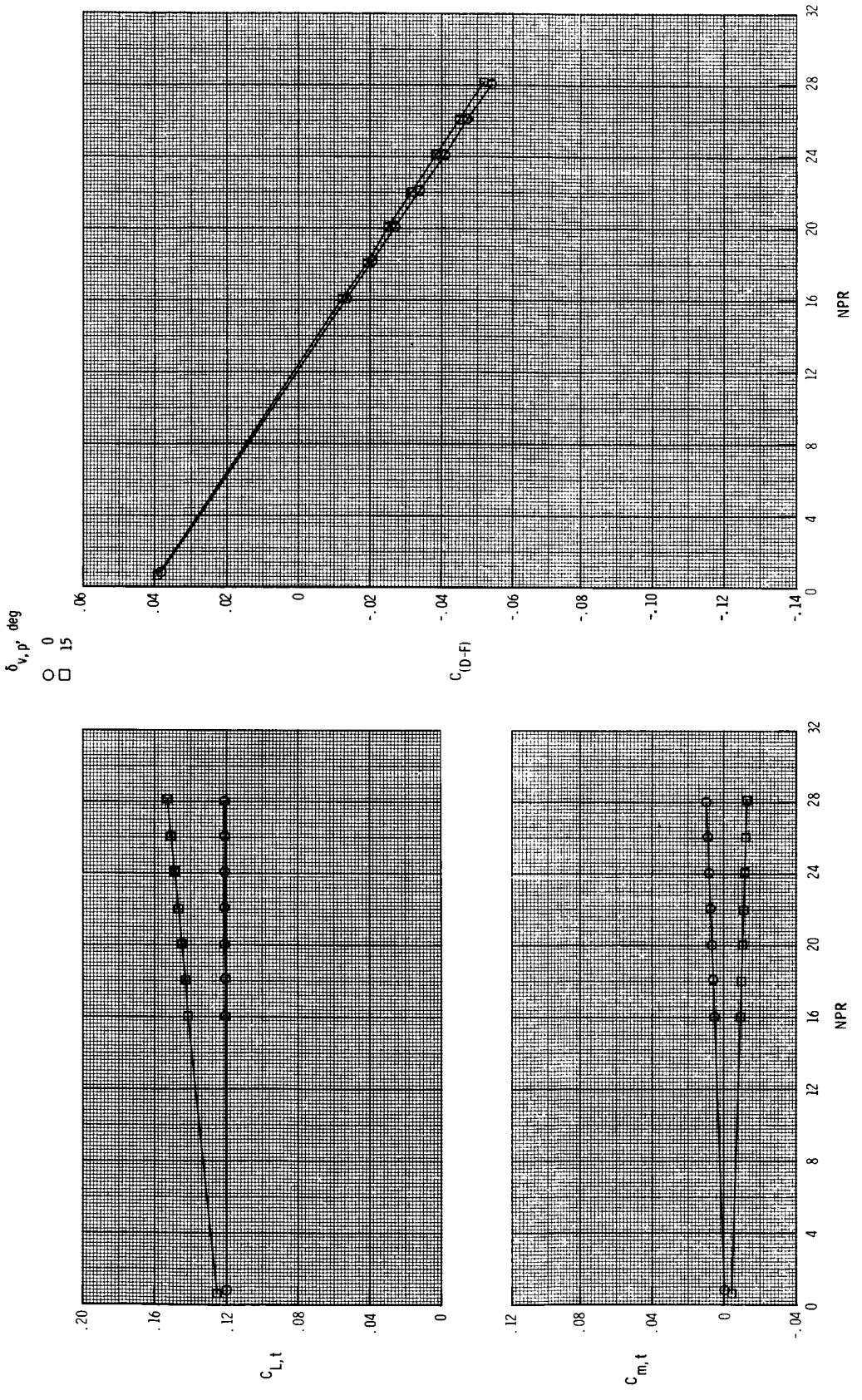

(g) $M = 2.47$.

Figure 16. Concluded.

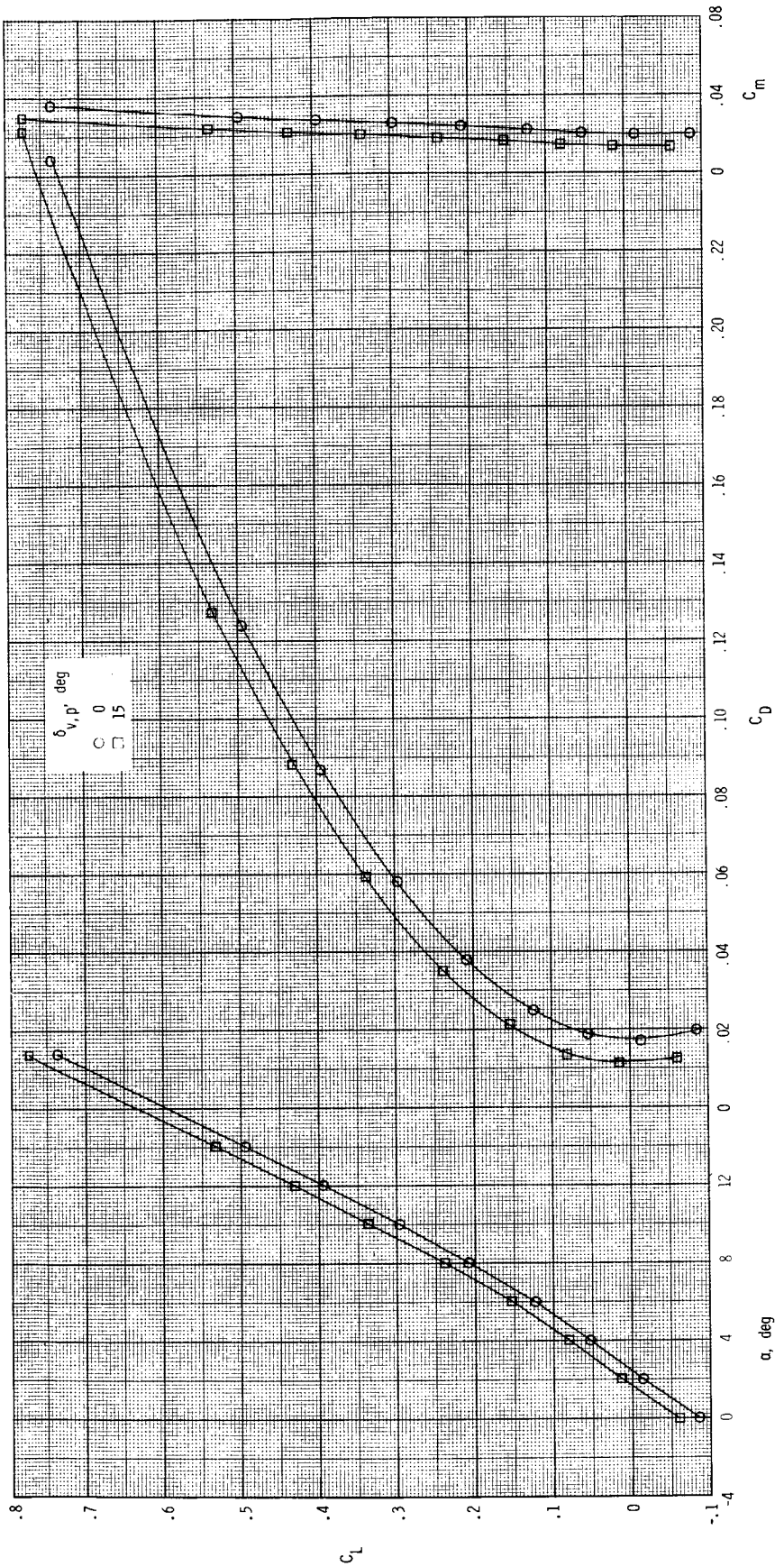

(a) $M = 0.20$; NPR $= 1.0$.

Figure 17. Effect of symmetric pitch vectoring on total longitudinal aerodynamic characteristics for $\delta_{v,y} = 0°$.

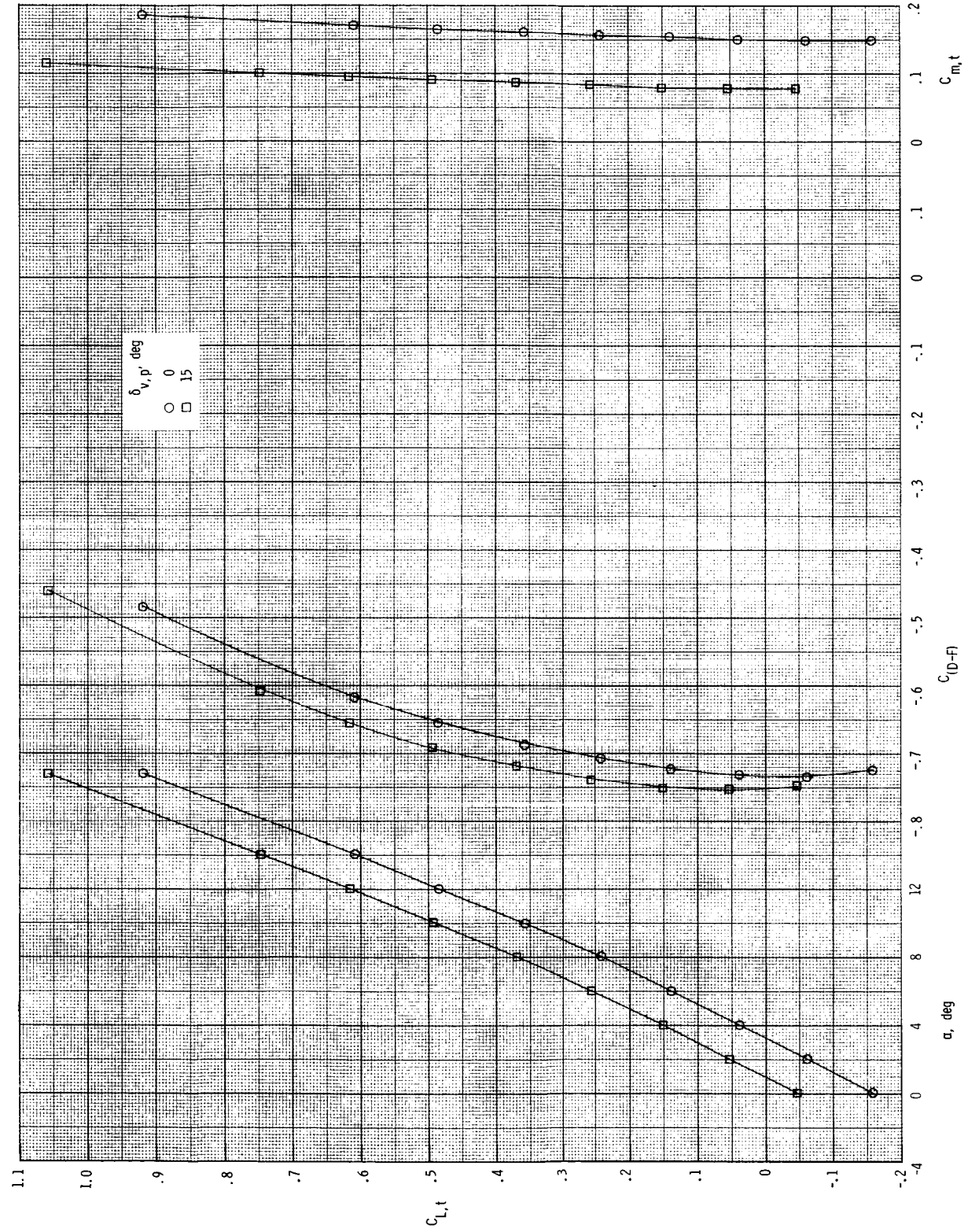

(b) $M = 0.20$; NPR = 2.5.

Figure 17. Continued.

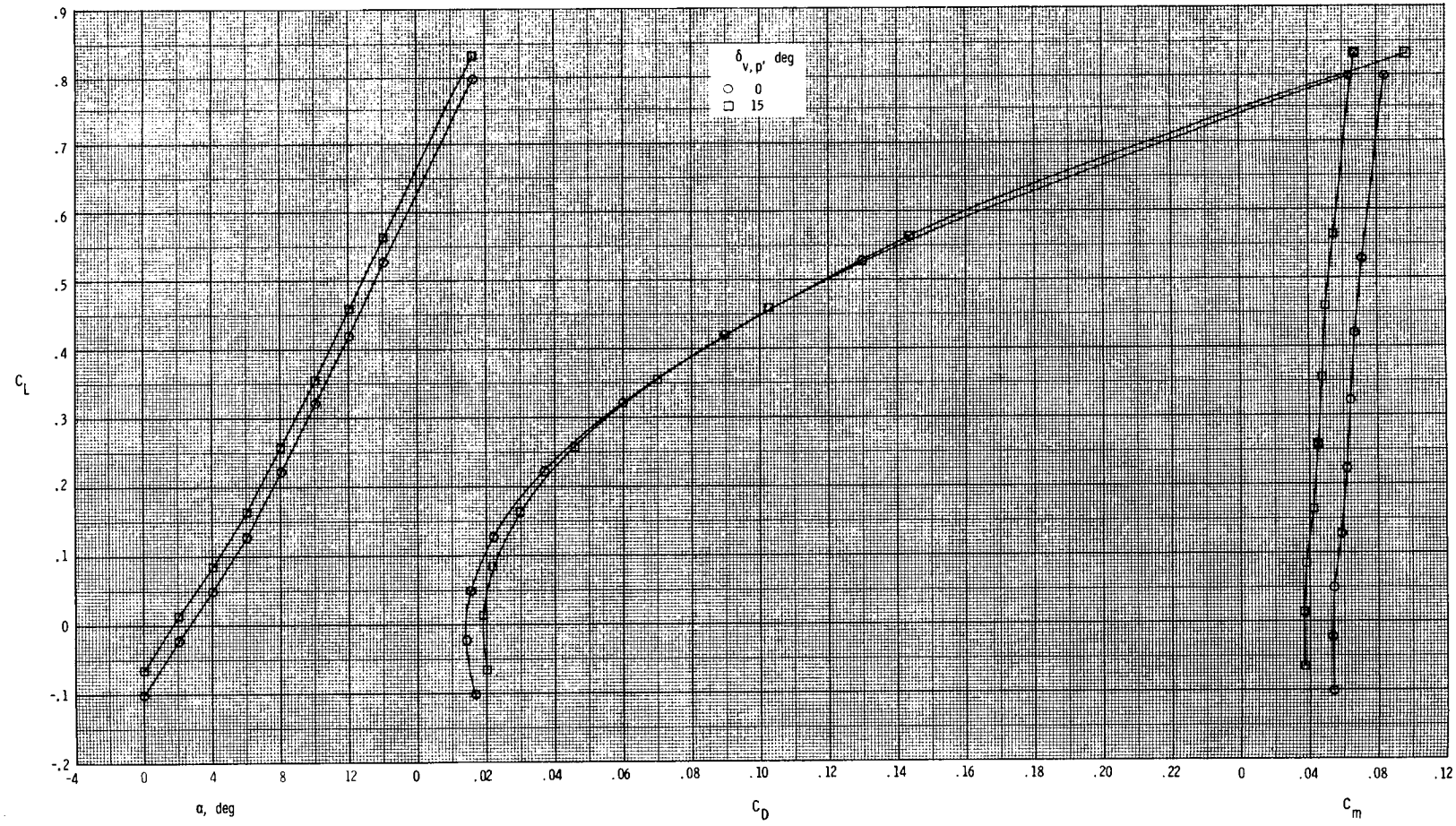

(c) $M = 0.60$; NPR = 1.0.

Figure 17. Continued.

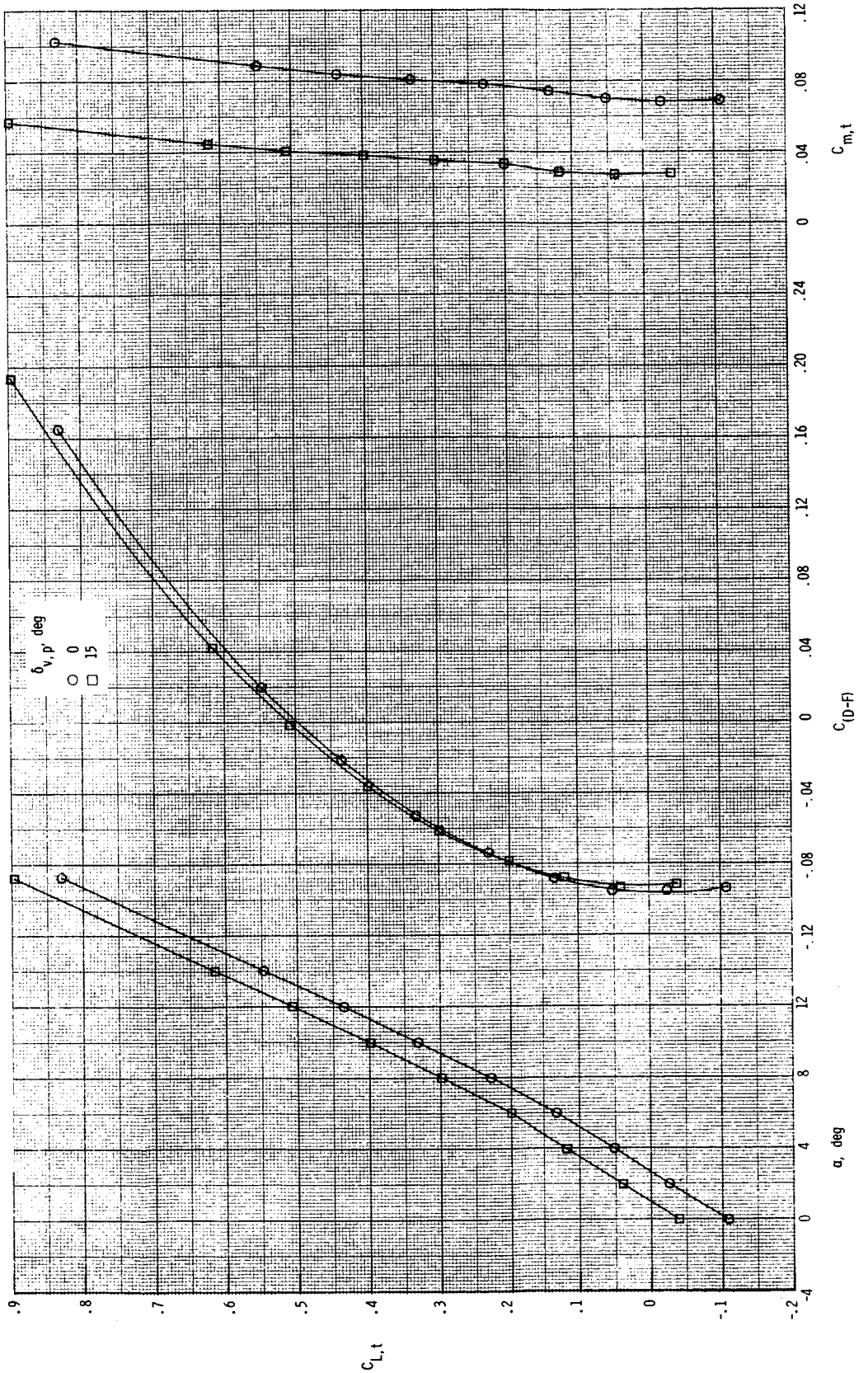

(d) $M = 0.60$; NPR $= 3.0$.

Figure 17. Continued.

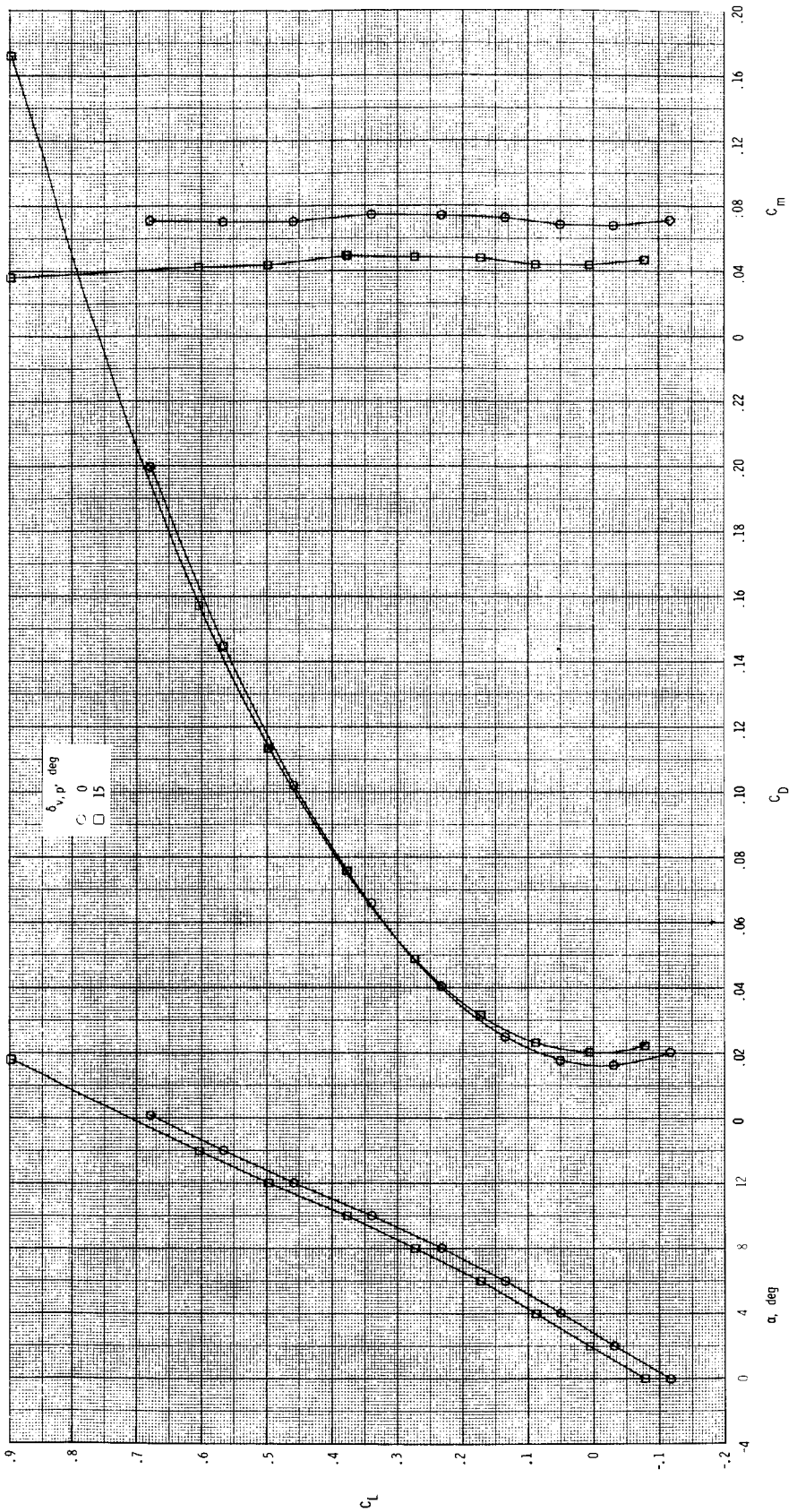

(e) $M = 0.87$; NPR = 1.0.

Figure 17. Continued.

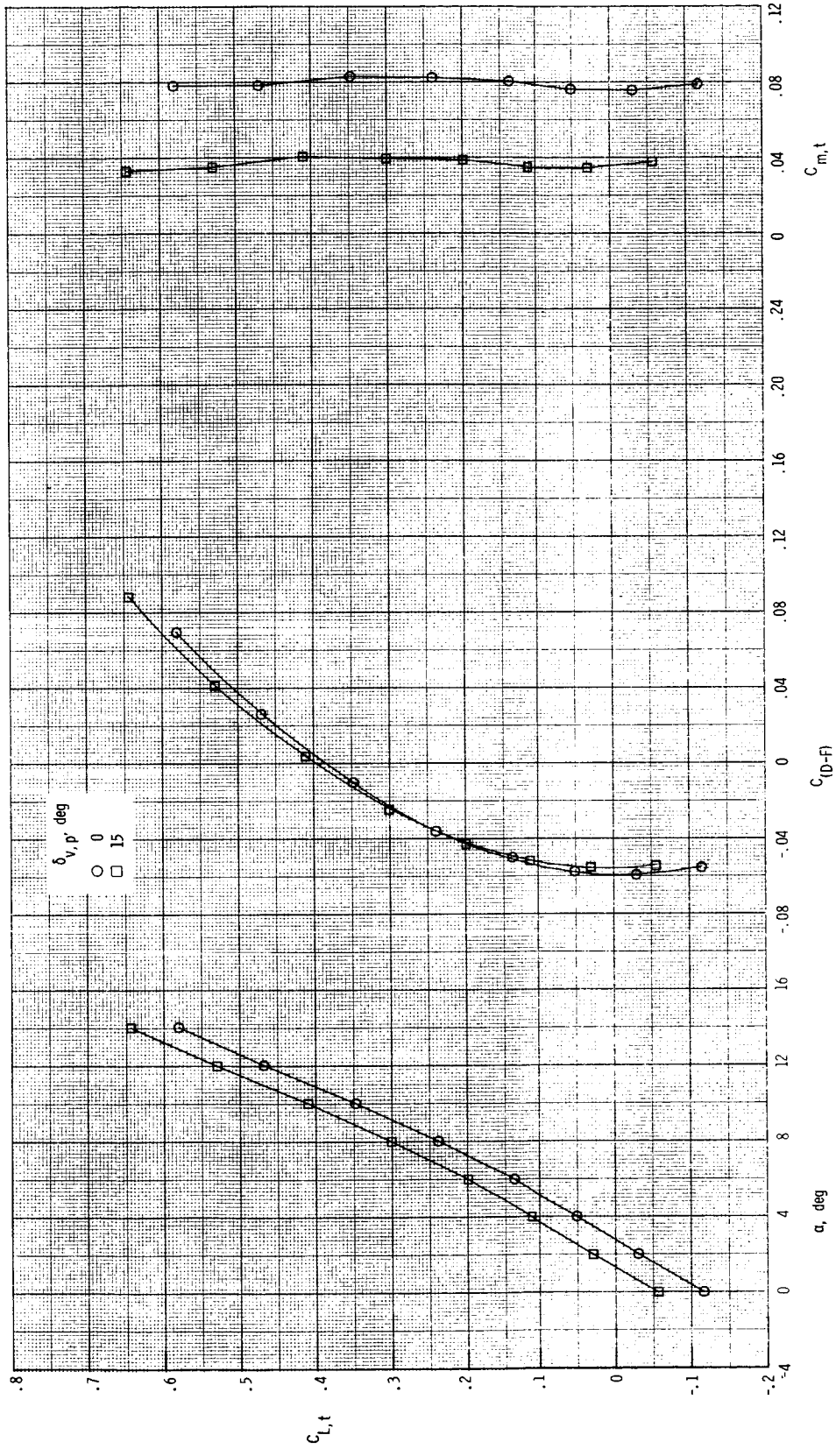

(f) $M = 0.87$; NPR $= 3.9$.

Figure 17. Continued.

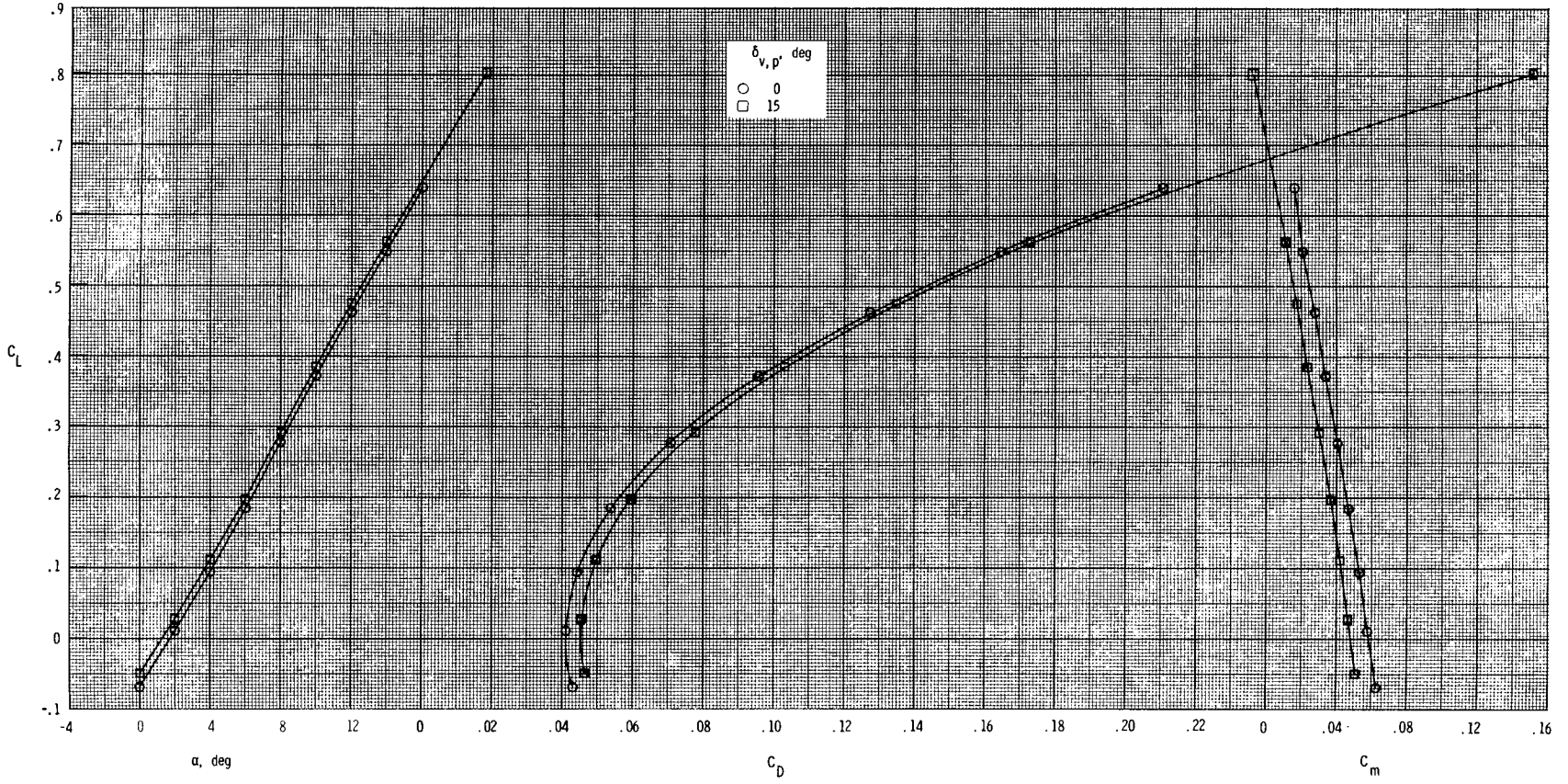

(g) $M = 1.20$; NPR = 1.0.

Figure 17. Continued.

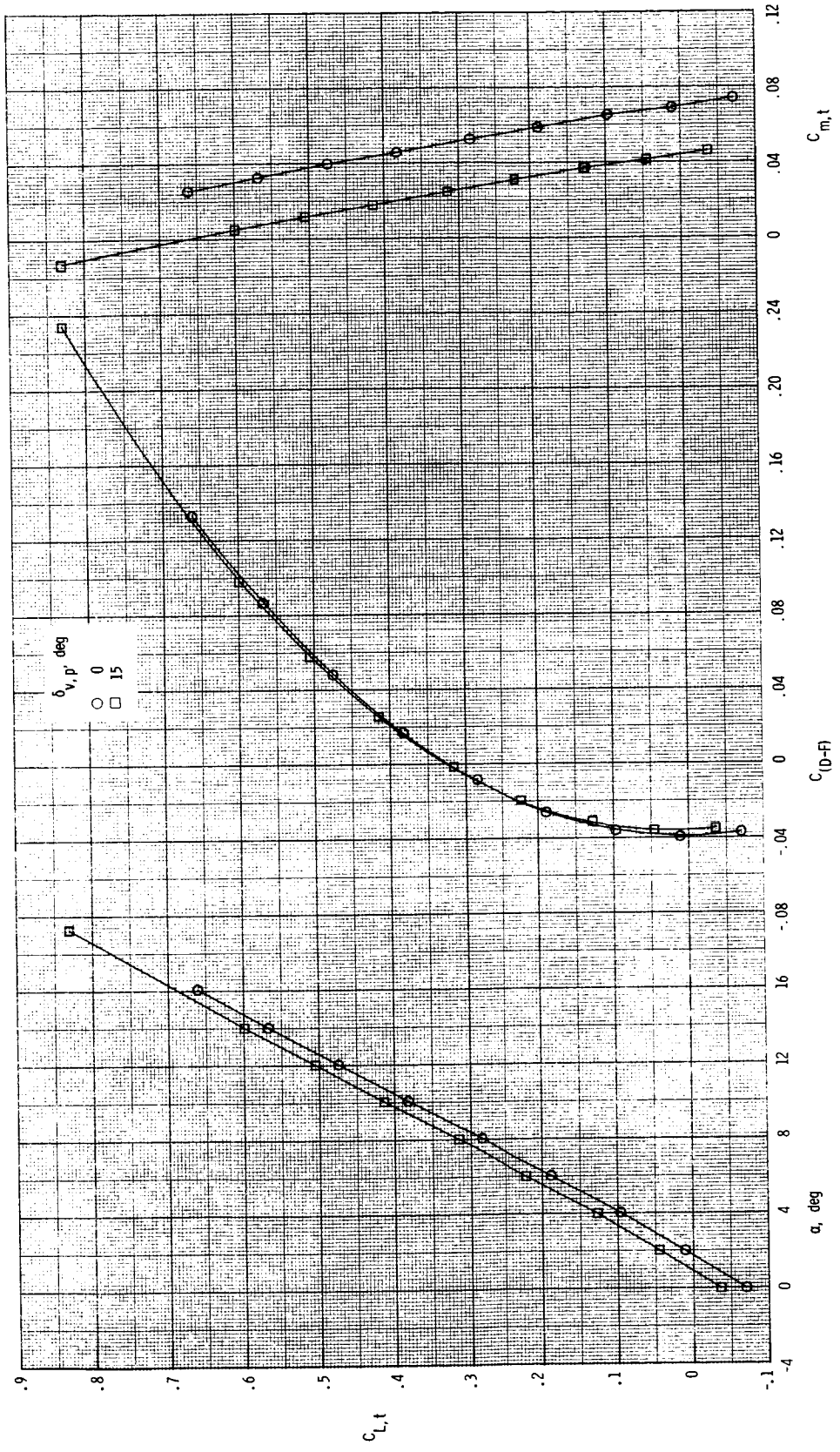

(h) $M = 1.20$; NPR = 6.6.

Figure 17. Continued.

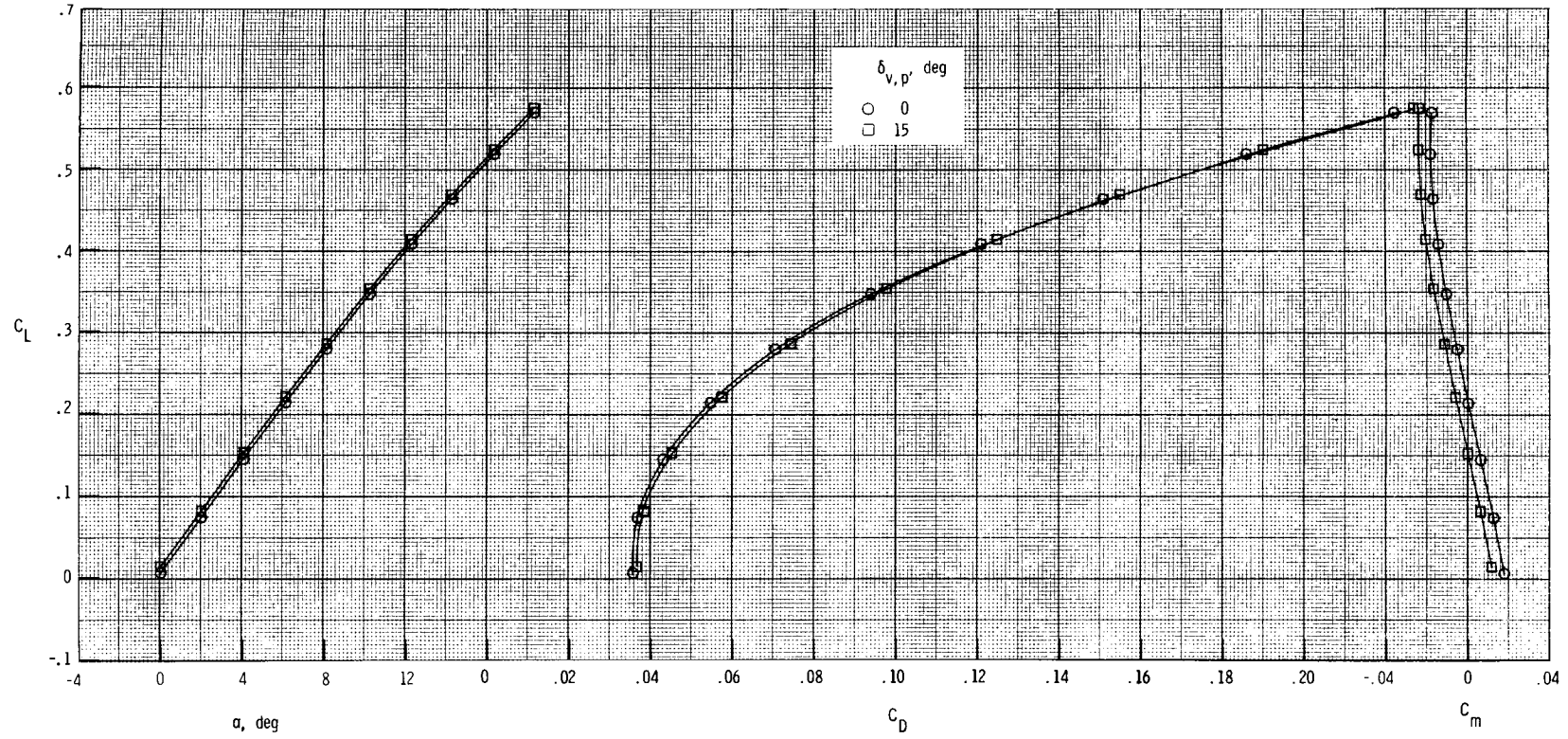

(i) $M = 2.00$; NPR = 1.0.

Figure 17. Continued.

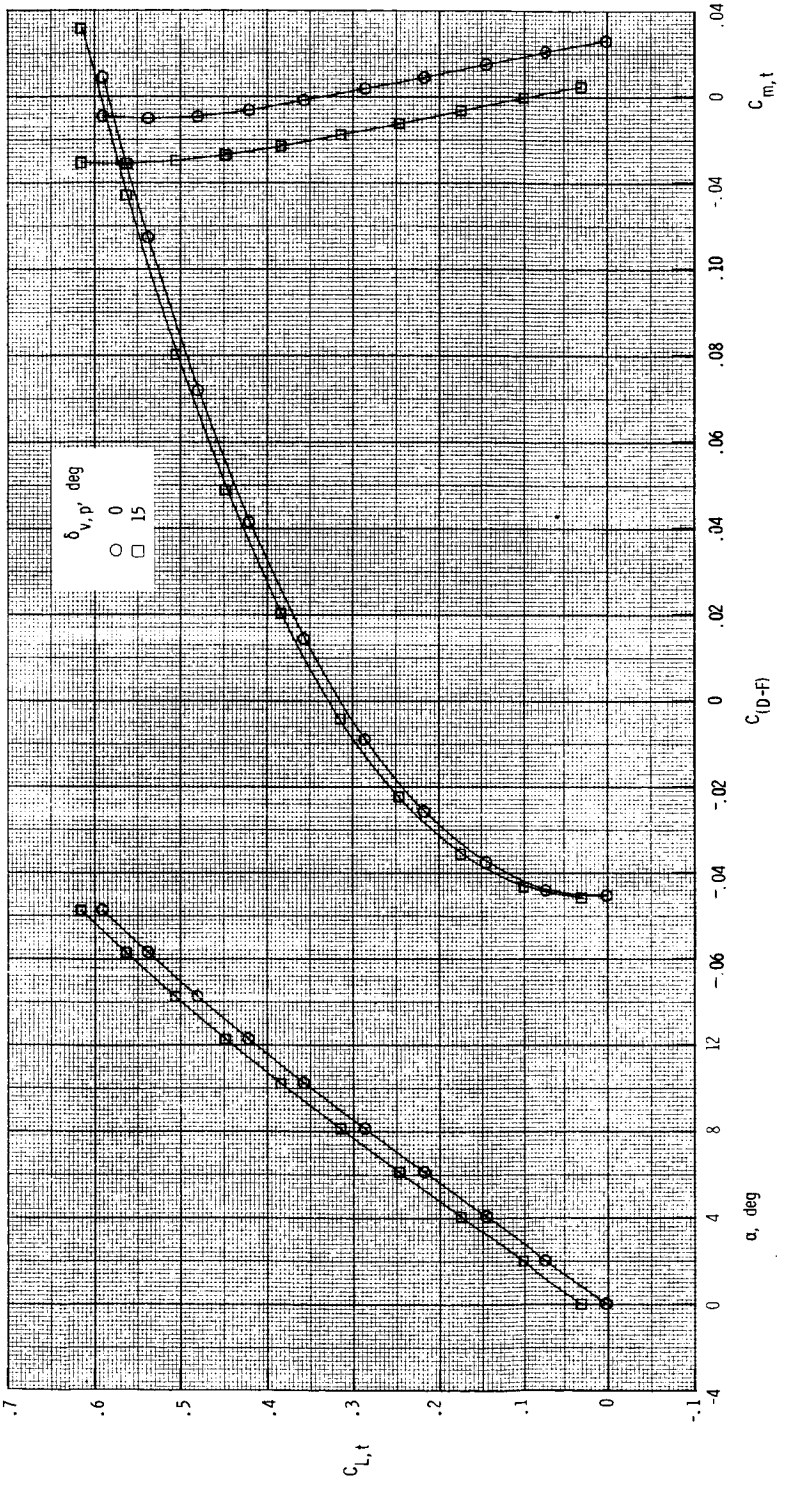

(j) $M = 2.00$; NPR $= 20.0$.

Figure 17. Continued.

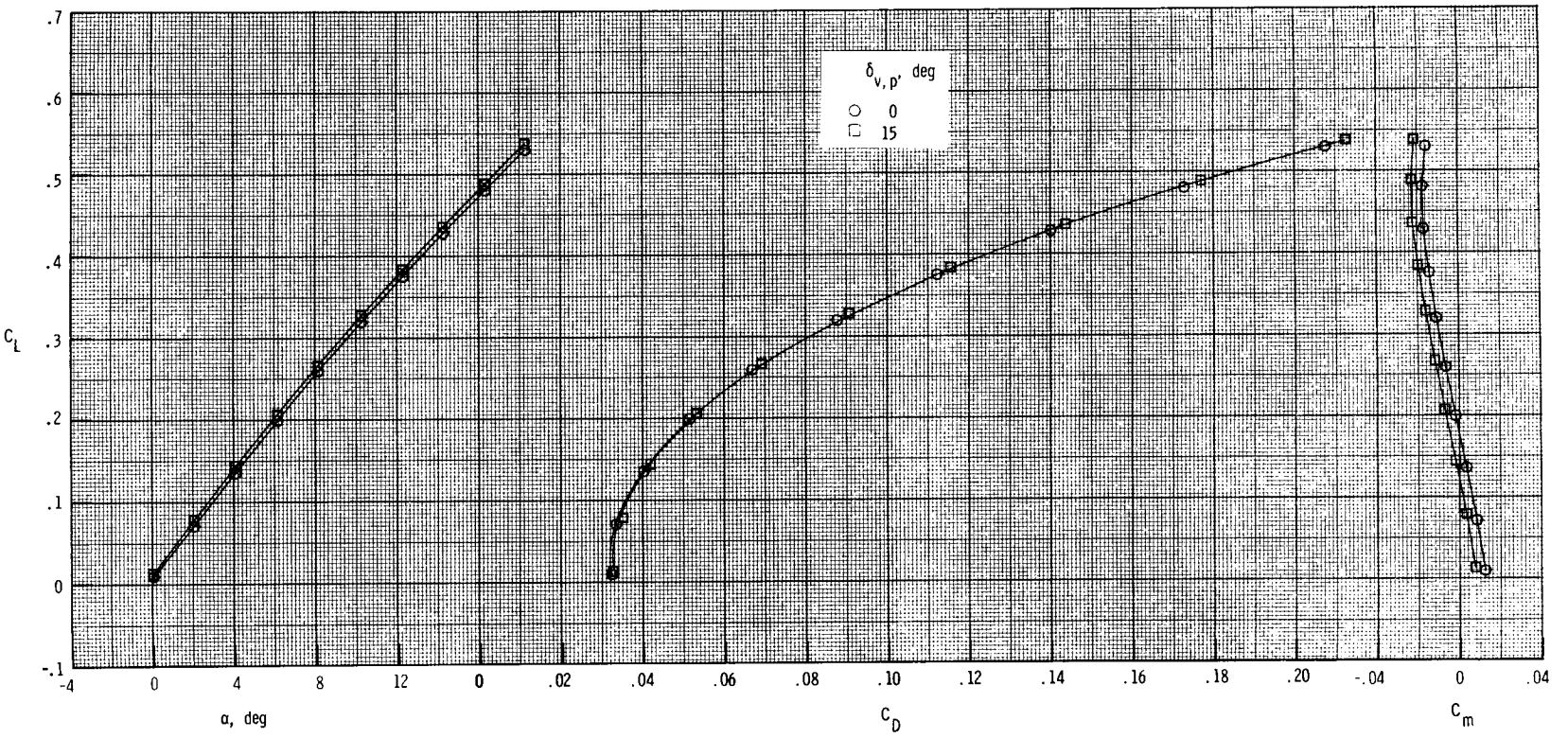

(k) $M = 2.17$; NPR = 1.0.

Figure 17. Continued.

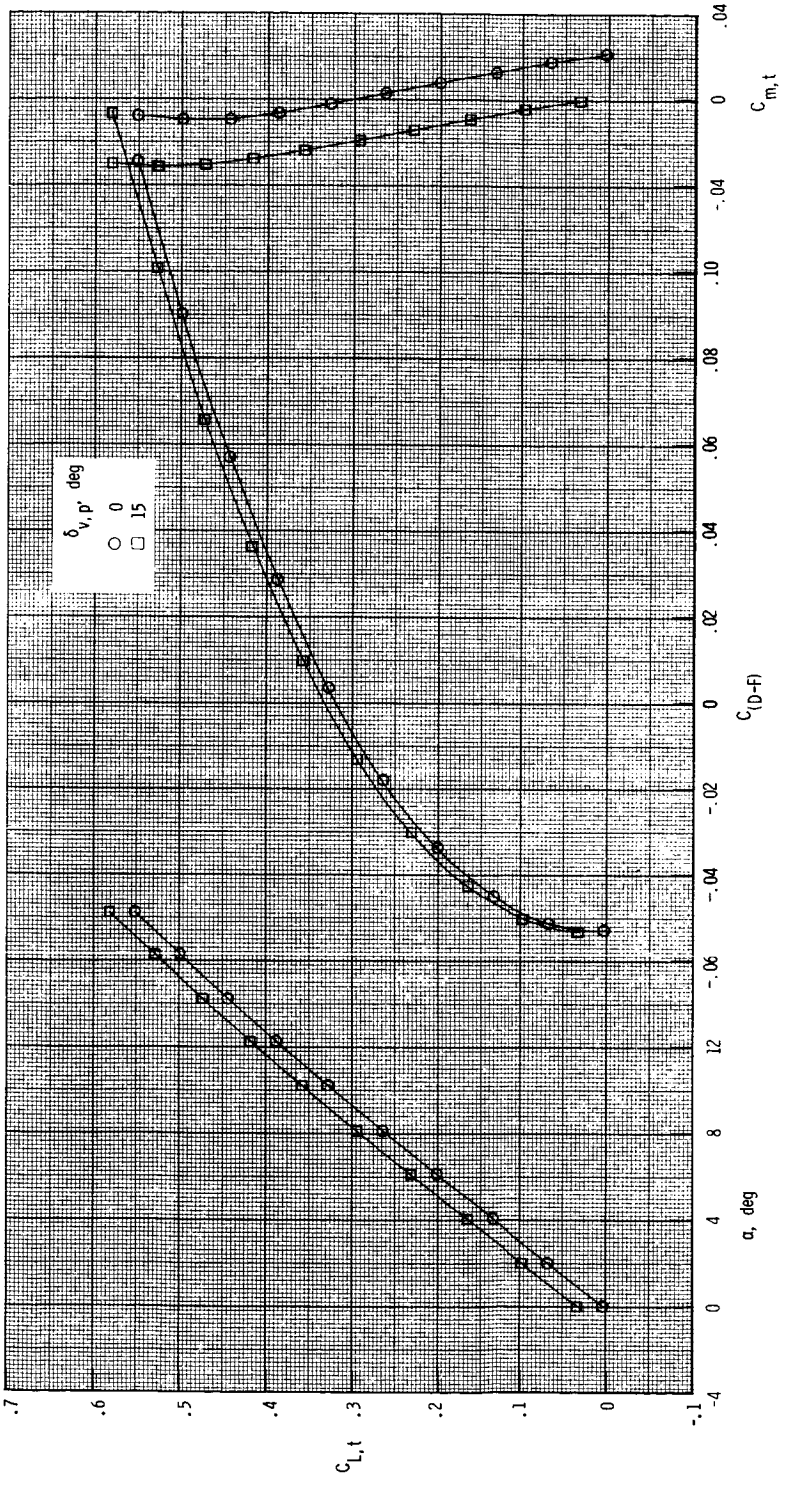

(l) $M = 2.17$; NPR = 20.0.

Figure 17. Continued.

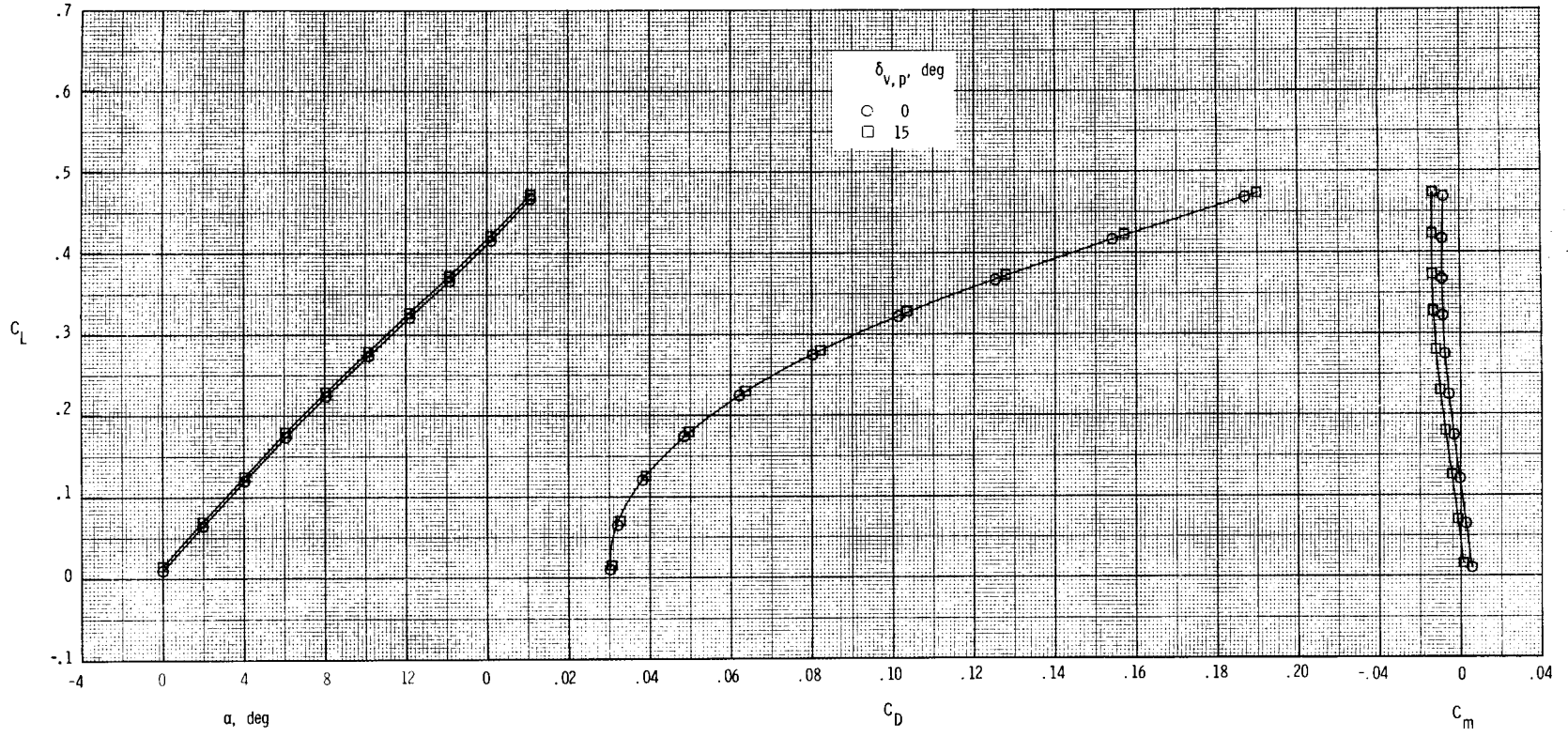

(m) $M = 2.47$; NPR = 1.0.

Figure 17. Continued.

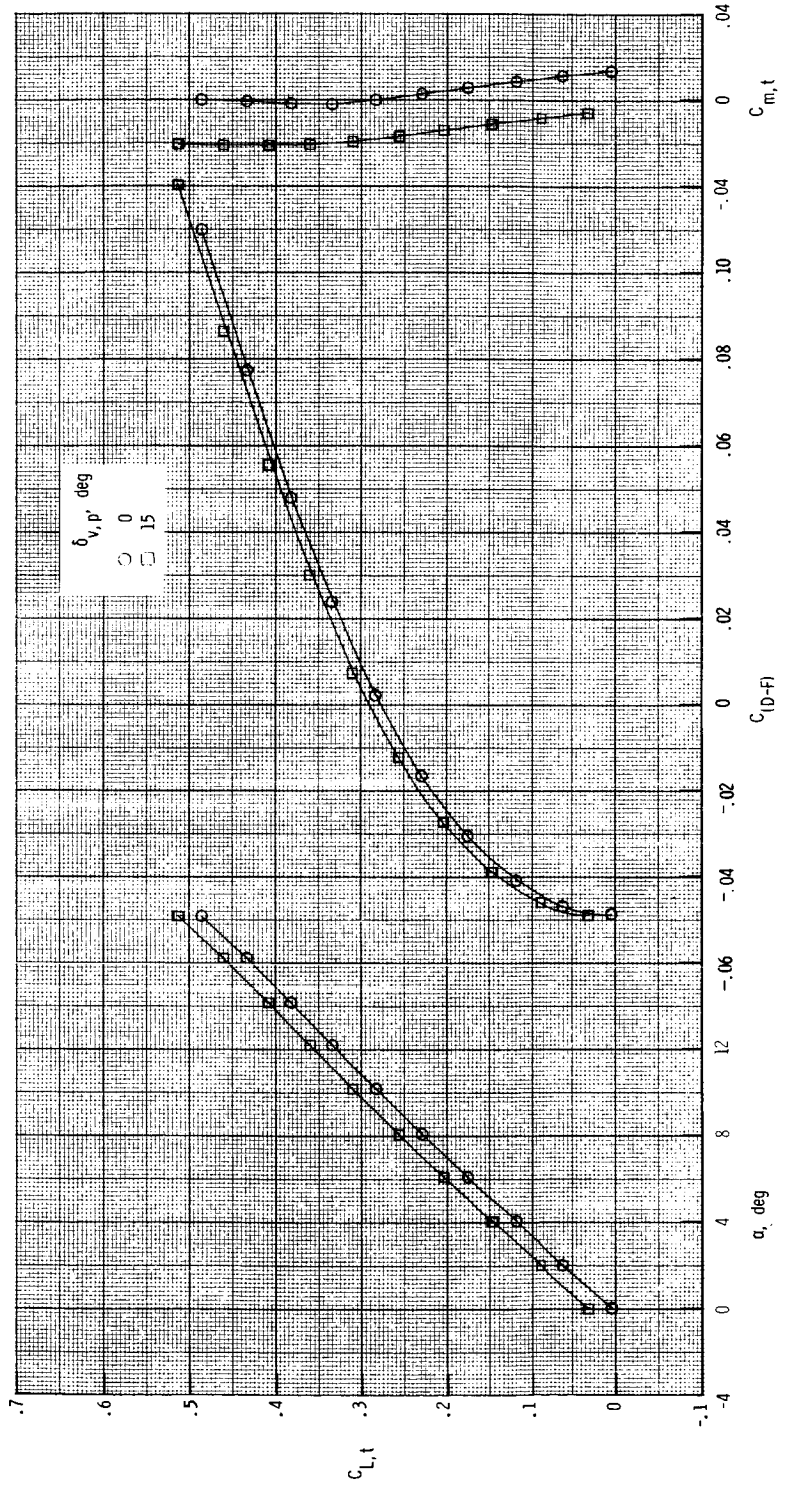

(n) $M = 2.47$; NPR = 24.0.

Figure 17. Concluded.

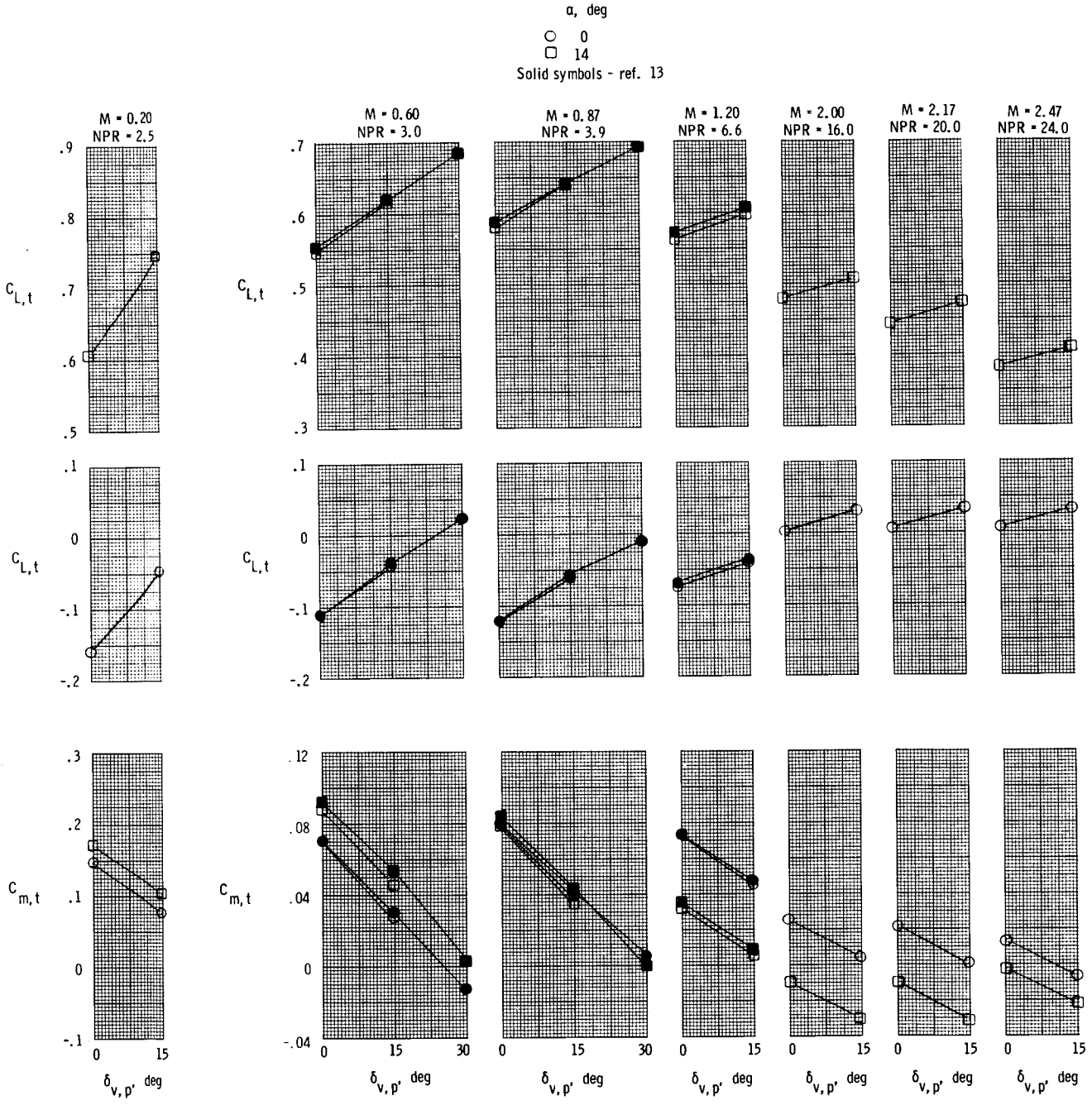

Figure 18. Summary of pitch vectoring for $\delta_{v,y} = 0°$.

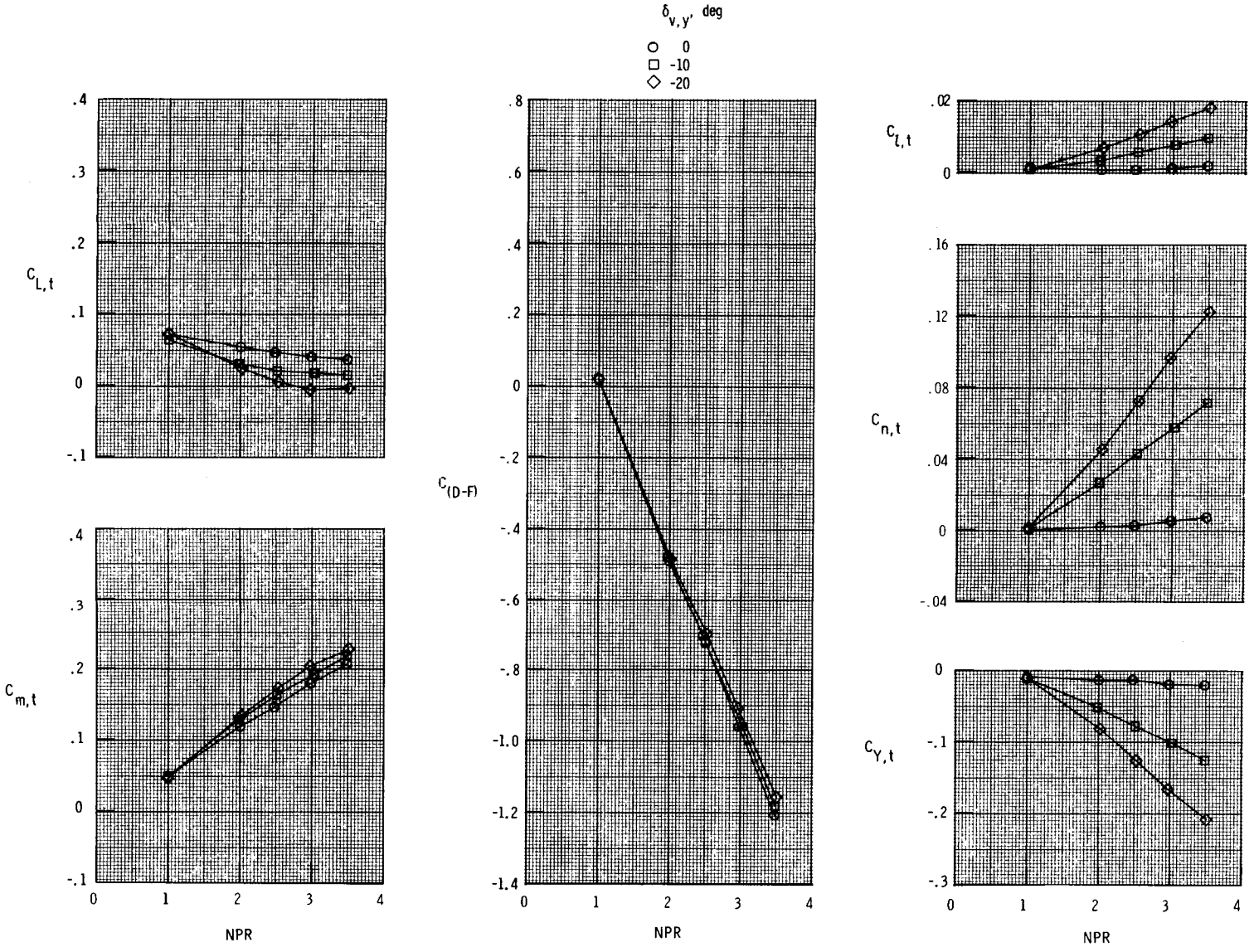

(a) $M = 0.20$.

Figure 19. Effect of nozzle pressure ratio and yaw vectoring on total aerodynamic characteristics for $\delta_{v,p} = 0°$ and $\alpha = 4°$.

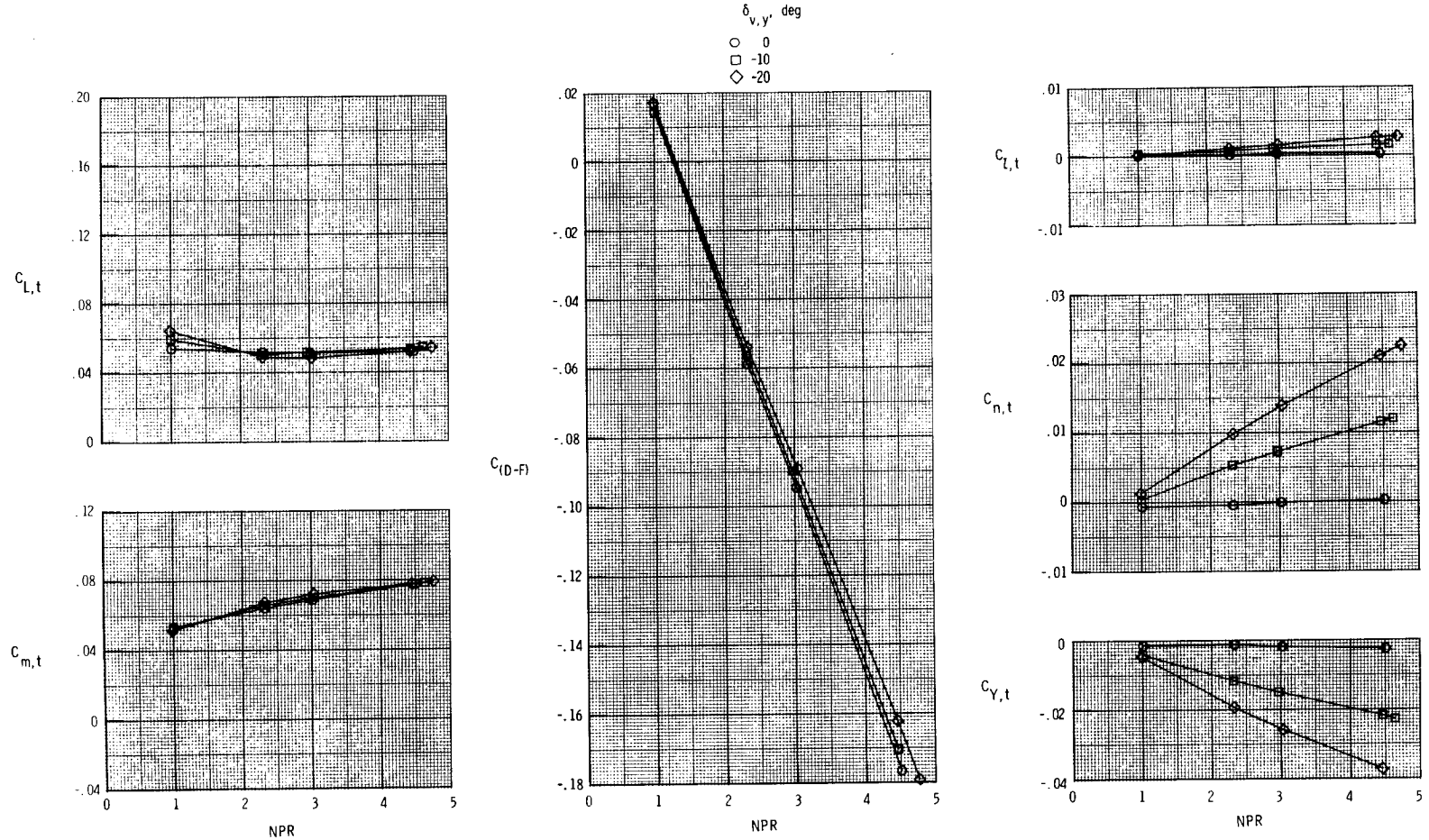

(b) $M = 0.60$.

Figure 19. Continued.

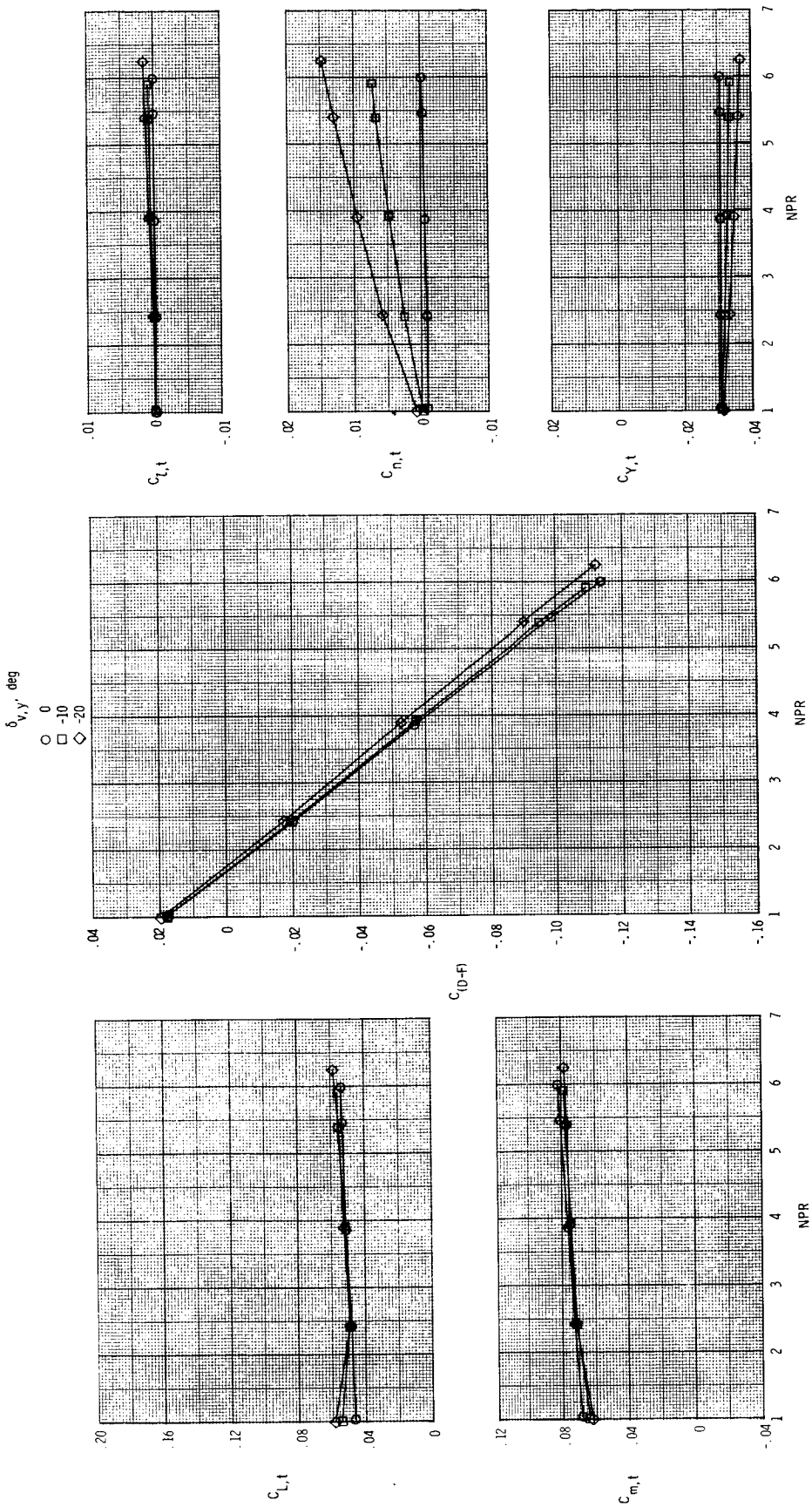

(c) $M = 0.87$.

Figure 19. Continued.

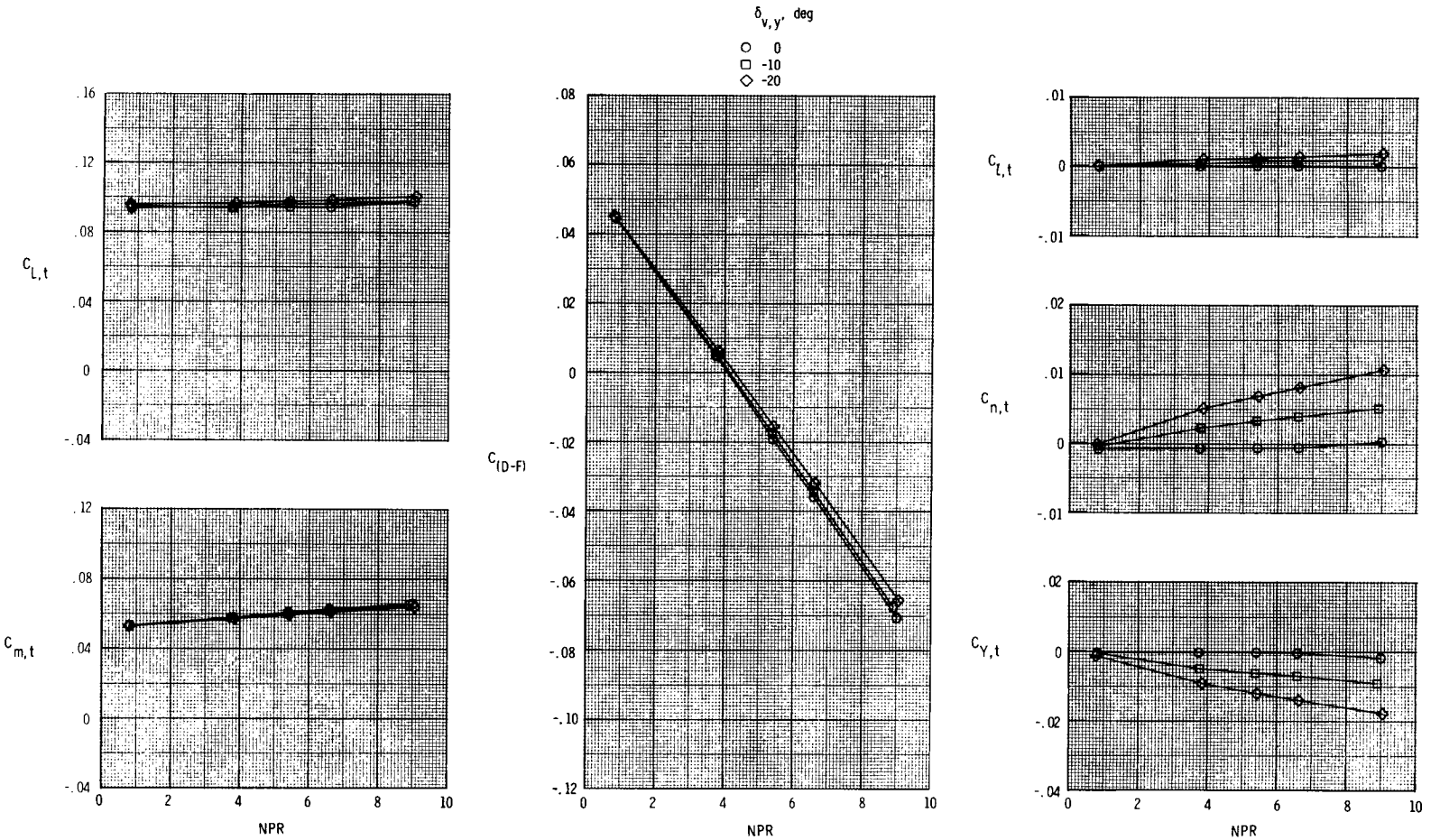

(d) $M = 1.20$.

Figure 19. Continued.

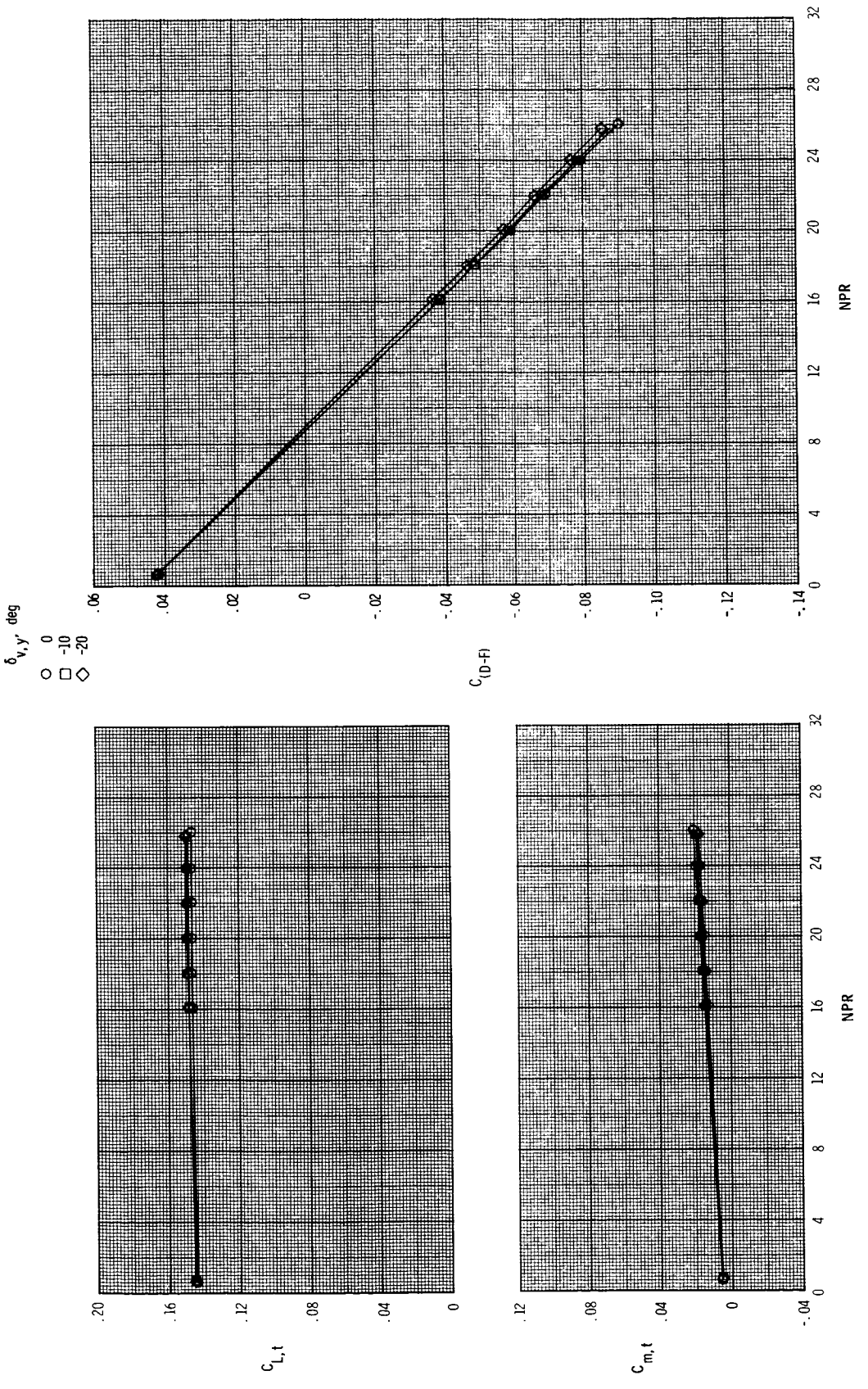

(e) $M = 2.00$.

Figure 19. Continued.

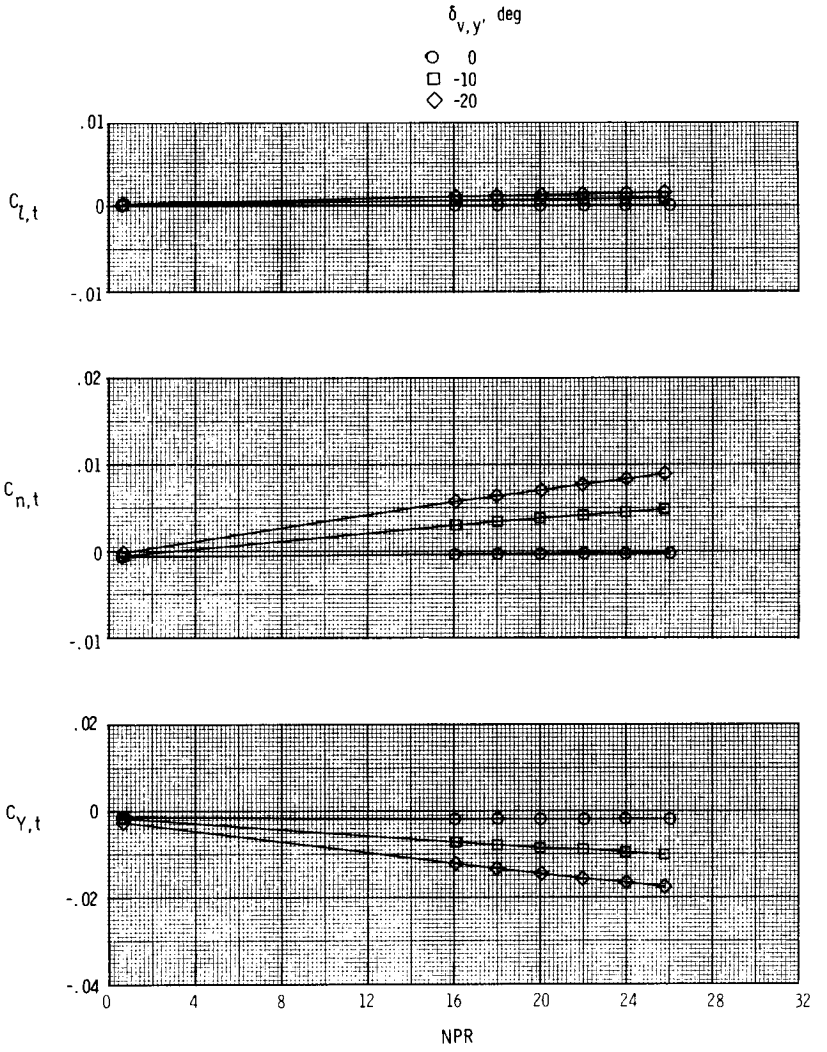

(e) Concluded.

Figure 19. Continued.

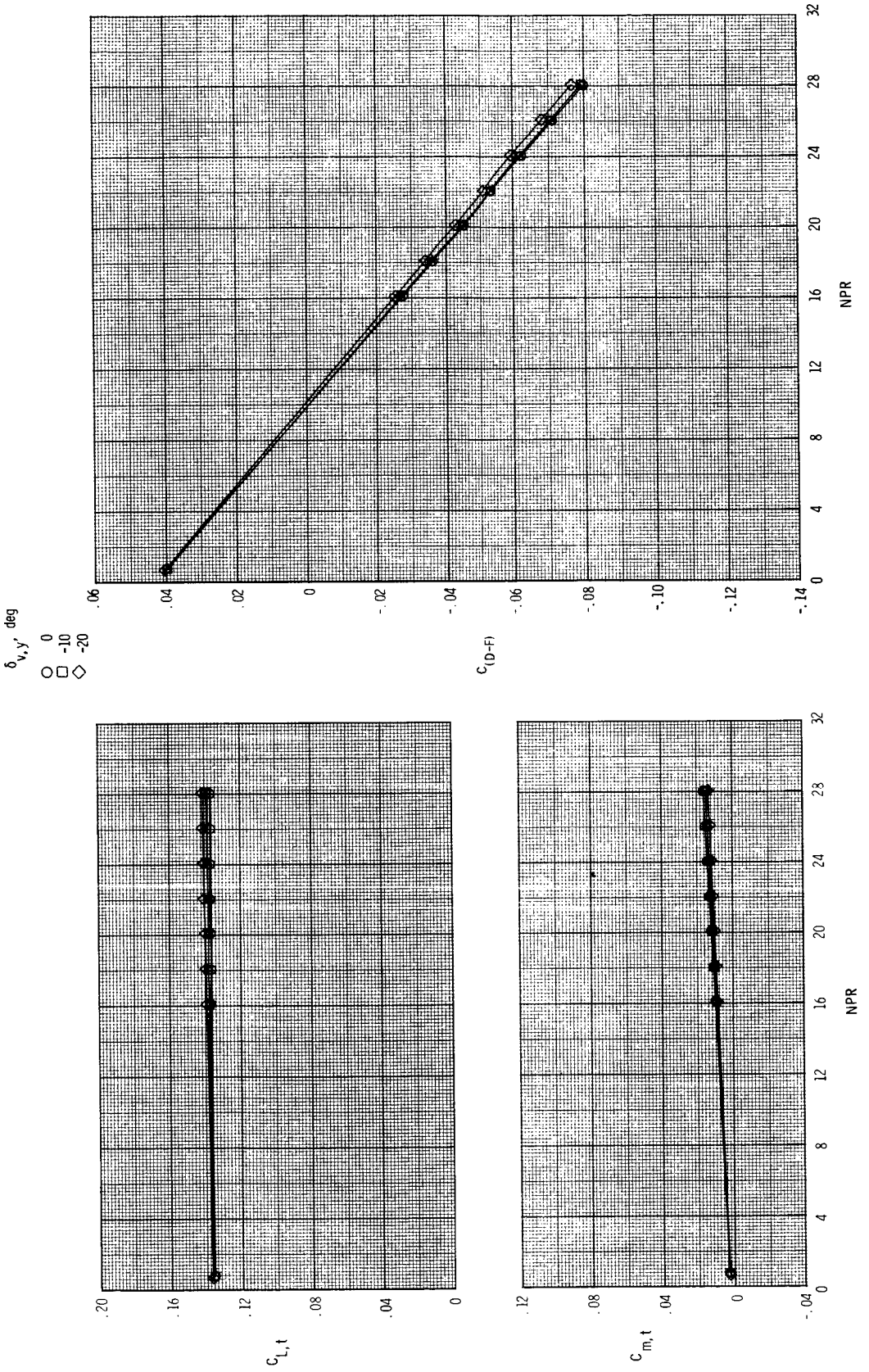

(f) $M = 2.17$.

Figure 19. Continued.

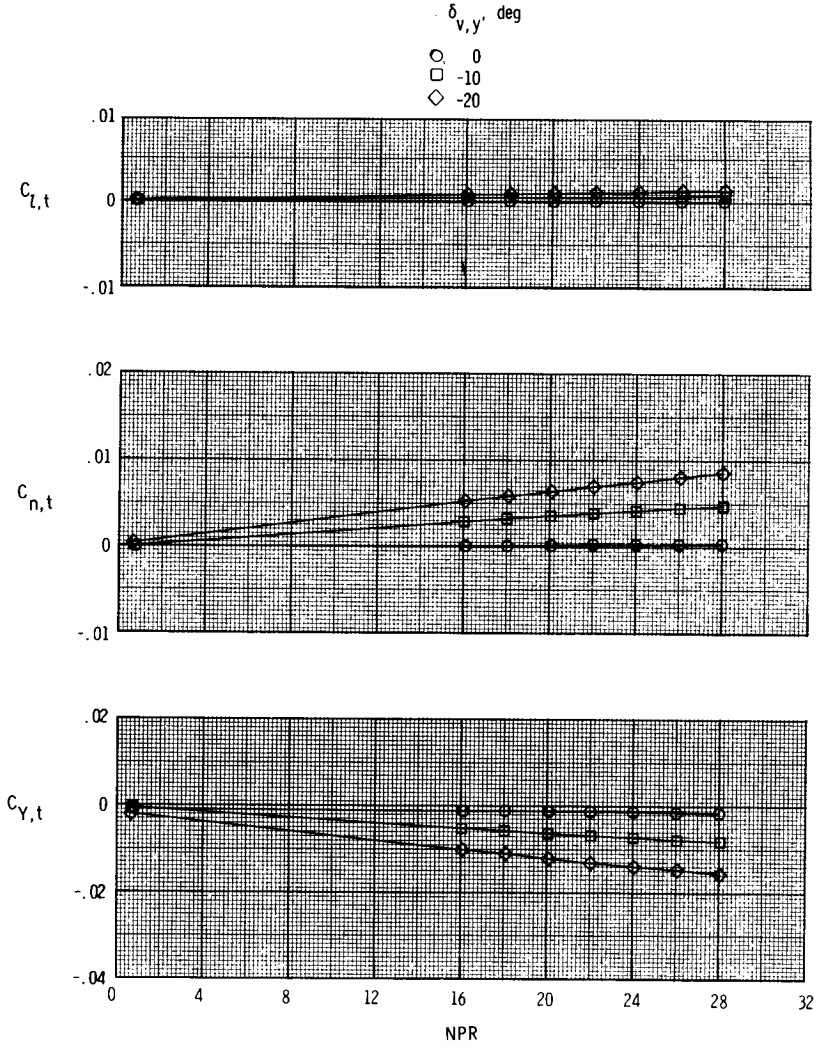

(f) Concluded.

Figure 19. Continued.

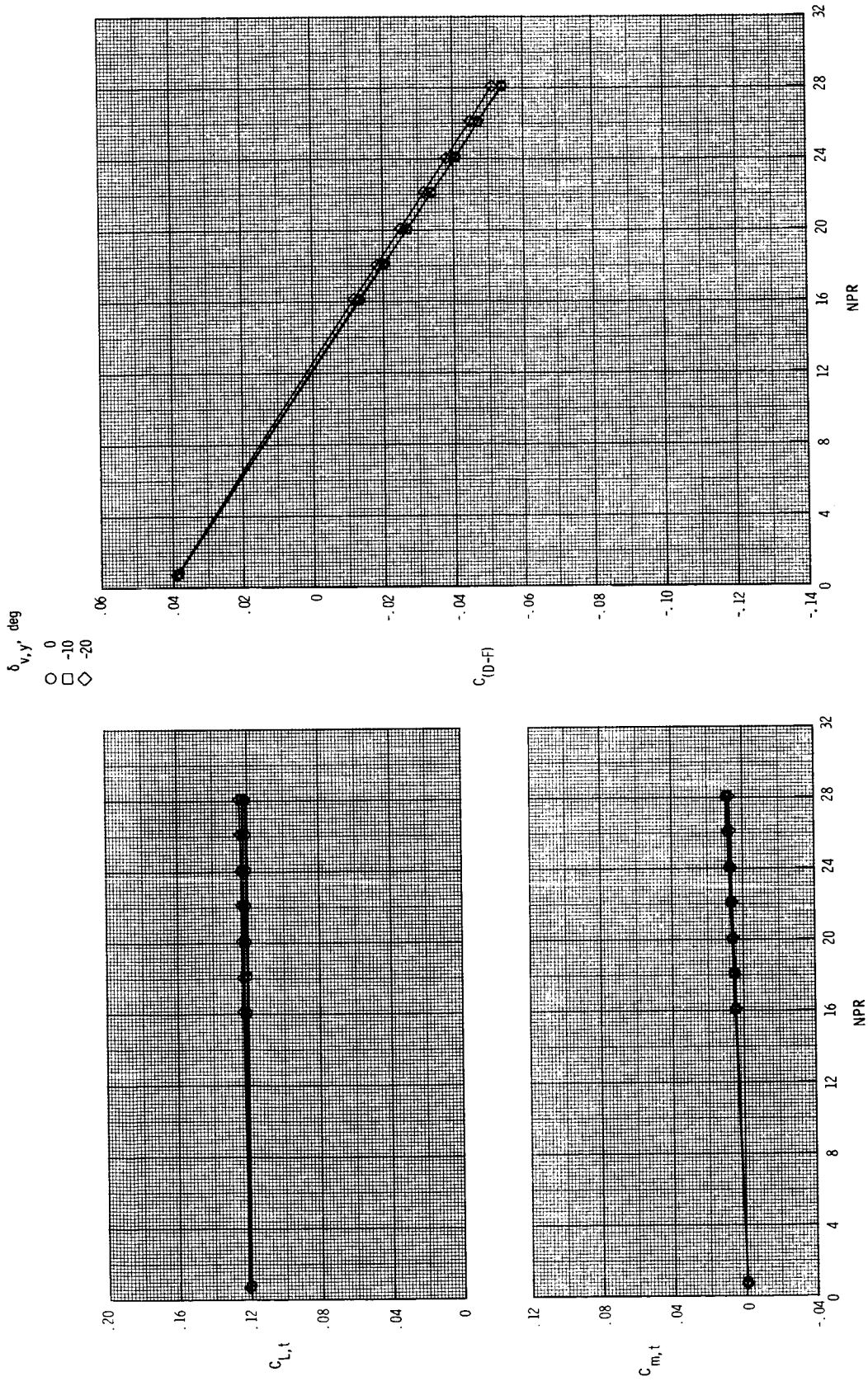

(g) $M = 2.47$.

Figure 19. Continued.

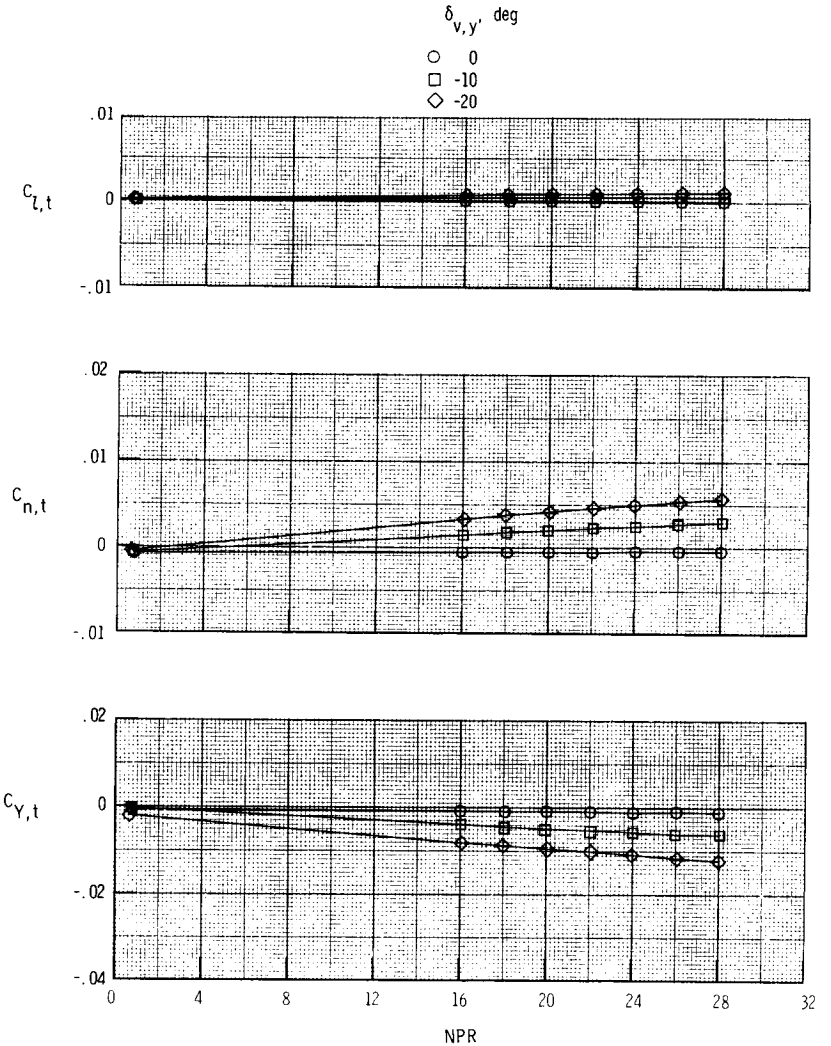

(g) Concluded.

Figure 19. Concluded.

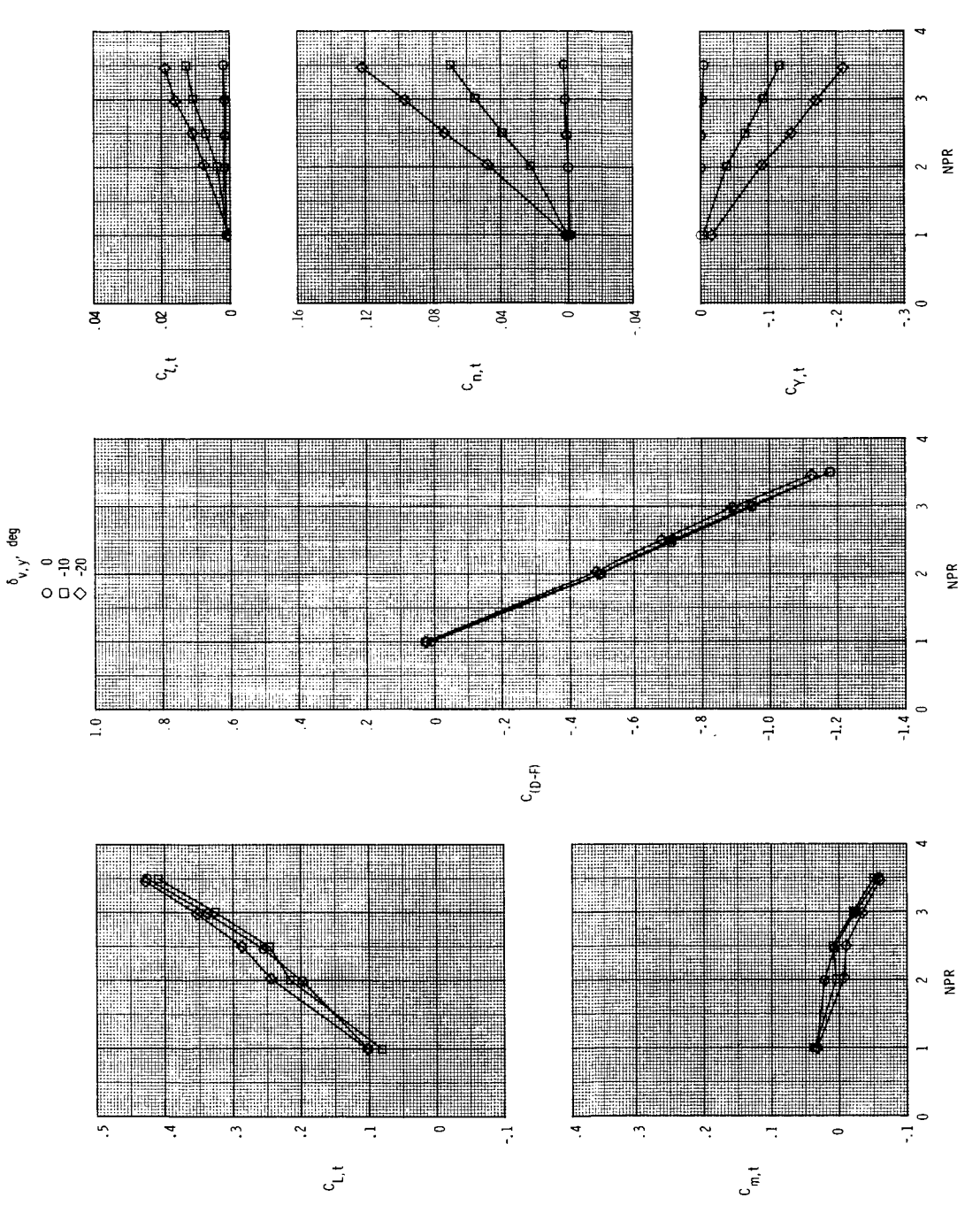

(a) $M = 0.20$.

Figure 20. Effect of nozzle pressure ratio and yaw vectoring on total aerodynamic characteristics for $\delta_{v,p} = 15°$ and $\alpha = 4°$.

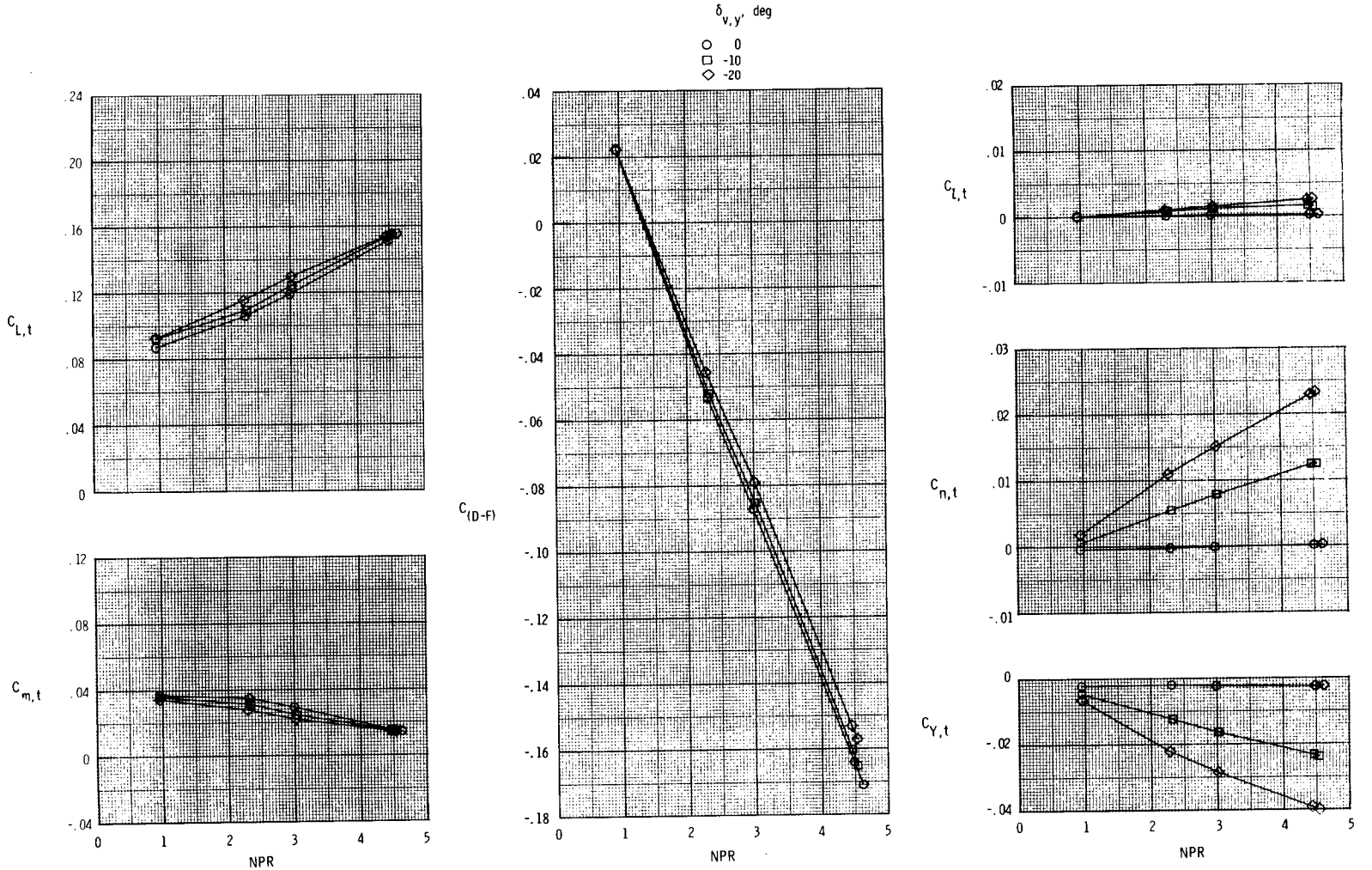

(b) $M = 0.60$.

Figure 20. Continued.

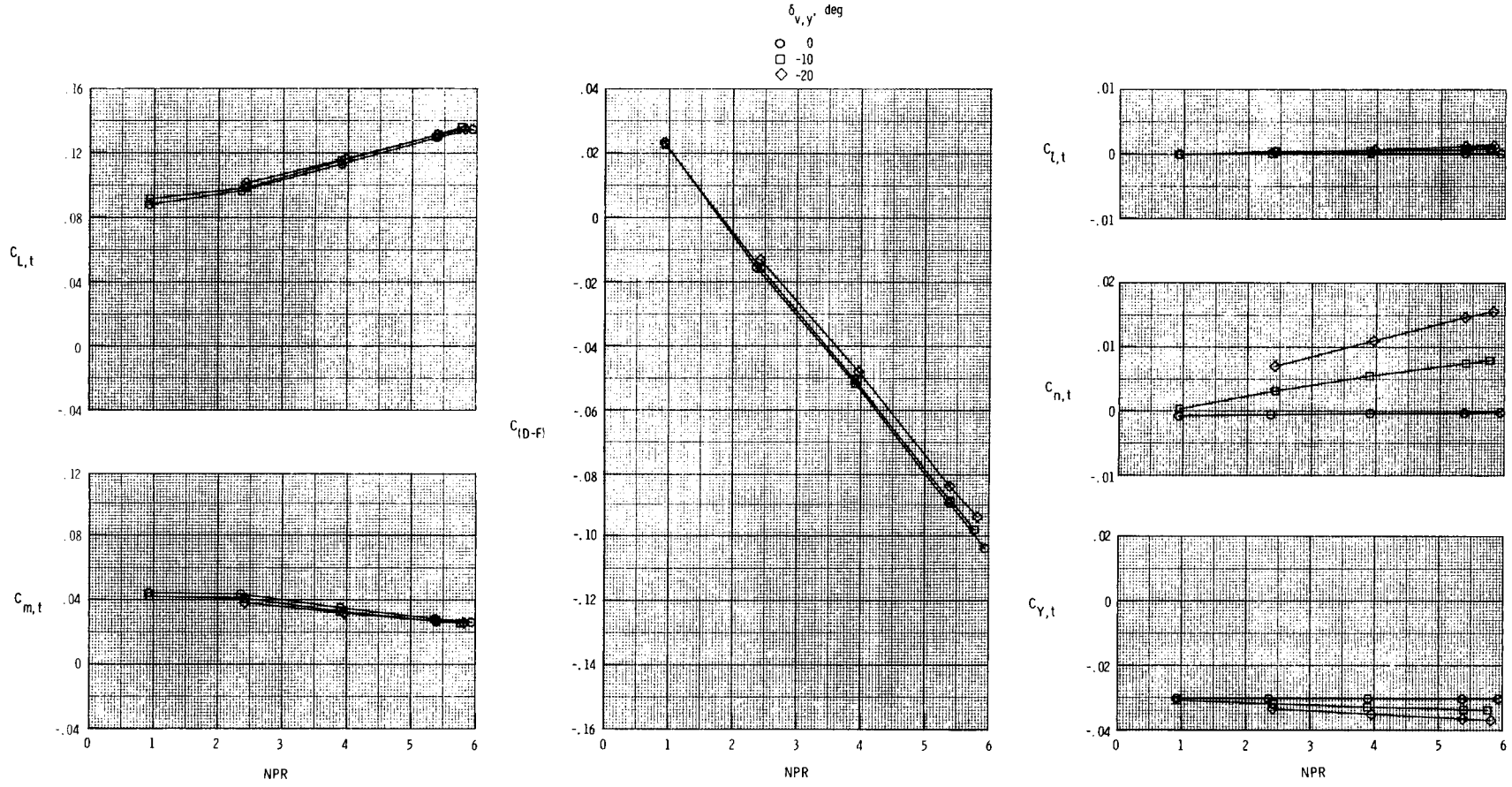

(c) $M = 0.87$.

Figure 20. Continued.

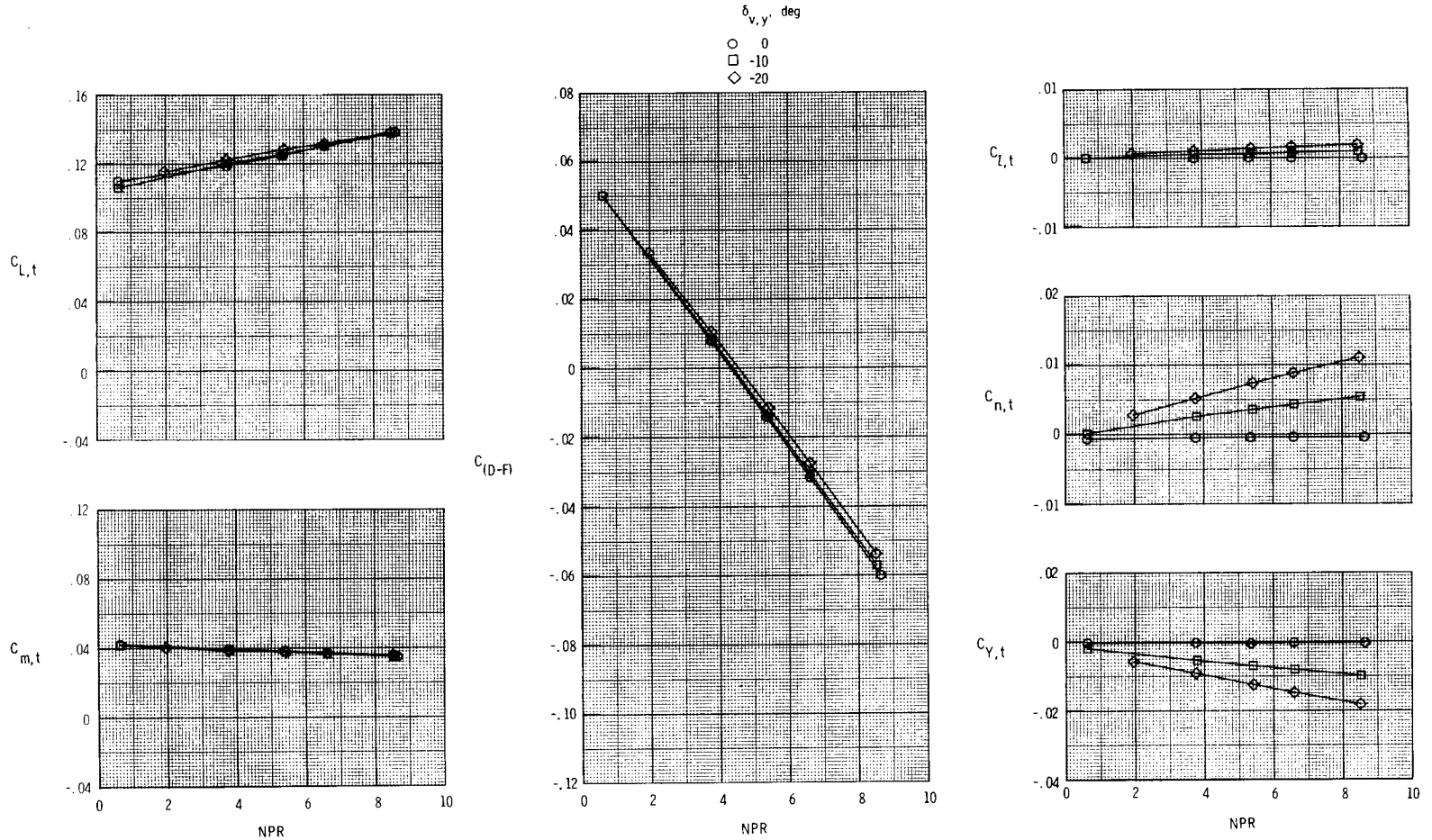

(d) $M = 1.20$.

Figure 20. Concluded.

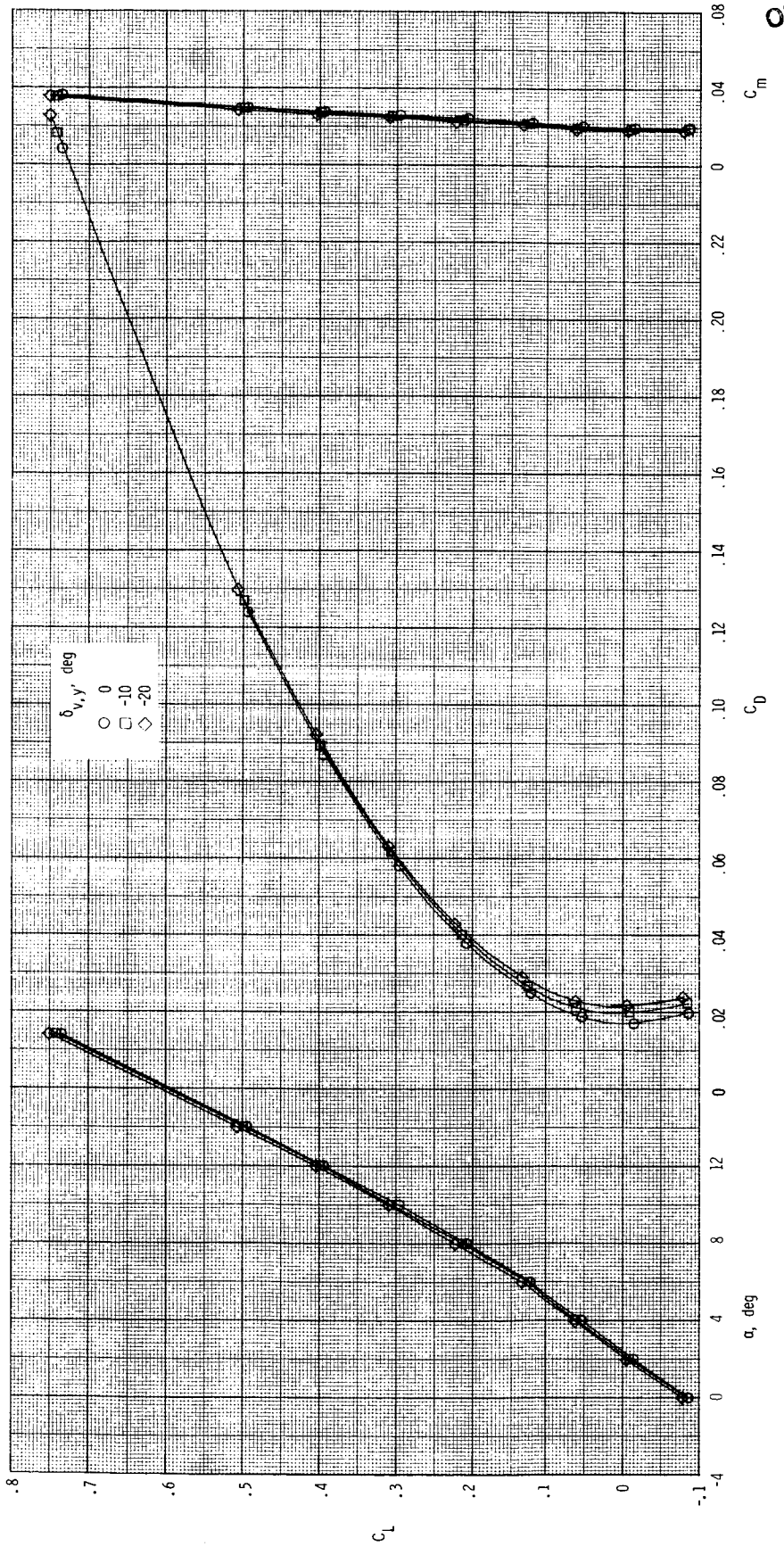

(a) $M = 0.20$; NPR $= 1.0$.

Figure 21. Effect of yaw vectoring on total aerodynamic characteristics for $\delta_{v,p} = 0°$.

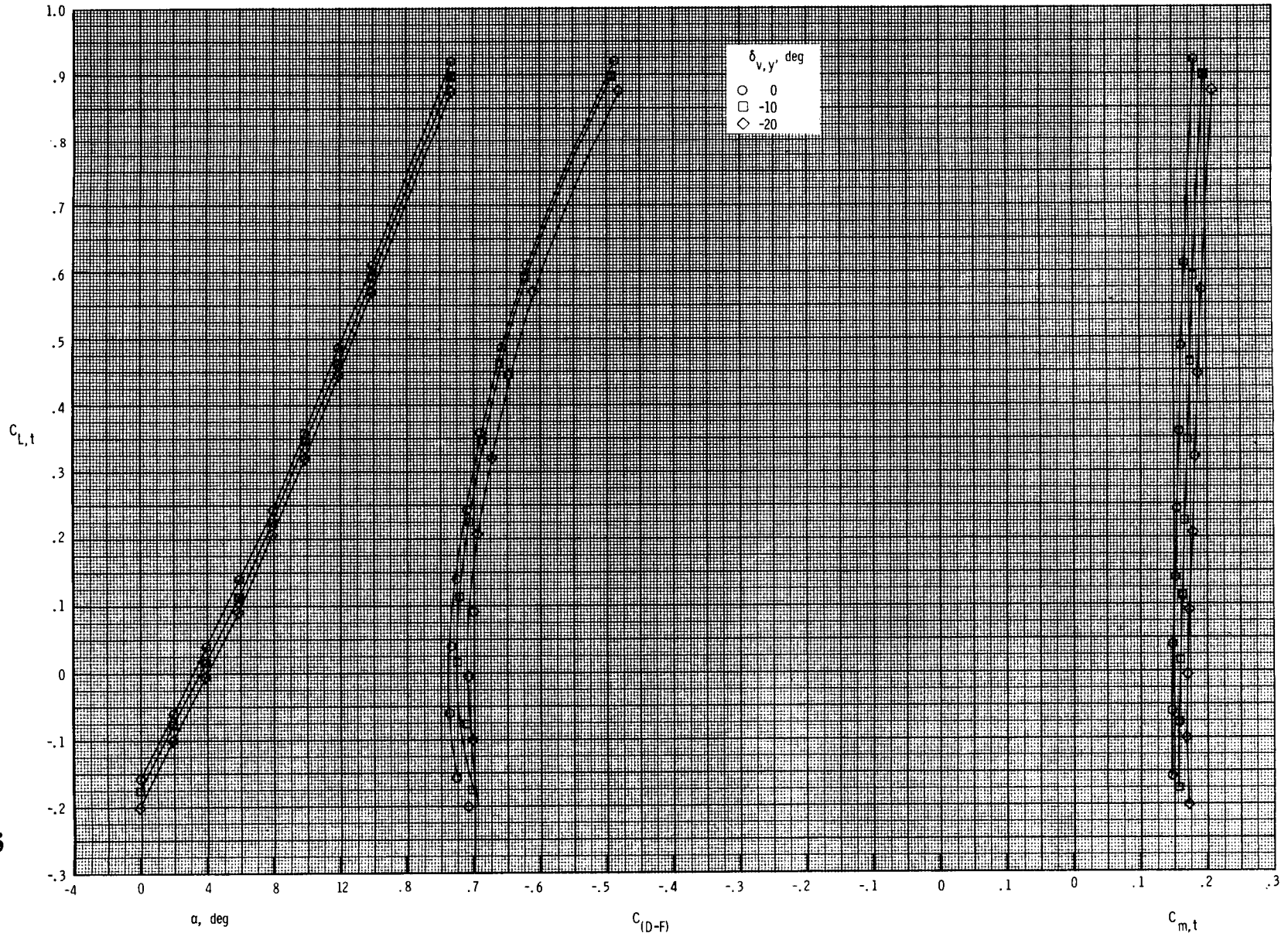

(b) $M = 0.20$; NPR $= 2.5$.

Figure 21. Continued.

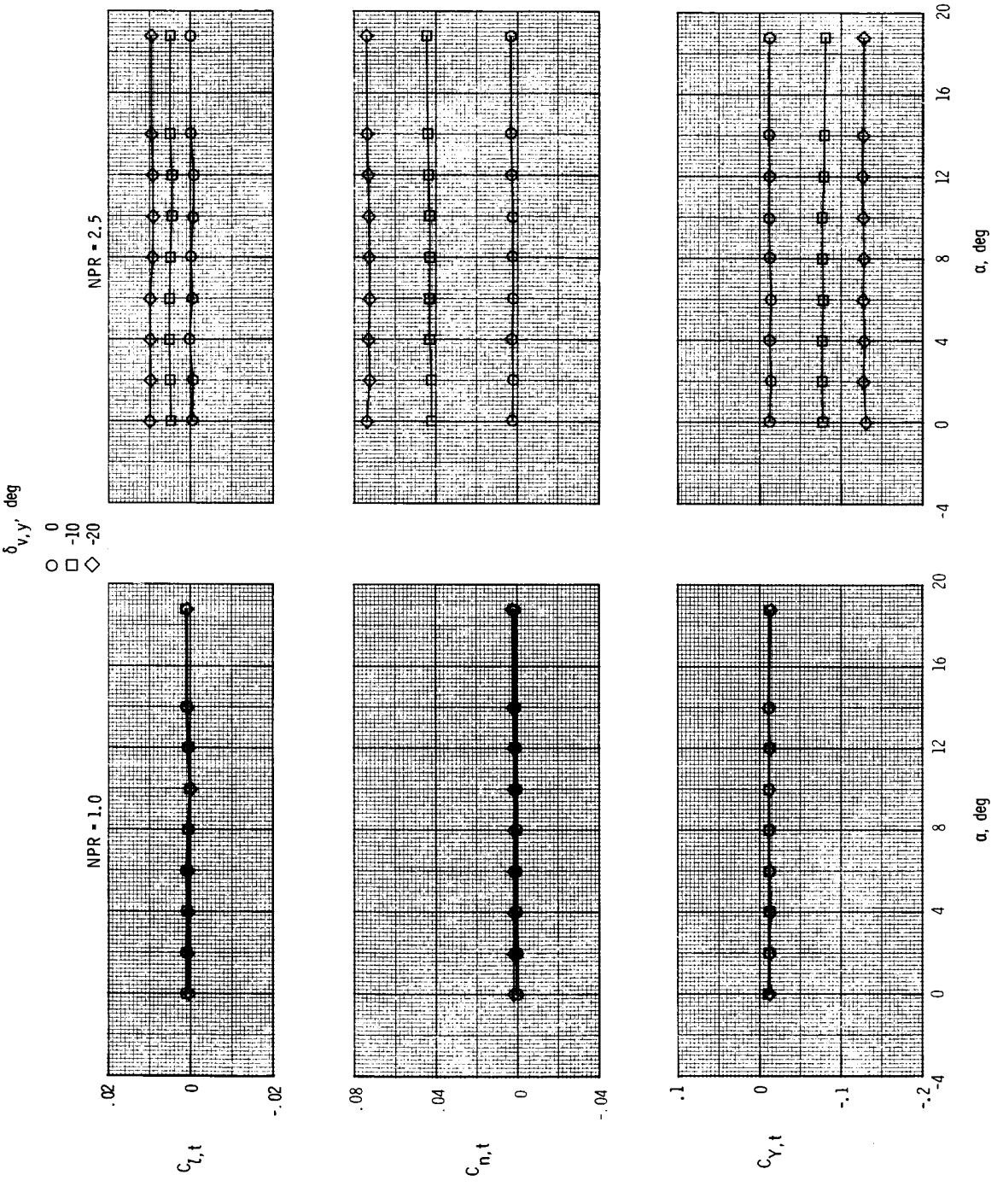

(c) $M = 0.20$; NPR = 1.0 and 2.5.

Figure 21. Continued.

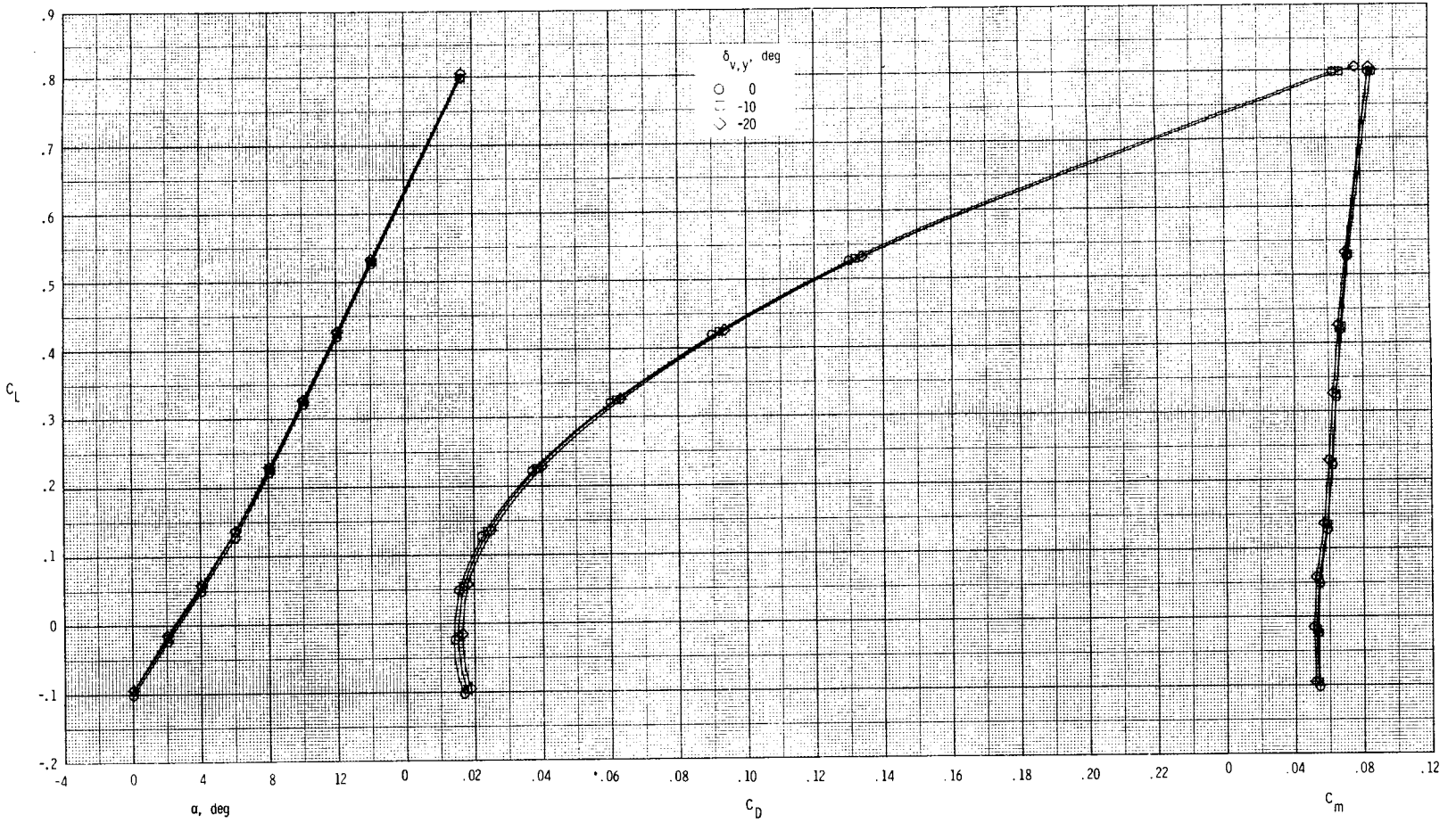

(d) $M = 0.60$; NPR = 1.0.

Figure 21. Continued.

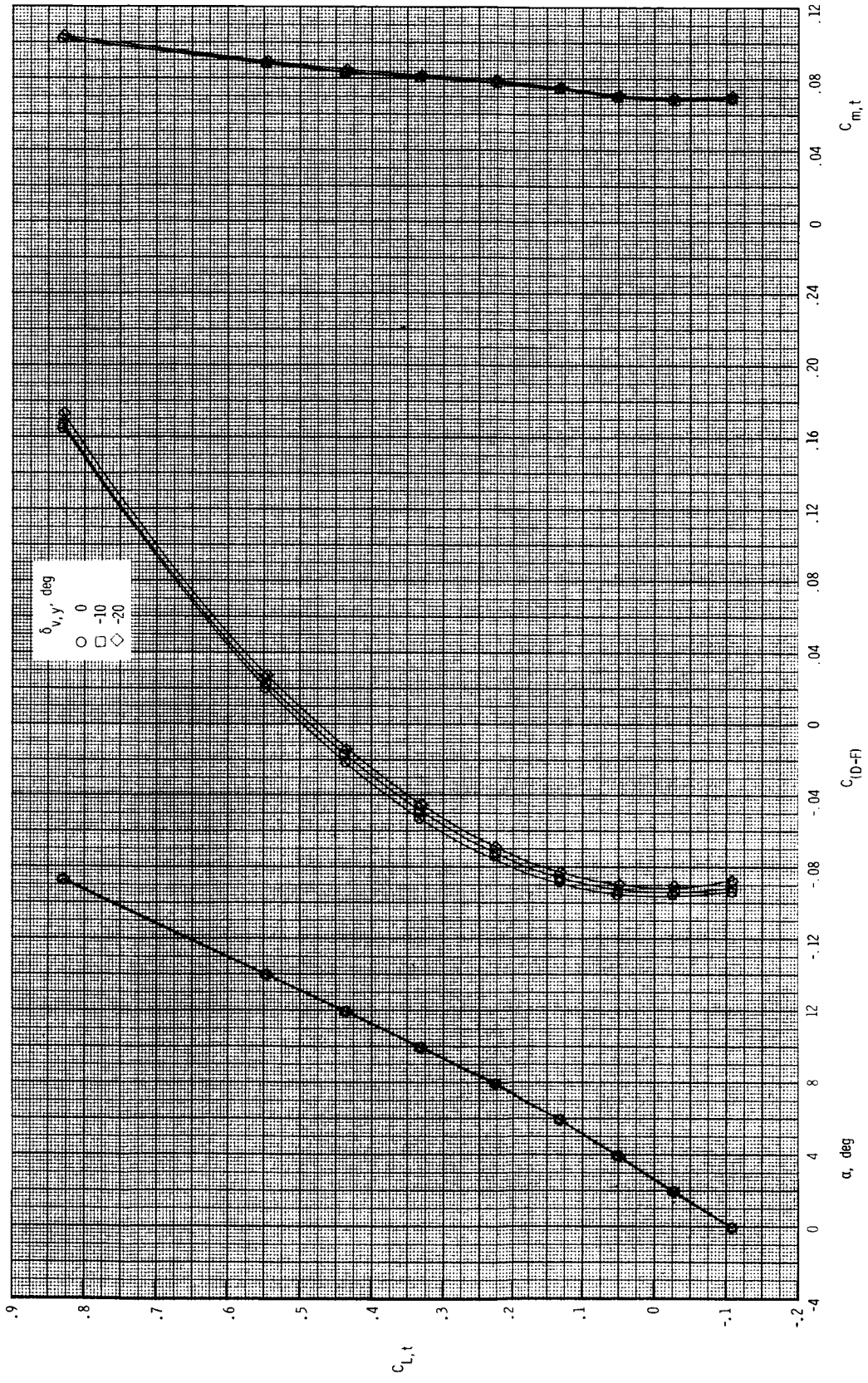

(e) $M = 0.60$; NPR $= 3.0$.

Figure 21. Continued.

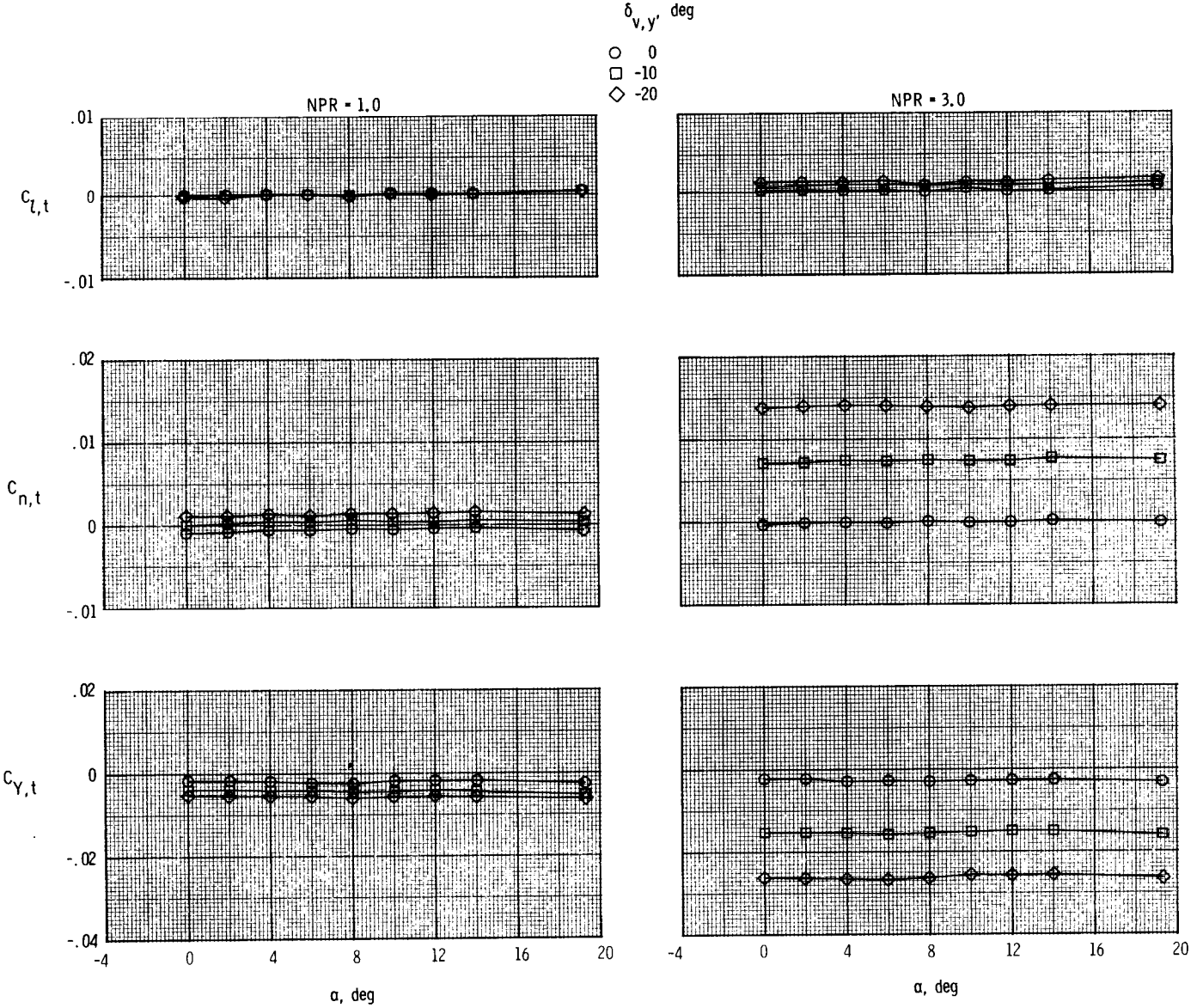

(f) $M = 0.60$; NPR = 1.0 and 3.0.

Figure 21. Continued.

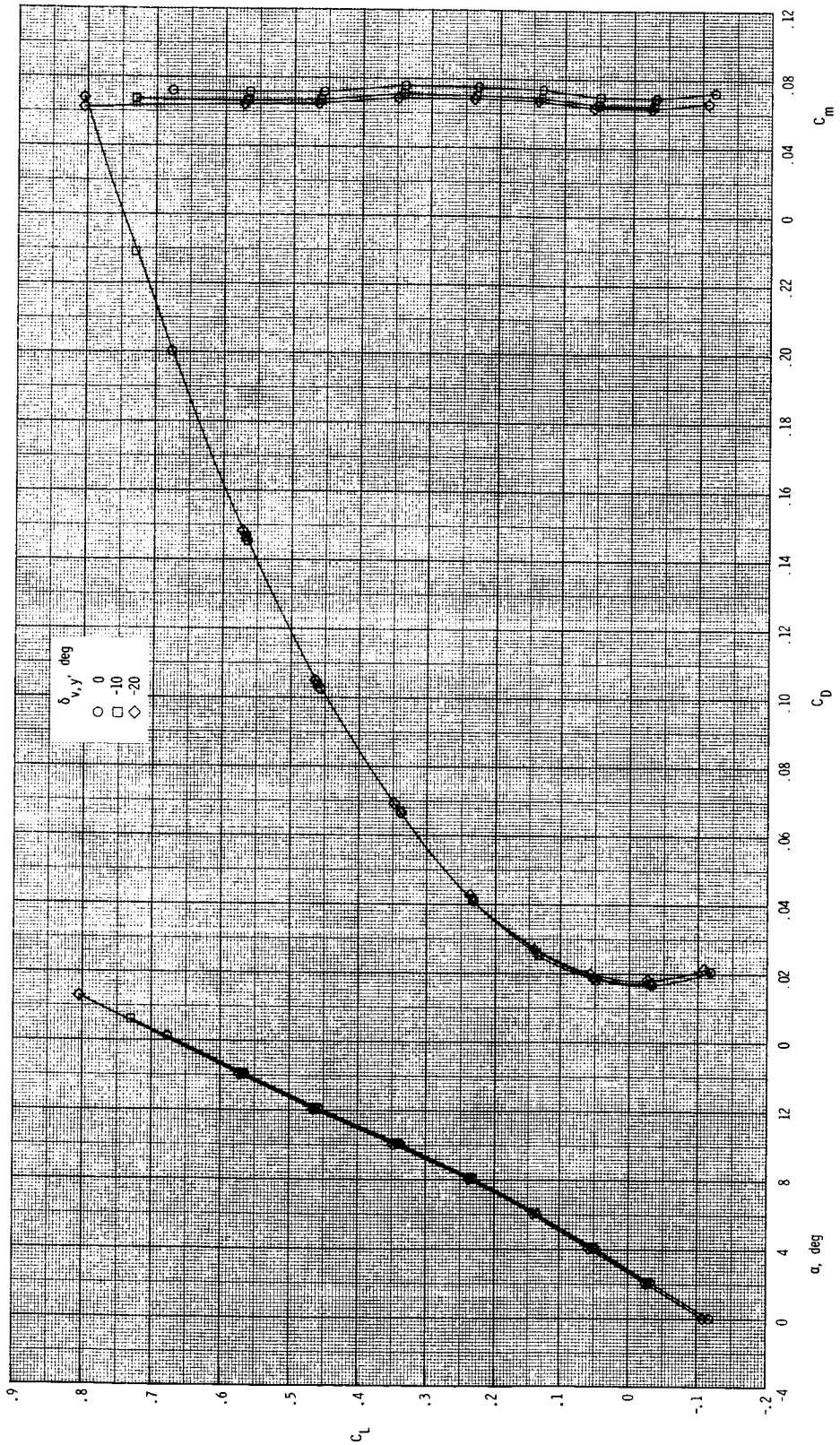

(g) $M = 0.87$; NPR = 1.0.

Figure 21. Continued.

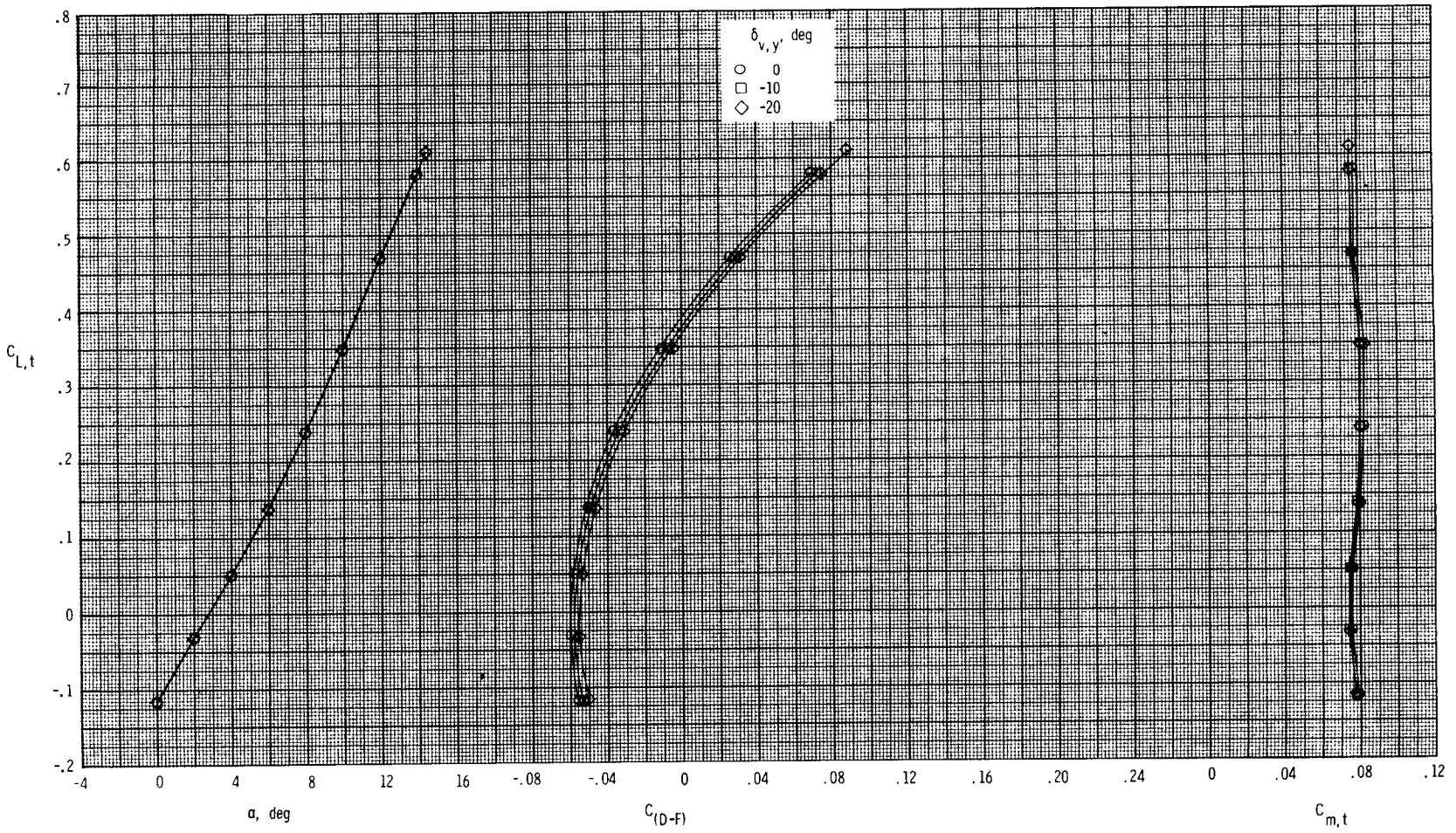

(h) $M = 0.87$; NPR = 3.9.

Figure 21. Continued.

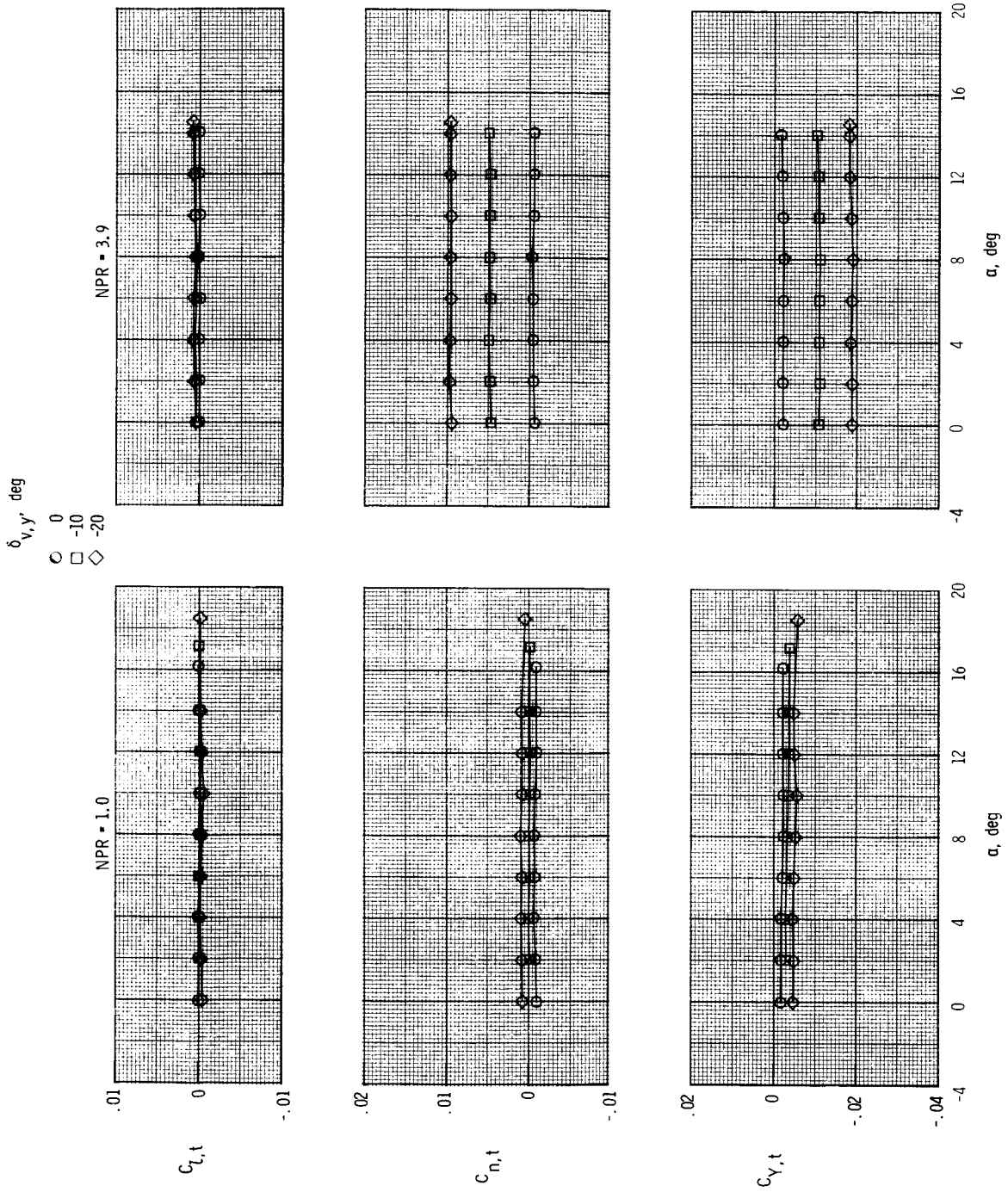

(i) $M = 0.87$; NPR = 1.0 and 3.9.

Figure 21. Continued.

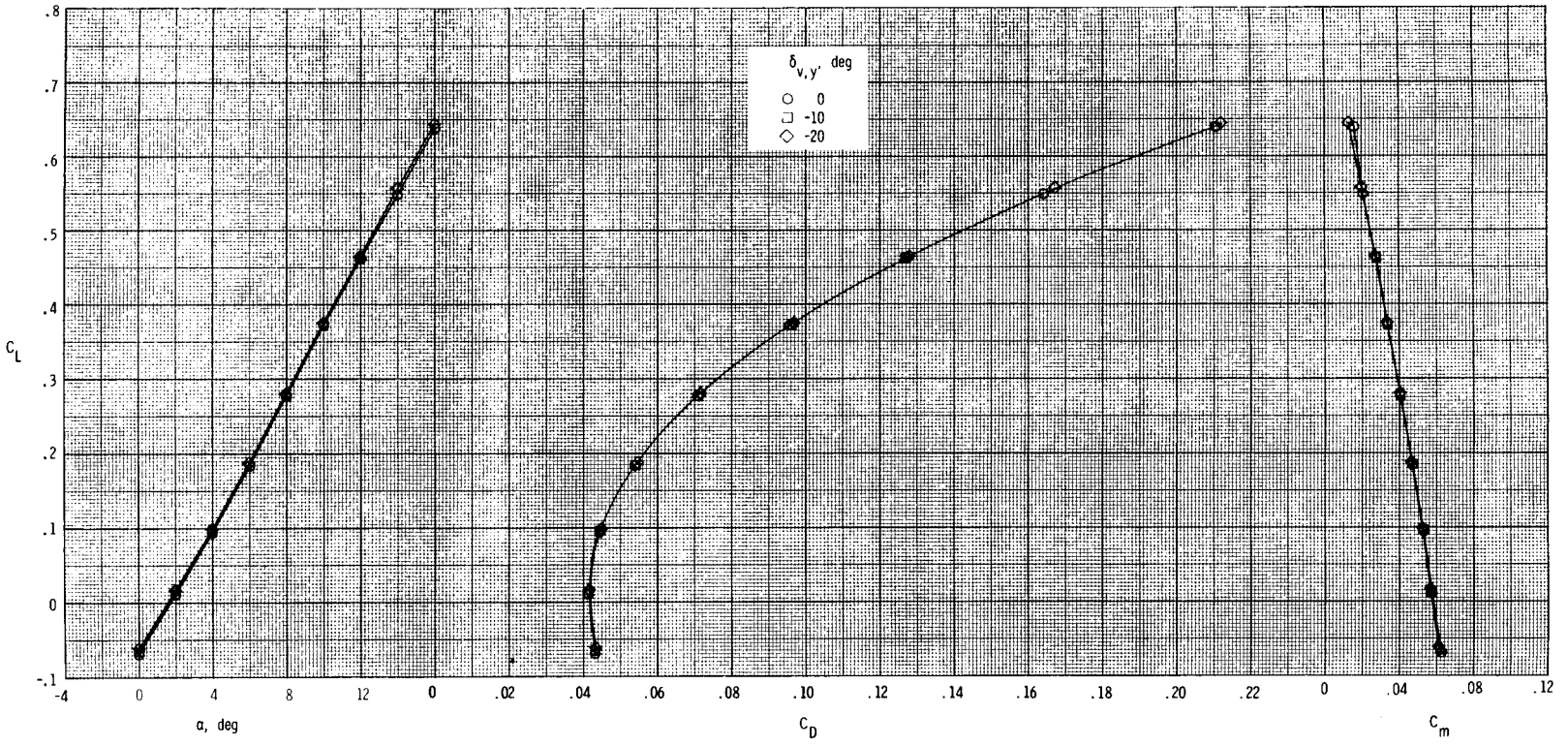

(j) $M = 1.20$; NPR = 1.0.

Figure 21. Continued.

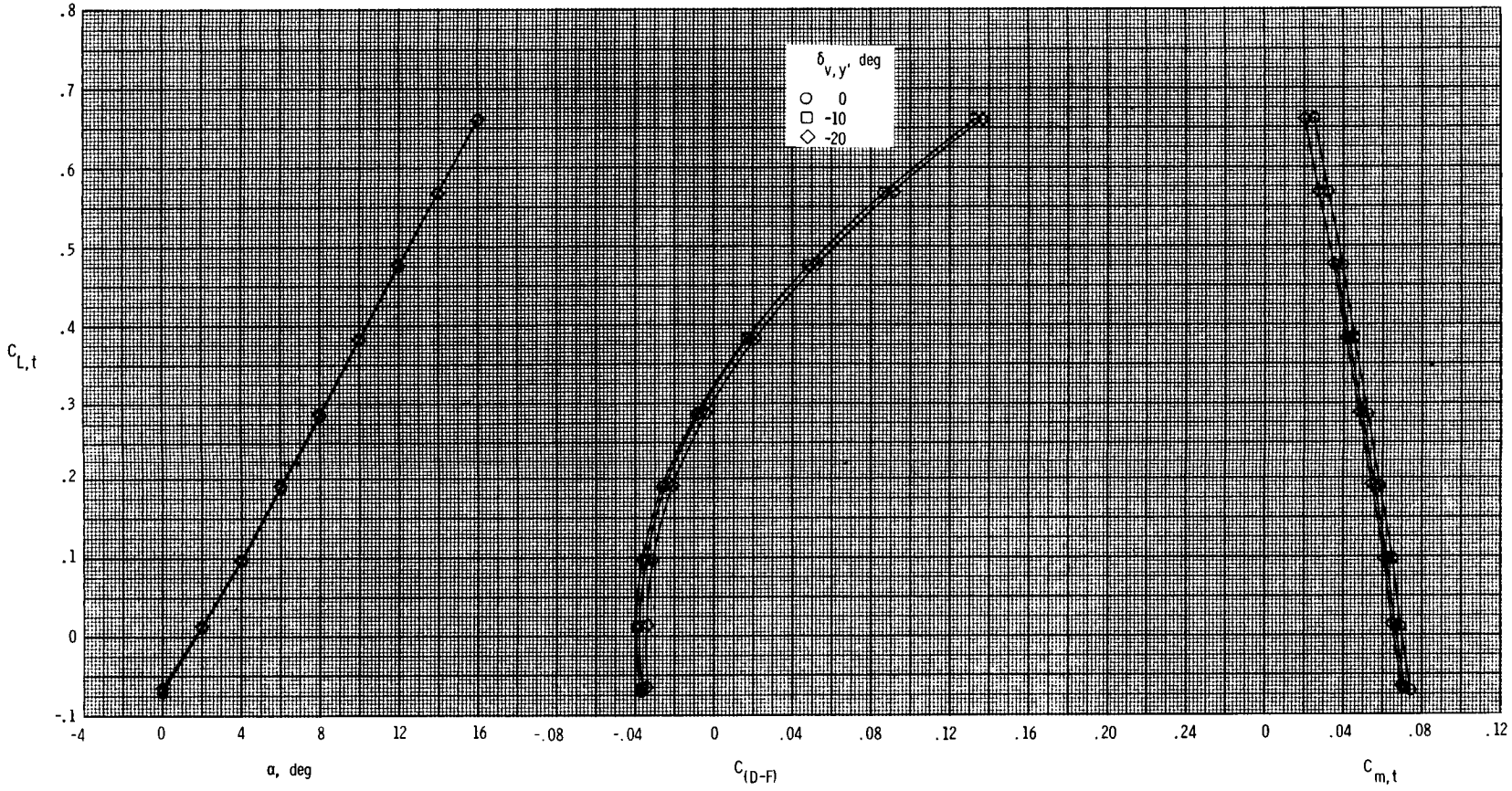

(k) $M = 1.20$; NPR = 6.6.

Figure 21. Continued.

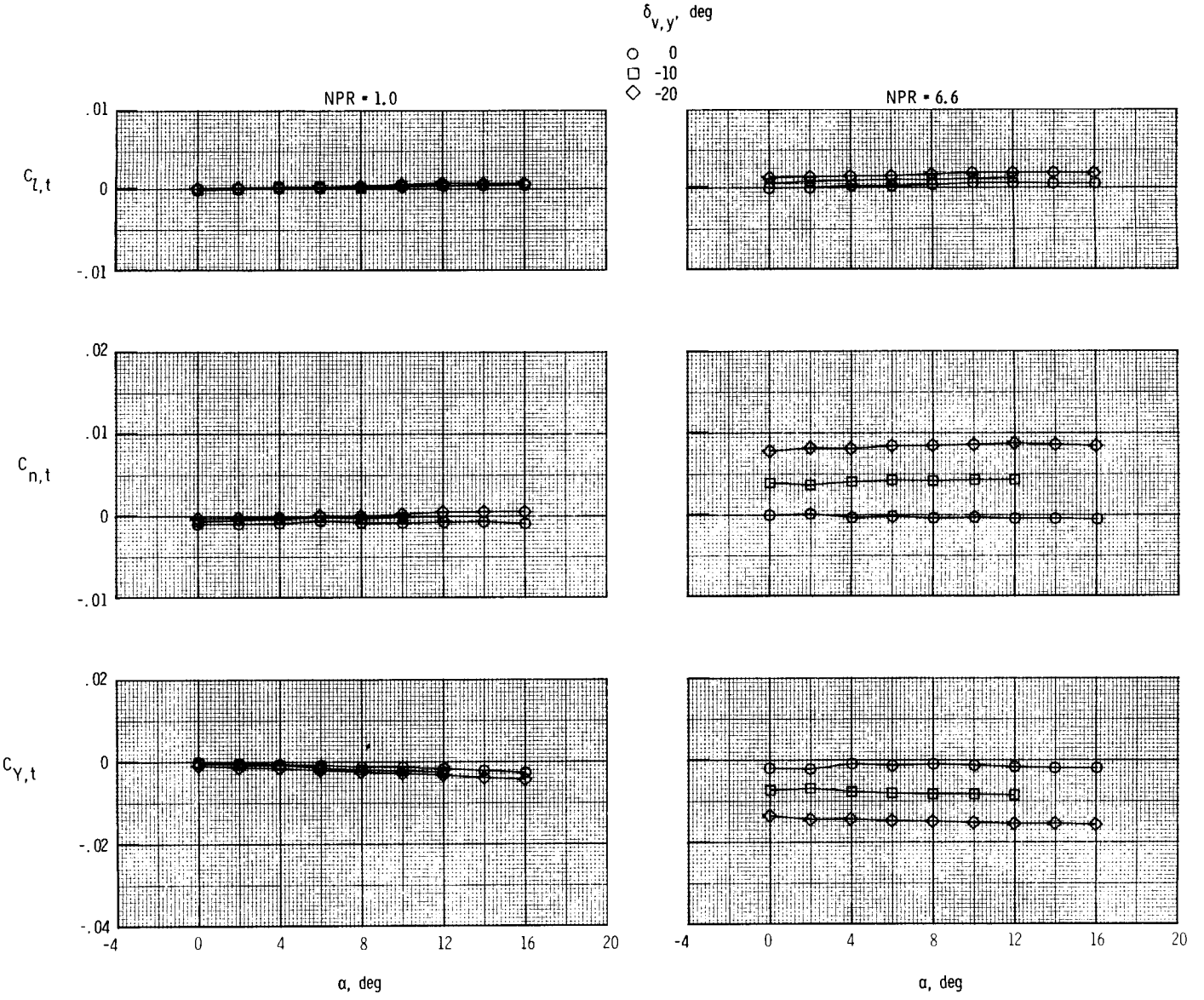

(l) $M = 1.20$; NPR = 1.0 and 6.6.

Figure 21. Continued.

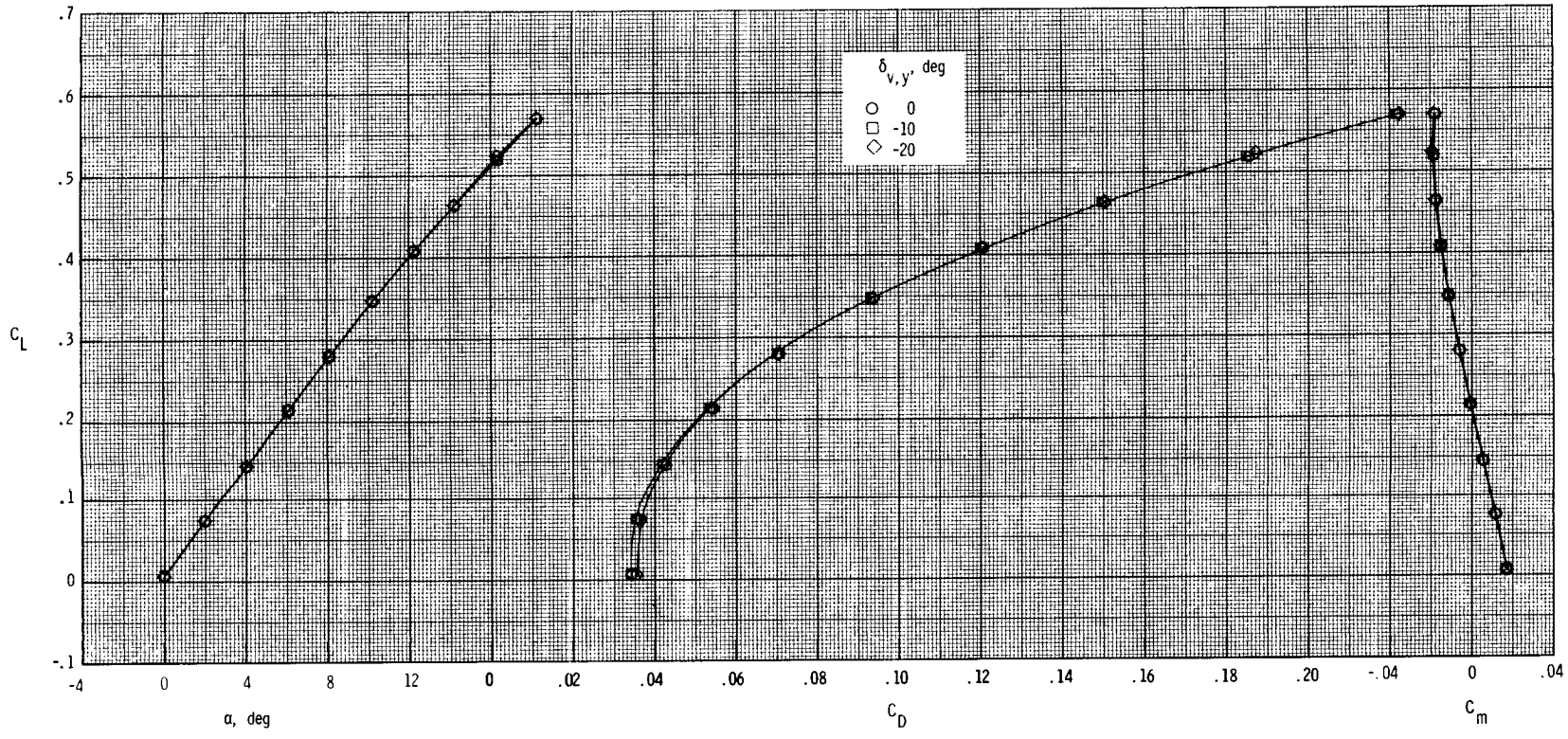

(m) $M = 2.00$; NPR = 1.0.

Figure 21. Continued.

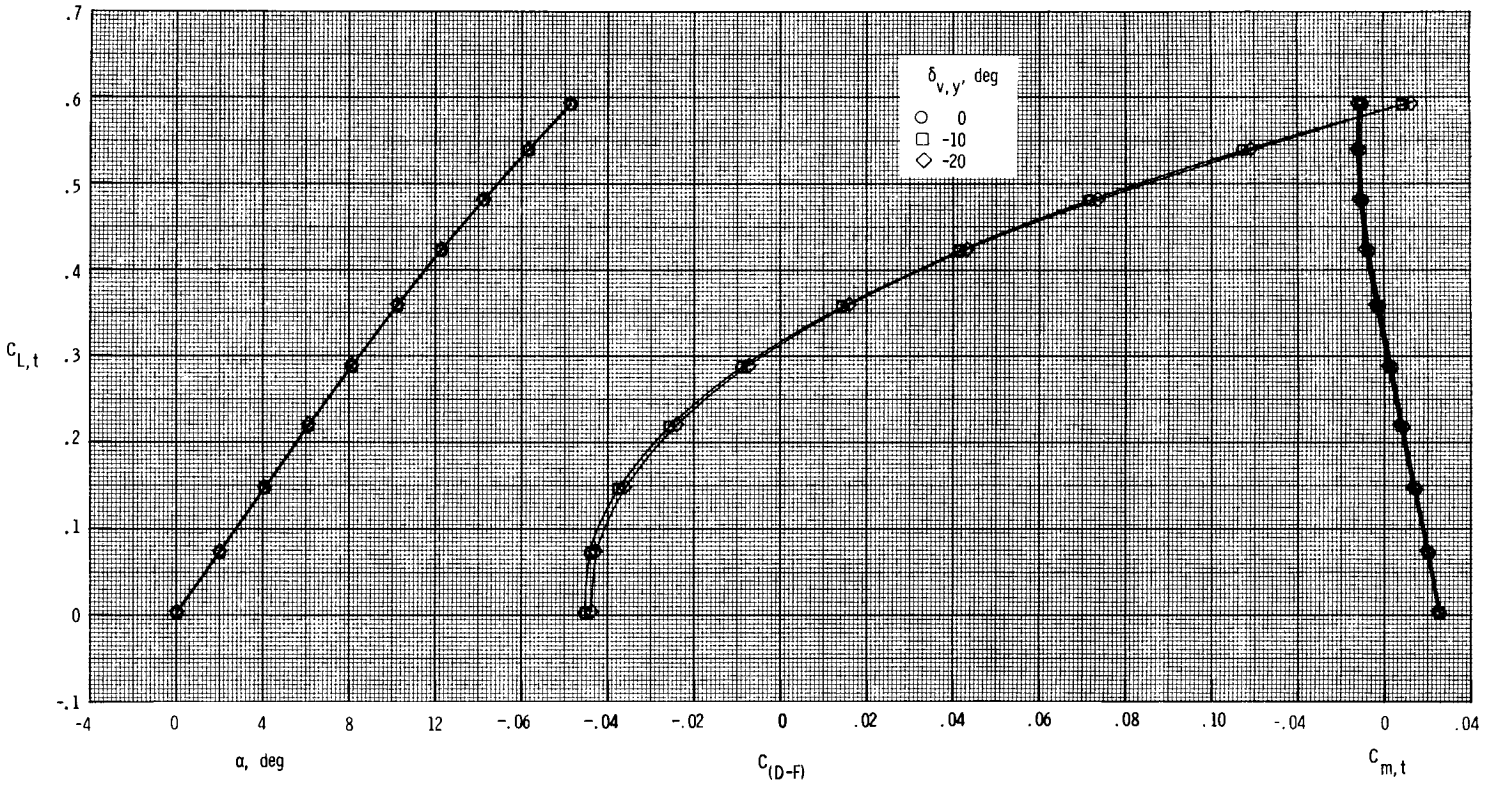

(n) $M = 2.00$; NPR = 16.0.

Figure 21. Continued.

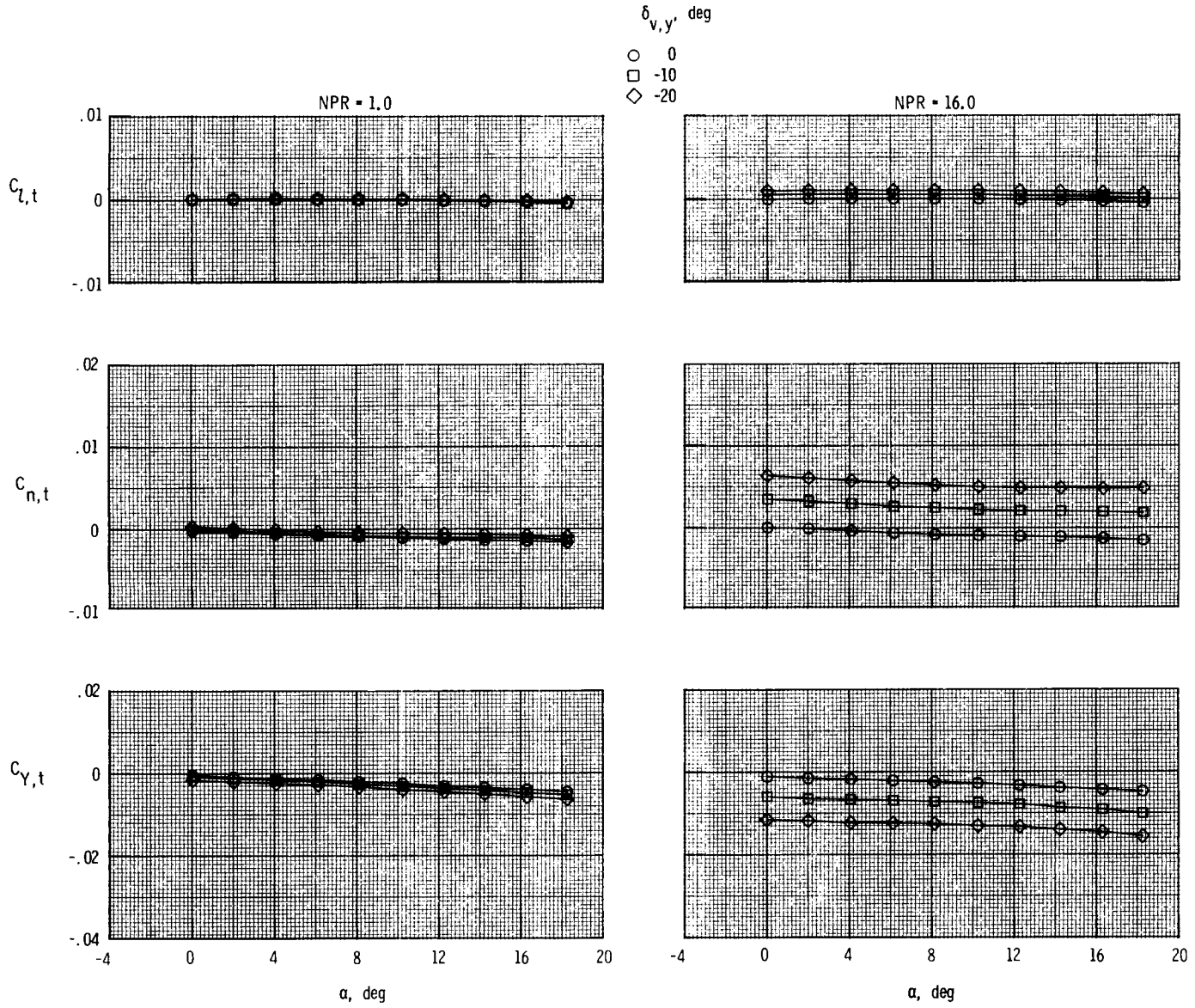

(o) $M = 2.00$; NPR = 1.0 and 16.0.

Figure 21. Continued.

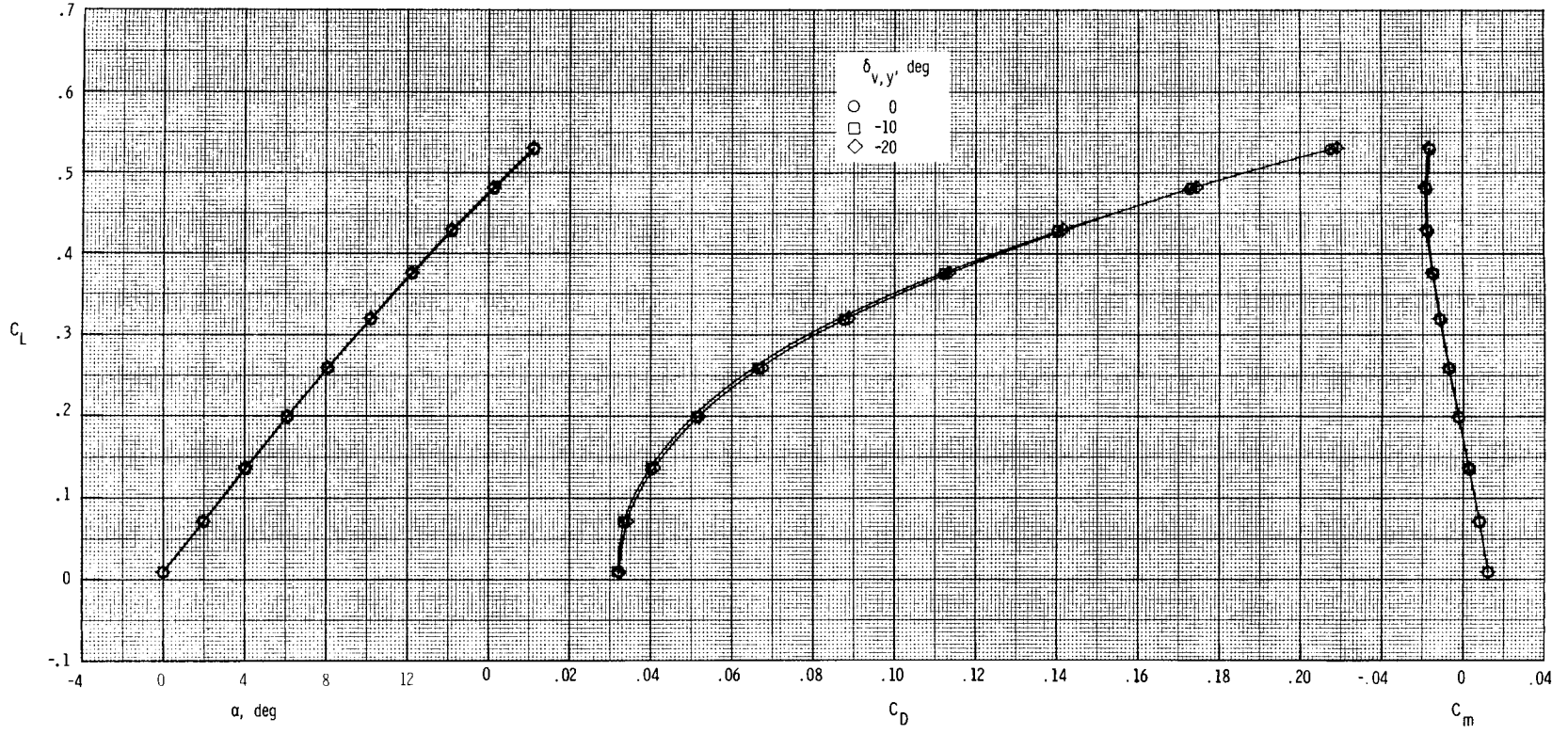

(p) $M = 2.17$; NPR = 1.0.

Figure 21. Continued.

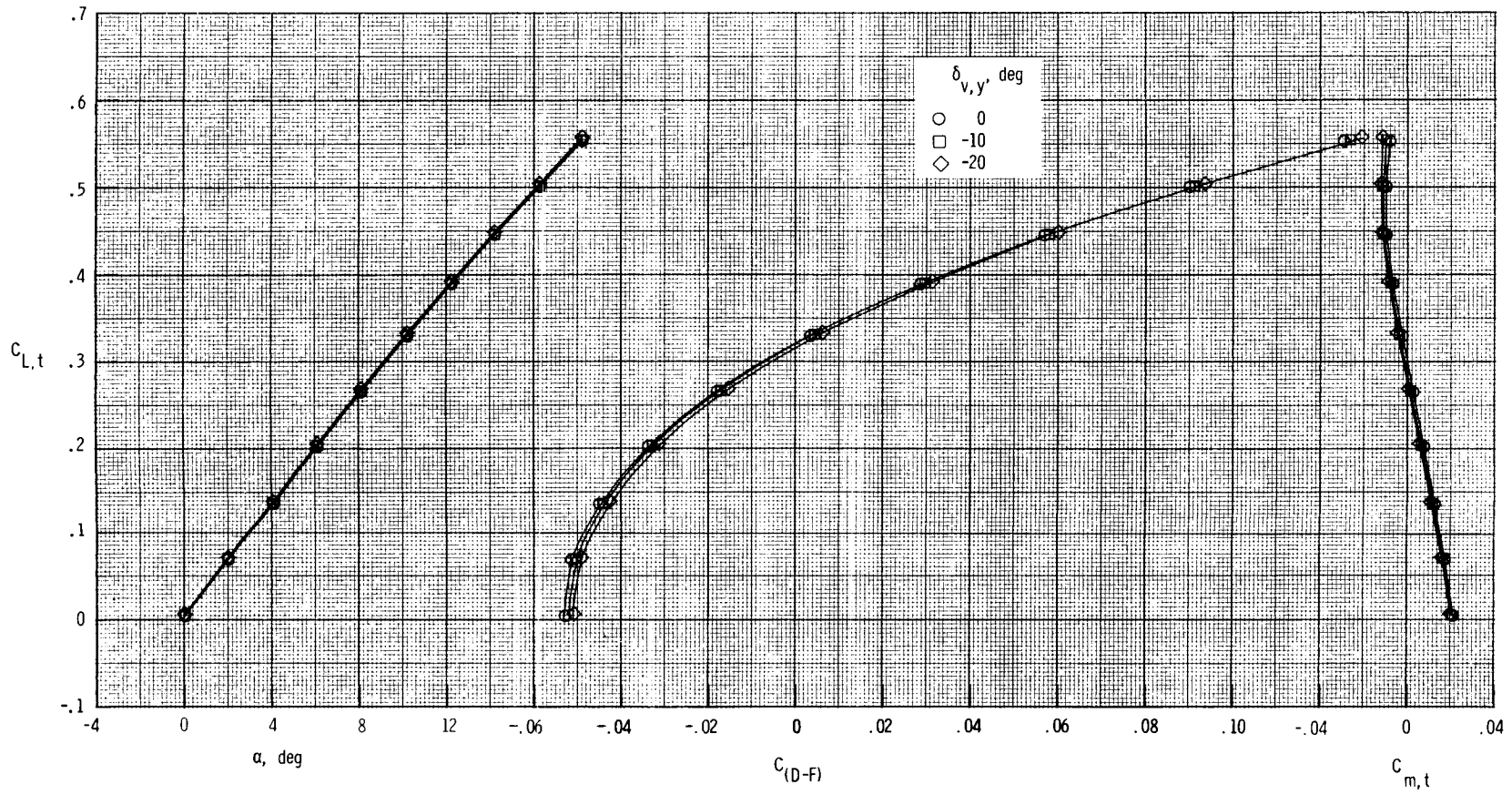

(q) $M = 2.17$; NPR = 20.0.

Figure 21. Continued.

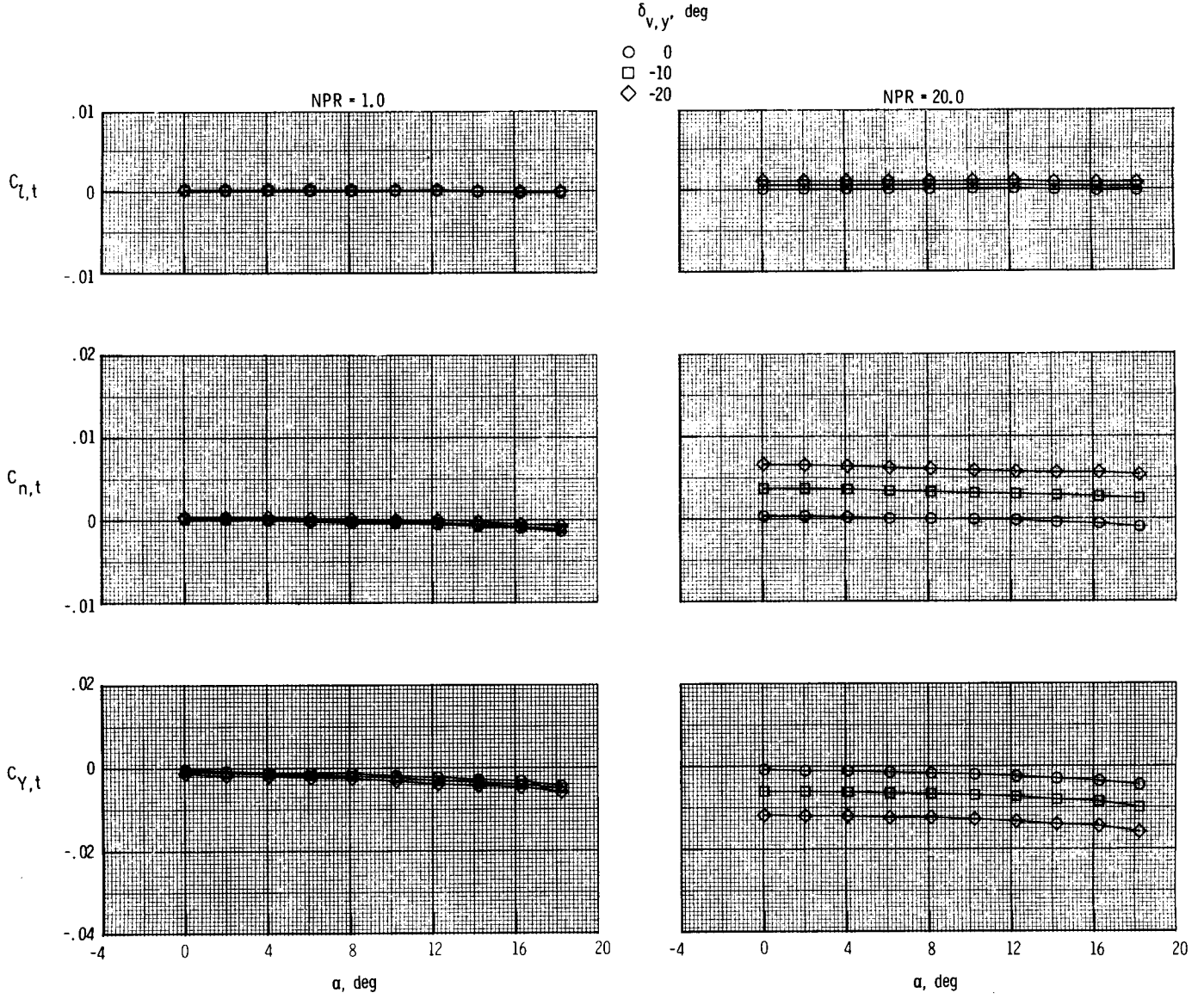

(r) $M = 2.17$; NPR = 1.0 and 20.0.

Figure 21. Continued.

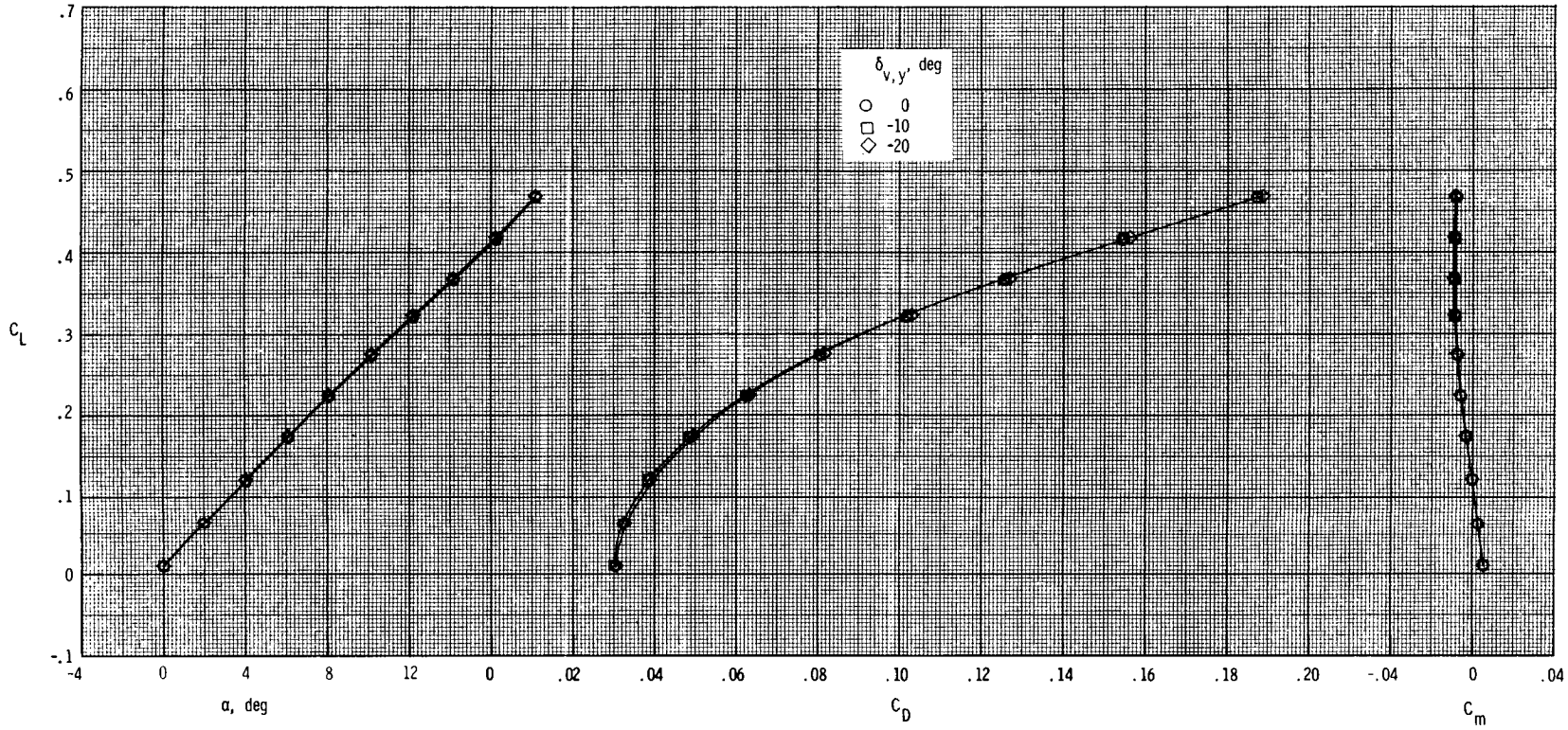

(s) $M = 2.47$; NPR = 1.0.

Figure 21. Continued.

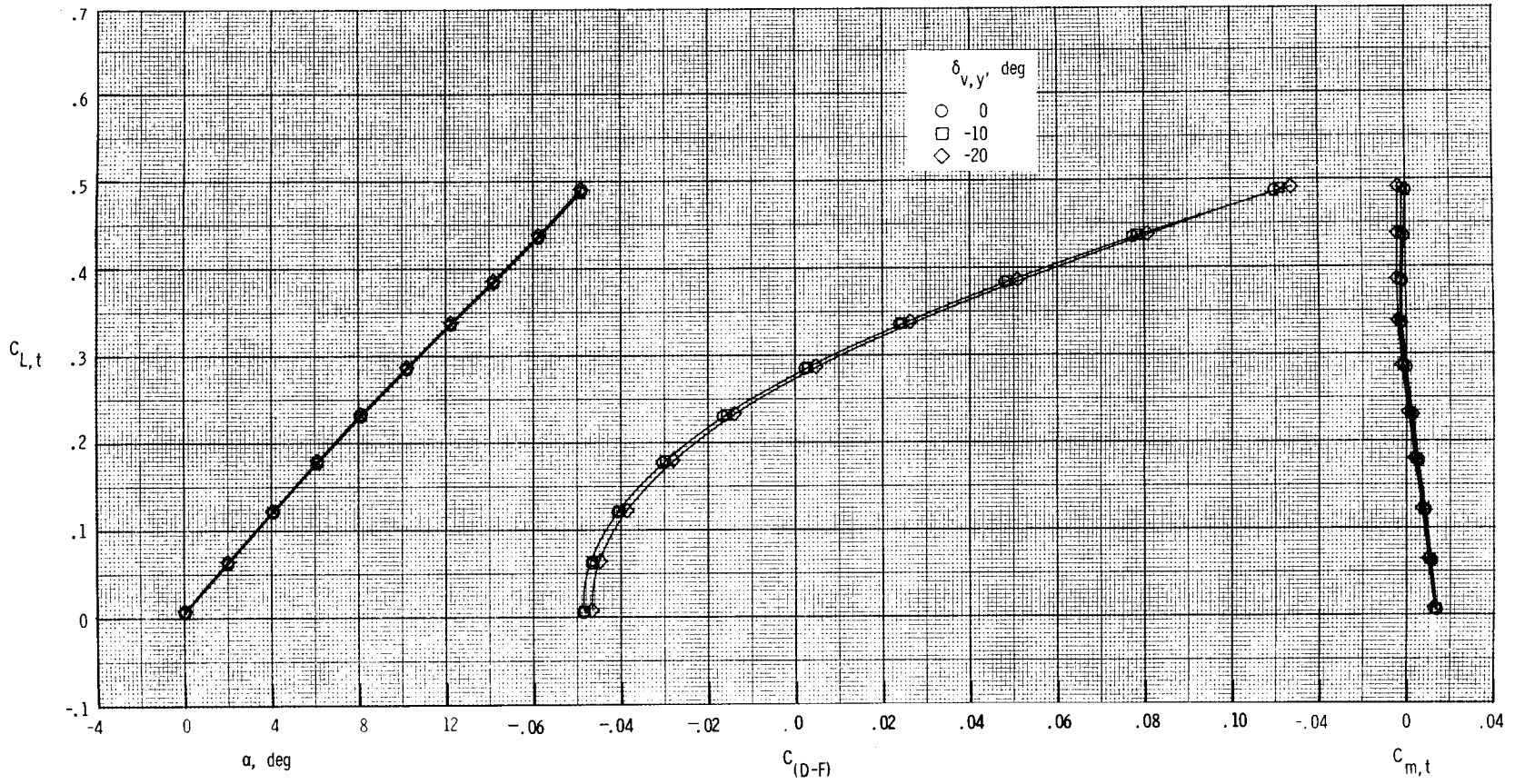

(t) $M = 2.47$; NPR = 24.0.

Figure 21. Continued.

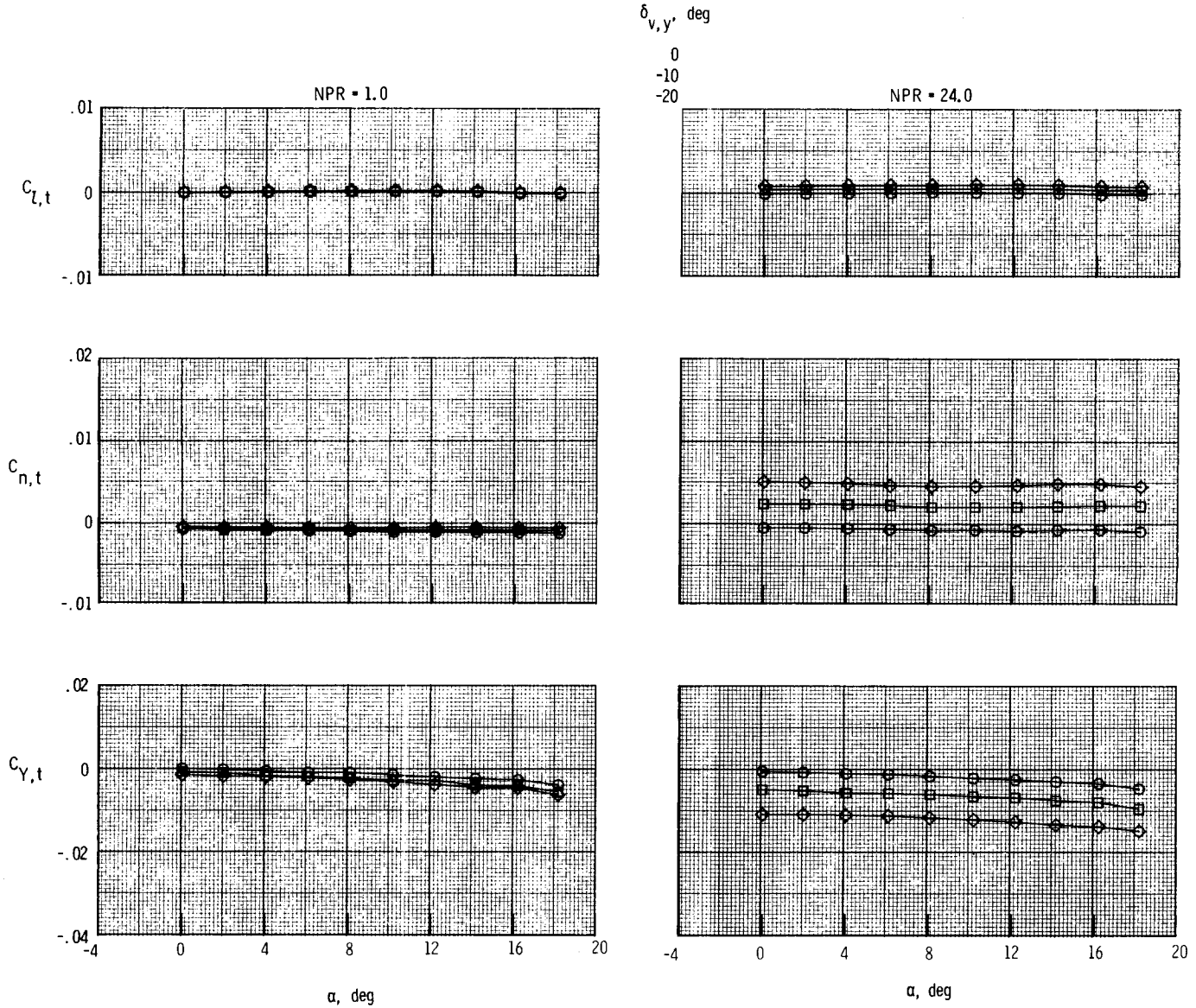

(u) $M = 2.47$; NPR = 1.0 and 24.0.

Figure 21. Concluded.

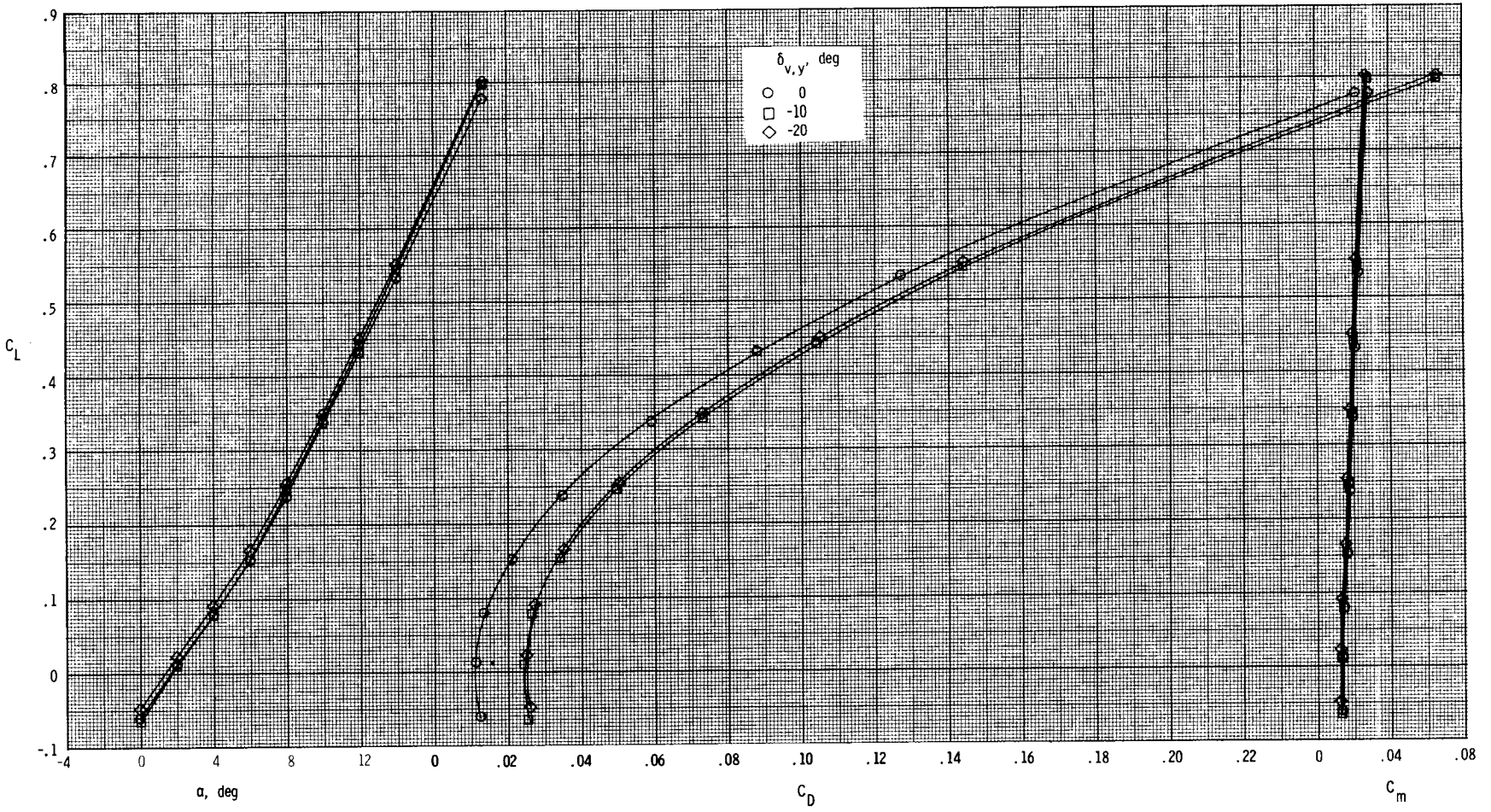

(a) $M = 0.20$; NPR = 1.0.

Figure 22. Effect of yaw vectoring on total aerodynamic characteristics for $\delta_{v,p} = 15°$.

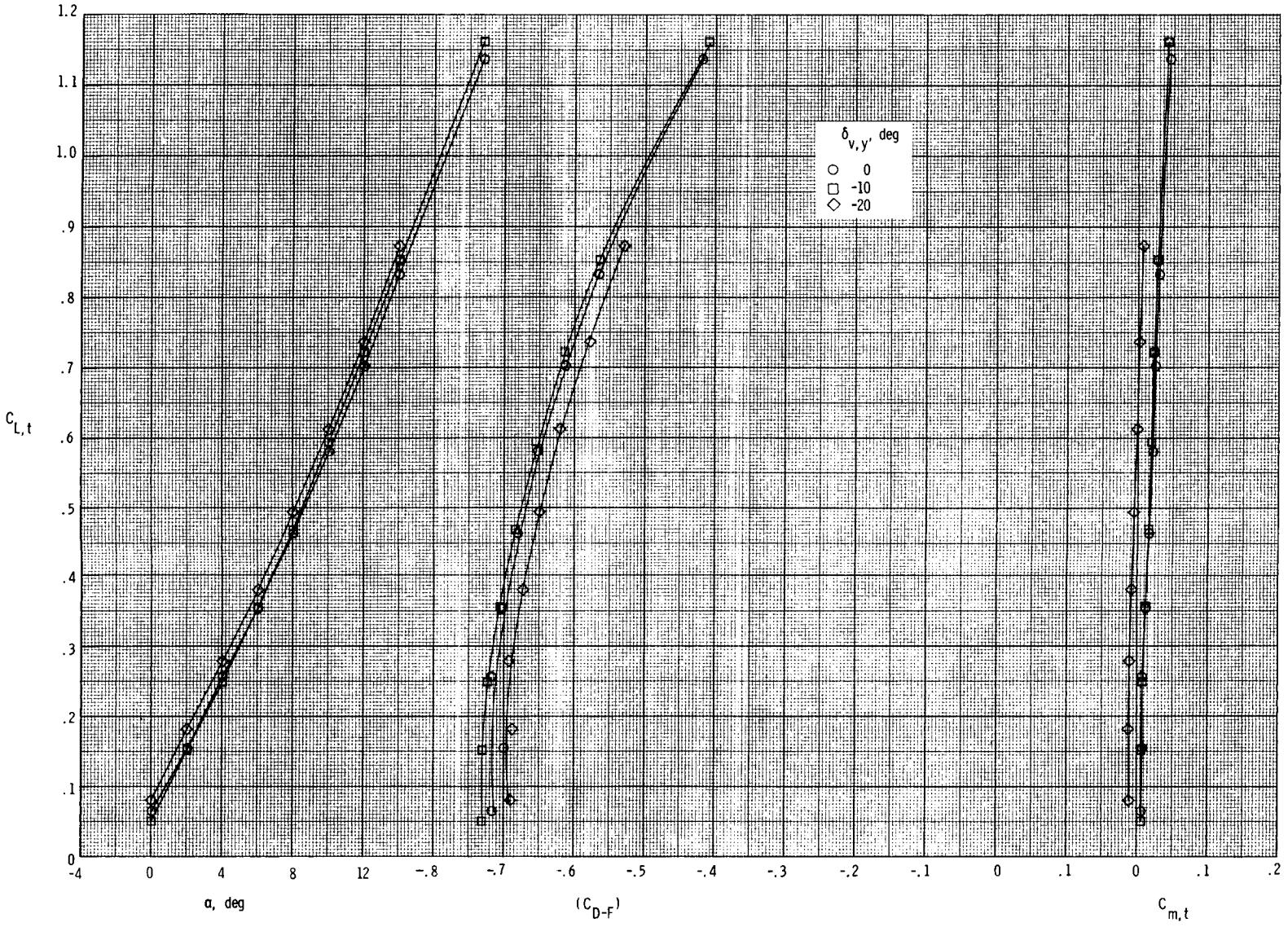

(b) $M = 0.20$; NPR $= 2.5$.

Figure 22. Continued.

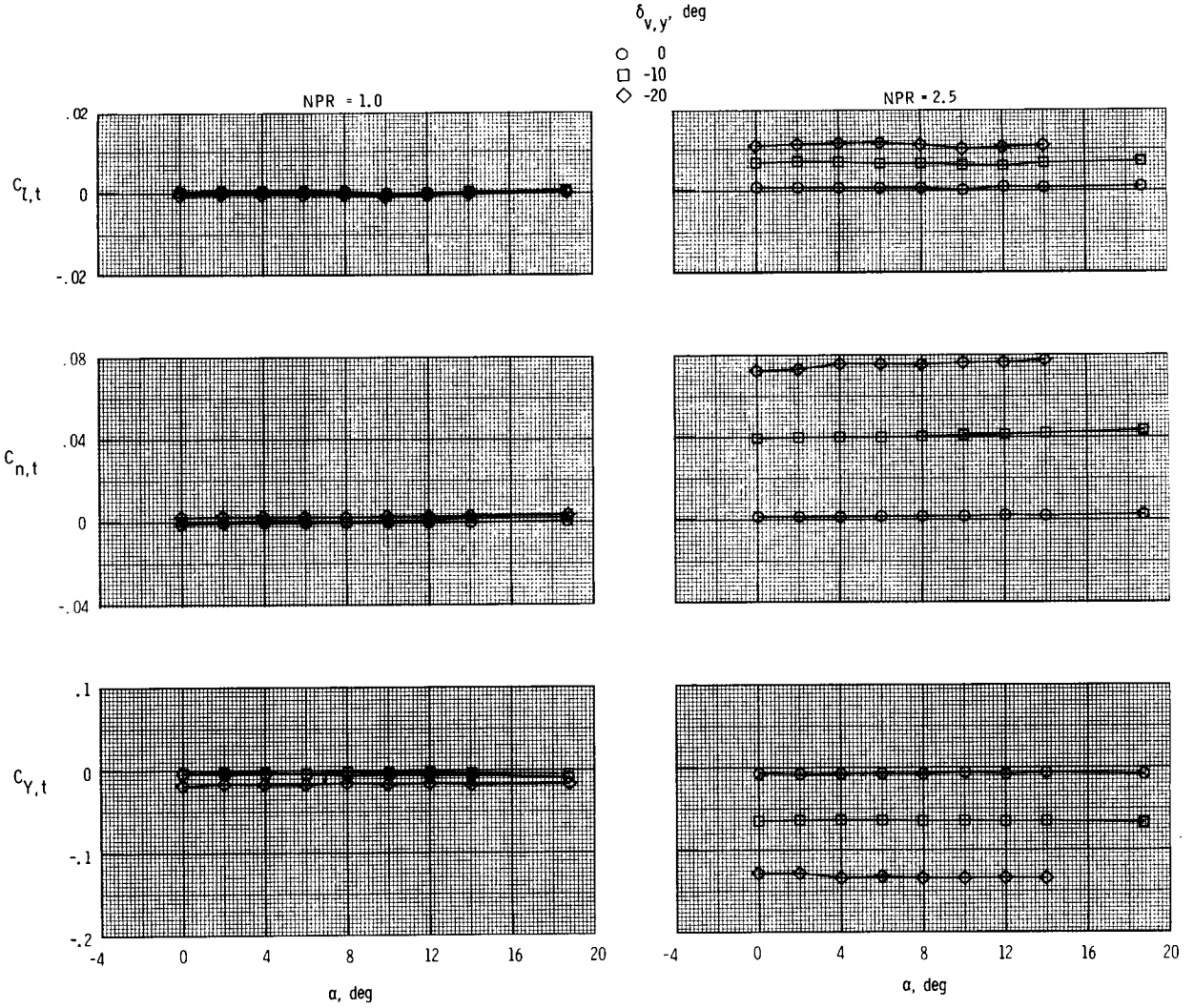

(c) $M = 0.20$; NPR = 1.0 and 2.5.

Figure 22. Continued.

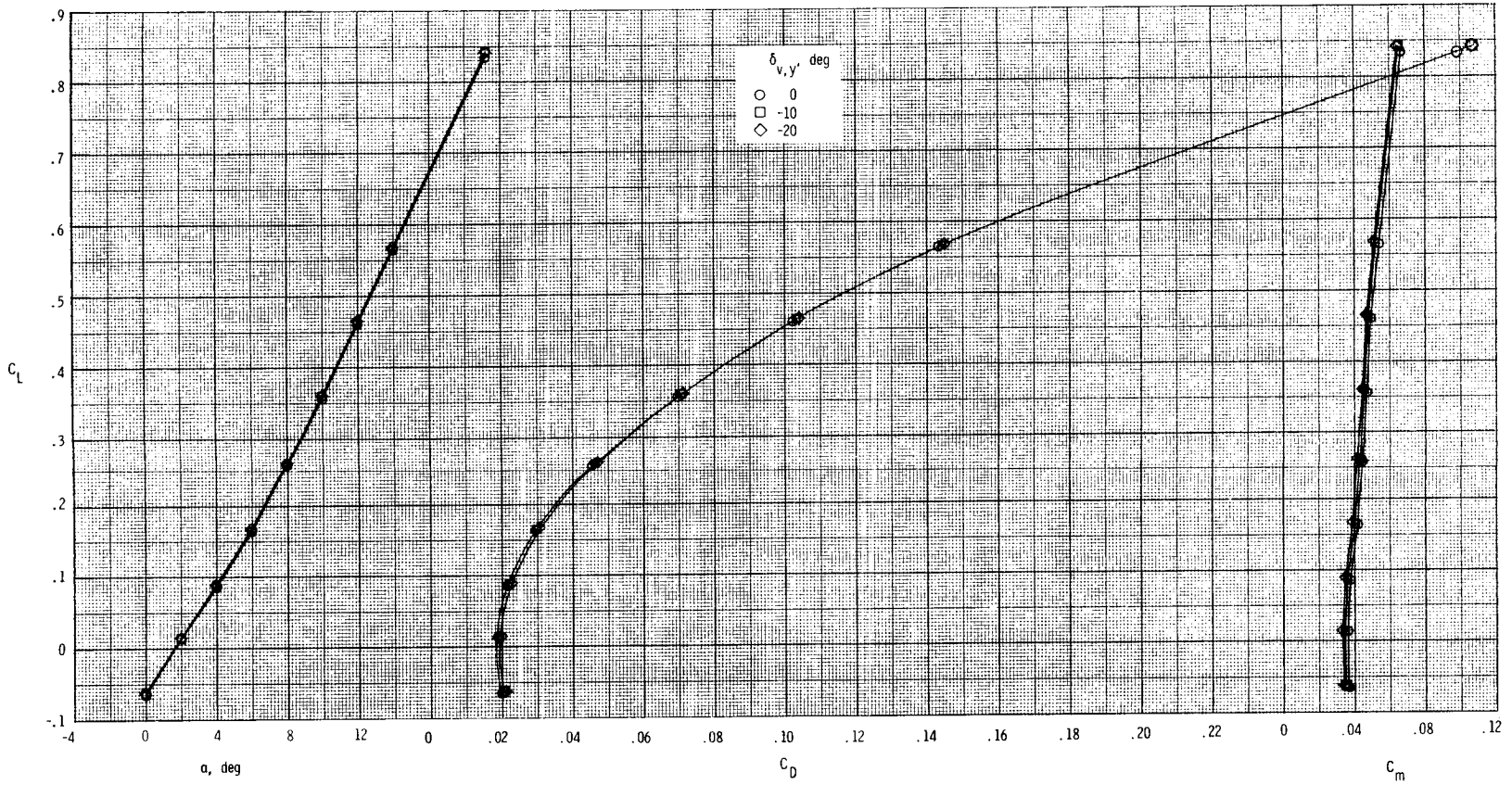

(d) $M = 0.60$; NPR $= 1.0$.

Figure 22. Continued.

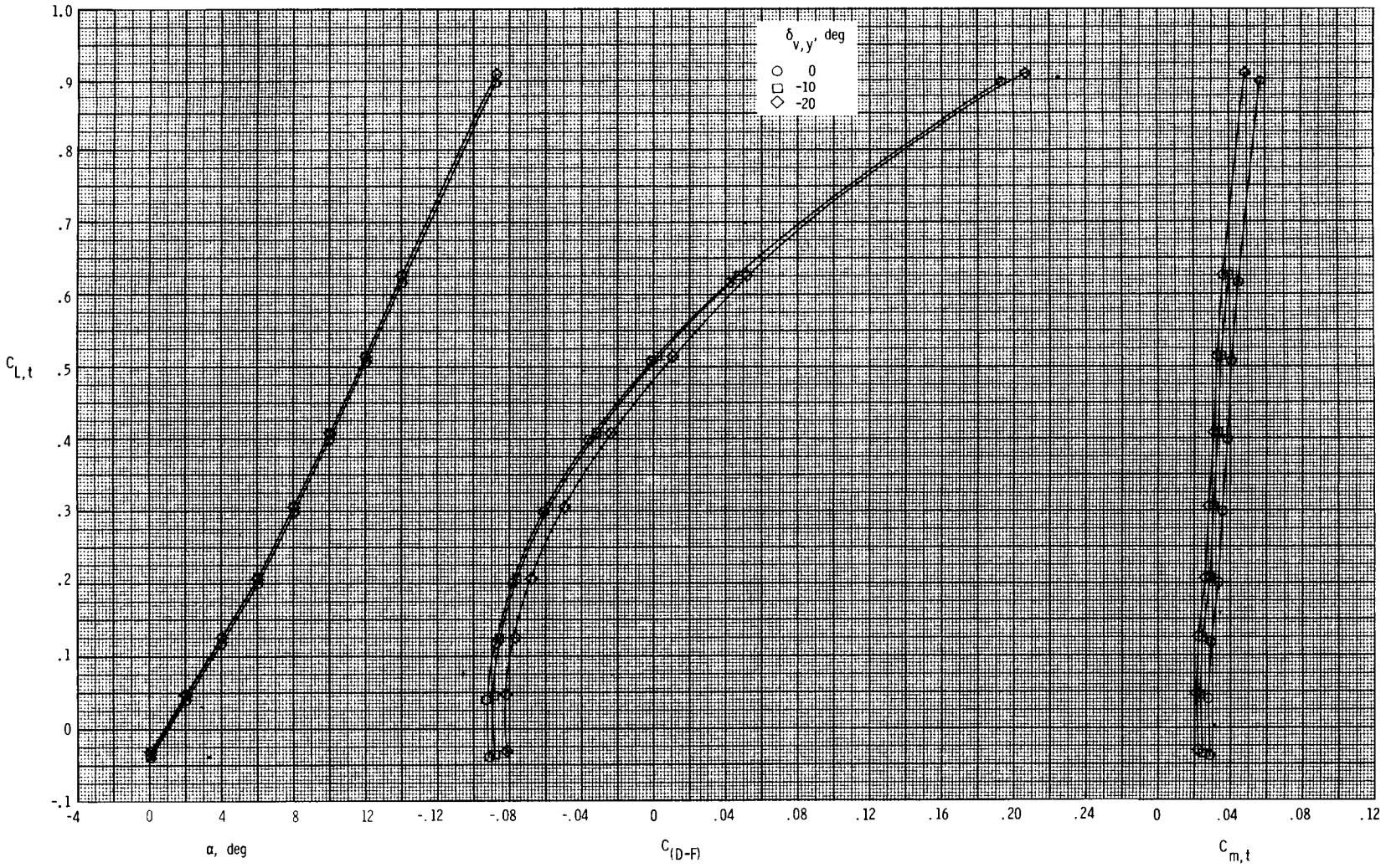

(e) $M = 0.60$; NPR = 3.0.

Figure 22. Continued.

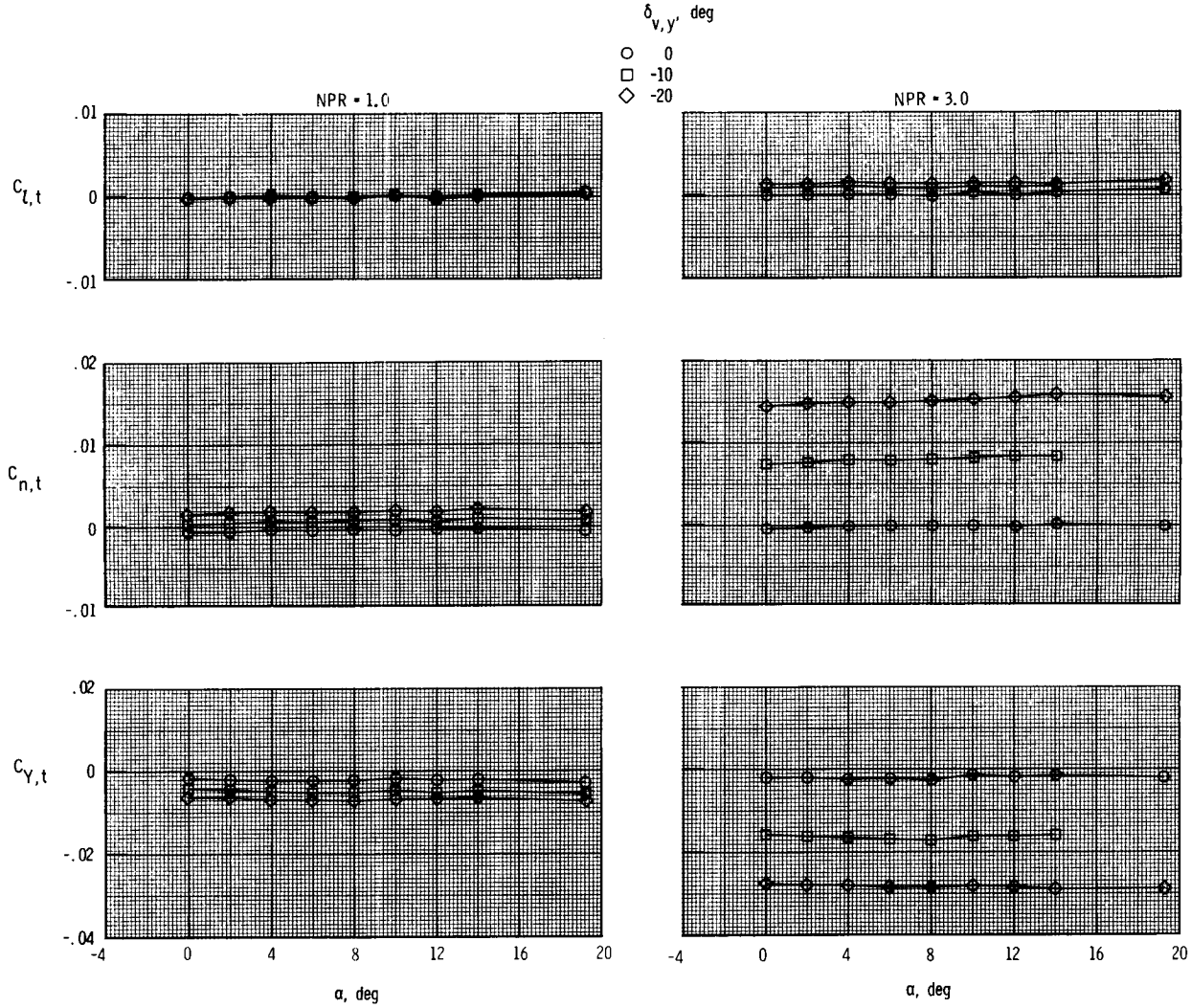

(f) $M = 0.60$; NPR = 1.0 and 3.0.

Figure 22. Continued.

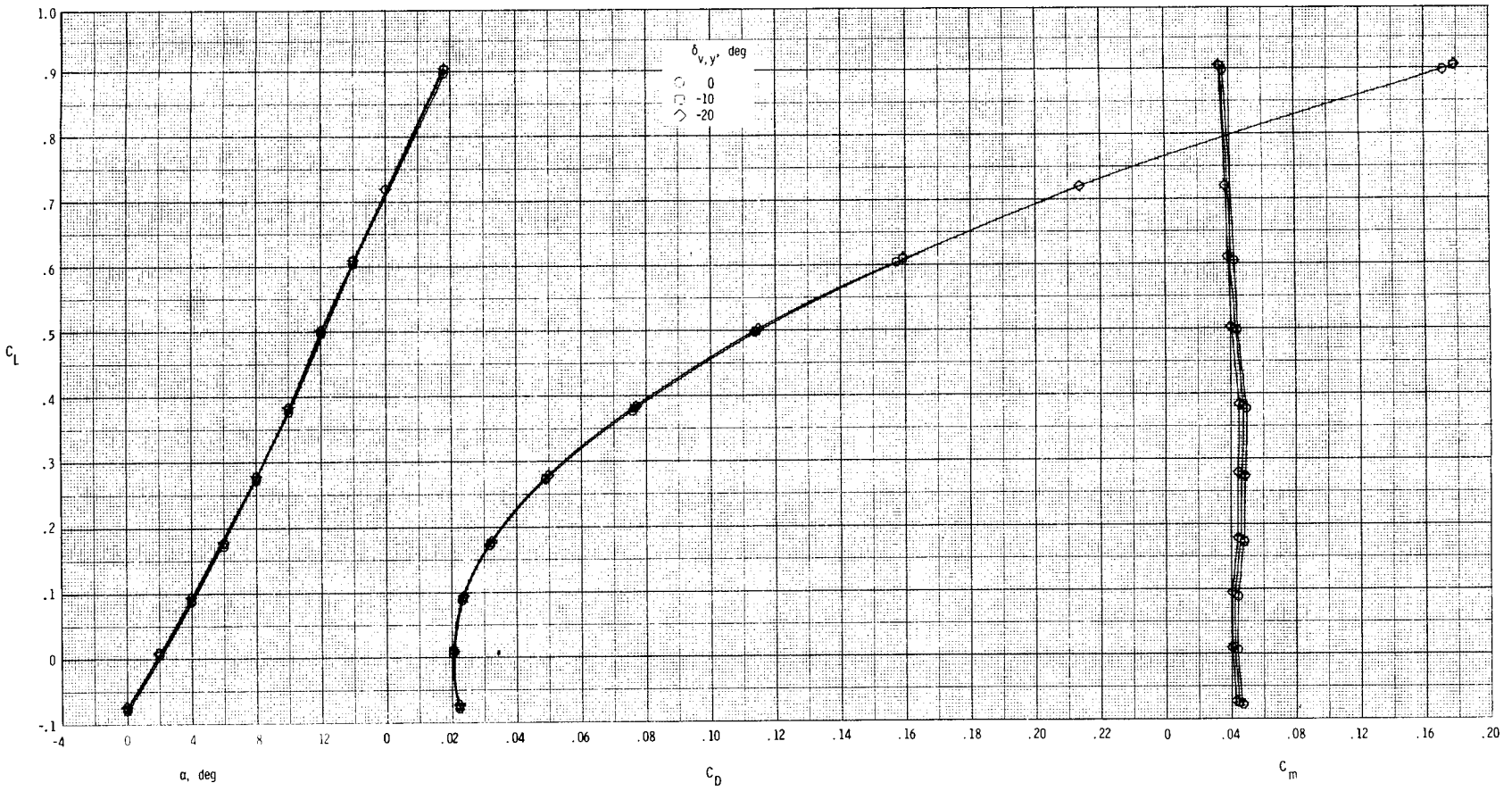

(g) $M = 0.87$; NPR = 1.0.

Figure 22. Continued.

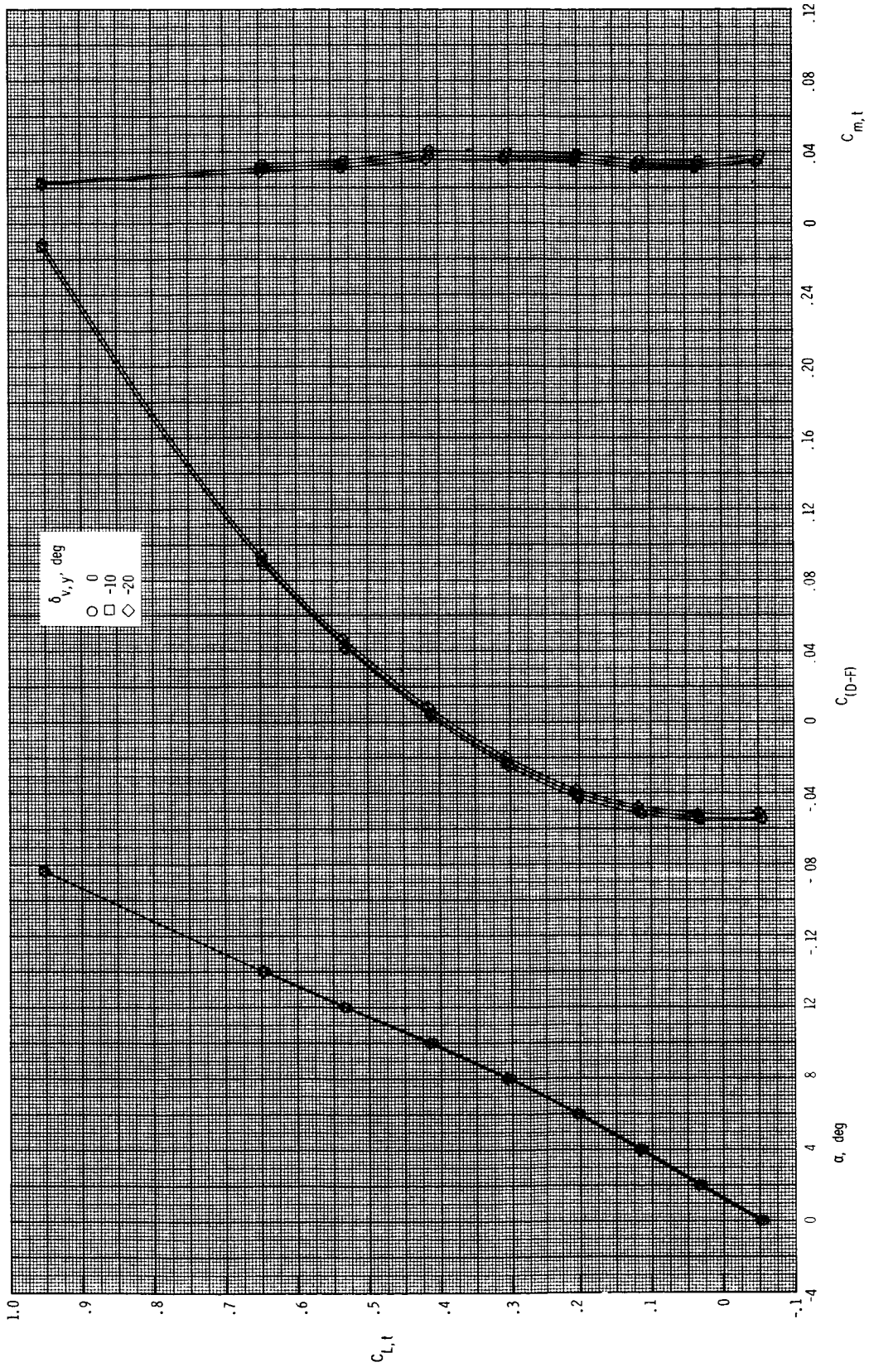

(h) $M = 0.87$; NPR $= 3.9$.

Figure 22. Continued.

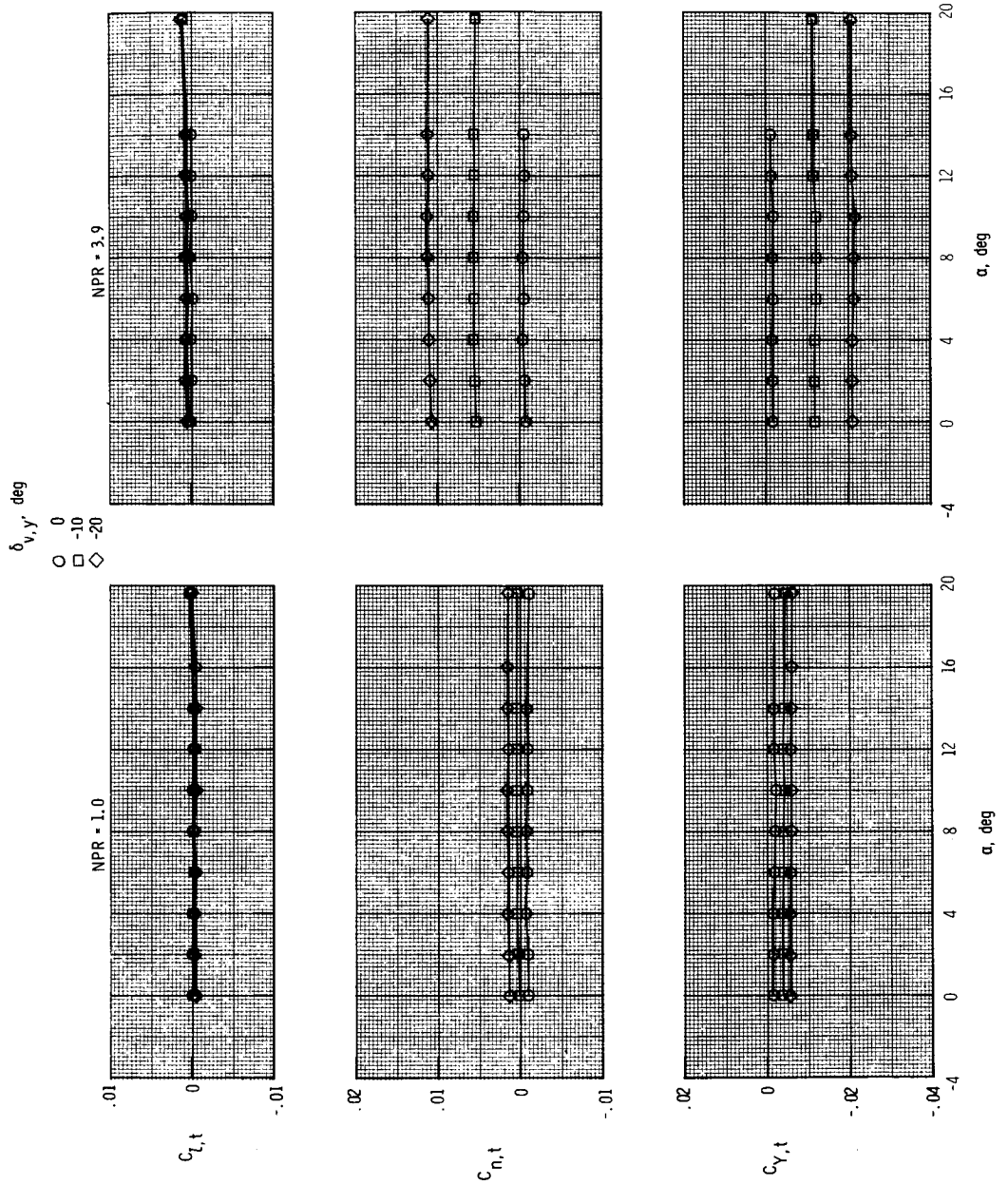

(i) $M = 0.87$; NPR = 1.0 and 3.9.

Figure 22. Continued.

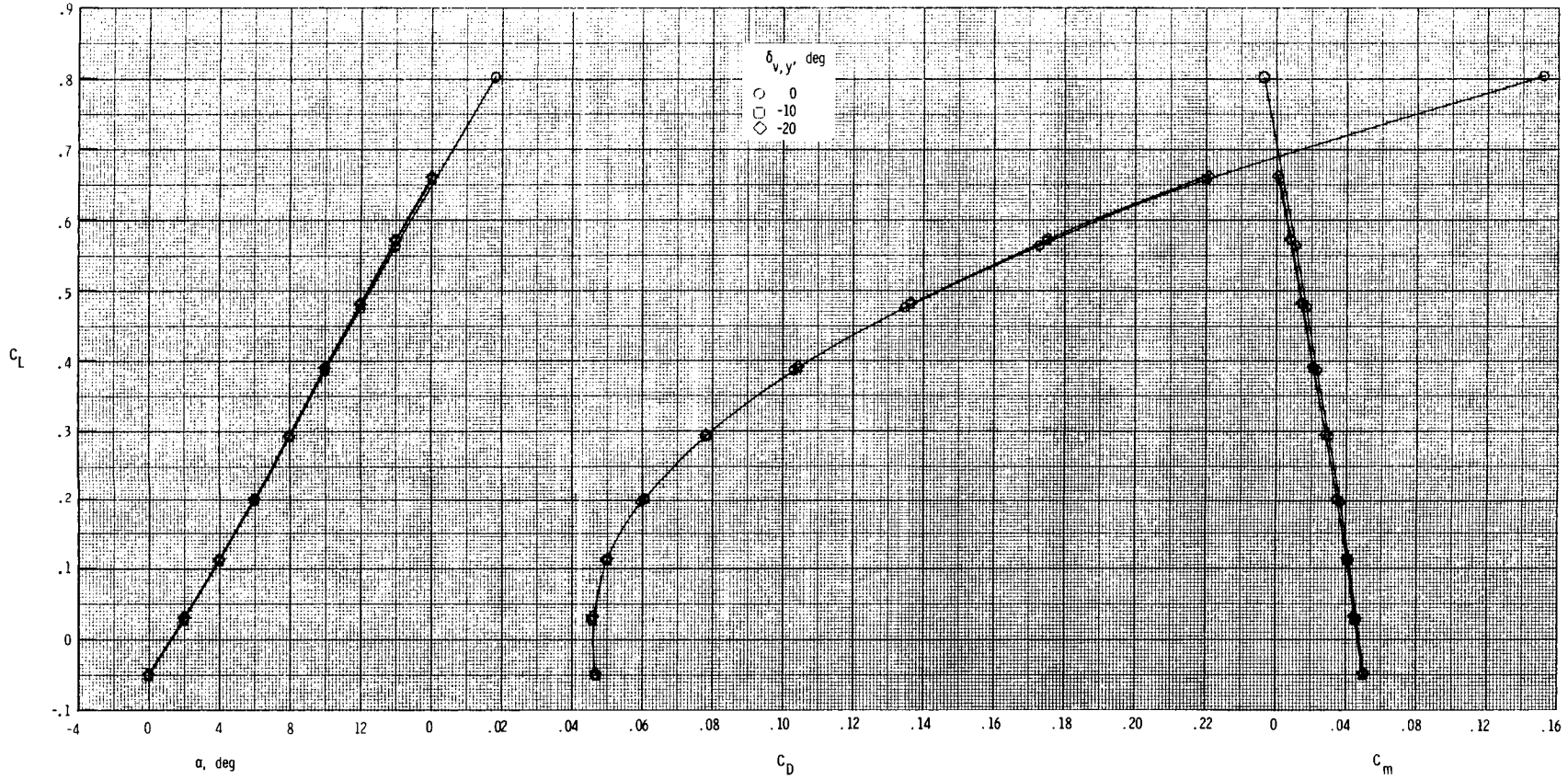

(j) $M = 1.20$; NPR = 1.0.

Figure 22. Continued.

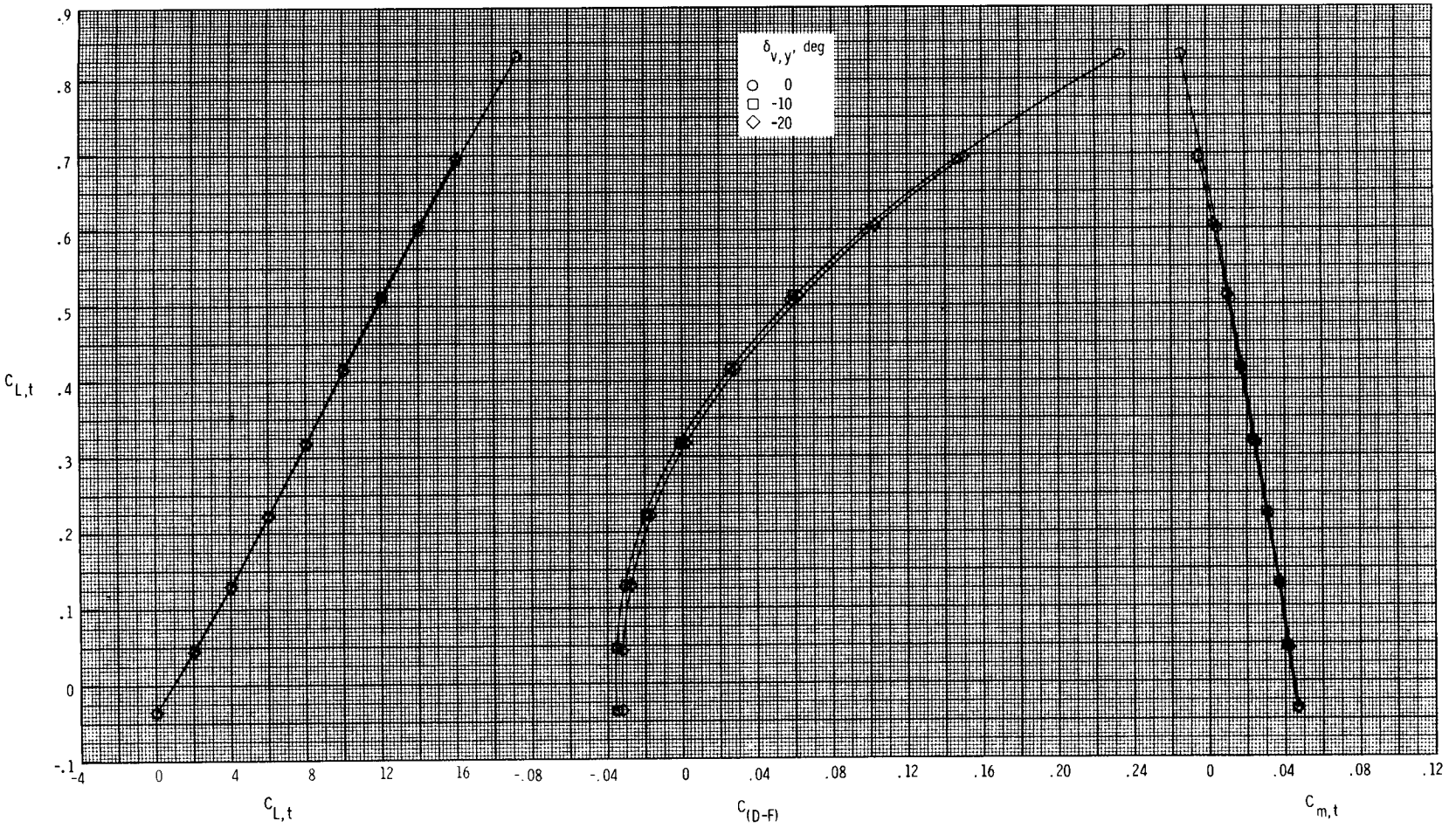

(k) $M = 1.20$; NPR = 6.6.

Figure 22. Continued.

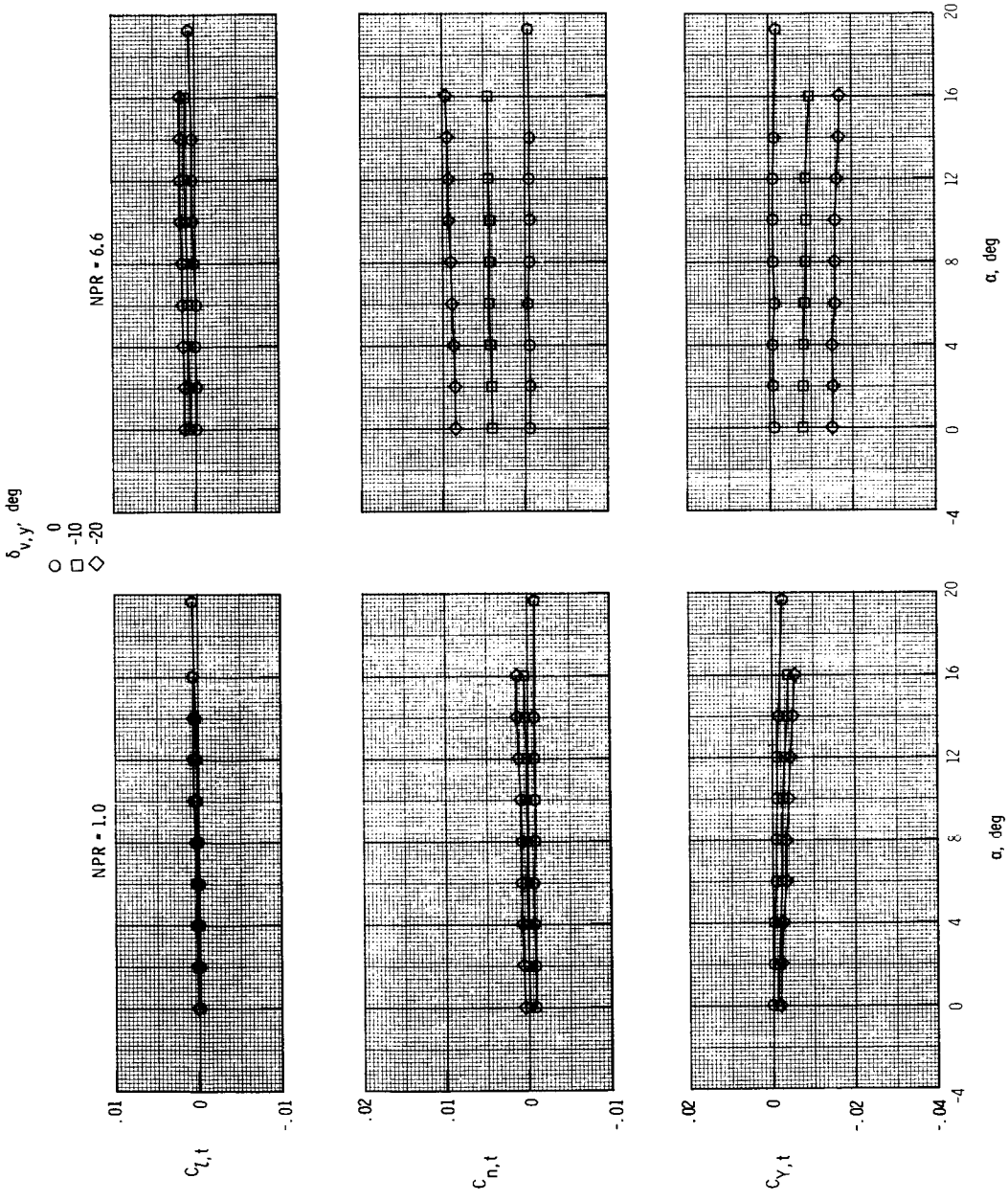

(l) $M = 1.20$; NPR = 1.0 and 6.6.

Figure 22. Concluded.

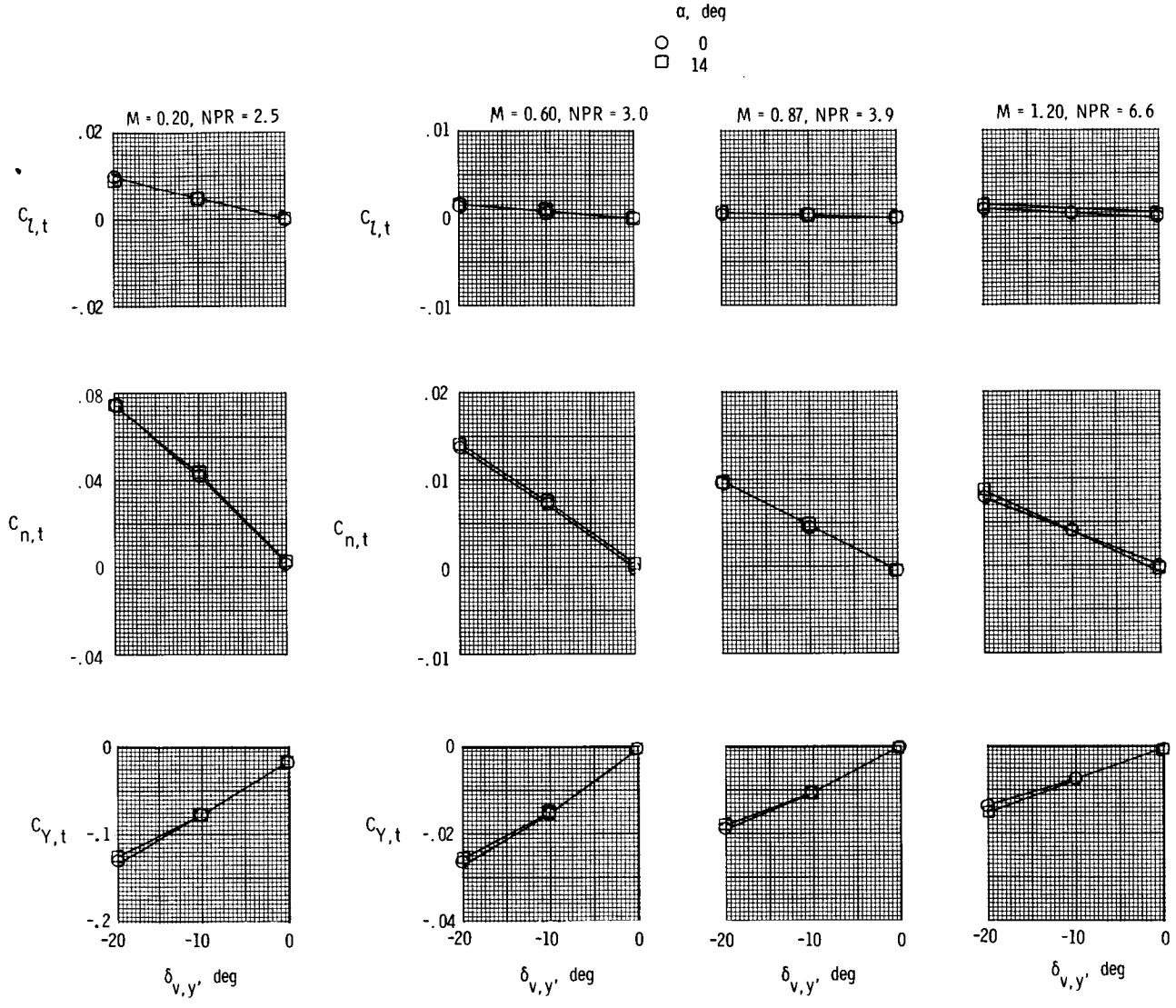

(a) $M = 0.20$ to 1.20.

Figure 23. Summary of yaw vectoring for $\delta_{v,p} = 0°$.

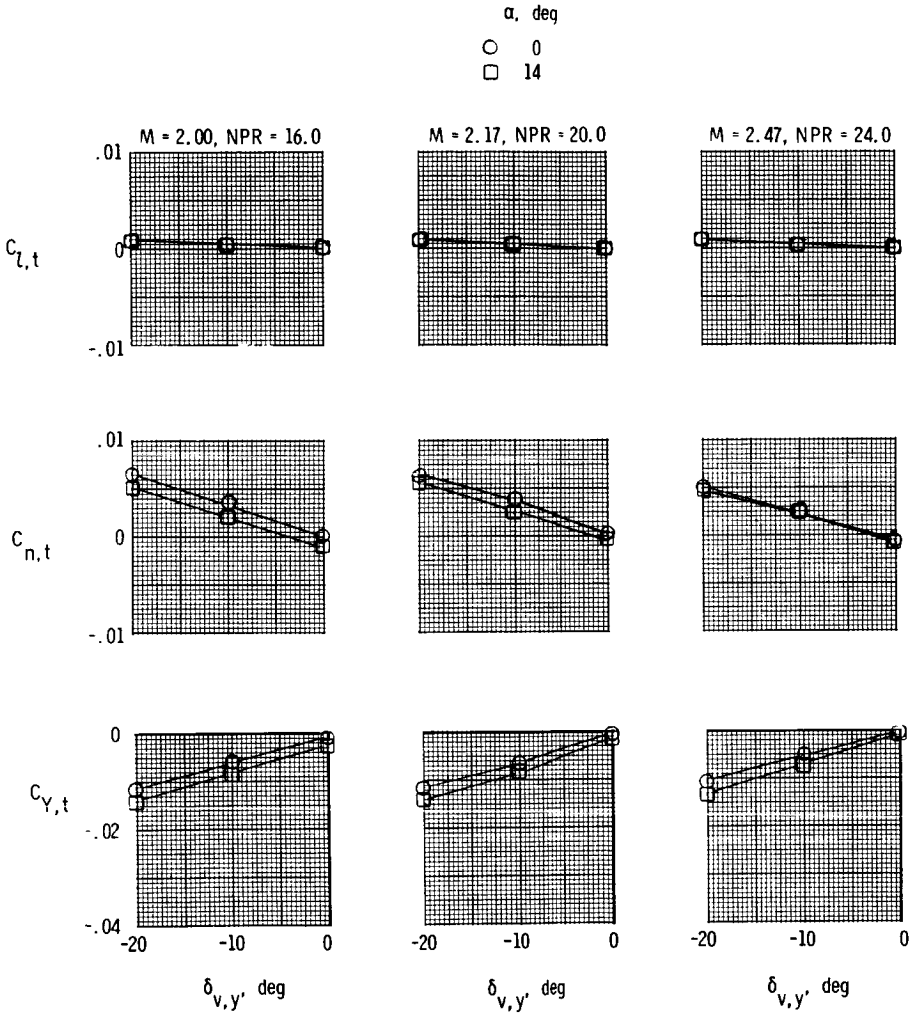

(b) $M = 2.00$ to 2.47.

Figure 23. Concluded.

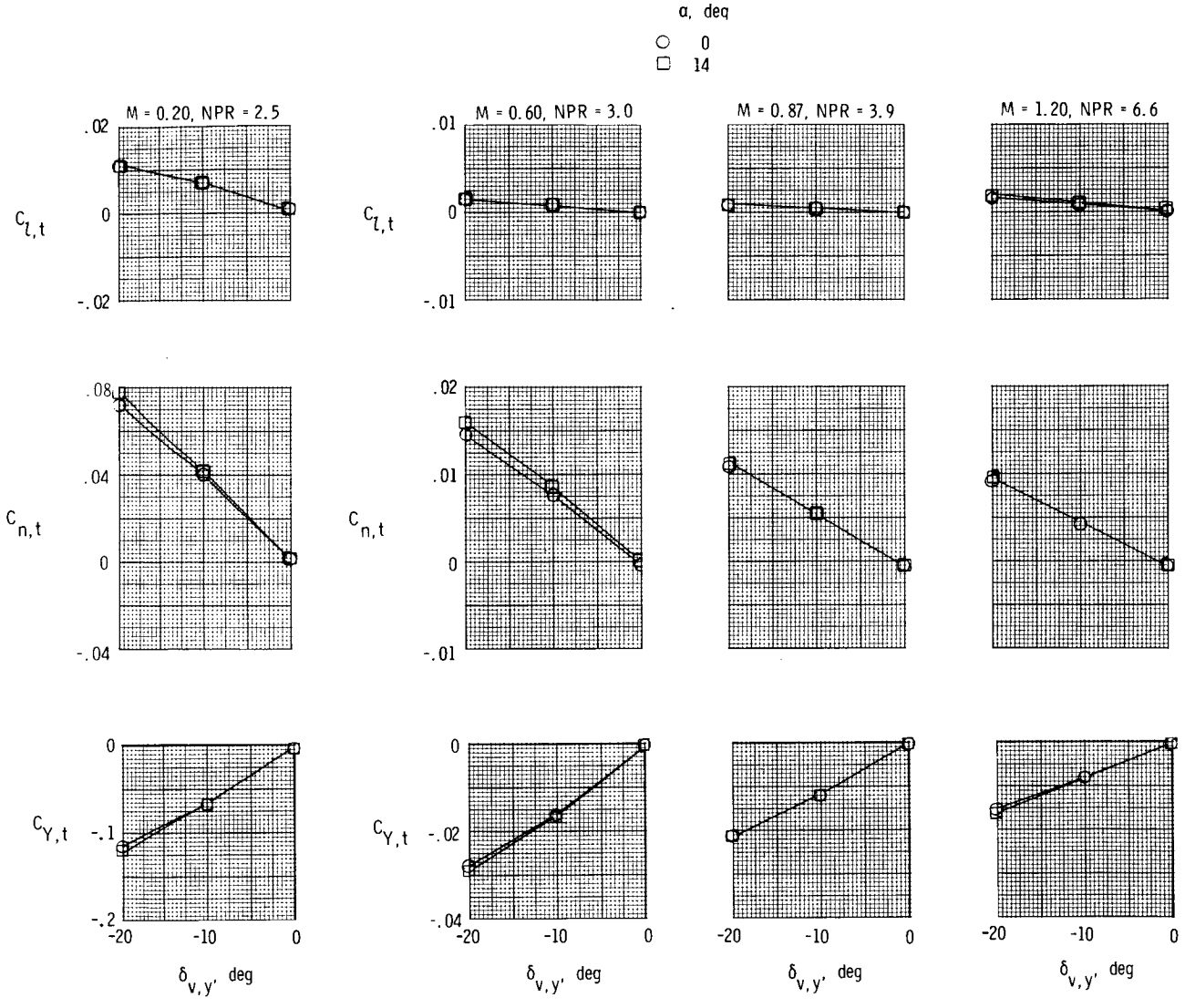

Figure 24. Summary of yaw vectoring for $\delta_{v,p} = 15°$.

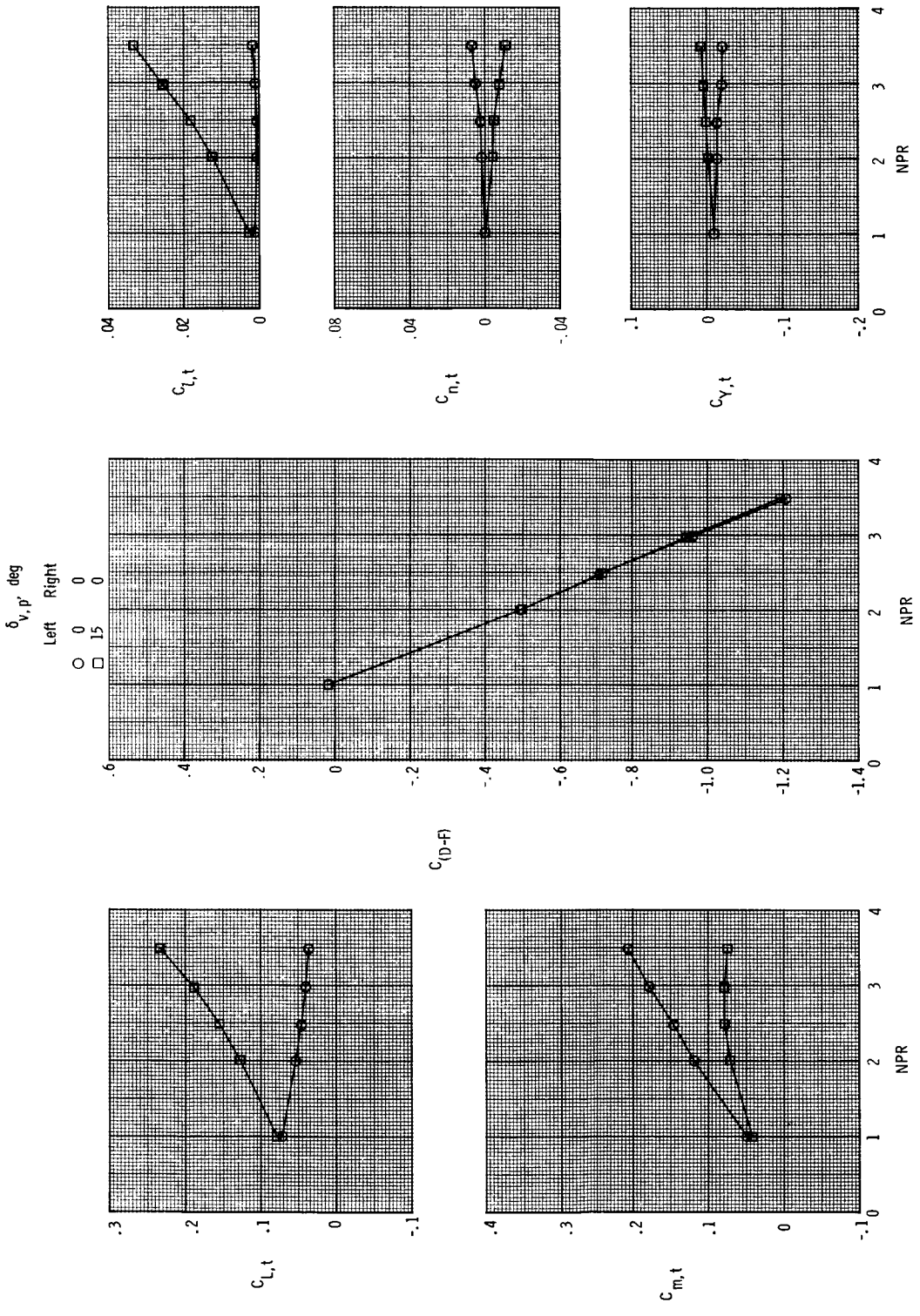

(a) $M = 0.20$.

Figure 25. Effect of nozzle pressure ratio and differential pitch vectoring on total aerodynamic characteristics for $\delta_{v,y} = 0°$ and $\alpha = 4°$.

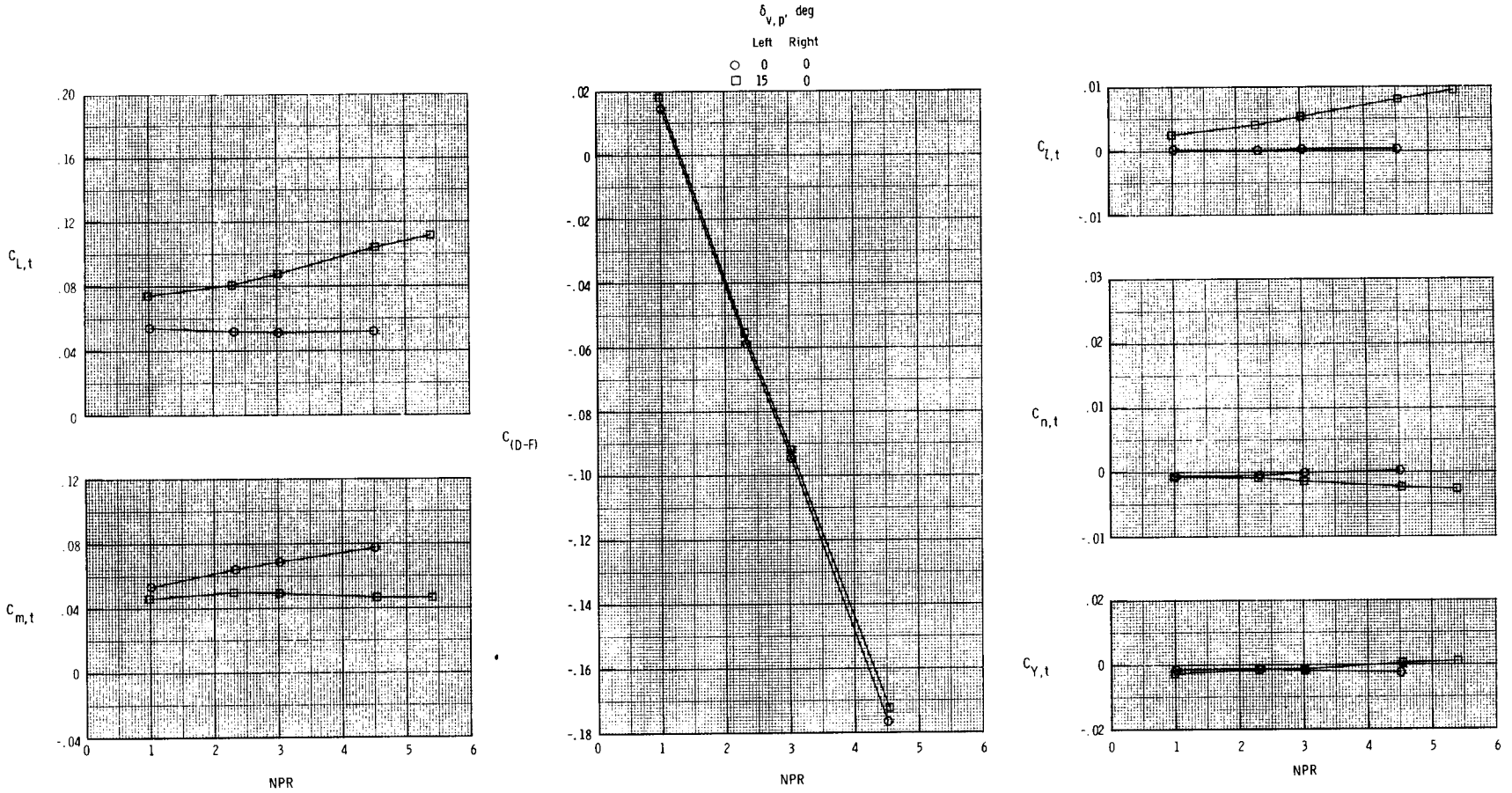

(b) $M = 0.60$.

Figure 25. Continued.

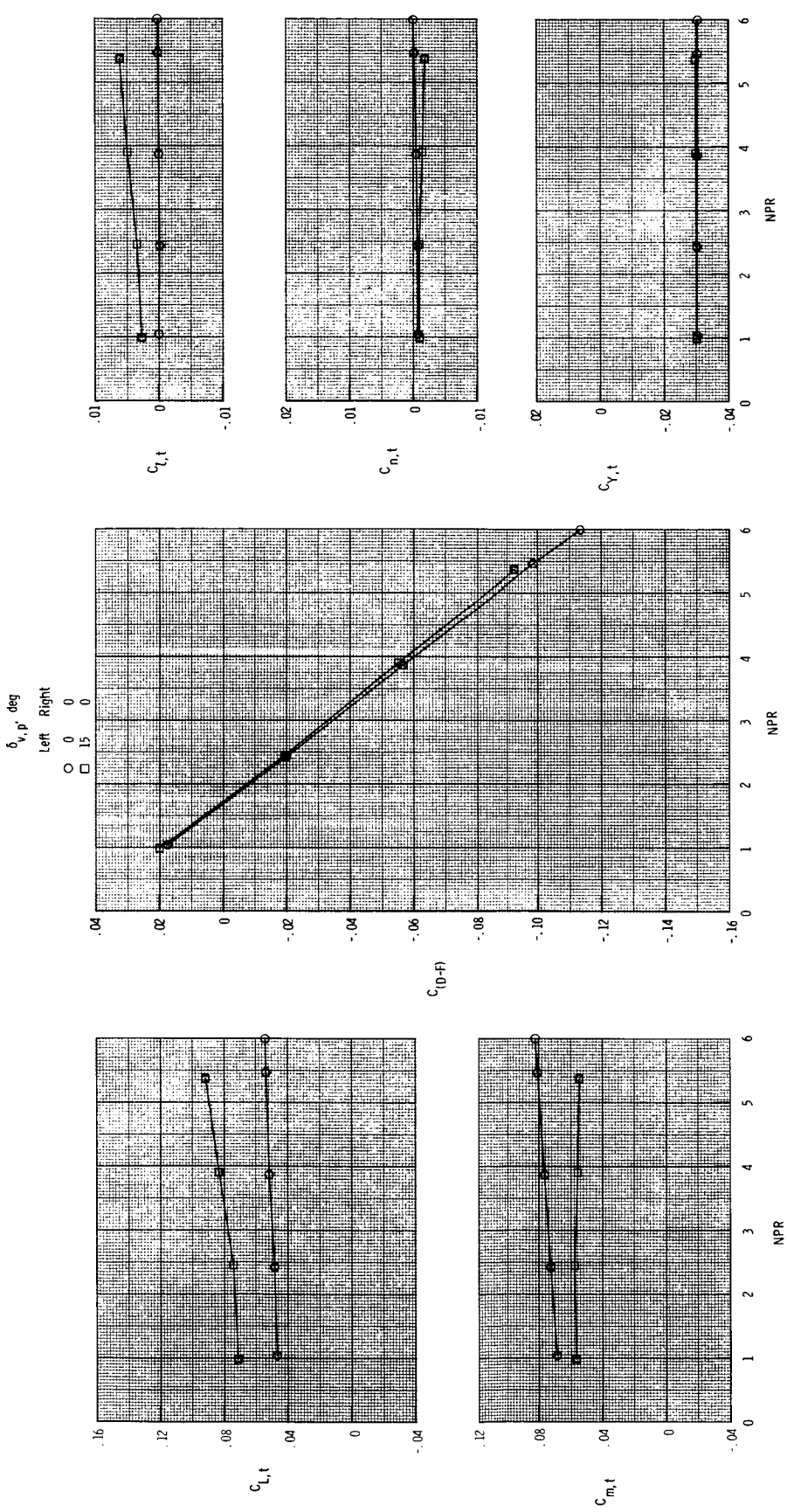

(c) $M = 0.87$.

Figure 25. Continued.

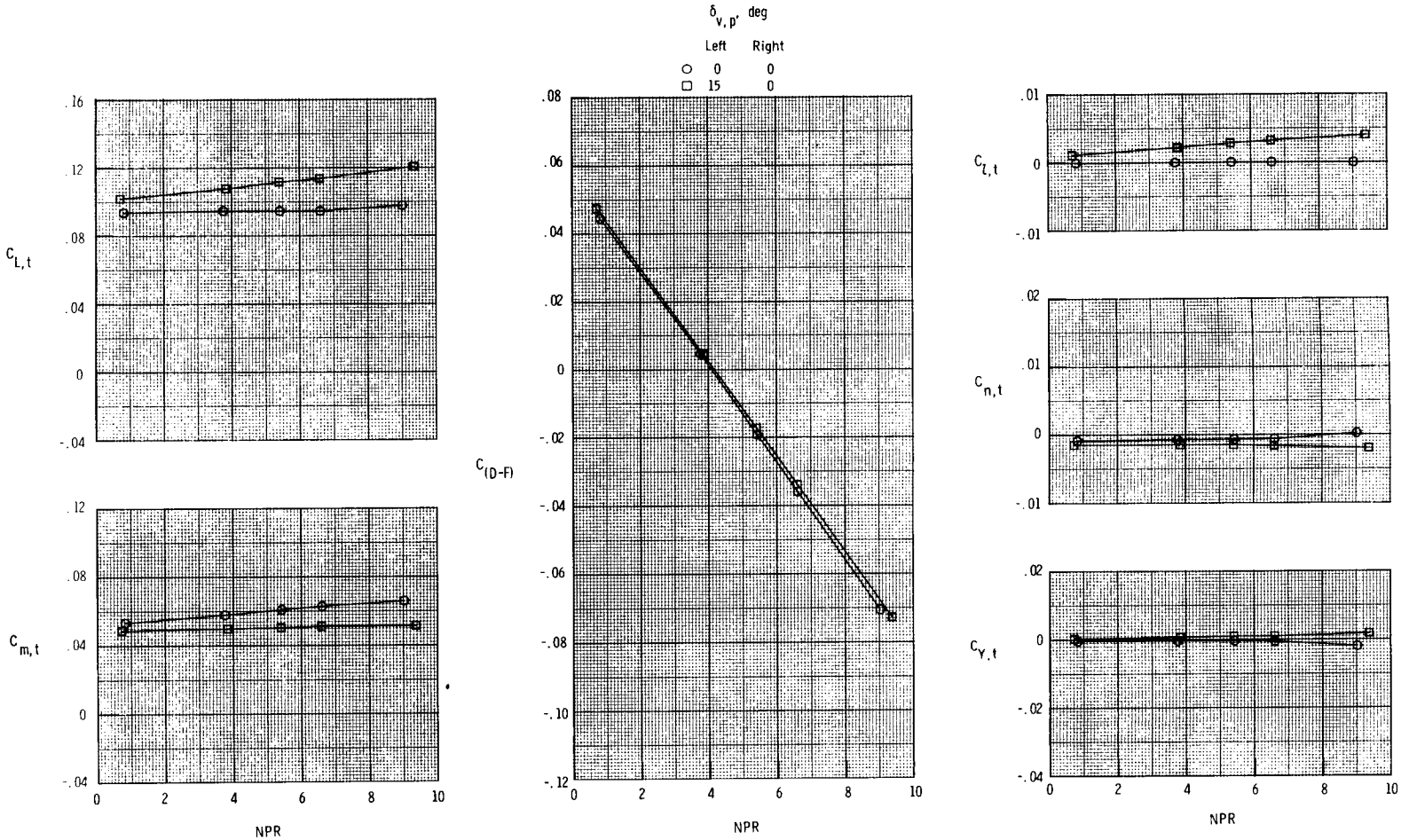

(d) $M = 1.20$.

Figure 25. Continued.

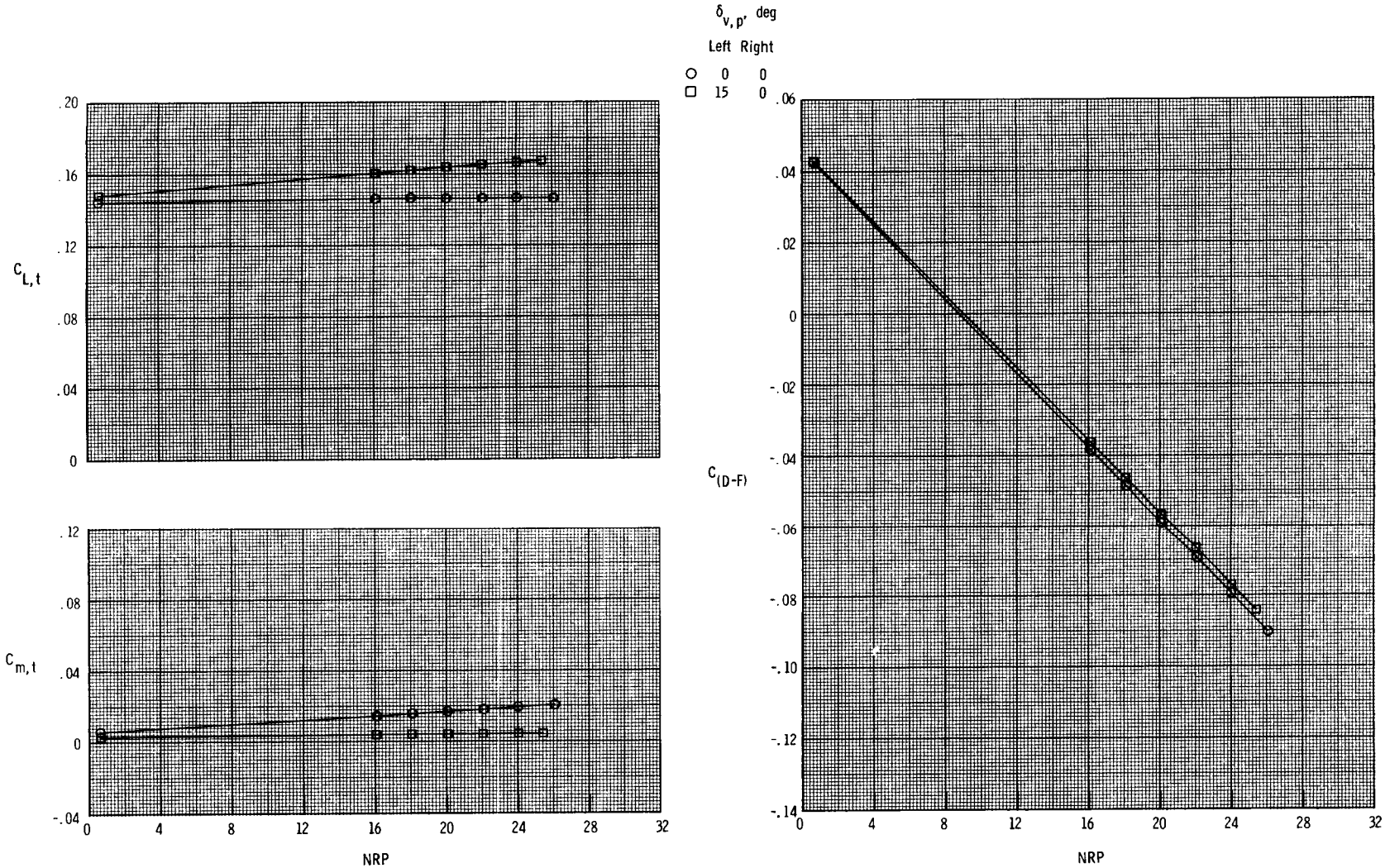

(e) $M = 2.00$.

Figure 25. Continued.

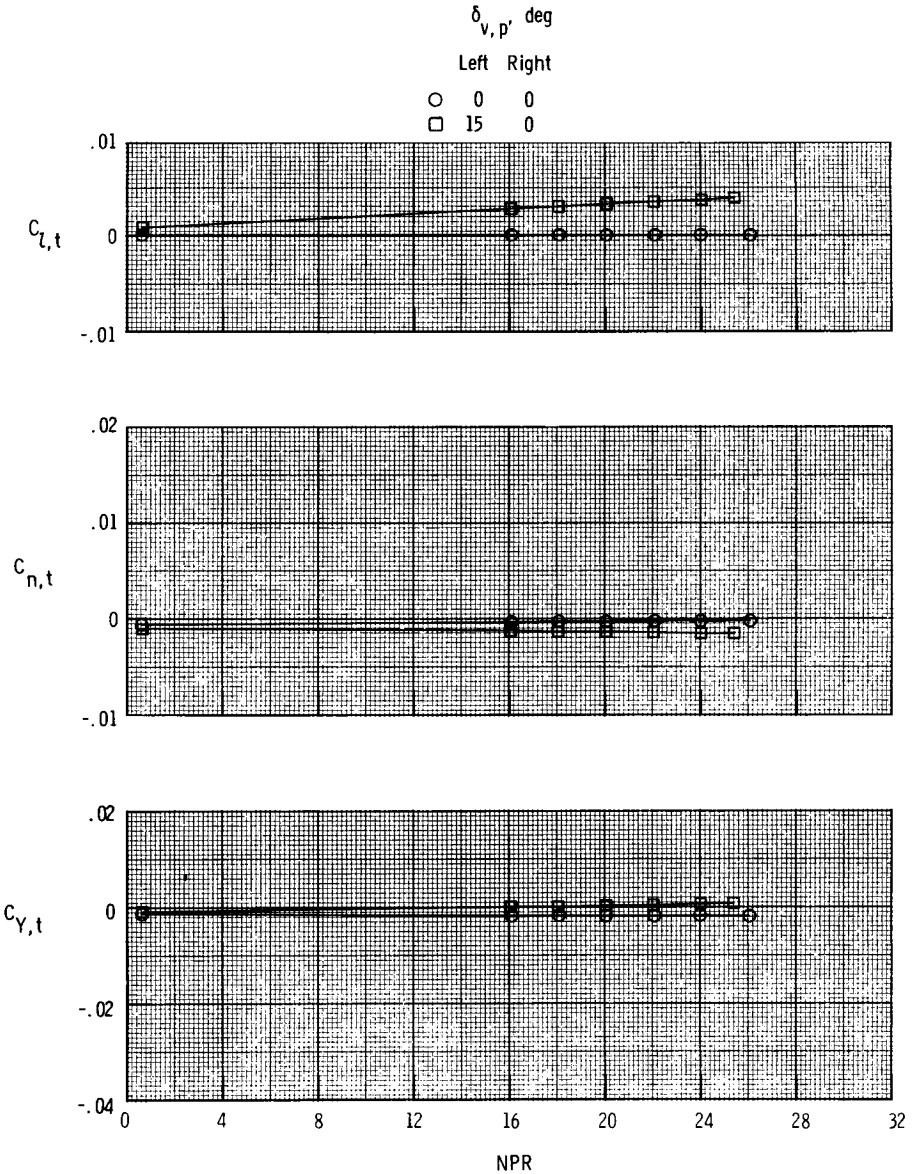

(e) Concluded.

Figure 25. Continued.

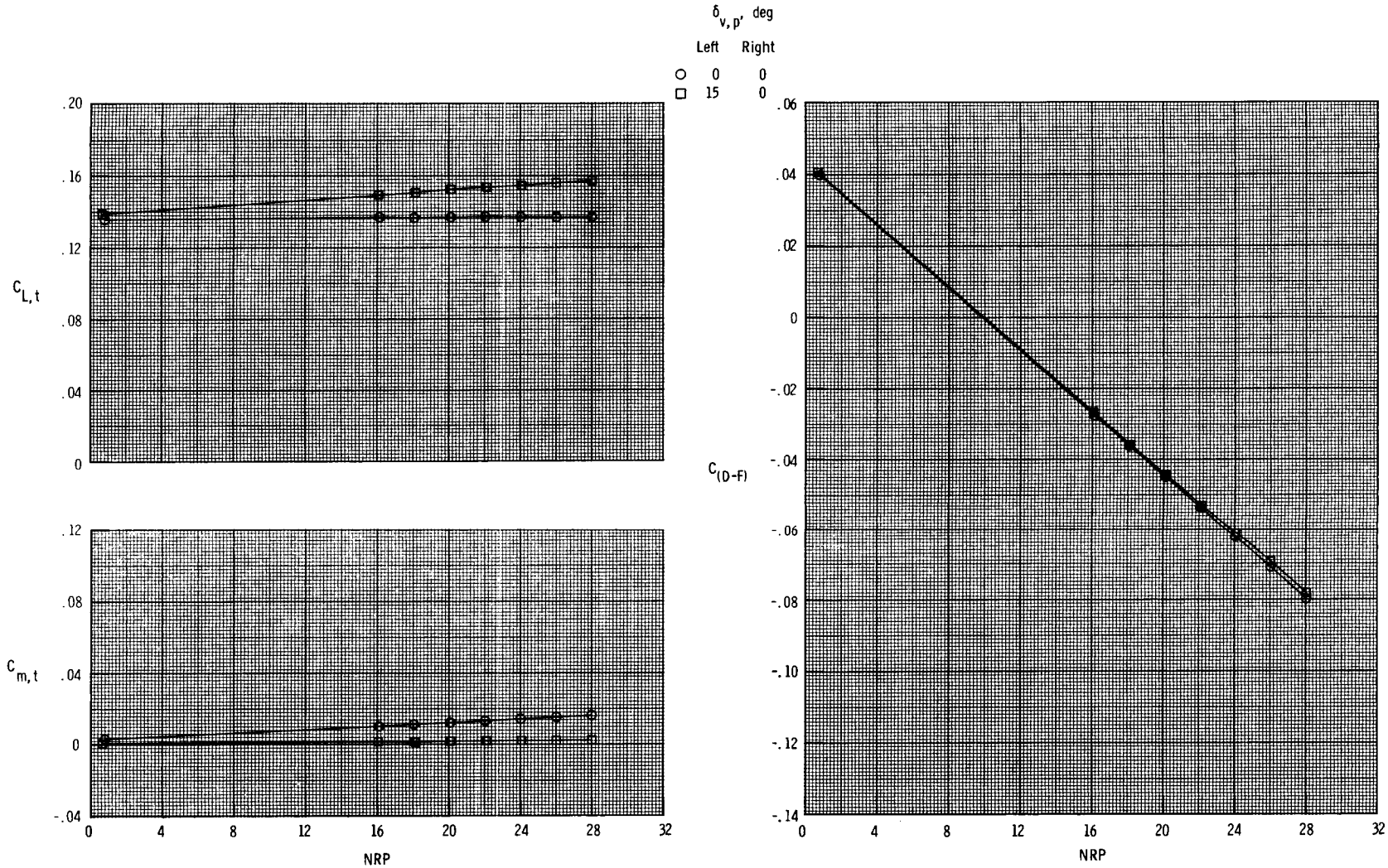

(f) $M = 2.17$.

Figure 25. Continued.

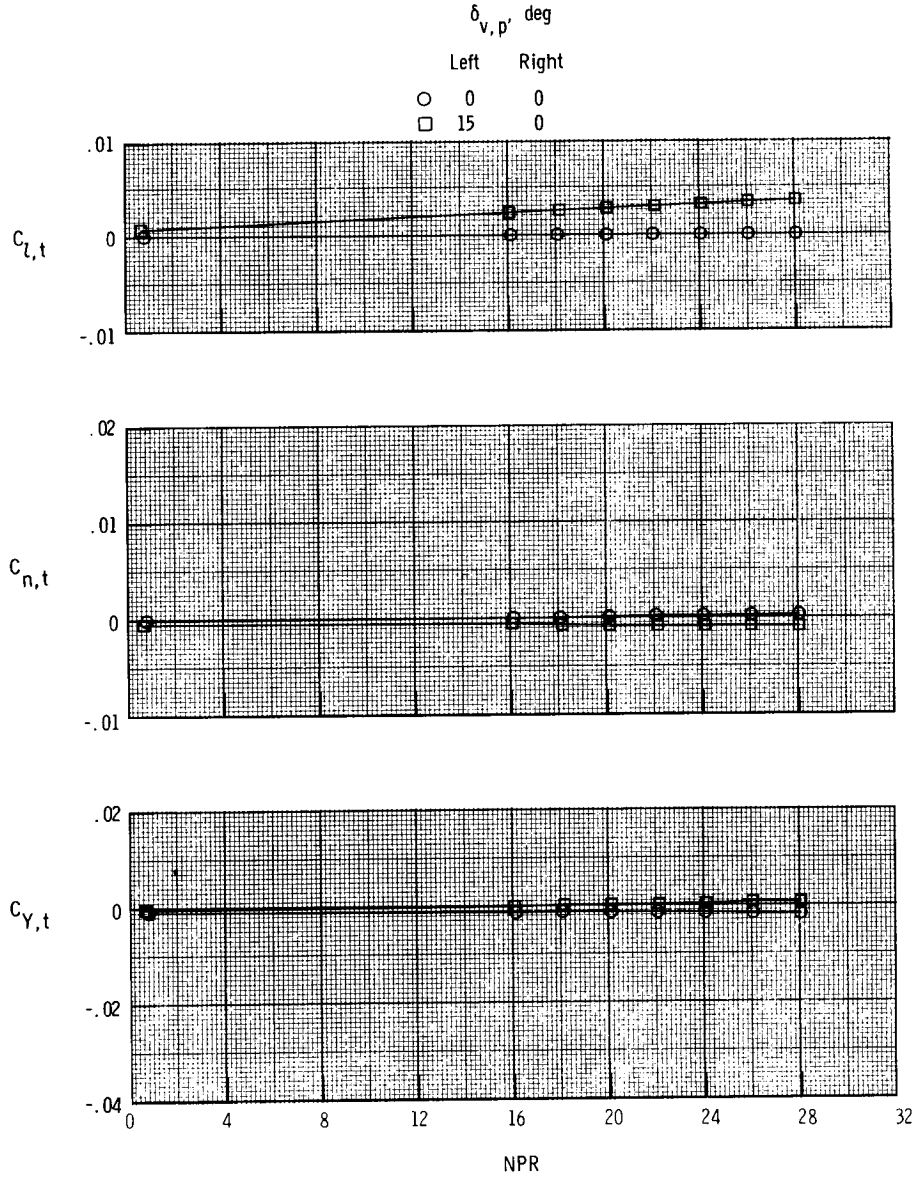

(f) Concluded.

Figure 25. Continued.

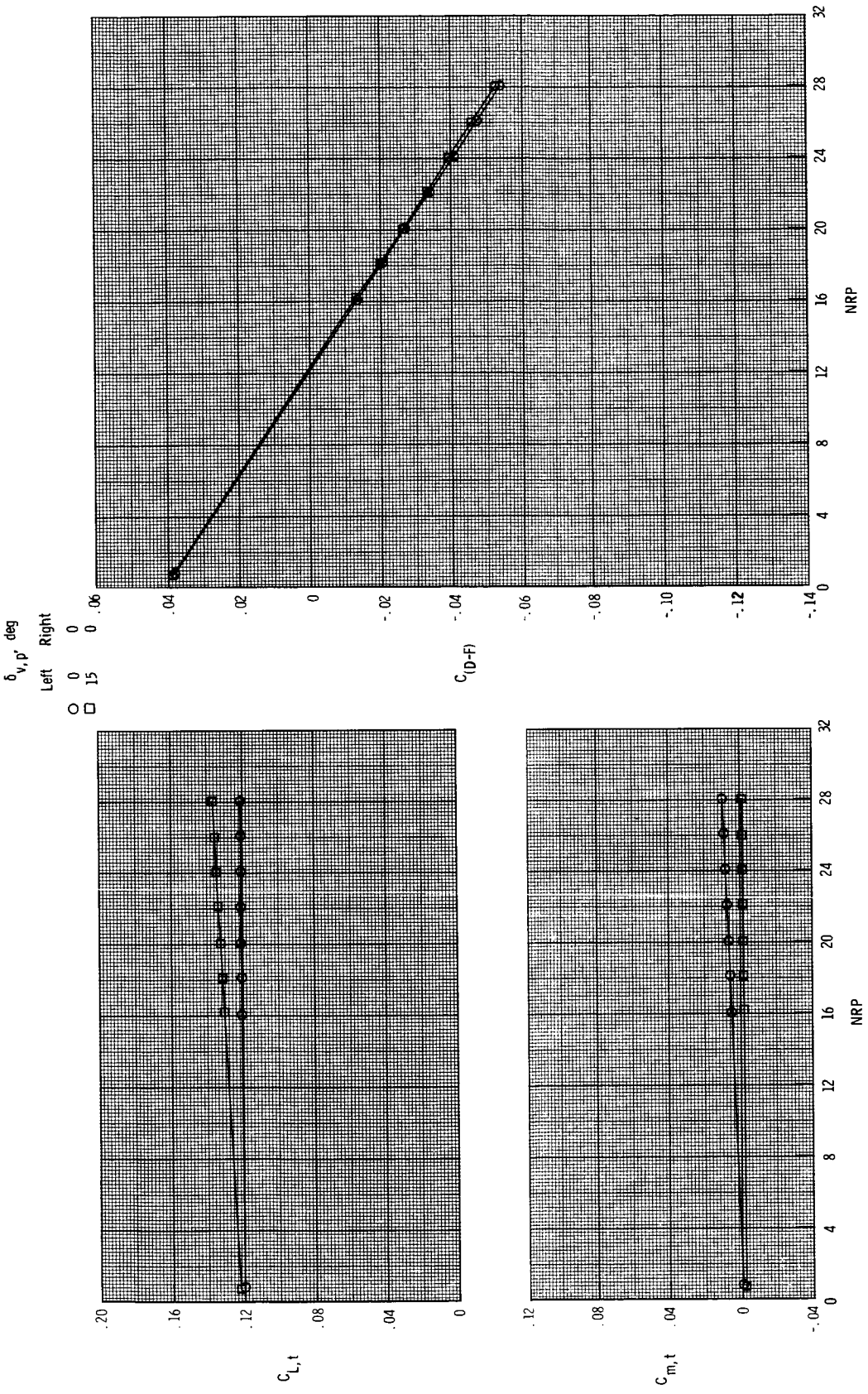

(g) $M = 2.47$.

Figure 25. Continued.

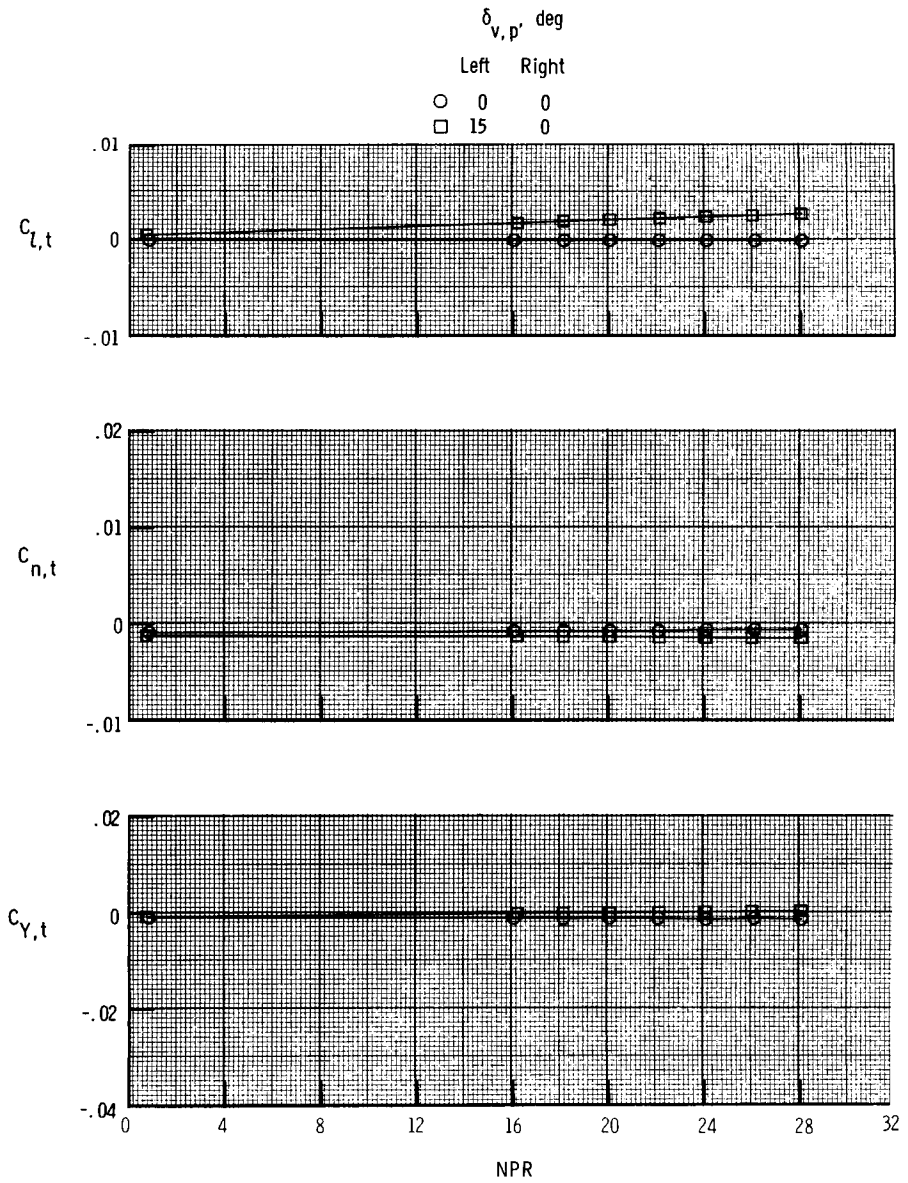

(g) Concluded.

Figure 25. Concluded.

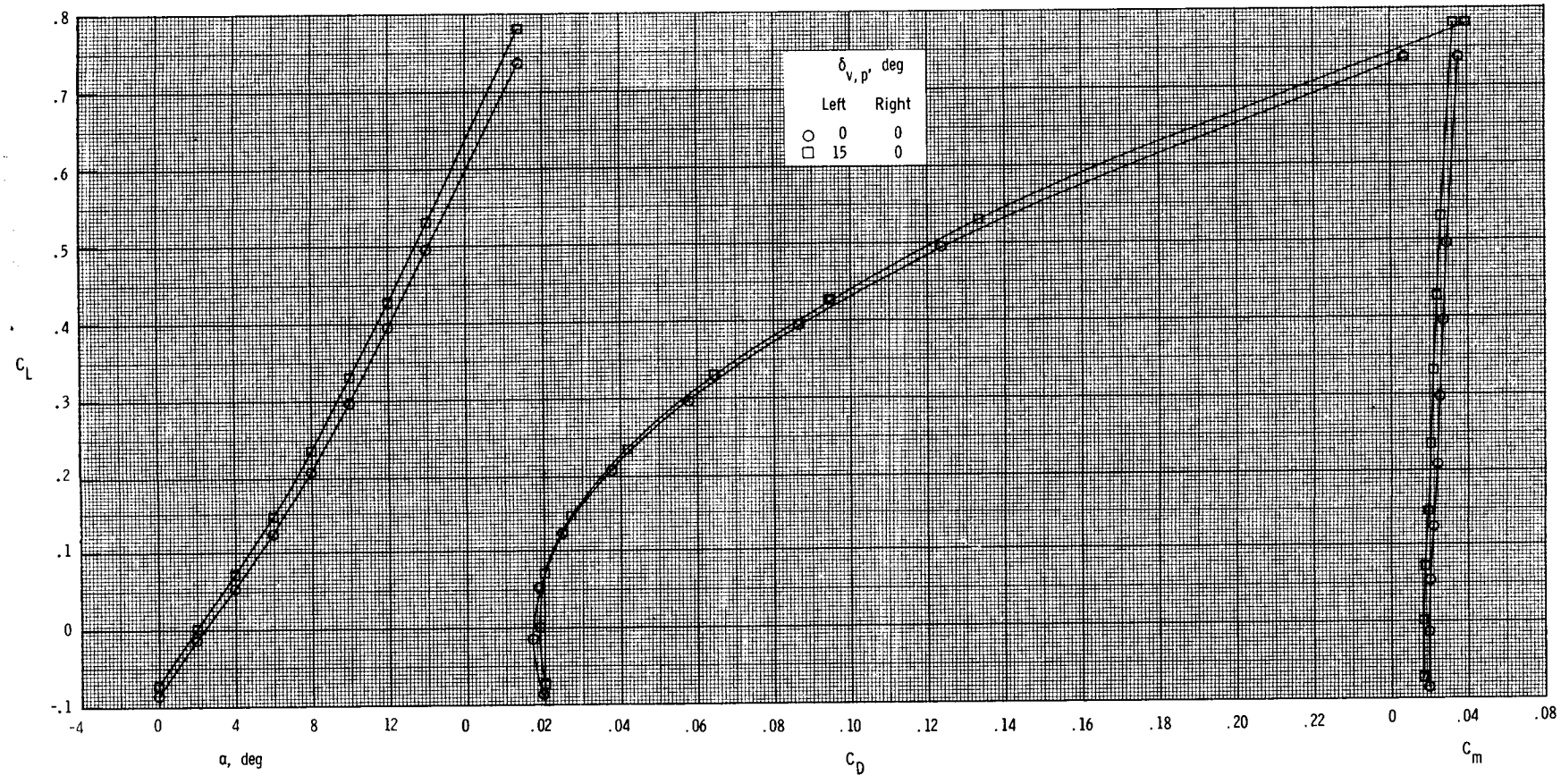

(a) $M = 0.20$; NPR = 1.0.

Figure 26. Effect of differential pitch vectoring on total aerodynamic characteristics for $\delta_{v,y} = 0°$.

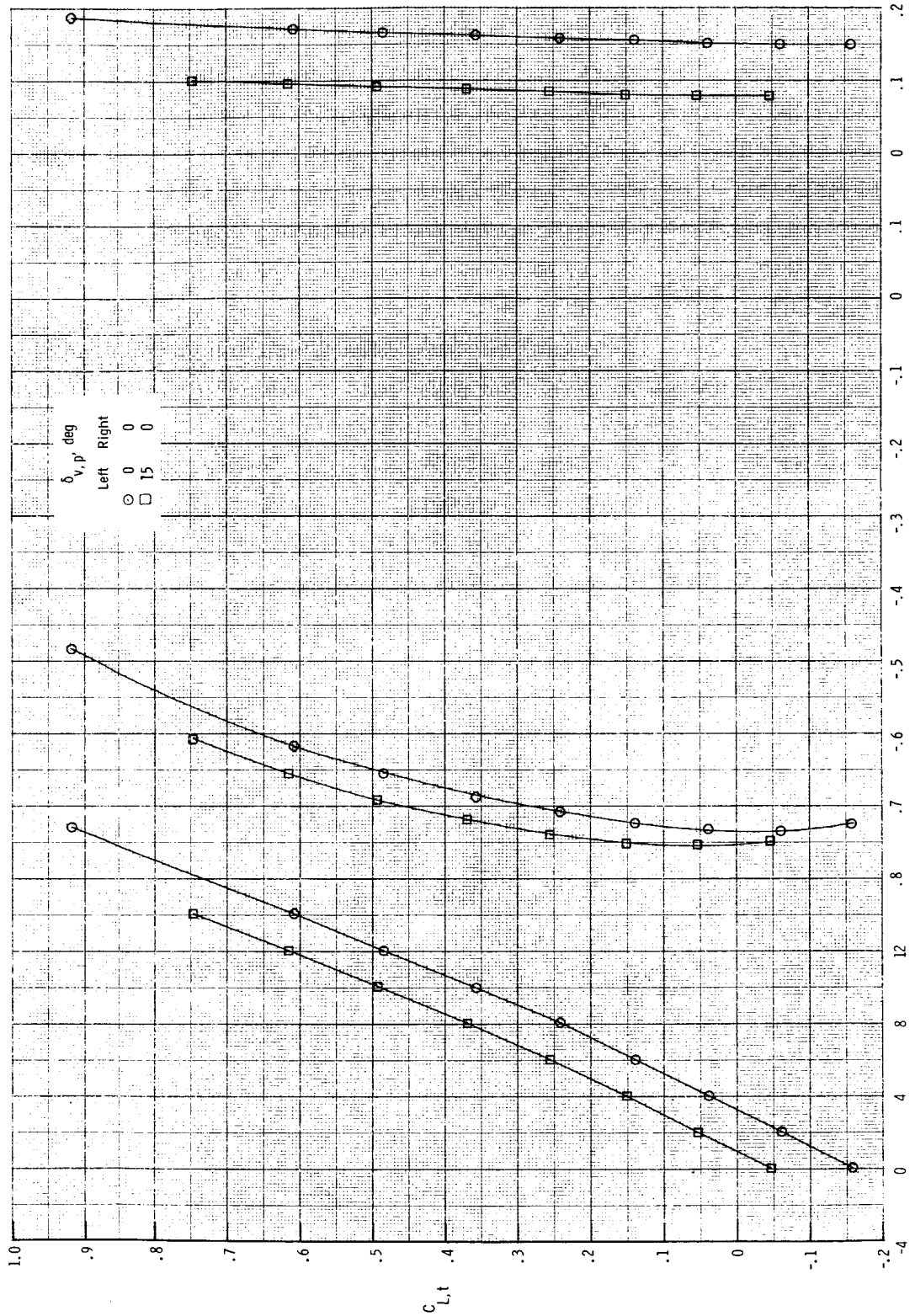

(b) $M = 0.20$; NPR = 2.5.

Figure 26. Continued.

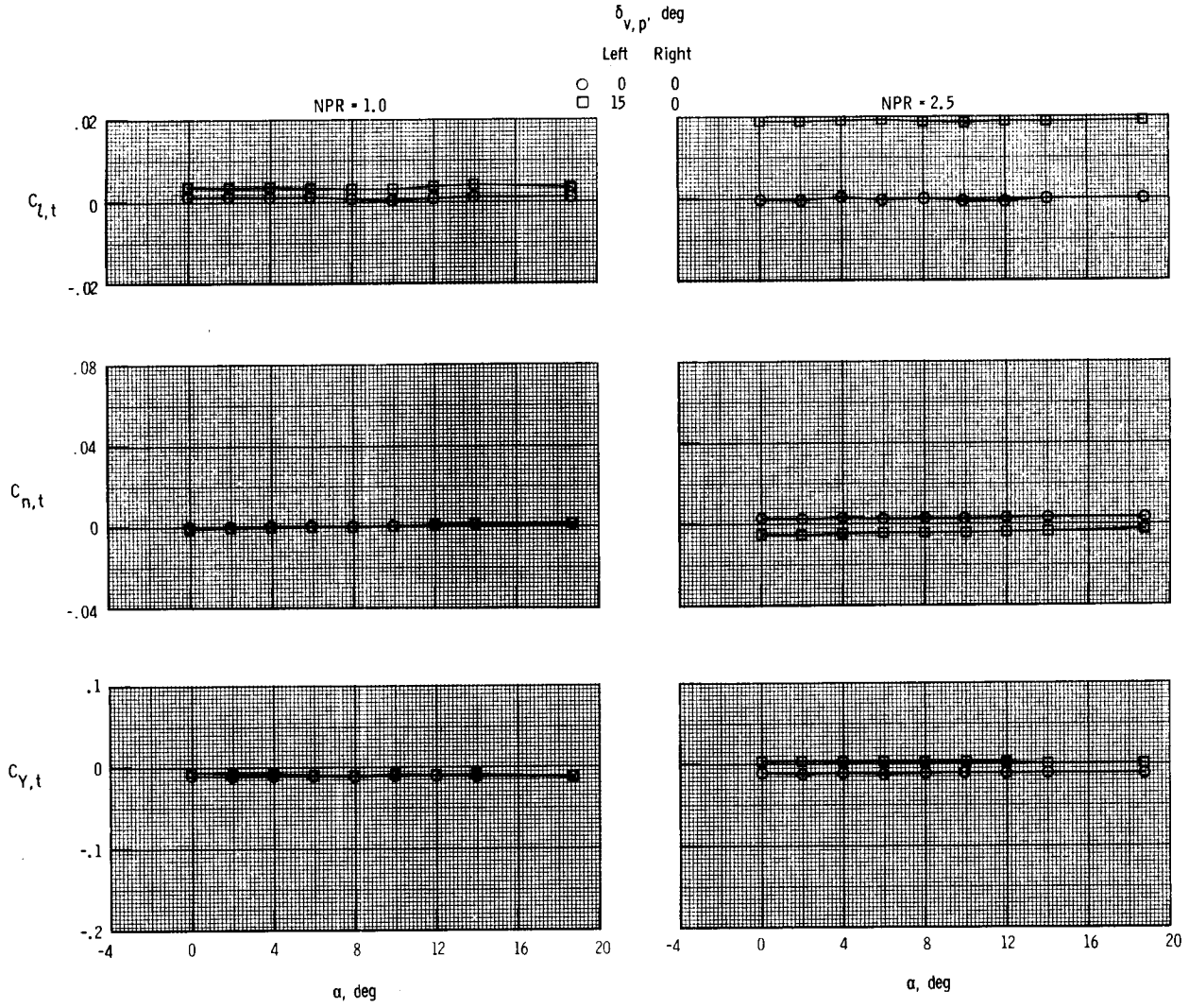

(c) $M = 0.20$; NPR = 1.0 and 2.5.

Figure 26. Continued.

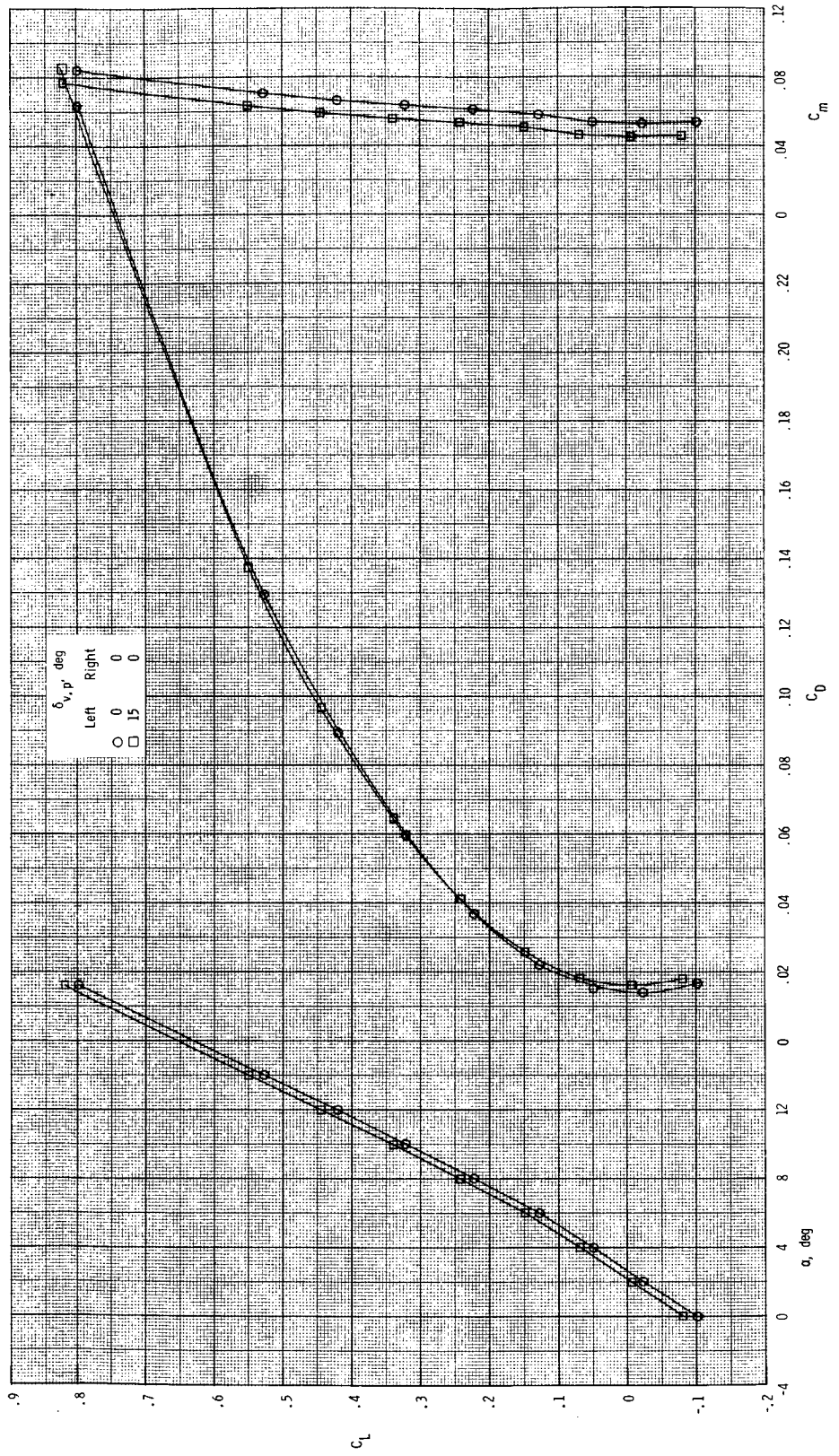

(d) $M = 0.60$; NPR = 1.0.

Figure 26. Continued.

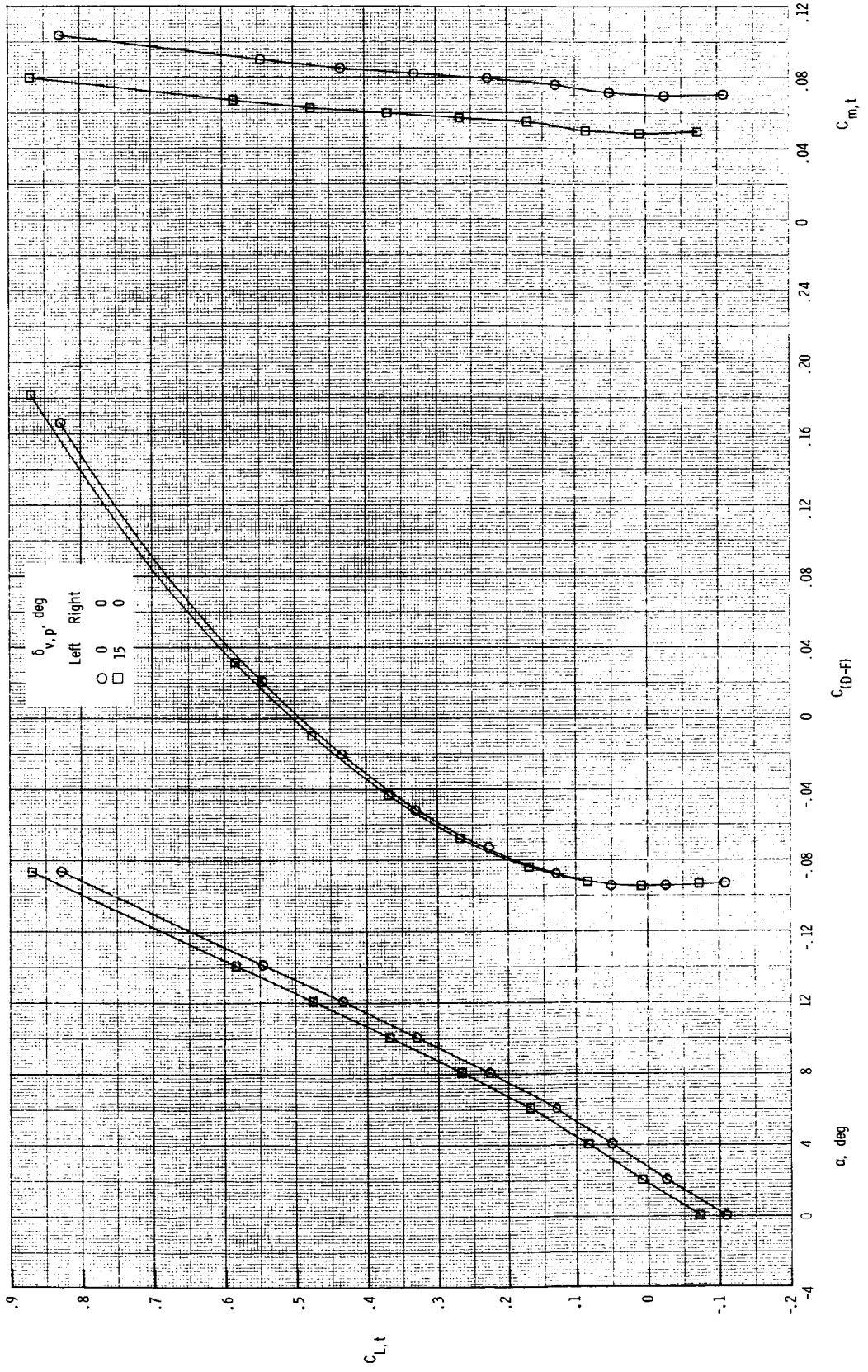

(e) $M = 0.60$; NPR = 3.0.

Figure 26. Continued.

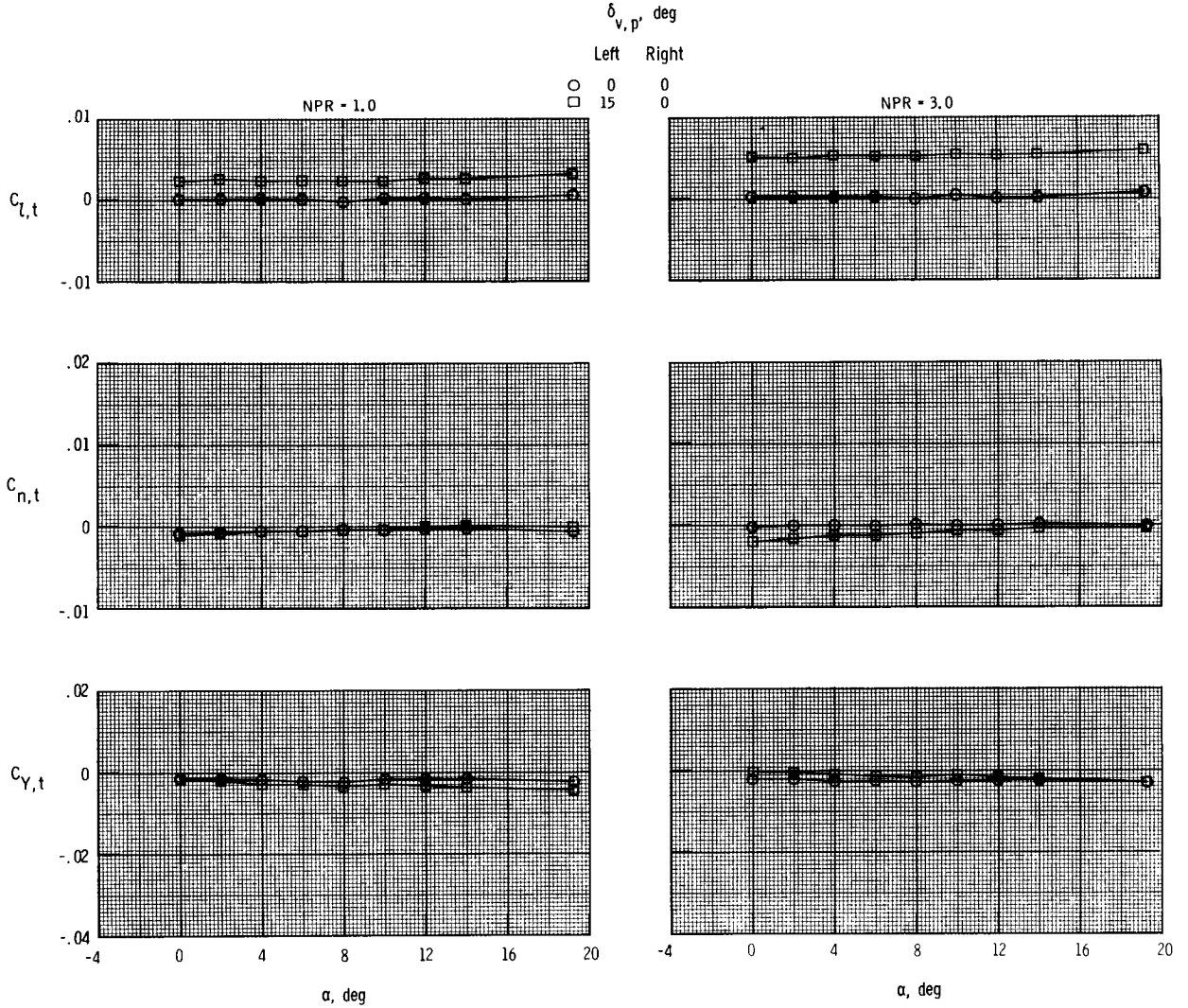

(f) $M = 0.60$; NPR = 1.0 and 3.0.

Figure 26. Continued.

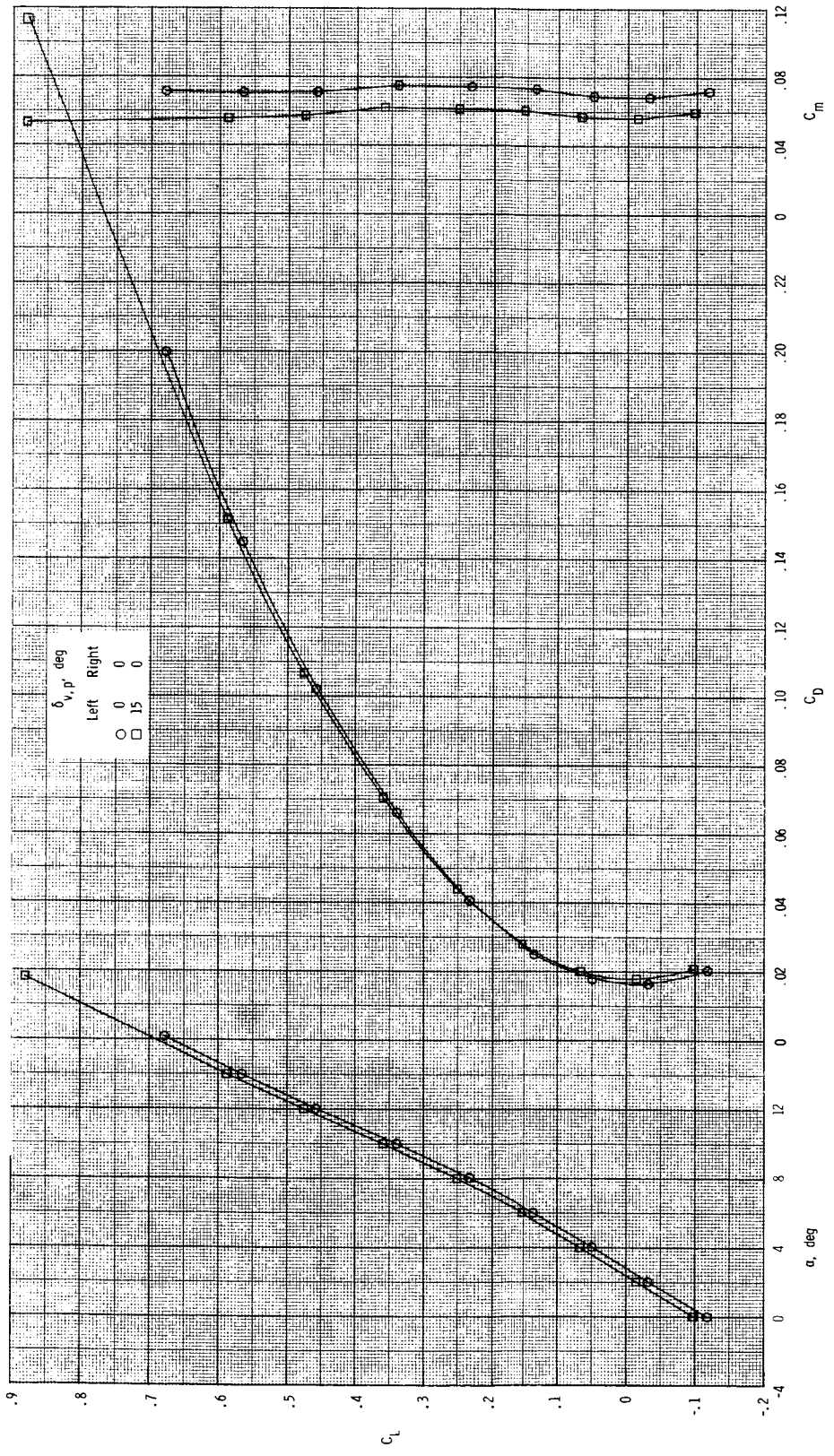

(g) $M = 0.87$; NPR = 1.0.

Figure 26. Continued.

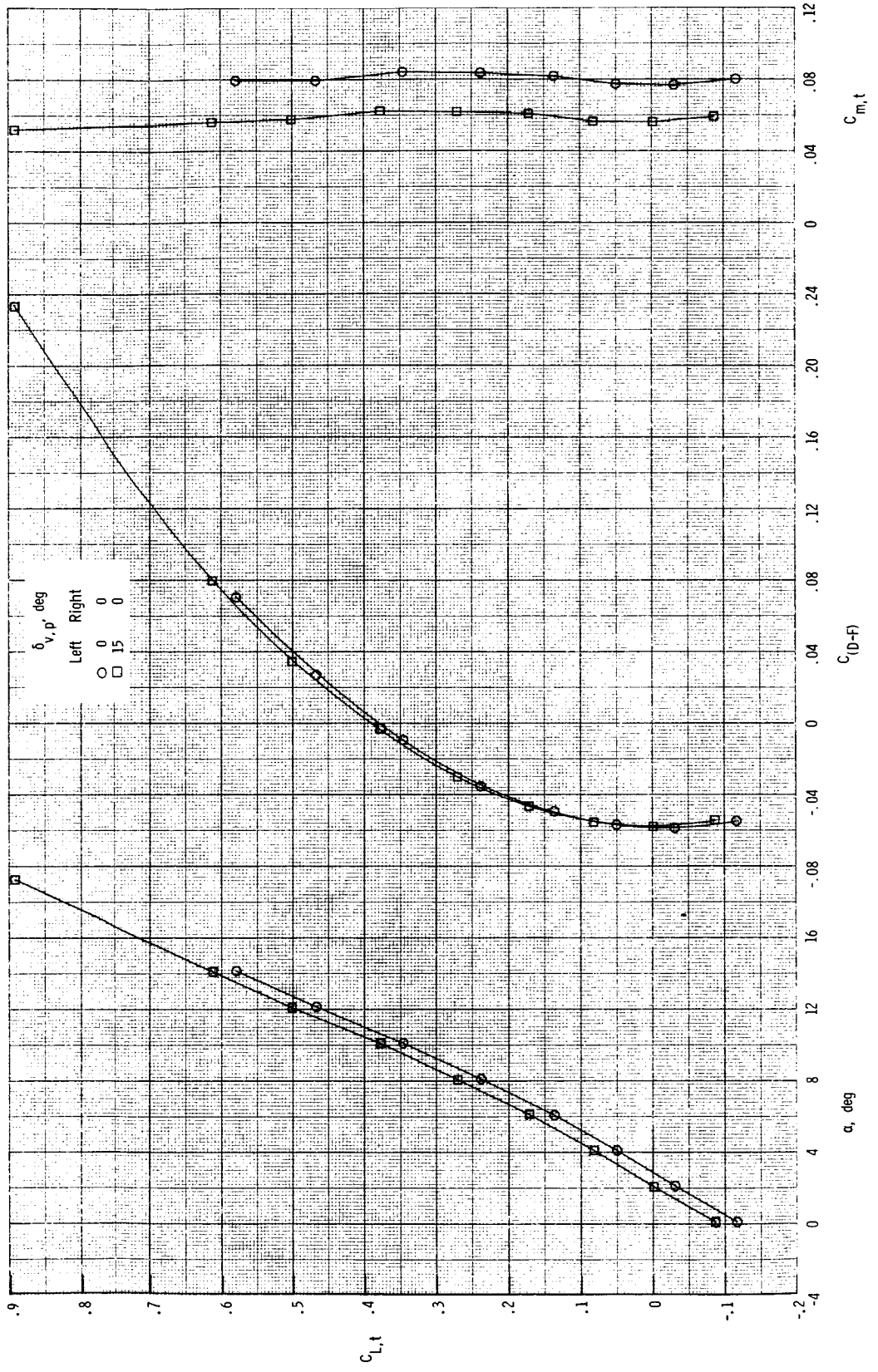

(h) $M = 0.87$; NPR = 3.9.

Figure 26. Continued.

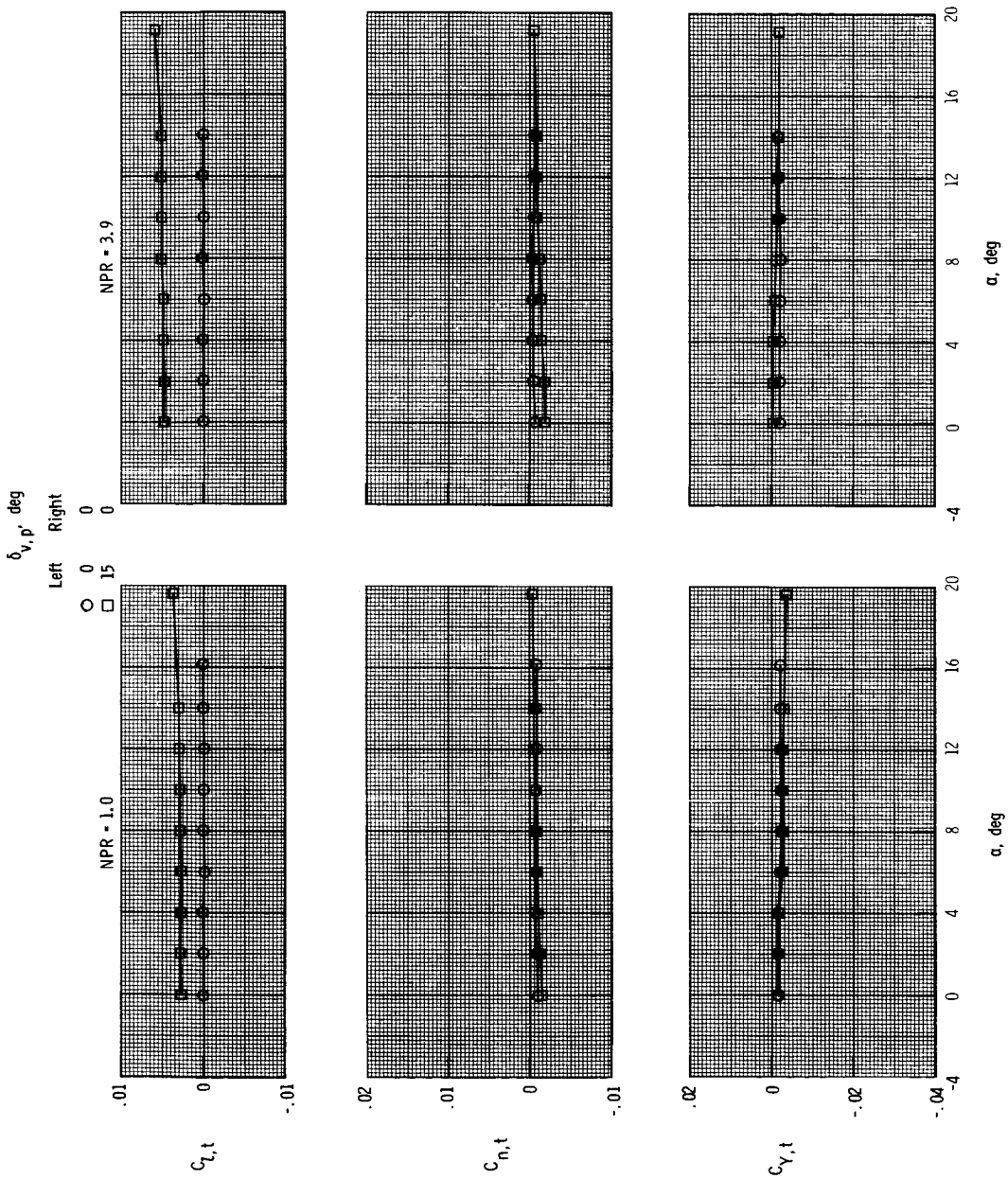

(i) $M = 0.87$; NPR = 1.0 and 3.9.

Figure 26. Continued.

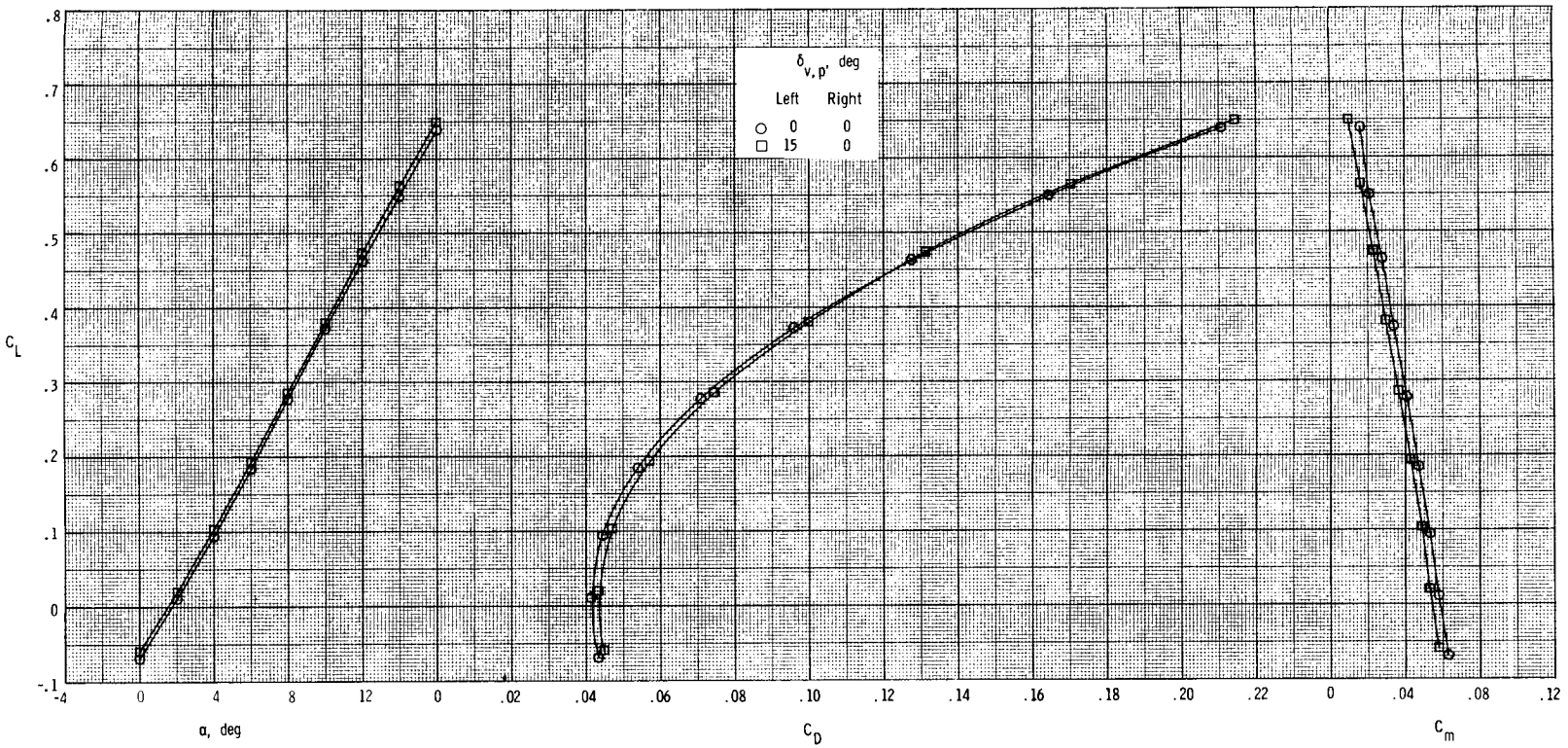

(j) $M = 1.20$; NPR = 1.0.

Figure 26. Continued.

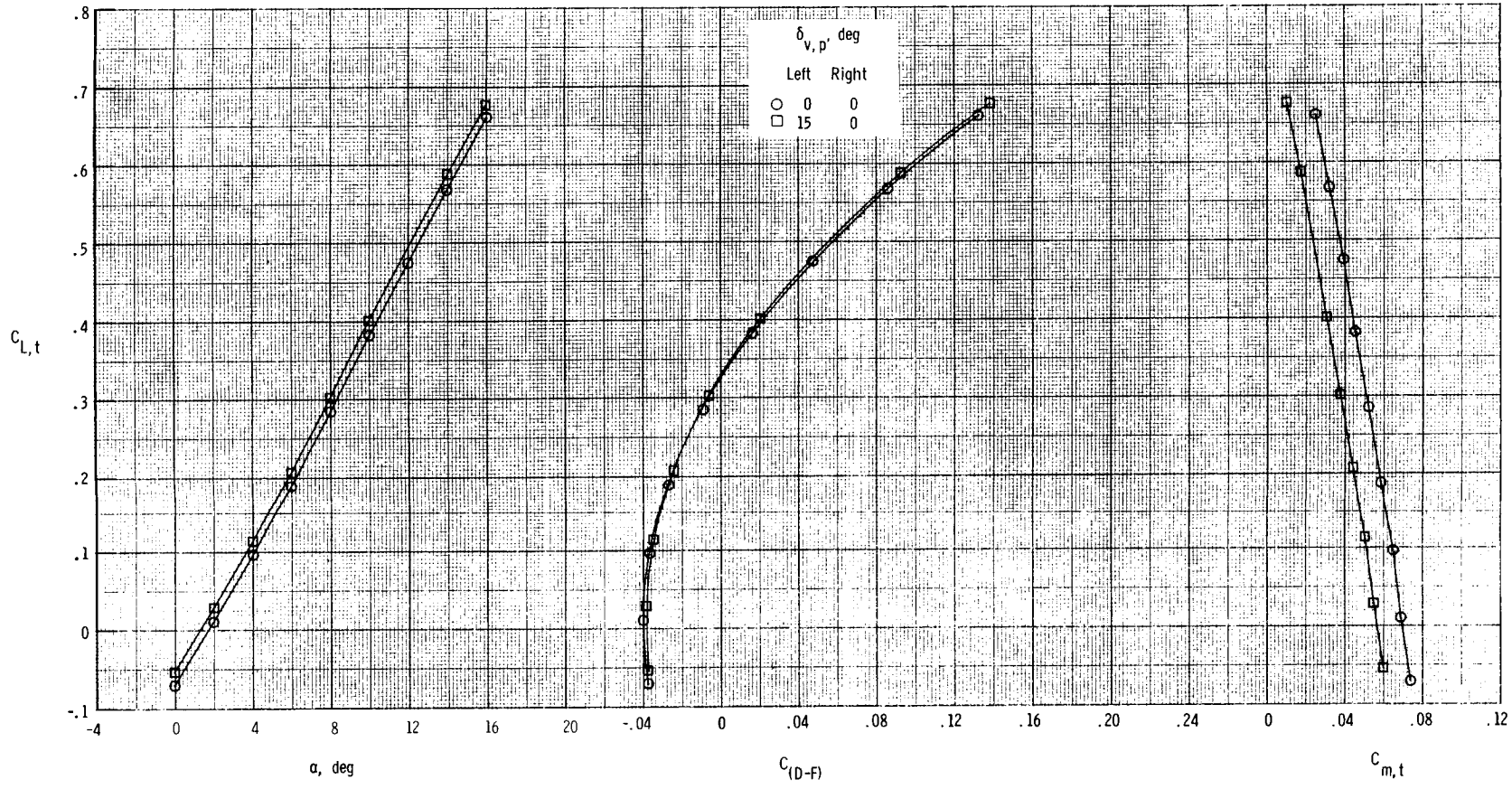

(k) $M = 1.20$; NPR = 6.6.

Figure 26. Continued.

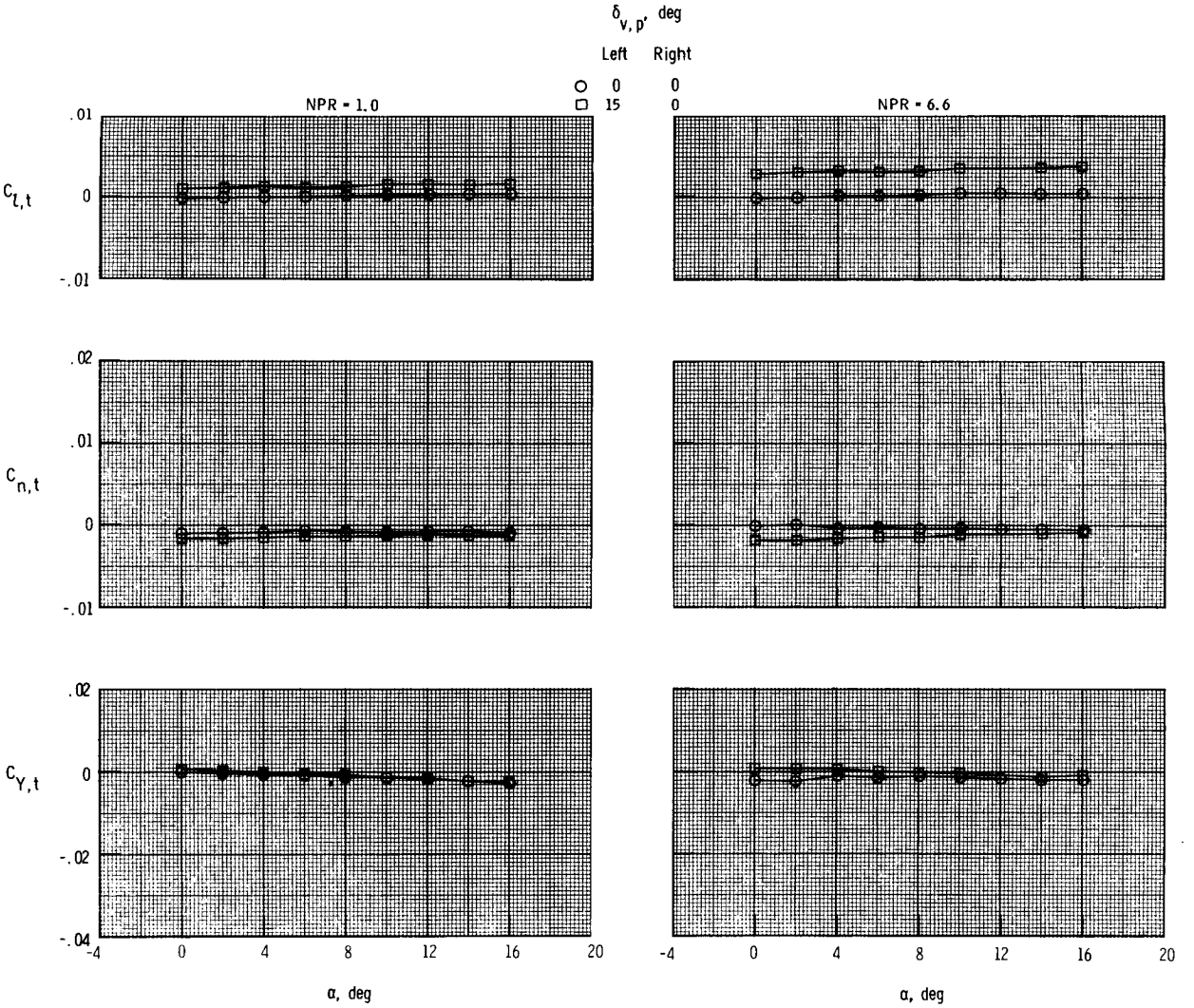

(l) $M = 1.20$; NPR = 1.0 and 6.6.

Figure 26. Continued.

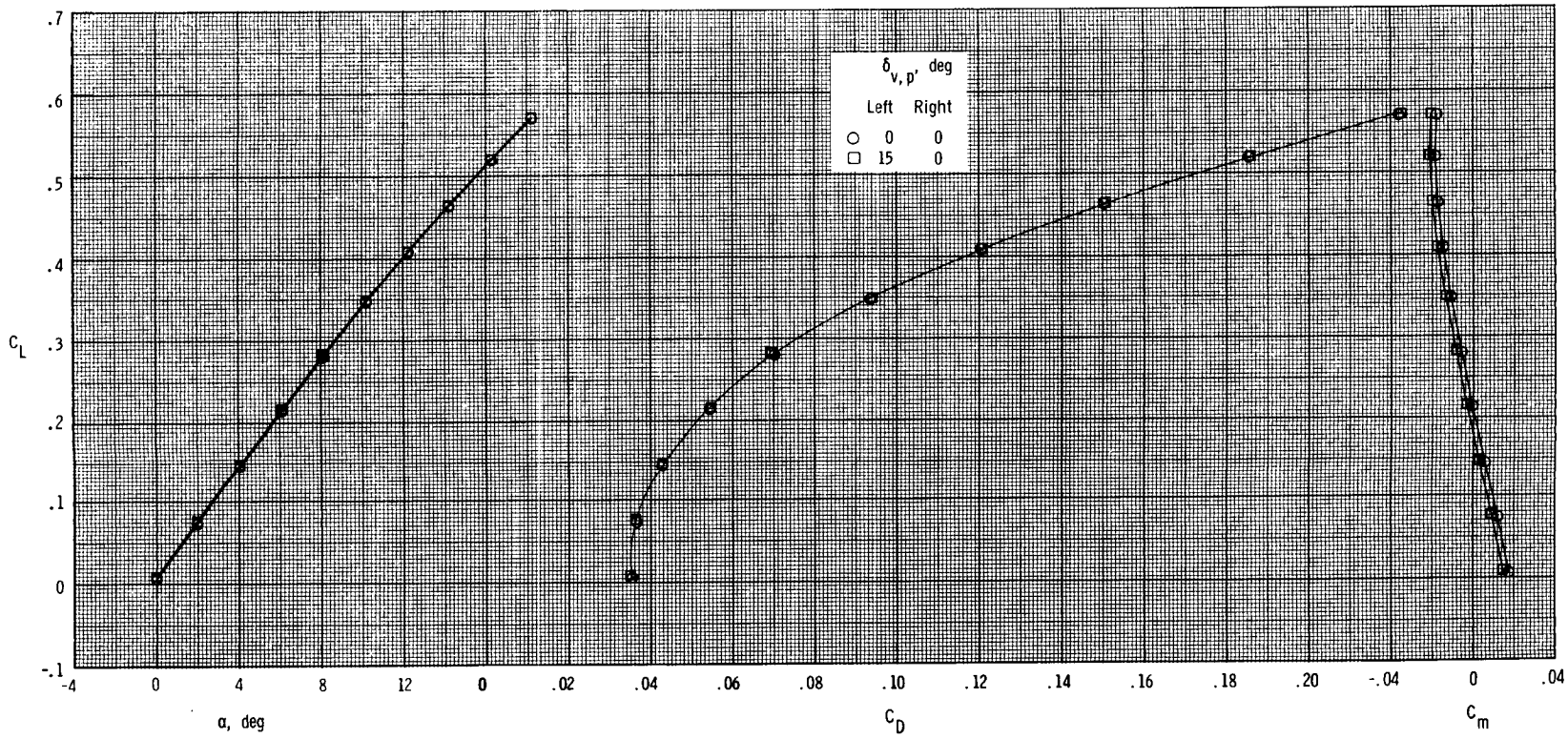

(m) $M = 2.00$; NPR = 1.0.

Figure 26. Continued.

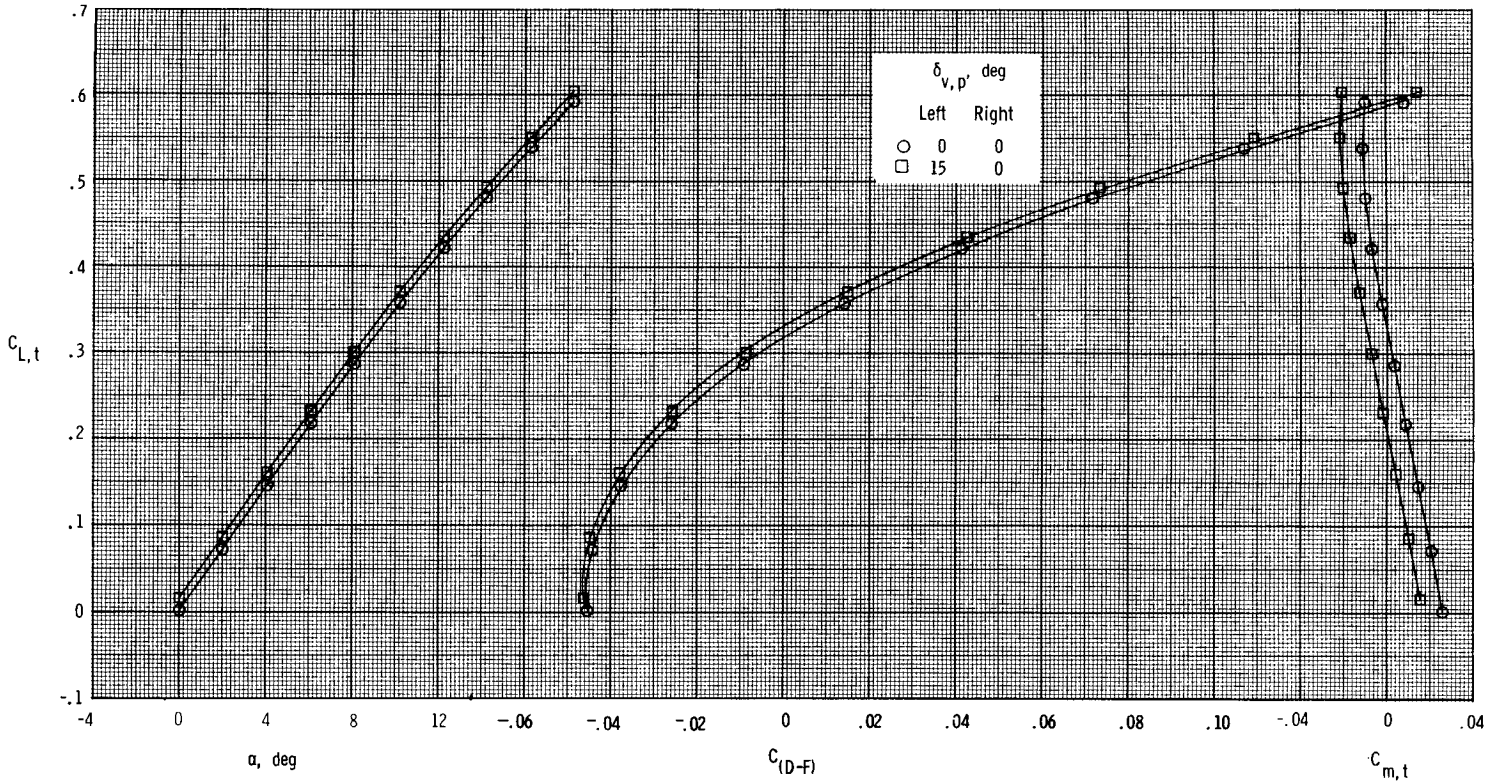

(n) $M = 2.00$; NPR = 16.0.

Figure 26. Continued.

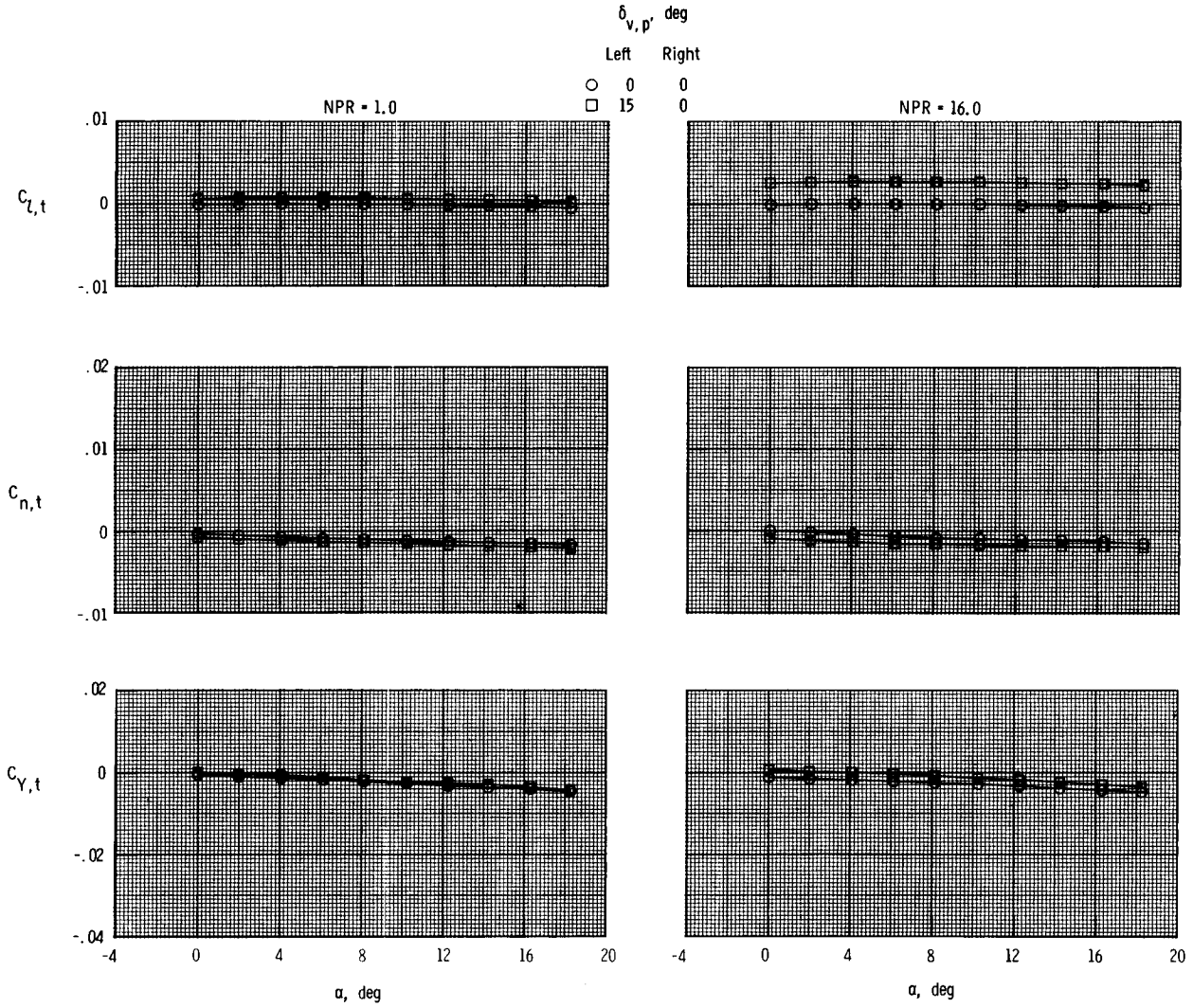

(o) $M = 2.00$; NPR = 1.0 and 16.0.

Figure 26. Continued.

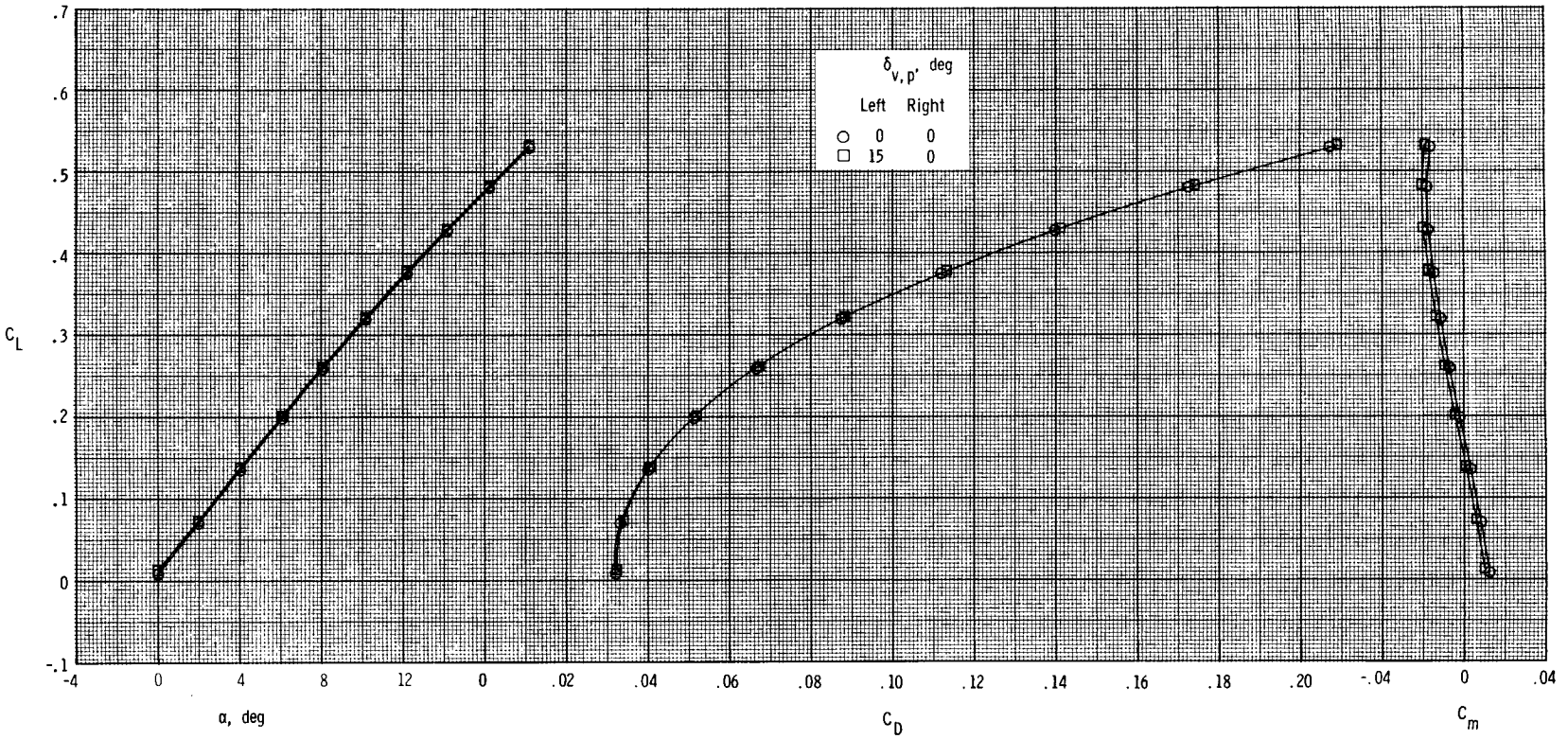

(p) $M = 2.17$; NPR = 1.0.

Figure 26. Continued.

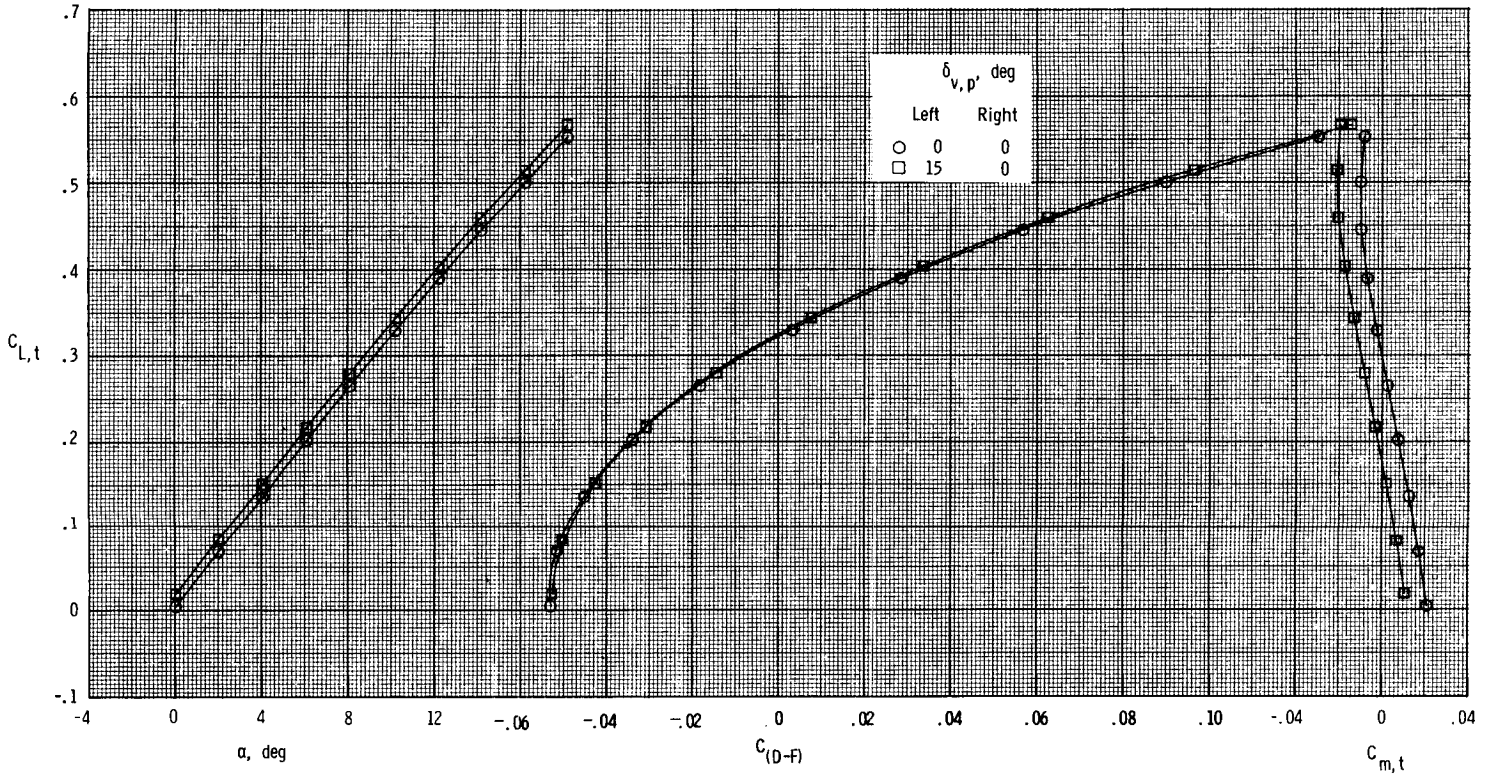

(q) $M = 2.17$; NPR = 20.0.

Figure 26. Continued.

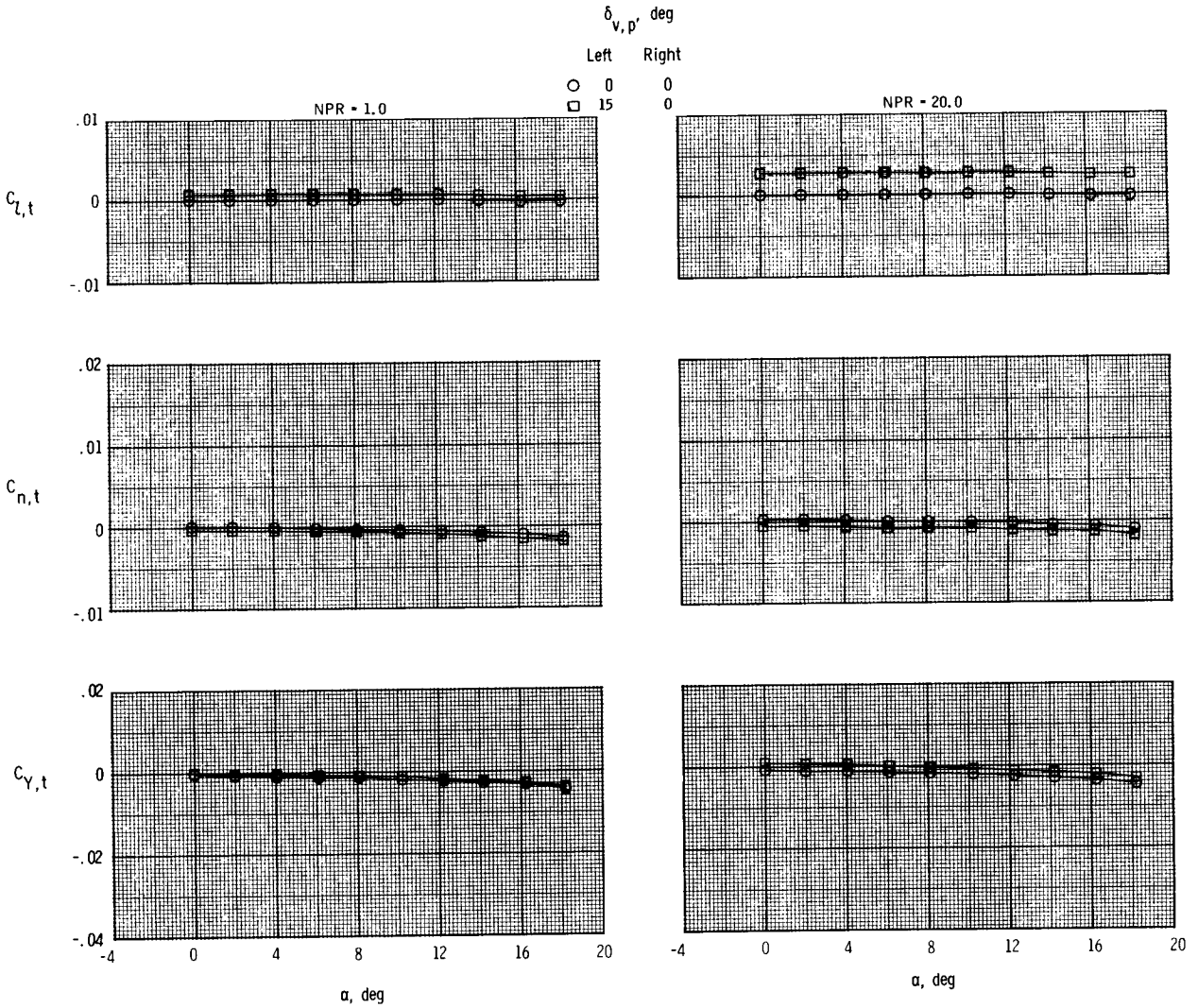

(r) $M = 2.17$; NPR = 1.0 and 20.0.

Figure 26. Continued.

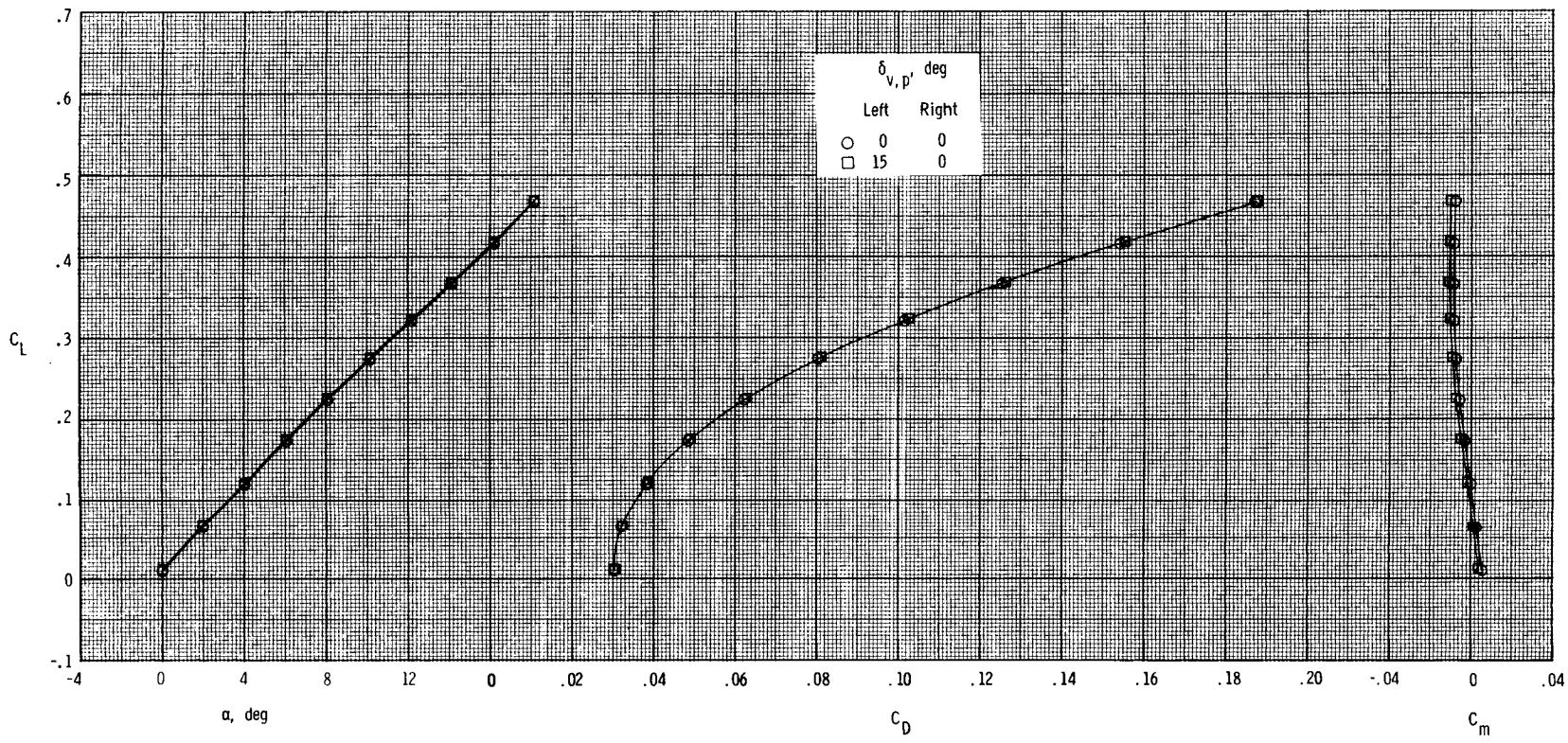

(s) $M = 2.47$; NPR = 1.0.

Figure 26. Continued.

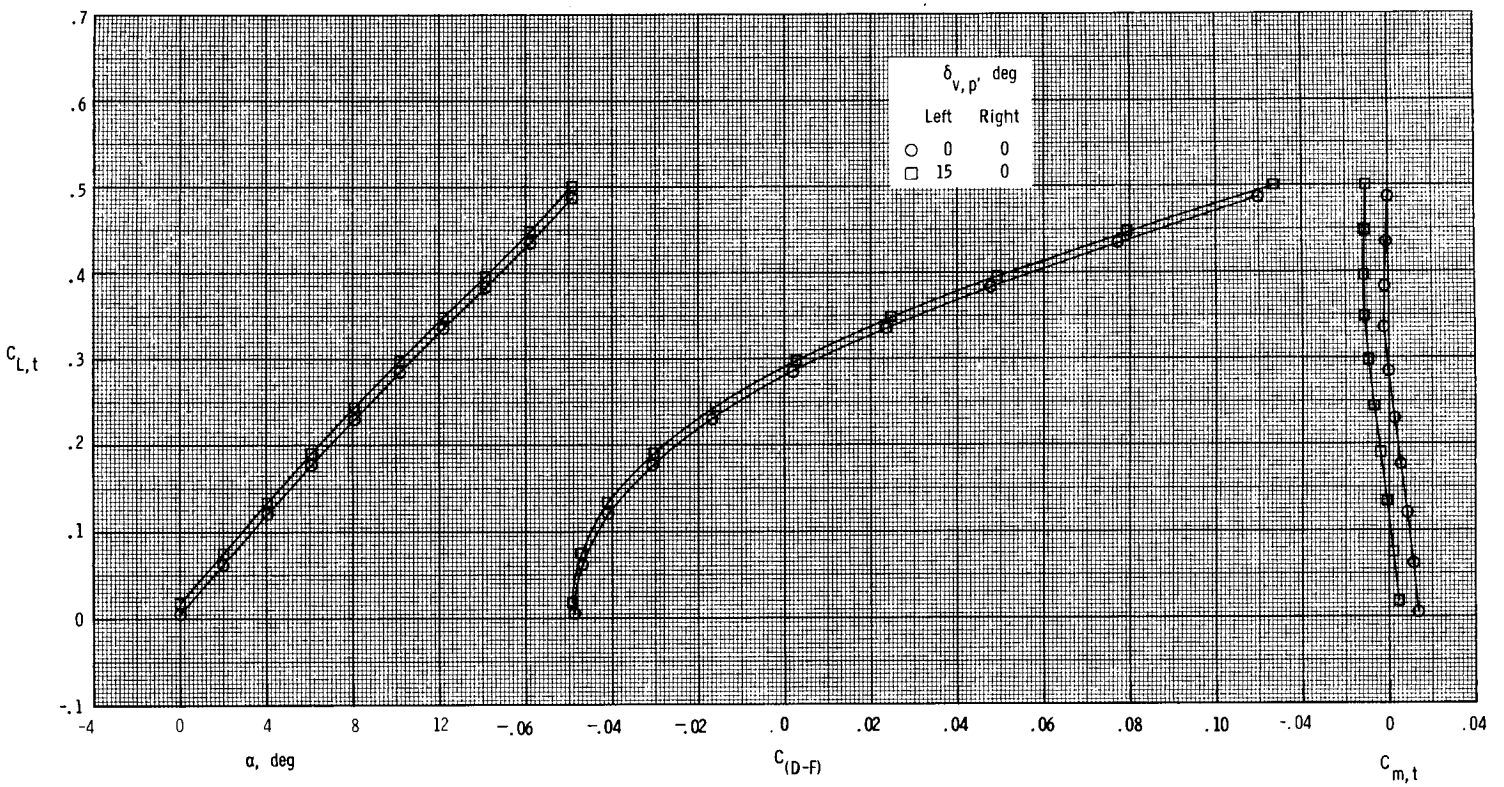

(t) $M = 2.47$; NPR = 24.0.

Figure 26. Continued.

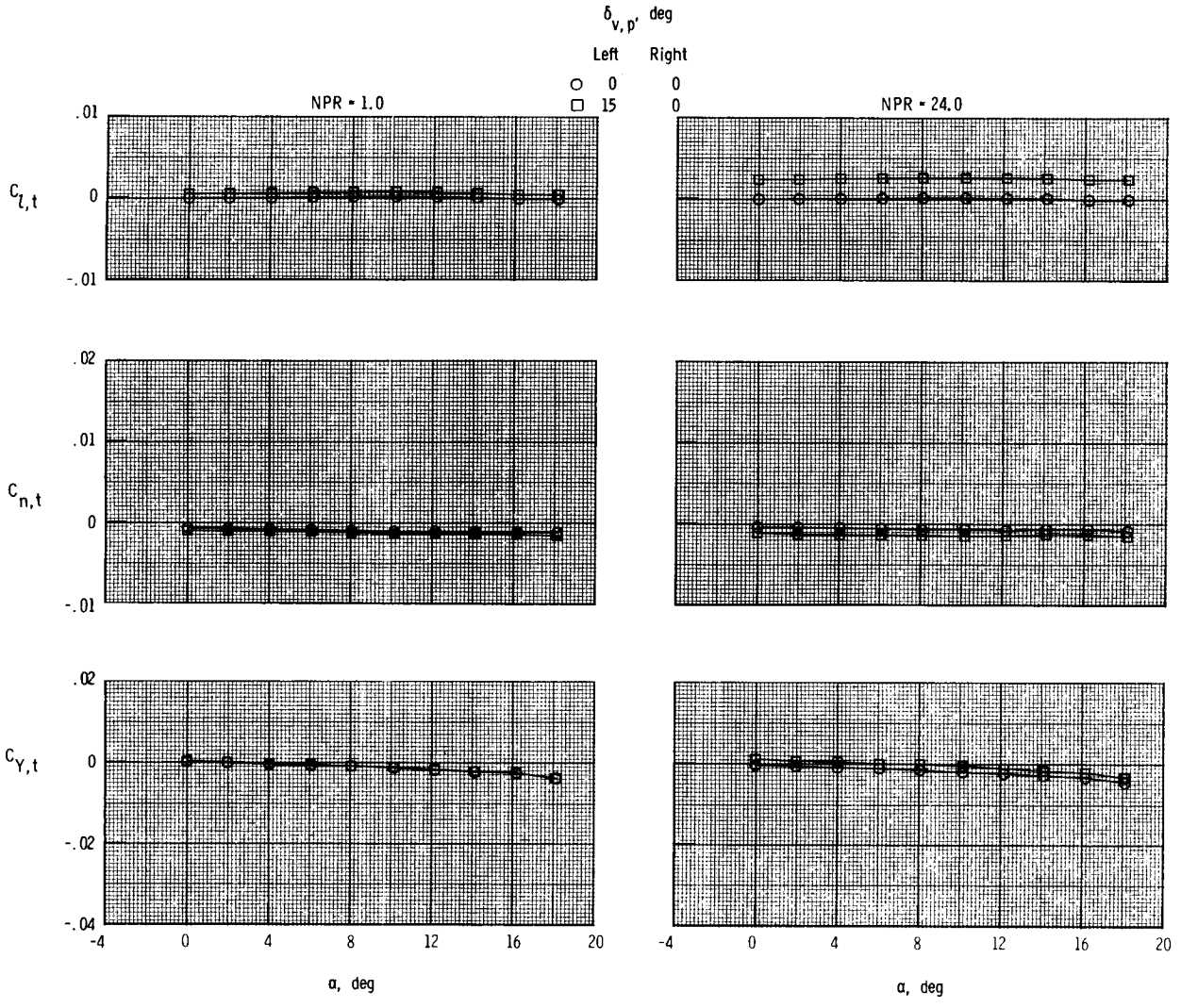

(u) $M = 2.47$; NPR = 1.0 and 24.0.

Figure 26. Concluded.

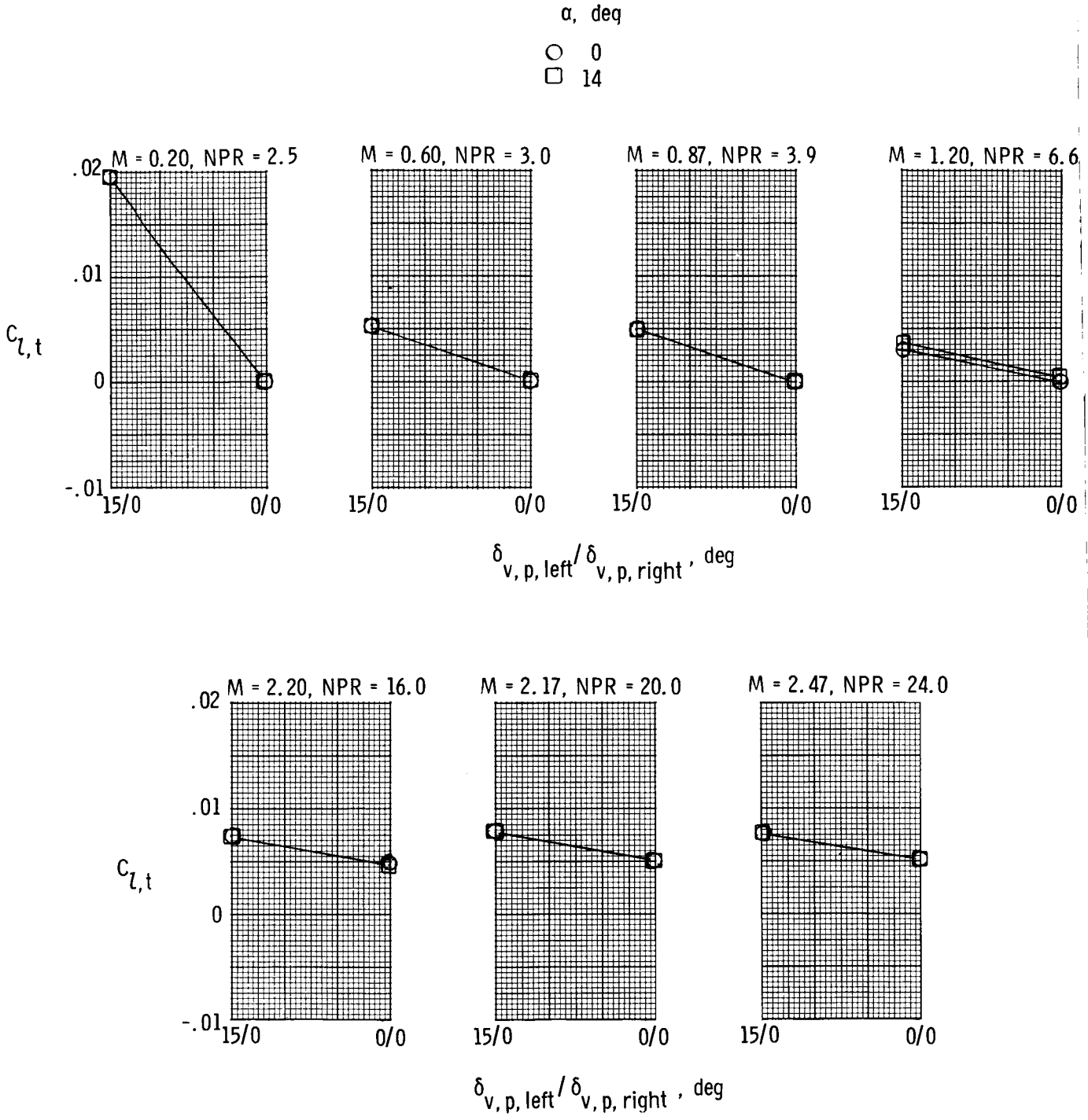

Figure 27. Summary of differential pitch vectoring for $\delta_{v,y} = 0°$.

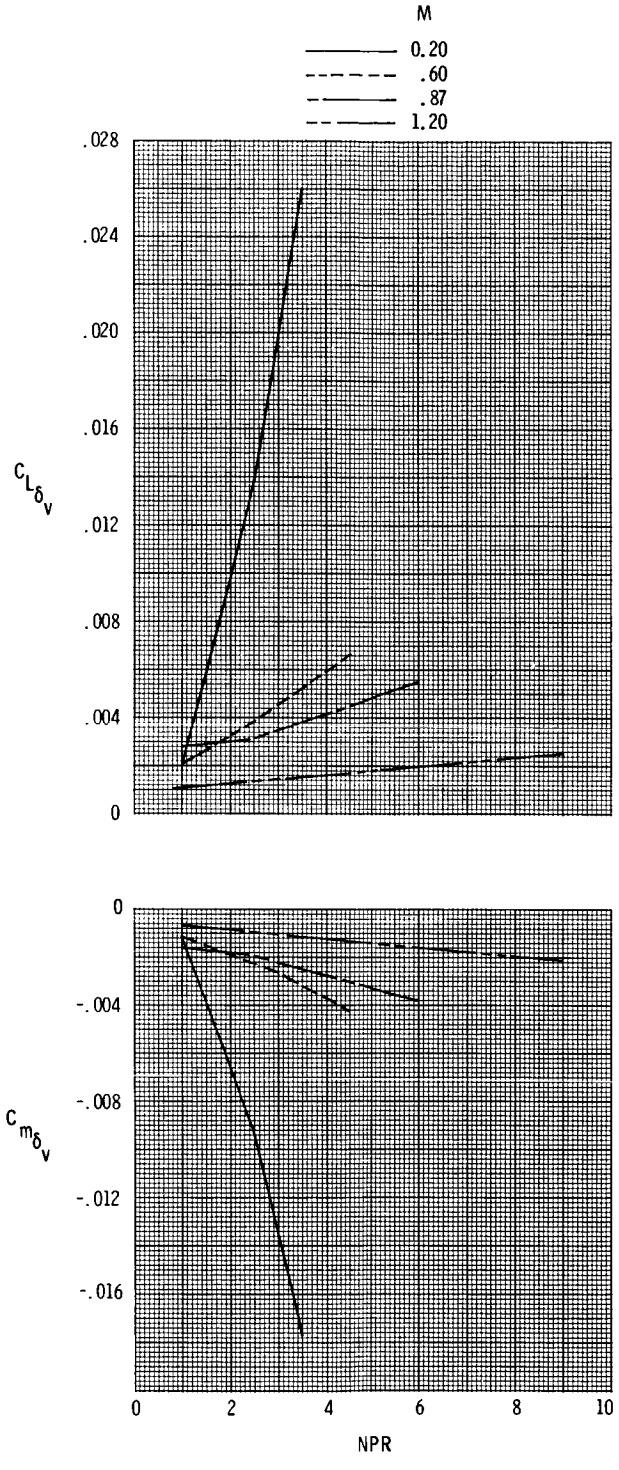

(a) $M = 0.20$ to 1.20.

Figure 28. Effect of nozzle pressure ratio on longitudinal control power and lift effectiveness due to pitch vectoring for $\delta_{v,y} = 0°$ and $\alpha = 4°$. (Evaluated between $\delta_{v,p} = 15°$ and 0°.)

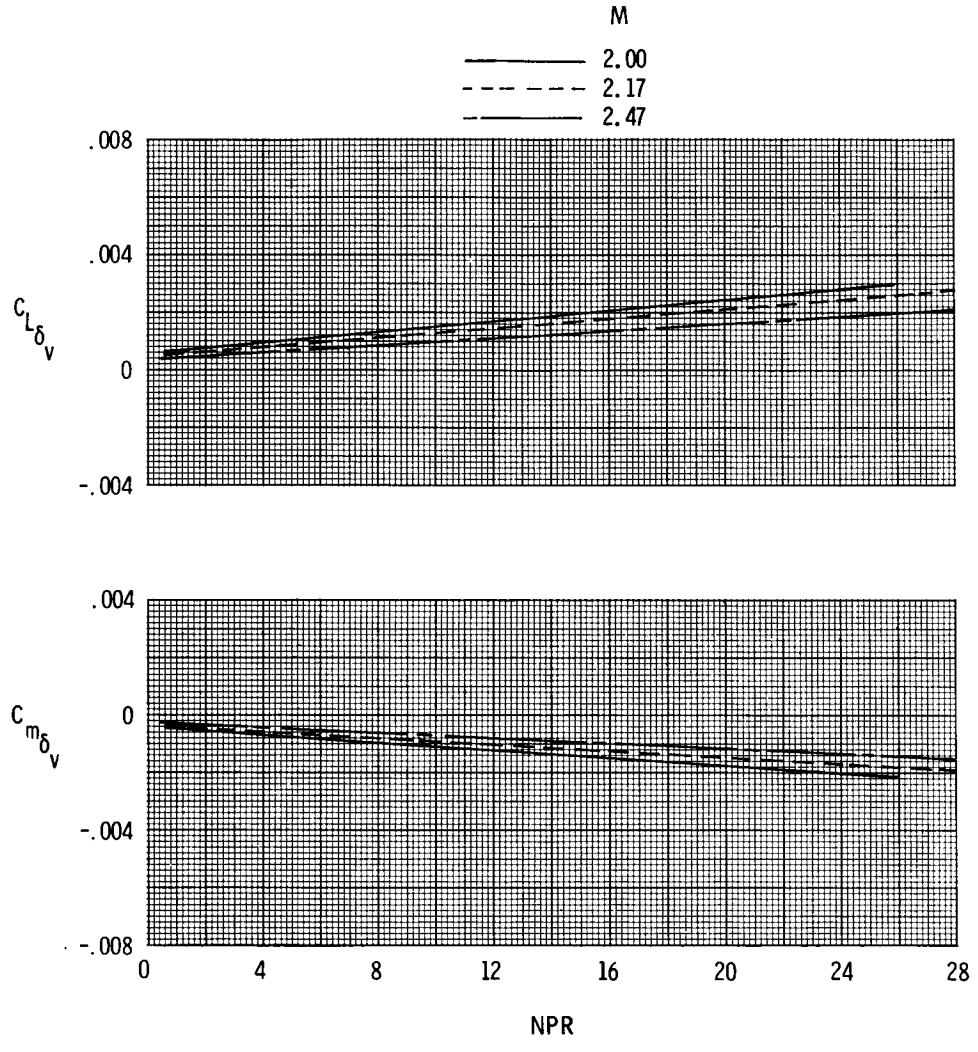

(b) $M = 2.00$ to 2.47.

Figure 28. Concluded.

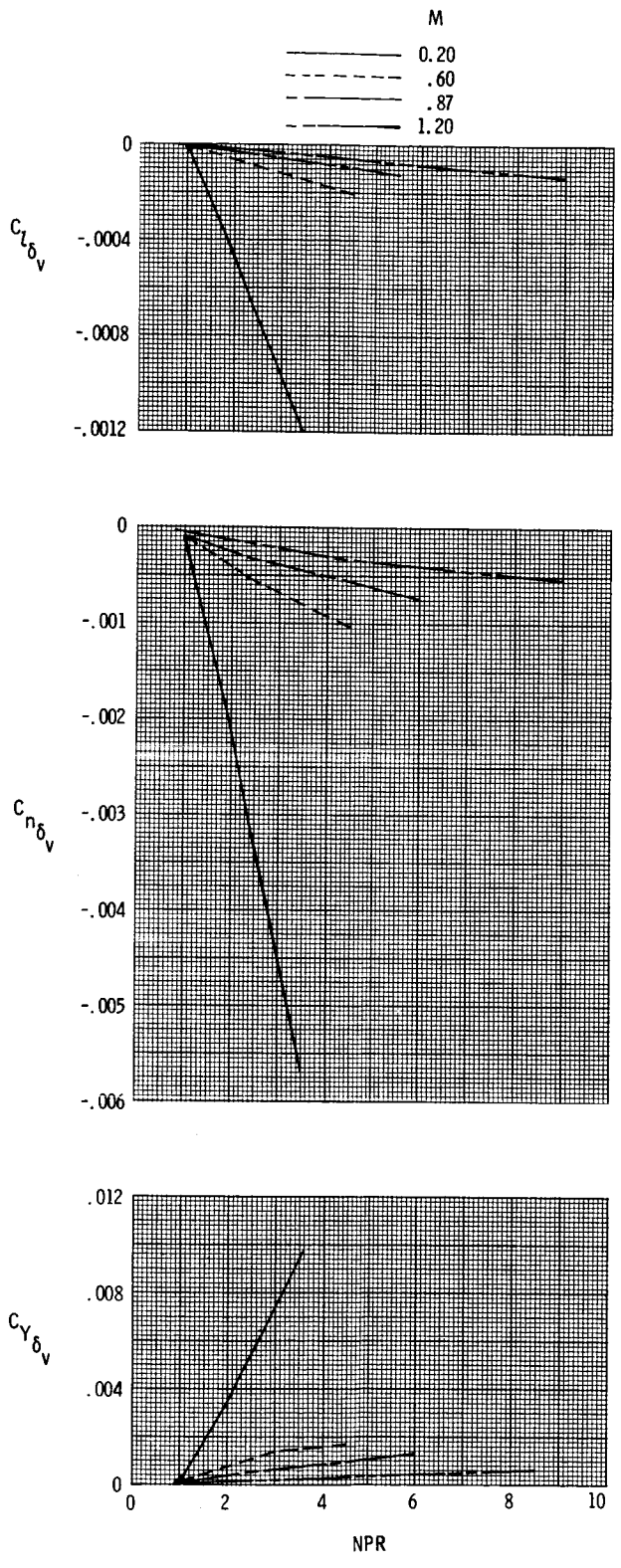

(a) $M = 0.20$ to 1.20.

Figure 29. Effect of nozzle pressure ratio on directional control power and side-force and rolling-moment effectiveness due to yaw vectoring for $\delta_{v,p} = 0°$ and $\alpha = 4°$. (Evaluated between $\delta_{v,y} = -20°$ and 0°.)

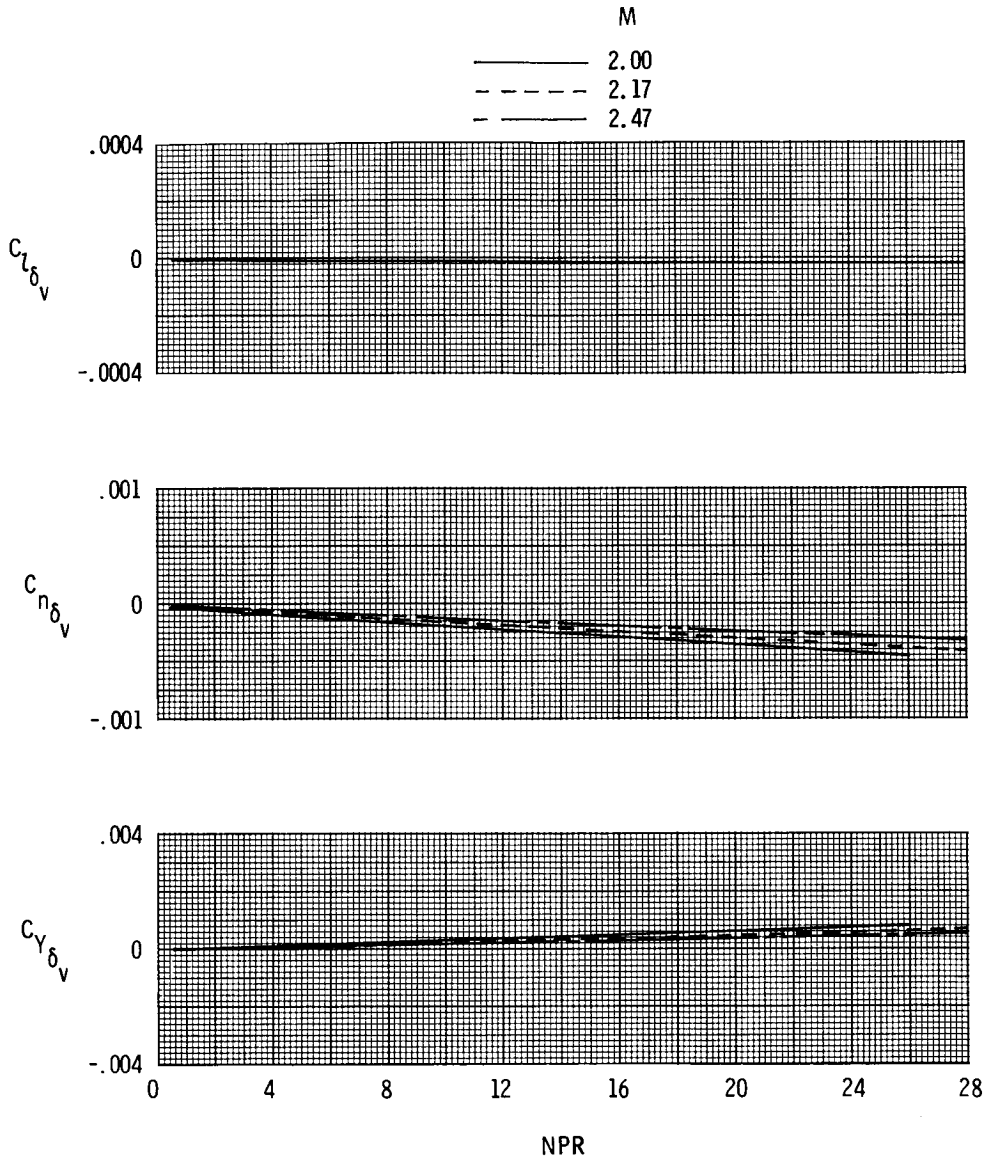

(b) $M = 2.00$ to 2.47.

Figure 29. Concluded.

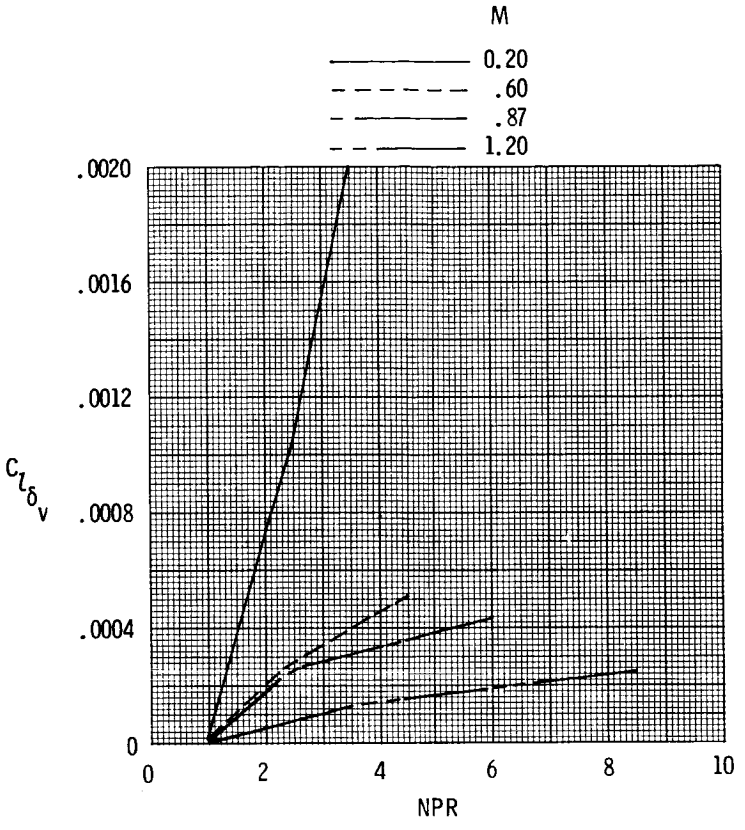

(a) $M = 0.20$ to 1.20.

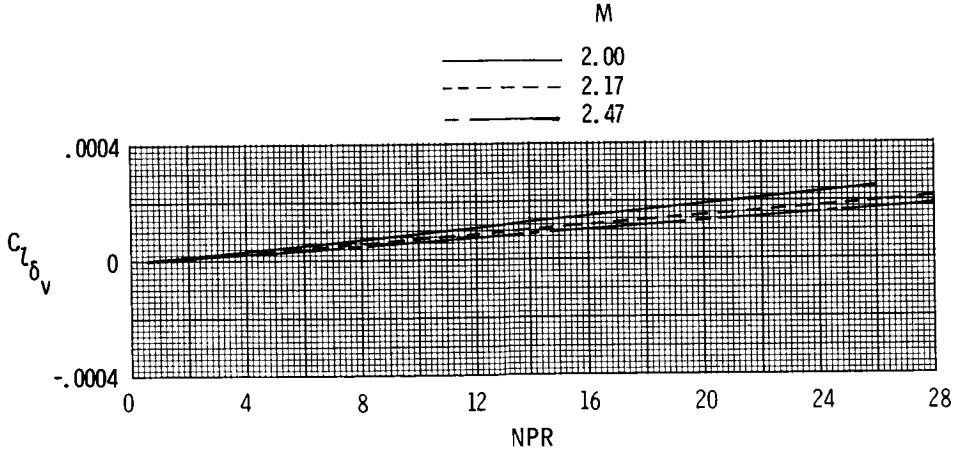

(b) $M = 2.00$ to 2.47.

Figure 30. Effect of nozzle pressure ratio on rolling-moment control power due to differential pitch vectoring for $\delta_{v,y} = 0°$ and $\alpha = 4°$. (Evaluated between $\delta_{v,p,\text{left}} = 15°$ and $\delta_{v,p,\text{right}} = 0°$.)

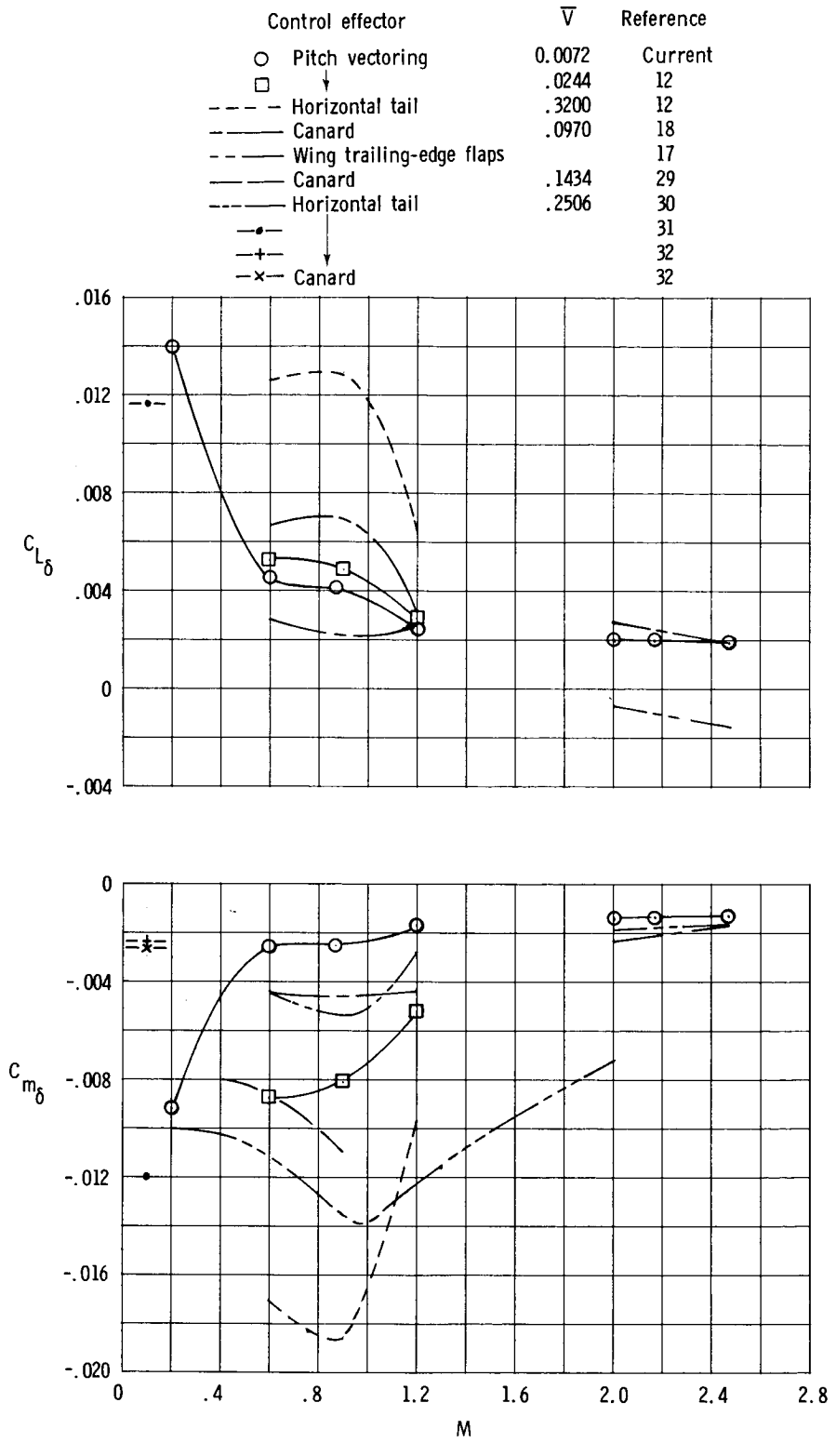

Figure 31. Comparison of longitudinal control power from powered and aerodynamic control effectors for $\alpha = 0°$.

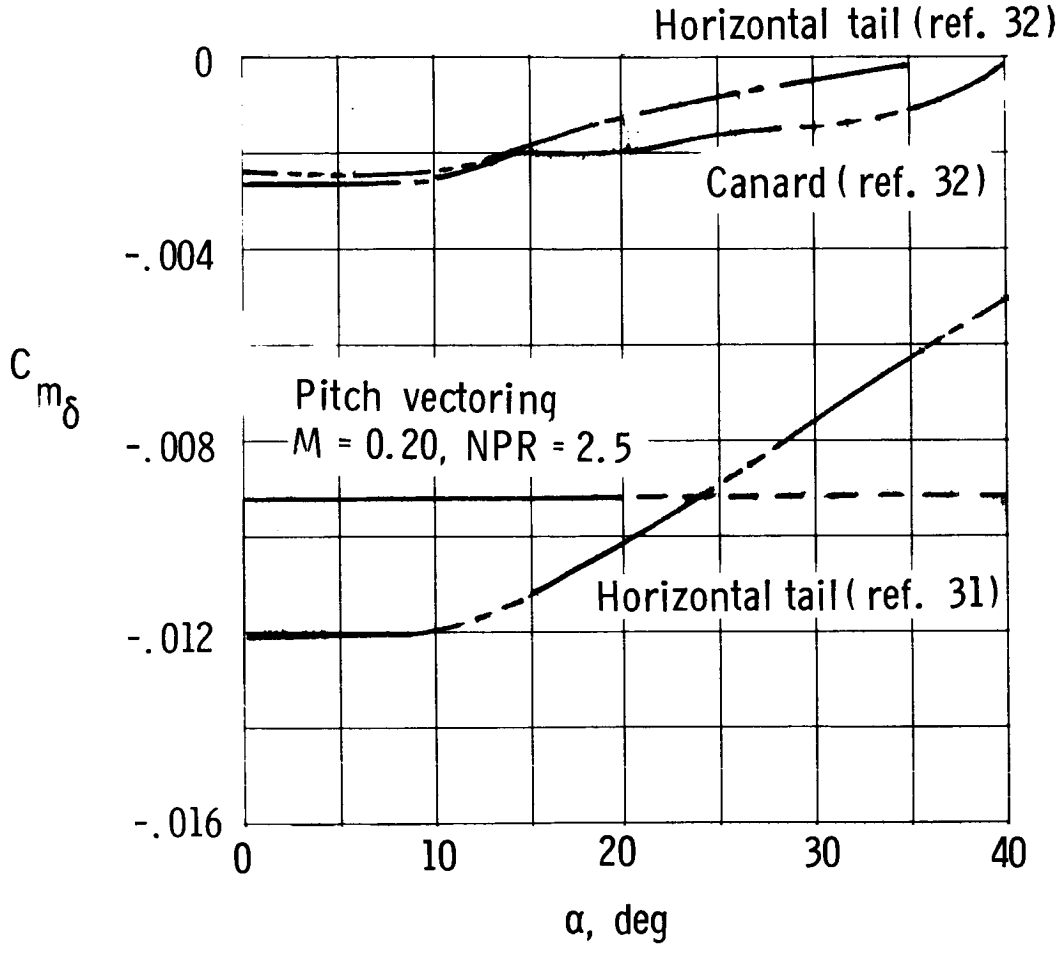

Figure 32. Effect of angle of attack on longitudinal control power from powered and aerodynamic control effectors.

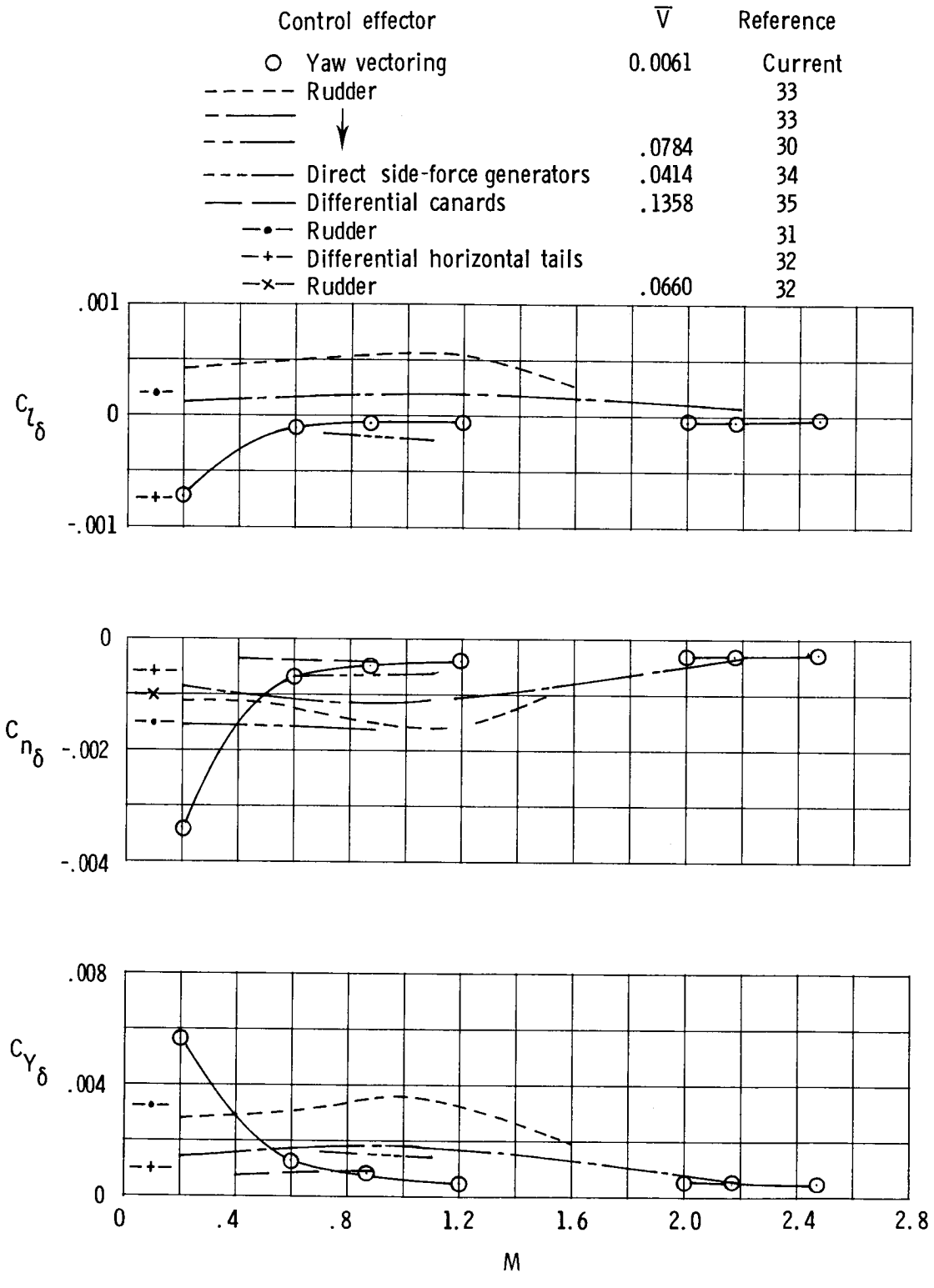

Figure 33. Comparison of directional control power from powered and aerodynamic control effectors for $\alpha = 0°$.

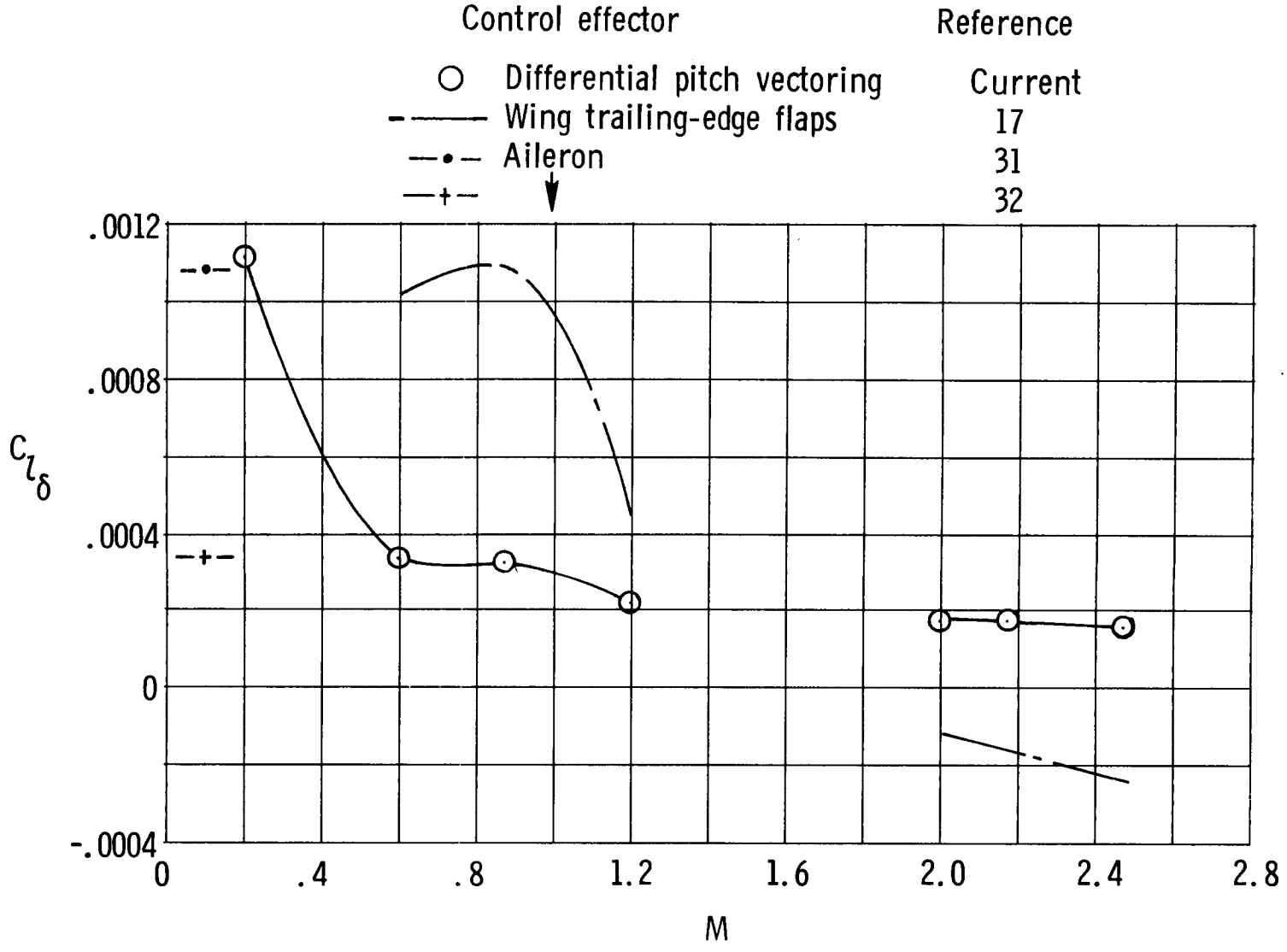

Figure 34. Comparison of rolling-moment control power from powered and aerodynamic control effectors for $\alpha = 0°$.

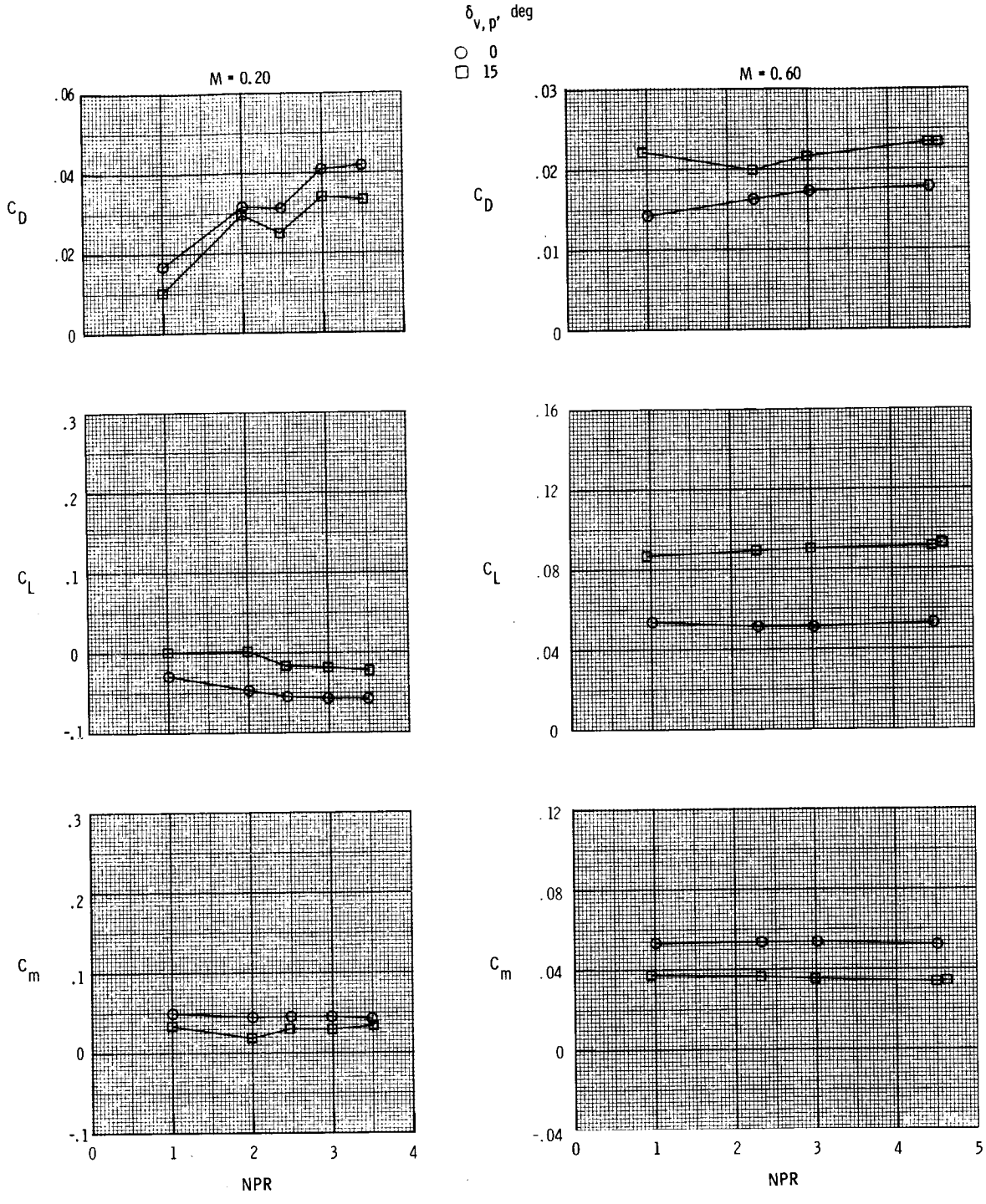

(a) $M = 0.20$ and 0.60.

Figure 35. Effect of nozzle pressure ratio and symmetric pitch vectoring on thrust-removed longitudinal aerodynamic characteristics for $\delta_{v,y} = 0°$ and $\alpha = 4°$.

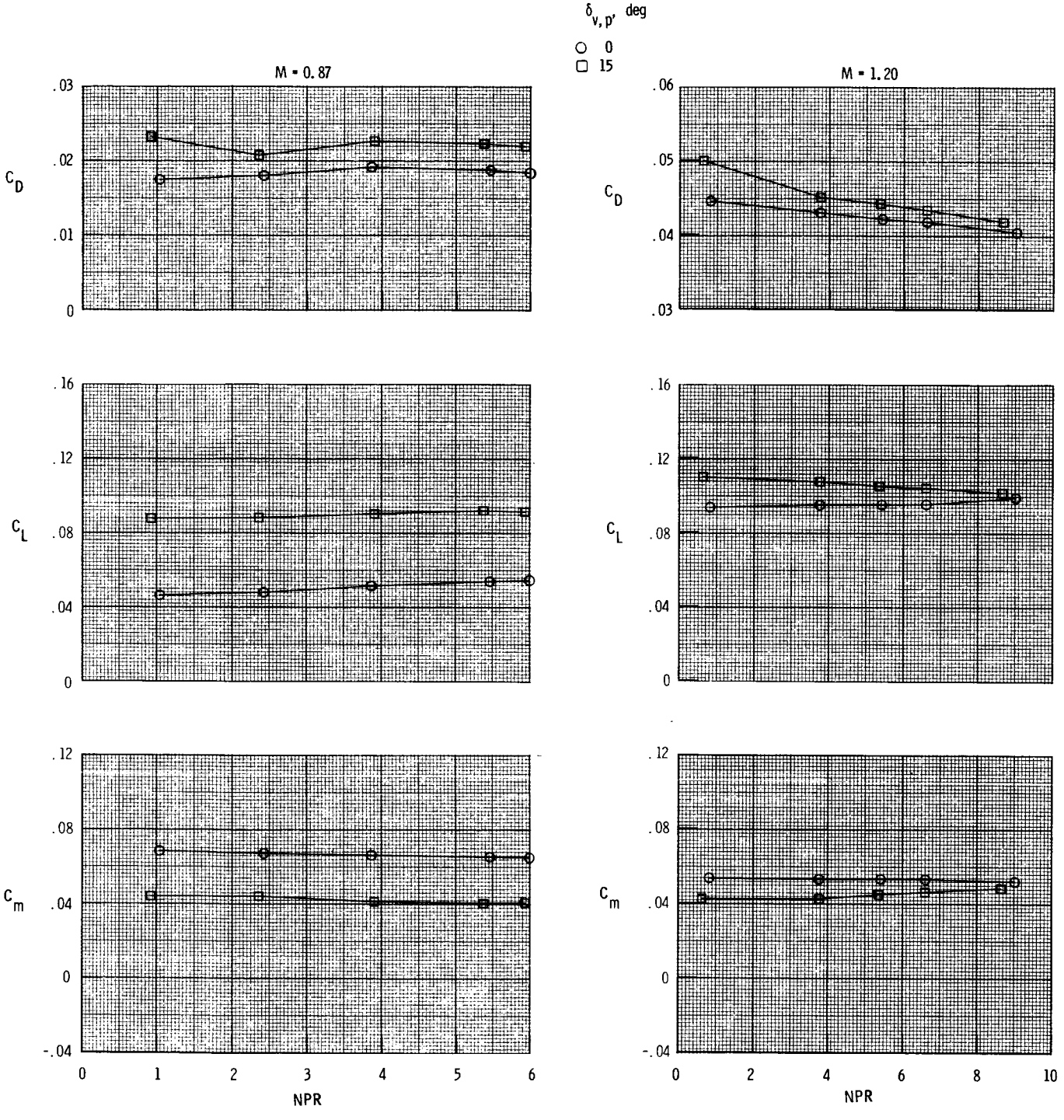

(b) $M = 0.87$ and 1.20.

Figure 35. Continued.

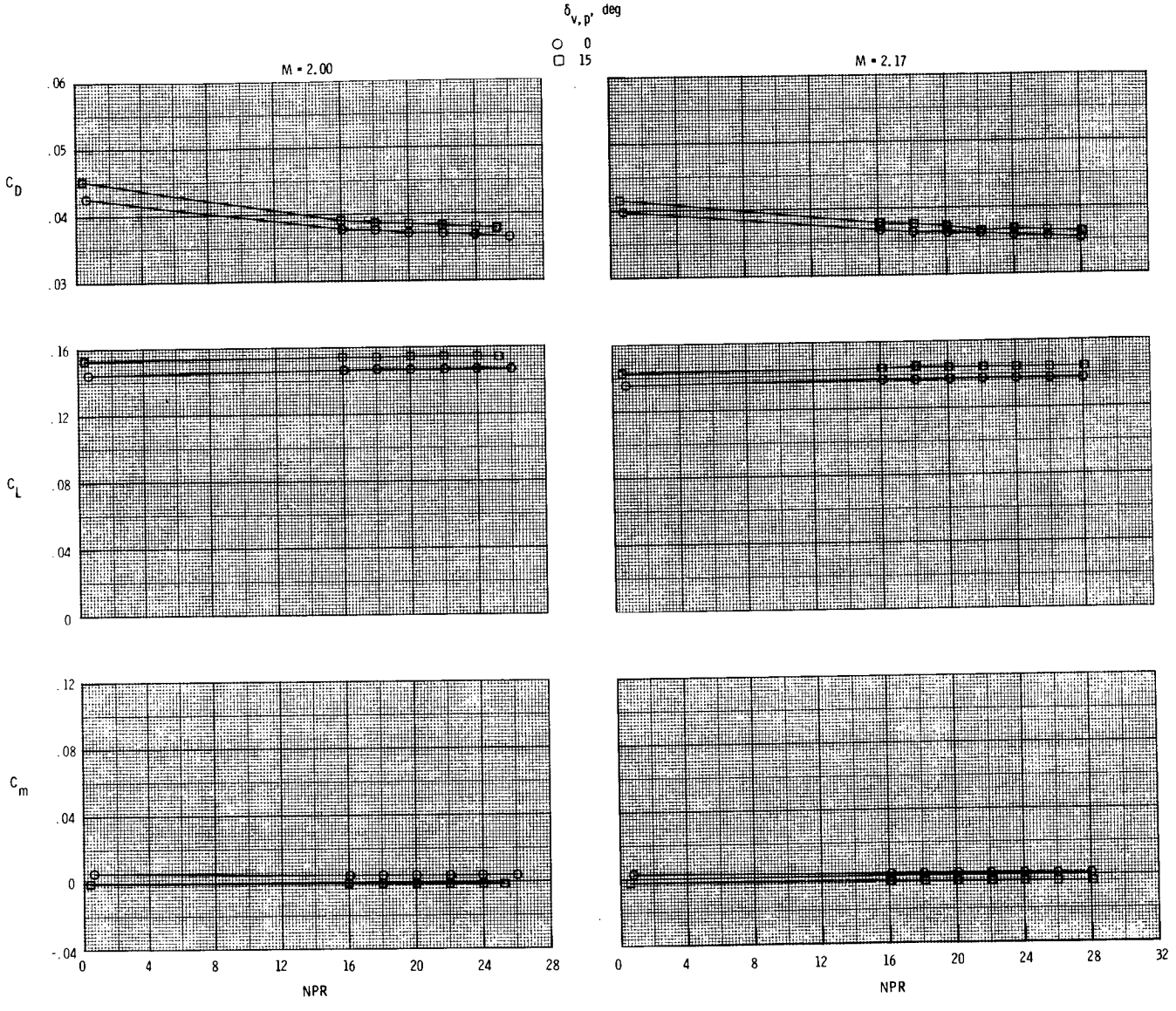

(c) $M = 2.00$ and 2.17.

Figure 35. Continued.

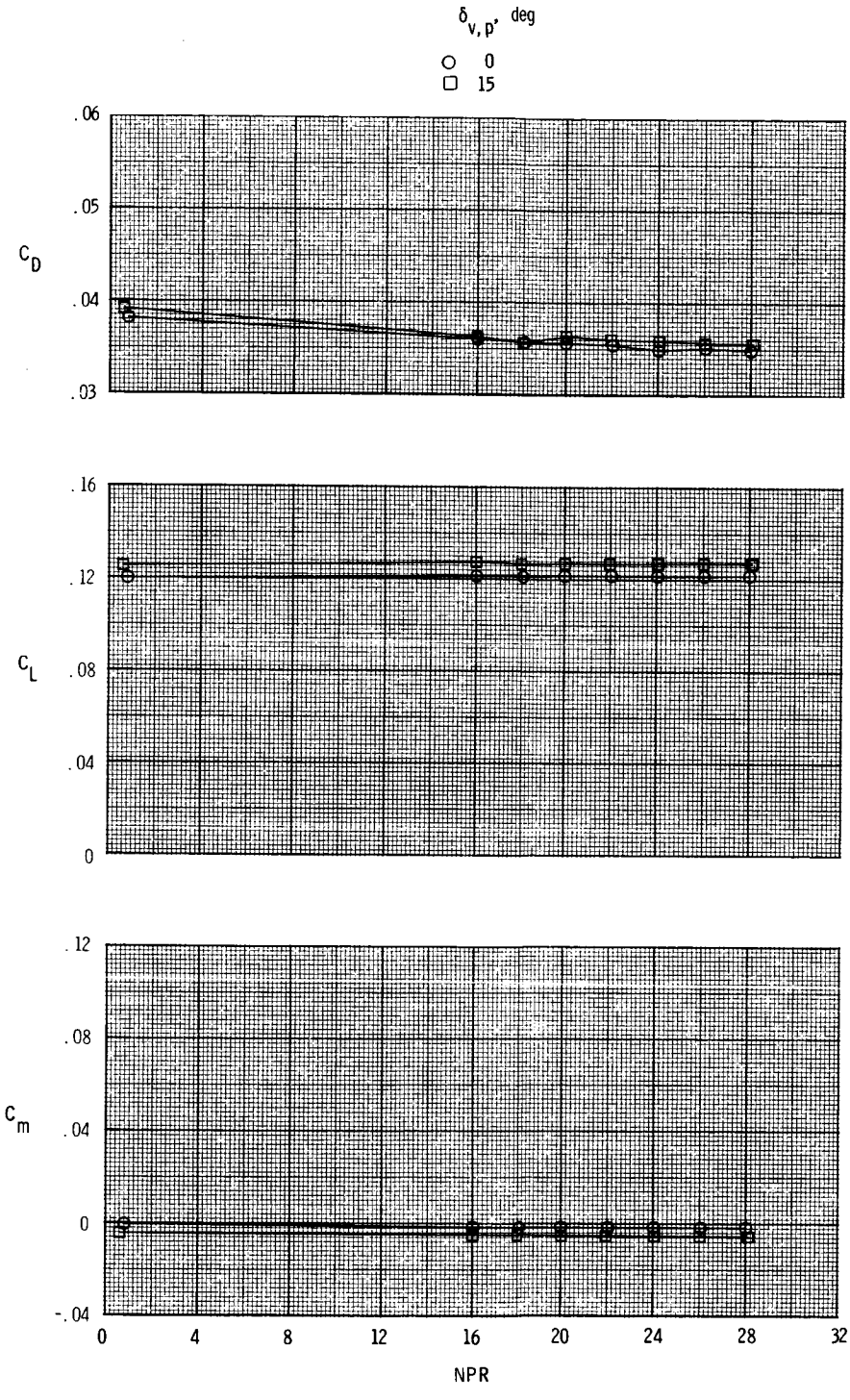

(d) $M = 2.47$.

Figure 35. Concluded.

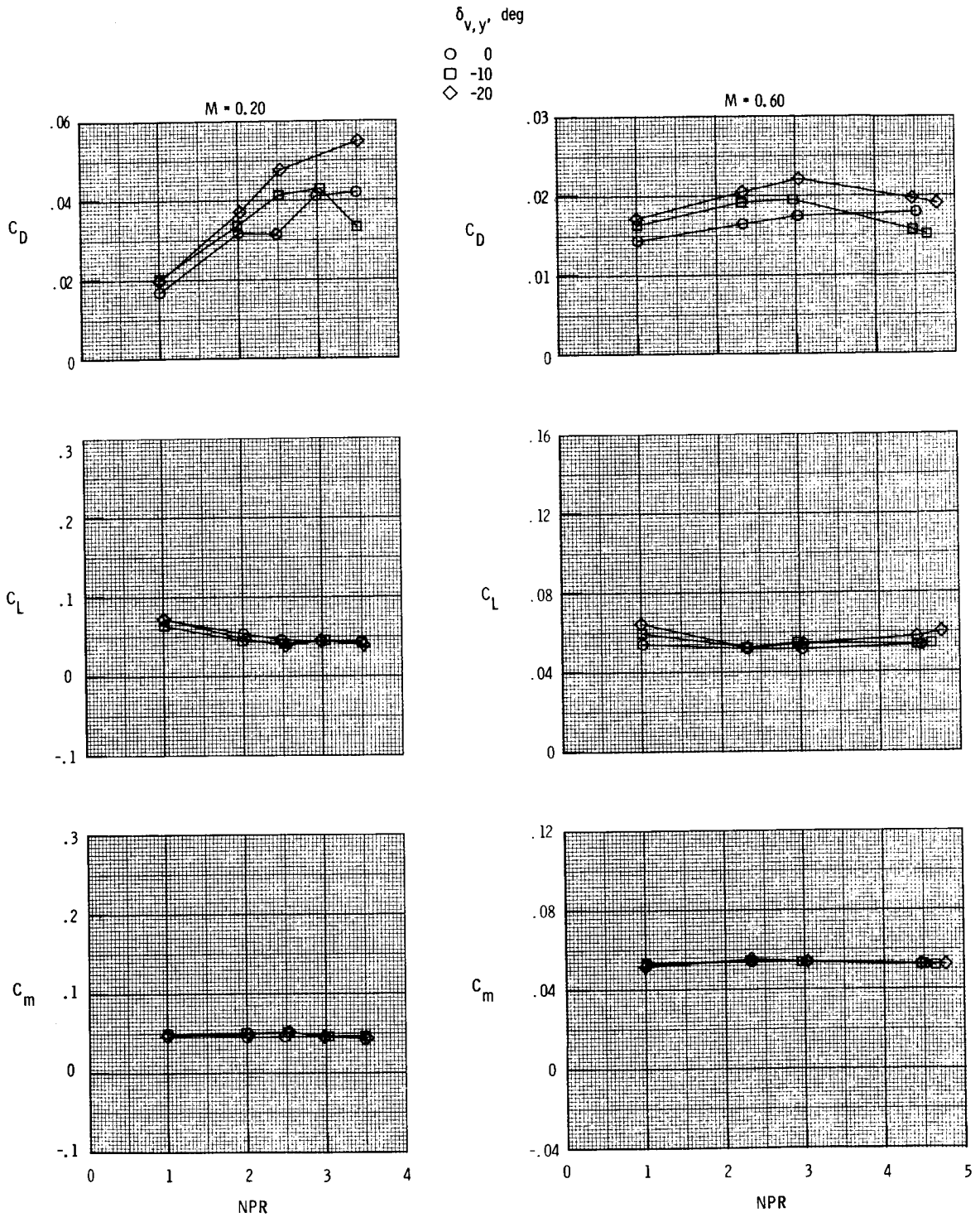

(a) $M = 0.20$ and 0.60.

Figure 36. Effect of nozzle pressure ratio and yaw vectoring on thrust-removed longitudinal aerodynamic characteristics for $\delta_{v,p} = 0°$ and $\alpha = 4°$.

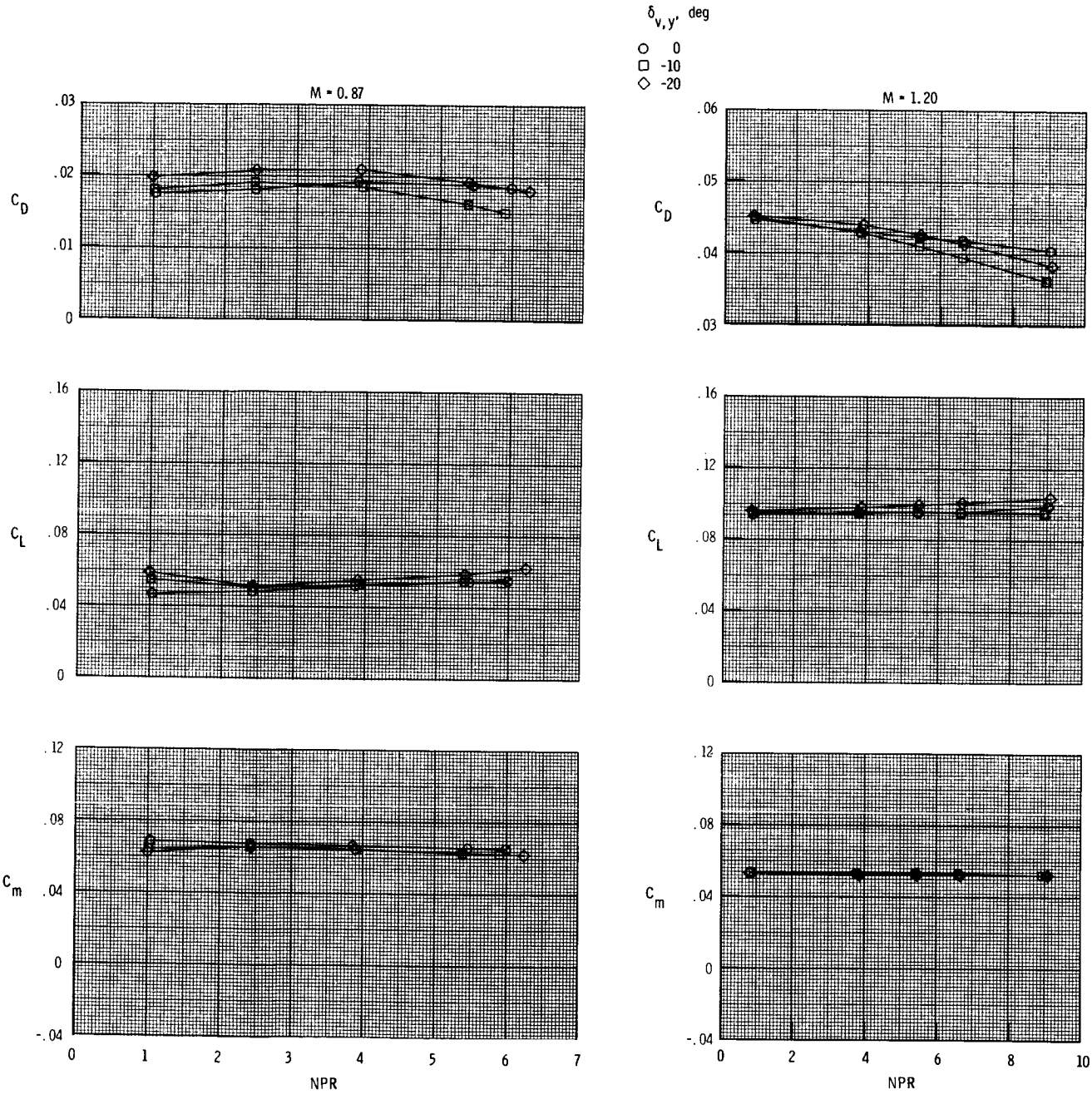

(b) $M = 0.87$ and 1.20.

Figure 36. Continued.

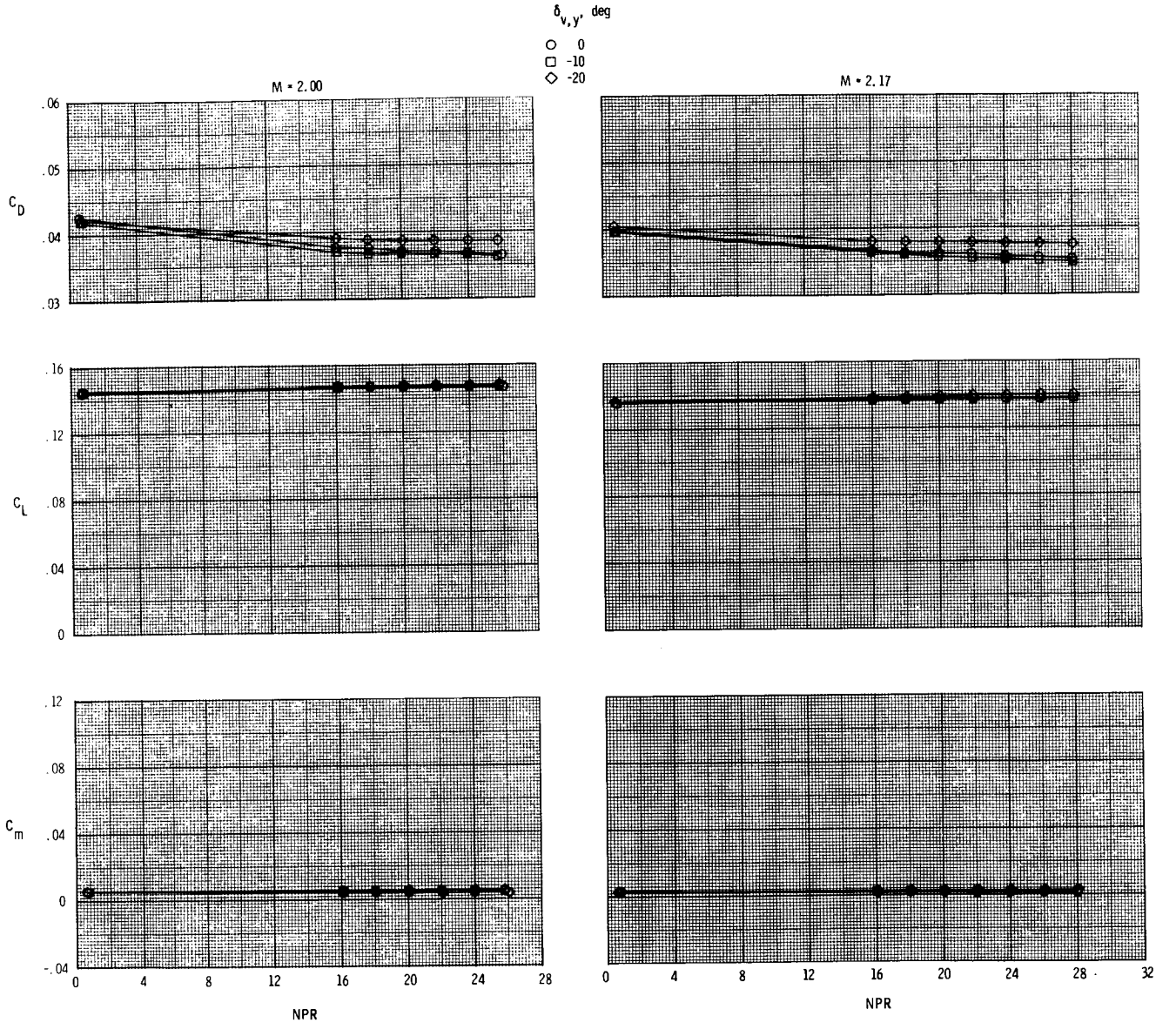

(c) $M = 2.00$ and 2.17.

Figure 36. Continued.

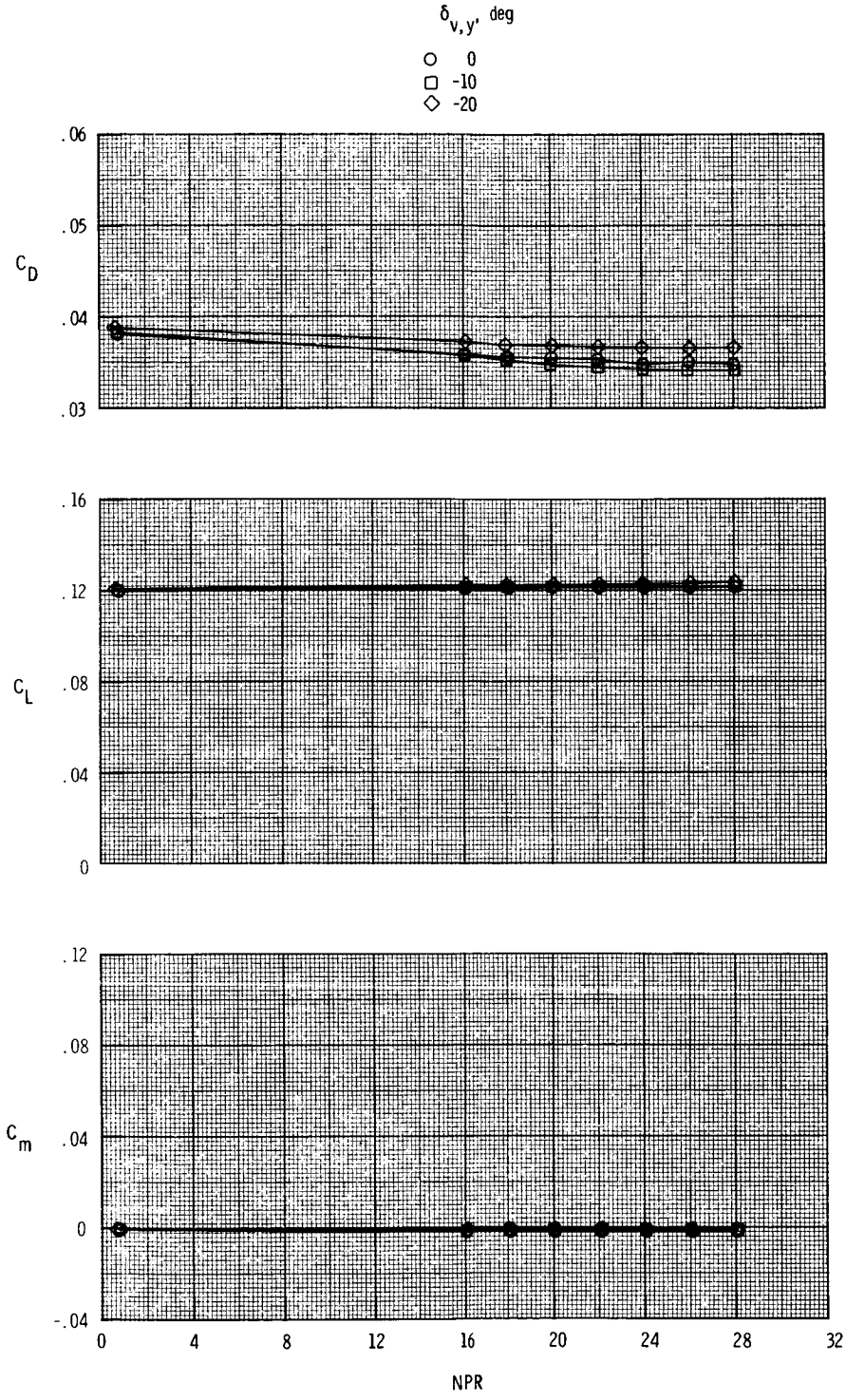

(d) $M = 2.47$.

Figure 36. Concluded.

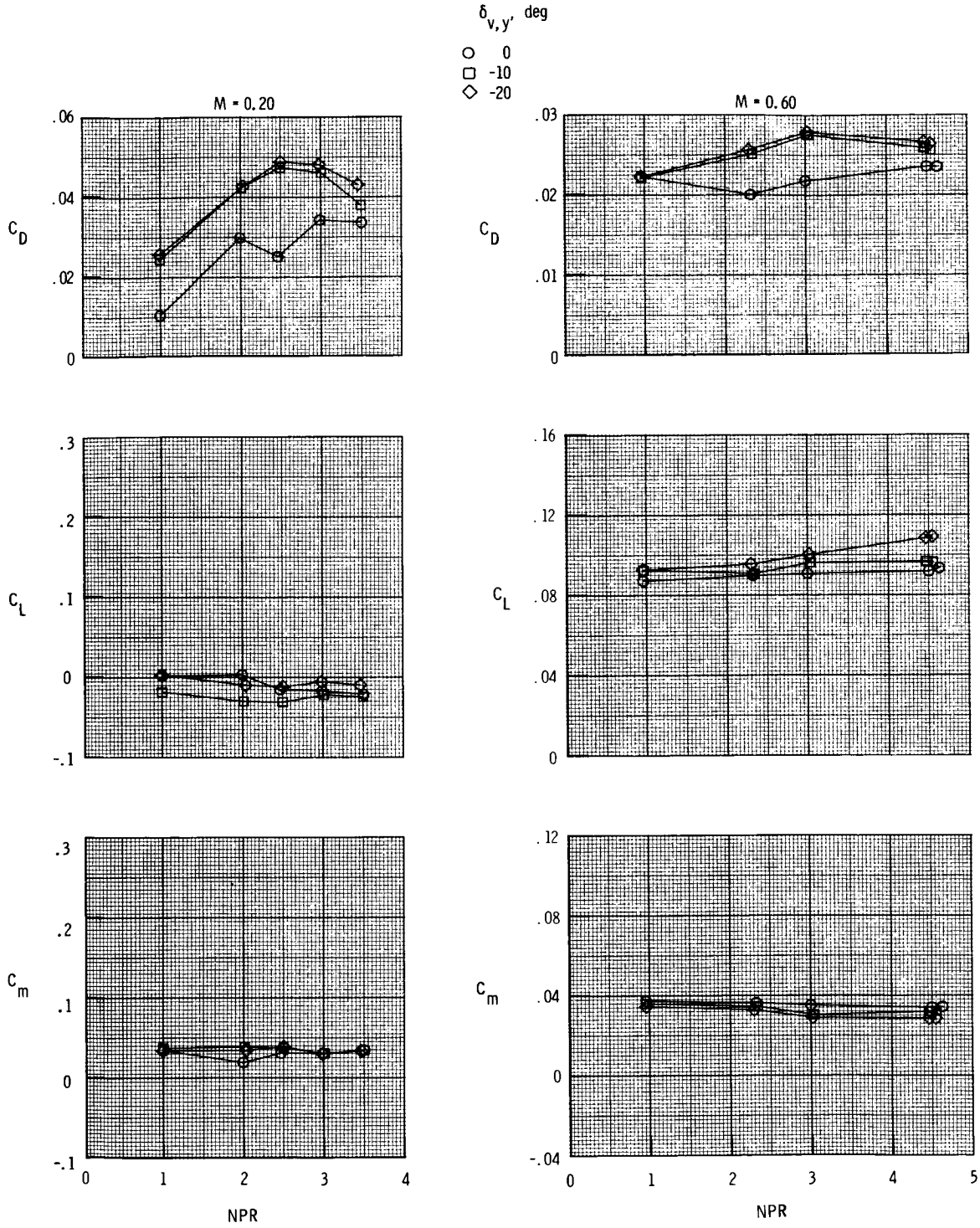

(a) $M = 0.20$ and 0.60.

Figure 37. Effect of nozzle pressure ratio and yaw vectoring on thrust-removed longitudinal aerodynamic characteristics for $\delta_{v,p} = 15°$ and $\alpha = 4°$.

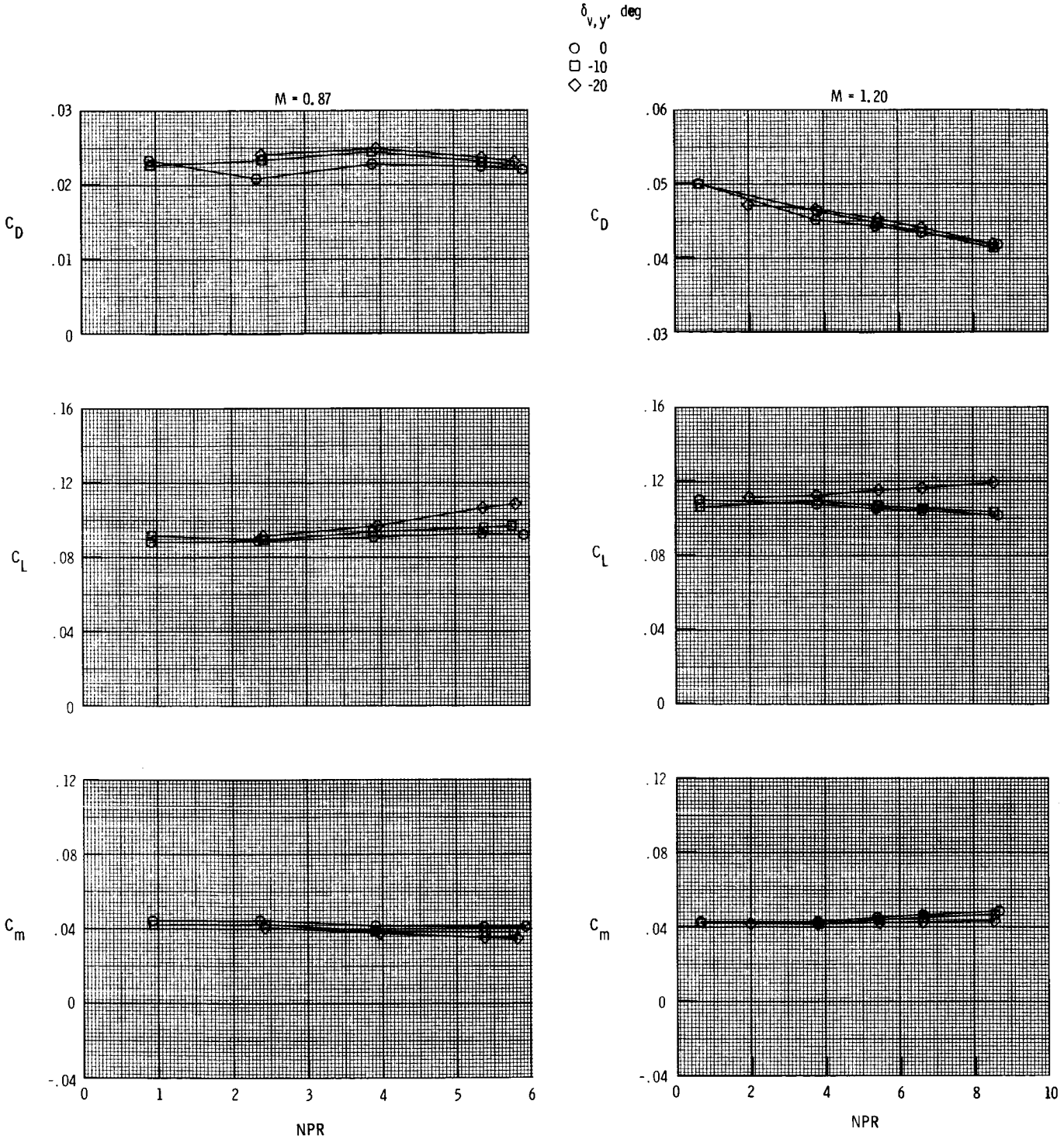

(b) $M = 0.87$ and 1.20.

Figure 37. Concluded.

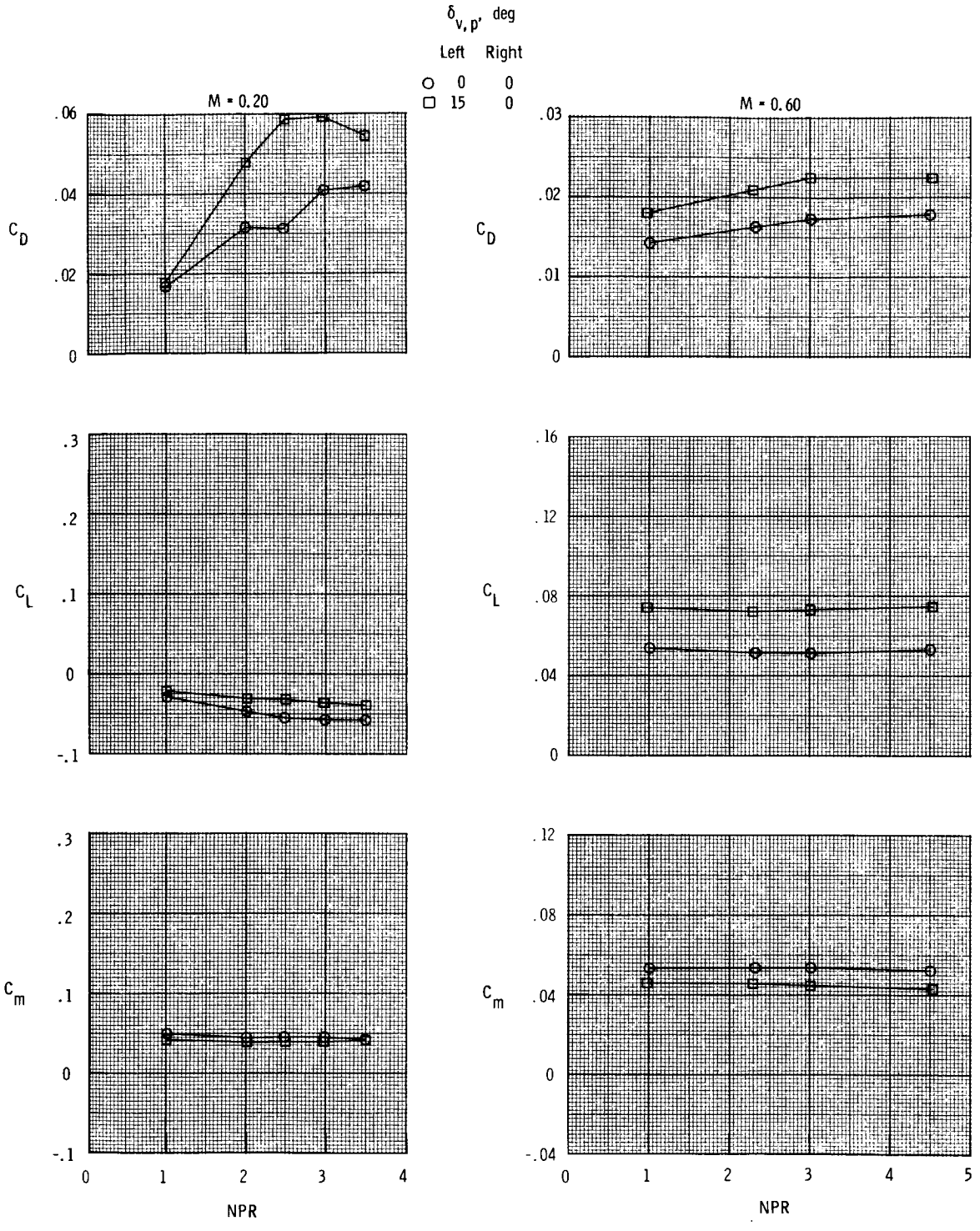

(a) $M = 0.20$ and 0.60.

Figure 38. Effect of nozzle pressure ratio and differential pitch vectoring on thrust-removed longitudinal aerodynamic characteristics for $\delta_{v,y} = 0°$ and $\alpha = 4°$.

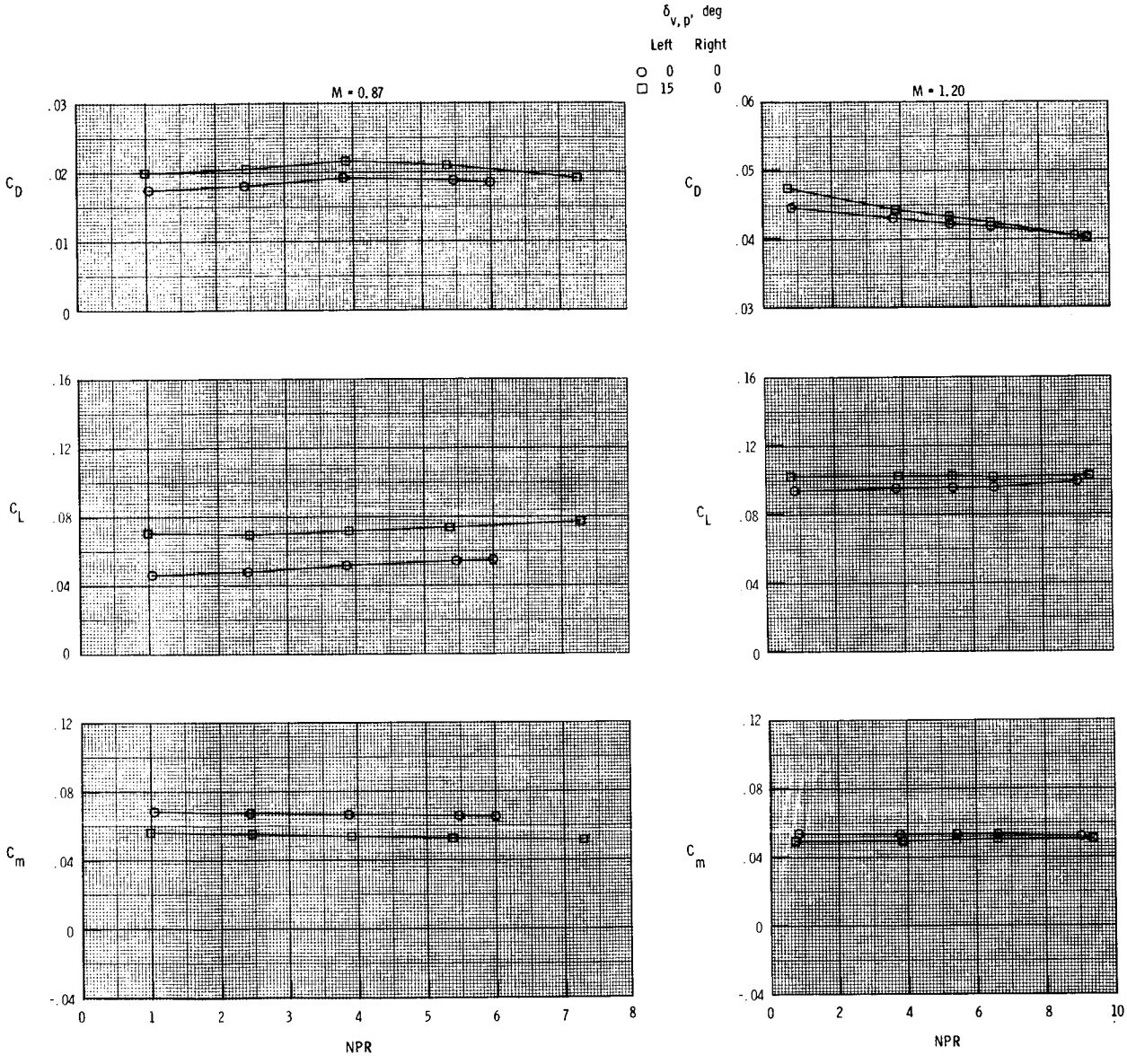

(b) $M = 0.87$ and 1.20.

Figure 38. Continued.

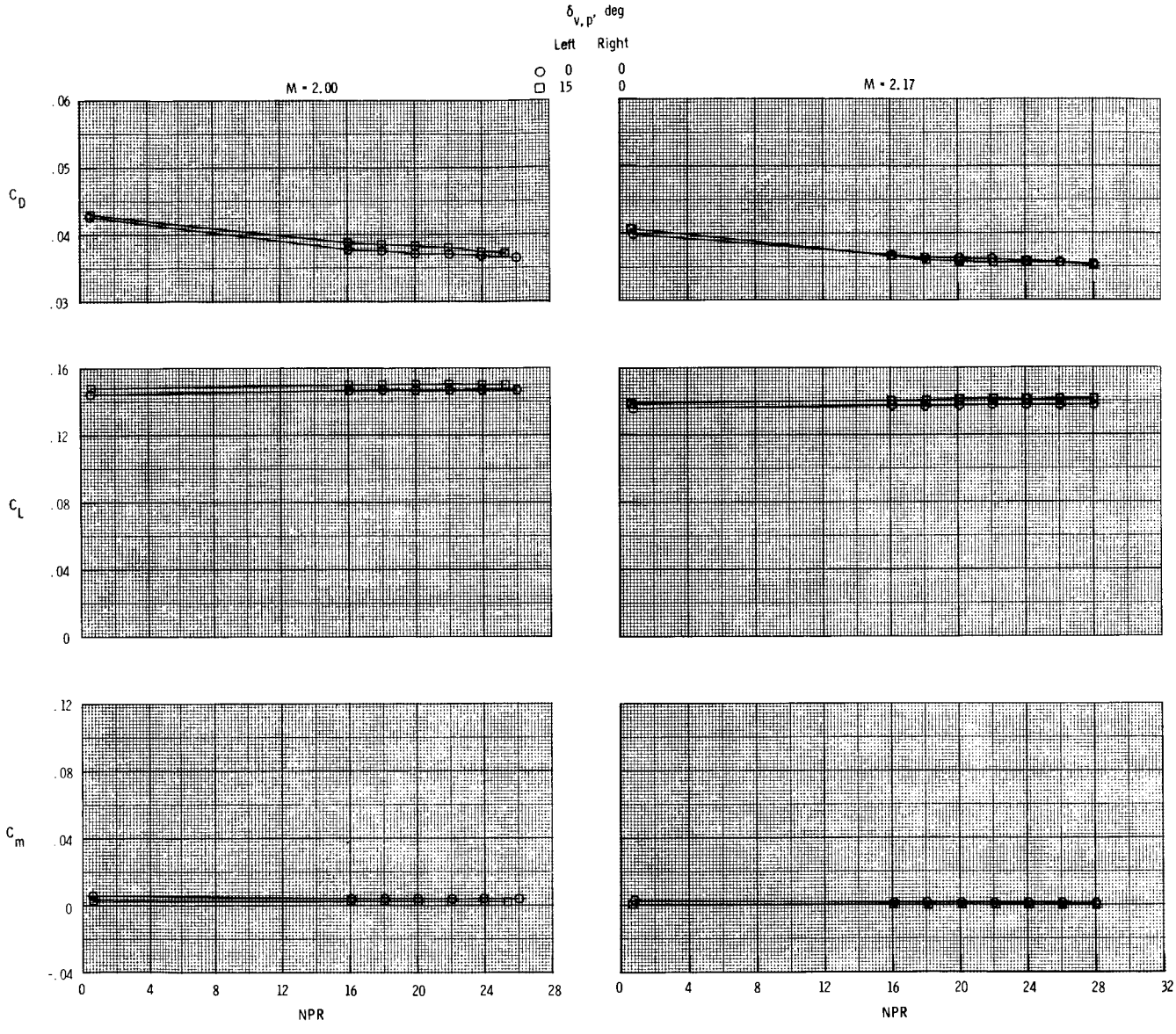

(c) $M = 2.00$ and 2.17.

Figure 38. Continued.

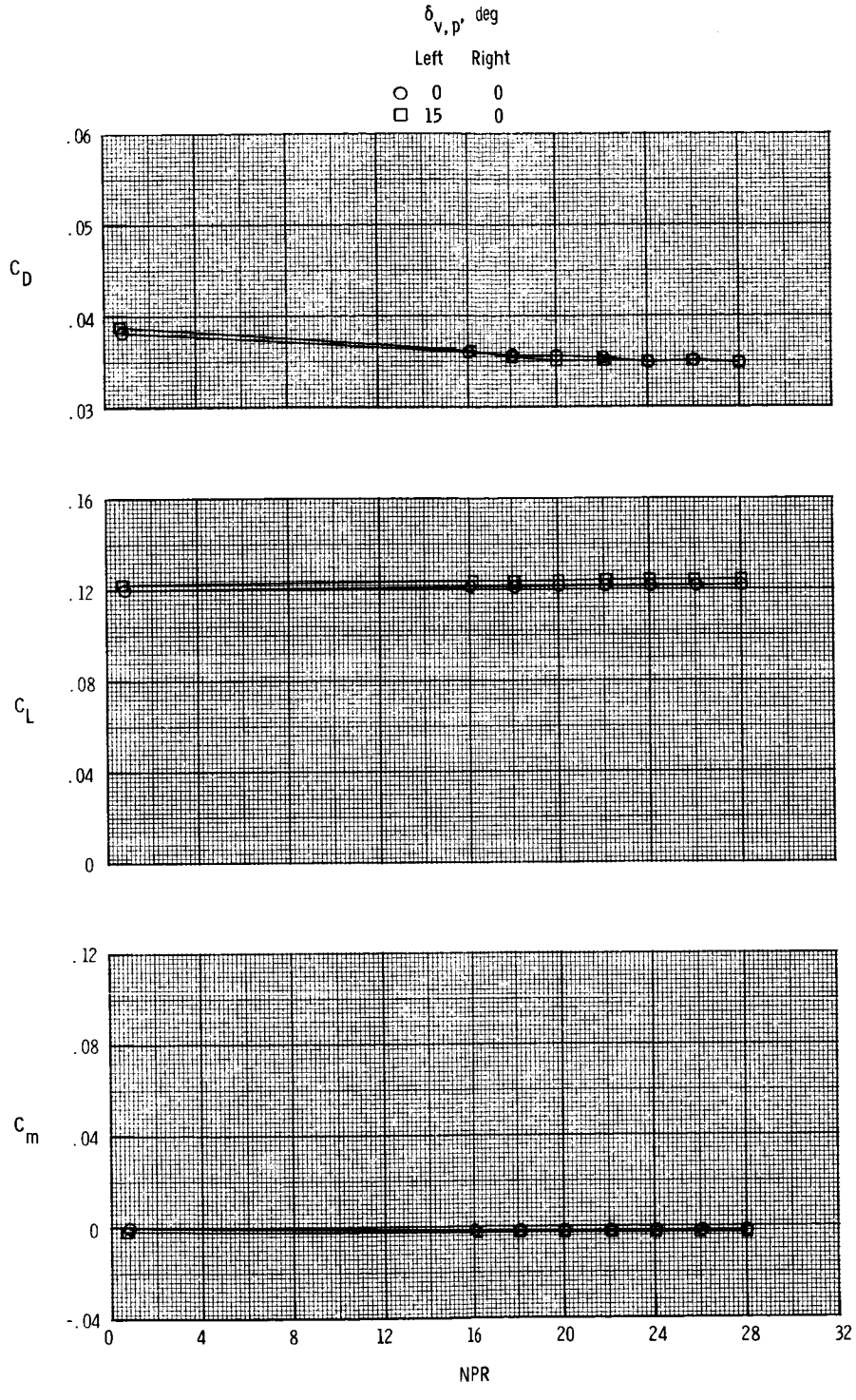

(d) $M = 2.47$.

Figure 38. Concluded.

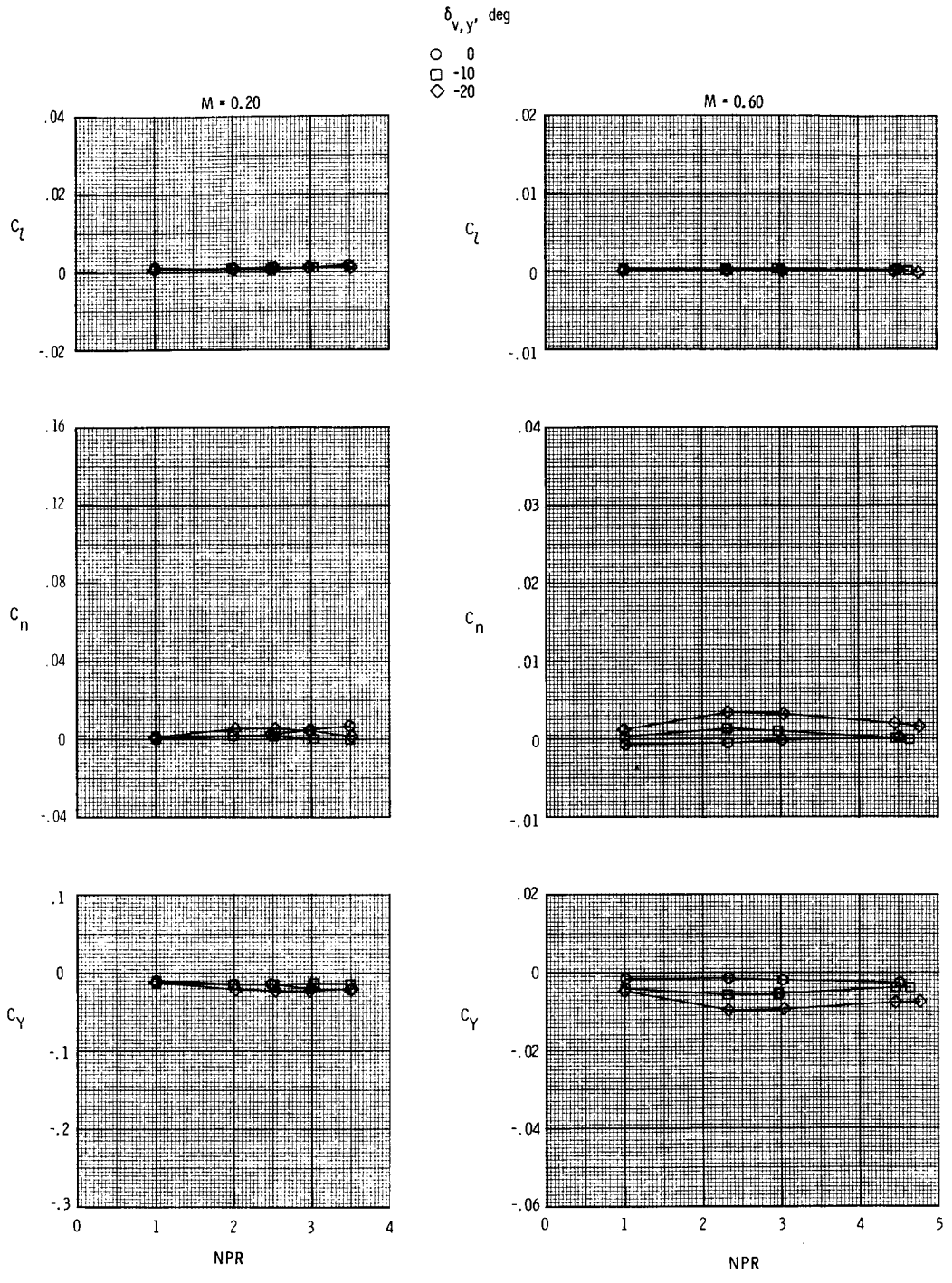

(a) $M = 0.20$ and 0.60.

Figure 39. Effect of nozzle pressure ratio and yaw vectoring on thrust-removed lateral aerodynamic characteristics for $\delta_{v,p} = 0°$ and $\alpha = 4°$.

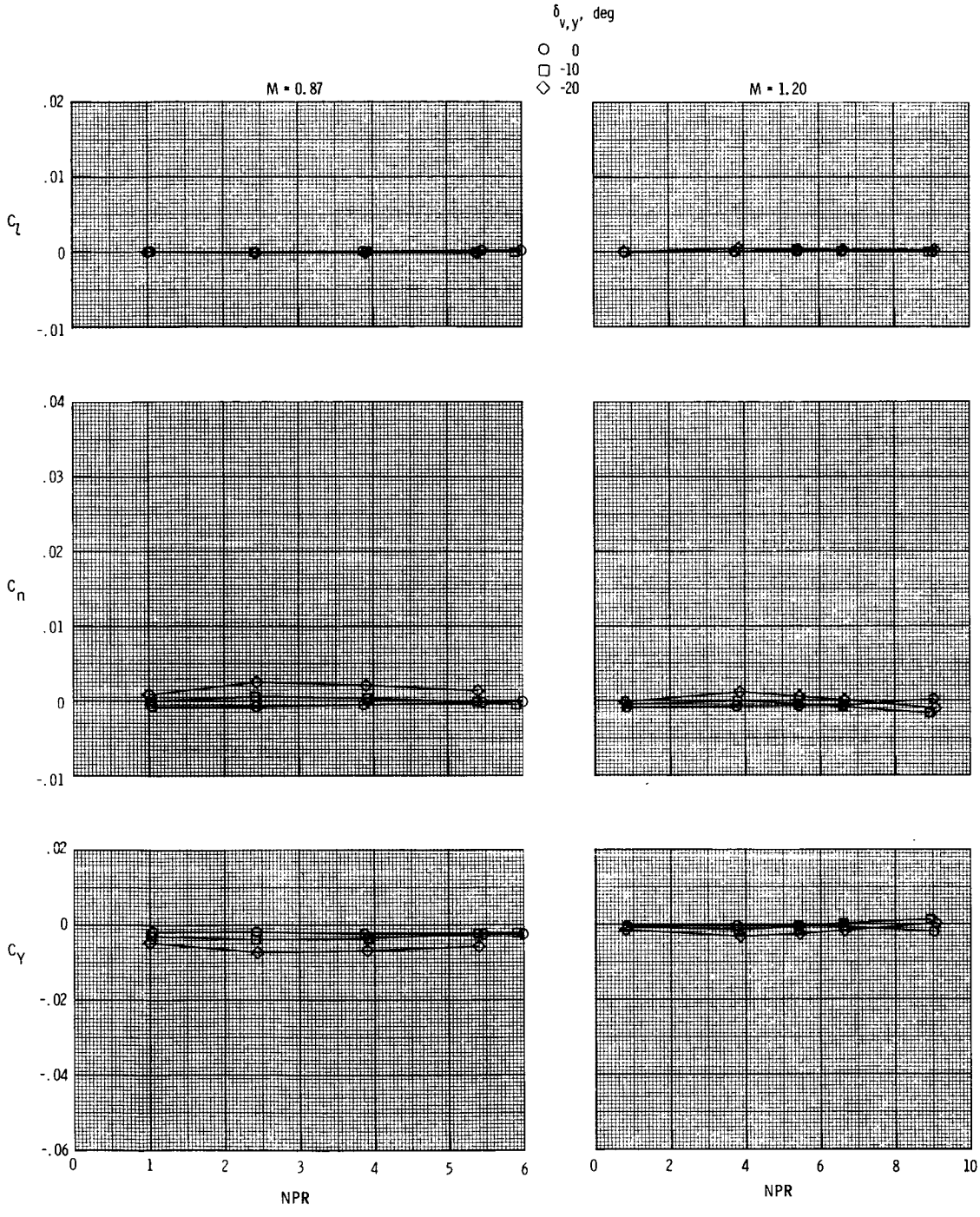

(b) $M = 0.87$ and 1.20.

Figure 39. Continued.

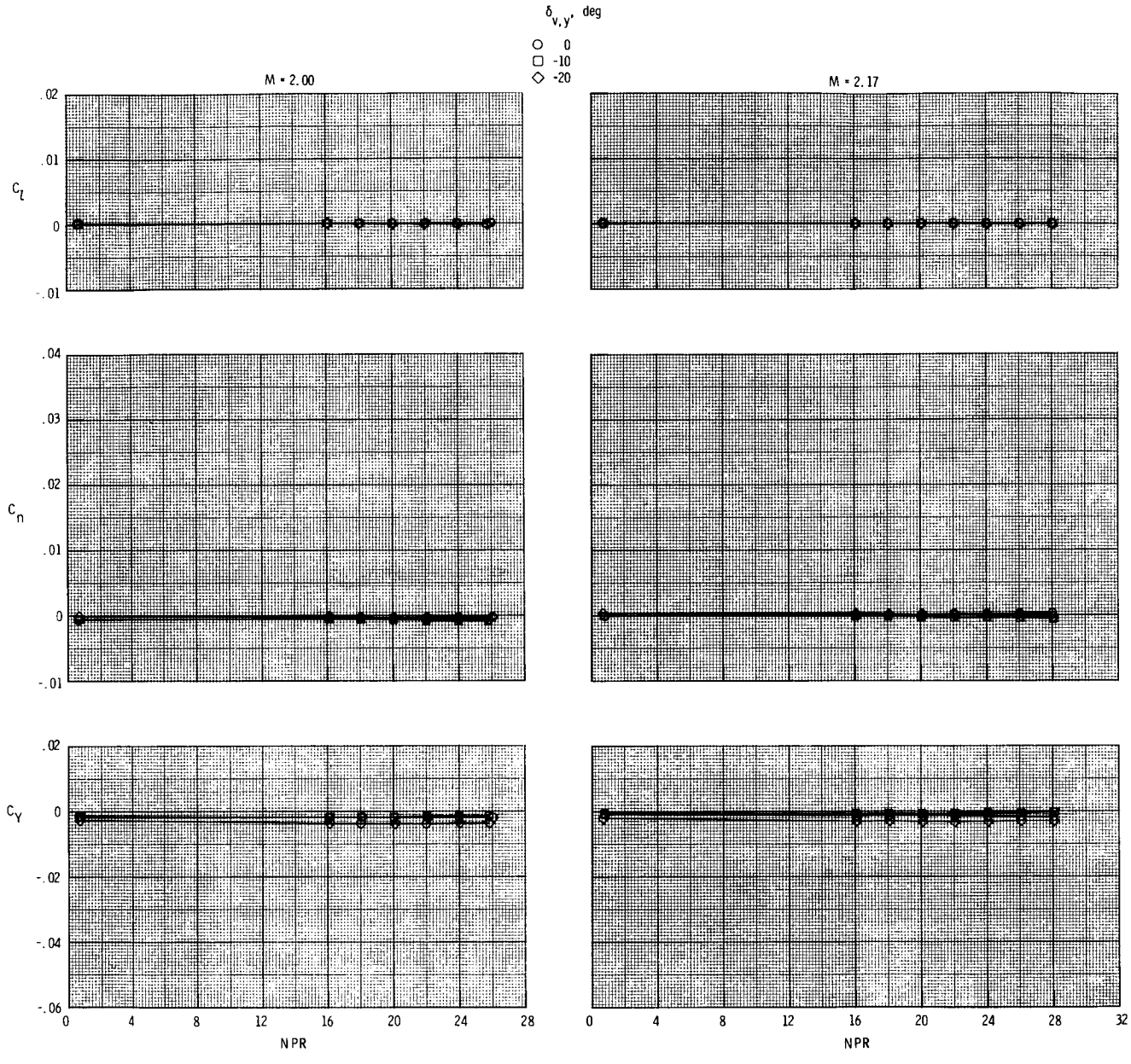

(c) $M = 2.00$ and 2.17.

Figure 39. Continued.

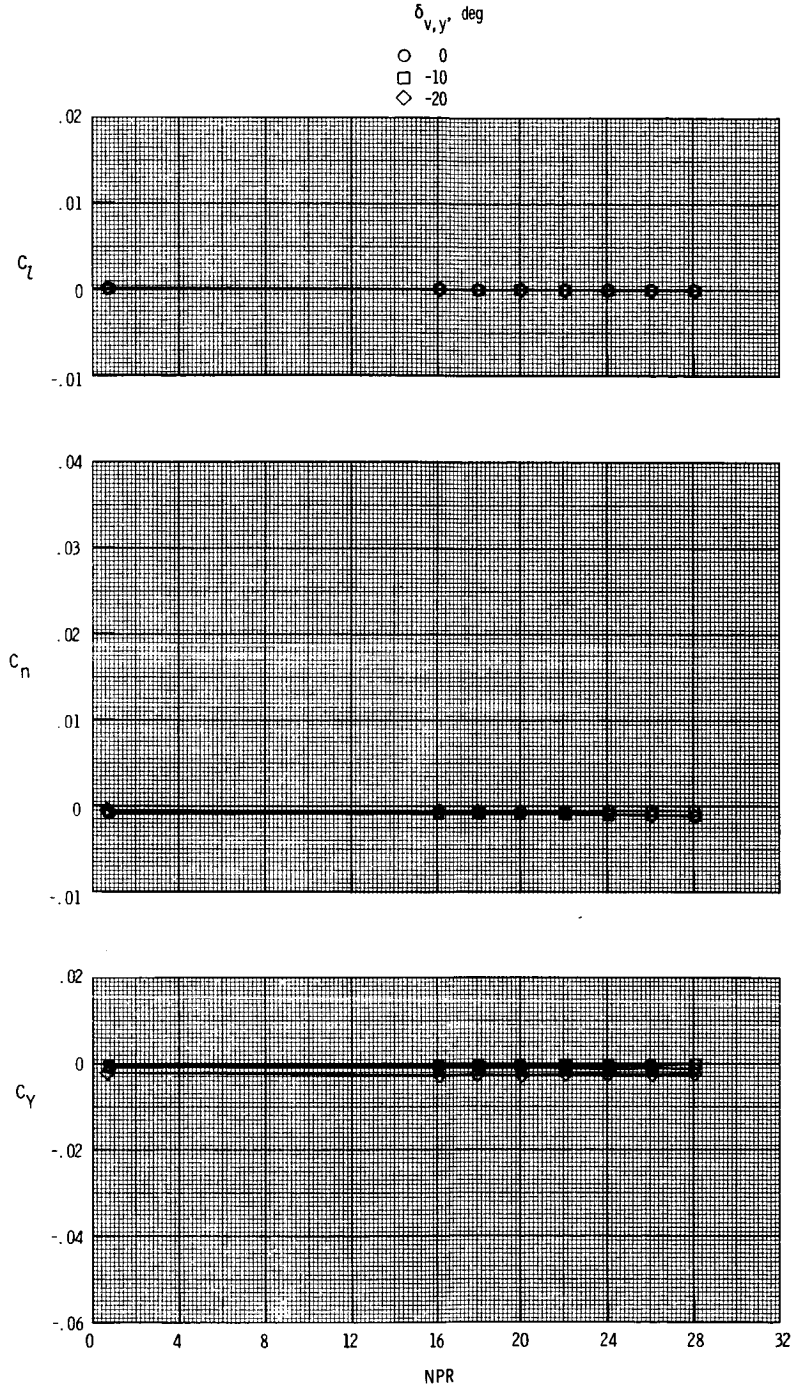

(d) $M = 2.47$.

Figure 39. Concluded.

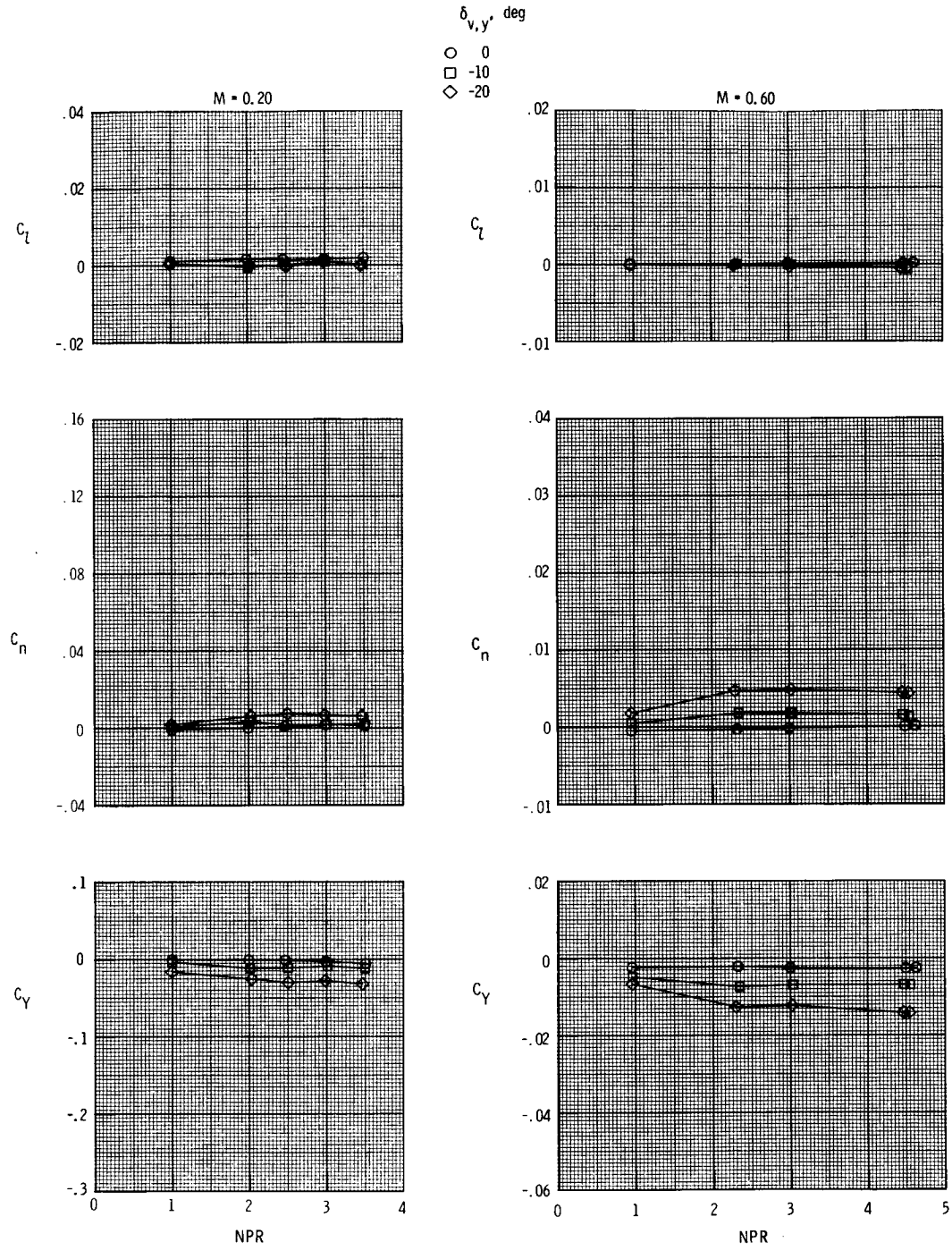

(a) $M = 0.20$ and 0.60.

Figure 40. Effect of nozzle pressure ratio and yaw vectoring on thrust-removed lateral aerodynamic characteristics for $\delta_{v,p} = 15°$ and $\alpha = 4°$.

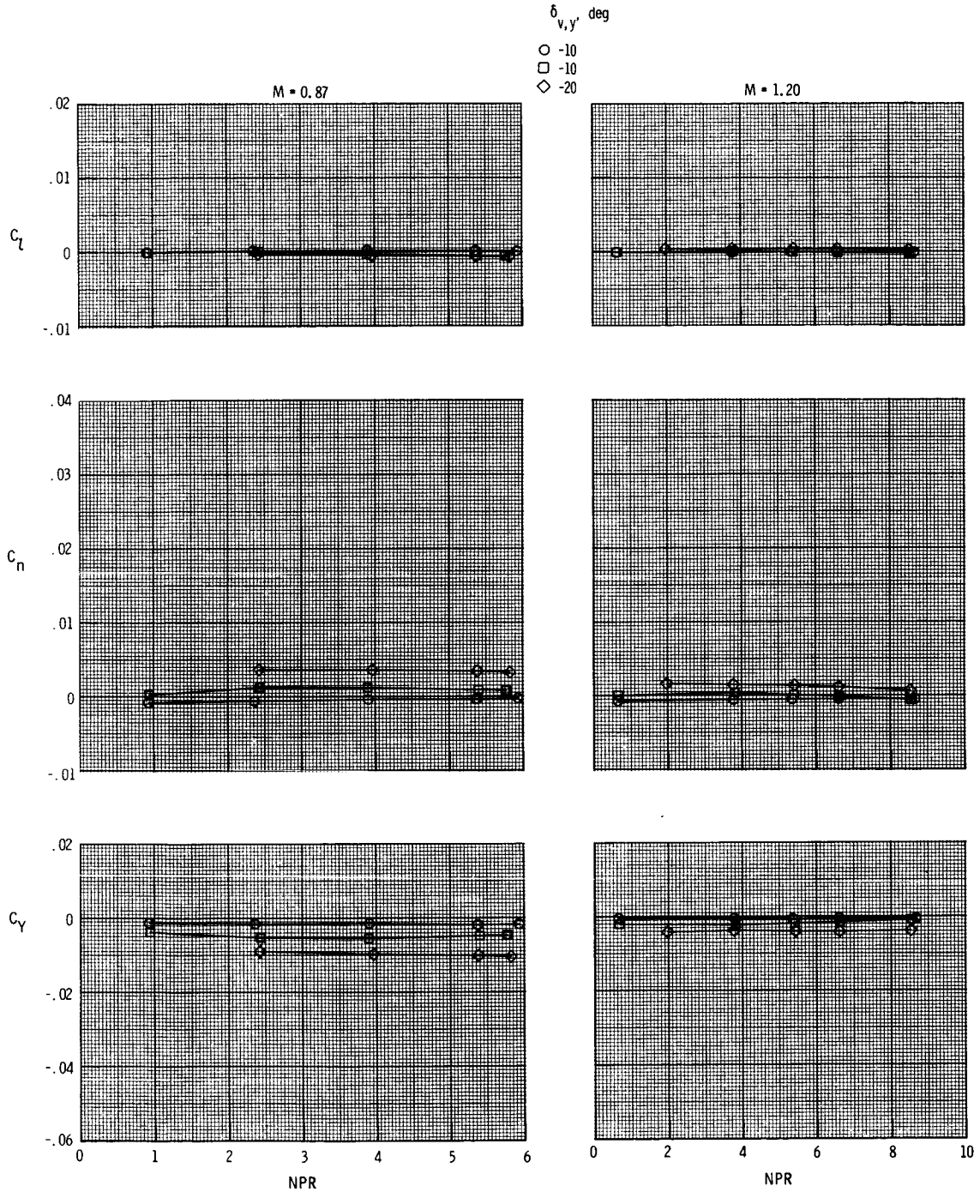

(b) $M = 0.87$ and 1.20.

Figure 40. Concluded.

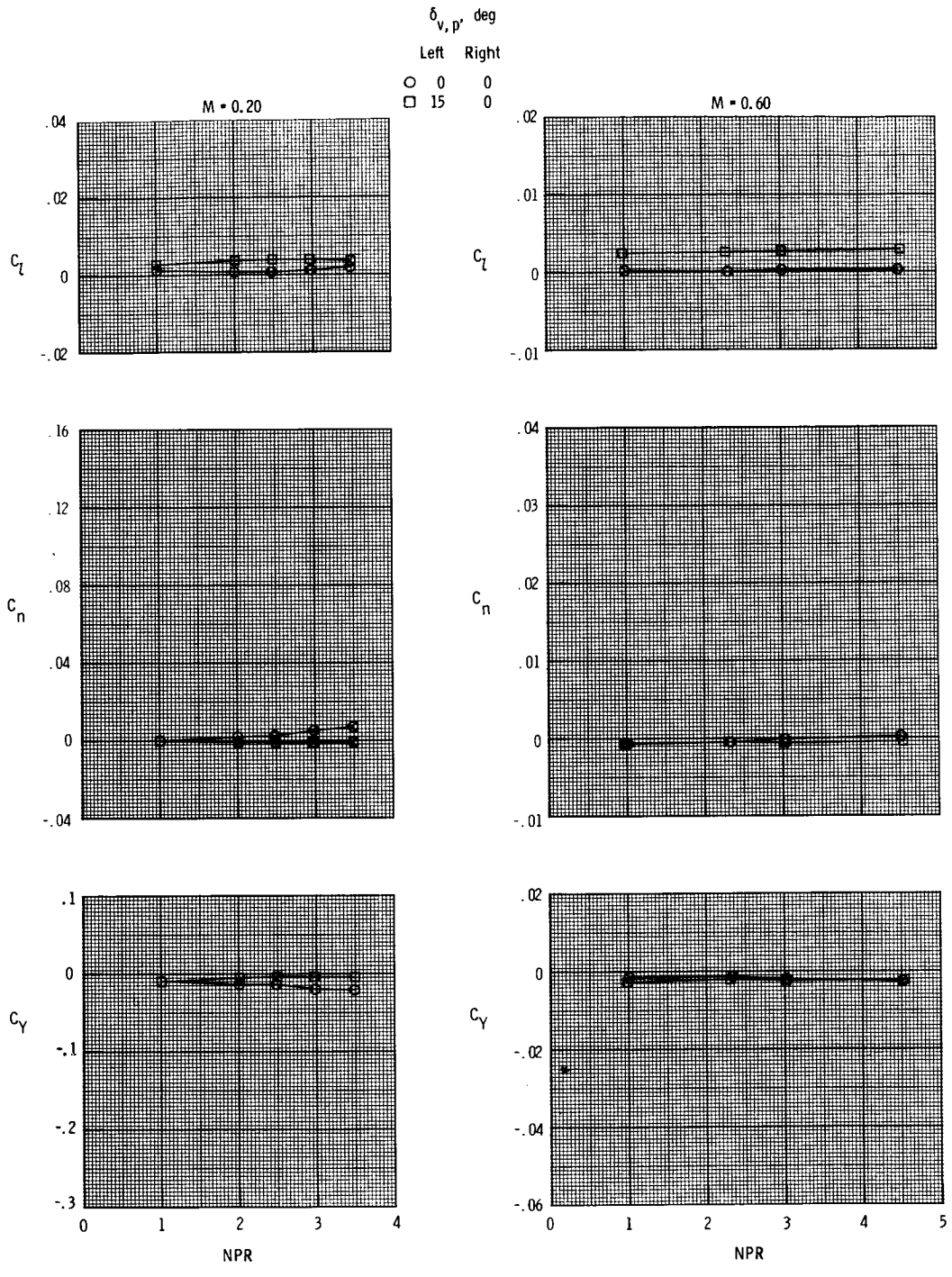

(a) $M = 0.20$ and 0.60.

Figure 41. Effect of nozzle pressure ratio and differential pitch vectoring on thrust-removed lateral aerodynamic characteristics for $\delta_{v,y} = 0°$ and $\alpha = 4°$.

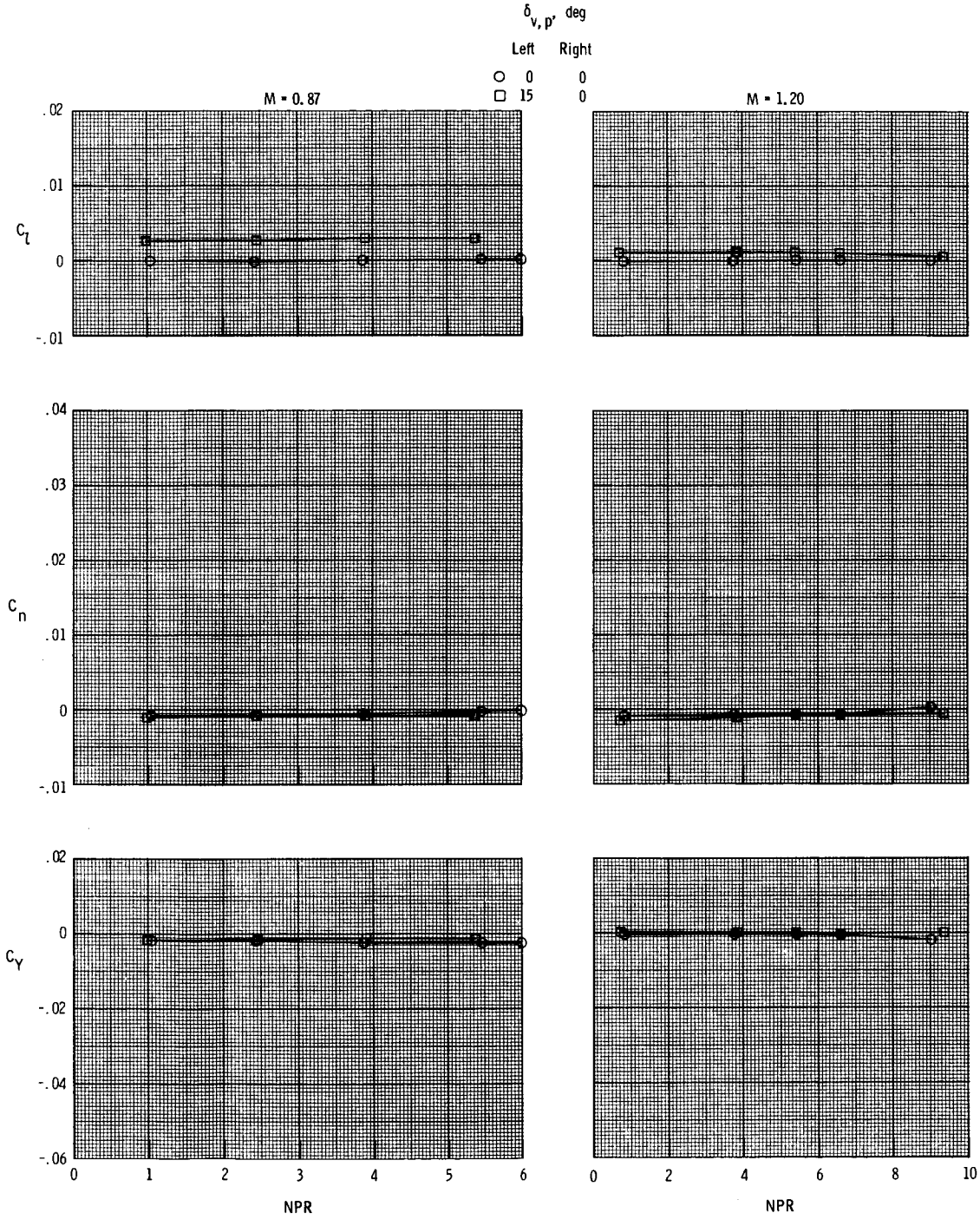

(b) $M = 0.87$ and 1.20.

Figure 41. Continued.

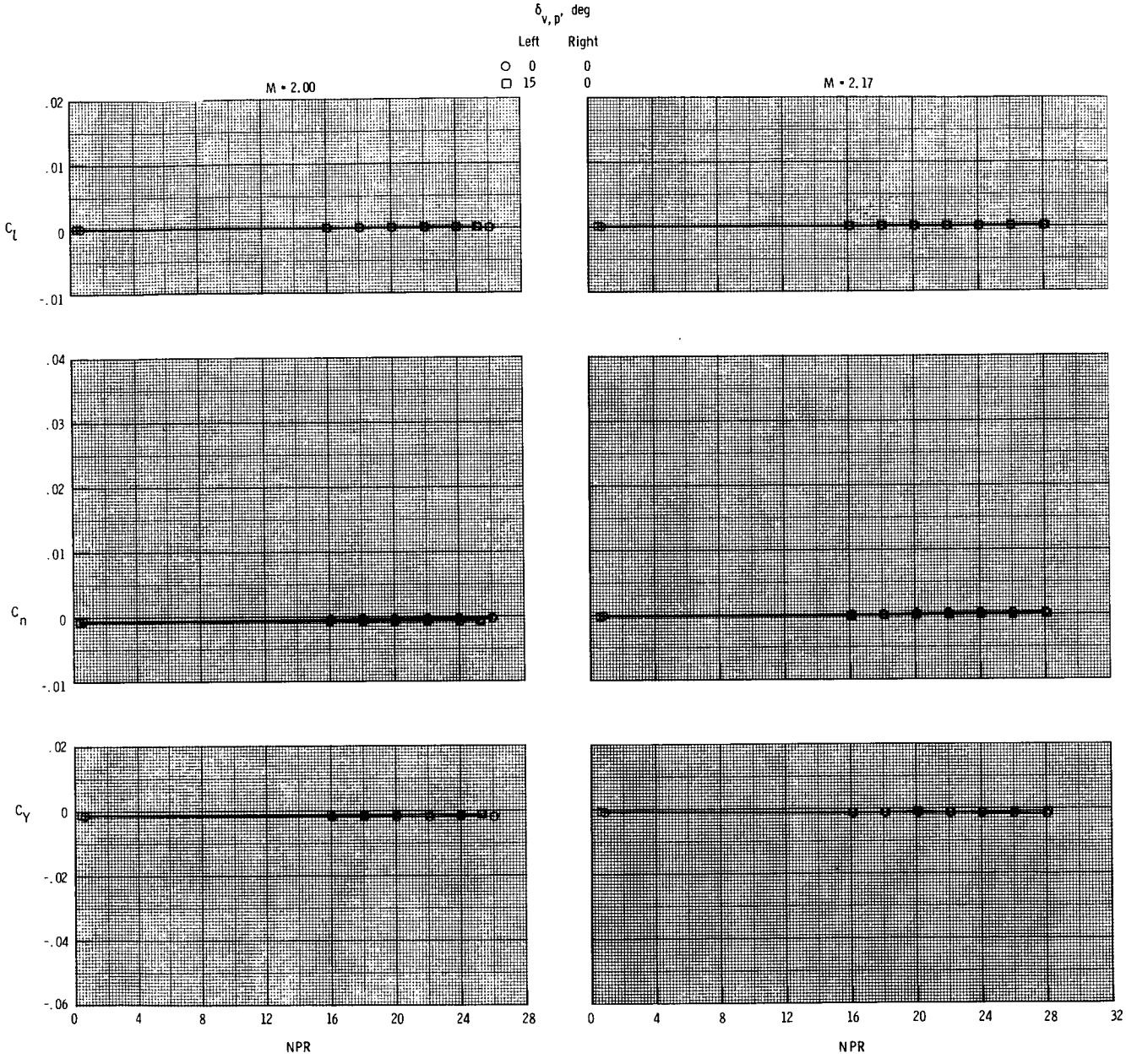

(c) $M = 2.00$ and 2.17.

Figure 41. Continued.

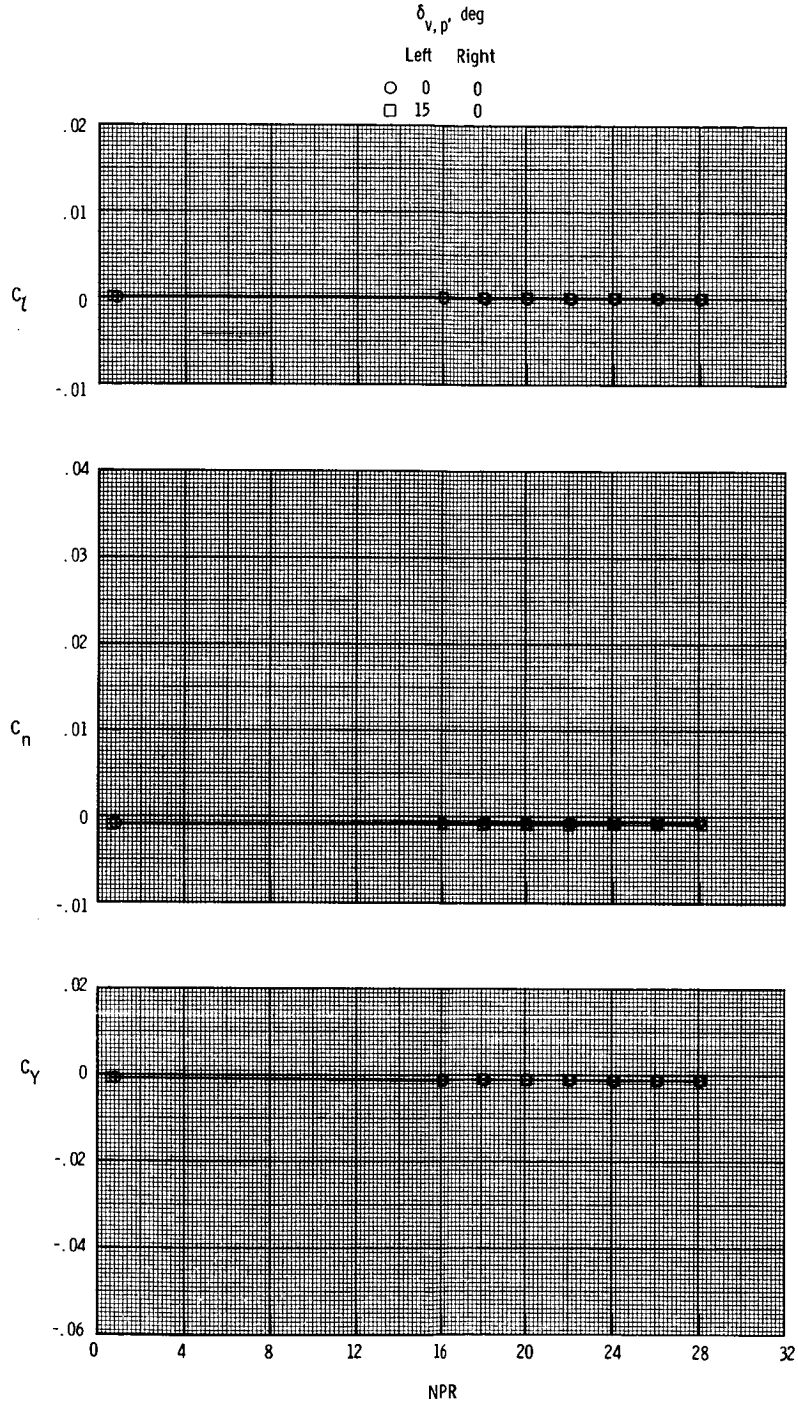

(d) $M = 2.47$.

Figure 41. Concluded.

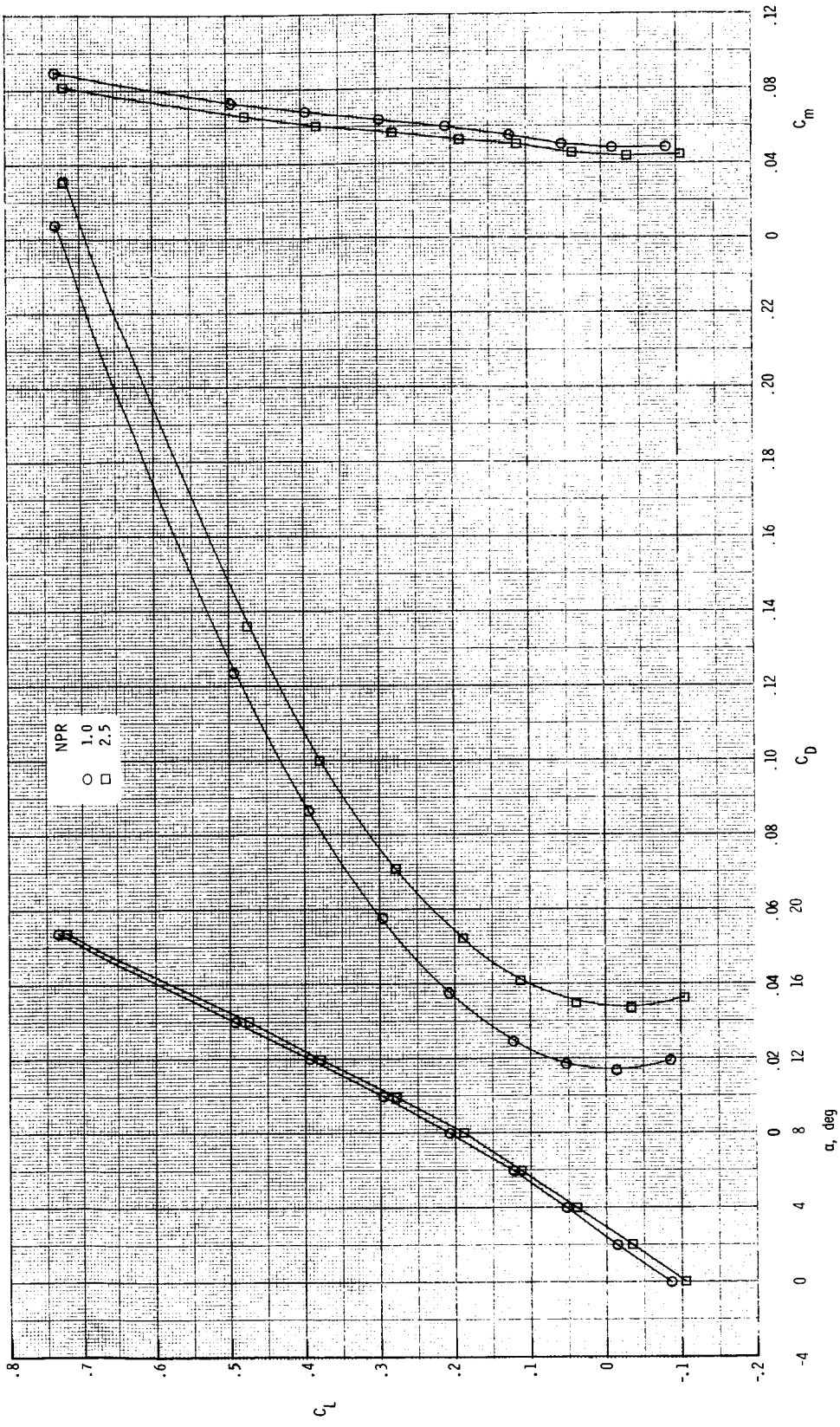

(a) $M = 0.20$.

Figure 42. Thrust-removed longitudinal aerodynamic characteristics for $\delta_{v,p} = 0°$ and $\delta_{v,y} = 0°$.

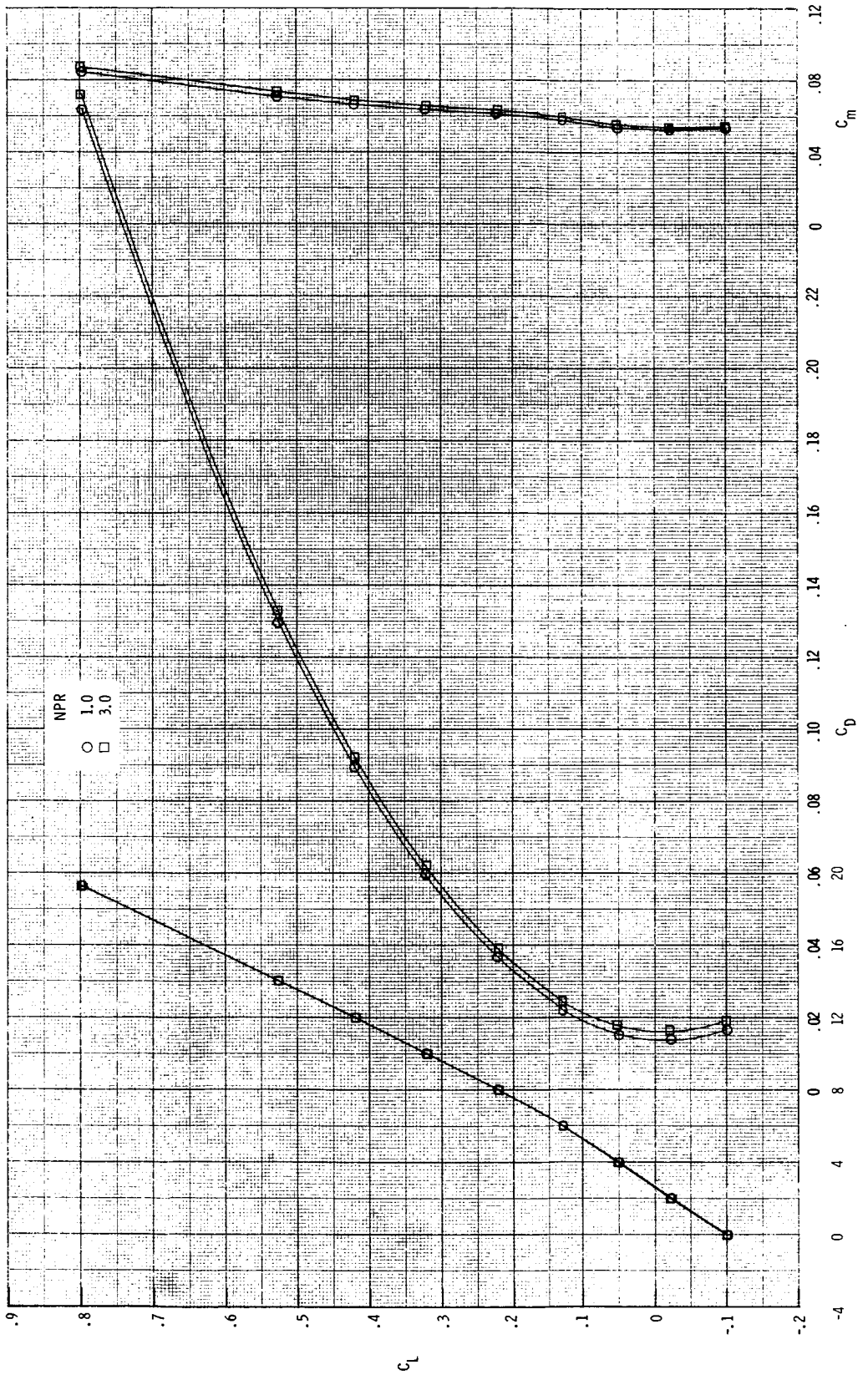

(b) $M = 0.60$.

Figure 42. Continued.

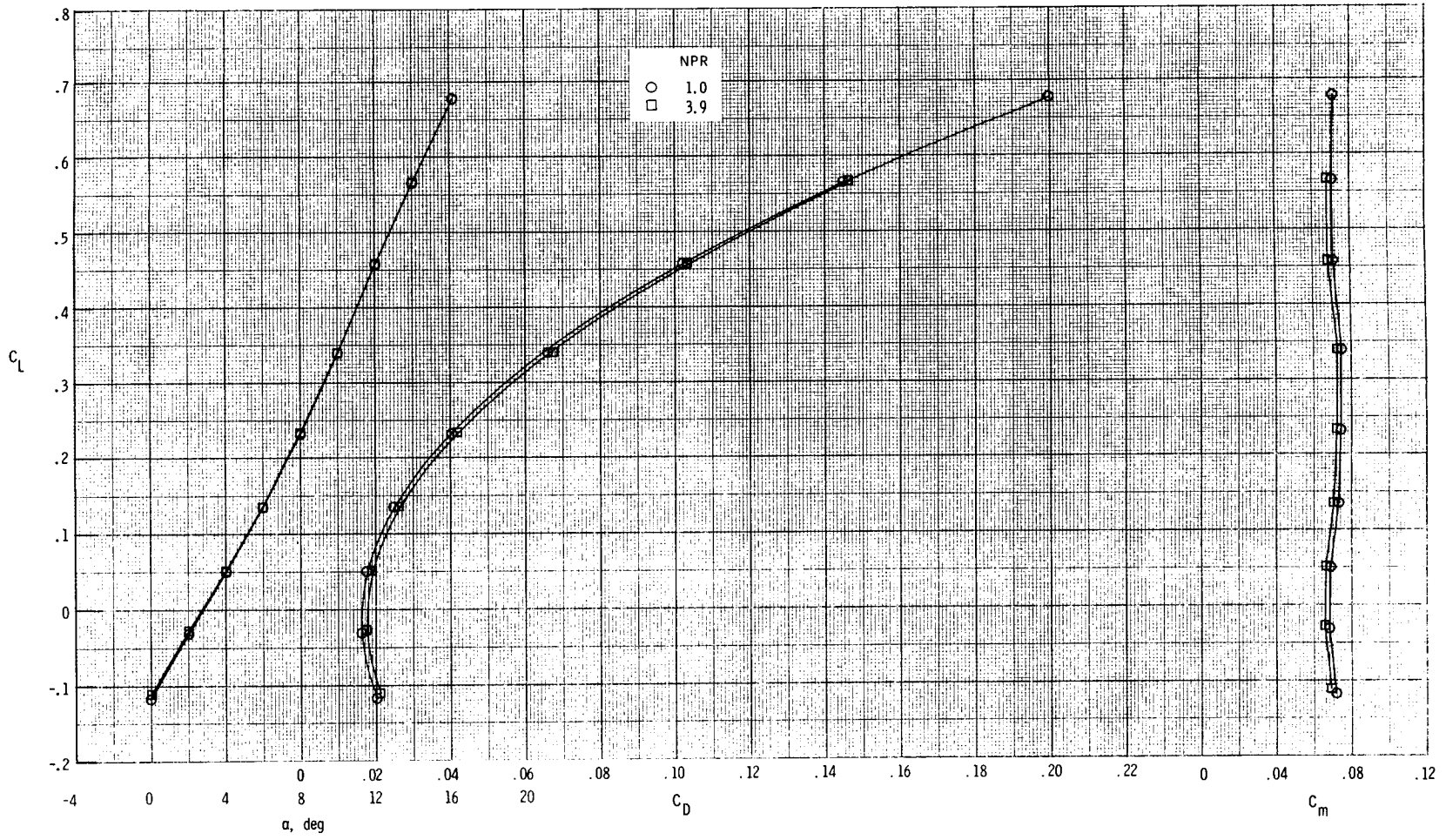

(c) $M = 0.87$.

Figure 42. Continued.

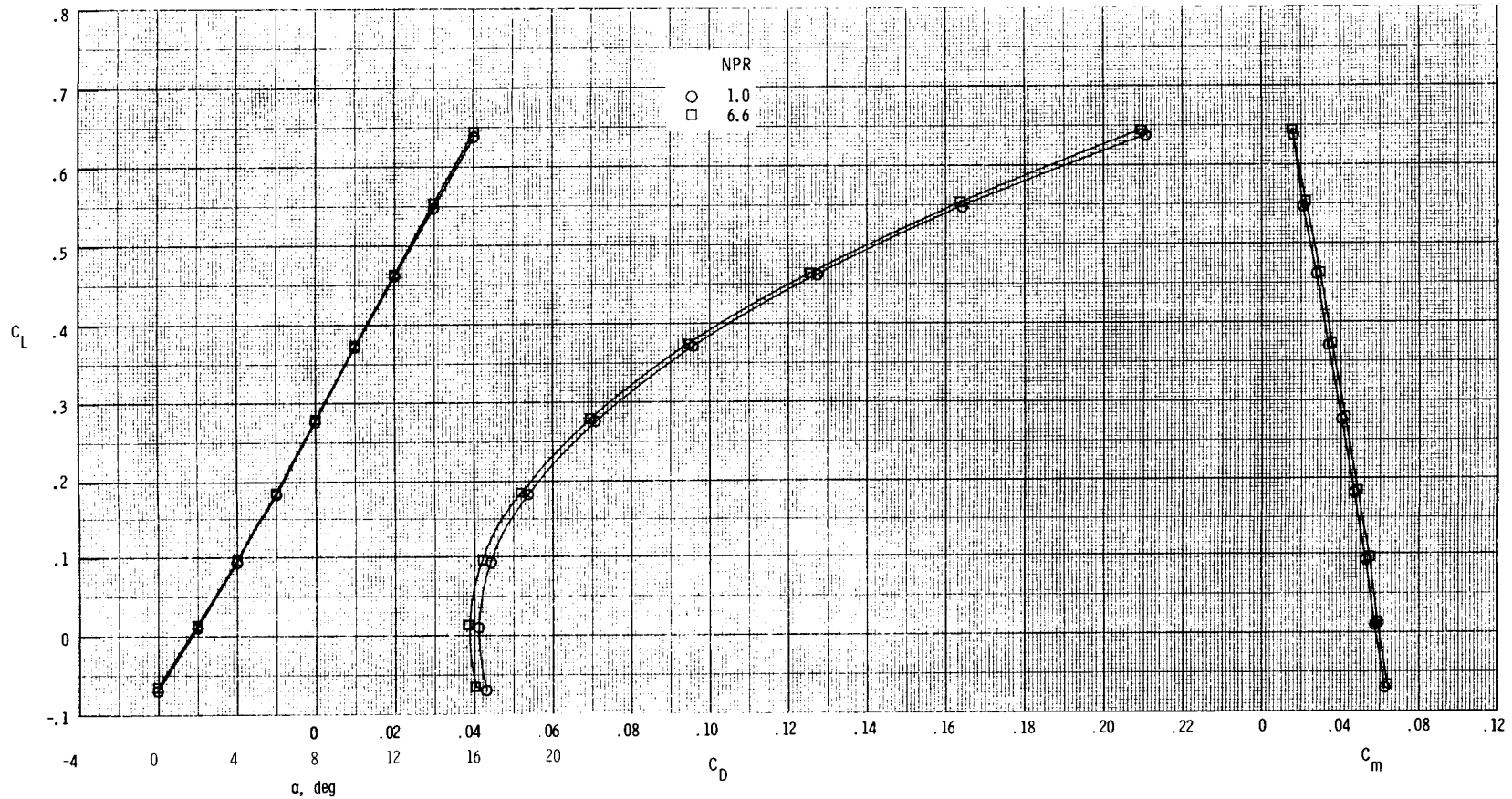

(d) $M = 1.20$.

Figure 42. Continued.

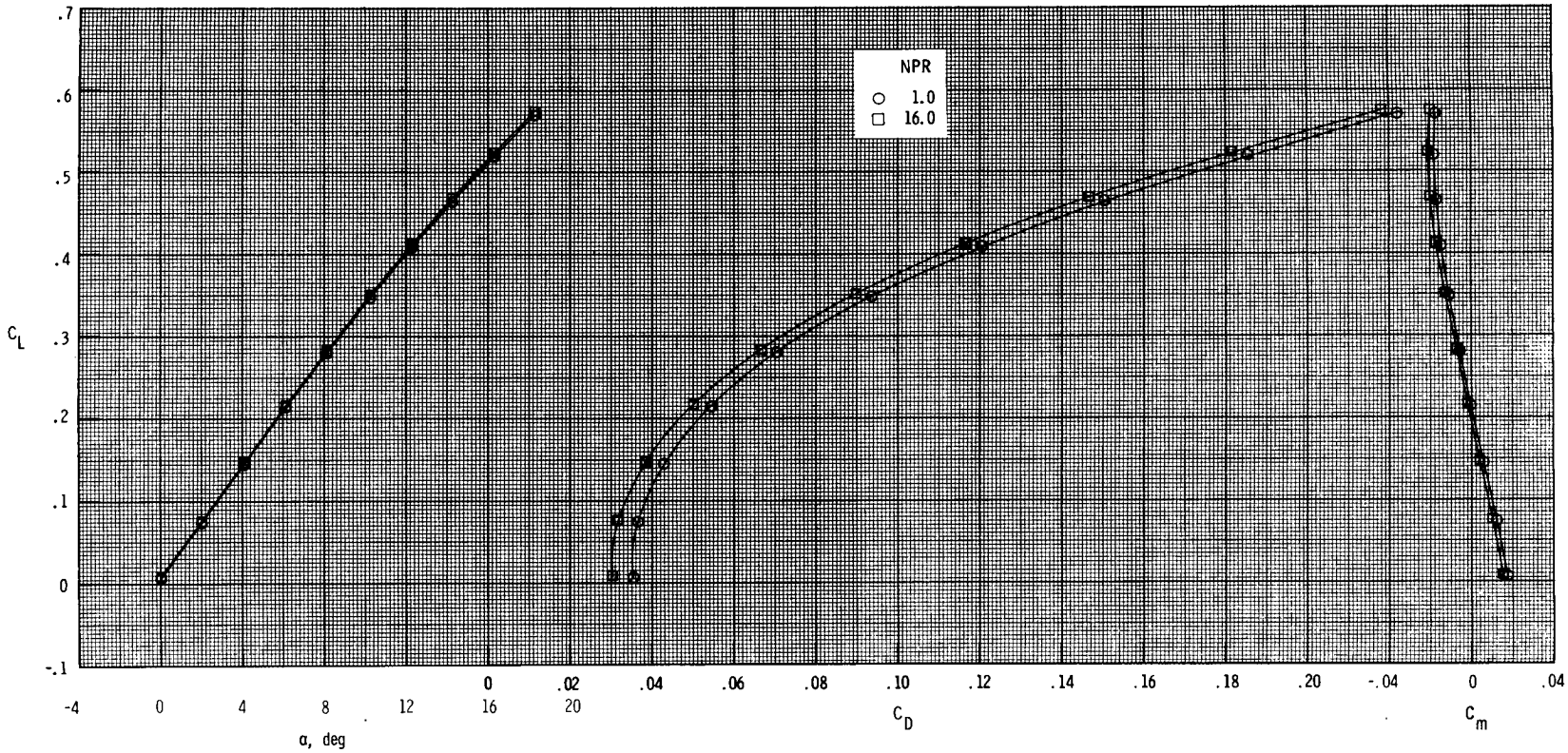

(e) $M = 2.00$.

Figure 42. Continued.

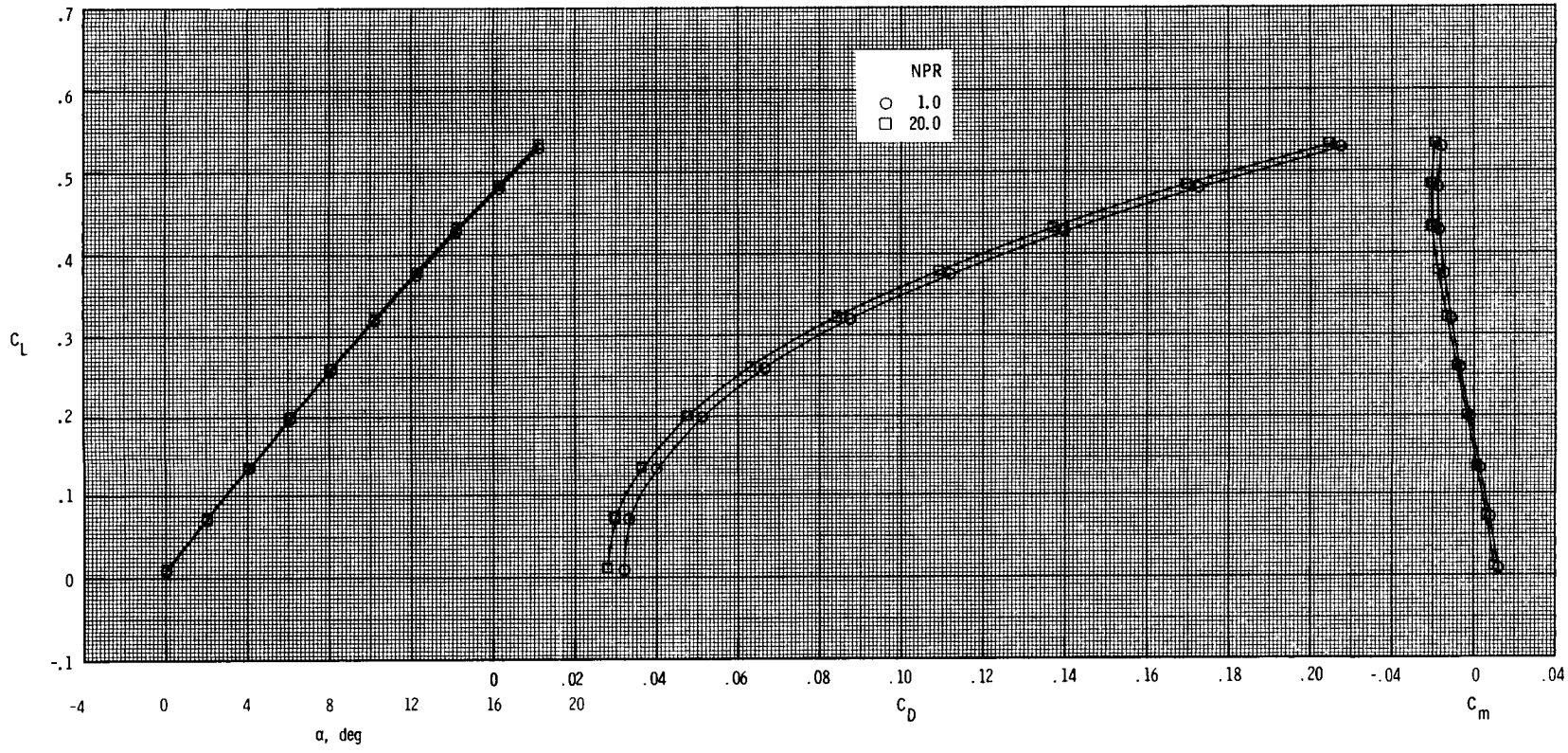

(f) $M = 2.17$.

Figure 42. Continued.

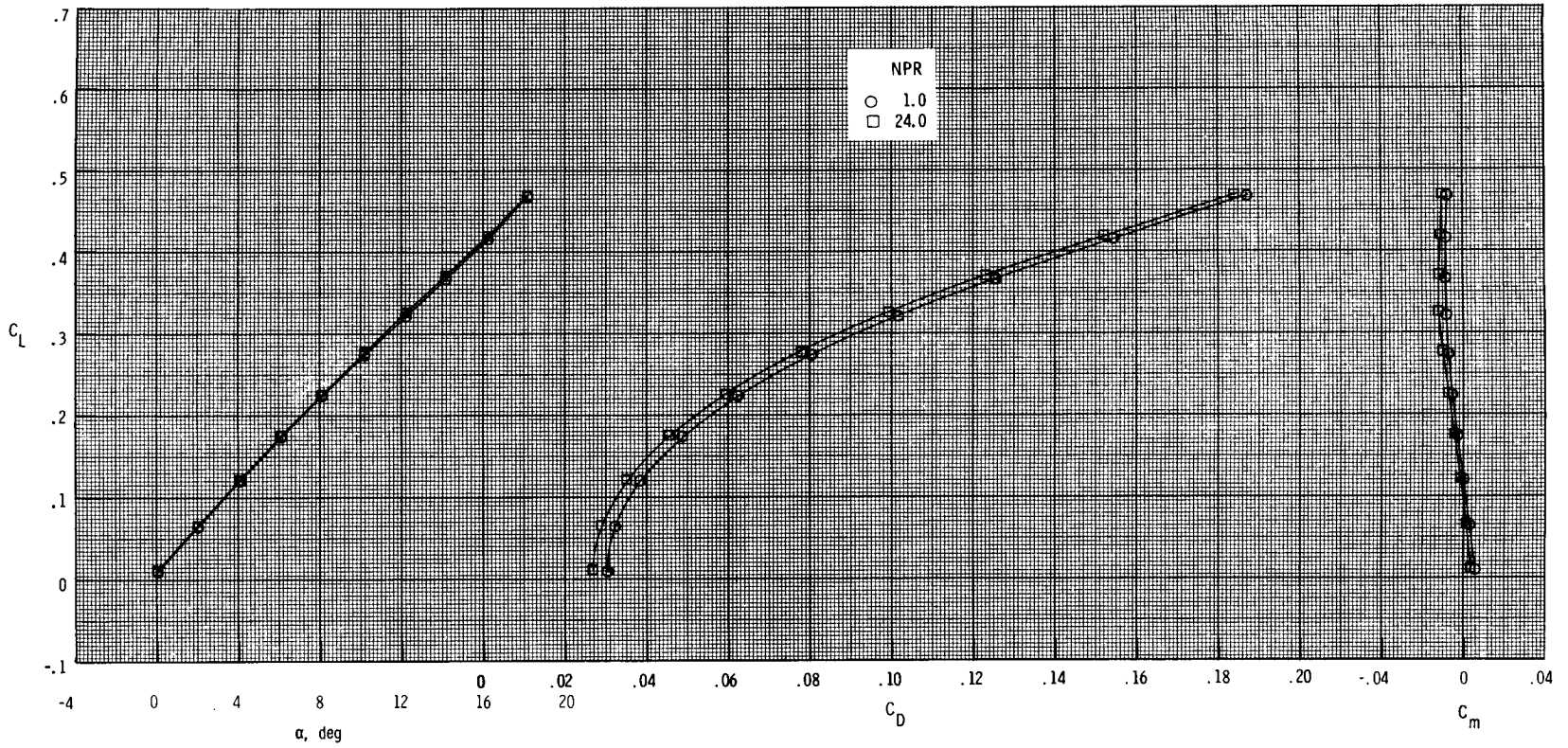

(g) $M = 2.47$.

Figure 42. Concluded.

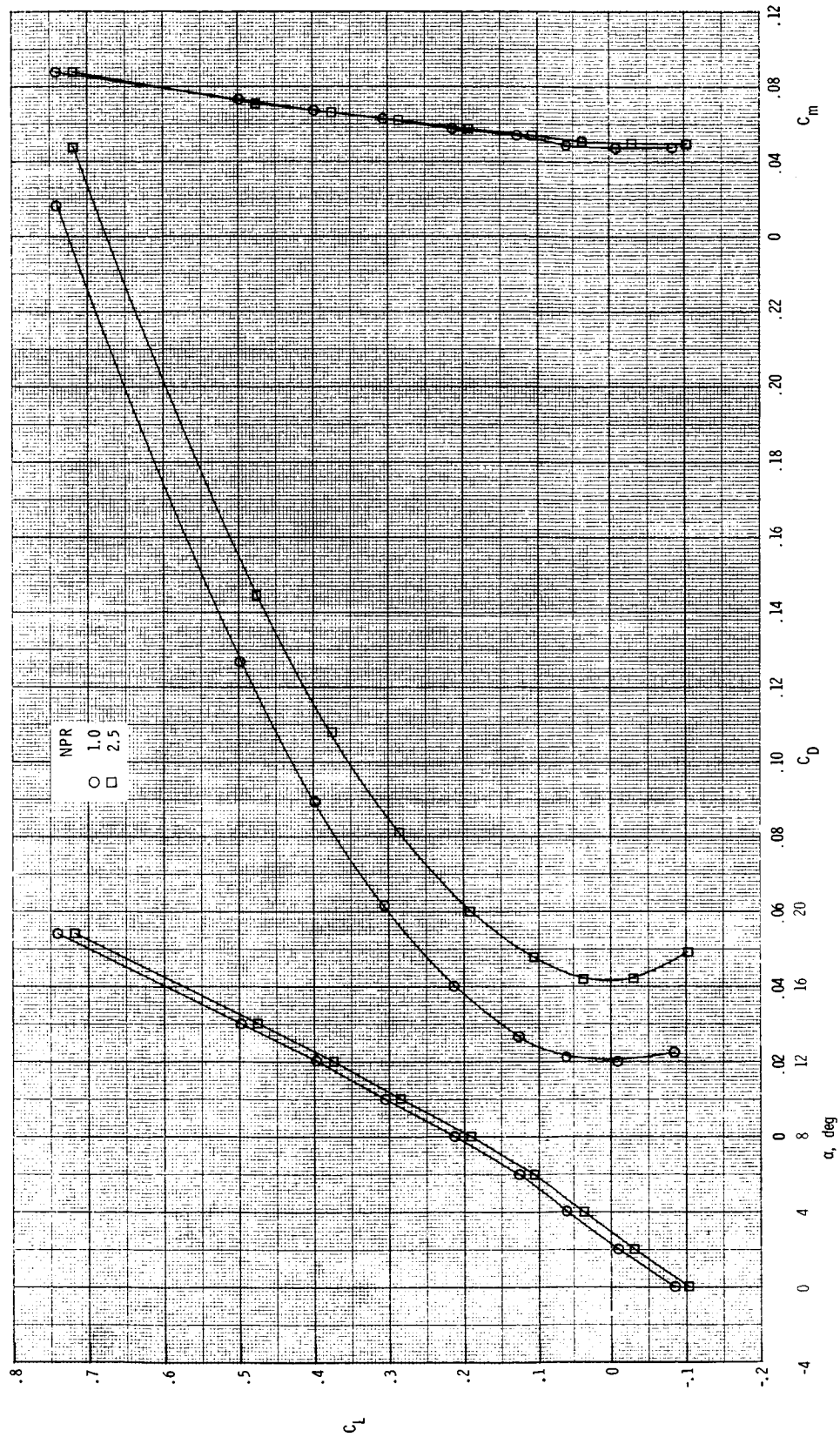

(a) $M = 0.20$.

Figure 43. Thrust-removed longitudinal aerodynamic characteristics for $\delta_{v,p} = 0°$ and $\delta_{v,y} = -10°$.

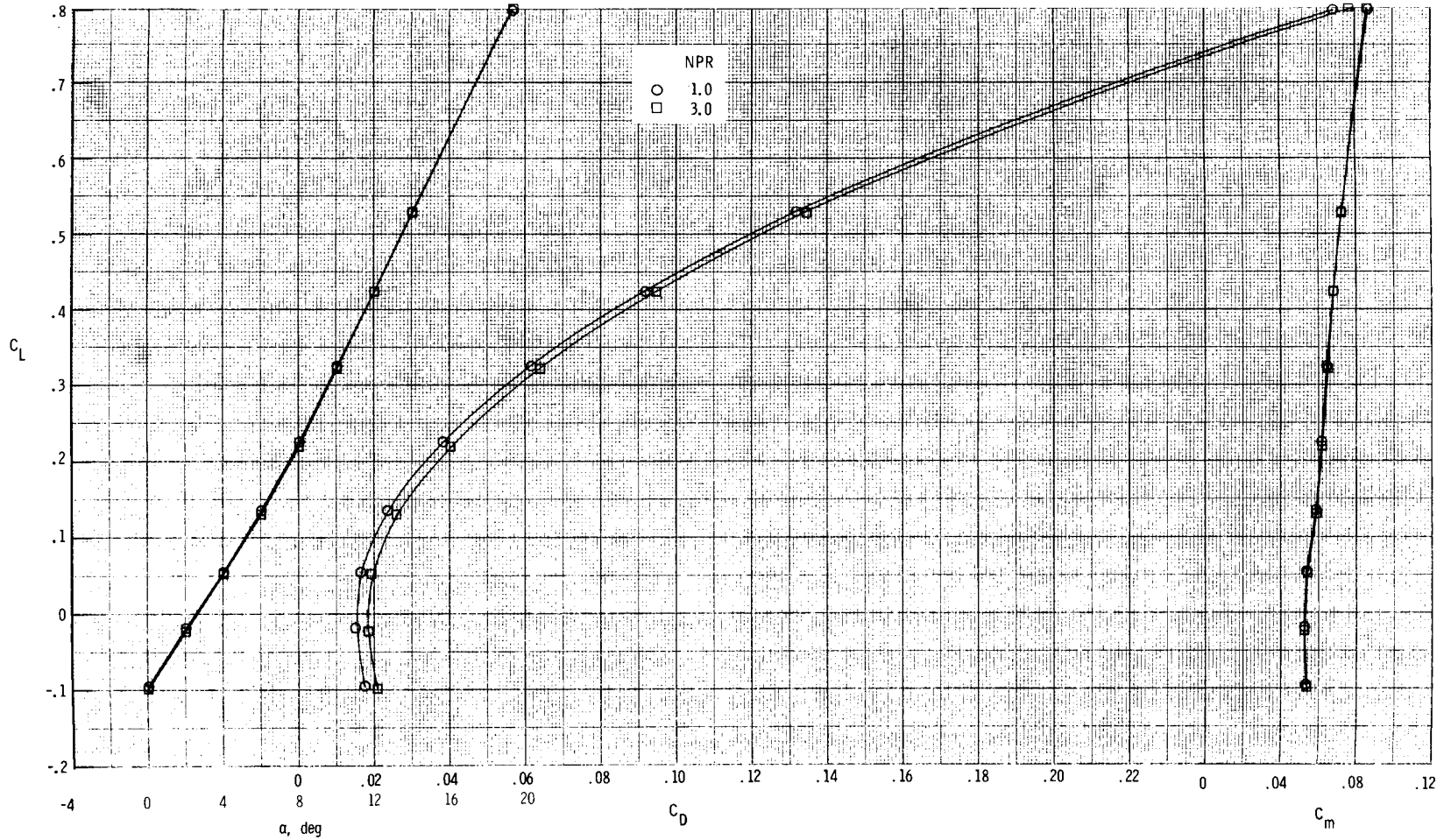

(b) $M = 0.60$.

Figure 43. Continued.

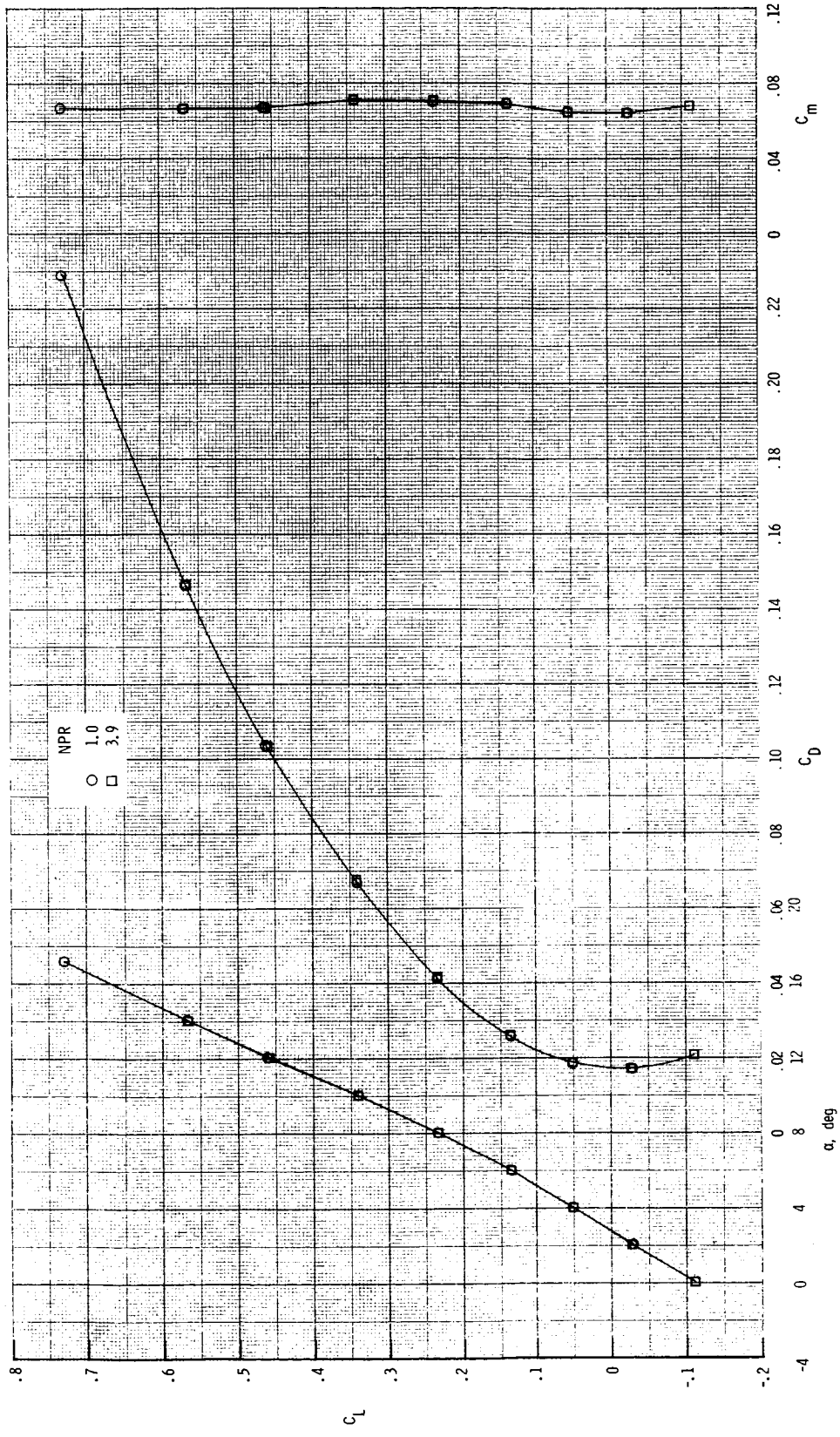

(c) $M = 0.87$.

Figure 43. Continued.

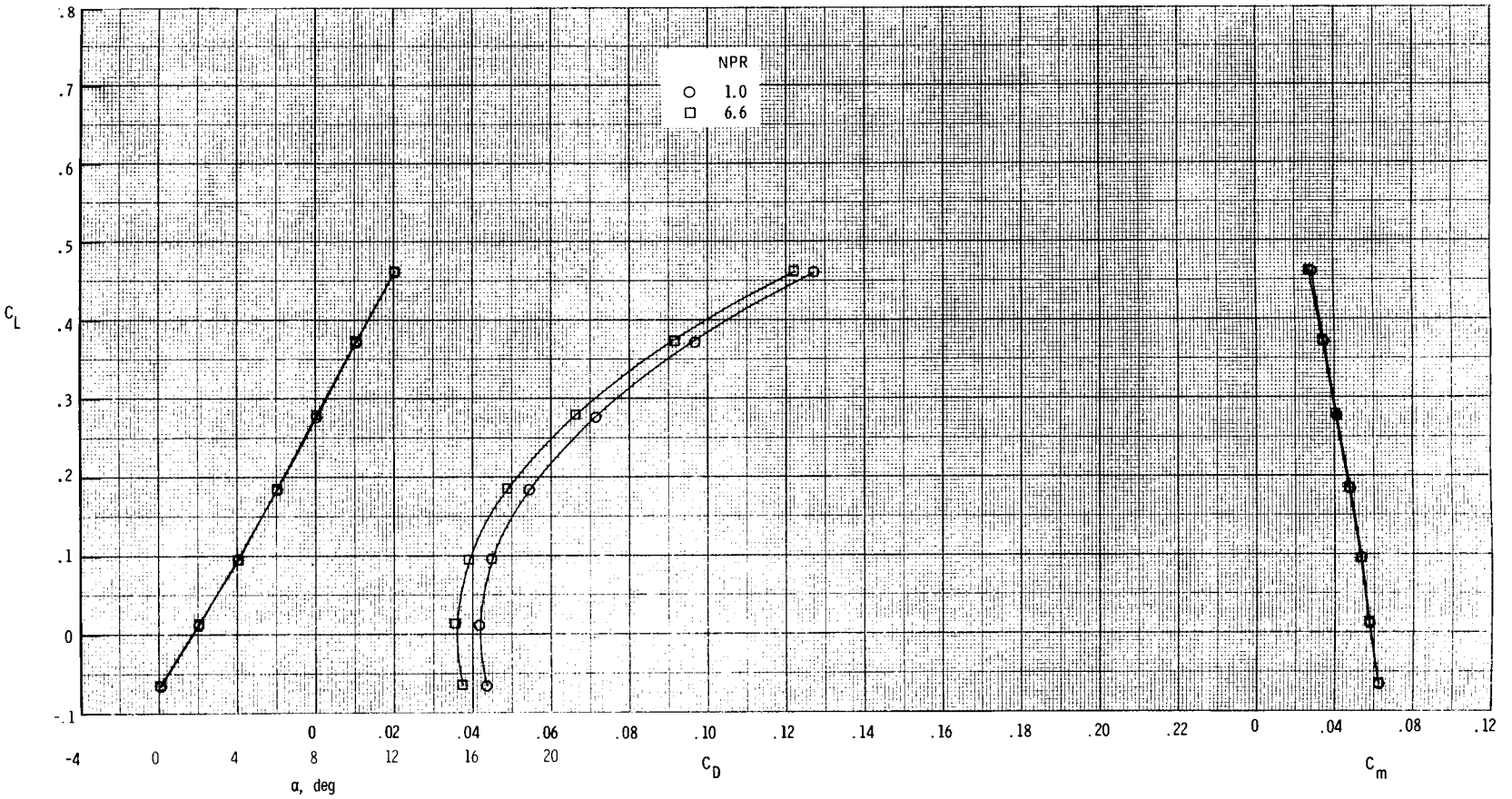

(d) $M = 1.20$.

Figure 43. Continued.

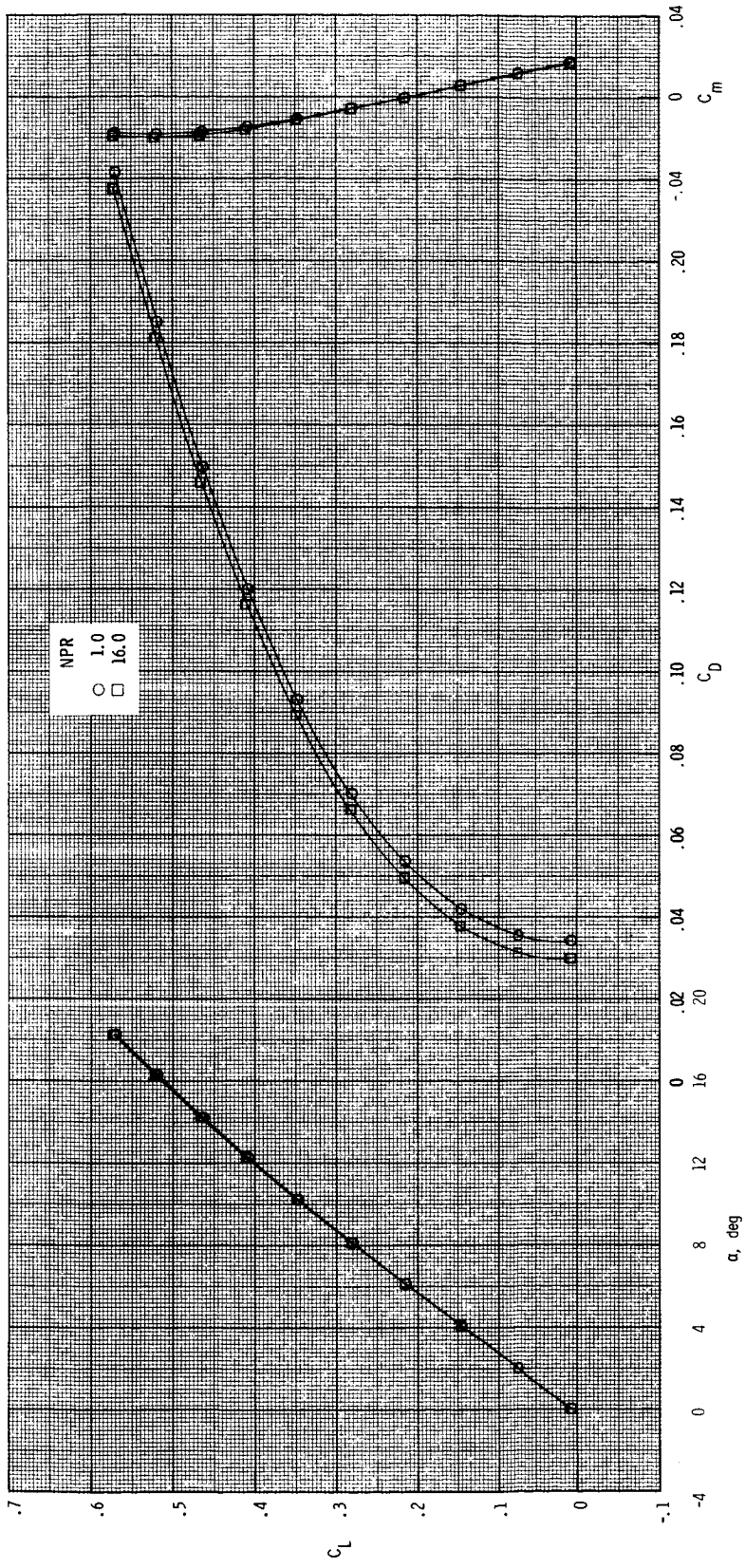

(e) $M = 2.00$.

Figure 43. Continued.

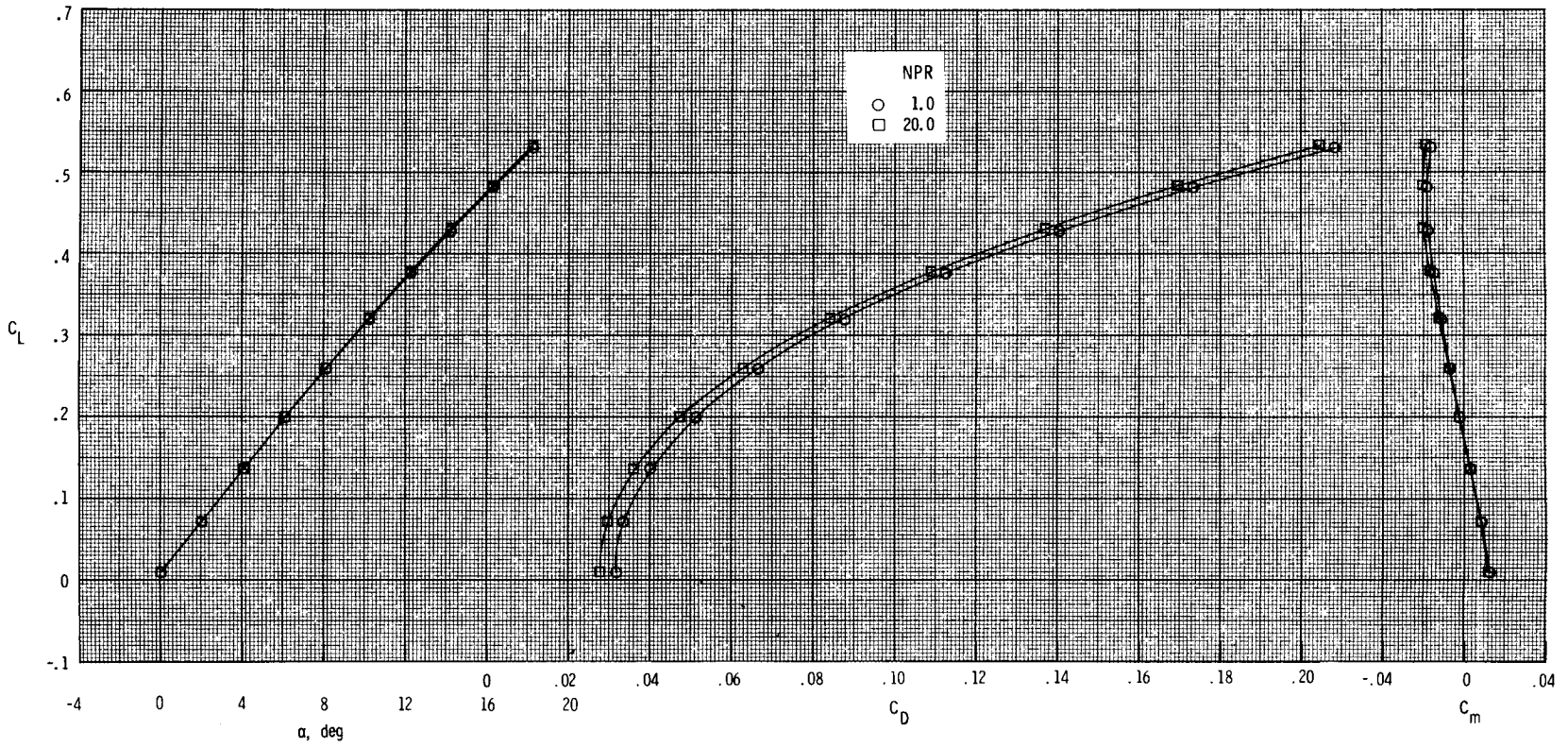

(f) $M = 2.17$.

Figure 43. Continued.

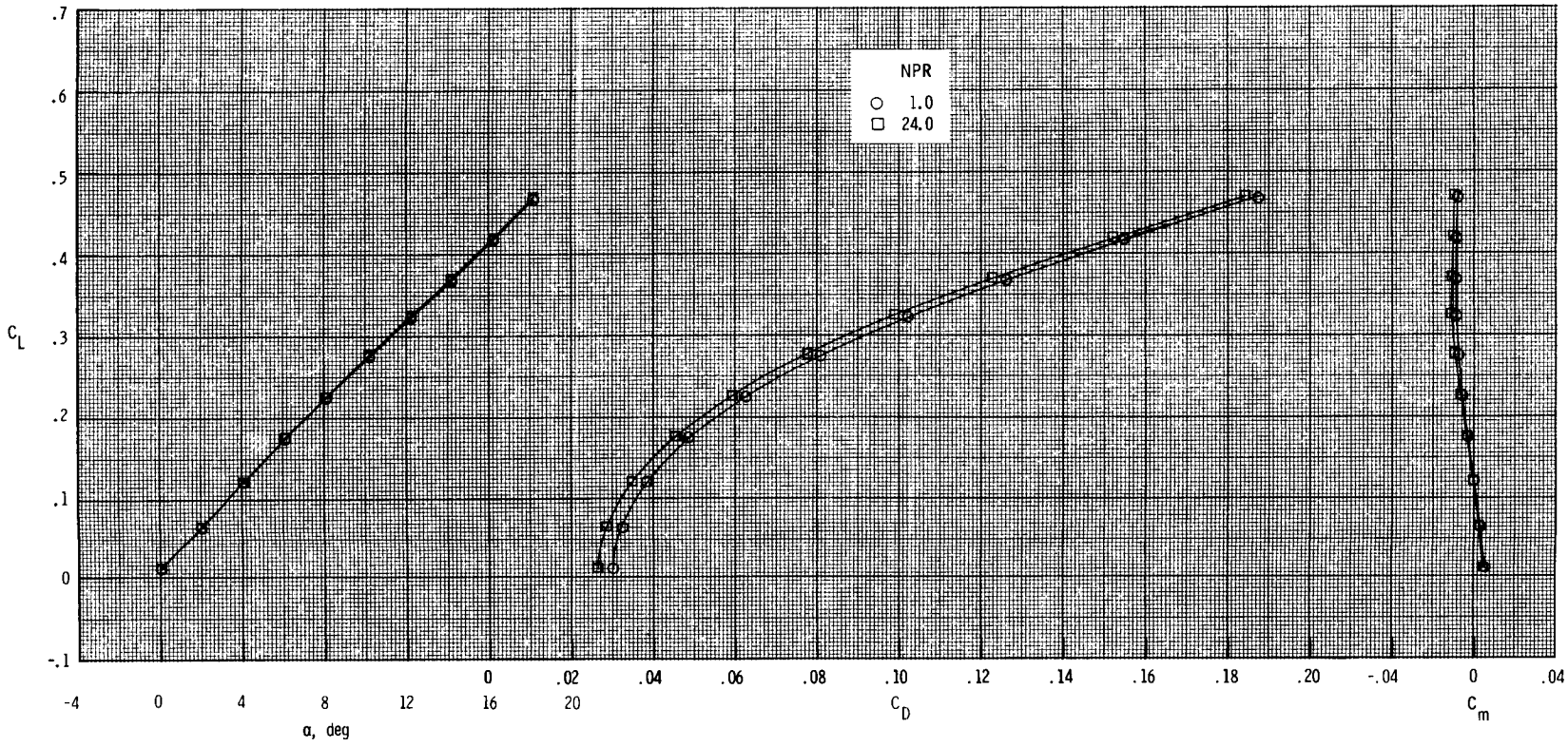

(g) $M = 2.47$.

Figure 43. Concluded.

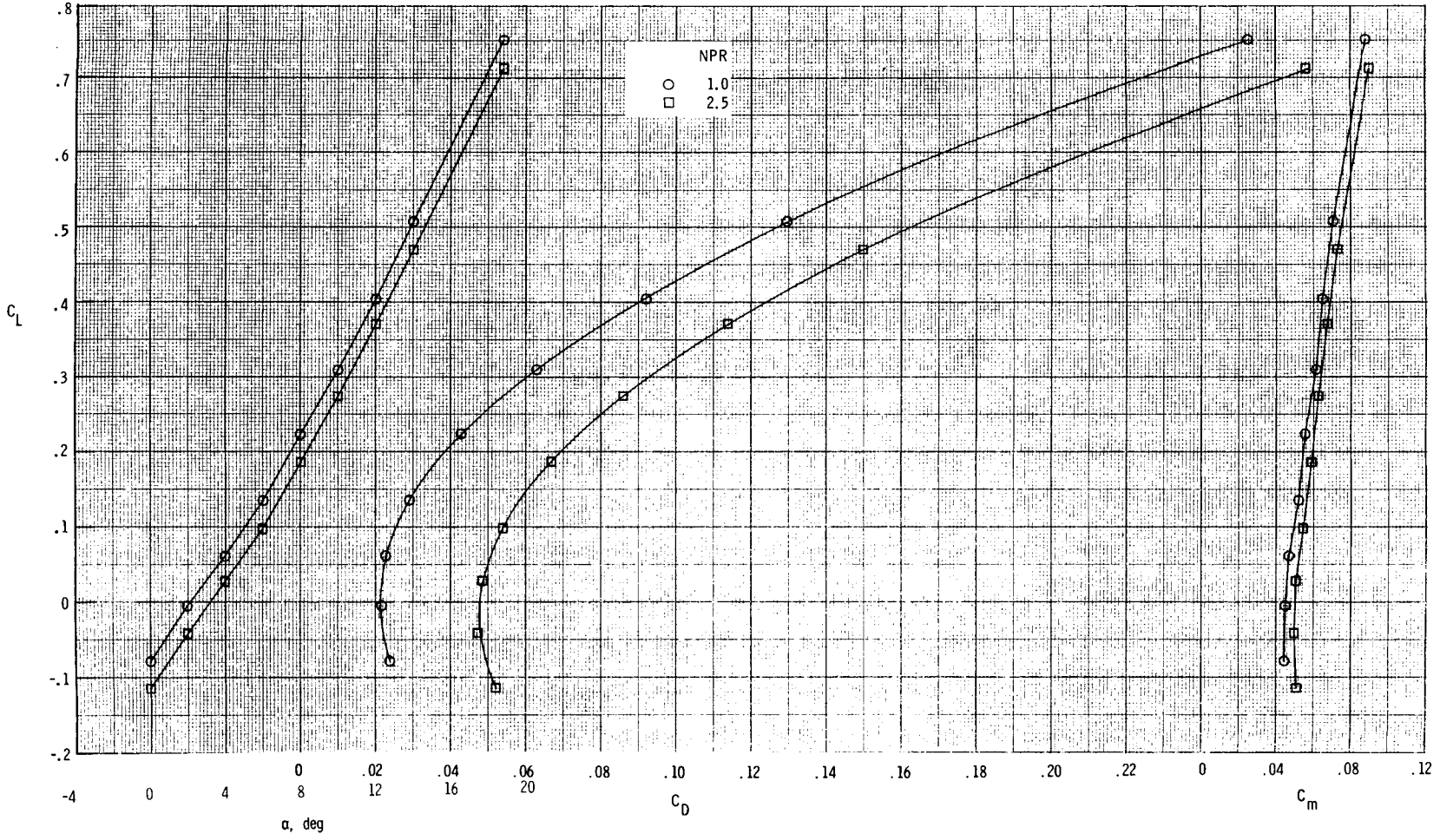

(a) $M = 0.20$.

Figure 44. Thrust-removed longitudinal aerodynamic characteristics for $\delta_{v,p} = 0°$ and $\delta_{v,y} = -20°$.

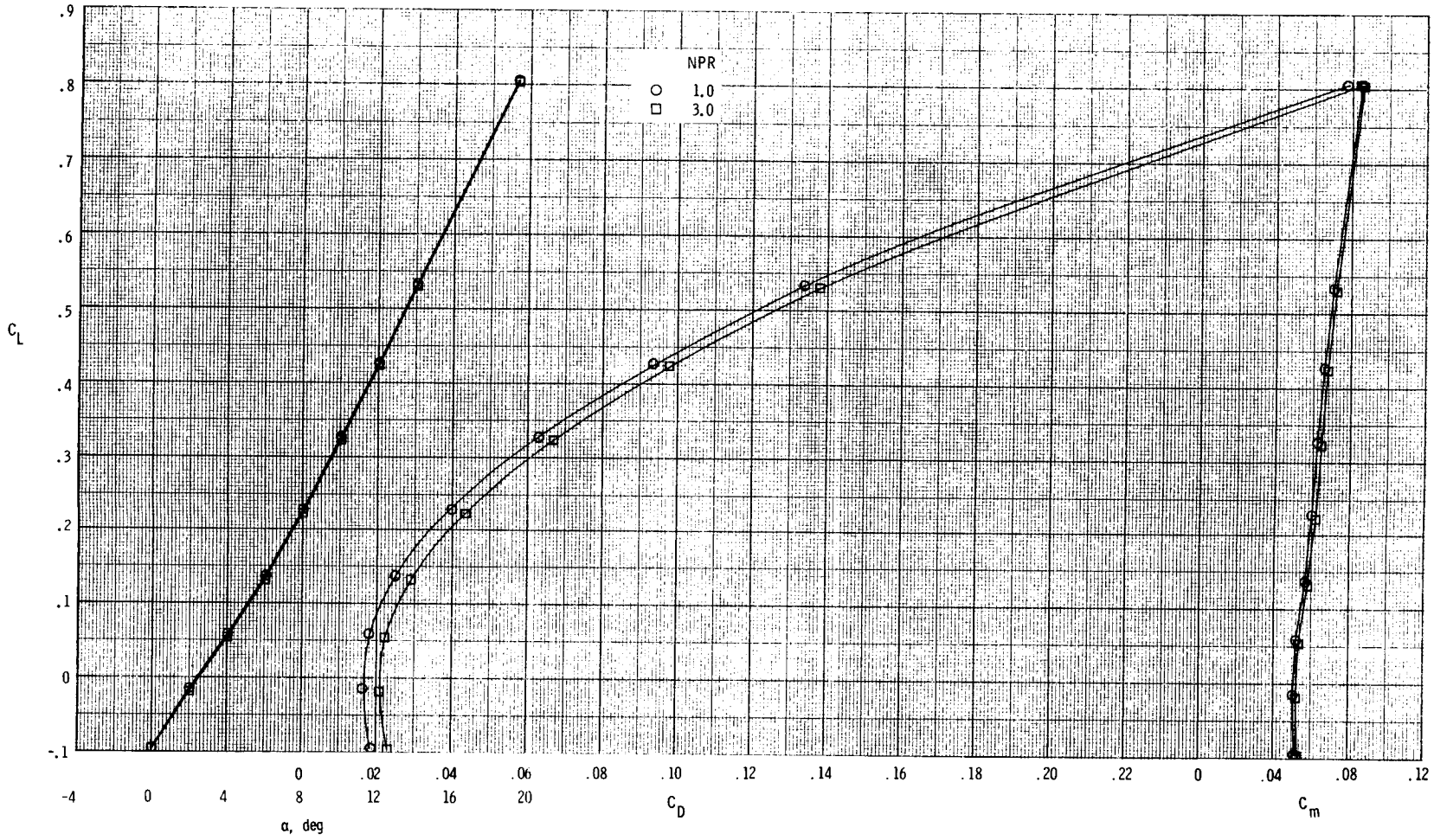

(b) $M = 0.60$.

Figure 44. Continued.

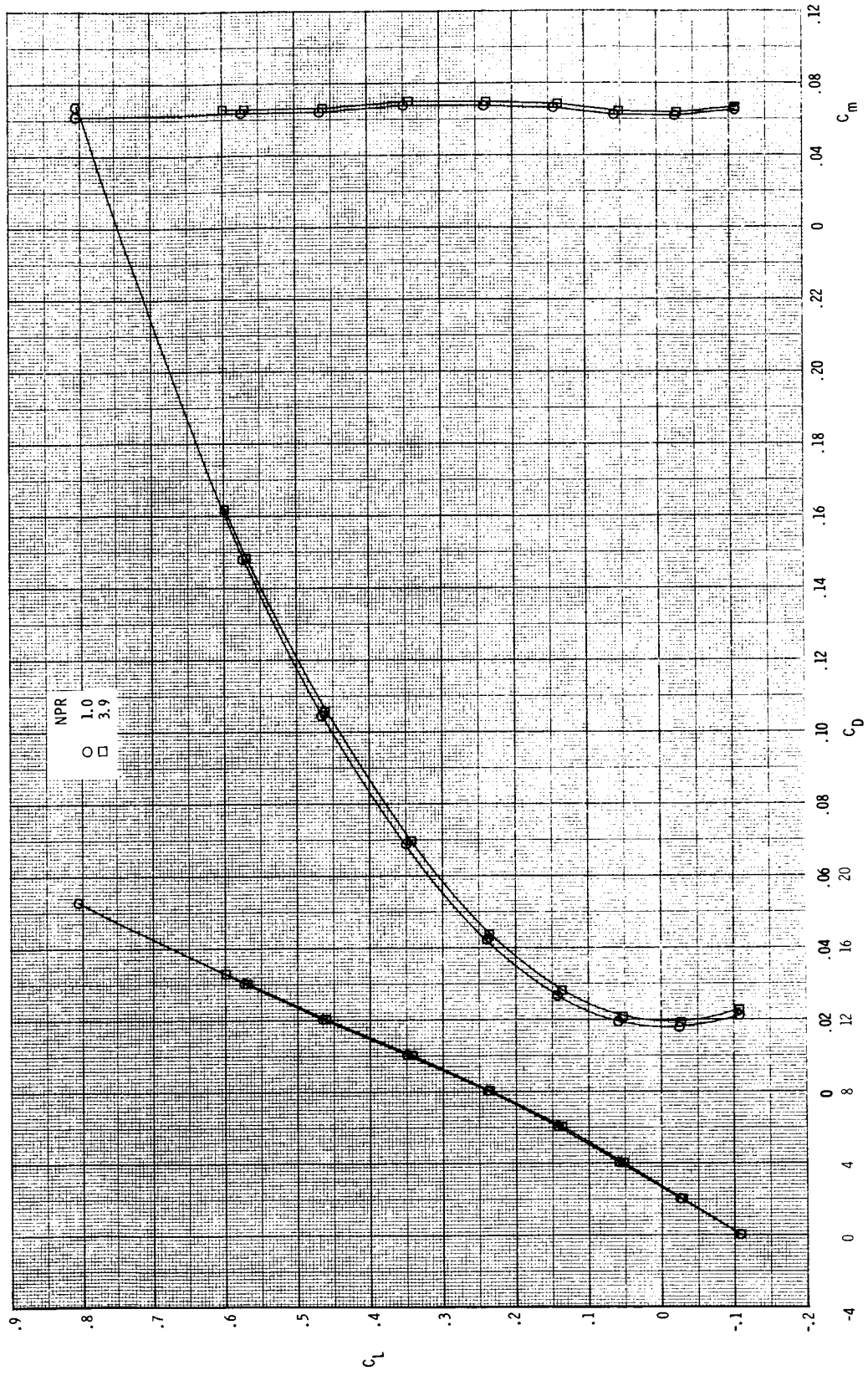

(c) $M = 0.87$.

Figure 44. Continued.

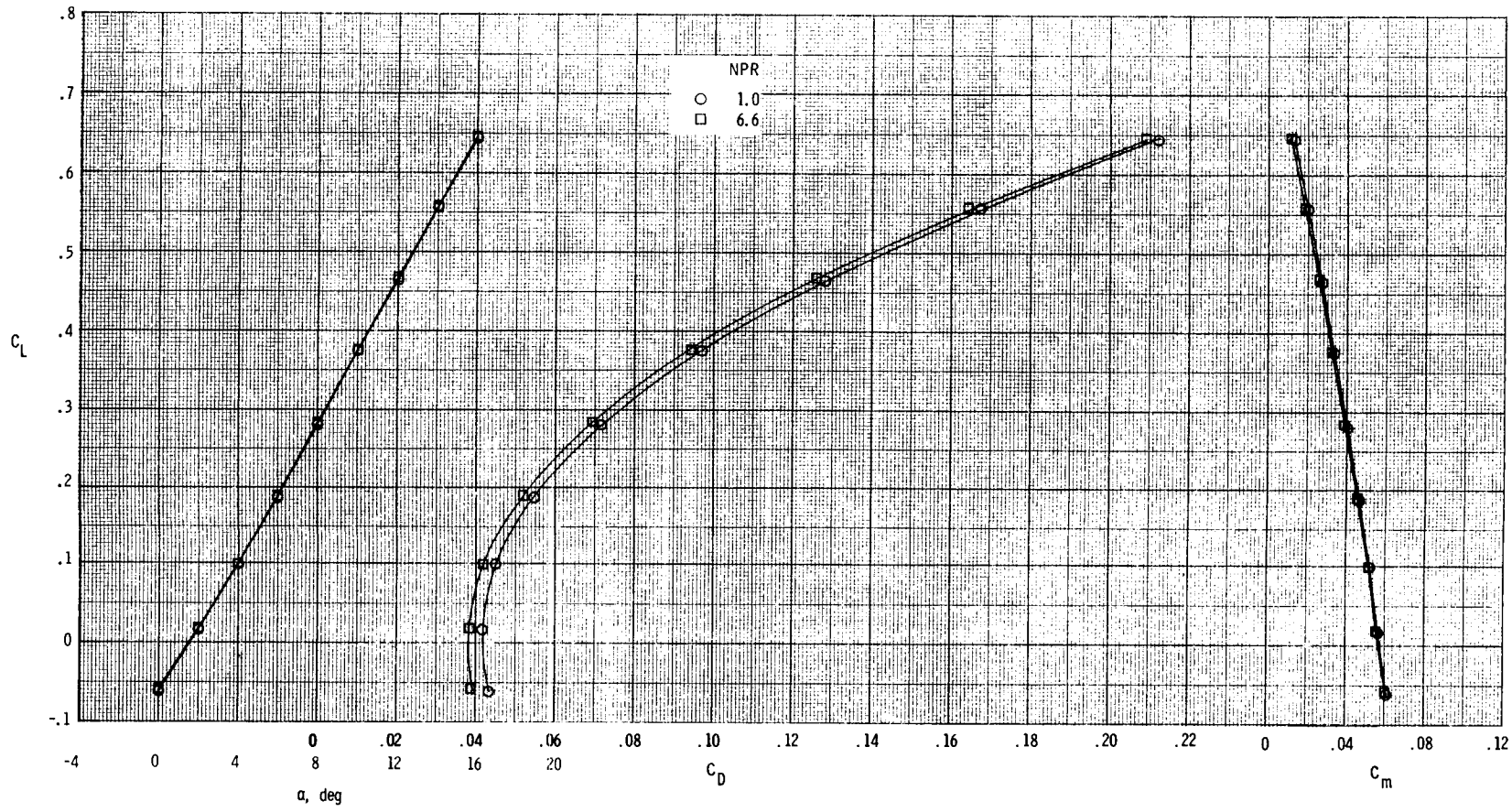

(d) $M = 1.20$.

Figure 44. Continued.

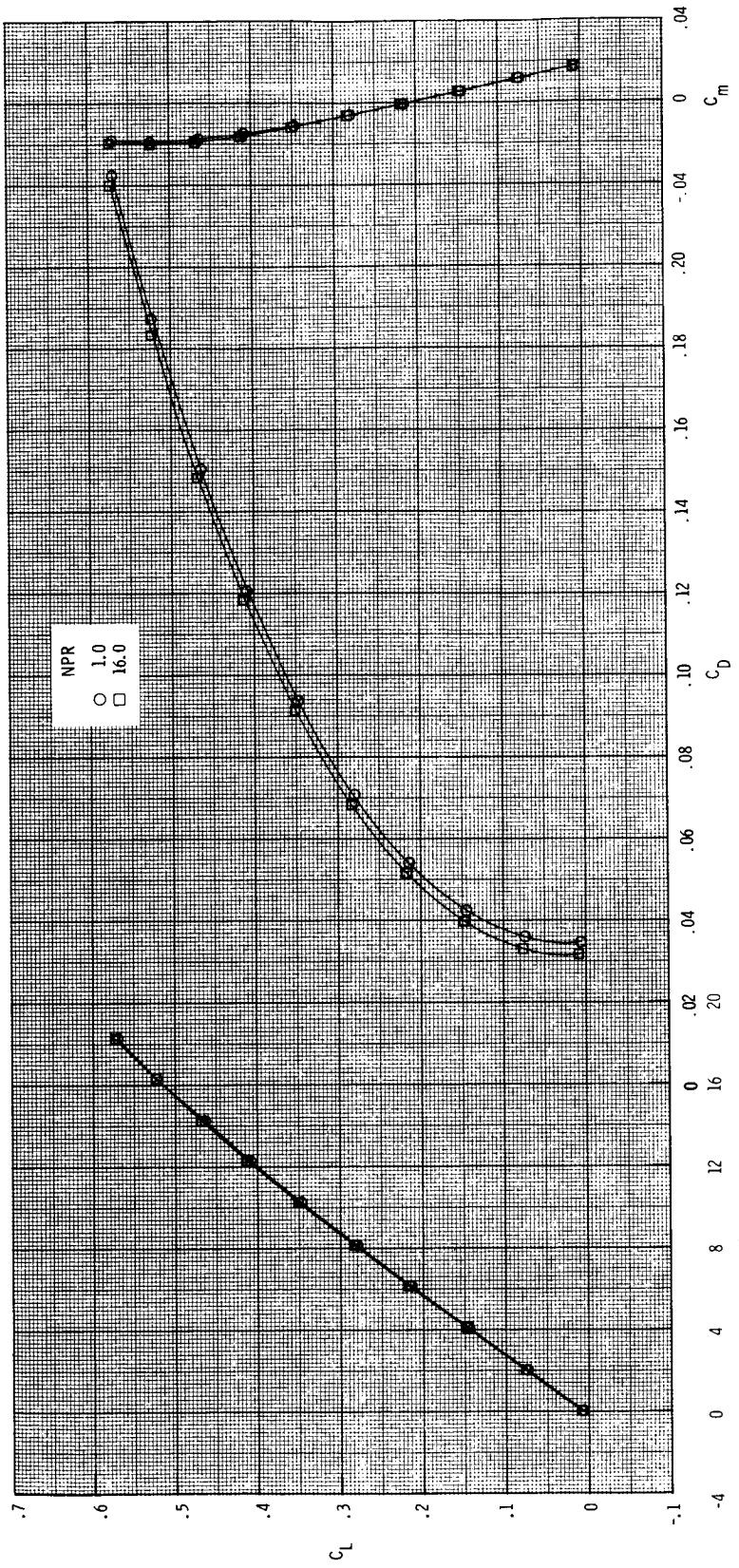

(e) $M = 2.00$.

Figure 44. Continued.

C-3

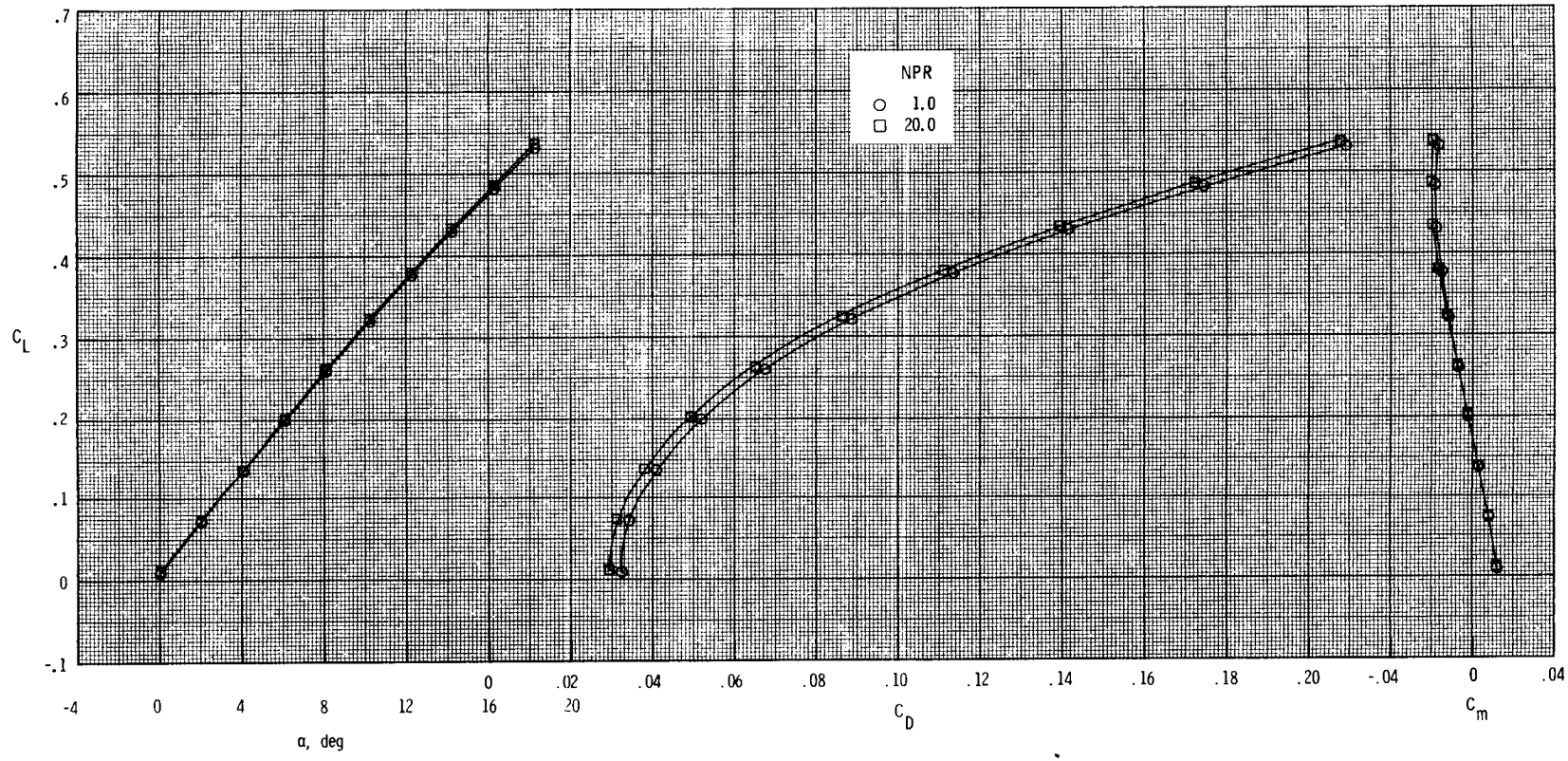

(f) $M = 2.17$.

Figure 44. Continued.

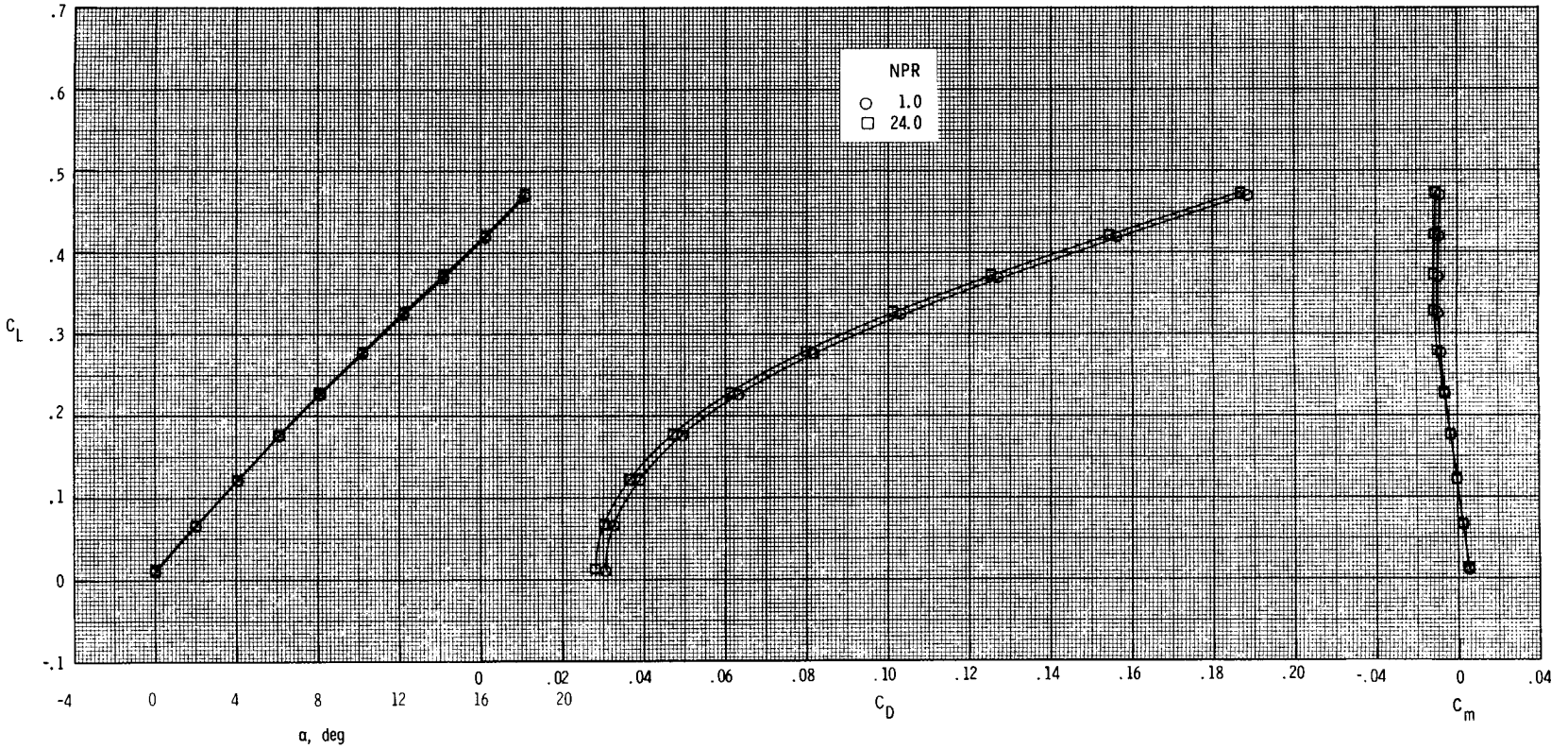

(g) $M = 2.47$.

Figure 44. Concluded.

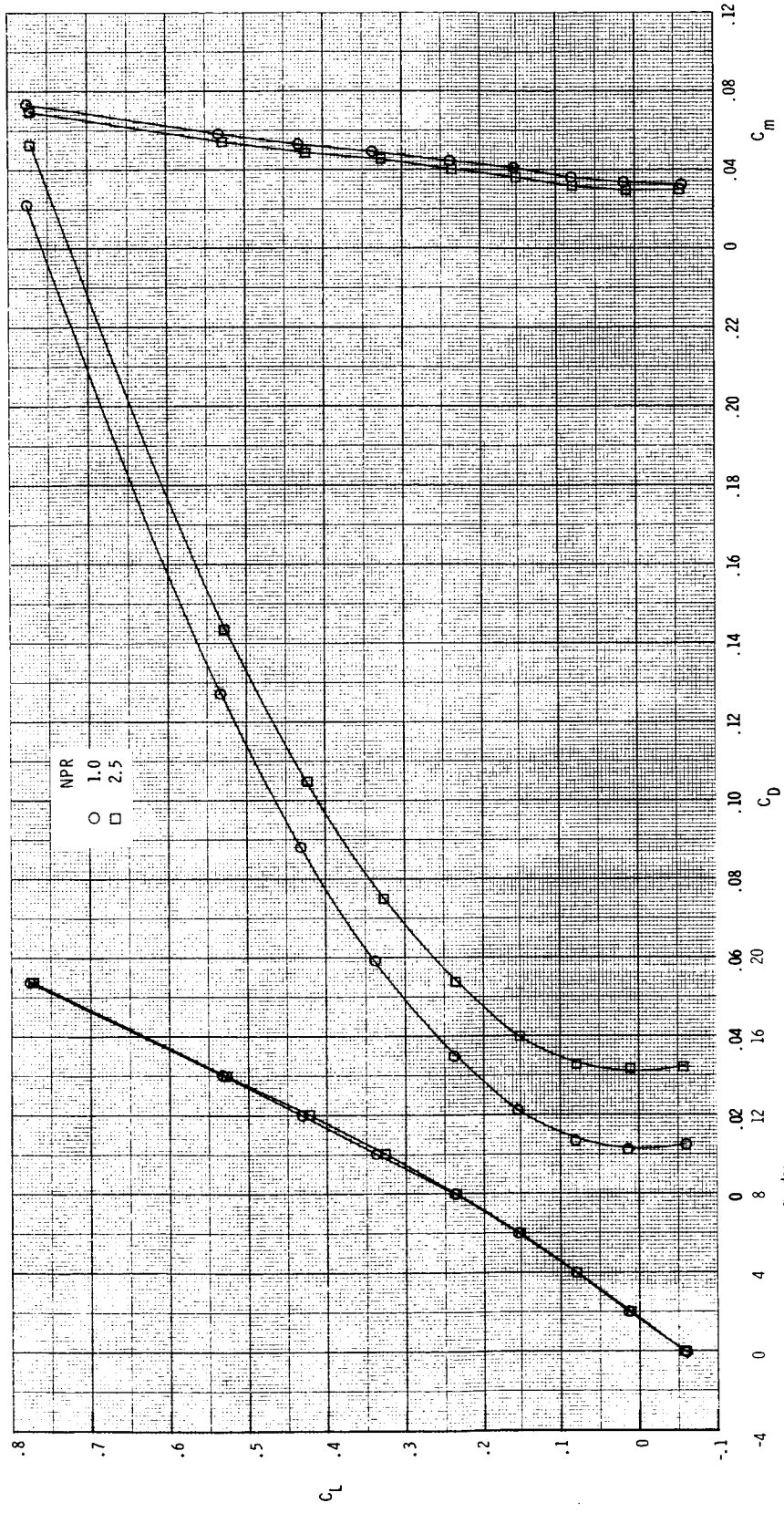

(a) $M = 0.20$.

Figure 45. Thrust-removed longitudinal aerodynamic characteristics for $\delta_{v,p} = 15°$ and $\delta_{v,y} = 0°$.

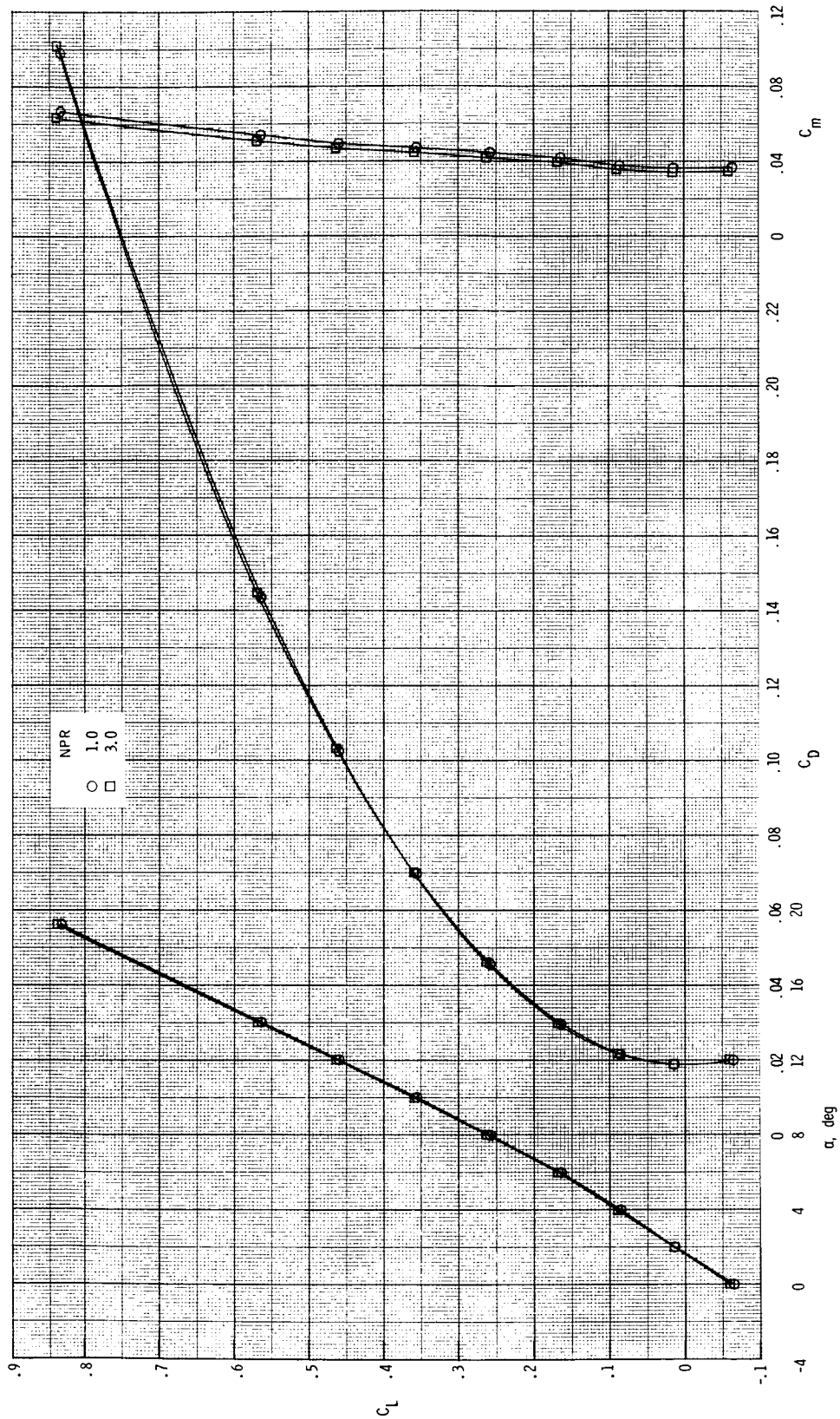

(b) $M = 0.60$.

Figure 45. Continued.

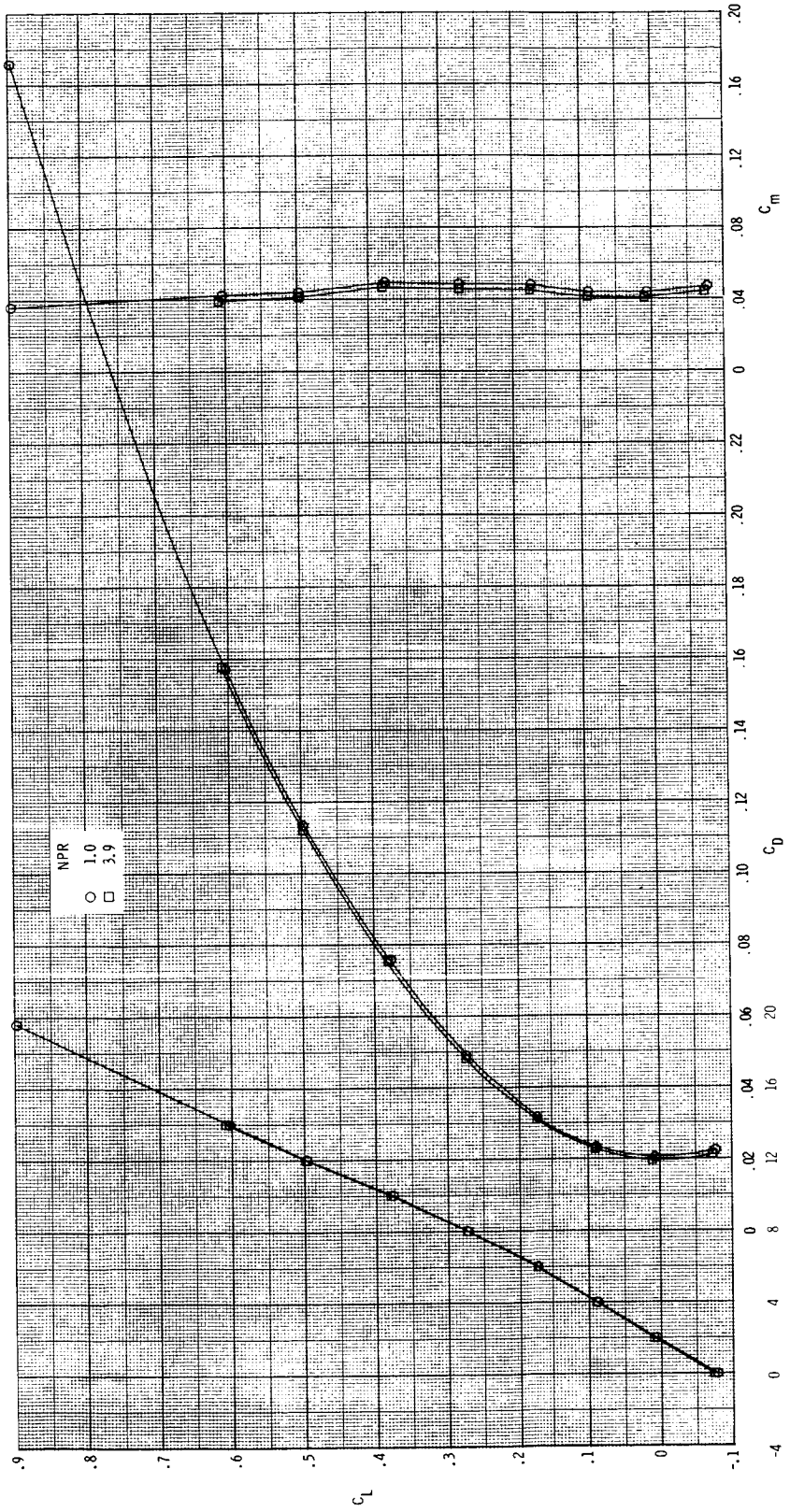

(c) $M = 0.87$.

Figure 45. Continued.

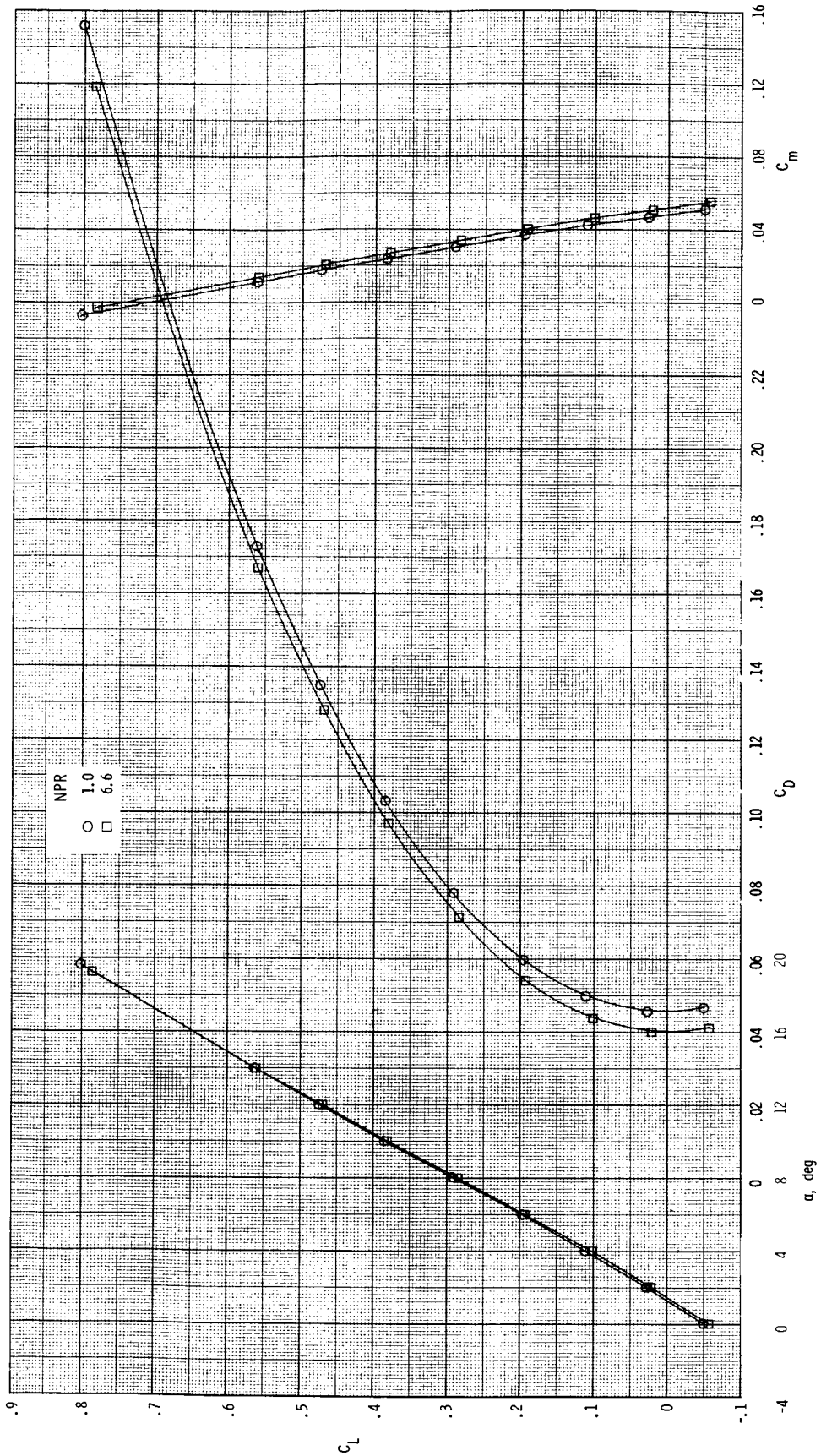

(d) $M = 1.20$.

Figure 45. Continued.

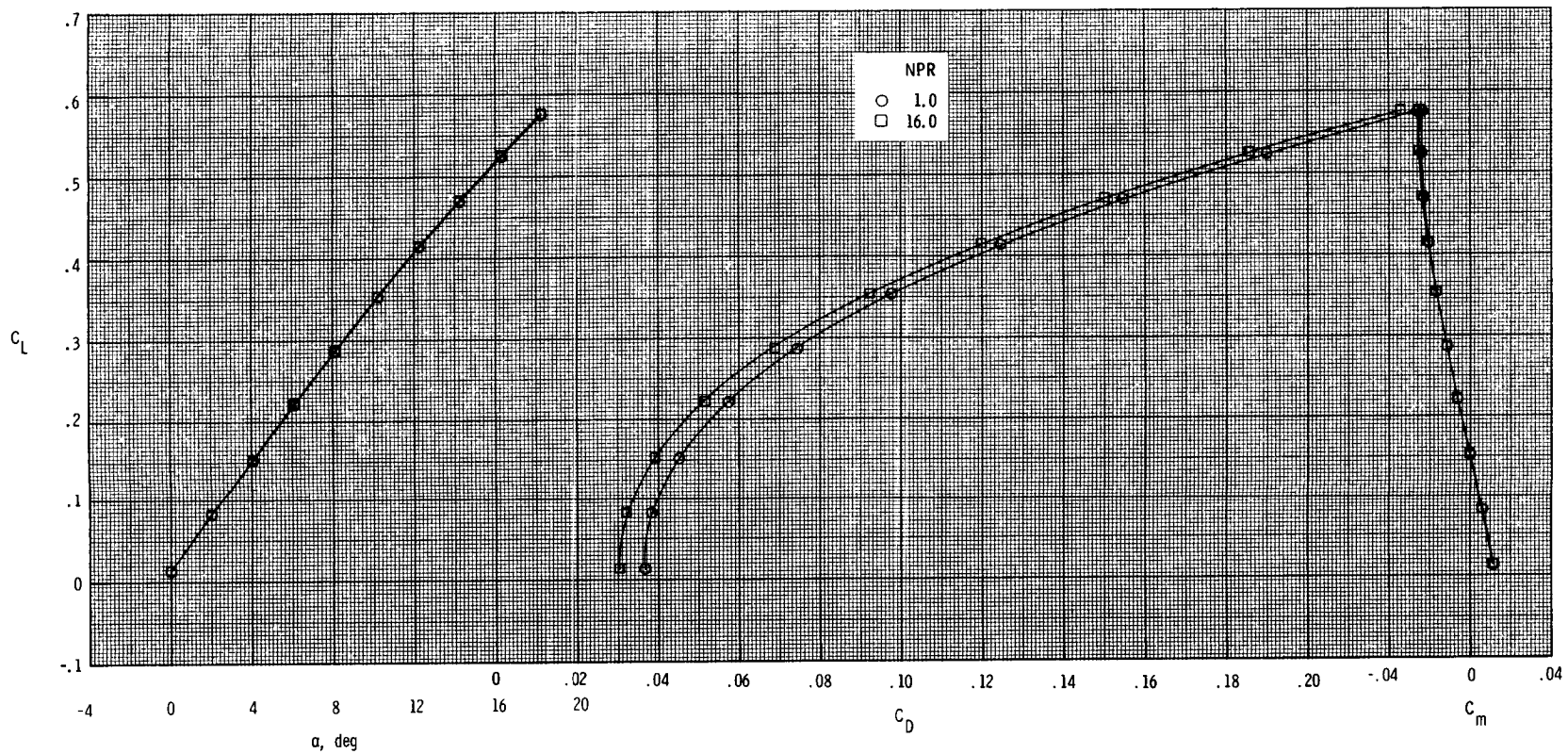

(e) $M = 2.00$.

Figure 45. Continued.

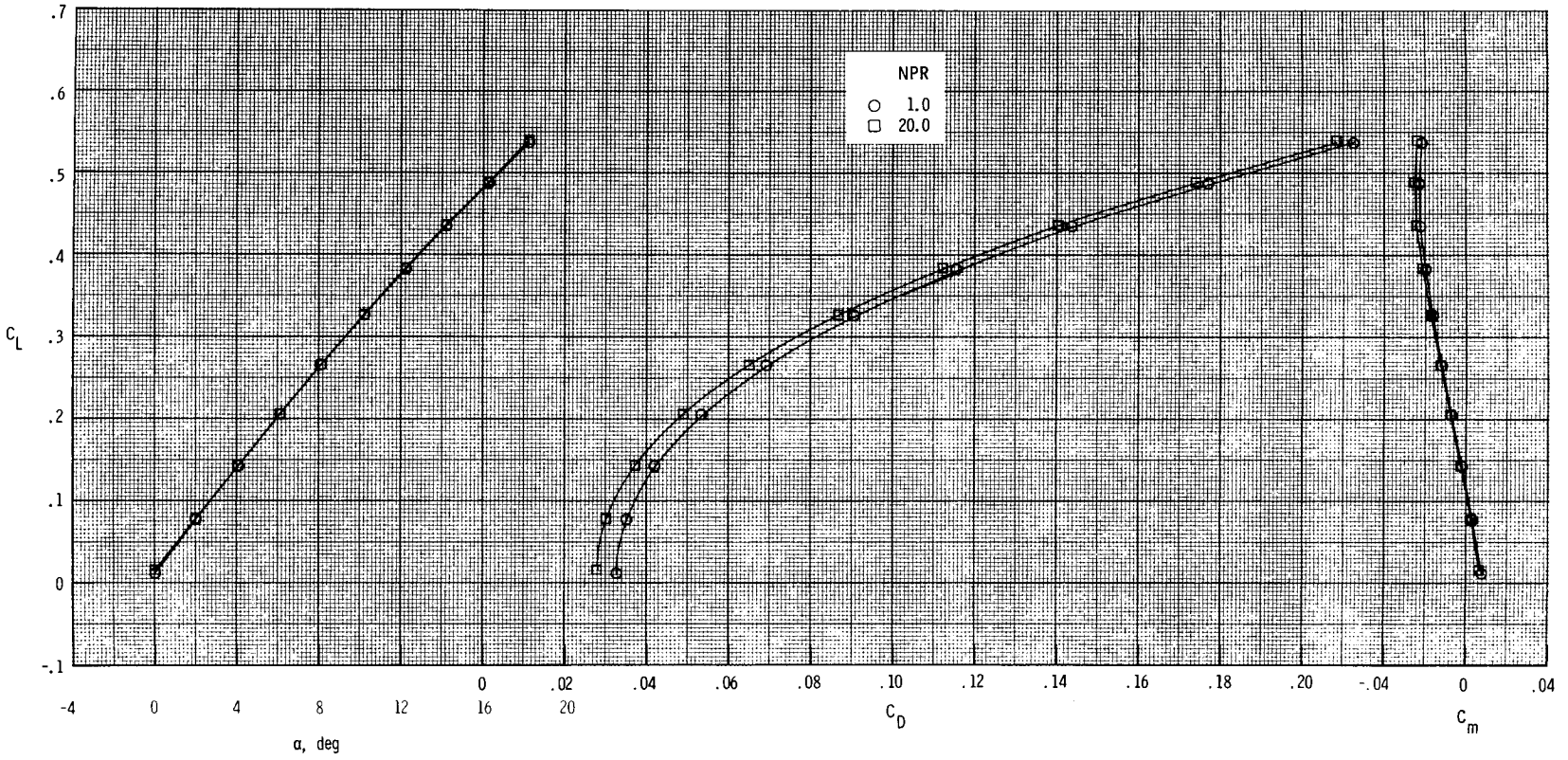

(f) $M = 2.17$.

Figure 45. Continued.

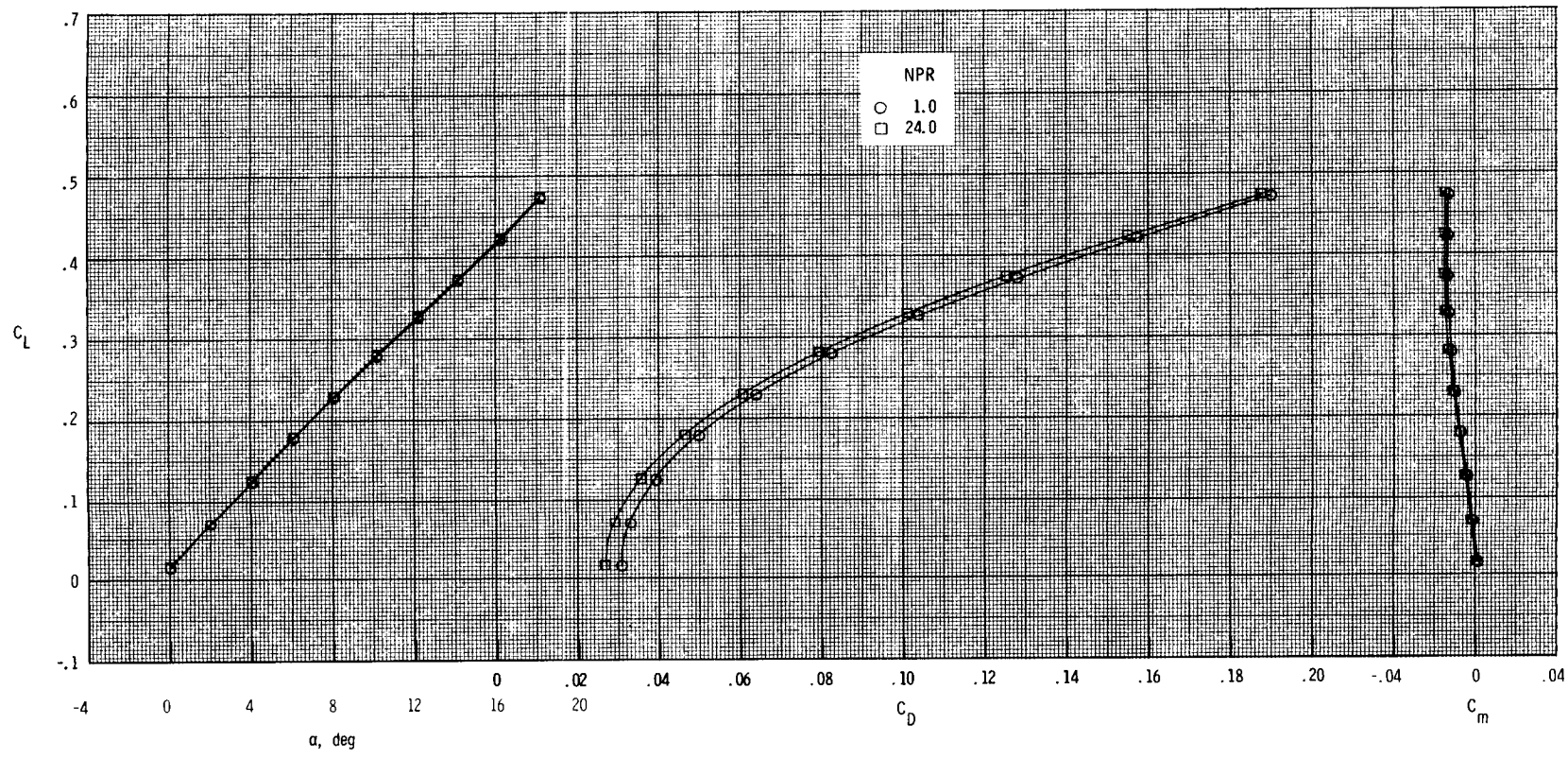

(g) $M = 2.47$.

Figure 45. Concluded.

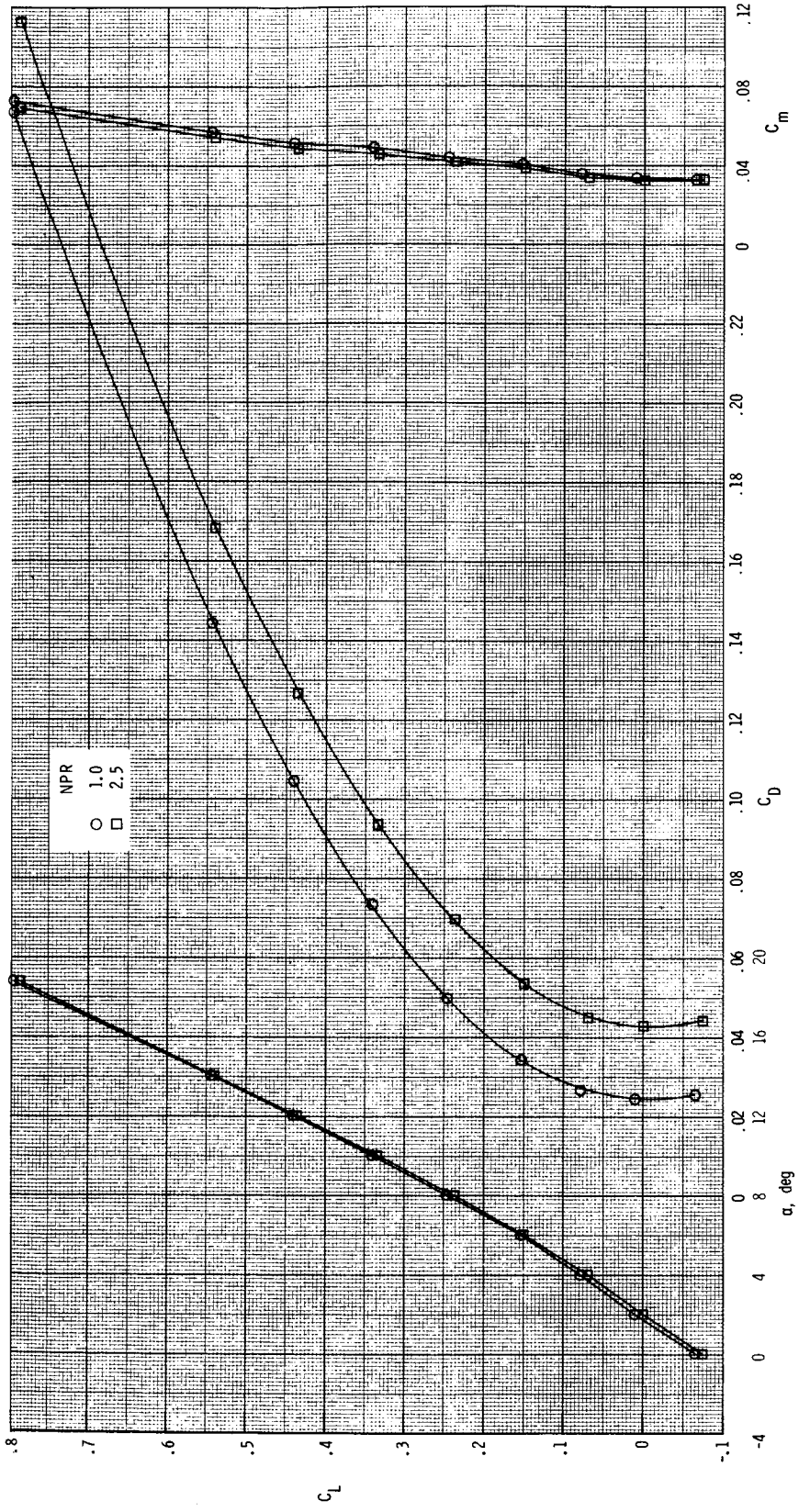

(a) $M = 0.20$.

Figure 46. Thrust-removed longitudinal aerodynamic characteristics for $\delta_{v,p} = 15°$ and $\delta_{v,y} = -10°$.

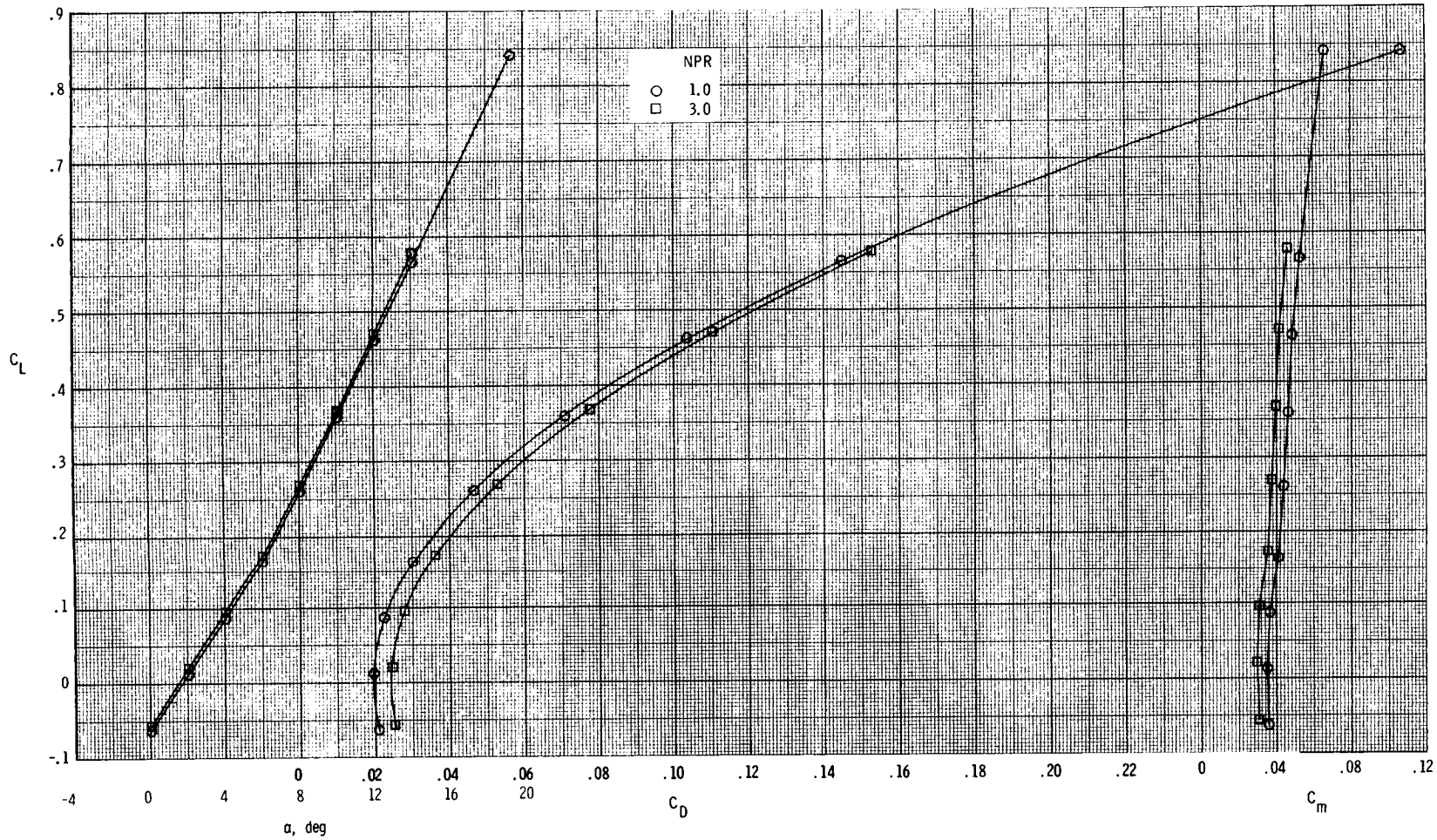

(b) $M = 0.60$.

Figure 46. Continued.

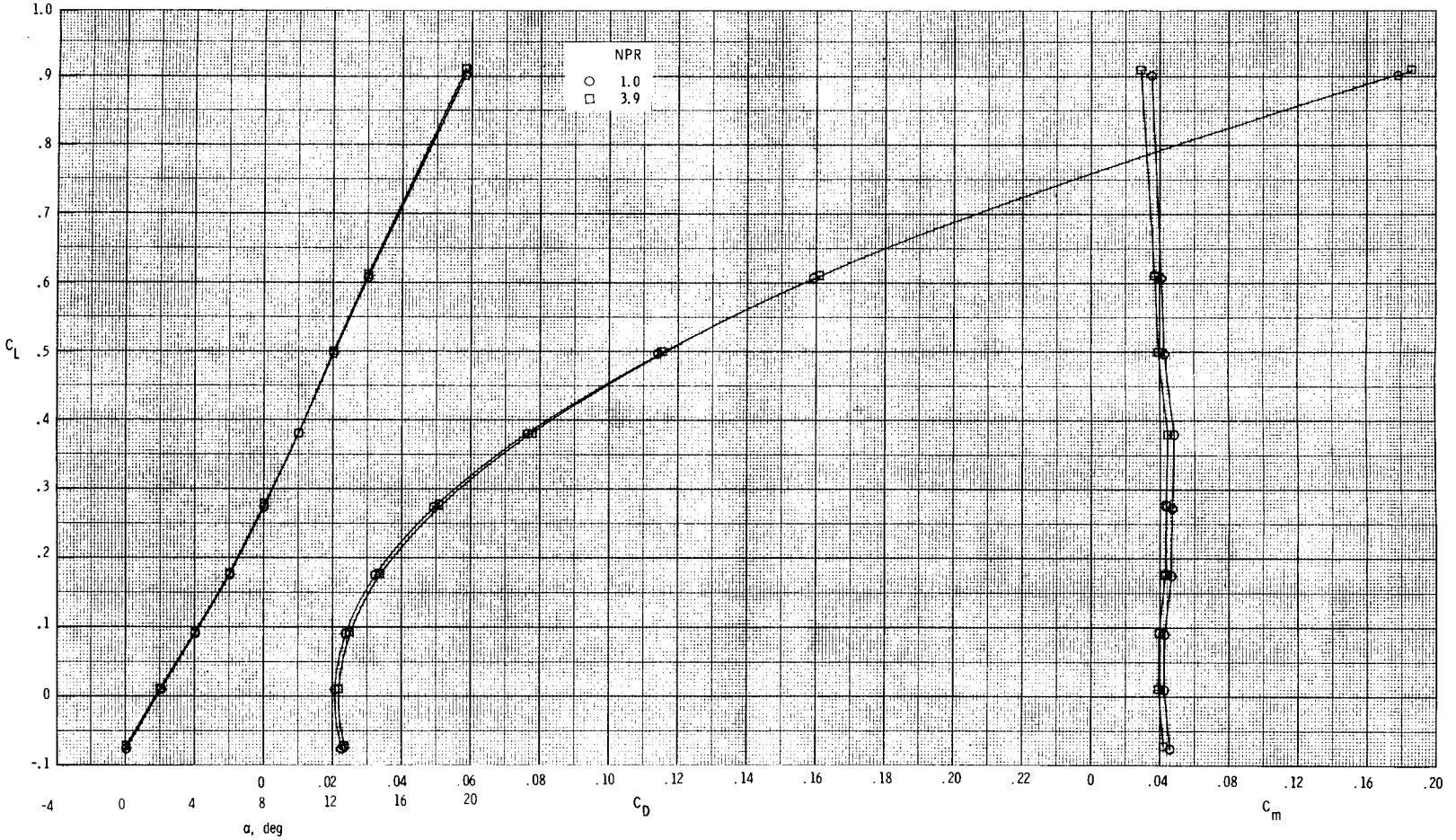

(c) $M = 0.87$.

Figure 46. Continued.

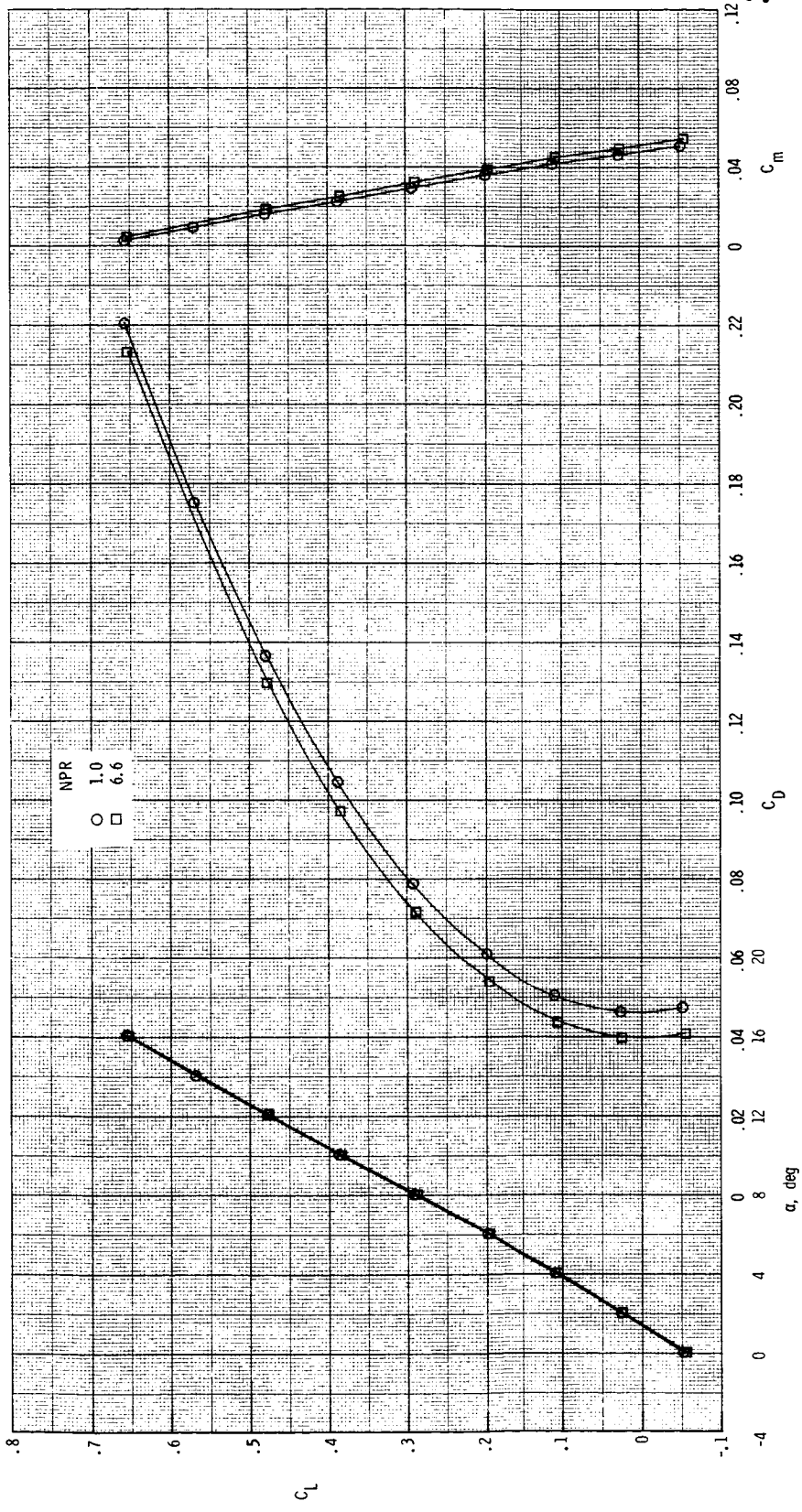

(d) $M = 1.20$.

Figure 46. Concluded.

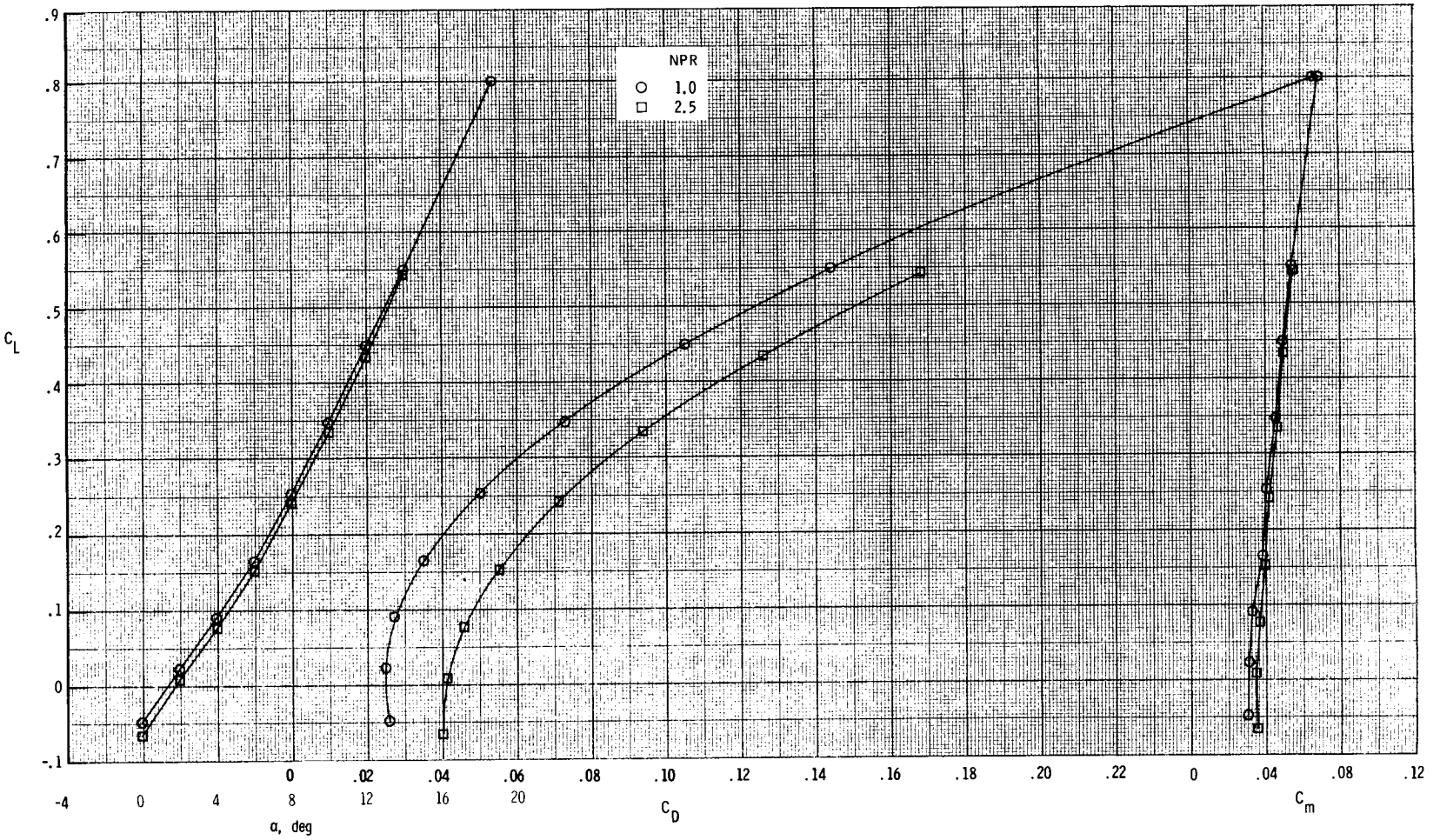

(a) $M = 0.20$.

Figure 47. Thrust-removed longitudinal aerodynamic characteristics for $\delta_{v,p} = 15°$ and $\delta_{v,y} = -20°$.

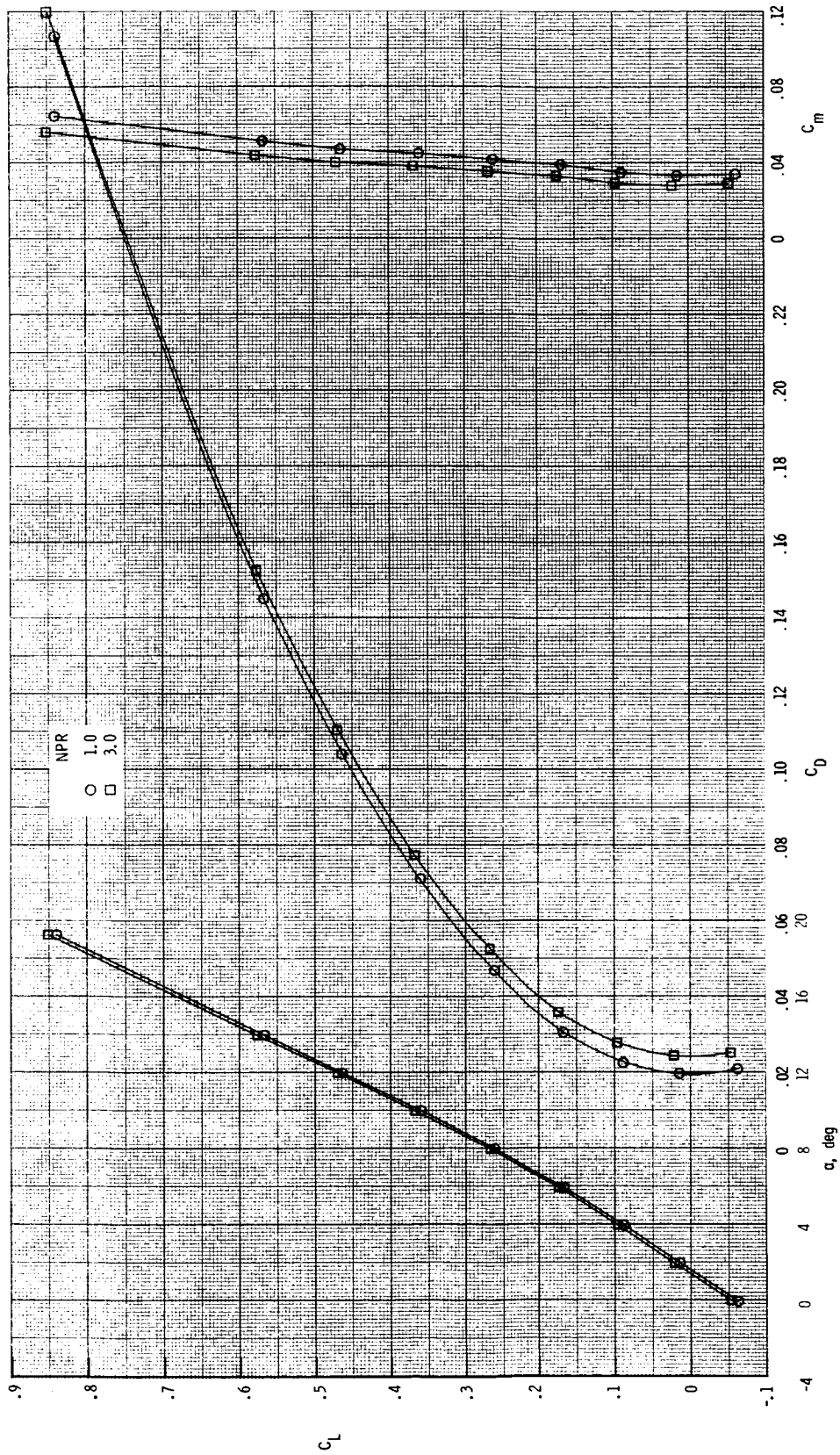

(b) $M = 0.60$.

Figure 47. Continued.

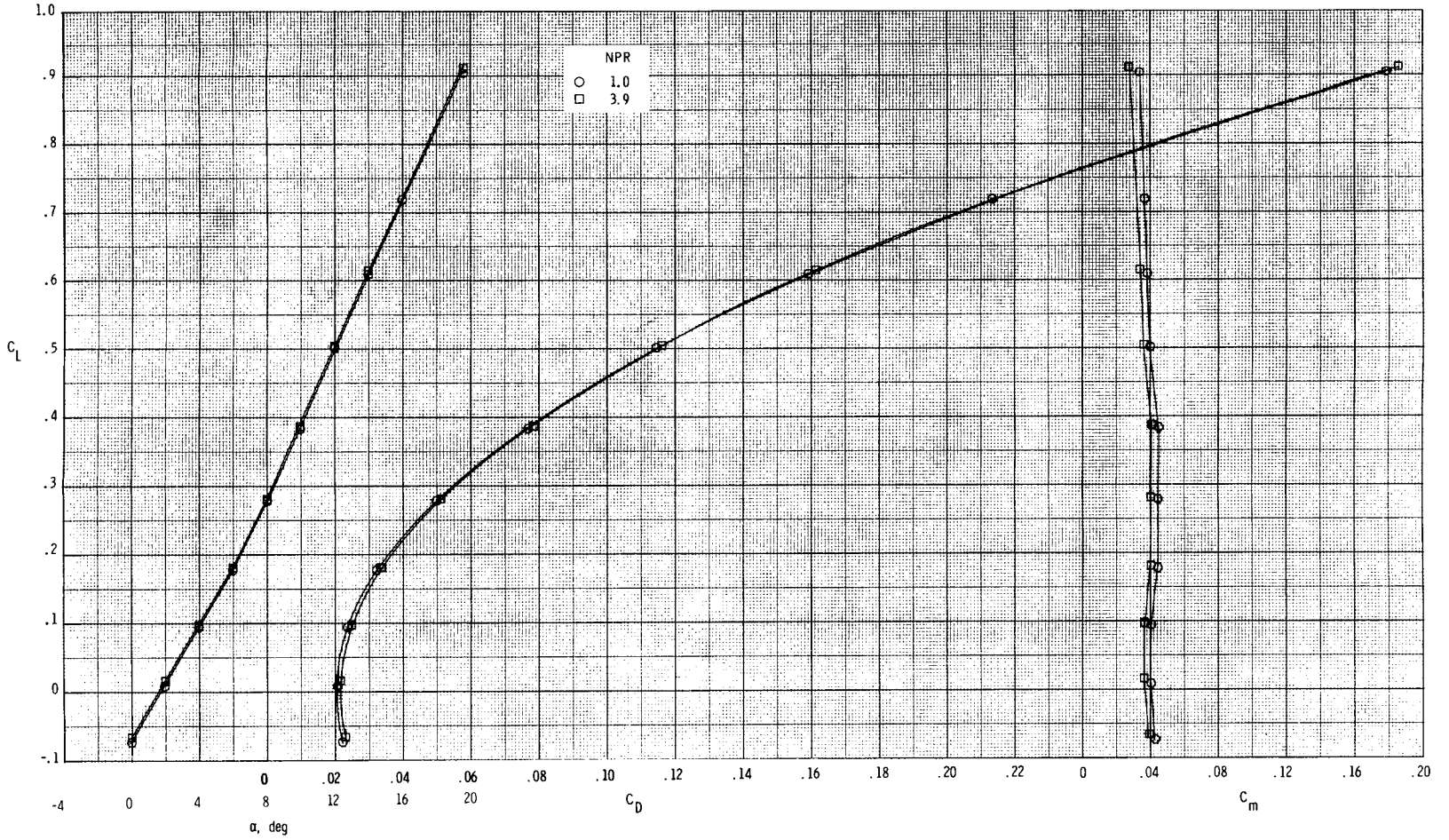

(c) $M = 0.87$.

Figure 47. Continued.

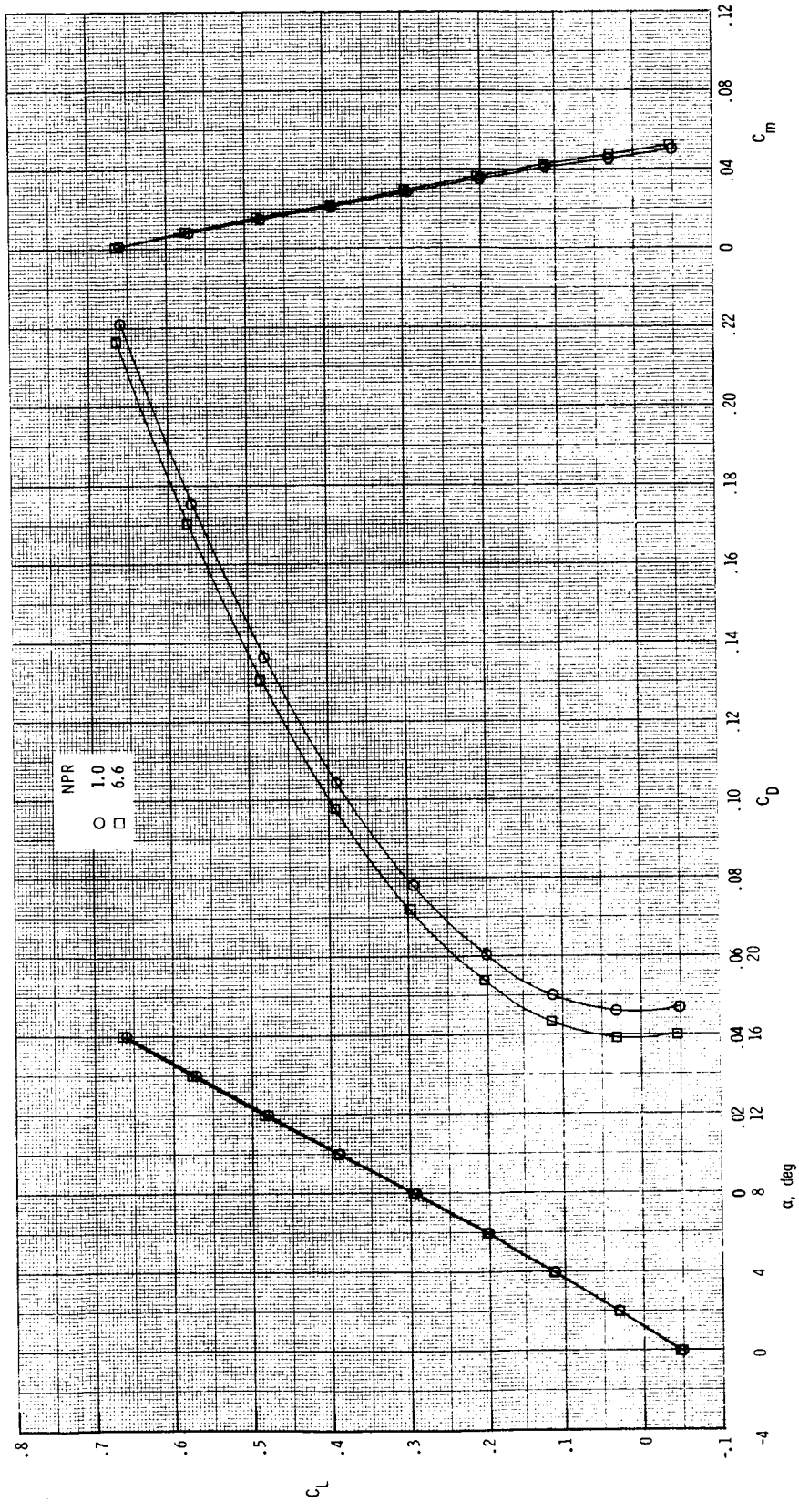

(d) $M = 1.20$.

Figure 47. Concluded.

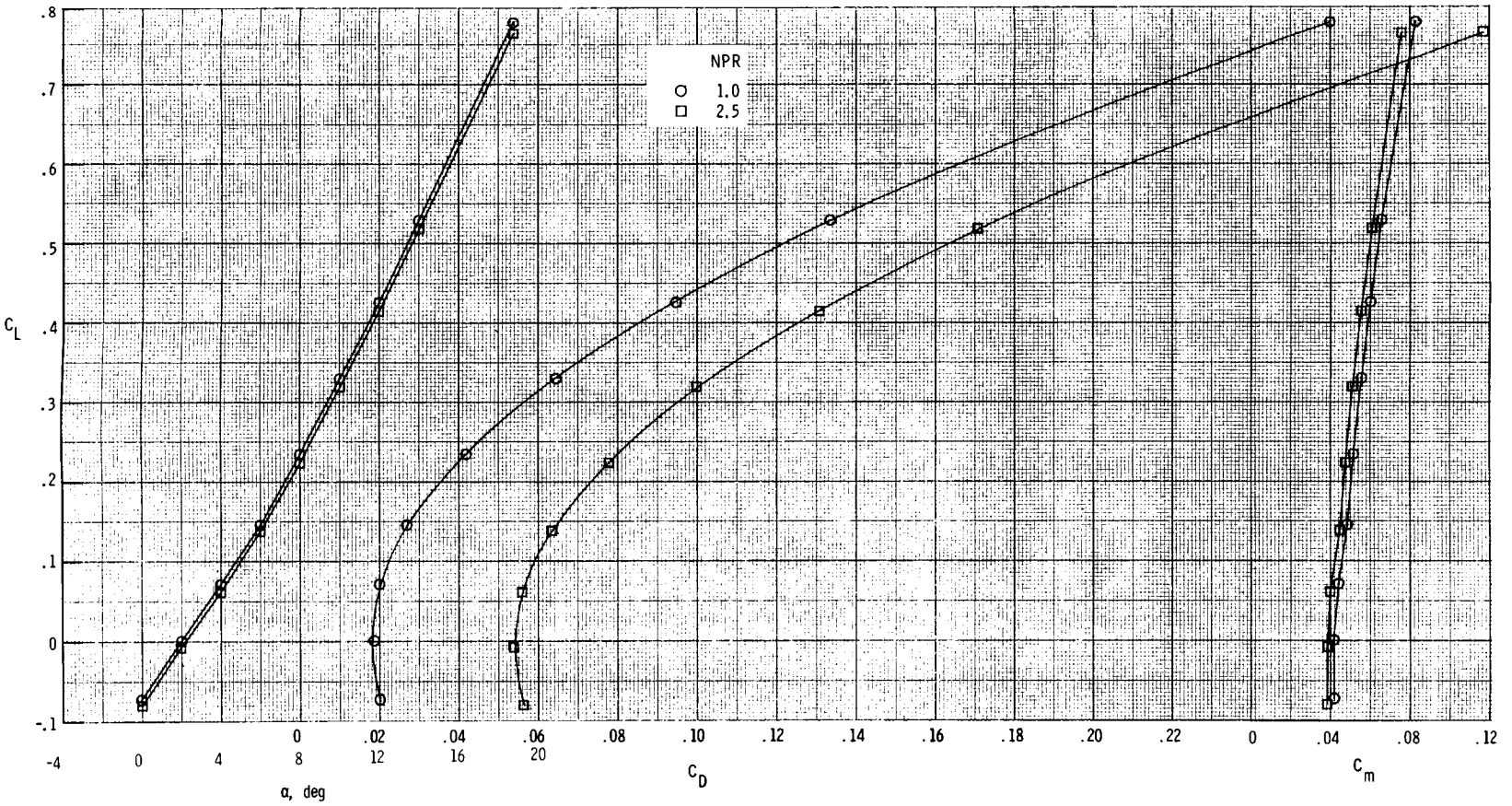

(a) $M = 0.20$.

Figure 48. Thrust-removed longitudinal aerodynamic characteristics for $\delta_{v,p,\text{left}} = 15°$, $\delta_{v,p,\text{right}} = 0°$ and $\delta_{v,y} = 0°$.

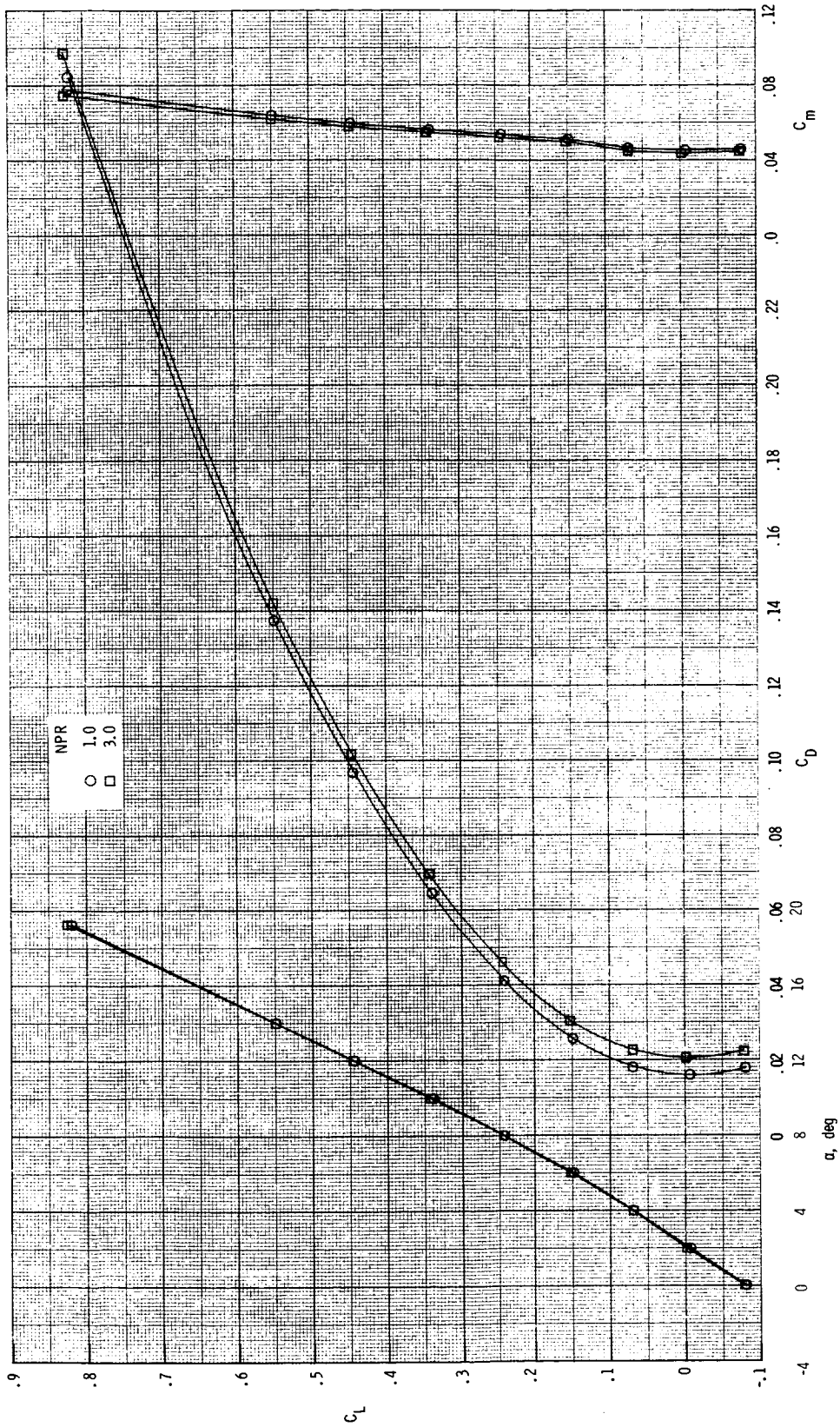

(b) $M = 0.60$.

Figure 48. Continued.

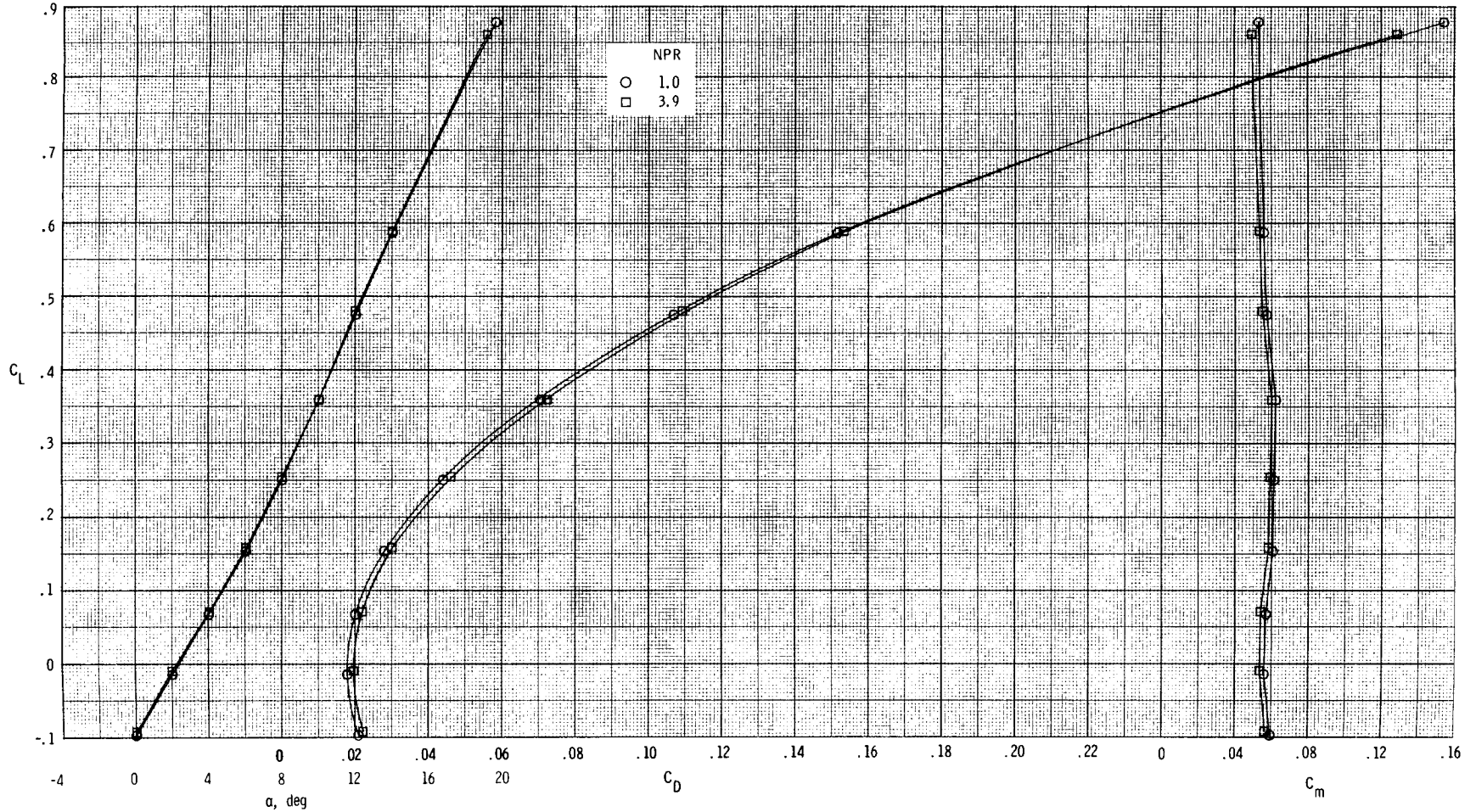

(c) $M = 0.87$.

Figure 48. Continued.

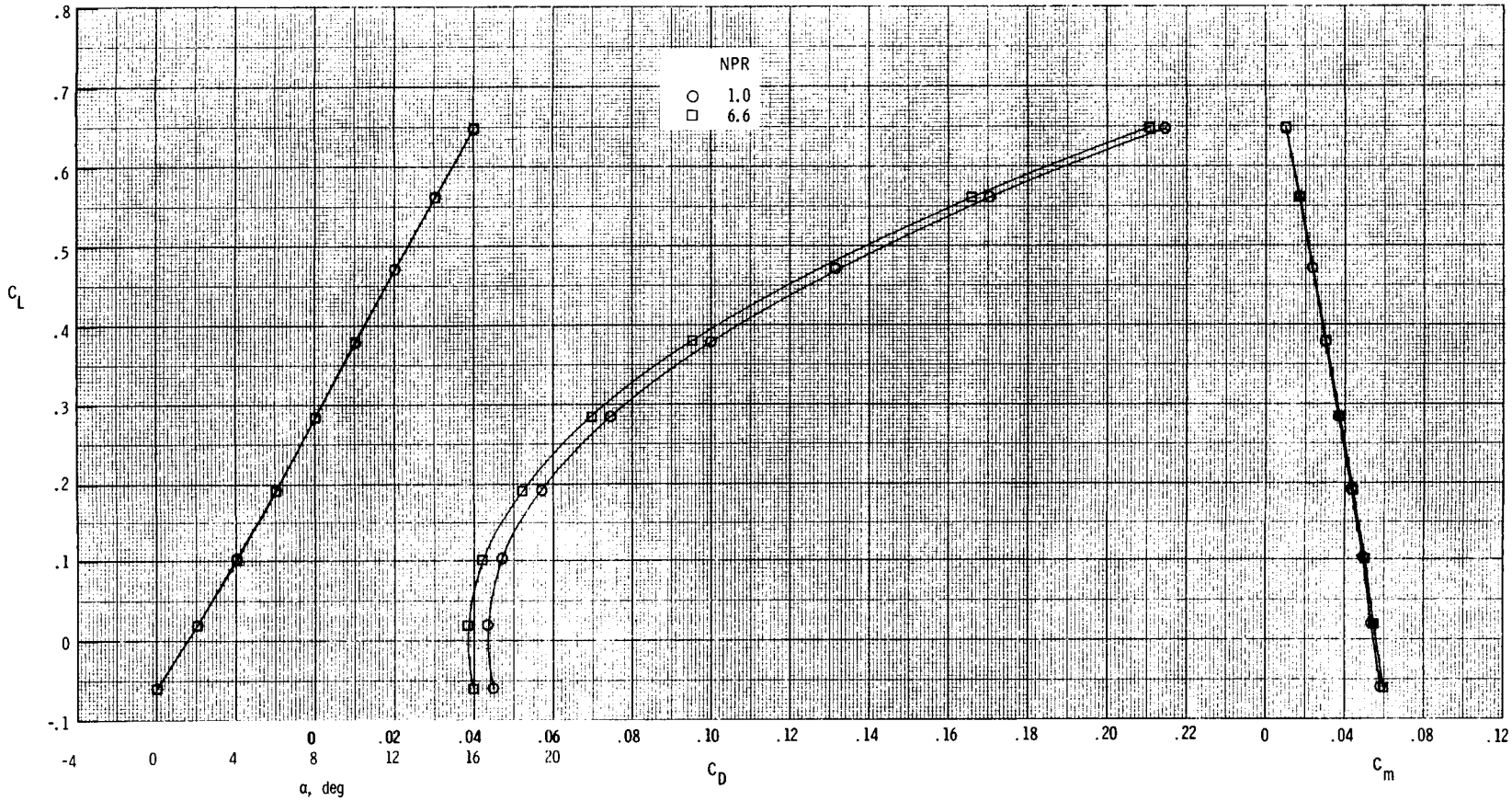

(d) $M = 1.20$.

Figure 48. Continued.

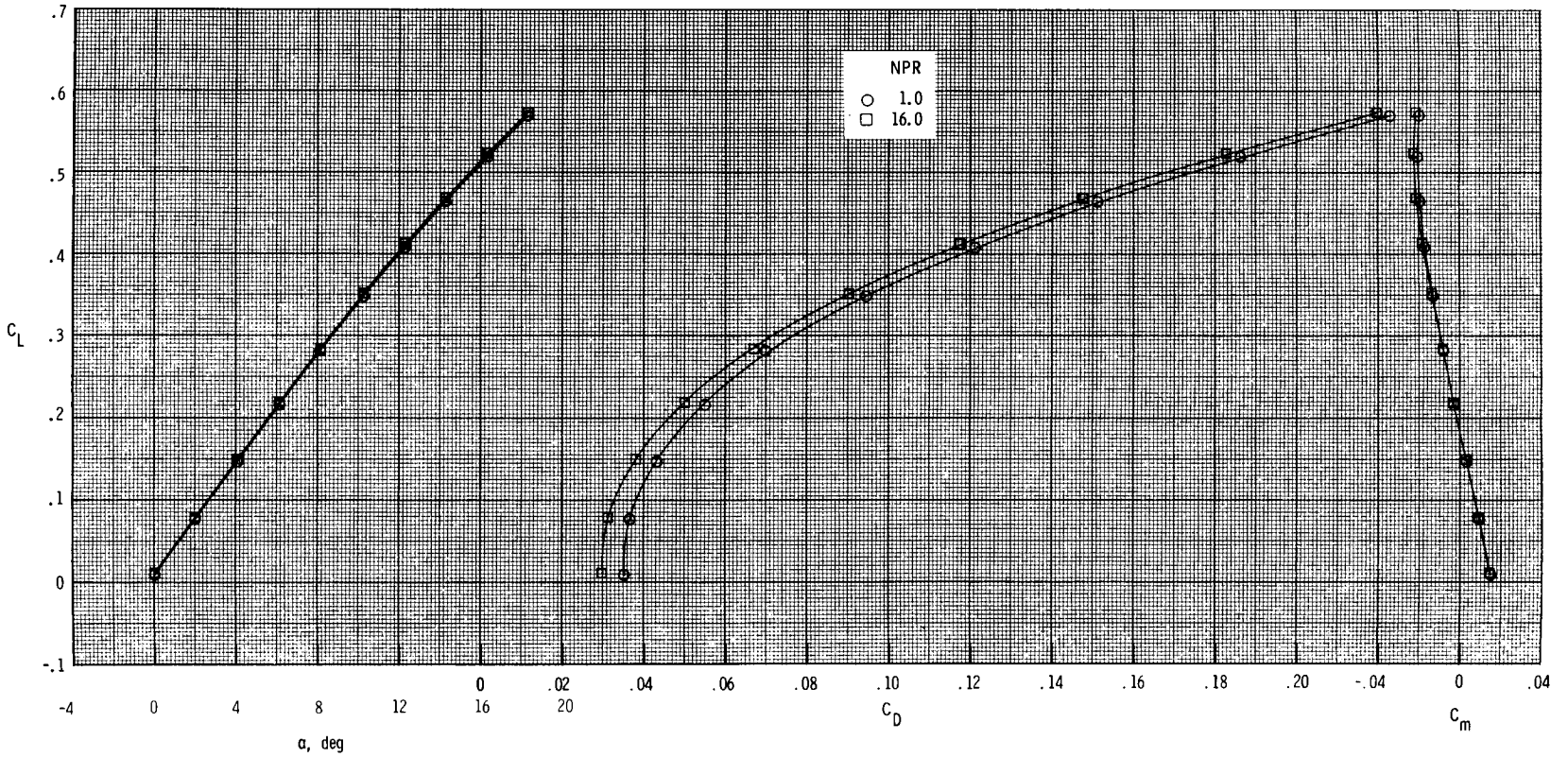

(e) $M = 2.00$.

Figure 48. Continued.

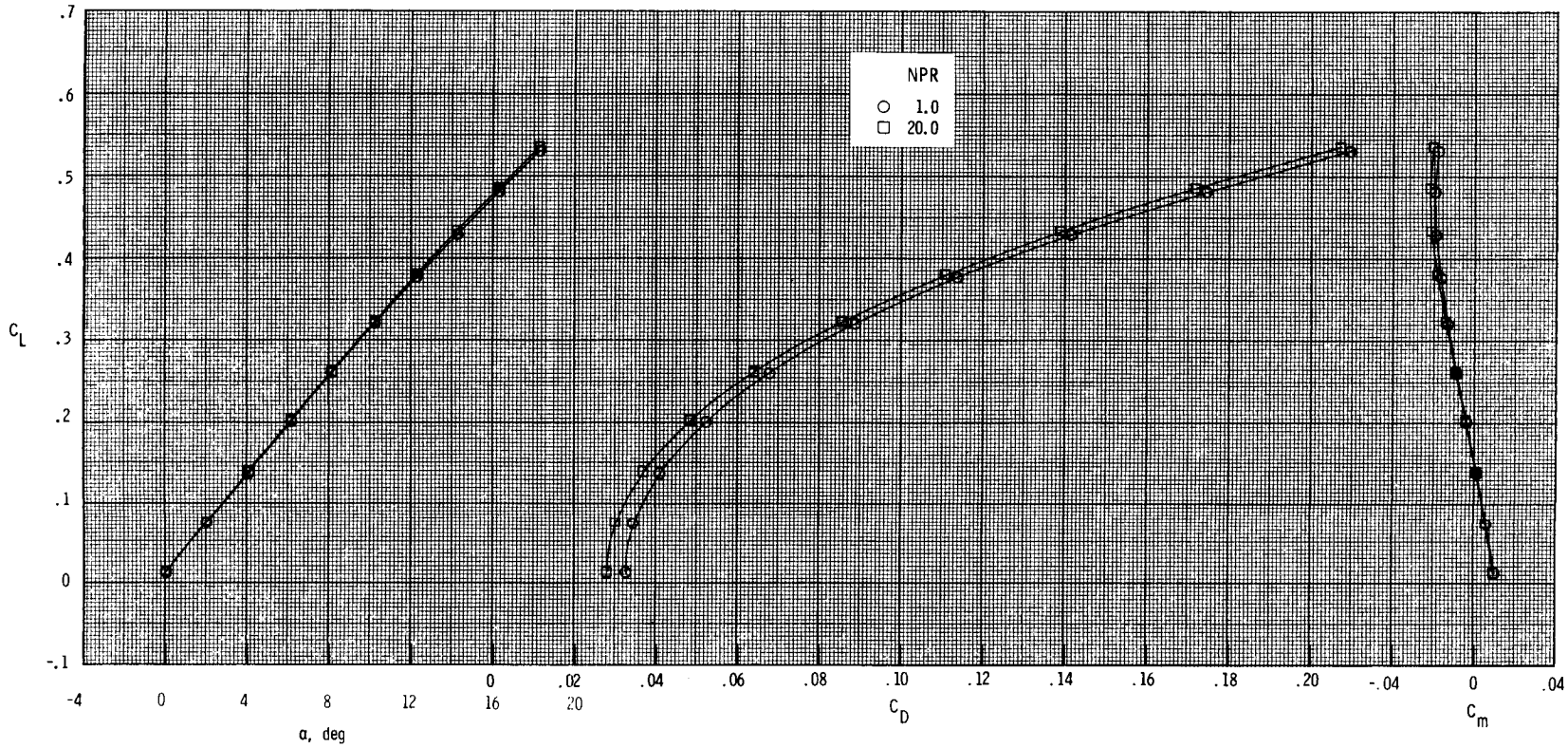

(f) $M = 2.17$.

Figure 48. Continued.

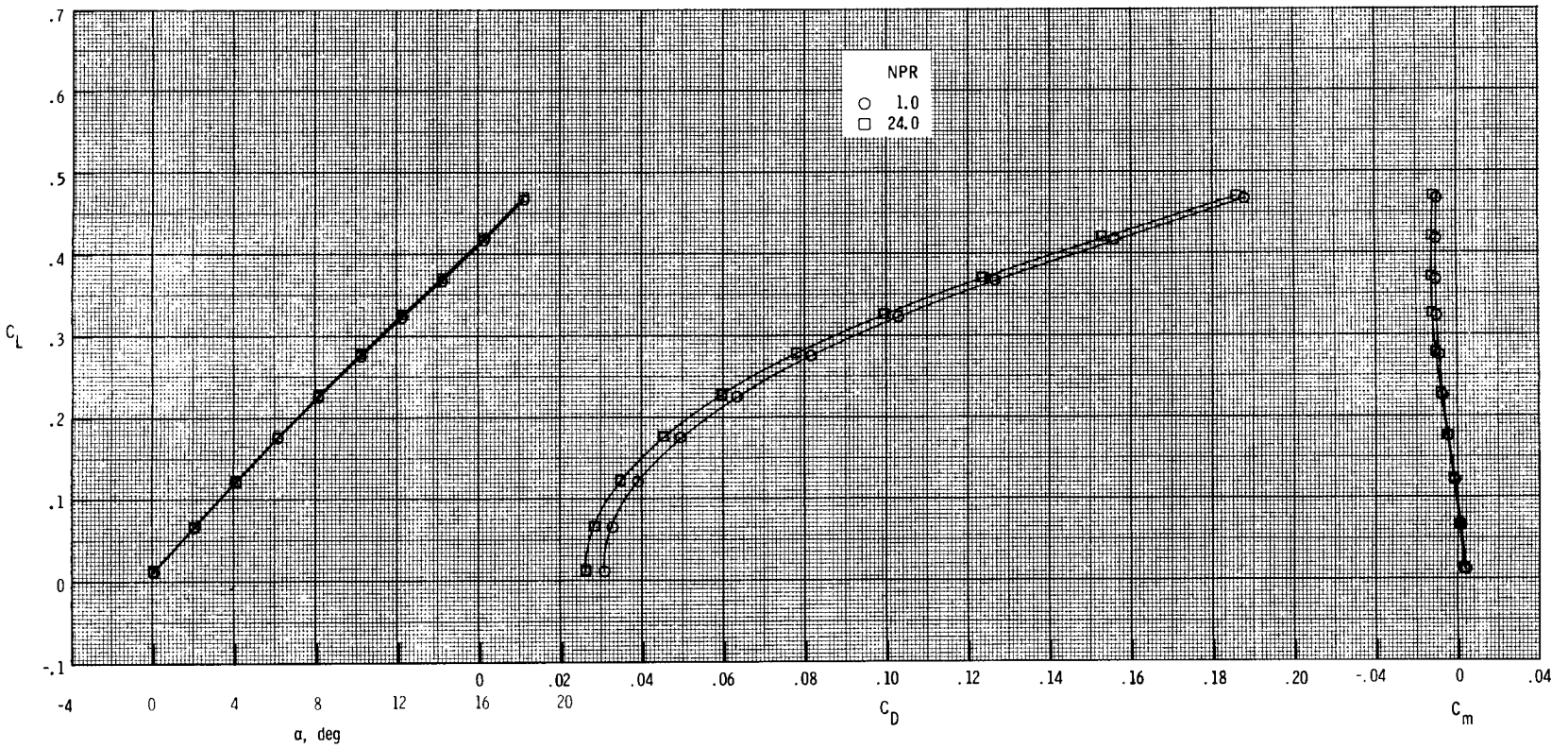

(g) $M = 2.47$.

Figure 48. Concluded.

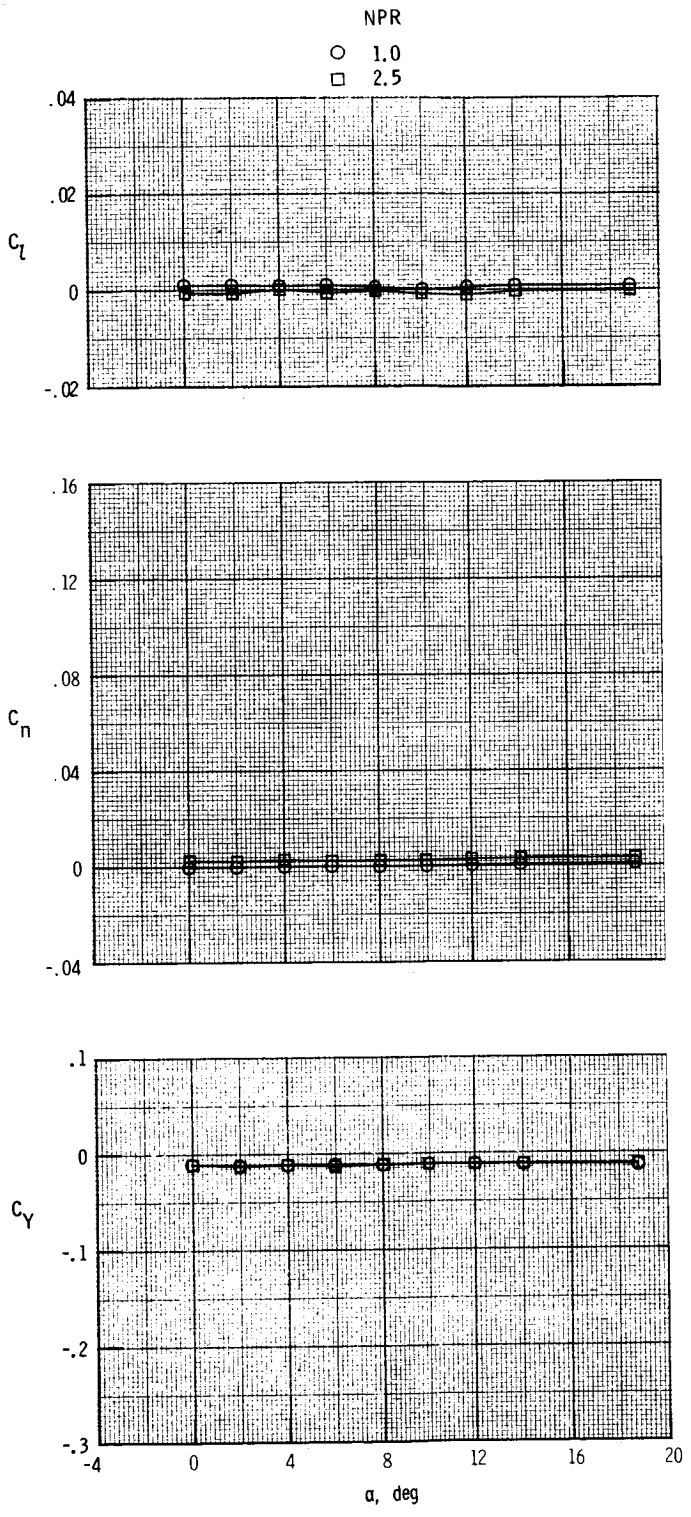

(a) $M = 0.20$.

Figure 49. Thrust-removed lateral aerodynamic characteristics for $\delta_{v,p} = 0°$ and $\delta_{v,y} = 0°$.

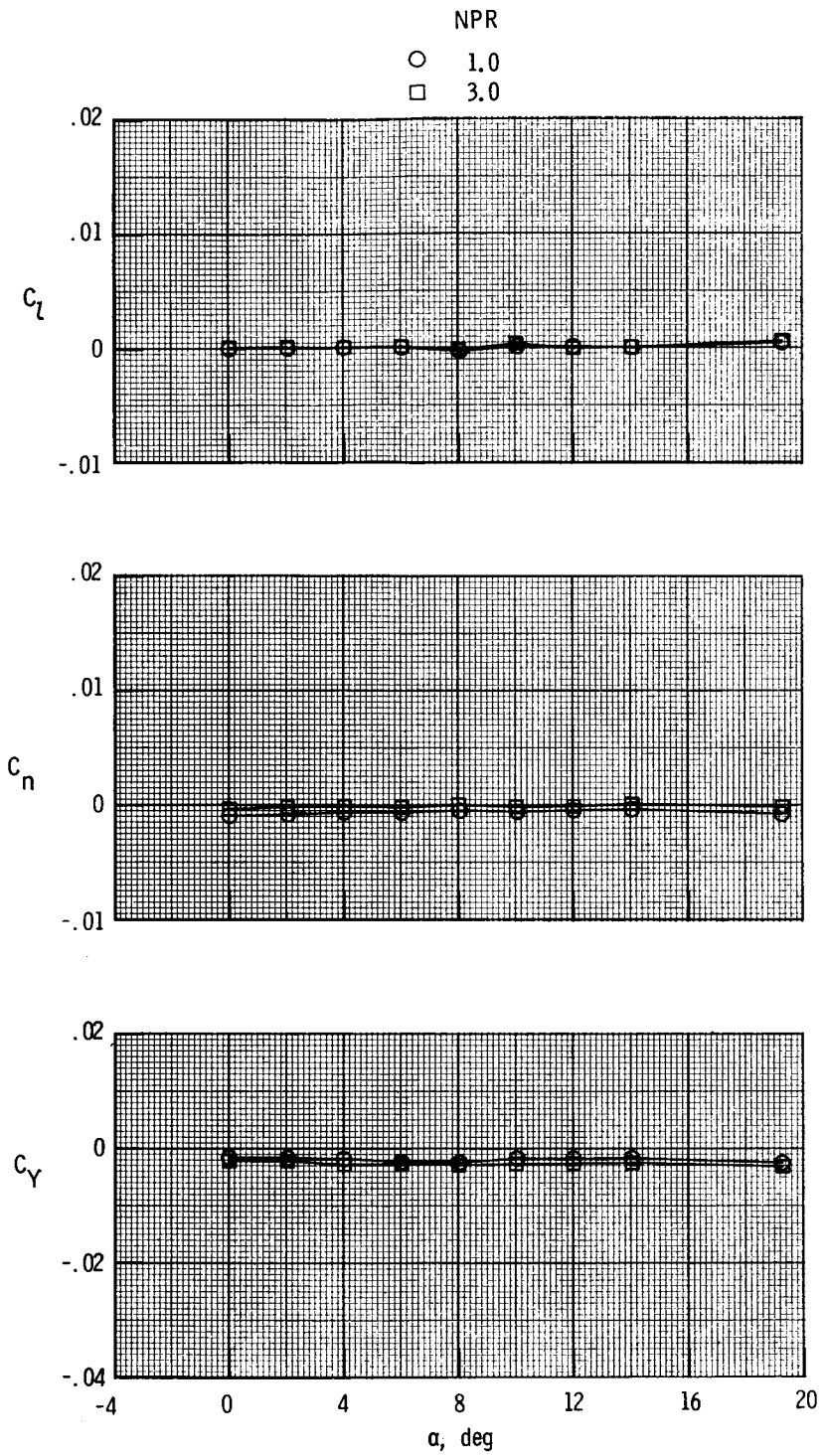

(b) $M = 0.60$.

Figure 49. Continued.

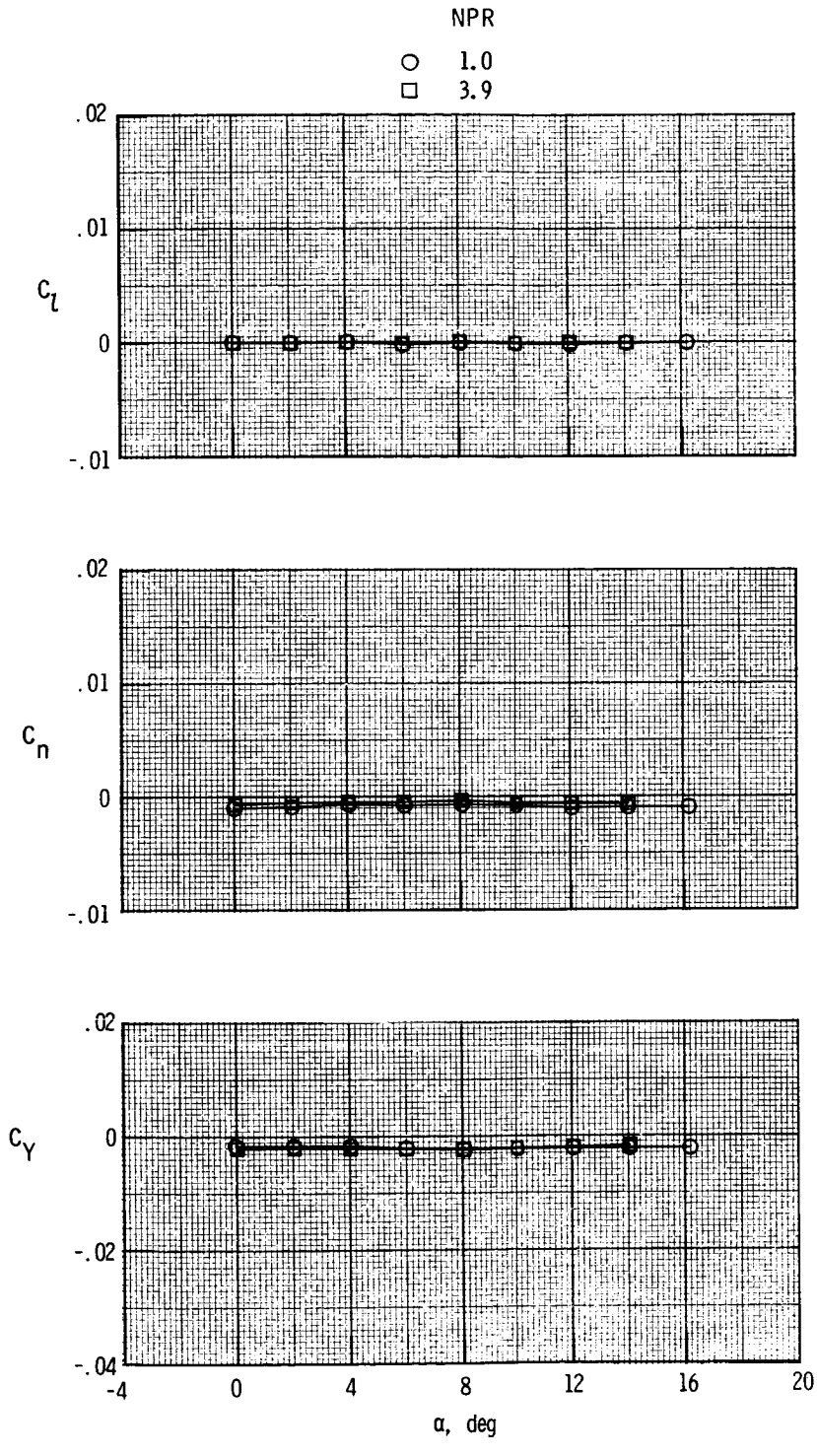

(c) $M = 0.87$.

Figure 49. Continued.

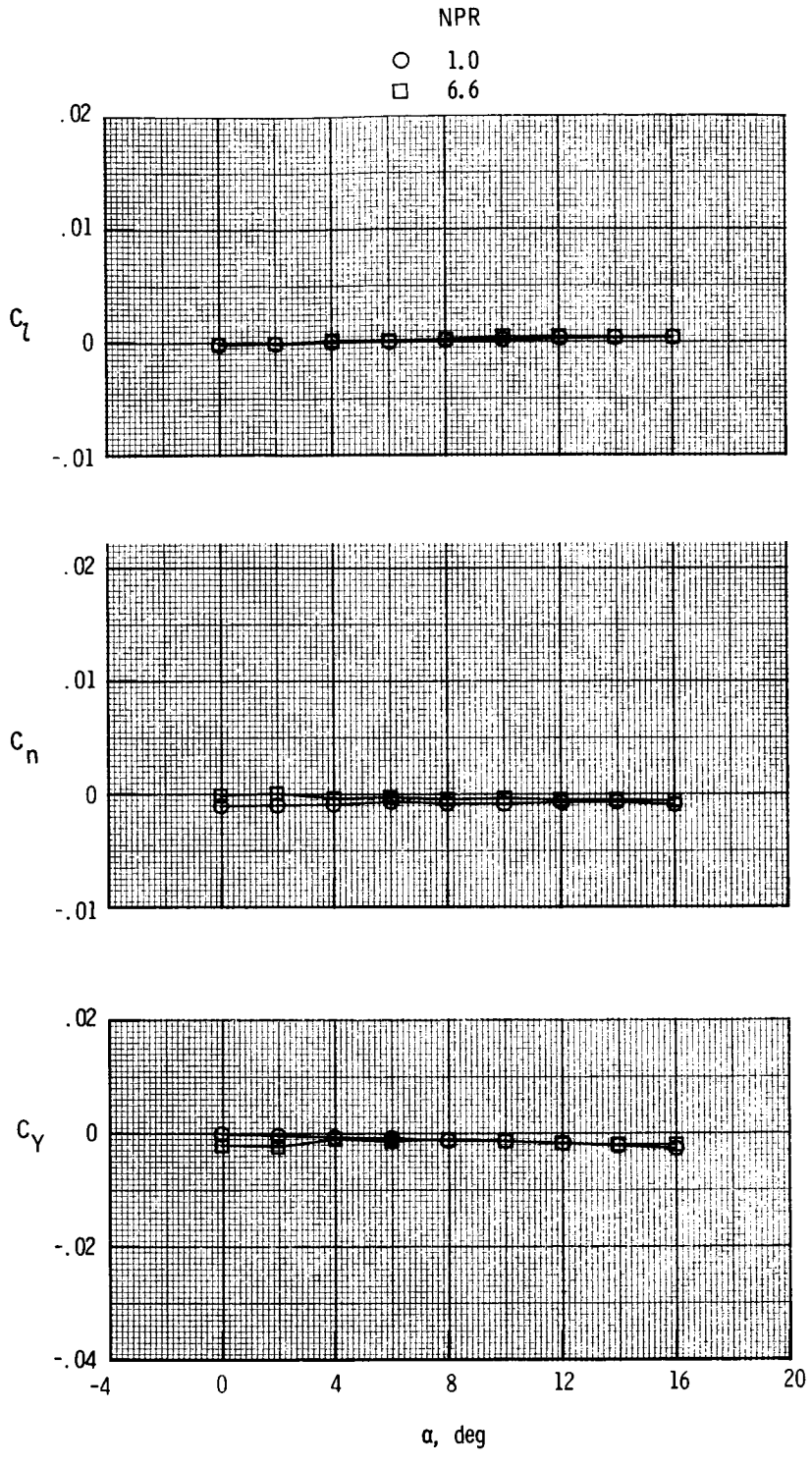

(d) $M = 1.20$.

Figure 49. Continued.

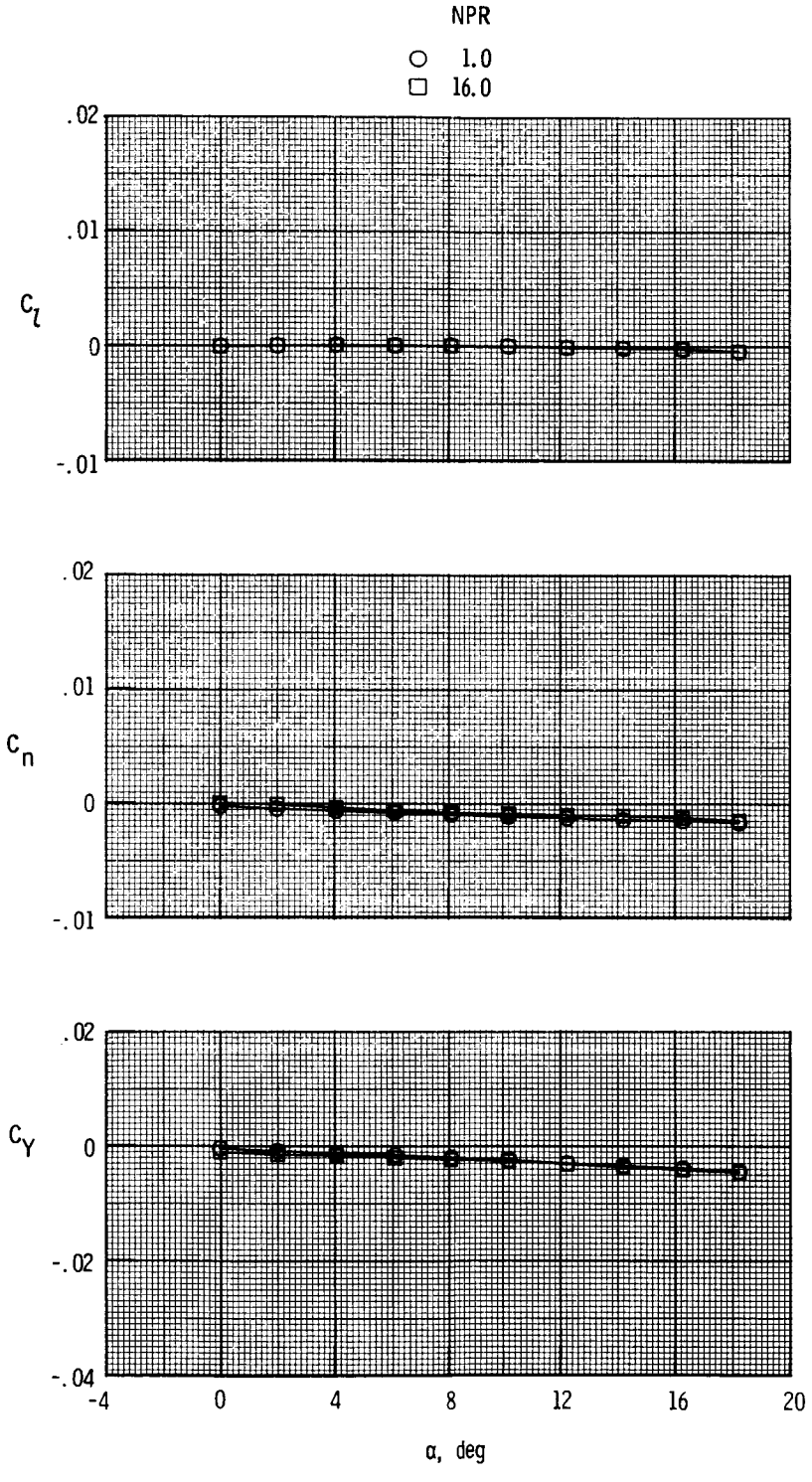

(e) $M = 2.00$.

Figure 49. Continued.

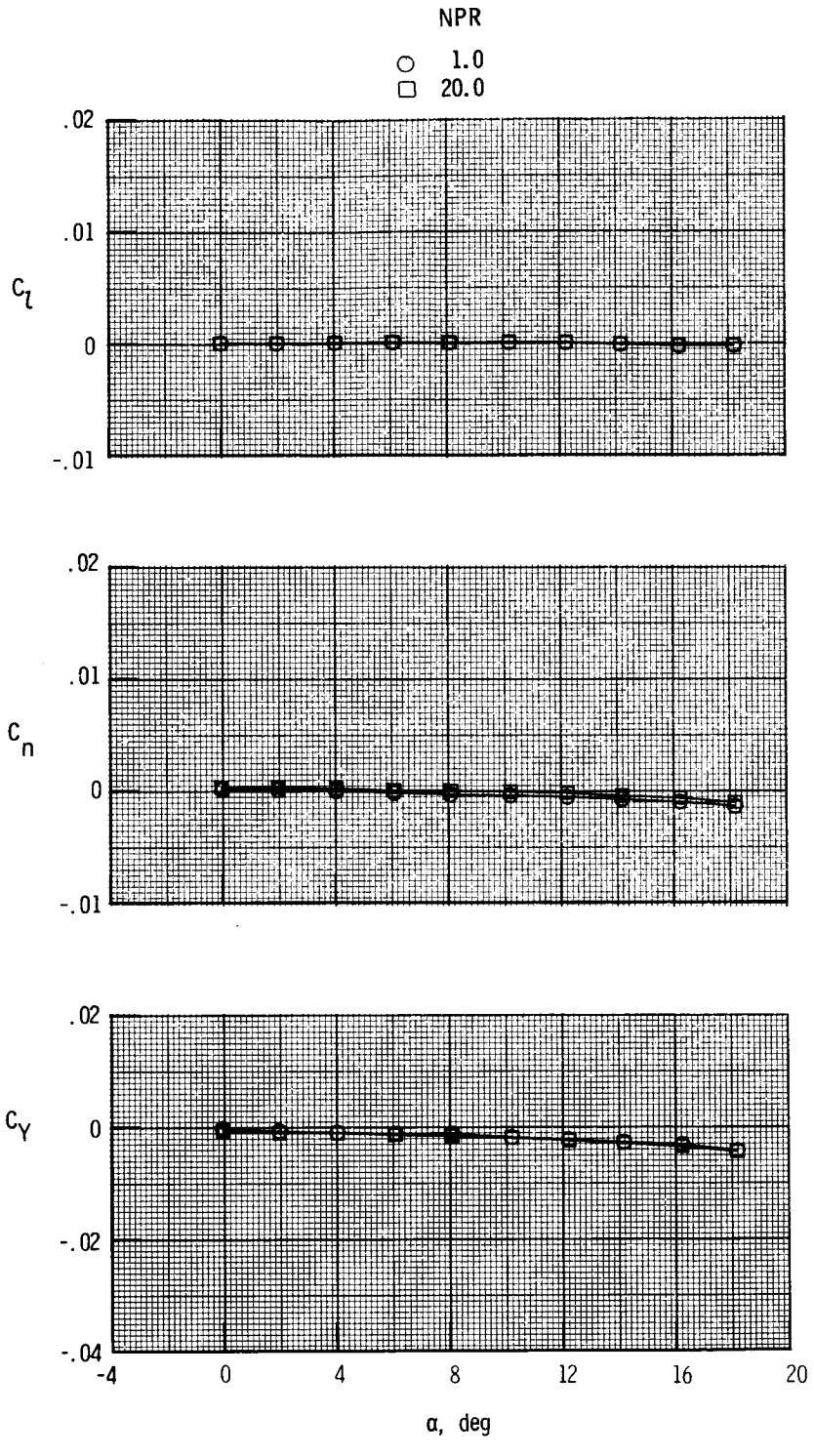

(f) $M = 2.17$.

Figure 49. Continued.

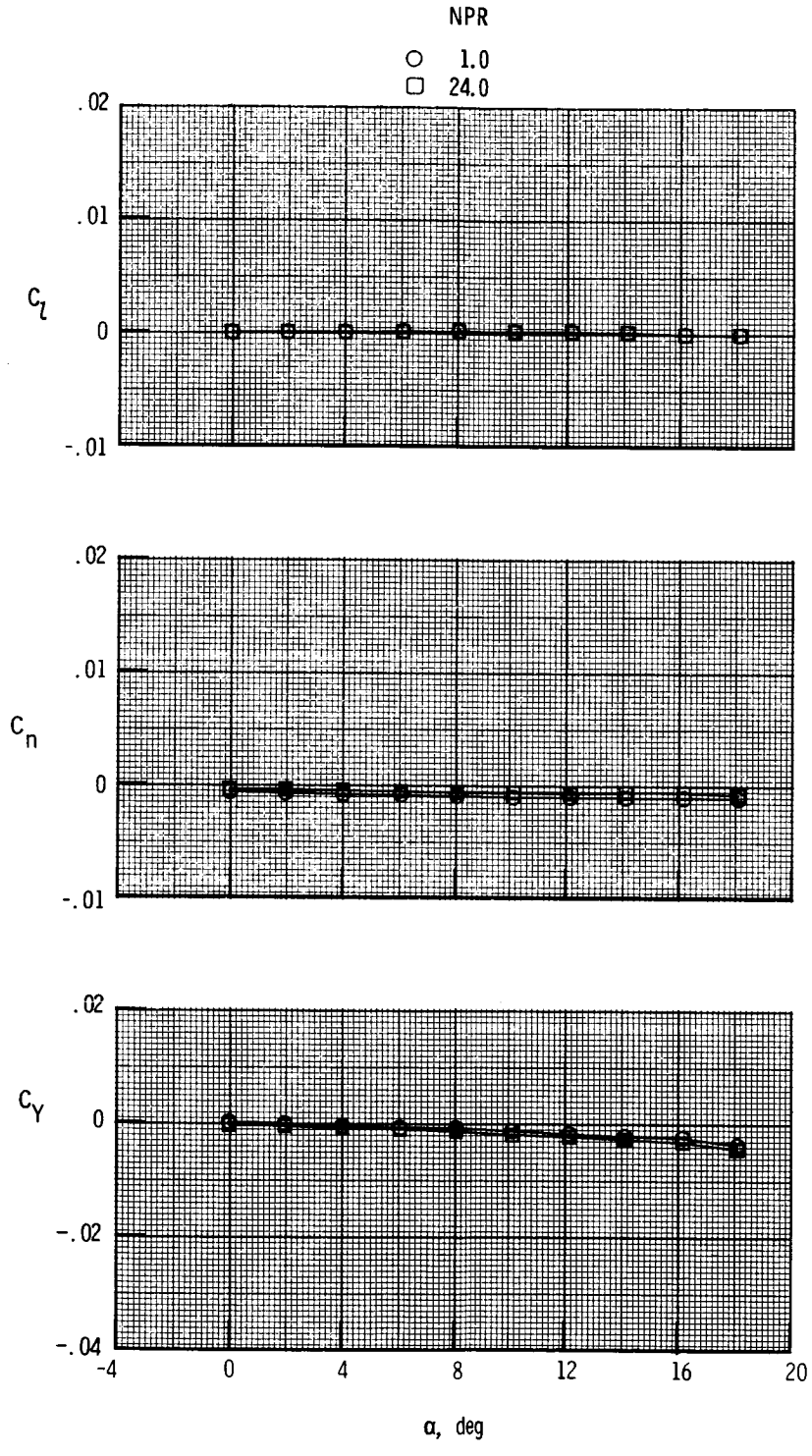

(g) $M = 2.47$.

Figure 49. Concluded.

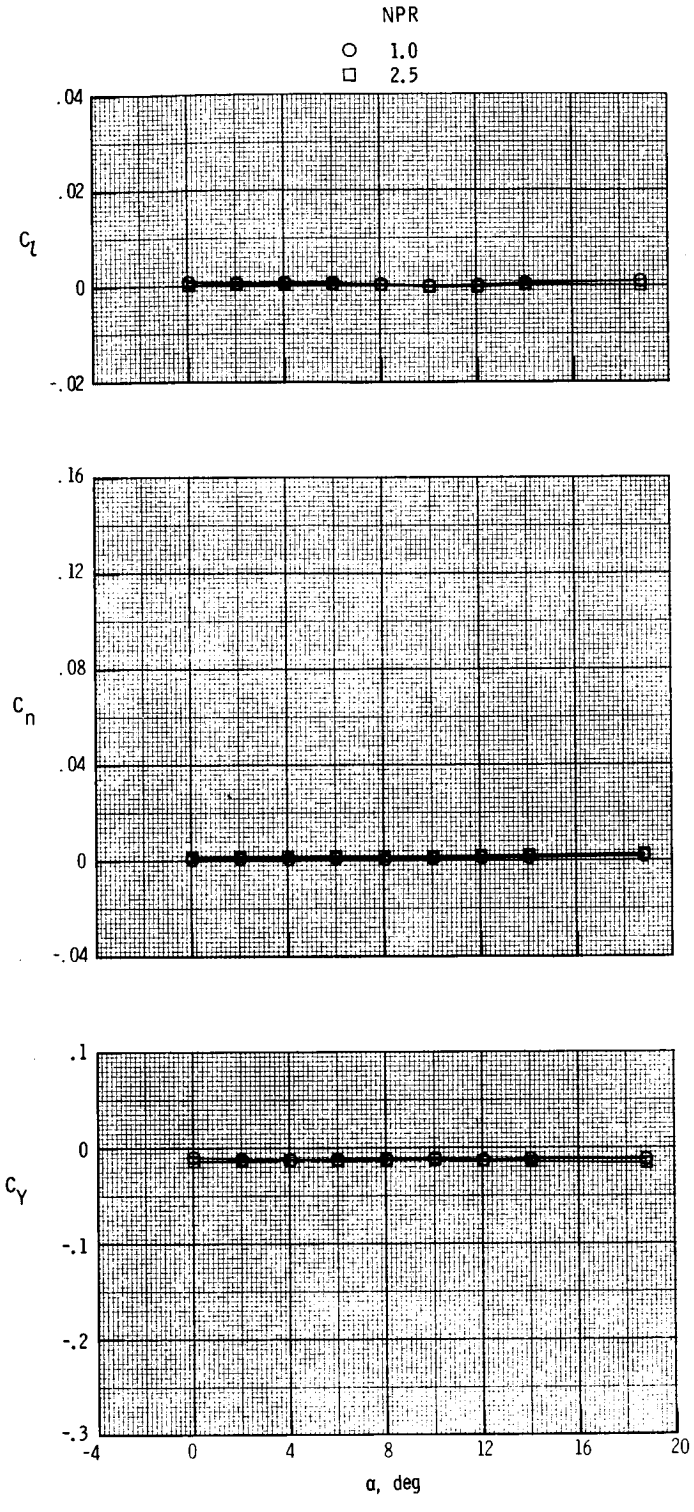

(a) $M = 0.20$.

Figure 50. Thrust-removed lateral aerodynamic characteristics for $\delta_{v,p} = 0°$ and $\delta_{v,y} = -10°$.

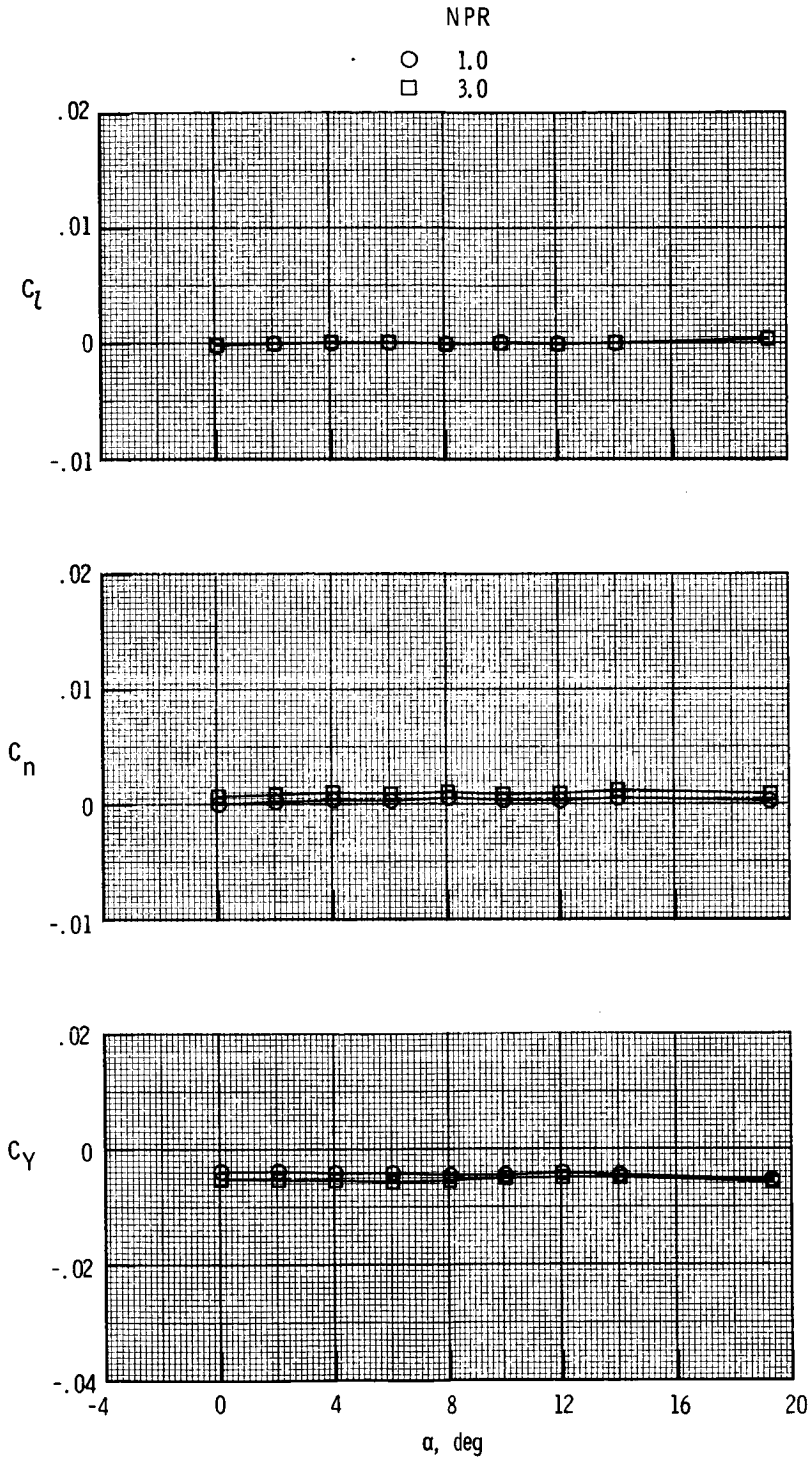

(b) $M = 0.60$.

Figure 50. Continued.

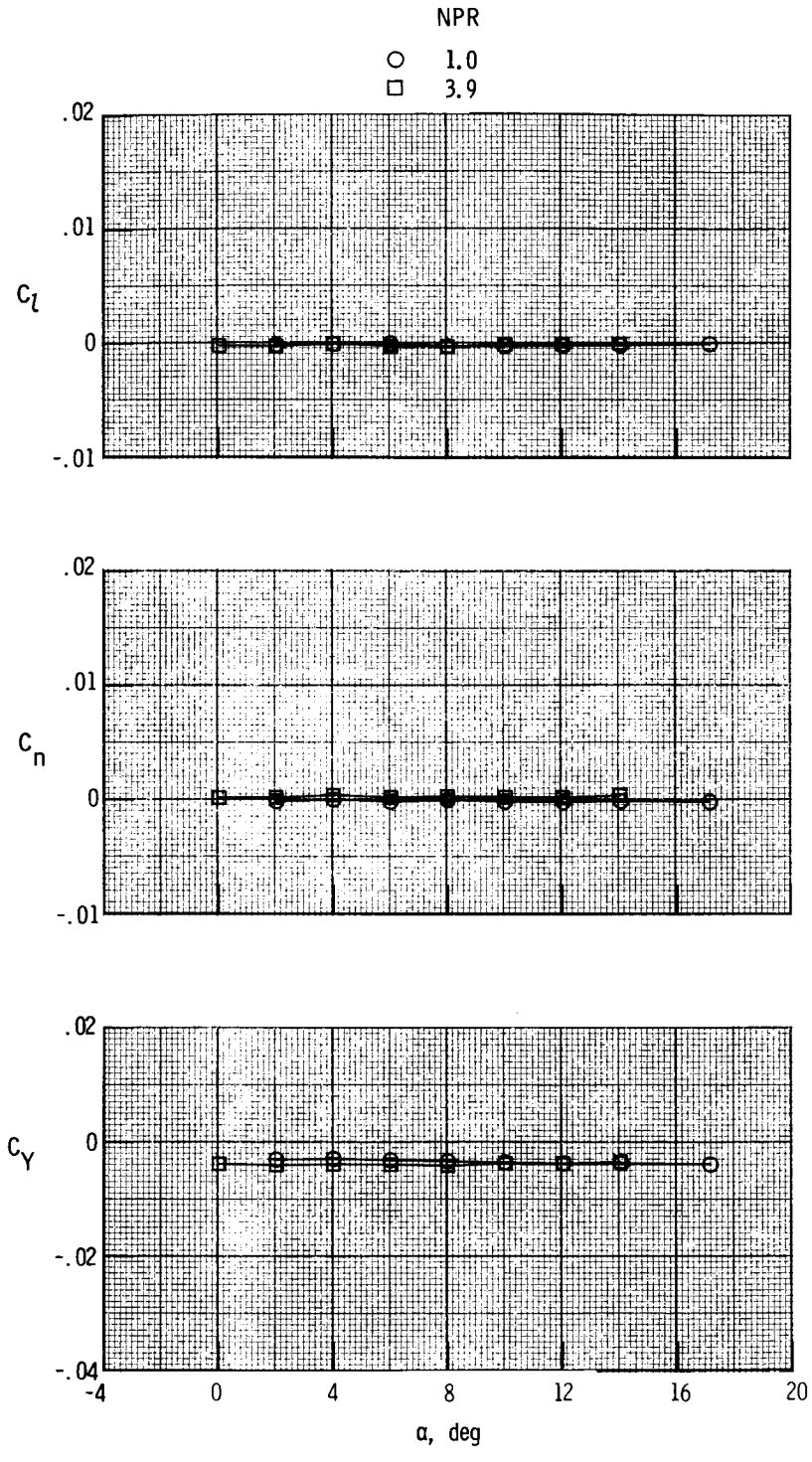

(c) $M = 0.87$.

Figure 50. Continued.

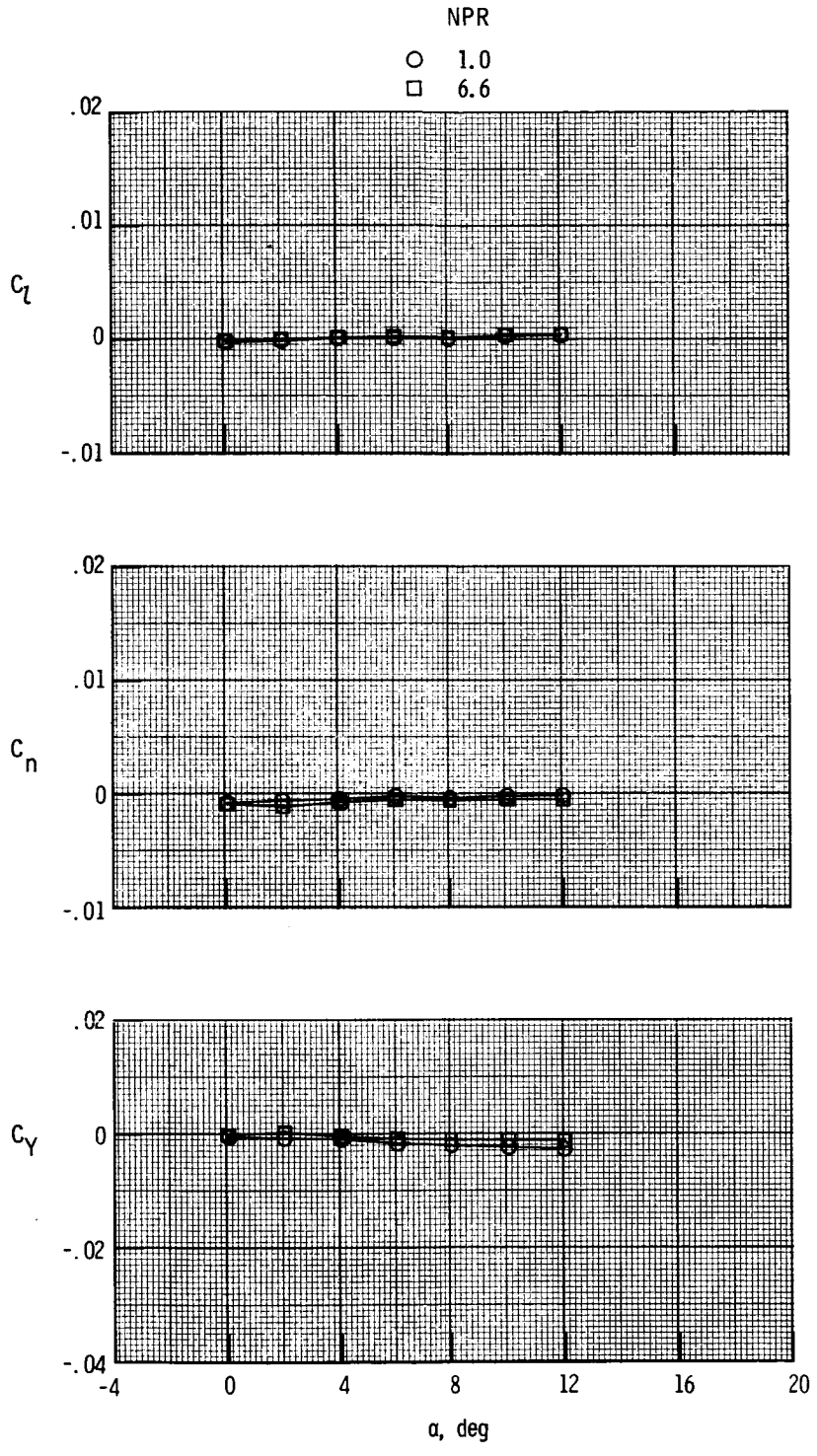

(d) $M = 1.20$.

Figure 50. Continued.

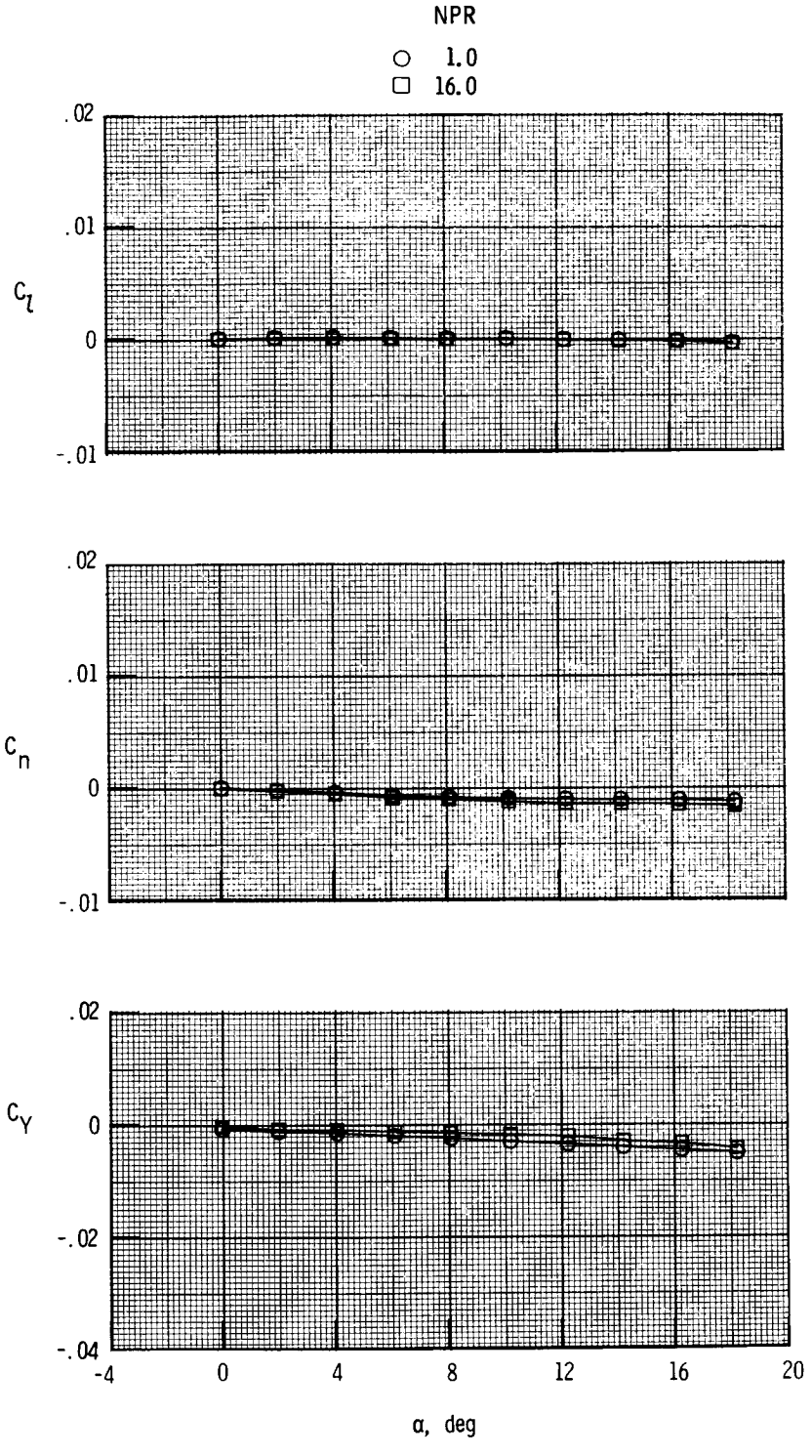

(e) $M = 2.00$.

Figure 50. Continued.

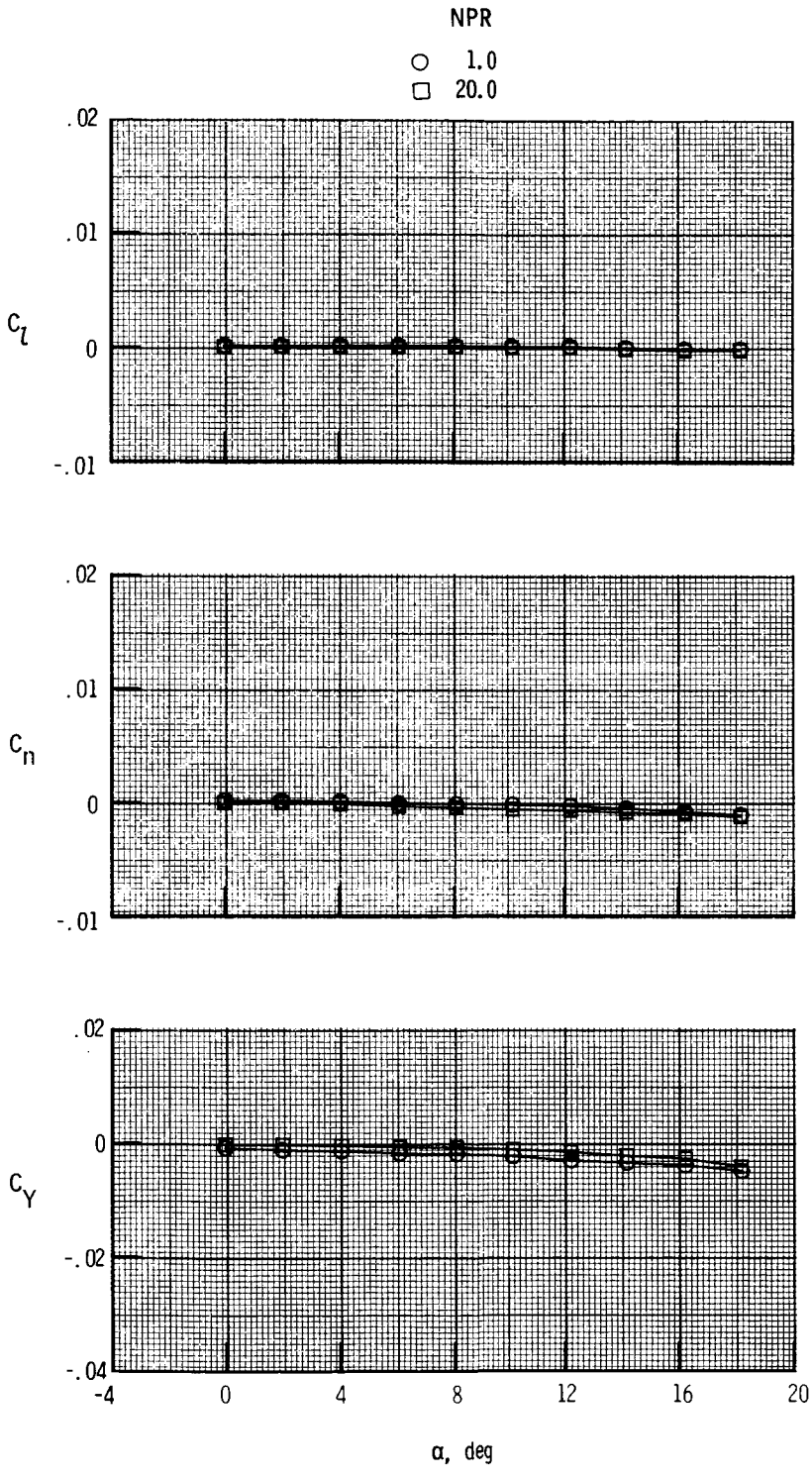

(f) $M = 2.17$.

Figure 50. Continued.

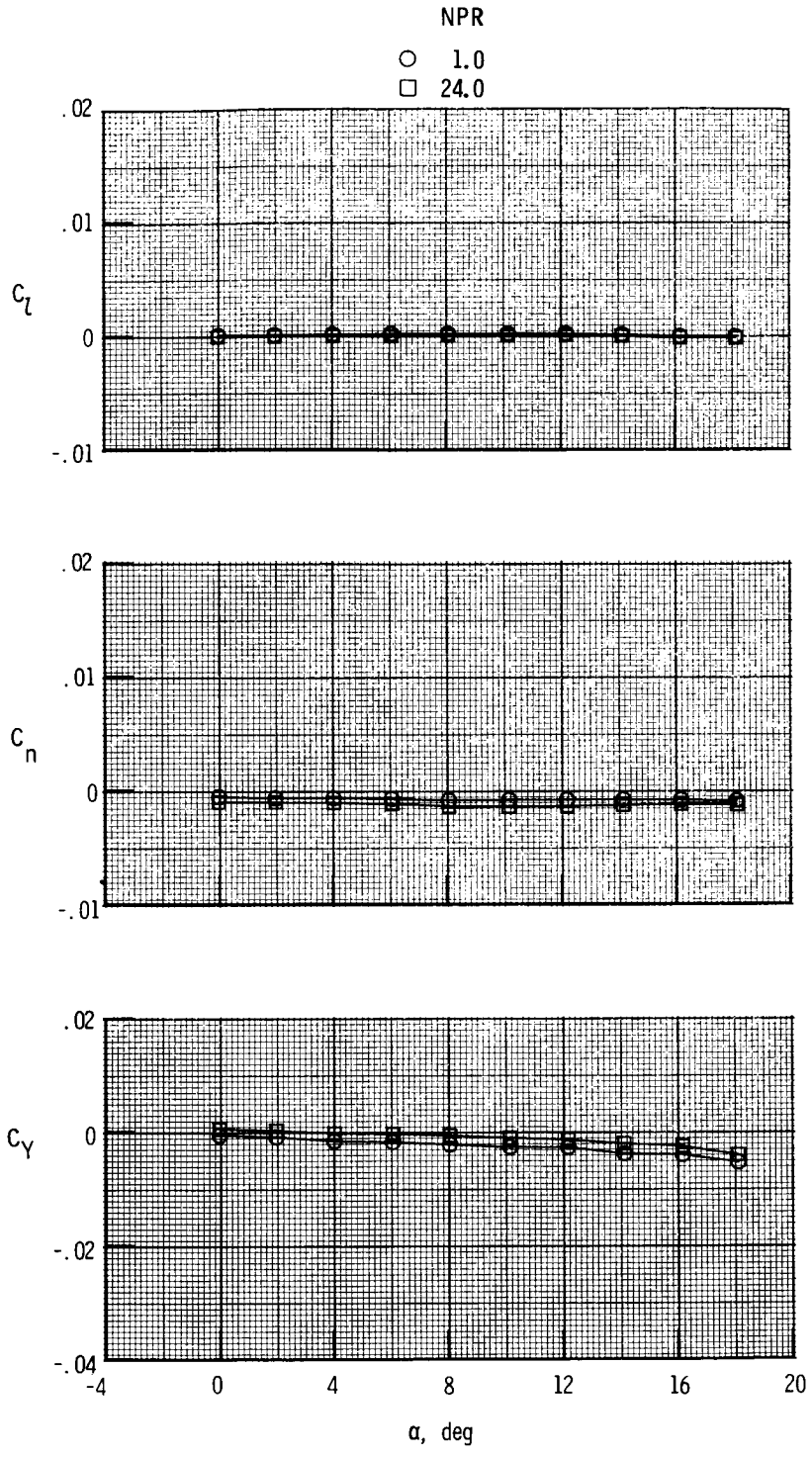

(g) $M = 2.47$.

Figure 50. Concluded.

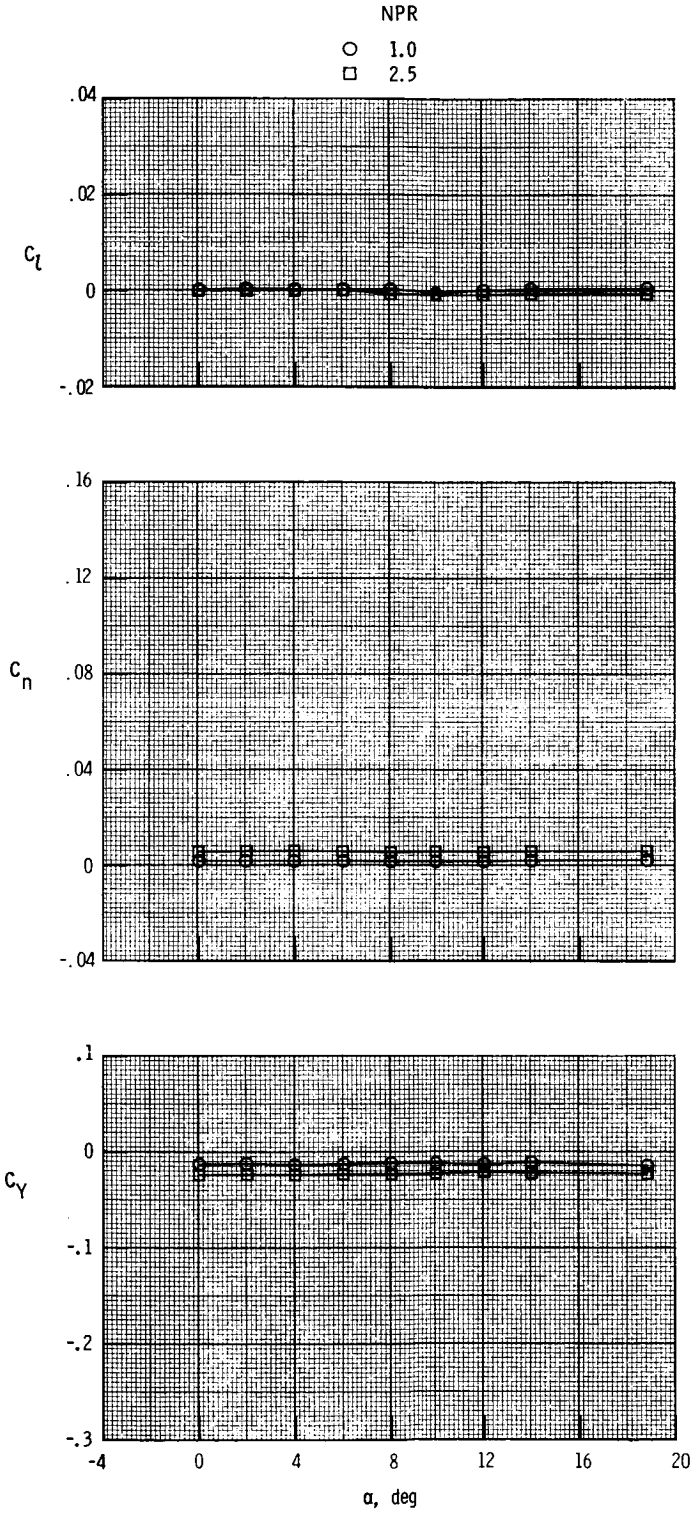

(a) $M = 0.20$.

Figure 51. Thrust-removed lateral aerodynamic characteristics for $\delta_{v,p} = 0°$ and $\delta_{v,y} = -20°$.

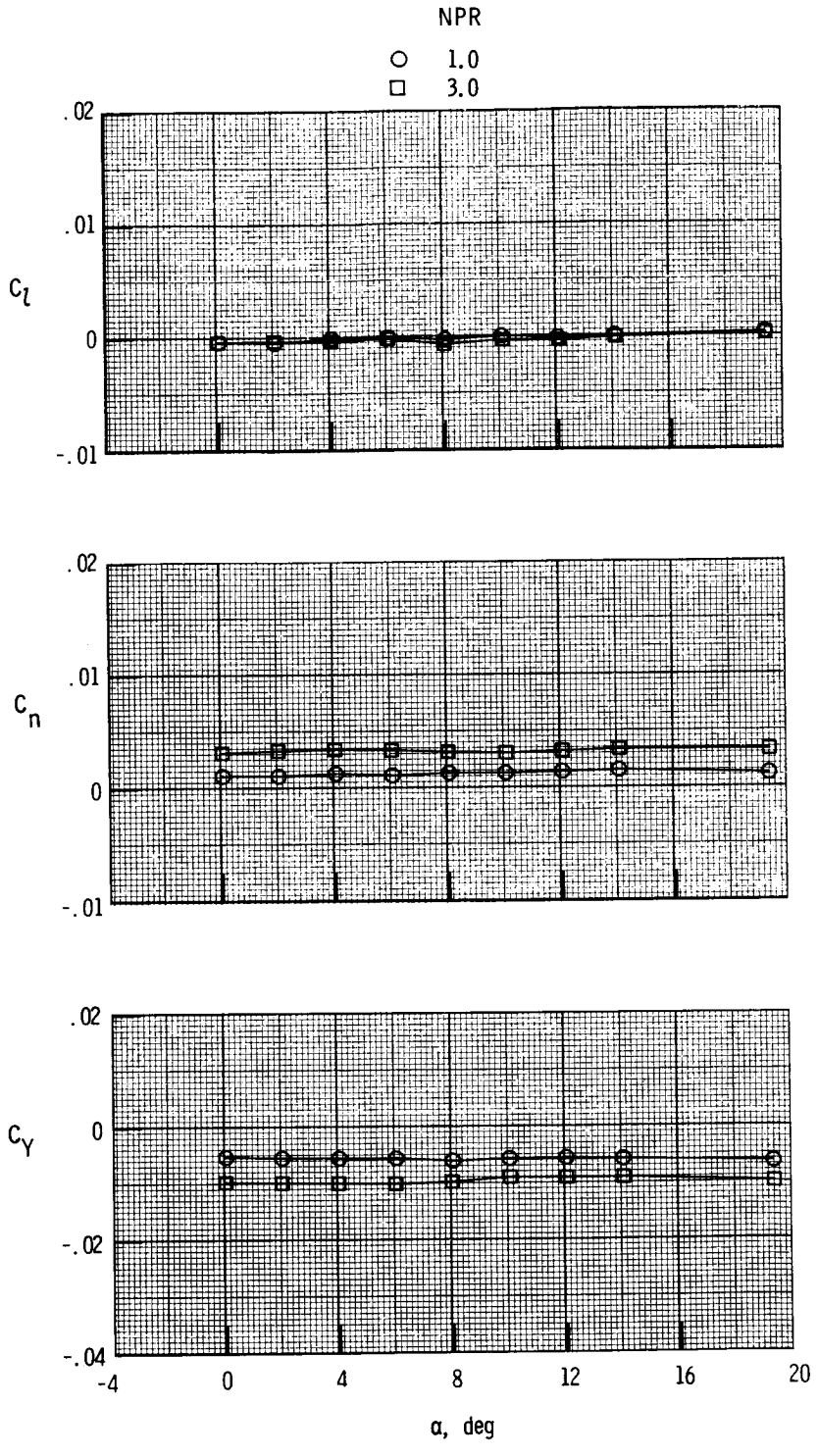

(b) $M = 0.60$.

Figure 51. Continued.

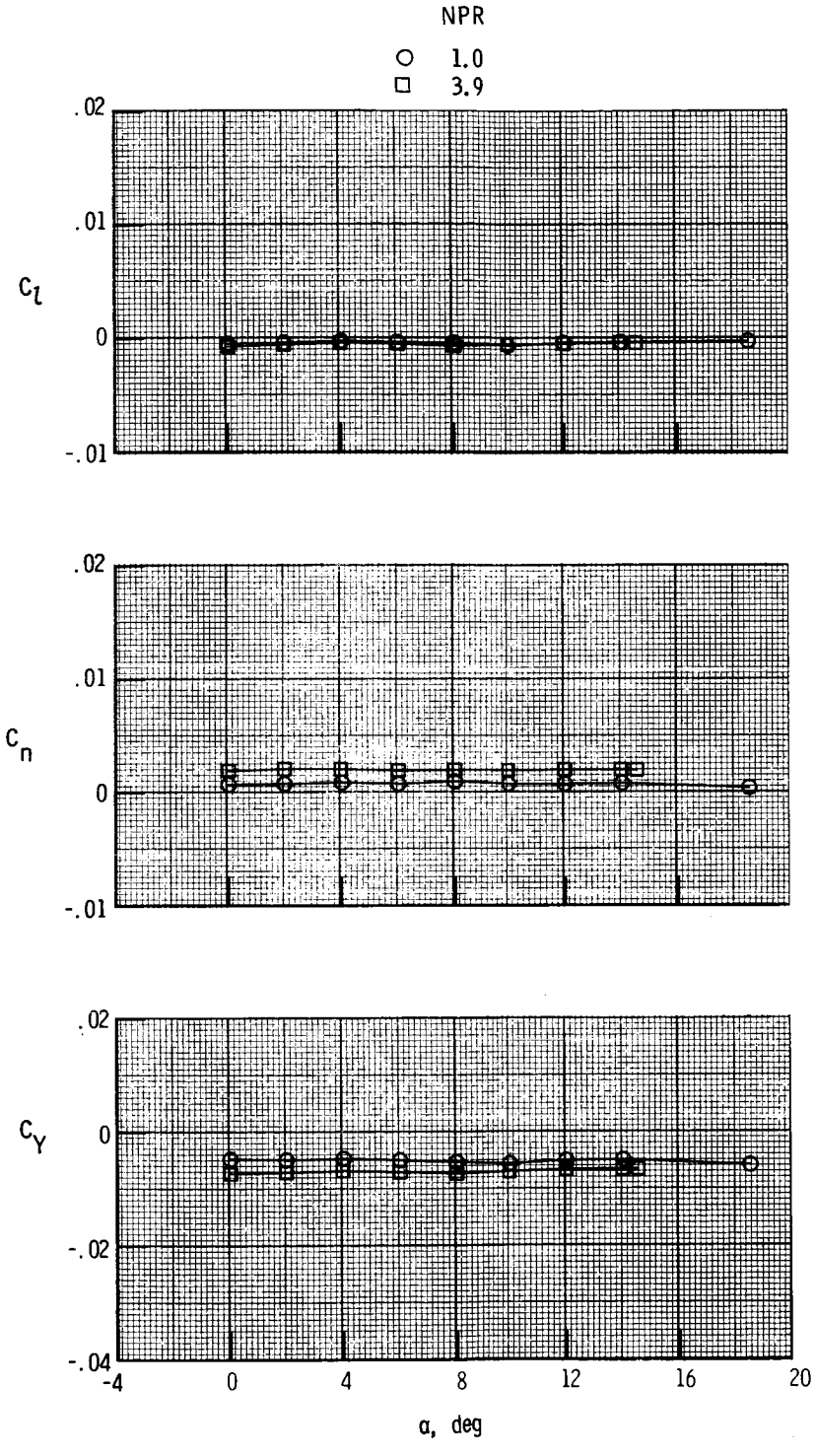

(c) $M = 0.87$.

Figure 51. Continued.

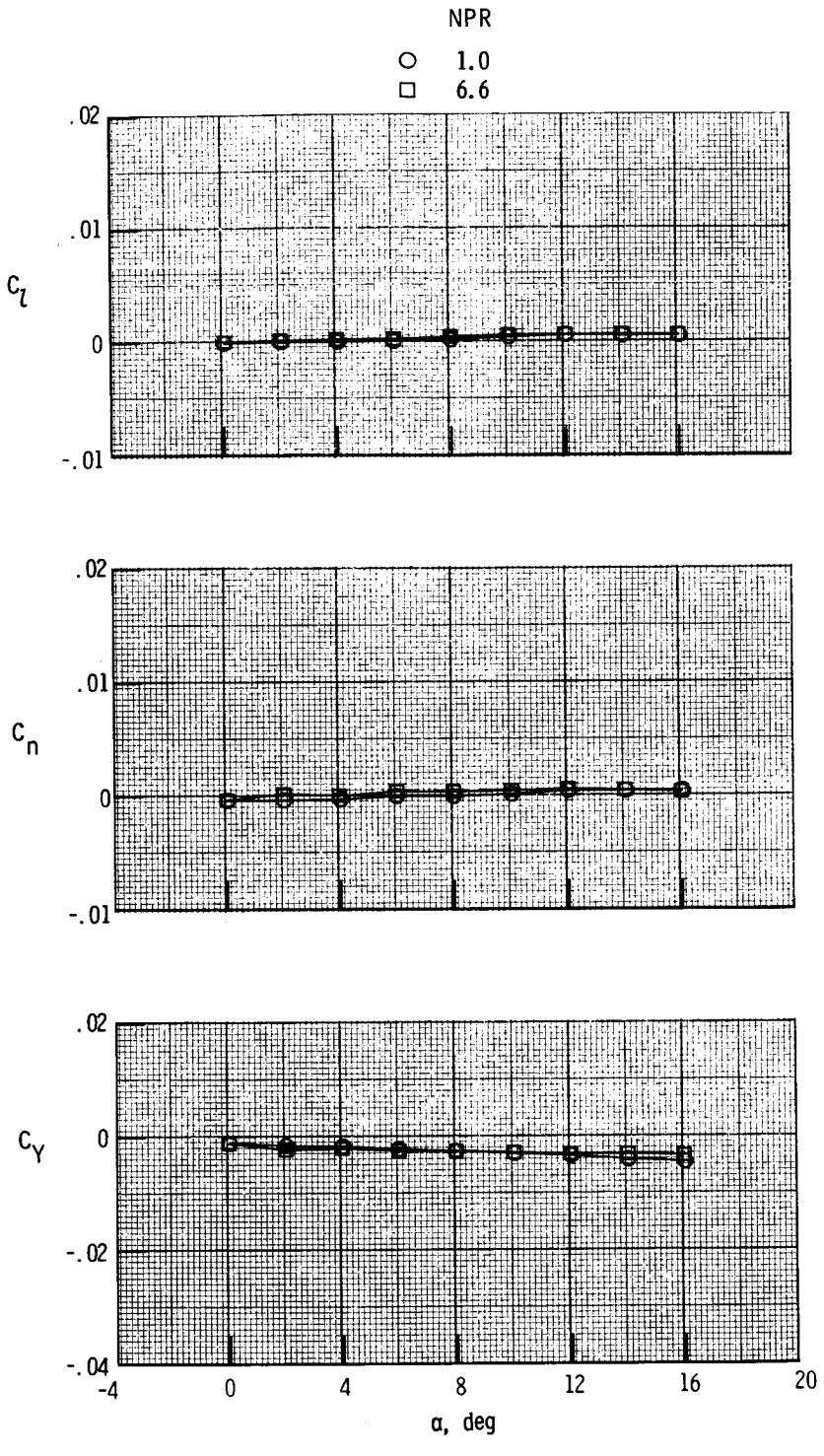

(d) $M = 1.20$.

Figure 51. Continued.

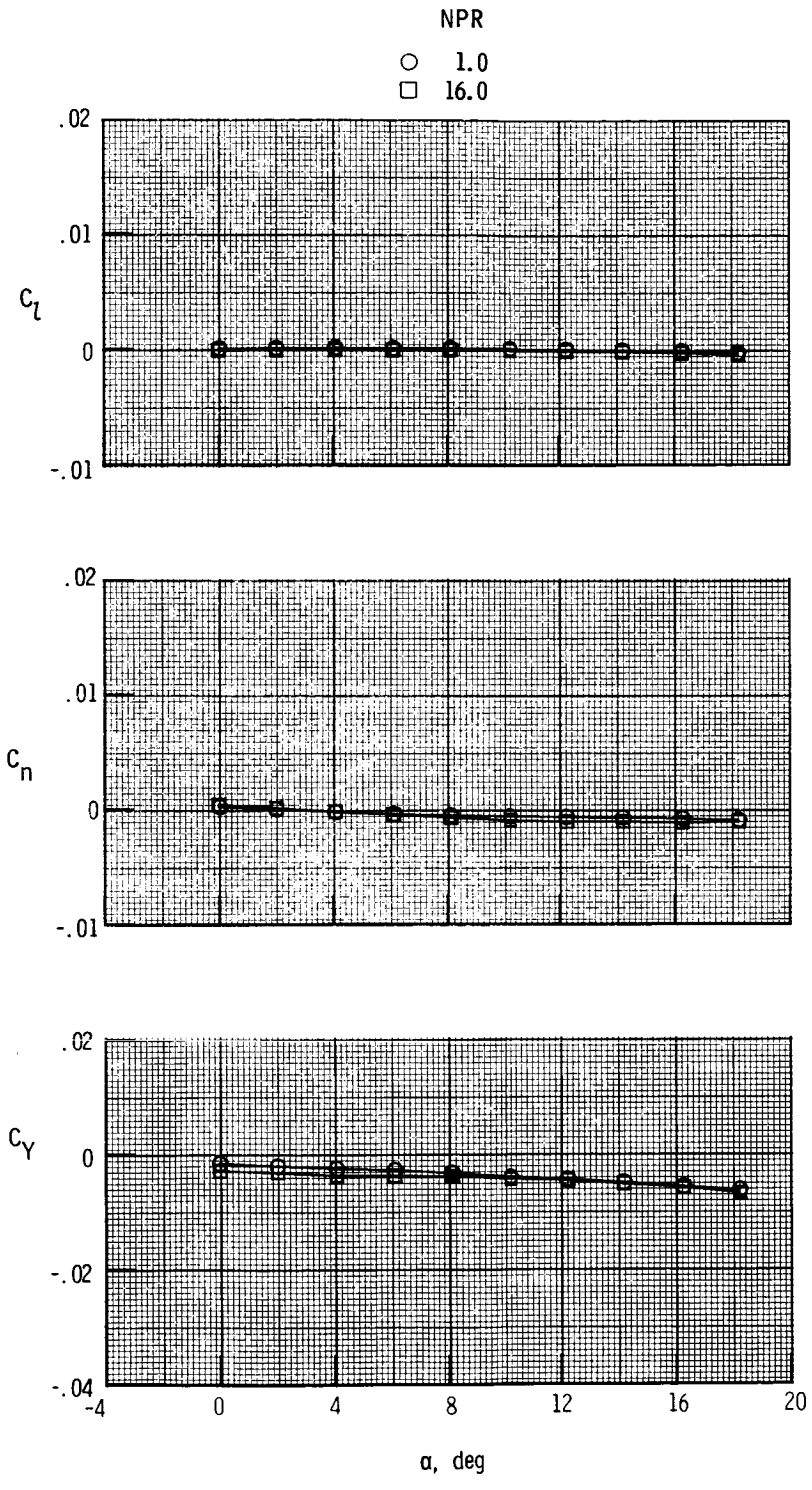

(e) $M = 2.00$.

Figure 51. Continued.

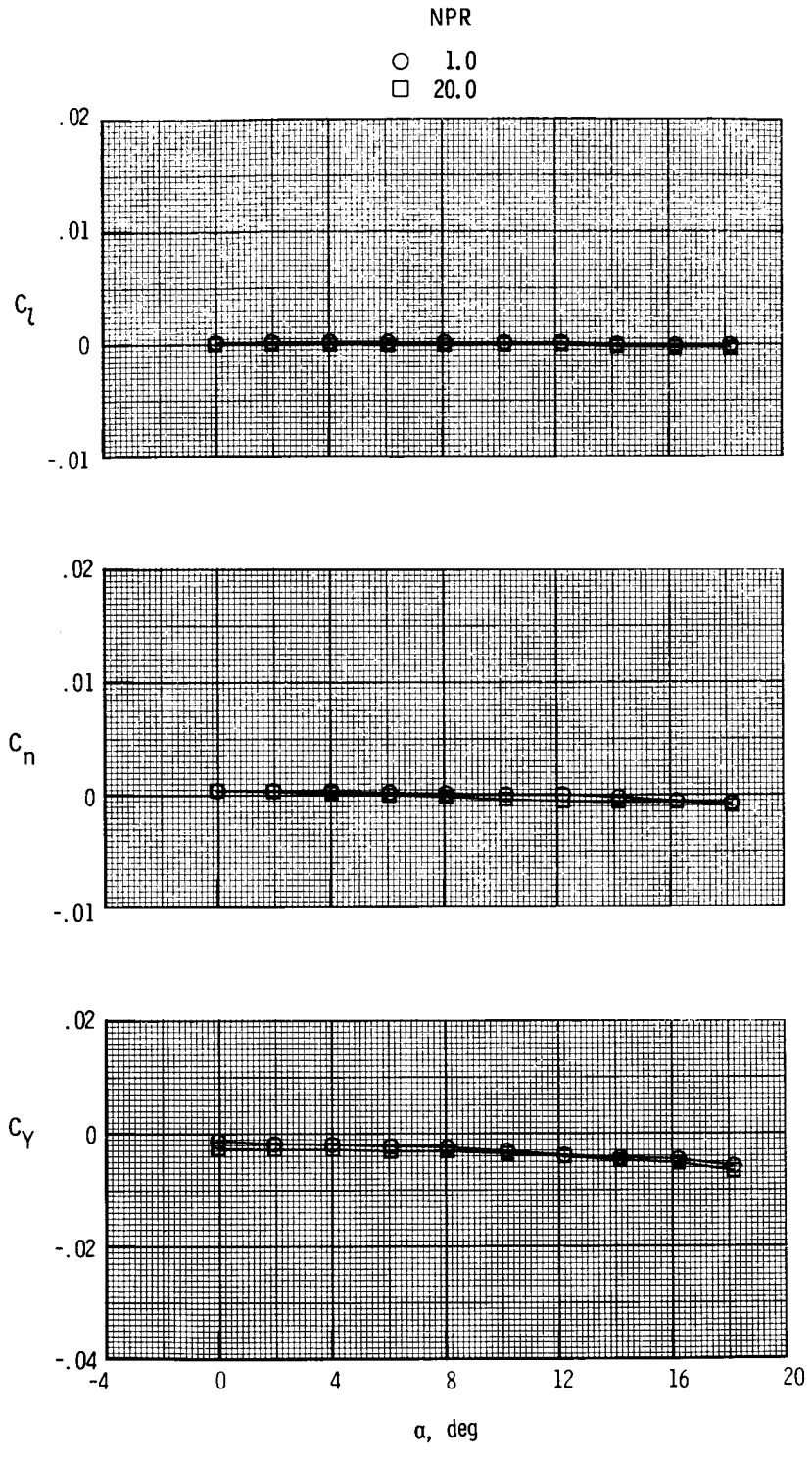

(f) $M = 2.17$.

Figure 51. Continued.

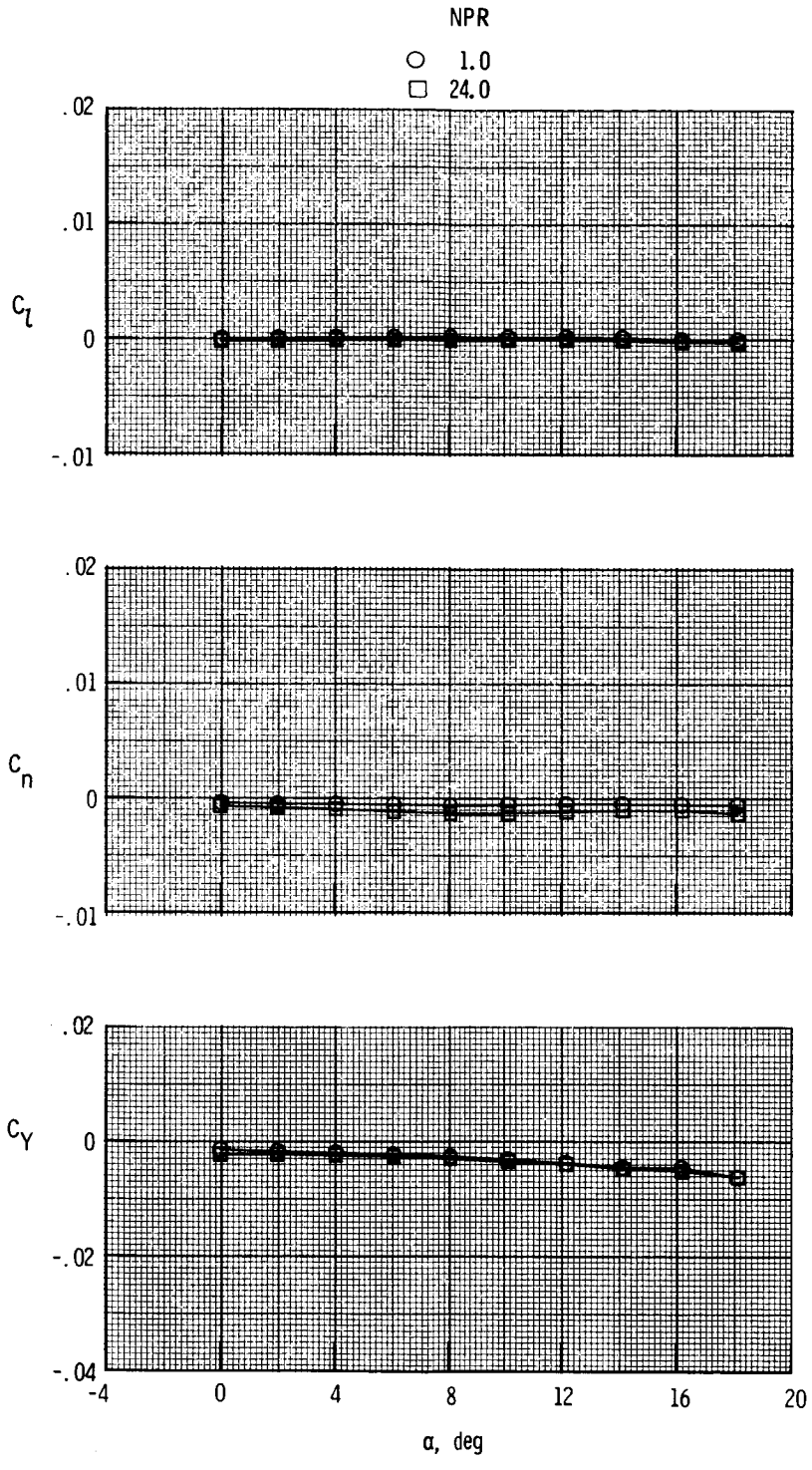

(g) $M = 2.47$.

Figure 51. Concluded.

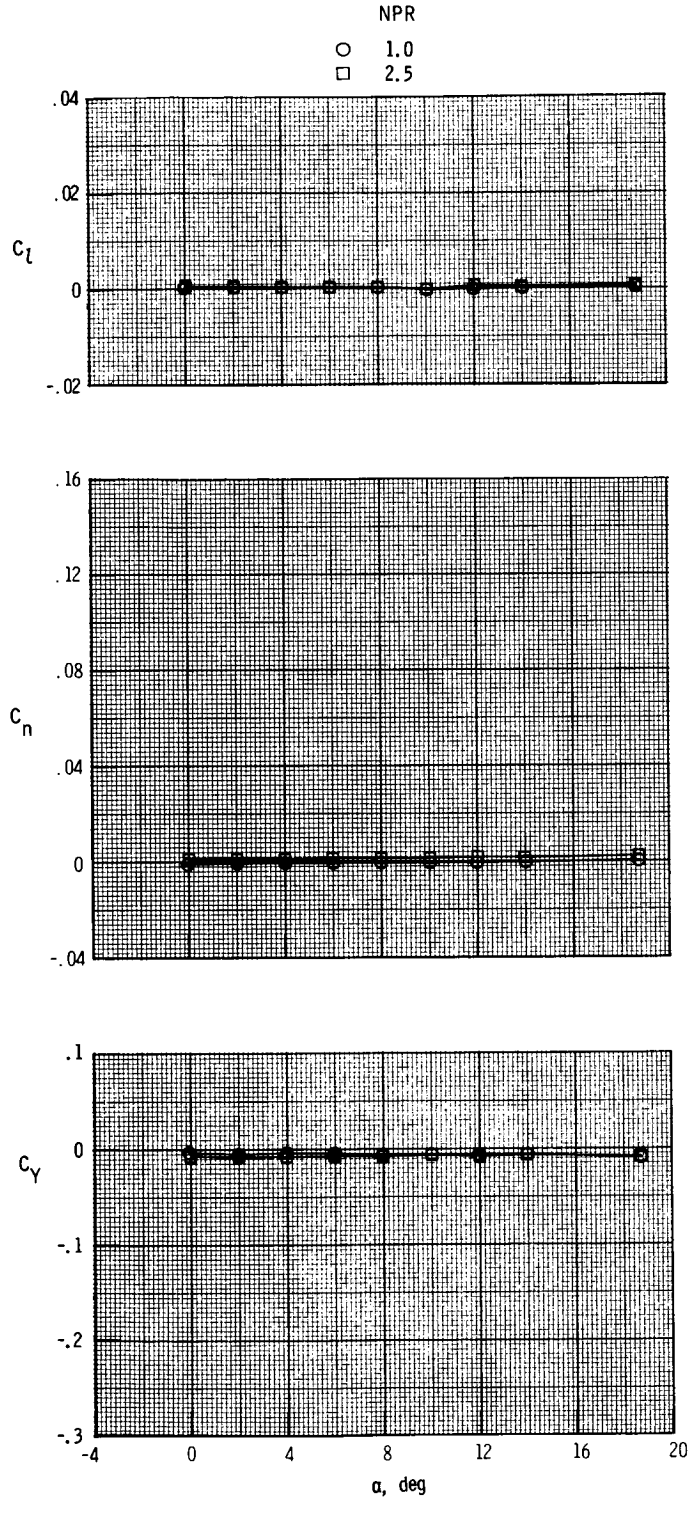

(a) $M = 0.20$.

Figure 52. Thrust-removed lateral aerodynamic characteristics for $\delta_{v,p} = 15°$ and $\delta_{v,y} = 0°$.

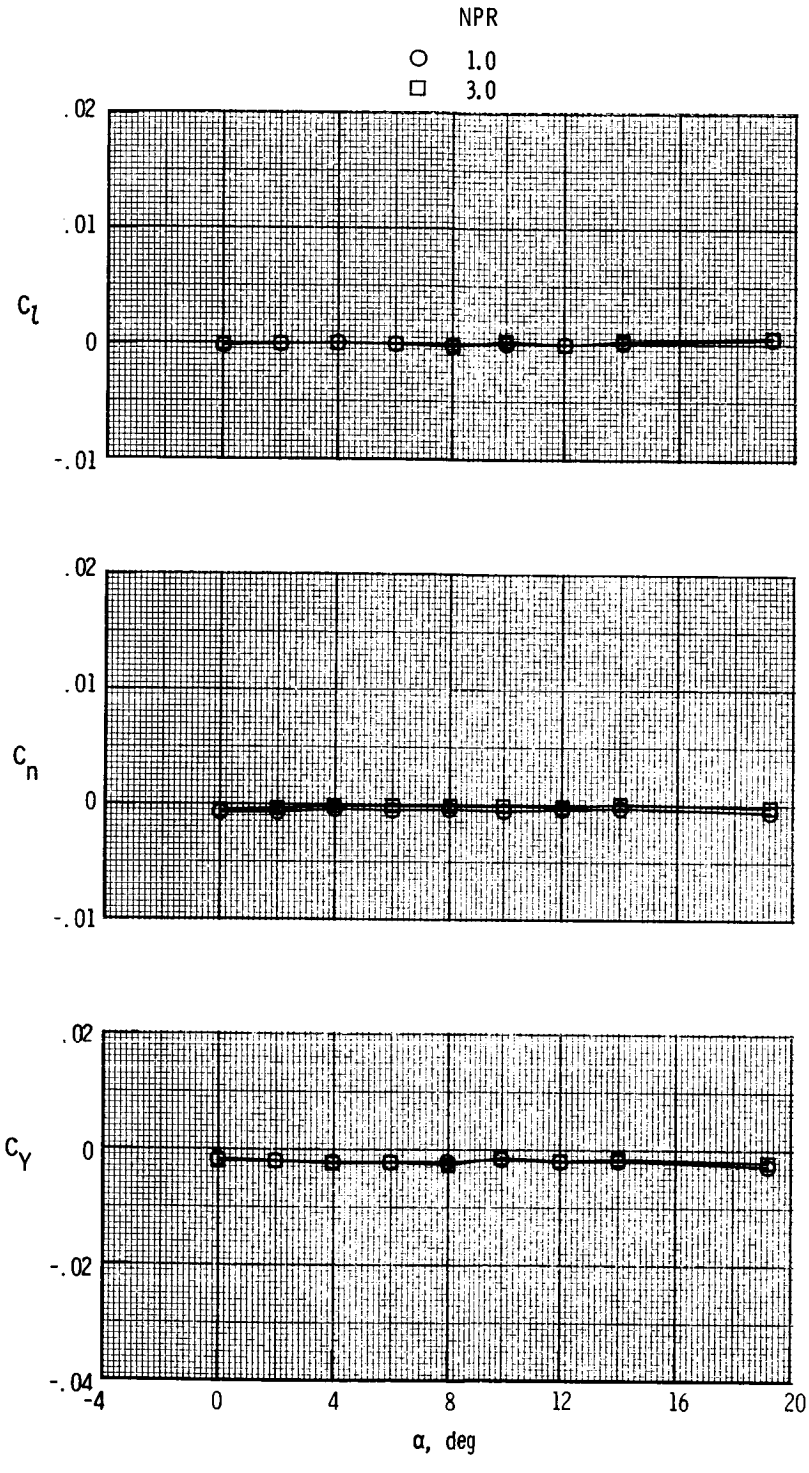

(b) $M = 0.60$.

Figure 52. Continued.

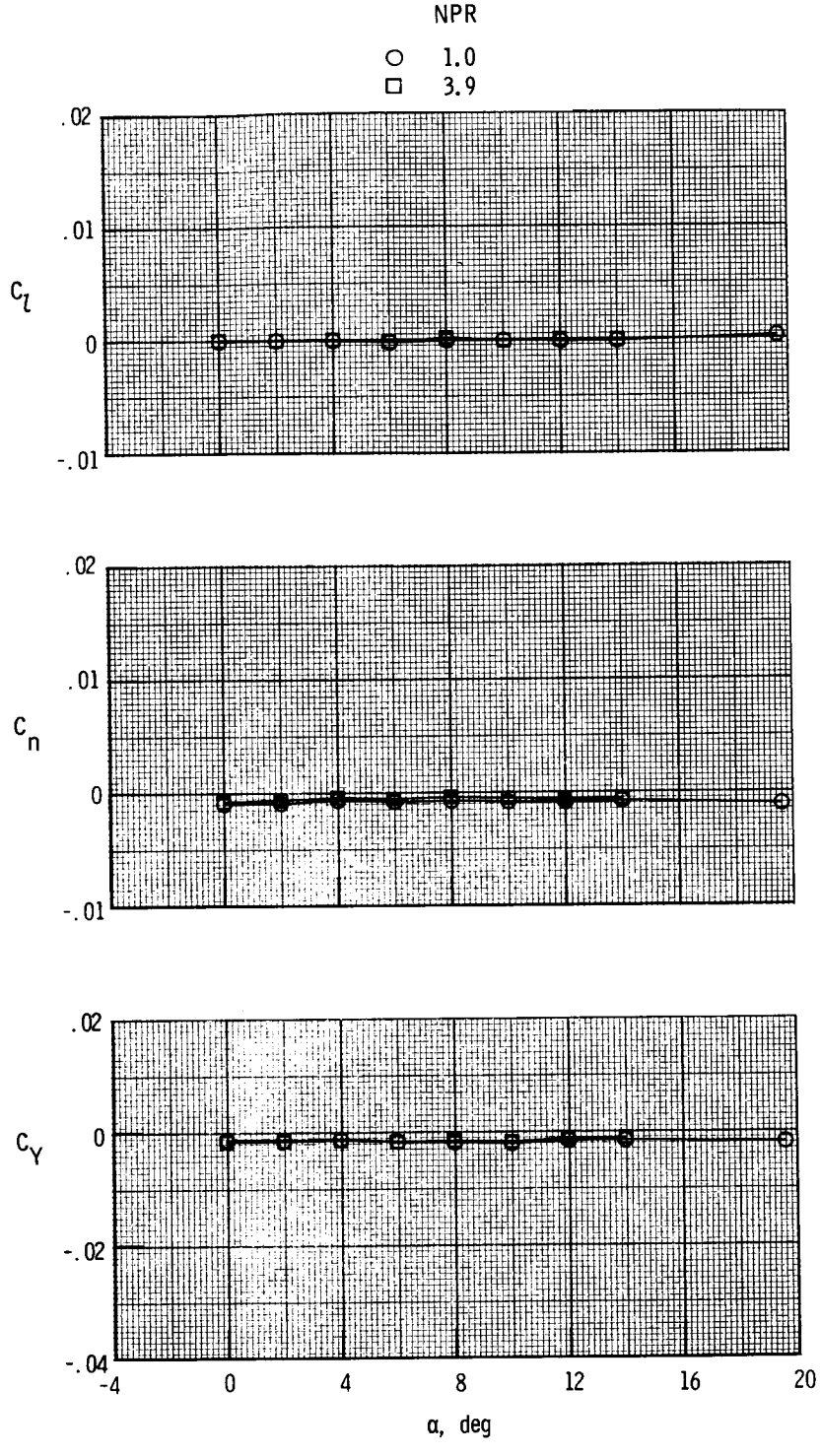

(c) $M = 0.87$.

Figure 52. Continued.

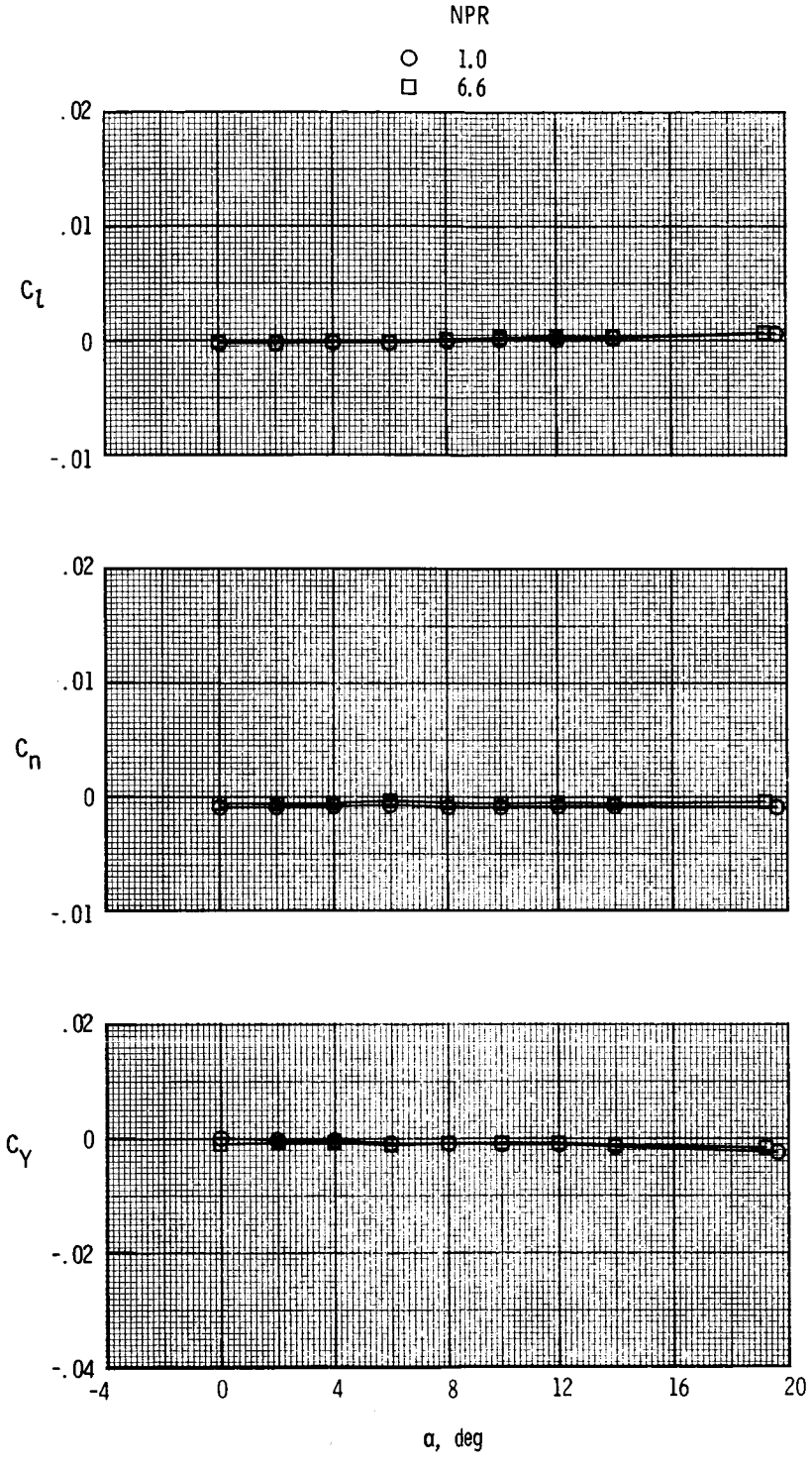

(d) $M = 1.20$.

Figure 52. Concluded.

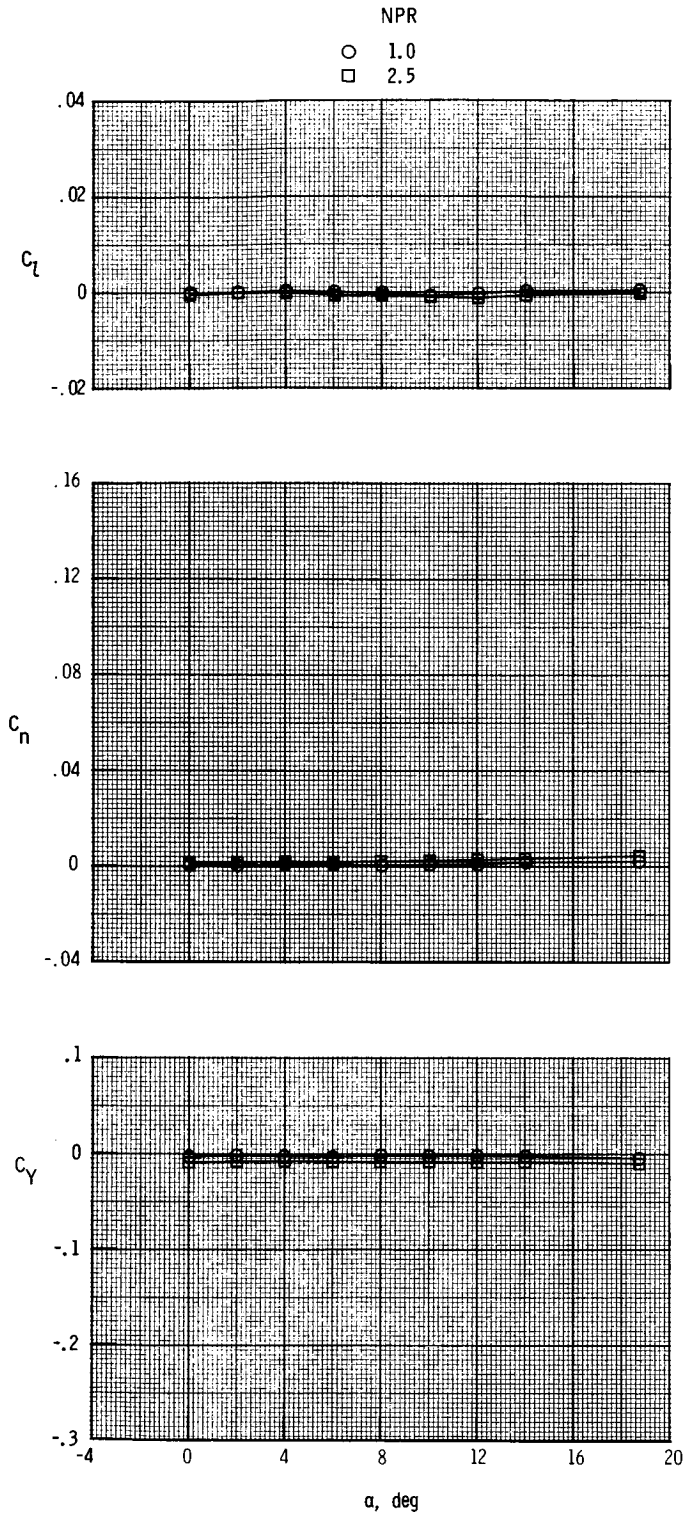

(a) $M = 0.20$.

Figure 53. Thrust-removed lateral aerodynamic characteristics for $\delta_{v,p} = 15°$ and $\delta_{v,y} = -10°$.

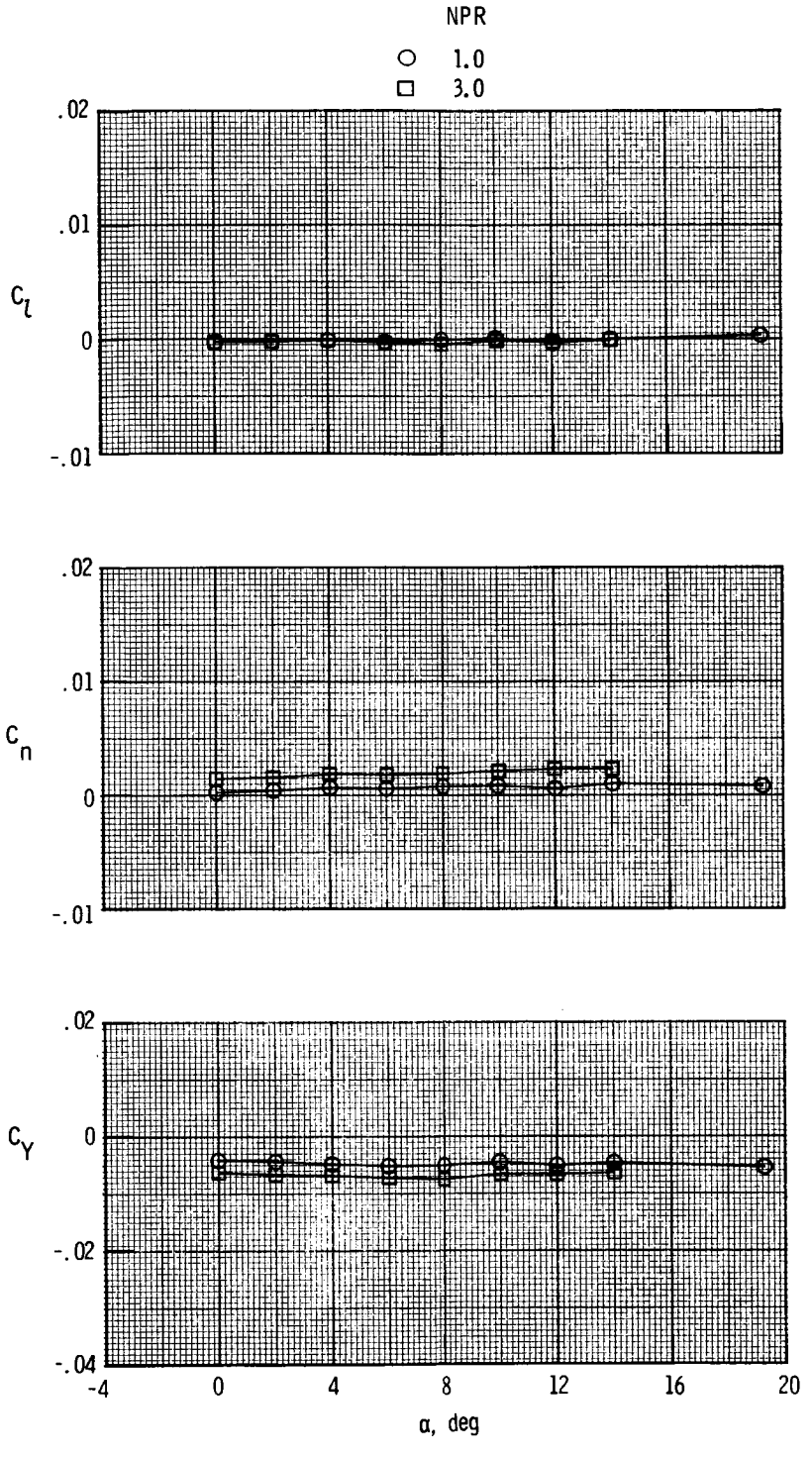

(b) $M = 0.60$.

Figure 53. Continued.

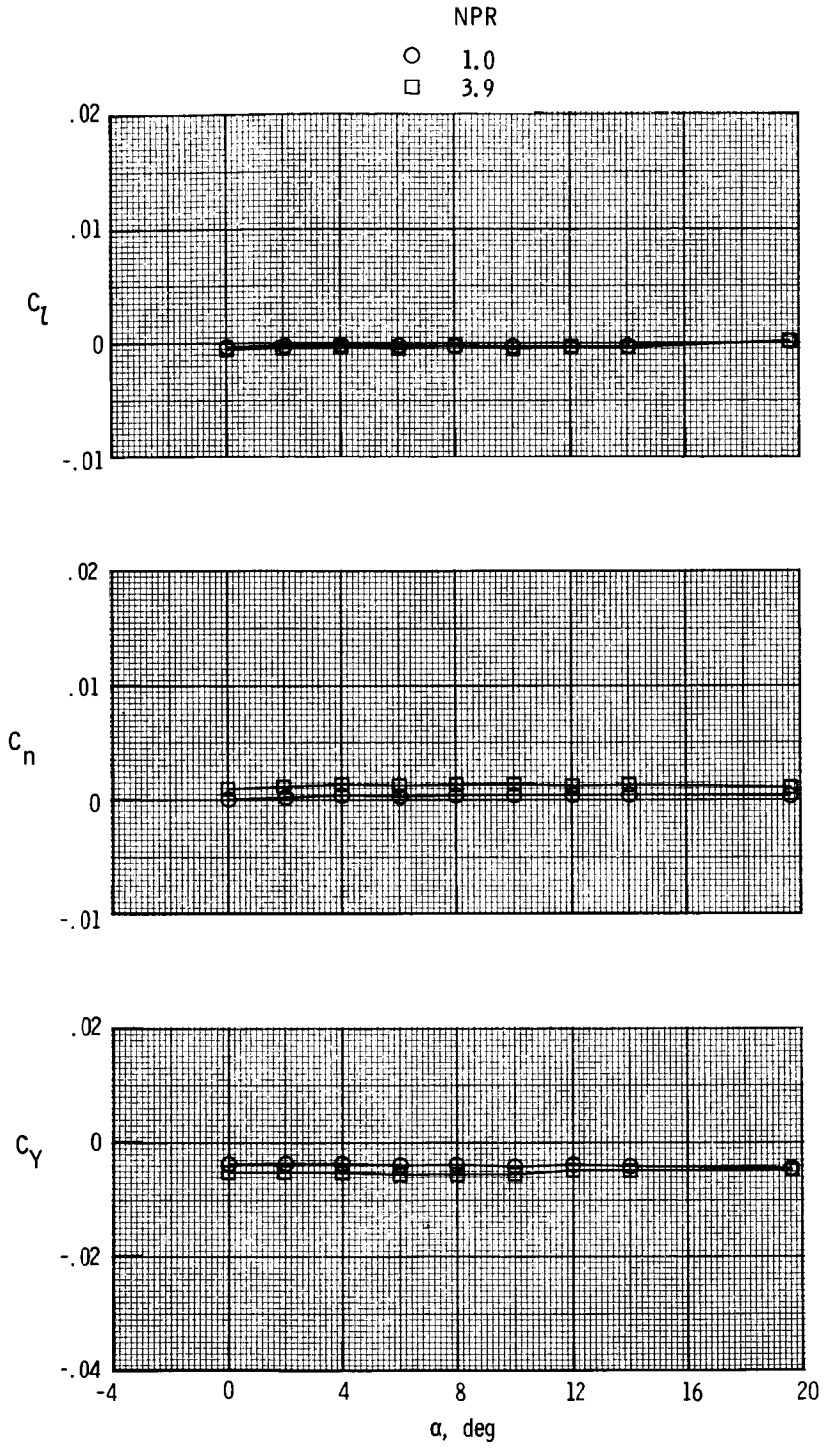

(c) $M = 0.87$.

Figure 53. Continued.

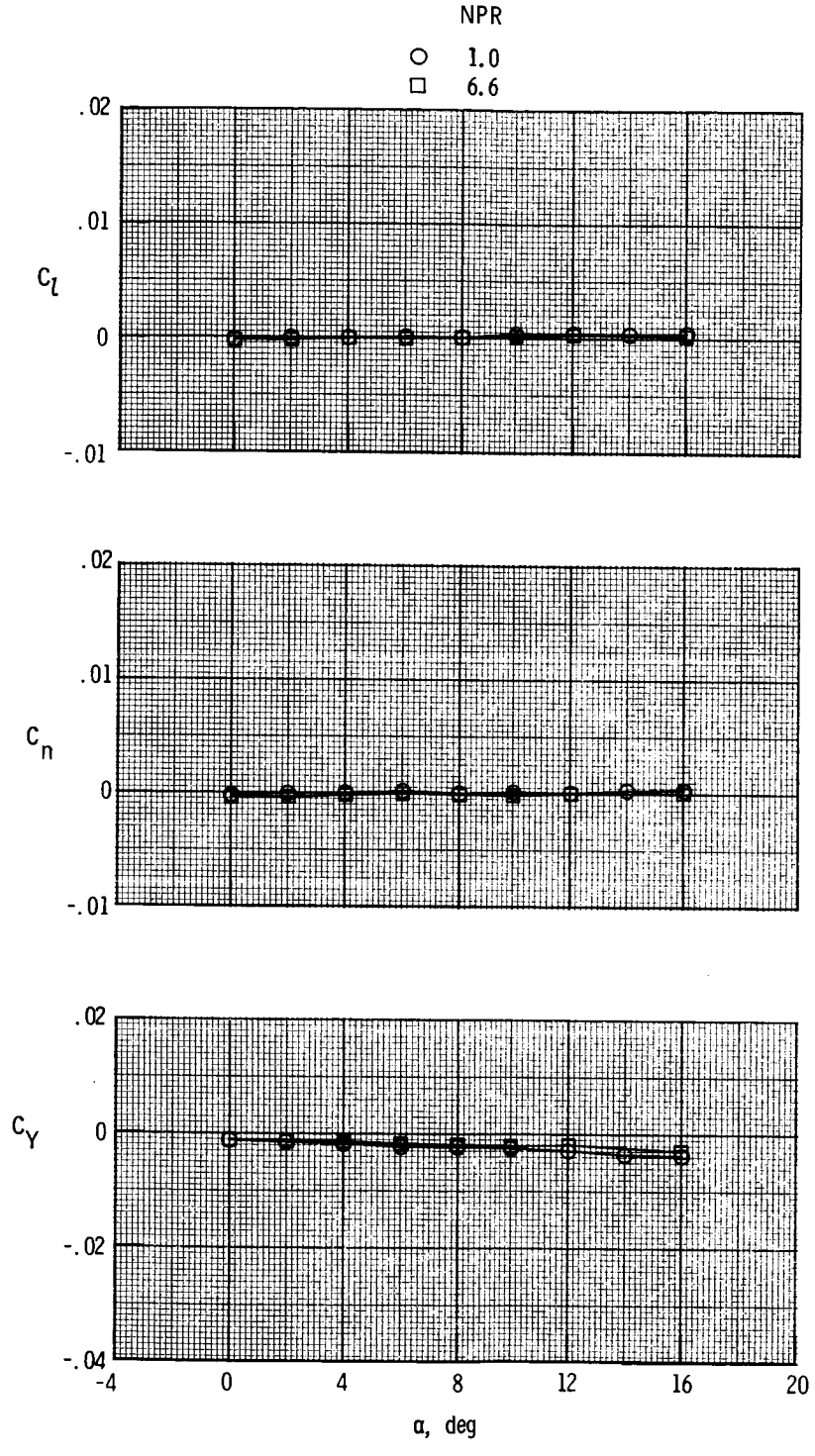

(d) $M = 1.20$.

Figure 53. Concluded.

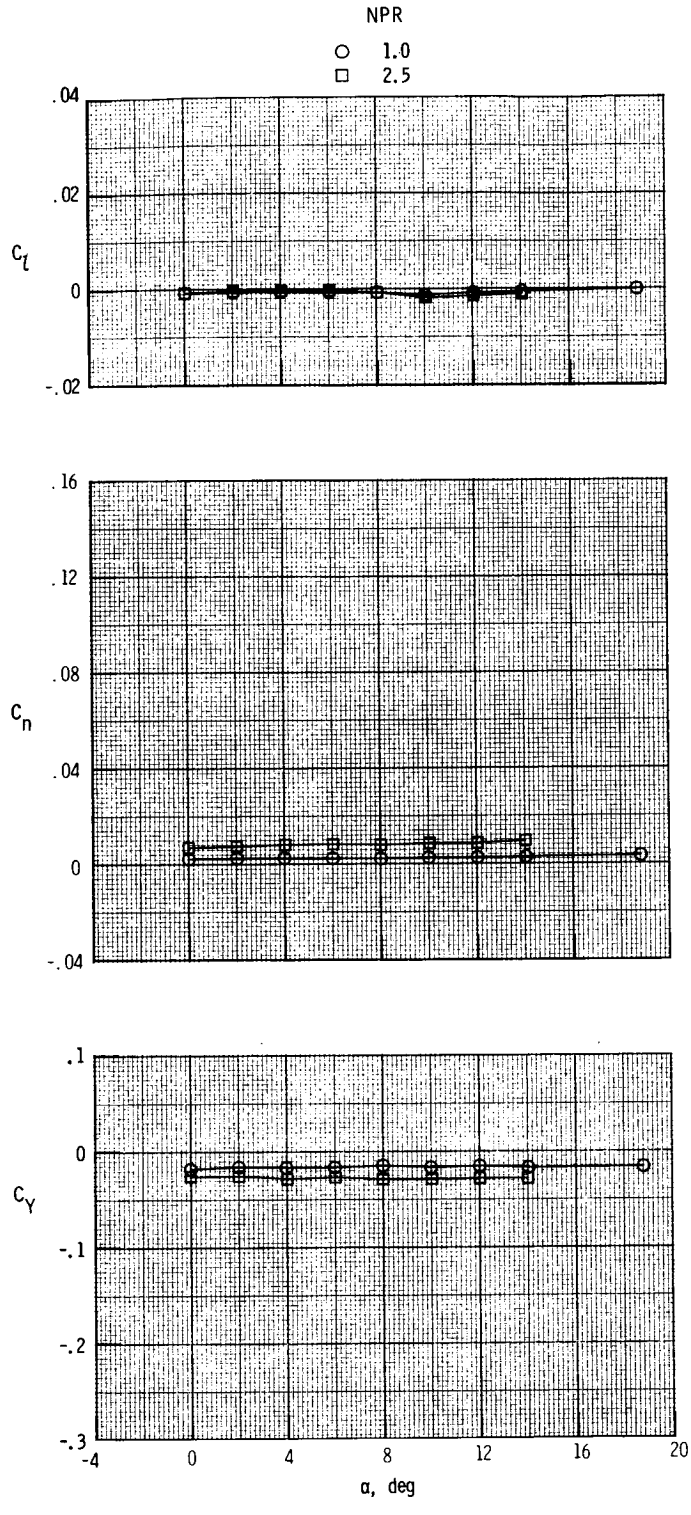

(a) $M = 0.20$.

Figure 54. Thrust-removed lateral aerodynamic characteristics for $\delta_{v,p} = 15°$ and $\delta_{v,y} = -20°$.

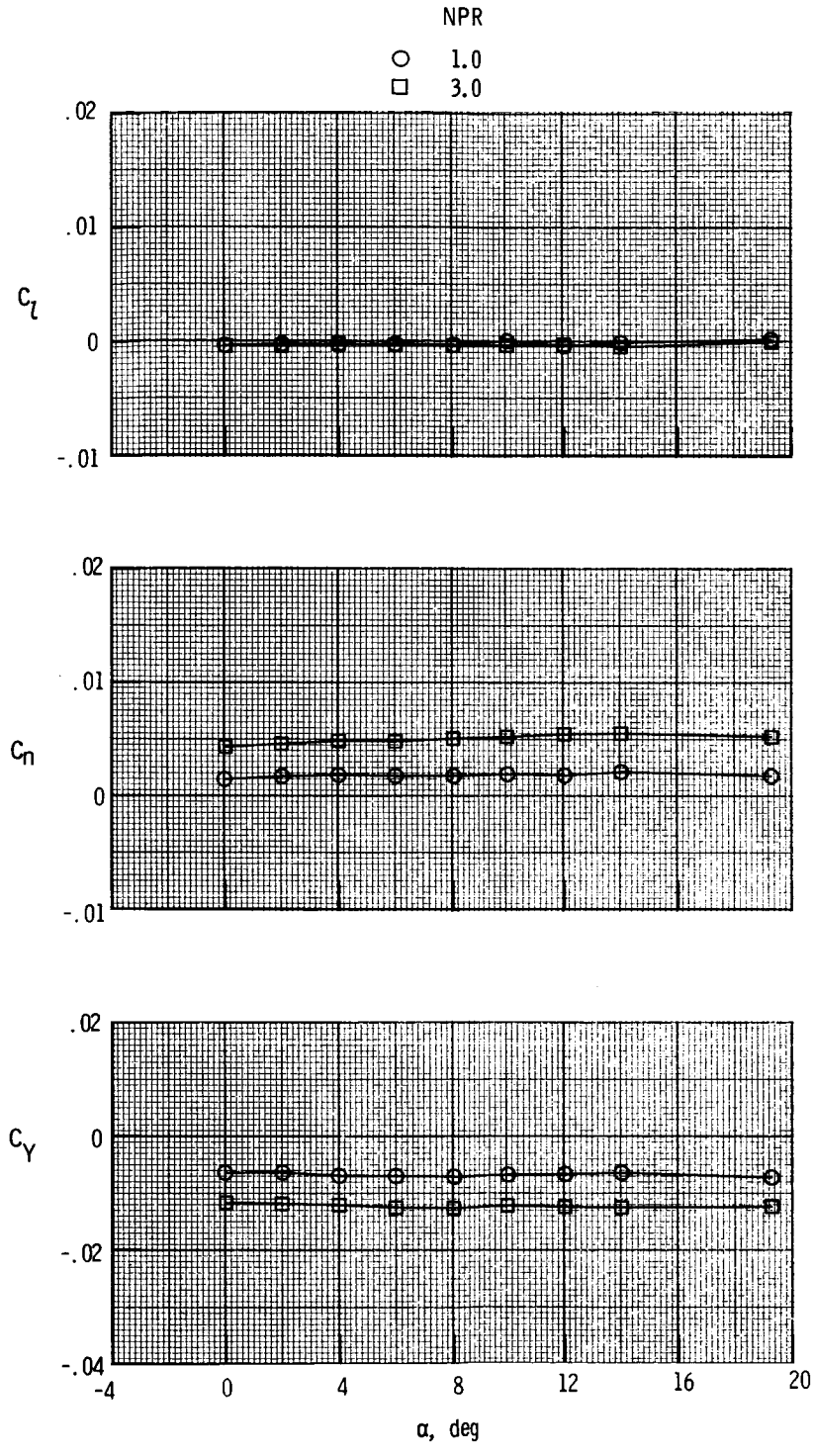

(b) $M = 0.60$.

Figure 54. Continued.

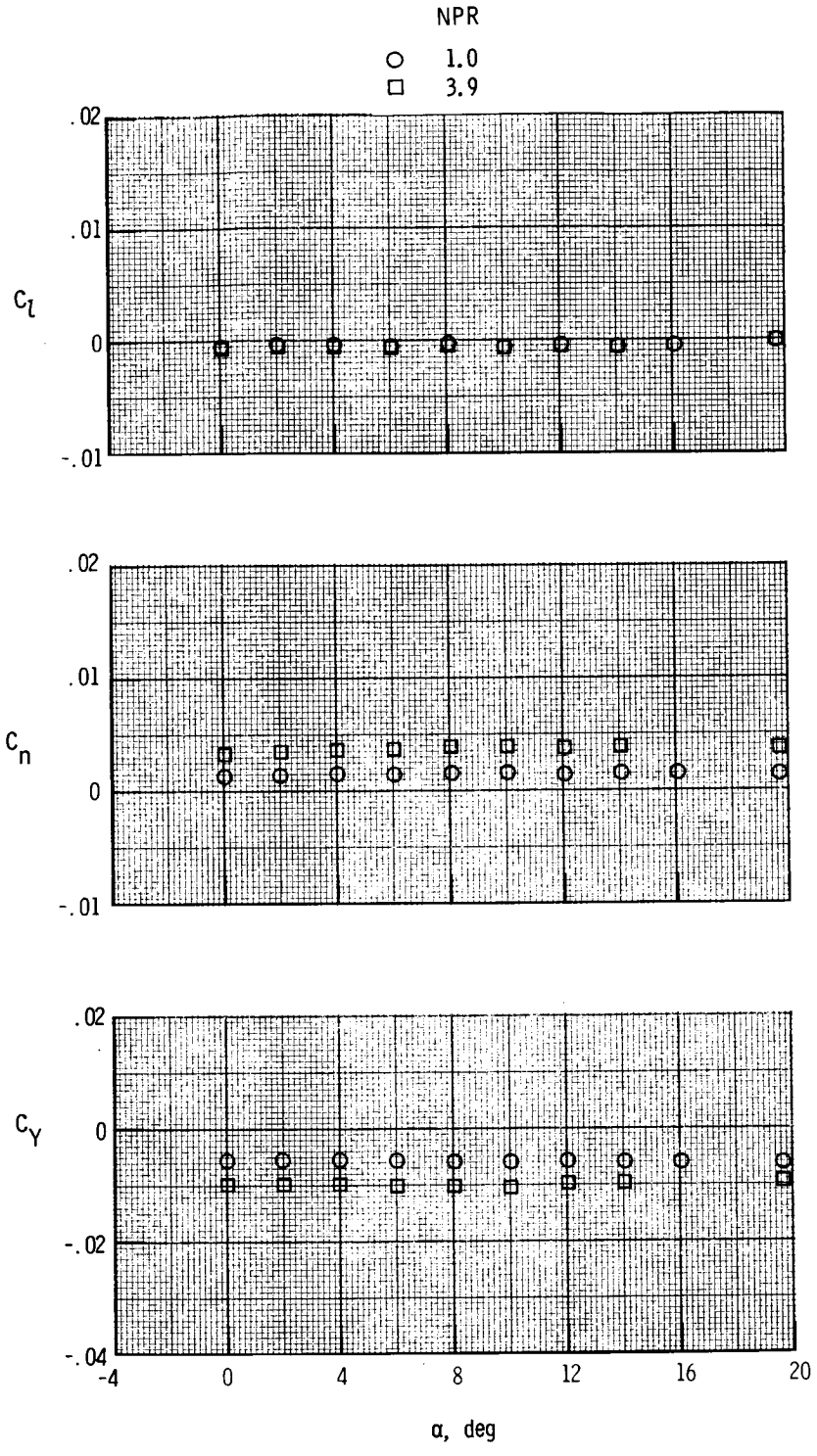

(c) $M = 0.87$.

Figure 54. Continued.

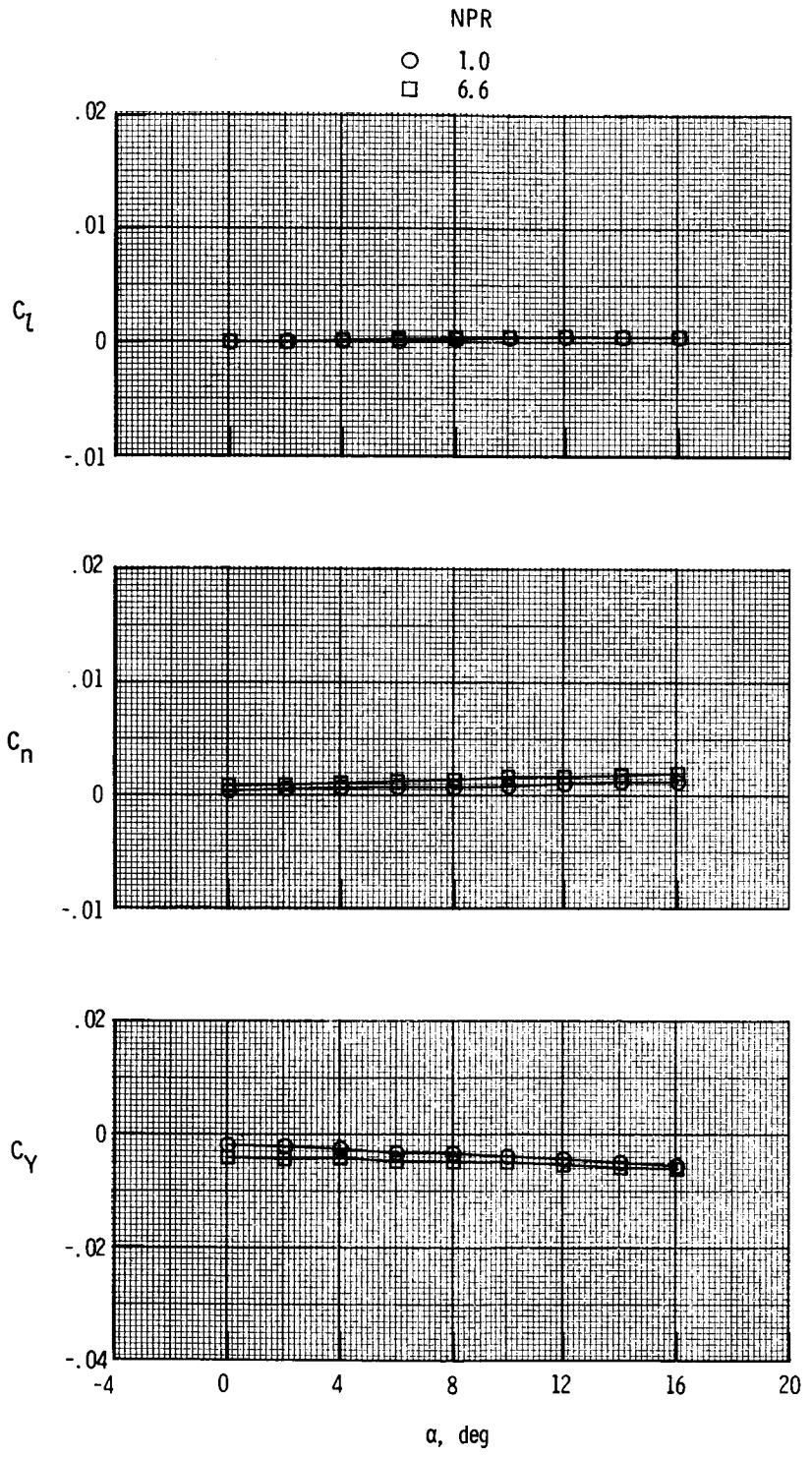

(d) $M = 1.20$.

Figure 54. Concluded.

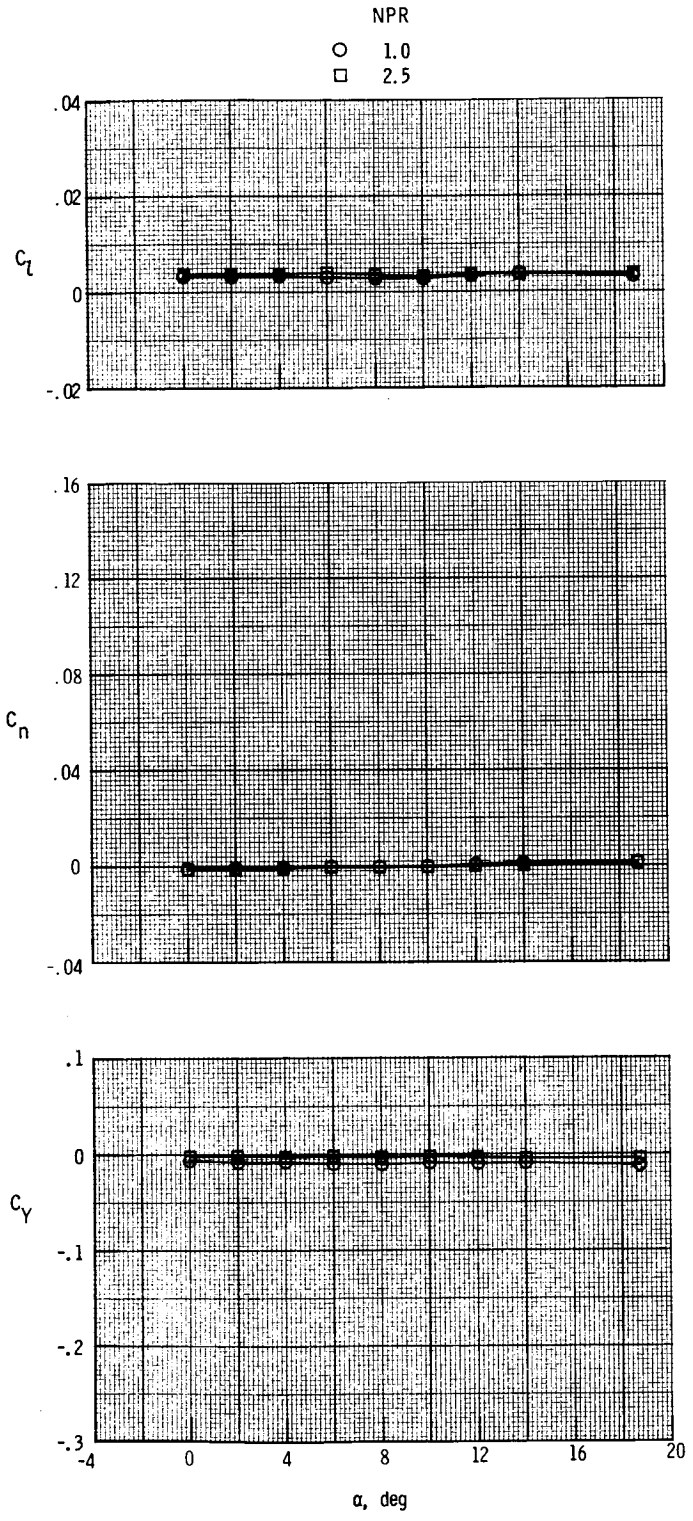

(a) $M = 0.20$.

Figure 55. Thrust-removed lateral aerodynamic characteristics for $\delta_{v,p,\text{left}} = 15°$, $\delta_{v,p,\text{right}} = 0°$, and $\delta_{v,y} = 0°$.

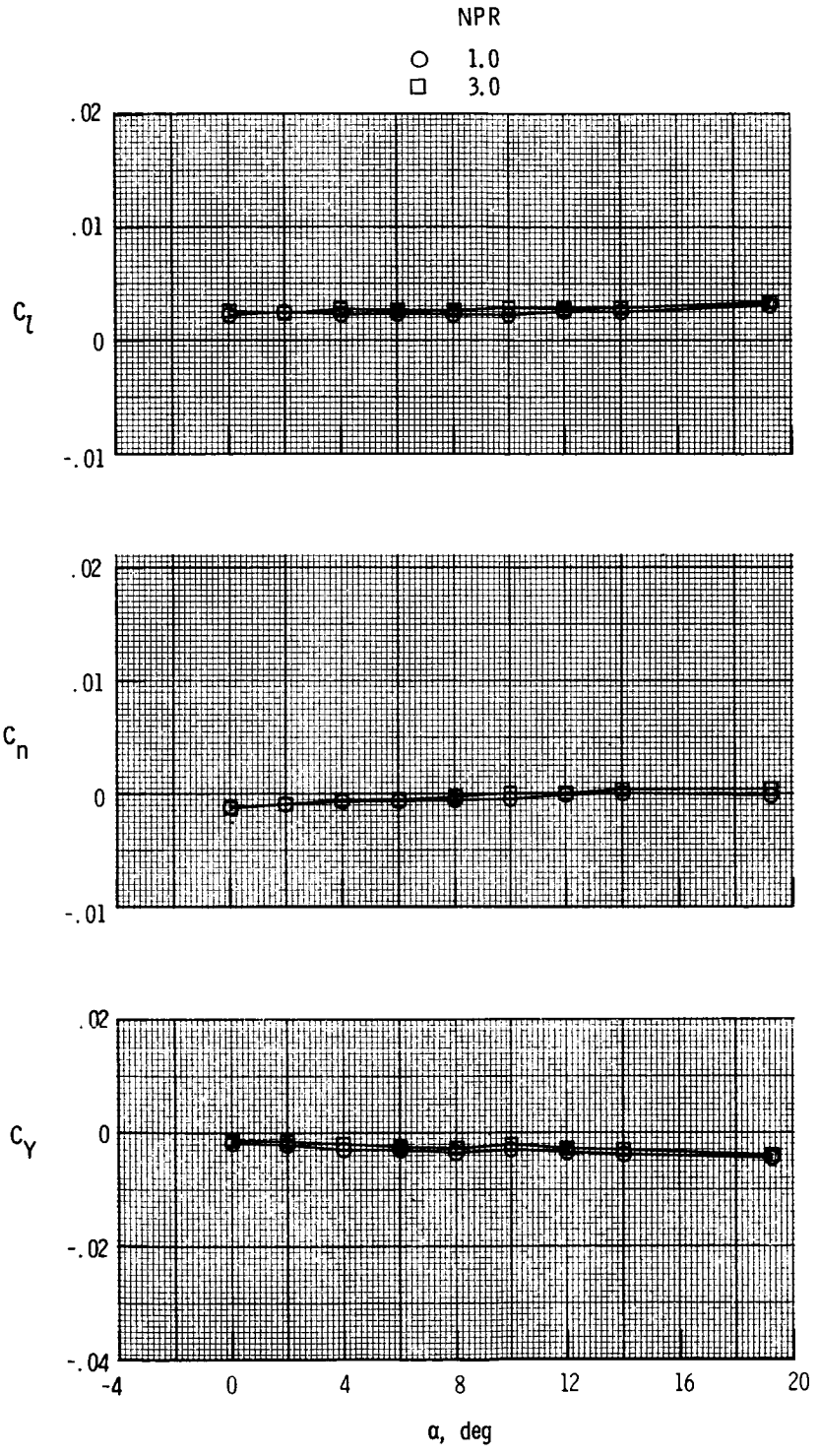

(b) $M = 0.60$.

Figure 55. Continued.

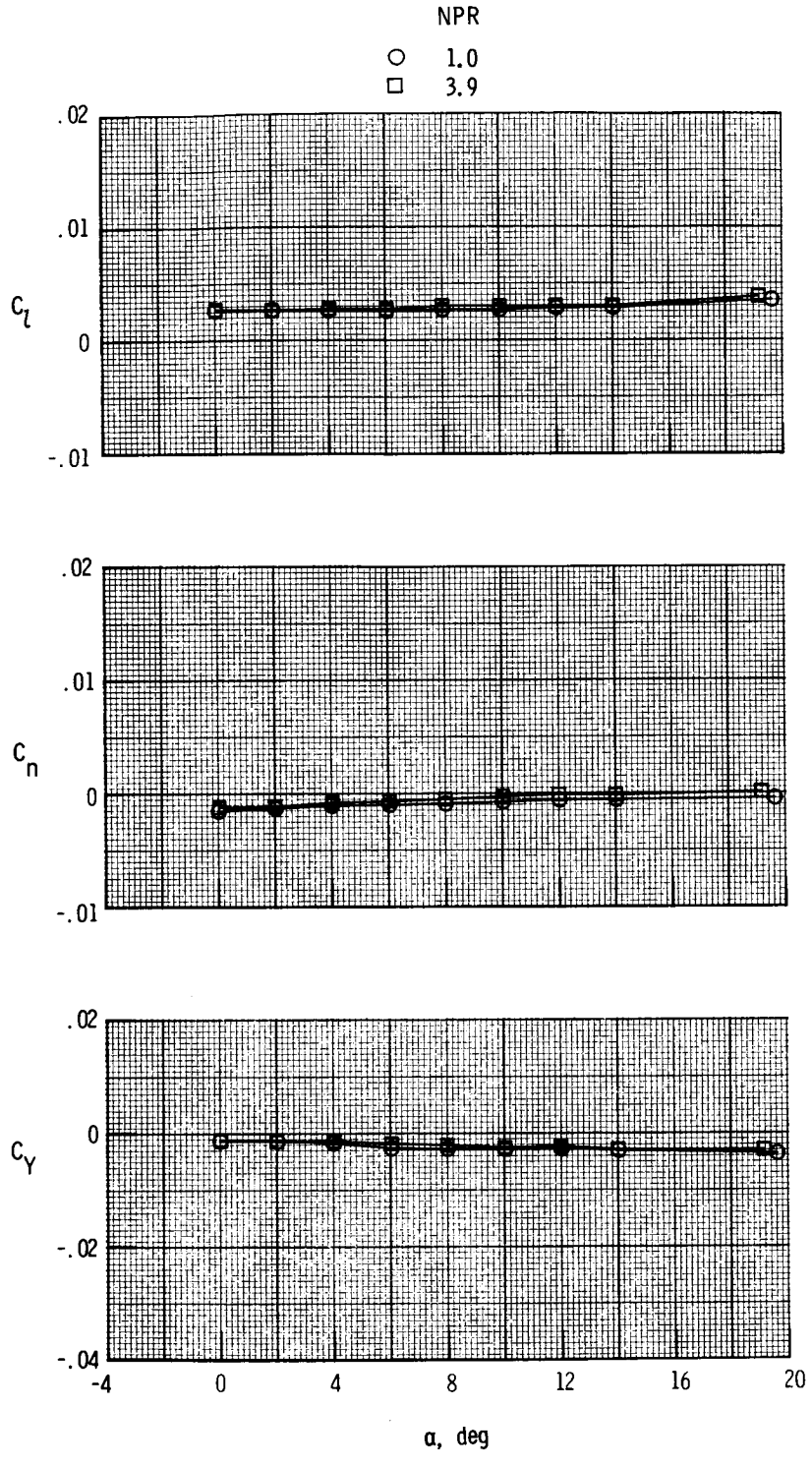

(c) $M = 0.87$.

Figure 55. Continued.

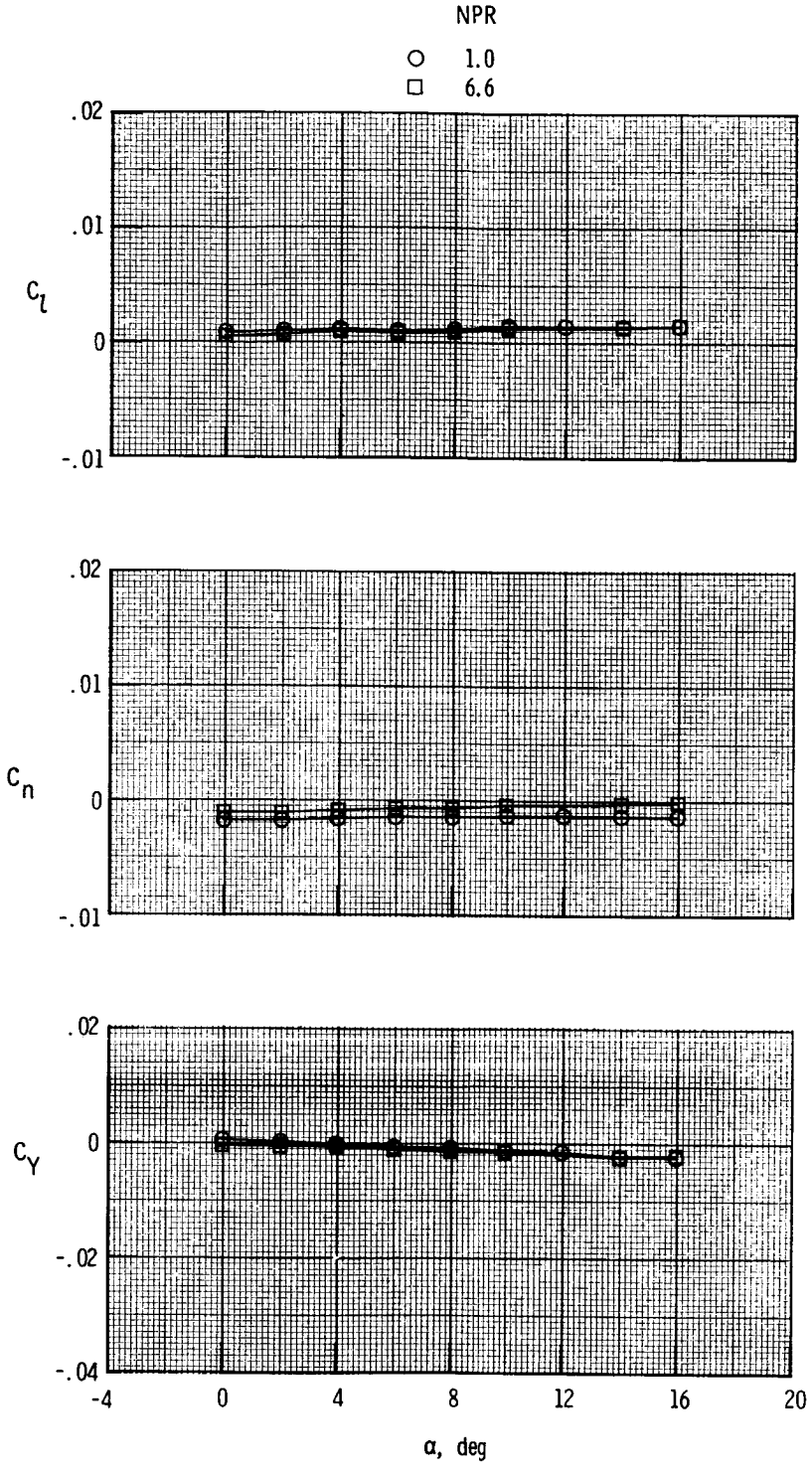

(d) $M = 1.20$.

Figure 55. Continued.

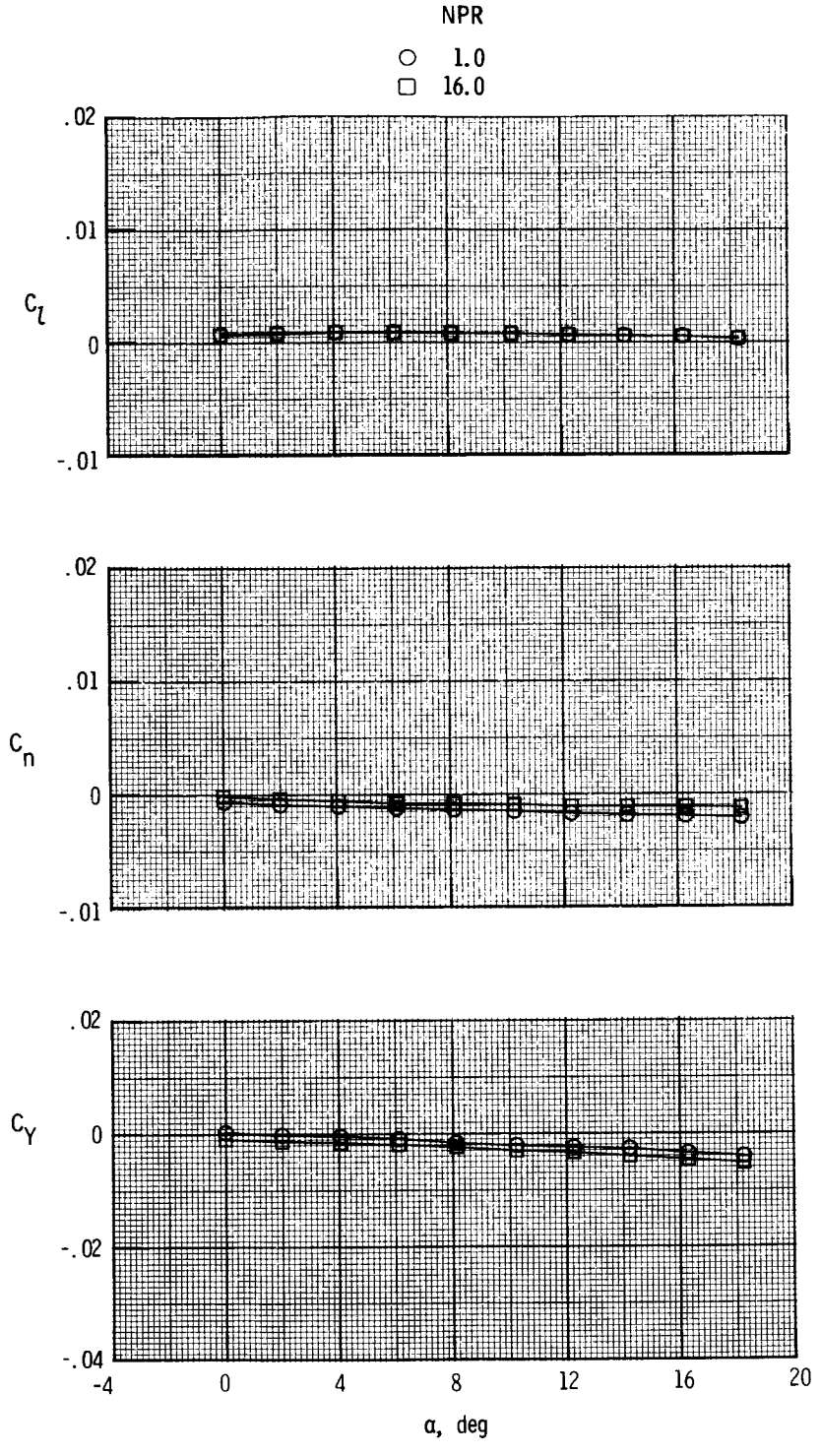

(e) $M = 2.00$.

Figure 55. Continued.

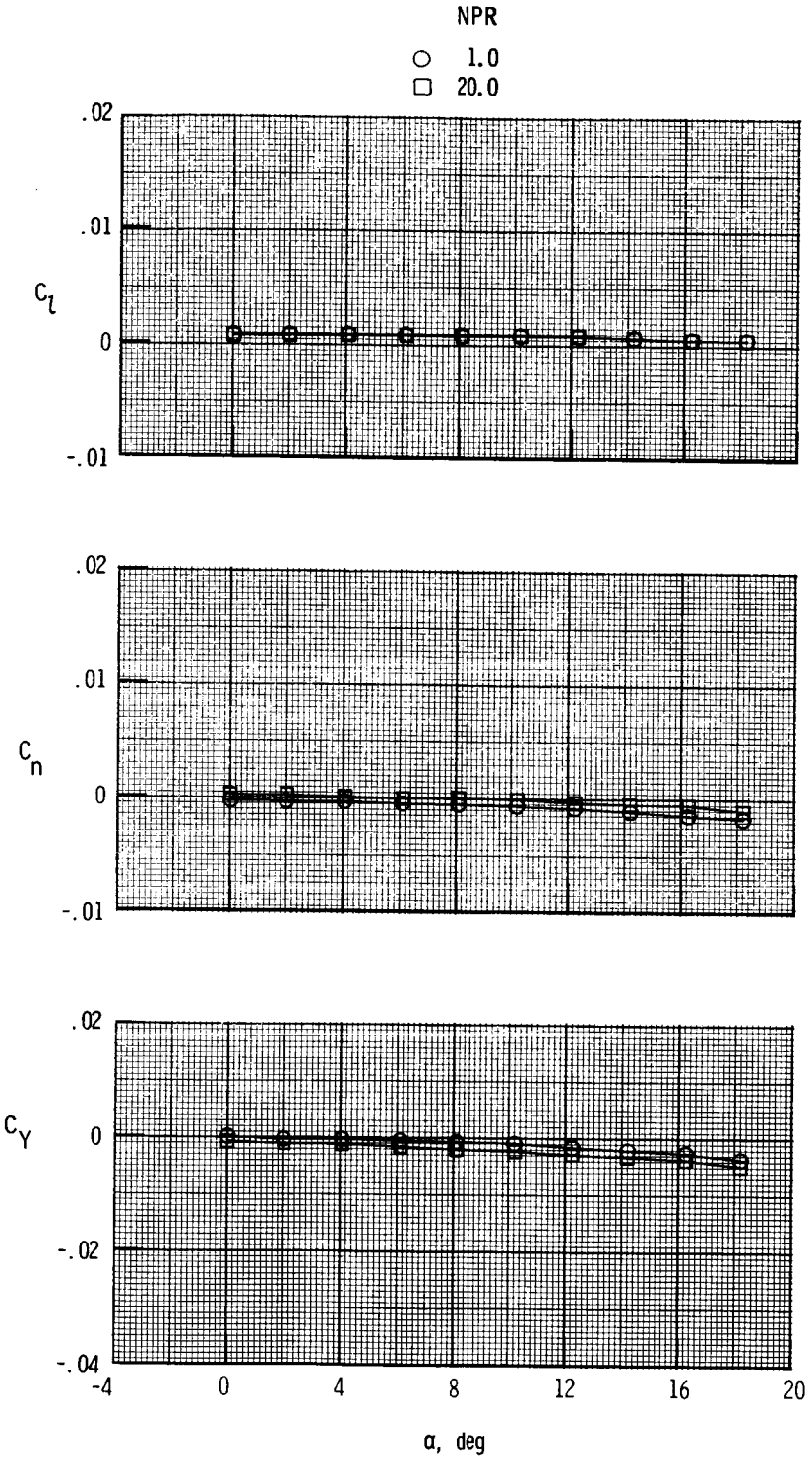

(f) $M = 2.17$.

Figure 55. Continued.

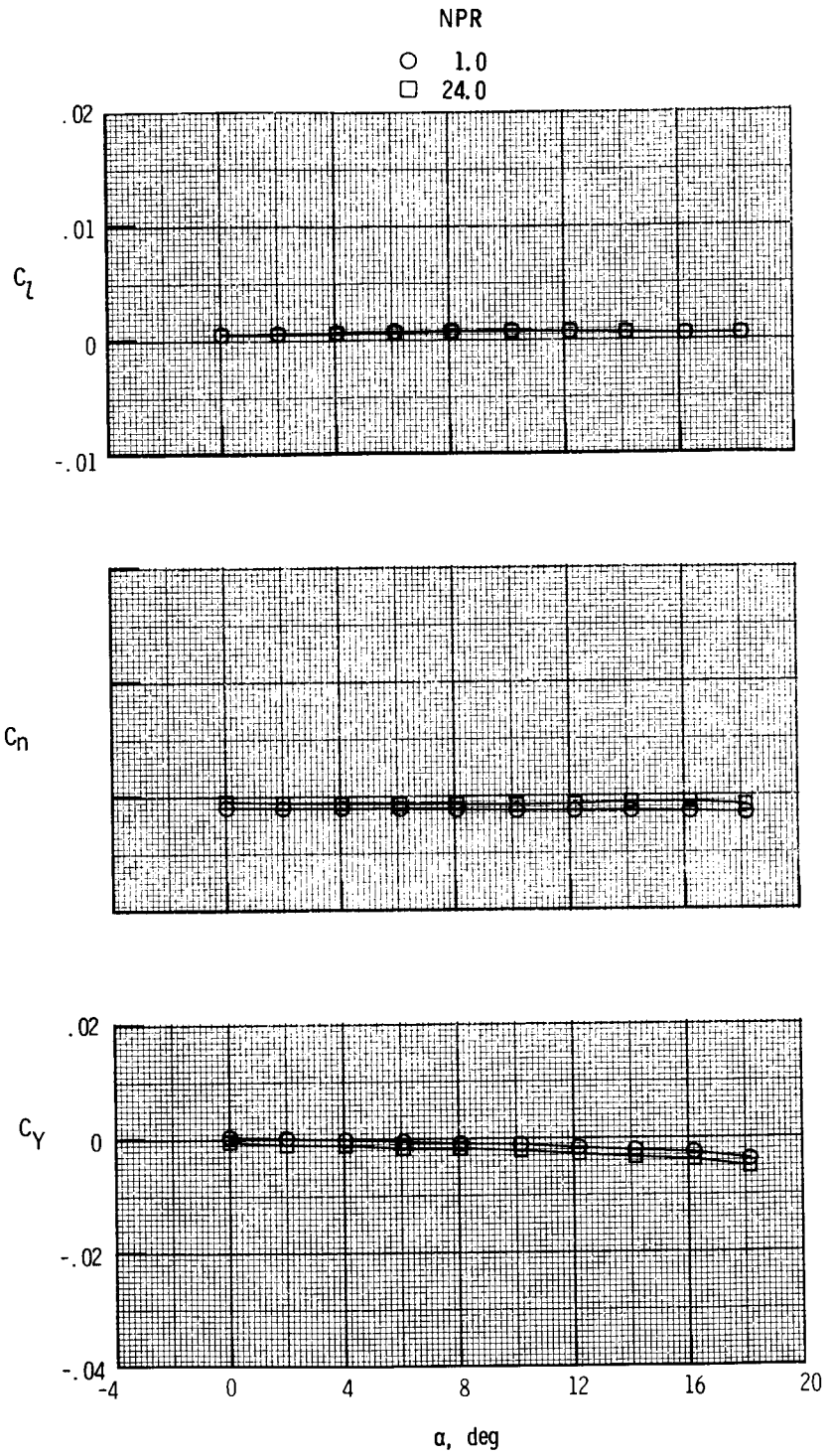

(g) $M = 2.47$.

Figure 55. Concluded.

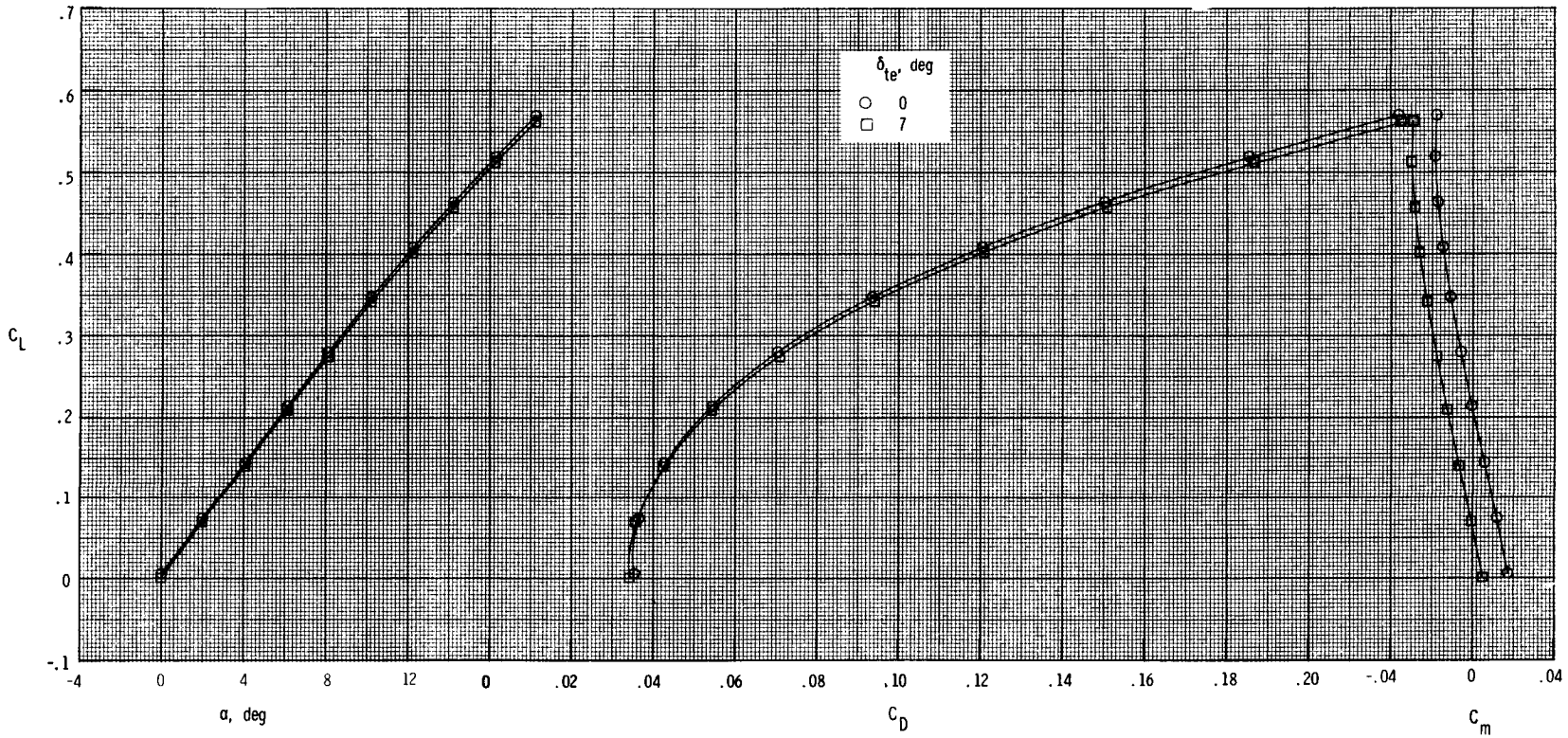

(a) $M = 2.00$.

Figure 56. Effect of wing trailing-edge flap deflection on longitudinal aerodynamic characteristics for $\delta_{v,p} = 0°$, $\delta_{v,y} = 0°$, and NPR = 1.0.

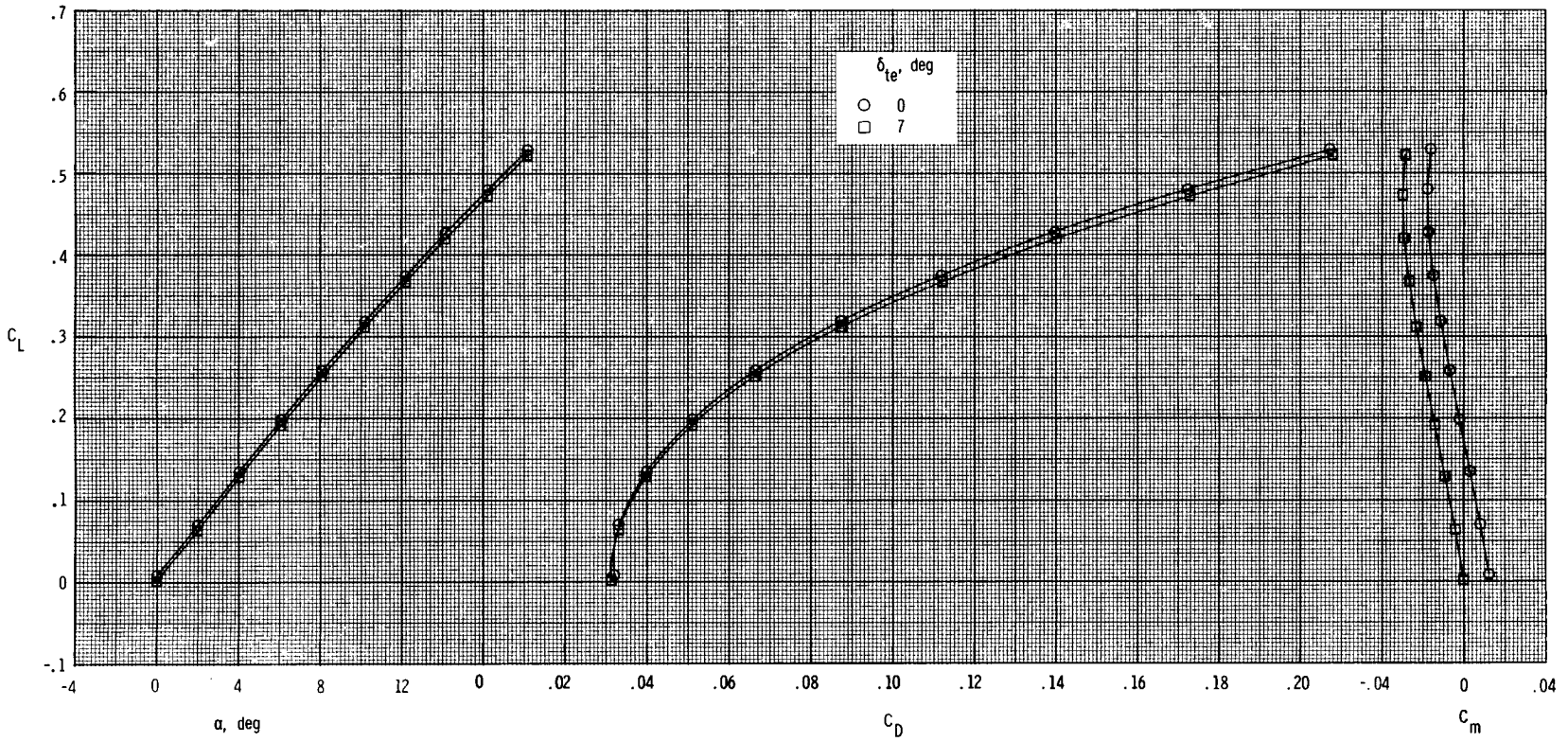

(b) $M = 2.17$.

Figure 56. Continued.

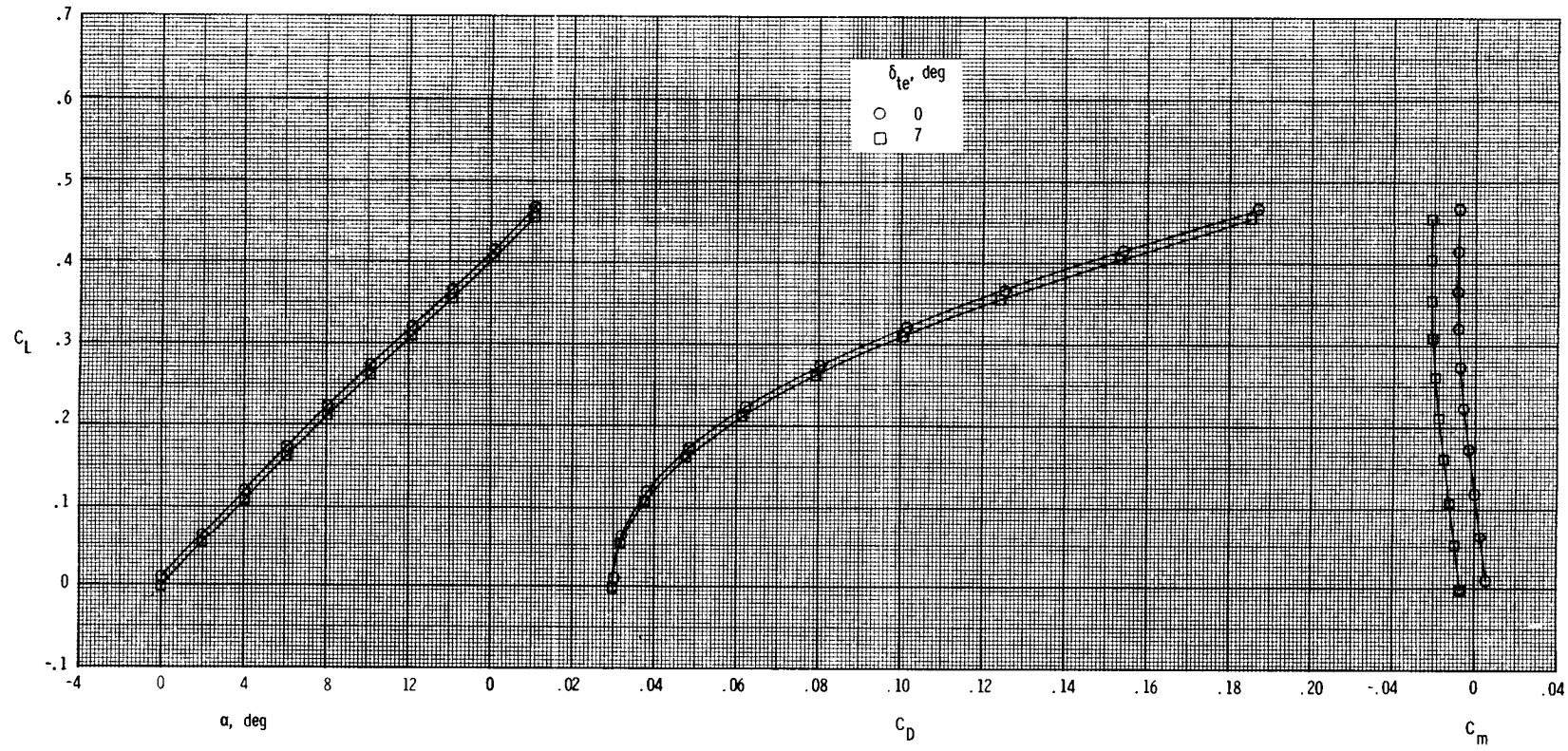

(c) $M = 2.47$.

Figure 56. Concluded.

NASA
National Aeronautics and Space Administration

Report Documentation Page

1. Report No.	2. Government Accession No.	3. Recipient's Catalog No.
NASA TP-2712		

4. Title and Subtitle	5. Report Date
Multiaxis Control Power From Thrust Vectoring for a Supersonic Fighter Aircraft Model at Mach 0.20 to 2.47	July 1987
	6. Performing Organization Code
7. Author(s)	8. Performing Organization Report No.
Francis J. Capone and E. Ann Bare	L-16213
9. Performing Organization Name and Address	10. Work Unit No.
NASA Langley Research Center Hampton, VA 23665-5225	505-62-91-01
	11. Contract or Grant No.
12. Sponsoring Agency Name and Address	13. Type of Report and Period Covered
National Aeronautics and Space Administration Washington, DC 20546-0001	Technical Paper
	14. Sponsoring Agency Code

15. Supplementary Notes

16. Abstract

The aeropropulsive characteristics of an advanced twin-engine fighter aircraft designed for supersonic cruise have been studied in the Langley 16-Foot Transonic Tunnel and the Lewis 10- by 10-Foot Supersonic Tunnel. The objective of this investigation was to determine multiaxis control-power characteristics from thrust vectoring. A two-dimensional convergent-divergent nozzle was designed to provide geometric yaw vector angles of 0°, −10°, and −20° combined with geometric pitch vector angles of 0° and 15°. Yaw thrust vectoring was provided by yaw flaps located in the nozzle sidewalls. Roll control was obtained from differential pitch vectoring. This investigation was conducted at Mach numbers from 0.20 to 2.47. Angle of attack was varied from 0° to about 19°, and nozzle pressure ratio was varied from about 1 (jet off) to 28, depending on Mach number. Increments in force or moment coefficient that result from pitch or yaw thrust vectoring remain essentially constant over the entire angle-of-attack range for all Mach numbers tested. There was no effect of pitch vectoring on the lateral aerodynamic forces and moments and only very small effects of yaw vectoring on the longitudinal aerodynamic forces and moments. This result indicates little cross-coupling of control forces and moments for combined pitch-yaw vectoring.

17. Key Words (Suggested by Authors(s))	18. Distribution Statement
Longitudinal control power Directional control power Thrust vectoring Fighter aircraft Supersonic cruise	Unclassified—Unlimited Subject Category 02

19. Security Classif.(of this report)	20. Security Classif.(of this page)	21. No. of Pages	22. Price
Unclassified	Unclassified	262	A12

NASA FORM 1626 OCT 86

NASA-Langley, 1987

For sale by the National Technical Information Service, Springfield, Virginia 22161-2171